Mathematical modelling of macrophage functioning in inflammatory bowel disease



Joanneke E. Jansen
New College
University of Oxford

A thesis submitted in partial fulfilment of the requirements for
Doctor of Philosophy

Michaelmas 2020

Abstract

Macrophages play a central role in host defence and the orchestration of the immune response. Macrophage functioning defects contribute to the development of inflammatory bowel disease (IBD), in particular Crohn's disease. Mechanistic understanding of IBD is needed to improve clinical care. We combined mathematical modelling with existing and novel experimental data to drive insight in the role of macrophages in IBD.

We developed a method to extract a minimal, weighted network from cytokine interaction data using ordinary differential equations and the Akaike information criterion. By applying our method to an existing PBMC flow cytometry dataset, we extracted a network of the regulation of IL-23, a key cytokine in IBD. Our findings suggest that IL-1 is an important regulator of cytokine responses and a promising therapeutic target for IBD patient subgroups.

Genetic studies in IBD suggest that that the hyper-inflammatory phenotype in subgroups of Crohn's disease patients could be driven by a degree of immunodeficiency causing defective antibacterial activity and subsequent inflammation. We studied this immunodeficiency component using a combination of mathematical modelling and killing and cytokine concentration assays. Our framework, complemented with literature data, suggests that, in the presence of an impairment in cytokine production capability due to genetic defects in the NOD2 pathway, elevated cytokine levels could be solely driven by an increased bacterial load during infection.

We constructed a bacterial-load structured model to study what factors drive granuloma formation and verified our model against an existing agent-based model. We parametrised our model to represent an *in vitro* granuloma model and found that macrophage fusion, implemented as non-local source and sink terms in our model, does not play a large role in this context.

In summary, we combined mathematical modelling with experimental data to drive insight in macrophage functioning in IBD, while focussing on cytokine signalling, anti-microbial activity, and granuloma formation.

Acknowledgements

First of all, I would like to thank my supervisors. Eamonn, Mark, and Holm, this thesis would not have been here without you. Thank you for your ongoing support until the very end. Eamonn, thank you for trusting me to find my own direction, while always being there for help and criticism. Mark, thank you for guiding me through the world of immunology from the very start, and for always reminding me of the bigger picture. Holm, your enthusiasm for new ideas is inspiring. Thank you for allowing me to make this work truly interdisciplinary and welcoming me to your lab. Jon and Antoine, thank you for your guidance.

Special thanks also to Sumeet, for the many hours you spent teaching and helping me during my time in the lab. Thank you Athena and Dominik, for letting me include your data in this thesis. Thanks to Maxi, Róisín, Duncan, and Simon, my peers from office S4.16. Thanks to all other group members based both up, and down the hill. Thank you for learning with, and from you, but also for making daily life at the office so enjoyable. The WCMBeers and TGU tea breaks might have come to an early end this year, but I have no doubts they will return.

Thanks to my parents, sister, and brother, for your ongoing love and support. Spending so much more time with you over the past year than anticipated was one of the few positive notes of the pandemic.

When I finally got back to Oxford, in October 2020, it did feel like returning home. I had missed, and will miss this stimulating, academic environment. Thanks to my wonderful house mates at Huize Henley, the Cave Girls, and Princes Street, thanks to my friends and peers from the New College MCR, the MSc in MMSC, Vincent's Club, the cycling club (OUCC), and both boat clubs (NCBC and OUWBC), and thanks to all others who made my time at Oxford unforgettable.

COVID-19 statement

During the Coronavirus disease 2019 (COVID-19) pandemic, my experimental work, along with those of colleagues all over the world, was affected. Various experiments that would have been able to be performed in the Translational Gastroenterology Unit by me or others in normal times might have been part of this thesis. I was for instance not able to obtain additional patient blood samples to further validate the bacterial handling driven mechanism of cytokine hyper-production in Chapter 3, or to supplement the model on granuloma formation with *in vitro* data in Chapter 4. The Translational Gastroenterology Unit, where the laboratory is based, was closed from March 2020 until October 2020.

Contents

List of acronyms v

1 Introduction **1**

1.1 Biological background 1

1.1.1 Inflammatory bowel disease 1

1.1.1.1 Cytokine signalling 2

1.1.1.2 Genetic markers 3

1.1.2 Monocyte-derived macrophages 9

1.1.2.1 The role of macrophages in IBD 9

1.1.2.2 Macrophage development 10

1.1.2.3 Macrophage differentiation 13

1.1.2.4 Receptor systems 14

1.1.2.5 Anti-microbial activity 14

1.2 Mathematical modelling 18

1.2.1 Examples of model driven-experimentation 18

1.2.1.1 Modelling macrophage-fibroblast interactions 18

1.2.1.2 Modelling the NF-κB signalling pathway 20

1.2.2 Modelling cytokine interactions 23

1.2.2.1 Connection with our study 24

1.2.3 Modelling host-pathogen interactions 24

1.2.3.1 Connection with our study 25

1.2.4 Modelling granuloma formation 25

1.2.4.1 Connection with our study 26

1.3 Modelling tools and methods 26

1.3.1 Cautionary tales. The possible failure modes of mechanistic modelling 26
1.3.2 Parameter estimation 28
1.3.3 Parameter identifiability 31
1.3.3.1 The scaling invariance method 31
1.3.3.2 Non-observability 33
1.3.3.3 The profile likelihood approach 34
1.3.4 Parameter sensitivity analysis 40
1.3.5 Model selection 42
1.3.6 Differential equations 43
1.3.7 Alternative modelling techniques 47
1.4 Thesis aims 49
1.4.1 Chapter 2: cytokine interaction networks 50
1.4.2 Chapter 3: bacterial handling 51
1.4.3 Chapter 4: granuloma formation 52
1.5 Thesis structure 53

2 Inference of an inflammatory cytokine interaction network 55
2.1 Introduction 55
2.2 Data 59
2.3 Model construction 62
2.4 Structural parameter identifiability 71
2.5 Model fitting 75
2.6 Model selection 84
2.6.1 Network selection algorithm 85
2.7 Extended model 93
2.8 Practical parameter identifiability 95
2.8.1 The 20-edge model 98
2.8.2 Comparison between the selected 20-edge model and the 31-edge model 101
2.9 Parameter sensitivity analysis 104
2.10 Validation 106

2.10.1 General modelling approach . . . 106
2.10.2 Four toy models . . . 117
2.10.3 Cytokine addition . . . 120
2.10.4 Coverage of the confidence intervals . . . 122
2.10.5 Validation of the optimisation strategy . . . 123
2.11 Knock-outs . . . 127
2.12 Discussion . . . 128

3 The balance between defective antibacterial activity and cytokine production impairment in driving Crohn's Disease pathogenesis 139

3.1 Introduction . . . 139
3.1.1 Aims and objectives . . . 142
3.1.2 Novelty . . . 142
3.1.3 Structure . . . 143
3.2 Methods . . . 144
3.2.1 Gentamicin protection assay . . . 145
3.2.2 Protein level analysis . . . 146
3.2.3 Viability assay . . . 146
3.2.4 Confocal microscopy . . . 146
3.2.5 Mathematical modelling . . . 147
3.3 Results . . . 147
3.3.1 Bacterial handling dynamics . . . 147
3.3.1.1 Comparison of donor dependent and independent parameter values . . . 151
3.3.2 Macrophage distributions . . . 151
3.3.3 Cytokine dynamics . . . 162
3.3.4 Further model assumptions . . . 167
3.3.5 Further model developments . . . 168
3.3.6 Macrophage viability . . . 180
3.3.7 Handling defects versus hyper-inflammation . . . 180

3.3.8 Exploration of the effects of varying the bacterial growth rate 190
3.3.9 Literature comparison 191
3.4 Discussion 200
3.4.1 Bacterial handling dynamics 203
3.4.2 Distribution of infection 204
3.4.3 Cytokine dynamics 205
3.4.4 Handling defects 207
3.4.5 Literature data 208
3.4.6 Summary and future work 209

4 A bacterial load-structured model of granuloma formation 229
4.1 Introduction 229
4.1.1 Aims, research questions, and novelty 232
4.1.2 Structure 233
4.2 Model statement 233
4.2.1 Recruitment: $R(E(t), B(t))$ 238
4.2.2 Bacterial growth: $Z(b,t)$ and $\Xi(E)$ 239
4.2.3 Apoptosis: $A(g(b,t))$ 239
4.2.4 Fusion: $F(g(b,t))$ and $F'(g(b,t))$ 239
4.2.5 Full system 241
4.2.6 Characteristics 242
4.3 System-size expansion 245
4.3.1 Background 246
4.3.2 Derivation of the bacterial-load structured model 250
4.4 Model exploration 255
4.4.1 Non-dimensionalisation 255
4.4.2 Numerical solutions 256
4.4.3 Silica beads 258
4.4.3.1 Constant recruitment 260
4.4.3.2 Non-constant recruitment 263

4.4.3.3 Fusion . . . 263
4.4.4 Pathogens . . . 267
4.4.4.1 Extracellular growth . . . 267
4.4.4.2 Intracellular growth and killing . . . 268
4.5 Model verification against an agent-based model . . . 270
4.5.1 The impact of fusion . . . 280
4.6 Differentiating between Crohn's disease and intestinal tuberculosis . . . 281
4.7 Discussion . . . 288
4.7.1 Summary and conclusions . . . 292

5 Discussion **296**

5.1 Thesis summary . . . 296
5.1.1 Introduction . . . 297
5.1.2 Correlation does not imply causation: inference of an inflammatory cytokine network . . . 297
5.1.2.1 Biological importance . . . 298
5.1.2.2 Connection to the wider systems biology field . . . 298
5.1.3 Getting it just right: the balance between immunodeficiency and hyper-inflammation . . . 299
5.1.3.1 Biological importance . . . 300
5.1.3.2 Connection to the wider systems biology field . . . 301
5.1.4 The whole is more than it parts: a bacterial load-structured model of granuloma formation . . . 302
5.1.4.1 Biological importance . . . 303
5.1.4.2 Connection to the wider systems biology field . . . 304
5.2 Future work . . . 305
5.3 Challenges of mechanistic model driven experimentation . . . 307
5.4 Perspective on mechanistic modelling . . . 308
Bibliography . . . 310

Acronyms

ABC approximate Bayesian computation. 40

ABM agent-based model. 25

AIC Akaike information criterium. 42

AIEC adherent-invasive *Escherichia coli*. 24

aIL10R anti IL10 receptor. 56

CD Crohn's disease. 1

CFU colony forming unit. 144

FDR false discovery rate. 60

GM-CSF granulocyte-macrophage colony-stimulating factor. 59

GWAS genome wide association study. 3

IBD inflammatory bowel disease. 1

IFN interferon. 3

IL interleukin. 2

IMID immune mediated inflammatory disease. 2

LAP LC3-associated phagocytosis. 14

LB lysogeny broth. 144

LC3 microtubule-associated protein 1A/1B-light chain 3. 14, 9

LPS lipopolysaccharide. 56

MCMC Markov chain Monte Carlo. 30

M-CSF macrophage colony-stimulating factor. 13

MD-IBD Mendelian disorder-associated inflammatory bowel disease. 8

MDM monocyte derived macrophage. 203

MDP muramyl dipeptide. 7

MFI mean fluorescence intensity. 60

MGC multinucleated giant cell. 16

MOI multiplicity of infection. 144

NADPH the reduced form of nicotinamide adenine dinucleotide phosphate. 14

NF-κB nuclear factor κ-light-chain-enhancer of activated B cells. 20

NK natural killer. 56

NOD2 nucleotide-binding oligomerization domain-containing protein 2. 7

OD optical density. 151

PBMC peripheral blood mononuclear cell. 56

PDE partial differential equation. 231

PI propidium iodide. 146

ROS reactive oxygen species. 14

SNP single nucleotide polomorphism. 3

Th1 type 1 helper T cel. 2

Th17 type 17 helper T cel. 2

Th2 type 2 helper T cel. 2

TLR toll-like receptor. 13

TNF-α tumour necrosis factor α. 1

Treg anti-inflammatory regulatory T cell. 2

UC ulcerative colitis. 1

XIAP X-linked inhibitor of apoptosis. 139

Chapter 1

Introduction

We will start this chapter with a literature review of the relevant biological and mathematical modelling background on the role of macrophages in inflammatory bowel disease and related chronic inflammatory diseases. We will then give an overview of the thesis aims and structure. Material for this chapter has been partly drawn from our 2019 perspective article "Combining mathematical models with experimentation to drive novel mechanistic insights into macrophage function" that was published in Frontiers of Immunology whereof I (JEJ) was the primary author [165].

1.1 Biological background

1.1.1 Inflammatory bowel disease

Inflammatory bowel disease (IBD) is characterised by severe inflammation of the gastrointestinal system. Two main types of IBD exist: Crohn's disease (CD) and ulcerative colitis (UC). IBD is a lifelong condition without a cure and that is most commonly first manifested in adolescence [21]. The disease can have a profound impact on a patient's quality of life and is associated with major health care costs [226]. IBD is a multifactorial disease, caused by a combination of genetic predisposition, environmental factors, and the resulting composition of the gut microbiome. IBD prevalence is highest in industrialised countries, with an estimated prevalence of 0.32% (CD) and 0.51% (UC) in Europe [234]. The increasing incidence of IBD over the past decade in Asia and the Middle-East, and in second-generation Asian immigrants living in Europe, points towards an important role for environmental factors, such as lifestyle and diet [14]. In contrast to classical IBD patients, a minor fraction

of IBD patients develop IBD as part of a single genetic defect with a large effect on the functioning of the gene it affects [339]. Such Mendelian-type IBD patients often display an extreme phenotype due to the gene defect. IBD can also present as an adverse event of cancer immunotherapies, such as anti-CTLA-4, necessitating (temporarily) discontinuation of the immunotherapy treatment [44]. IBD typically follows a pattern of particularly severe symptoms known as 'flare-ups', and periods of remission. The disease pattern and response to treatment varies dramatically between patients. Treatment options include immunosuppressants, biological therapy such as anti tumour necrosis factor α (TNF-α) therapy, and surgery. A better understanding of IBD onset, progression and variability is needed to improve clinical care.

1.1.1.1 Cytokine signalling

Inflammatory processes are tightly controlled by complex networks of cytokines, the messenger molecules of the immune system. Cytokine disregulation is common to the wide array of immune mediated inflammatory diseases (IMIDs) such as inflammatory bowel disease (IBD), rheumatoid arthritis, atherosclerosis, and Alzheimer's disease. Inhibition of the inflammatory cytokine TNFα has transformed the treatment of IBD and other IMIDs and has led to the development of various other anti-cytokine therapies, such as anti-p_{40}, the common subunit of interleukin (IL)-12 and IL-23 [100, 249, 338]. The success of the inhibition of a specific cytokine is disease specific. The inhibition of the cytokine IL-17A for instance aggravated CD, although it was effective in psoriasis and ankylosing spondylitis [27, 38, 156, 224]. Clinical results also vary within patient subgroups, and might be dependent on the mechanisms underlying each individual case. Understanding of disease mechanisms is therefore needed to improve clinical care.

Many cytokines are thought to play a role in IBD pathogenesis. We have highlighted the role of the key cytokines relevant in the context of this thesis in Table 1.1. We show a selection of the described interactions in Figure 1.1. We have focussed on the effects of cytokines produced by intestinal epithelial cells, macrophages, dendritic cells, and the four T cell subsets Th1, Th2, Th17, and anti-inflammatory regulatory T cells (Tregs). Th1, Th2 and Th17 are pro-inflammatory helper T cell subsets. Increased Th17 numbers and

increased Th17 secreted cytokines are observed in both CD and UC. Th1 and Th2 have been asscociated with CD and UC respectively, although this distinction is somewhat controversial [110, 161, 248]. We did not include the role of intraepithelial lymphocytes, stromal cells, myofibroblasts, eosinophils, innate lymphoid cells, mucosal-associated invariant T cells or B cells. For reviews including cytokines related to these cell types, we refer to [110, 116, 248].

We show the key pro-inflammatory macrophage produced cytokines (TNFα, IL-1β, IL-12, IL-18 and IL-23) in Figure 1.1. The function of macrophage produced IL-6 is context dependent. It can promote epithelial barrier repair, but can also stimulate pro-inflammatory T cell production and prevent T cell apoptosis [23, 160, 248]. While IL-12 drives Th1 differentiation, IL-23 and IL-1β shape the Th17 response [110]. T cell derived interferon (IFN)-γ increases macrophage activation. IL-10 is a key anti-inflammatory cytokine that regulates the inflammatory response of macrophages and other cell types.

The development of new anti-cytokine therapies for IBD and other IMIDs is an active field of research (summarized in [110]). Anti TNFα and anti IL-23p$_{40}$, the common subunit of IL-12 and IL-23, are approved drugs [110]. Promising is the blockage of IL-23p$_{19}$, the other subunit of IL-23 [100]. Anti IFNγ or anti IL-13 (associated with the Th2 response) have not yet been successful [110, 153, 287]. Targetting IL-17 in CD even aggravated disease, possibly due to its protective function in epithelial barrier repair [156, 333]. Targeting IL-6 does seem effective, but side effects due to its role in barrier functioning are a point of concern [77]. Inhibiting IL-1β and IL-18 signalling might be beneficial in subgroups of patients, as they have shown to be effective in certain Mendelian IBD cases [52, 197]. Finally, administering the anti-inflammatory cytokine IL-10 has not yet been effective [68, 110].

1.1.1.2 Genetic markers

Over 240 IBD susceptibility loci have been identified by genome wide association studies (GWAS) [16, 85, 106, 168, 202, 231]. In a GWAS, associations between genome wide genetic variants such as single nucleotide polomorphisms (SNPs), i.e. substitutions of one nucleotide by another, and traits such as IBD susceptibility are studied. Susceptibility loci identified by GWAS typically have very small effects. As gene regulatory networks are highly interconnected, complex traits can be driven by the combined effects of a large number of

Cytokine	Key producers	Function
TNFα	Th1 cells, IECs, DCs and macrophages	The pro-inflammatory cytokine TNFα has many effects, including induction of epithelial cell apoptosis and prevention of T cell death [24, 110, 274].
IL-1β	IECs, DCs, macrophages, and neutrophils	Increased IL-1β signalling can drive pathogenic Th17 responses featuring increased IFNγ, IL-17A and IL-17F production, and can downregulate Treg responses [110]. IL-1 also has a role in neutrophil recruitment and increases IL-6 production [248].
IL-23	DCs and macrophages	Increased IL-23 signalling can drive pathogenic Th17 responses featuring increased IFNγ, IL-17A and IL-17F production, and can downregulate Treg responses [110].
IL-18	IECs and macrophages	Activates the Th1 response featuring increased production of IFNγ and TNFα [116]. IL-18 has also been shown to have a disruptive effect on barrier functioning in mice [252].
IL-6	IECs, macrophages, and Th1 cells	The function of IL-6 is context dependent. It can promote epithelial barrier repair, but can also stimulate pro-inflammatory T cell production and prevent T cell apoptosis [23, 160, 248].
IL-12	DCs and macrophages	Drives Th1 differentation [66, 110, 116]. Activates the Th1 response featuring increased production of IFNγ and TNFα [116].

Table 1.1: Overview of key cytokines relevant in the context of this thesis [110, 116, 248]. Table and legend continue on next page.

Cytokine	Key producers	Function
IFNγ	Th1 and Th17 cells	IFNγ activates macrophages and induces epithelial cell death [248].
IL-17A/F	Th17 cells	The role of IL-17A and IL-17F is context dependent. They can promote barrier integrity and antimicrobial defense, but can also be pathogenic by inducing neutrophil recruitment [180, 194].
IL-13	Th2 cells	Th2 produced IL-13 can induce epithelial cell death.
IL-10	Tregs	IL-10 has a key role in tissue homeostasis by downregulating pro-inflammatory cytokine production and activating Tregs [110].
IFNα/β	dendritic cells	promote barrier integrity and Treg responses [179, 183].
IL-22	Th17 cells	Promotes barrier integrity and activates production of antimicrobial peptides [248].

Table 1.1: (Continued table). Overview of key cytokines relevant in the context of this thesis [110, 116, 248]. We did not include the role of intra-epithelial lymphocytes, stromal cells, myofibroblasts, eosinophils, innate lymphoid cells, mucosal-associated invariant T cells, or B cells. Abbreviation: Treg, regulatory T cell; Th cell, helper T cell; IEC, intestinal epithelial cell; DC, dendritic cell.

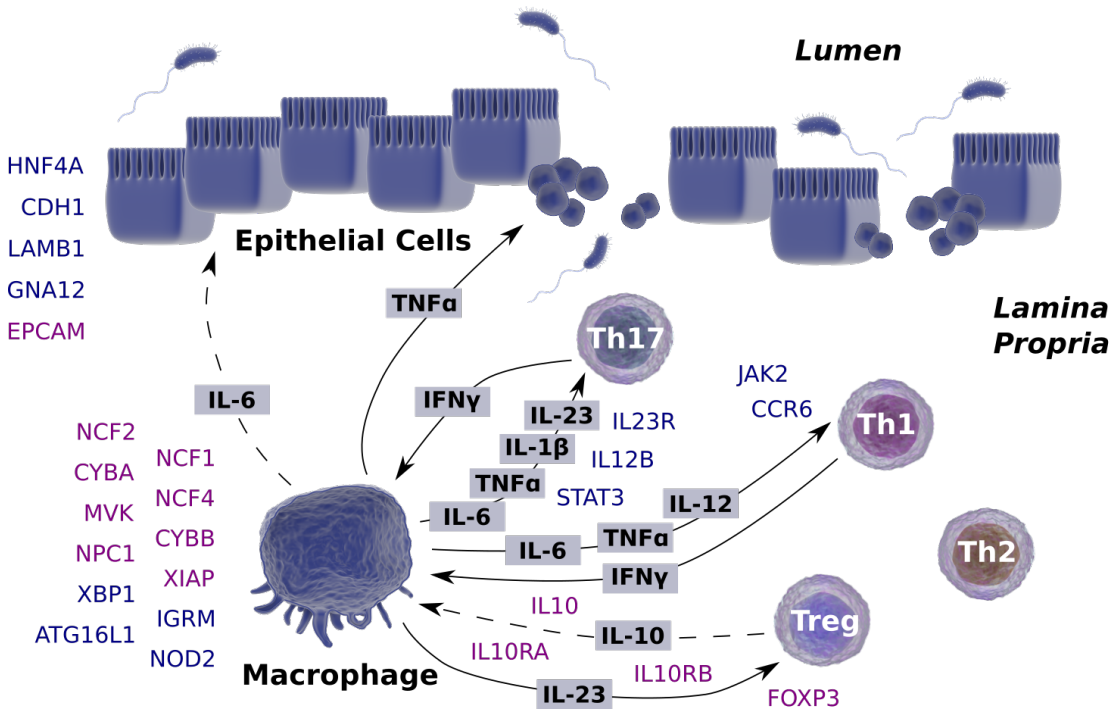


Figure 1.1: Overview of key cytokines (black), and a selection of genes associated with polygenic IBD (blue), and Mendelian IBD (pink). Solid and dashed arrows correspond to activating and regulatory cytokine effects respectively. The shown genes associated with polygenic IBD are involved in epithelial barrier functioning (HNF4A, CDH1, LAMB1, GNA12), the IL-23/IL-17 axis (IL-23R, STAT3, JAK2, IL-12b, CCR6), and innate immune responses (IRGM, ATG16L1, NOD2, XBP1). The shown Mendelian IBD genes are involved in epithelial barrier functioning (EPCAM), IL-10 signalling (IL-10, IL-10RA, IL-10RB), pathogen handling (CYBB, CYBA, NCF1, NCF2, NCF4, XIAP, NPC1), auto-inflammatory disease (MVK), and regulatory T cell activity (FOXP3). Bacteria are mainly found in the intestinal lumen, the inside of the intestines where digestion occurs, but can enter the lamina propria after epithelial barrier disruption.

genetic variants [46]. The vast majority of IBD susceptibility loci are not protein coding, but might play a role in gene expression regulation [231]. Due to linkage disequilibrium (i.e. the high correlation between various SNPs in neighbouring pieces of DNA), it is often unknown which SNPs are causative of the increased risk of developing IBD within a specific susceptibility locus.

Eighteen IBD susceptibility loci have been fine mapped to causal genetic variants, including protein coding variants in *IL23R* and *NOD2* [155, 231]. The gene *IL23R* encodes for the IL-23 receptor and is one of the several genes in the IL-23/Th17 pathway associated with polygenic IBD. Polymorphisms in *NOD2* are the strongest genetic risk factor for CD. The protein encoded by *NOD2* is nucleotide-binding oligomerization domain-containing protein 2 (NOD2). It is an intracellular receptor that recognizes the bacterial cell wall component muramyl dipeptide (MDP). NOD2 is expressed amongst other cell types in macrophages, dendritic cells and intestinal epithelial cells [5]. The exact mechanism of NOD2 deficiency in CD pathogenesis is still unknown, but many have been proposed [328]. Early studies highlighted the role of NOD2 in the release of antimicrobial peptides by Paneth cells, a type of epithelial cell [40, 352]. NOD2 signalling has been shown to promote monocyte recruitment in mice during infection [176].

NOD2 stimulation also has been shown to have a regulatory role in T cell function. Since NOD2 is largely expressed in antigen presenting cells, this regulatory role of NOD2 in T cell function is largely believed to be cell extrinsic [207, 251, 267, 351]. Watanabe et al. showed that MDP-induced NOD2 stimulation of murine antigen presenting cells inhibits a subsequent inflammatory response to PGN, a ligand of TLR2, in wild-type, but not in NOD2 deficient murine antigen presenting cells [351]. This inflammatory TLR2 mediated response includes increased IL-12 production. IL-12 drives Th1 cell differentiation and drives Th1 type cytokine production [248]. They later showed that MDP administration can protect wild-type but not NOD2 deficient mice from experimental colitis by suppression of multiple TLR signalling pathways. This suppression was associated with reduced Th1 type responses [350]. Hedl et al. showed that pre-treatment of human monocyte derived macrophages with MDP significantly decreased the production of TNFα, IL-8 and IL-1β after subsequent TLR2, TLR4 or NOD2 stimulation [142]. Thus NOD2 might tolerize innate

immune responses through direct (APC function) and indirect effects (cytokine effects on T cells). The increased TLR mediated innate response in the presence of NOD2 defects might lead to a secondary increased Th1 response. Additionally, NOD2 has been linked with autophagy, a mechanism that can be used by cells to kill and degrade intracellular pathogens [69, 336]. Most recently, a T cell intrinsic role of NOD2 signalling in suppressing Th17 signalling and uveitis, a disease of the eye, has been identified in mice. Adoptive transfer of Nod2−/− CD4+ T cells or retina-specific autoreactive CD4+ T cells into lymphopenic mice suggests a Ripk2-independent NOD2 signalling mechanism within T cells [246].

In light of the overwhelming evidence for a innate function of NOD2, we decided to focus on the well established MDP sensing mechanism in the thesis (Chapter 3). We hypothesize that a heightened bacterial load due to impairments in autophagy in the presence of a NOD2 deficiency might drive increased levels of cytokine production. This could be an alternative explanation for the inflammatory innate immune response and subsequent increased Th1 response observed in NOD deficient contexts. We did not focus on T cell responses themselves, as the increased Th1 response in a NOD2 deficient context seems to follow an impairment in the innate response, and clear evidence for T cell intrinsic functions was lacking at the time of the experiments.

Another key gene associated with polygenic IBD that is involved in the autophagy pathway is *ATG16L1*. In addition to the connections with innate and adaptive immune responses, genes thought to be linked to IBD susceptibility loci are involved in epithelial barrier functioning [116, 341].

In contrast to classical forms of polygenic IBD, Mendelian IBD-like disorders are driven by a single gene defect. Such Mendelian defects are so rare that they are not included in current GWAS studies, which only consider variants with a minimal minor allele frequency in the general population, e.g. 5%, [16], 1% [202], 0.1% [85]. In contrast, the minor allele frequency of, for instance, rare variants in X-linked inhibitor of apoptosis (XIAP) associated with IBD is typically below 0.001% [339]. Mendelian disorder-associated inflammatory bowel diseases (MD-IBDs) also point towards key pathways involved in (various subtypes of) IBD, such as IL-10 signalling, pathogen handling, and regulatory T cell activity [341].

It is a key open question to what extent the various type of MD-IBD map to classical IBD (sub)types [339].

We show some of the key genes thought to play a role in polygenic IBD (in blue), and genes involved in mendelian IBD (in purple) in Figure 1.1 [339, 341].

1.1.2 Monocyte-derived macrophages

The macrophage is a heterogeneous cell type with key functions in inflammatory responses, wound healing, and immune regulation [240]. Gut macrophages are mainly derived from monocytes, which are macrophage-precursor cells that are found in the blood (Section 1.1.2.2). Freshly recruited monocytes can differentiate into monocyte-derived macrophages with varying phenotypes and functions, depending on the specific stimuli they receive (Section 1.1.2.2).

Monocyte-derived macrophages have a major impact on the host interaction with pathogens, but also on the pathogenesis and progression of many chronic inflammatory diseases, including IBD. As discussed above, monocyte-derived macrophages produce all inflammatory cytokines that have been successfully targeted to treat IBD, such as TNFα, IL-12/23, via their common subunit p_{40}, or IL-6 (Section 1.1.1.1). Furthermore, many common polymorphisms and Mendelian disorders that can present with IBD and other immune mediated inflammatory diseases are clearly linked with important macrophage signalling pathways (Section 1.1.1.2). However, the complex molecular interactions within macrophages and the interactions of macrophages with their environment are still poorly understood. The monocyte-derived macrophage is therefore the object of our study, with an emphasis on its role in sensing, engulfing, and degrading pathogens, and the accompanying cytokine response.

1.1.2.1 The role of macrophages in IBD

The disregulation of the adaptive side of the immune system has long been at the centre of IBD research [243]. More recently, the focus has shifted to the innate immune system, and in particular monocyte derived macrophages. The importance of macrophages in IBD has been established by genetic research and functional studies [150, 231]. After the identification of

NOD2 in 2001, GWAS studies have identified multiple IBD associated genes involved in the innate immune response, including *ATG16L1* (See Section 1.1.1.2) [85, 157, 168, 202, 231]. An example of a study that points towards a key role of macrophages in IBD pathogenesis is a study by Baillie et al [28]. Baillie et al. identified promoters, i.e. sequences of DNA to which proteins can bind to initiate transcription of the downstream gene, that were regulated in LPS stimulated monocyte-derived macrophages [28]. The majority of loci associated with IBD were enriched for the identified promotors. This enrichment was specific to IBD, as loci associated with rheumatoid arthritis and unrelated traits were not enriched for the identified promotors.

Monocytes are constantly recruited to the gut and differentiate into non-inflammatory macrophages during homeostasis (See Section 1.1.1.2) [322]. In CD pathogenesis, defects in the resolution of inflammation might cause a disregulated differentiation of monocytes to non-inflammatory macrophages. This impaired differentiation could cause excessive cytokine production [243]. For instance, Kamada et al. identified an inflammatory intestinal macrophage subset (CD14+CD33+) that produced larger amounts of pro-inflammatory cytokines (e.g. TNFα, IL-23 and IL-6) than CD14-CD33+ intestinal macrophages [170]. This macrophage population was significantly increased in CD patients and the patient cells also produced larger amounts of pro-inflammatory cytokines than controls. Further, Ogino et al. found that monocyte-like macrophages from CD patients induced the development of Th17 cells [255]. Increased Th17 activity is associated with IBD (Section 1.1.1.1). In addition to a disregulated cytokine response, CD associated defects in innate pathways such as the NOD2 pathway have been linked to an impaired abilitiy of innate immune cells to kill intracellular bacteria [69, 306]. Such defects in antimicrobial activity might drive increased cytokine responses leading to a self-perpetuating process. Together, these findings point towards an important role for monocyte-derived macrophages in IBD pathogenesis.

1.1.2.2 Macrophage development

It is a relatively recent insight that the two main origins of macrophages are the blood and the tissue [133]. The macrophages originating from the blood and the tissue are known

as monocyte and yolk-sac derived macrophages respectively (see Figure 1.2). During embryonic development, yolk-sac derived macrophages are seeded in the tissues. Yolk-sac derived macrophages have tissue-specific functions, but are in general important for tissue renewal, debris engulfment and resolution of inflammation. The other type of macrophage that can be found in the tissues is the monocyte-derived macrophage. In general, monocytes are recruited from the blood during inflammation and subsequently differentiated into macrophages. Once arrived in the tissues, these plastic cells will either resolve inflammation, or contribute to the inflammatory environment, depending on the various stimuli they receive. Experimental distinction between monocyte-derived and embryonic macrophages is difficult. No reliable marker exists to accurately distinguish between the two [133]. However, using parabiosis and genetic fate-mapping experiments in animal models [133], and by studying organ transplantation in humans [256], it has been established that tissue-resident macrophages are self-maintaining and are not constantly replenished by monocytes in most tissues. For the fate-mapping experiments used by Hashimoto et al., a gene was selected that was highly expressed in monocytes [138]. Mice were bred with cells that expressed a fluorescent protein whenever this gene was expressed, therefore allowing to determine whether macrophages found in the tissues were derived from monocytes or not. This, and other fate-mapping experiments suggest that the macrophage population in most tissues does not get replenished by monocytes in homeostasis [122, 151, 303, 361]. For the parabiosis experiments used by Hashimoto et al., two mice at a time were joined, thus having a shared vasculature, and the percentage of non-host derived cells in both mice was determined a couple of months after the operation [138]. The percentage of non-host tissue resident macrophages was negligible for the tissues studied. Other parabiosis experiments also found that monocytes do not differentiate into tissue-resident macrohages for most tissues in homeostasis [132, 163]. In humans, studies on organ transplantation similarly indicate that long-lived populations of non-host tissue resident macrophages exist in most tissues, e.g. a study on human liver transplantation by Pallett et al. [256, 258]. However, there are several tissues to which monocytes are constantly recruited, even in the absence of inflammation. One of these is the gut, which is under constant attack of microbes. Monocyte-derived macrophages can be key drivers of inflammation, but are conditioned

s

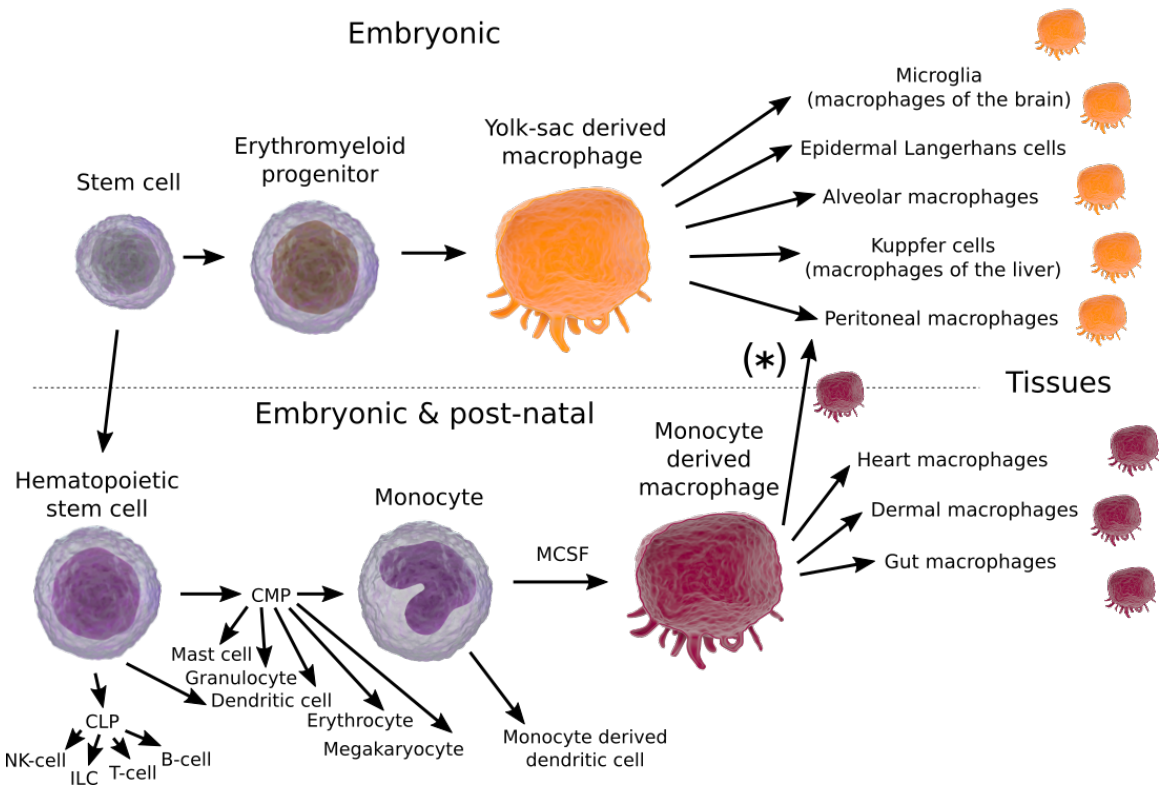


Figure 1.2: The different origins of human macrophages found in the tissues both during embryonic development and after birth [123, 144]. (∗) During inflammation or tissue injury, monocytes are recruited from the blood and differentiated into monocyte derived macrophages. At steady state conditions, most tissues are exclusively populated by macrophages of embryonic origin, except for the intestine, dermis and heart, where the main macrophage population consists of monocyte derived macrophages. Abbreviations: CMP, common myeloid progenitor; CLP, common lymphoid progenitor; ILC, innate lymphoid cell; M-CSF, macrophage colony-stimulating factor.

to be non-inflammatory in the healthy gut [123]. It is currently unknown to what extent differences in function between the two macrophage populations derive from their origin, and to what extent differences derive from their micro-environmental imprinting [219]. For instance, it was found that bone marrow-derived and resident liver macrophages display broadly similar biological functions, although subtle differences exist [30]. Resident liver macrophages were for instance poorer in taking up bacterial pathogens than bone marrow-derived macrophages.

1.1.2.3 Macrophage differentiation

Activated monocyte-derived macrophages have historically been divided in two mutually exclusive groups: the pro-inflammatory classically activated M1 and the anti-inflammatory alternatively activated M2 macrophages [219]. Differentiation into one of the two subtypes was assumed to occur depending on the different stimuli the macrophage received after recruitment from the blood. The distinction between M1 and M2 macrophages was based on in vitro stimulation experiments with selected macrophage receptor ligands, such as LPS+ IFNγ or TNFα stimulation for an M1 and IL-4, IL-10 or glucocorticoid stimulation for an M2 phenotype. *In vivo* evidence of classically activated M1 type macrophages during a *Listeria monocytogenes* infection in mice was first described by Mackaness in 1962 [206, 219]. *In vivo* evidence of alternatively activated M2 type macrophages during Helminth infection was given by Loke et al. and Hesse et al. [149, 166, 204]. Although the binary M1/M2 framework might provide a useful distinction between inflammatory and non-inflammatory populations of macrophages, they are much more heterogeneous than this simplified classification suggests [240]. The expression of the markers used to classify M1 and M2 phenotypes appear to be not mutually exclusive, allowing for 'mixed' M1/M2 phenotypes. Vogel et al. for instance found that 70% of foamy macrophages in multiple sclerosis express both M1 and M2 markers [348]. An analysis of tumor-associated macrophages (TAMs) by Pettersen et al. resulted in the identification of macrophages expressing M1 genes, M2 genes, and macrophages expressing both M1 and M2 genes. Macrophage phenotypes encountered *in vivo* are the result of a complex and dynamic interplay of received stimuli and do not map to the phenotypes found by *in vitro* stimulation with only a few key cytokines. In vivo macrophages are now thought to exist in different states of differentiation and activation, suggesting a heterogeneity of macrophages [219]. Single-cell RNA sequencing data of macrophage populations in multiple organs, including the gut [319], suggest that multiple macrophages exist under physiologic and non physiologic conditions. Although extreme states exist, there are many states of macrophages. It remains an open question how plastic their phenotype remains after having received specific stimuli.

1.1.2.4 Receptor systems

Macrophages sense and respond to various external stimuli from their tissue micro-environments. They express multiple receptor systems that permit the detection of pathogens (e.g. toll-like receptors (TLRs) and NOD-like receptors, via pathogen-associated molecular patterns [112, 43]), molecules that indicate cell damage (e.g. RAGE and TLRs via alarmins [37]), cytokines (cytokine receptors that detect growth factors such as macrophage colony-stimulating factor (M-CSF), interleukins such as IL-1, IL-6 and IL-10, TNFα, and chemokines), and neurotransmitter receptors [263]. Receptor responses can result in the production of activating and inhibitory cytokines that orchestrate the immune response (Figure 1.3) [173].

1.1.2.5 Anti-microbial activity

Macrophages engulf pathogens in a process known as phagocytosis. Phagocytosis is defined as the internalization of extracellular entities such as particles or pathogens into single membrane vesicles called phagosomes. Single membrane phagosomes undergo a maturation process during which they fuse with vesicles called lysosomes and subsequently degrade [254]. The killing and degradation process of intracellular pathogens by macrophages has been linked with autophagy. Autophagy is a degradation process used by cells to break down intracellular components and can be initiated by multiple processes such as energy depletion, starvation, or growth factor deprivation [196]. The autophagy machinery can also be used to clear pathogens. We distinguish between xenophagy (a form of canonical autophagy), and LC3-associated phagocytosis (LC3-associated phagocytosis (LAP), a form of phagocytosis that has been linked to components of the autophagy pathway). Both xenophagy and the LAP pathway are associated with microtubule-associated protein 1A/1B-light chain 3 (LC3, a marker for autophagy) recruitment, fusion with lysosomes, and subsequent pathogen degradation [140]. Canonical autophagy is characterised by the formation of a double-membrane autophagosome around the intracellular components (i.e. intracellular pathogens in the case of xenophagy) that are to be degraded. Xenophagy can for instance be initiated in response to damage of the phagosome when pathogens try to escape from the phagosome to gain access to the cytosol, the interior of the cell. In contrast, LAP is a form of phagocytosis. Various receptors play a role in initiating and

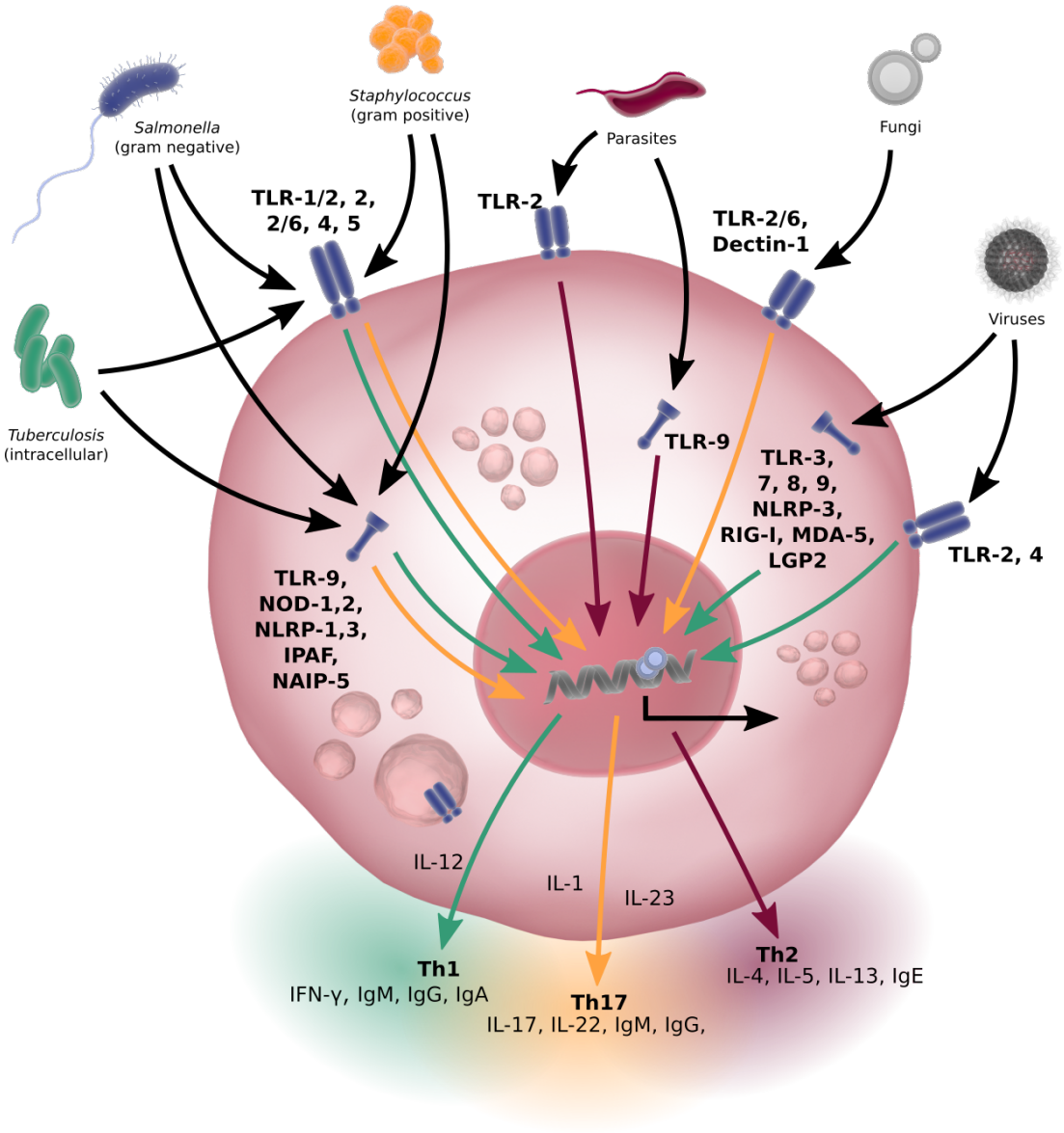


Figure 1.3: The activation of macrophage signalling pathways by various pathogens. Macrophage output in the form of cytokine production is amongst others dependent on the type of pathogen and the receptor location. Green, yellow and red arrows correspond to a Th1, Th17 and Th2 polarizing response respectively. Macrophage responses exist in a continuum.

stimulating LAP, such as the pathogen recognition receptors TLR2 and NOD2 [306, 342]. The LAP pathway is dependent on the reduced form of nicotinamide adenine dinucleotide phosphate (NADPH) oxidase complex formation, which is used by macrophages to produce antimicrobial reactive oxygen species (ROS), e.g. hydrogen peroxide. We note that autophagy proteins are not required for phagosome maturation [56]. Hence, we distinguish three ways in which intracellular pathogens can be cleared by macrophages: (1) via conventional phagocytosis and subsequent lysosomal degradation, independent of autophagy proteins, (2) via LAP (non-canonical autophagy) dependent phagocytosis and subsequent lysosomal degradation, or (3) via xenophagy (canonical autophagy), for instance after damage of the phagosome. In contrast to the double-membrane autophagosome that forms during xenophagy, LAP and conventional phagocytosis are characterised by single membrane phagosomes. Some intracellular pathogens have developed effective strategies to avoid degradation. *Mycobacterium tuberculosis* for instance, avoids LAP by secretion of a factor that inhibits NADPH oxidase recruitment [182, 342]. Some pathogens can replicate intra-cellularly, either within the phagosome or after escape to the cytosol. The ability to replicate is both pathogen and host-cell type dependent. Whereas in epithelial cells *Salmonella enterica serovar typhimurium* (*Salmonella*) for instance can replicate at high rates within the cytosol, in macrophages only replicating *Salmonella* within vacuoles have been observed [36, 48, 54].

Bacterial infection can induce cell death. Nod-like receptor signalling in response to *Salmonella* for instance activates the inflammasome resulting in IL-1β and IL-18 secretion that can induce pyroptosis, a rapid form of pro-inflammatory cell death [47, 103, 128]. A very high bacterial load can induce necrosis, another type of cell death, for instance during *Mycobacterium tuberculosis* infection. Necrosis might be a mechanism used by bacteria to escape the host cell and spread infection [193]. In contrast, TNFα induced apoptosis, a type of programmed cell death, can serve as a mechanism for infection containment [31].

Clusters of aggegrated macrophages form when macrophages can not effectively clear their intracellular pathogen load [257]. Such clusters are known as granuloma. Various types of granuloma can form in different parts of the body. Granuloma can be classified based on the stimulus that drives its formation. Granuloma can be caused by foreign bodies, such

as tattoo particles or biomedical implants, they can be caused by infectious agents, such as parasitic larvae or tuberculosis bacteria, or they can be found in inflammatory diseases such as Crohn's disease (CD), chronic granulomatous disease (CGD) or sarcoidosis. The factors and cellular processes that drive granuloma formation are still poorly understood. Granuloma formation is initiated by the clustering of macrophages. It has been shown that chronic activation of the metabolic checkpoint kinase mTORC1 can spontaneously initiate such clustering [200]. Within days of granuloma formation, macrophages can start to resemble epithelial cells [72]. This process is called epithelioid transformation. After some time, cell types other than macrophages can be recruited to the granuloma, most notably T cells, but also dendritic cells, neutrophils, B cells or eosinophils. Although T cells are found in all infectious granuloma, granulomas induced by tattoo pigments, talc or silica do not typically induce a T cell response [257]. The recruited T cells amplify macrophage microbicidal capacity by IFN-γ and TNF production [233]. Other features of granuloma include a necrotic core, common in *Mycobacterium tuberculosis* (TB) induced granuloma, and fibrosis, common in granuloma induced by parasitic eggs [78, 265]. Granuloma with a necrotic core, also called caseating granuloma, typically form a center of debris, surrounded by a ring of granuloma macrophages and an outer ring of lymphocytes [257]. Caseating granuloma are usually larger than non-caseating granuloma. A key feature of macrophages within a granuloma is also their ability to fuse, resulting in multinucleated giant cell (MGC) formation [145]. Fused macrophages might be better at degrading large particles [190, 239, 245, 257, 300]. A granuloma resolves when the granuloma-inducing agent is cleared. When the granuloma-inducing agent can not be cleared, a granuloma can become chronic. Chronic TB granuloma are thought to be able to persist for years and may never heal during the life of a patient [78]. Chronic TB Granuloma in the lung typically have a diameter of 2mm or more, while macrophages typically have a diameter of 20μm [307]. Lung TB Granuloma can consist of many thousands of macrophages [78]. TB Granuloma can also form in different parts of the body. In Chapter 4, we will be concerned with TB granuloma in the gut. The diameter of intestinal TB granuloma found in a study by Polimood et al., was approximately 200μm, while CD granuloma were found to have an average diameter of 100μm [278]. Counts of the number of macrophages per granuloma in the gut were not reported in this study.

However, assuming spherical granuloma and macrophages (with a diameter of 20μm), the volume of a TB and CD granuloma is 8000 and 1000 times larger than the volume of a single macrophage respectively. The life-span of CD granuloma is likely much shorter than the life-span of TB granuloma. The chance of observing CD granulomas in a histological biopsy, after having observed granulomas in an earlier biopsy, has been reported to be only 44% (2-6 biopsies, 52 CD patients, mean follow up time of 58 months) [146].

1.2 Mathematical modelling

Mechanistic mathematical models have been used to analyse the role of macrophages in inflammatory processes. In our perspective article Jansen et. al, "Combining Mathematical Models With Experimentation to Drive Novel Mechanistic Insights Into Macrophage Function", we argued that a synergistic cycle of modelling and experimentation can drive novel mechanistic insights in macrophage functioning [165]. In this article we highlighted two studies that took such an approach, one on macrophage-fibroblast interactions by Xu Zhou et al., and one on NF-κB signalling by Alexander Hoffmann et al. [152, 366]. In the following, we will first summarize these two modelling studies. We will refer to them in our discussion chapter (Chapter 5). We will then consider other modelling studies particularly relevant in the context of our thesis, while focussing on cytokine signalling, antimicrobial activity, and granuloma formation. In the second part of this section, we will give an overview of the techniques used in this thesis for parameter estimation, determination of parameter identifiability, and model selection. We will also give some background information on differential equations, and other modelling techniques.

1.2.1 Examples of model driven-experimentation

1.2.1.1 Modelling macrophage-fibroblast interactions

Mesenchymal derived fibroblasts support the integrity of intestinal and other mucosal barriers via synthesis of extracellular matrix and growth factors required for both barrier repair and macrophage homeostasis. Xu Zhou et. al utilized a combination of experimentation and modelling based on an in-vitro system of bone-marrow derived macrophages and primary mouse embryonic fibroblasts to dissect feedback signalling loops between macrophages and

stromal fibroblasts [9, 366]. In this experimental system the macrophages and fibroblasts were plated together in medium without the addition of further growth factors and cell numbers were determined by flow cytometry. The mathematical model describes how simple macrophage-fibroblast interactions can reach stable cell populations. This is an illustration of how modelling can provide a useful framework for qualitative understanding of dynamics between different cells. The model also proved to be useful on a quantitative level; it was found that cell-density had to be taken in consideration in order to match the experimentally observed cell numbers with the cell numbers predicted by the model. This in turn led to the experimentally verified finding that close cell-cell contact is essential for growth factor exchange between macrophages and fibroblasts. We elaborate on both findings below. First, it was experimentally determined that fibroblasts in the system produce both macrophage and fibroblast growth factors, while the macrophages only produce a fibroblast growth factor. Secondly, it was assumed and experimentally verified that the growth rate of the fibroblasts, but not the macrophages, was limited by their carrying capacity, which was found to be dependent on the available space. Based on these two assumptions, a mathematical model was constructed describing the macrophage and fibroblast cell counts and growth factor concentrations over time. Different wiring possibilities of the model network were explored mathematically. Of the 144 possibilities considered, only 48 networks allowed for a stable steady state for a wide range of parameters, corresponding to a stable number of macrophages and fibroblasts. It was found that all 48 networks that allowed for such a stable steady state included a negative regulatory loop on the macrophage growth factor. This is a necessary condition for stability, as a cell population that is not limited by its carrying capacity will keep expanding indefinitely if its growth factor is not regulated. Experimental verification showed that macrophage growth factor is negatively regulated by receptor internalization. Furthermore, it was found that fibroblast growth factor too is negatively regulated, both by receptor internalization and by inhibition by the macrophage growth factor, but the model indicates that this regulation of the fibroblast growth factor is not essential to reproduce the observed dynamics (Figure 1.4 (a)). The mathematical model based on the final circuit generated in this way predicts that apart from the stable steady state, there also exists a state with only fibroblasts, sustaining themselves, and a

state without macrophages and fibroblasts. Depending on the initial absolute cell numbers, the system is predicted to converge to one of these states (Figure 1.4 (b)), which was experimentally verified by quantifying cell numbers over time by a combination of flow cytometry and fluorescent imaging for different initial cell numbers. Finally, it was found that the initial cell numbers required to converge to the steady state of coexisting cell populations was larger than the model predicted. This was explained by density-dependent effects; the model assumes a perfectly mixed population, but cell-dependent contact decreases when cell numbers decrease. Thus, the discrepancy of the model predictions with the experimental results suggested that cell-cell contact is essential for growth factor dynamics and the regulation of tissue homeostasis.

1.2.1.2 Modelling the NF-κB signalling pathway

A key integrator of the different macrophage signalling pathways is the nuclear factor κ-light-chain-enhancer of activated B cells (NF-κB) pathway, which regulates the nuclear localization of NF-κB transcriptional regulators that control the expression of hundreds of genes involved in many aspects of inflammation [365]. One of the earlier mathematical models of NF-κB signalling was developed by Alexander Hoffmann et al. The model provides a quantitative description of the different roles of three NF-κB inhibitor isoforms, IκBα, IκBβ and IκBϵ (Figure 1.5 (a)) [152]. The model was calibrated with data obtained from an experimental mouse model with only one active NF-κB inhibitor isoform and provides a mechanism-based explanation for the oscillatory dynamics of the nuclear NF-κB concentration that are observed in wild-type mice, but not in mice that lack an active form of IκBα (Figure 1.5 (b)). Many more mathematical models of NF-κB dependent processes were subsequently constructed, including models of TNFα receptor signalling [353], TNFα secretion [51], TLR4 receptor signalling, and the addition of extrinsic noise to the synthesis rate of TLR4, the activation rates of TRIF and MyD88 and the endosomal maturation rate, in order to incorporate cell-to-cell variability [60]. Most of these studies integrated modelling with wet lab experimentation.

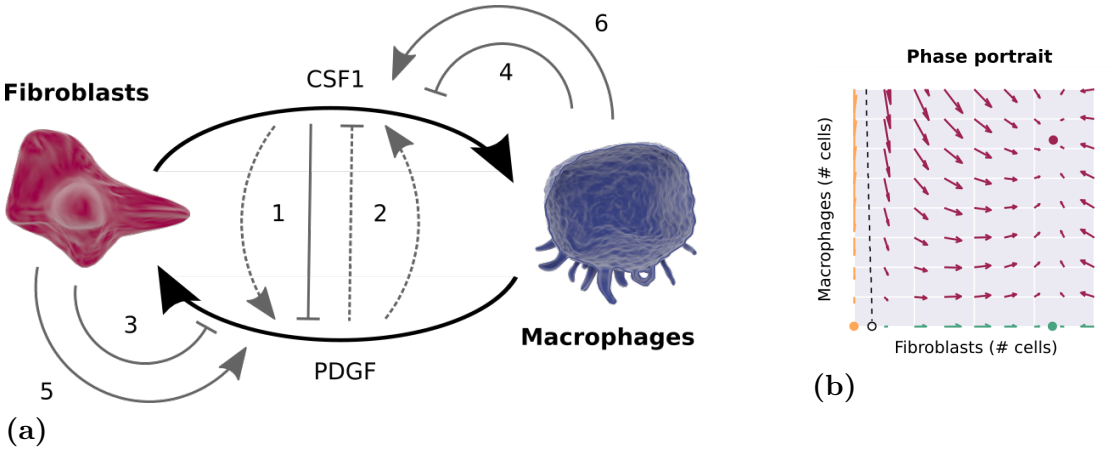


Figure 1.4: (a) Wiring diagram of the macrophage-fibroblast growth factor model by Xu Zhou et al. [9, 366]. Fibroblasts produce both macrophage growth factor (CSF1) and fibroblast growth factors (PDGFD, HBEGF), while macrophages produce a fibroblast growth factor (PDGFB), mediating cross talk between macrophages and stroma. The dimensionless model derived from this diagram consists of two ODEs describing the population sizes of the macrophages and fibroblasts and two algebraic equations describing the concentration of the two growth factors. Different wiring possibilities were explored (grey arrows), i.e. the addition of positive or negative feedback of one growth factor on the production rate of the other (1,2), removal of a growth factor through receptor mediated endocytosis (3,4), or autocrine growth factor production (5,6). Of the 144 possibilities considered, only 48 networks allowed for a stable steady state for a wide range of parameters, corresponding to a stable number of macrophages and fibroblasts. The final experimentally verified circuit is depicted by the solid arrows. (b) Phase portrait of the macrophage and fibroblast cell population numbers of the model by Xu Zhou et al. [9, 366]. Given initial cell numbers, the system will end up in one of the three stable steady states. All initial values at the left-hand side of the separatrix (dashed line) will converge to the trivial steady state (yellow, no fibroblasts or macrophages). At the right-hand side of the separatrix, the system will converge to the positive steady state if the initial system contains macrophages (red, positive numbers of fibroblasts and macrophages), and converge to the 'fibroblast only' steady state (green, only fibroblasts) otherwise.

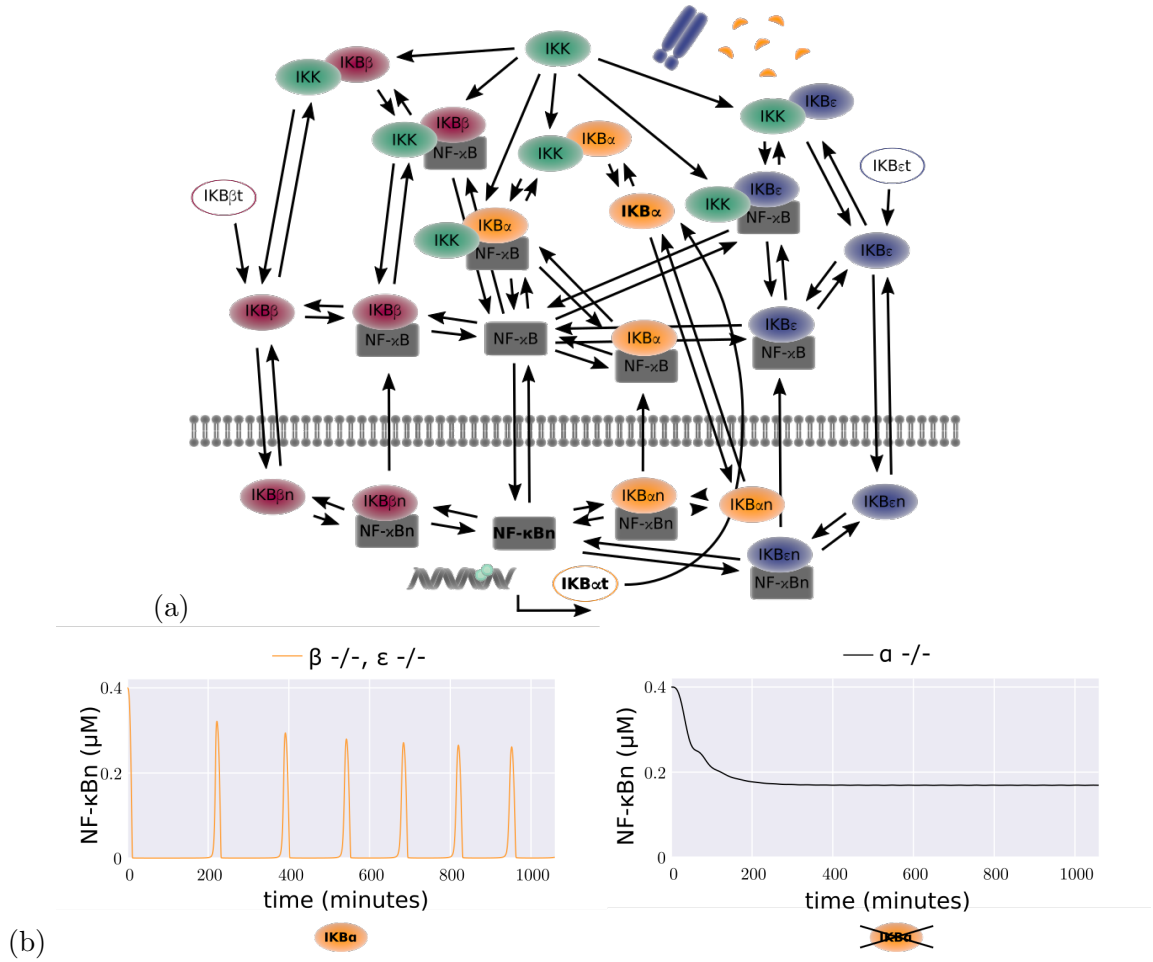


Figure 1.5: (a) Wiring diagram of the NF-κB model by Alexander Hoffmann et al. [152]. The model derived from this network consists of 26 ODEs, one for every node in the network. The interactions between nodes, denoted by arrows in the network, are included in the terms of these 26 ODEs. (b) The free nuclear NF-κB concentration against time generated by the equations of the model by Alexander Hoffmann et al. [152]. The model provides an explanation for the oscillatory dynamics of the nuclear NF-κB concentration that are observed in wild-type mice, but not in mice that lack an active form of IκBα. Each NF-κB inhibitor can bind to a NF-κB molecule, forming an NF-κB-inhibitor complex. When IκB kinase (IKK) also binds to this NF-κB-inhibitor complex, the inhibitor degrades, and the free NF-κB can travel to the nucleus and bind DNA. This results in the synthesis of various proteins, one of which is IκBα. The production rate of the NF-κB inhibitor IκBα is thus dependent on the concentration of free NF-κB. The negative NF-κB-IκBα feedback loop generates oscillations in the concentration of NF-κB. In contrast, the other two NF-κB inhibitors, IκBβ and IκBϵ, are produced at a constant rate, independent of the amount of free NF-κB. Therefore, they have a damping effect on the oscillations generated by the IκBα negative feedback loop. A model without IκBβ or IκBϵ, but with IκBα therefore produces oscillations (left, yellow), while a model without IκBα, but with IκBβ and IκBϵ does not (right, black).

1.2.2 Modelling cytokine interactions

In Chapter 2 of this thesis, we will be concerned with cytokine interactions. A better mechanistic understanding of the immune response, including the role of cytokine interactions, is needed to improve clinical care. Examples of mathematical modelling efforts to drive such understanding exist on various scales, and at different levels of granularity. At the intracellular scale, models have been constructed that include as much prior knowledge of the pathway of interest as possible. In such models the model components correspond to (the concentration of) individual molecules. An example is the model of NF-κB modelling we discussed above [152], and the subsequent NF-κB signalling studies [51, 60, 353]. A limitation of such an approach is the required certainty about both the pathway structure and the strength of the interactions of the various model components [227]. Insufficient knowledge about the studied system will lead to practical parameter unidentifiability. The amount of data required for model parametrisation further increases when considering processes at a larger scale, such as models on the whole-organ level. In many mechanistic modelling approaches, the problem of parameter unidentifiability is adressed by not including each individual pathway component in the model. The production rate of a cytokine might for instance be assumed to be dependent on the concentration of a certain cell type, without explicitly considering the various molecules part of the cytokine production pathway. This approach was taken in the study that we discussed above by Zhou et al. [366]. Other mechanistic, ordinary differential equation (ODE) based modelling studies involving cytokine interactions include models of *Mycobacterium tuberculosis* infection [83, 214], myocardial infarction [349], neuroinflammation [17], and wound inflammation [244].

Finally, purely data-driven approaches do not take into account any prior knowledge of the pathway at stake. Examples include information theoretic or directed acyclic graphs (DAGs, also known as Bayesian networks) [99, 101, 212, 238]. A limitation is their lack of providing detailed mechanistic insight. Further, their form might not be suitable to capture all relevant features of cytokine interactions, such as temporal oscillations or bi-stability. The level of model abstraction should be dependent on the purpose of the model.

1.2.2.1 Connection with our study

Our cytokine interaction model will be as simple as possible and only describe the concentrations of a limited set of cytokines of interest using ordinary differential equations (Chapter 2). Further, all cytokine interactions included in the model follow directly from the data set used. The use of ordinary differential equations over for instance a Boolean or Graphical Gaussian approach allows us to describe both the strength of the cytokine interactions and cytokine self-interactions, together with accommodating the continuous development of the cytokine concentrations over time [220, 221, 238, 358]. Other possible methods for analysing cytokine networks, such as Boolean and Graphical Gaussian Models, will be considered in Section 1.3.7.

1.2.3 Modelling host-pathogen interactions

In Chapter 3 of this thesis, we will construct a model on bacterial handling, that is intracellular kiling, by macrophages and the accompanying cytokine response. Mathematical models of host-pathogen interactions have been around for many years. The first mathematical models on HIV models arose more than thirty years ago, just three years after the virus was first isolated [70, 71]. Models have explored pathogen interactions at various scales, from intracellular pathway dynamics to the tissue, whole host, and wider population. Examples of innate host-pathogen modelling on an intra-cellular scale include models of the interaction between *Mycobacterium tuberculosis* and a killing mechanism dependent on nitric oxide and iron regulation [285], *Francisella tularensis*, TLR2 and the complement receptor (cr)3 [191], *Helicobacter pylori* and the pathogen recognizing receptor leucine-rich repeat-containing protein X1 [271], *Helicobacter pylori* and Lanthionine Synthetase C-Like 2 [192], *Cryptococcus neoformans* and NF-κB [139, 330], and the nematode *Acanthocheilonema viteae* and IL-10 signalling [102, 178] (see for a review [181]). Examples of studies on the cellular scale include stochastic models of macrophage dynamics during infection, focussing mainly on bursting of macrophages [53, 120, 277, 355]. J. Gog et al. studied the dynamics of a *Salmonella enterica* infection at early time points with an iterative approach of modelling and experimentation [127]. Restif et al. and Demarre et al. constructed models

based on *Salmonella* and adherent-invasive *Escherichia coli* (AIEC) infection assays respectively, while focussing on non-replicating bacteria (persisters) within macrophages [289, 87]. Examples of host-pathogen dynamics studied on a larger scale include influenza infection [264], *Streptococcus pneumoniae* infection, [321], *Streptococcus pneumoniae* and influenza co-infection [88, 320], fungal spore inhalation [331], *Leishmania* infection [316], *Francisella tularensis* infection [120], and HIV infection [94].

As showcased by the two exemplar modelling studies on NF-κB signalling and macrophage-fibroblast interaction, the combination of mechanistic modelling with wet-lab experimentation is important to drive mechanistic insight [152, 165, 366]. However, many of the existing mechanistic modelling efforts listed above have been disconnected from wet-lab experimentation. Further, we have previously found that when mechanistic modelling studies were complemented by wet-lab experimentation, the vast majority of associated experimental systems consisted of mouse models, murine or other animal/human immortalised cell lines [165]. Animal models and cell lines do not recapitulate all features of human disease pathophysiology and response to drug exposure [82, 363].

1.2.3.1 Connection with our study

We will study genetic defects associated with IBD that are still poorly understood at the mechanistic level using a combination of modelling and experimentation (Chapter 3). We will construct a novel, ordinary differential equation-based model that describes the bacterial load and associated cytokine response of several key cytokines in *in vitro* infected macrophages over time. We will use primary human cells as they are more relevant than murine cells or immortalized cell lines when studying the role of human genetic defects in IBD pathogenesis.

1.2.4 Modelling granuloma formation

In our final research chapter, we will study macrophage clustering into granulomatous structures in response to persistent stimuli (Chapter 4). Multiple mathematical model types of granuloma formation exist in the literature, including agent-based models (ABMs) [177], a spatial partial differential equation model [137] and a Petri net model [10]. Granulomatous

Mycobacterium tuberculosis infection in the lung has been modelled extensively by the group of Denise Kirschner. Their original ABM of granuloma formation GranSim was published in 2003 and has since been continuously updated and validated against human and animal experimental data [63, 98, 285, 307].

1.2.4.1 Connection with our study

We will construct a model of granuloma formation that considers the dynamics of pathogen load in a manner analogous to age structured models, to describe the granuloma size and distribution of infection over time (Chapter 4). The use of pathogen load as an internal structuring variable is a novel approach in mechanistic granuloma modelling. One of the key features we will include in our model is the ability of macrophages within a granuloma to fuse. Cell fusion has not yet been considered in existing models of granuloma formation. Finally, we will conduct an initial study into the difference between the granuloma found in CD and in intestinal TB (iTB). No granuloma modelling study has been parametrised before to study intestinal granulomas such as found in Crohn's disease.

1.3 Modelling tools and methods

In this thesis, we will construct deterministic, mechanistic models. We will first provide some background on the possible failure modes of mechanistic modelling and how they can be mitigated against. We then introduce the key modelling techniques used in this thesis for parameter estimation, determination of parameter identifiability, parameter sensitivity analysis, and model selection. We will give a brief overview of differential equations and the way they are solved in this thesis. We will also give a brief overview of some other modelling techniques not used in this thesis.

1.3.1 Cautionary tales. The possible failure modes of mechanistic modelling

The dynamics found in biological systems are often non-linear, complex, and hard to grasp by intuition alone. Mechanistic models can help shape our understanding of biology and make quantitative predictions. However, several key risks of failure should be kept in mind when using a mechanistic model to describe a biological process. We will focus on

deterministic differential equation modelling as this is the modelling technique used in this thesis. The first risk is that of model and error model misspecification. The structure of a differential equation has to be specified based on prior knowledge. Choices need to be made on what species should be included in the model and how to include the interactions between the different species. When comparing experimental data to model simulations, a model for the noise and systemic error in the data also needs to be specified. Using experimental data, we can then obtain estimates of the value of the model parameters. Practical parameter identifiability analysis can give insight into the feasability and accuracy of these estimates, given the data [281]. Sensitivity analysis gives insight in how uncertainty in the value of the model parameters and initial conditions impacts the model simulations [213]. Discrepancies between model simulations and experimental data can lead nonetheless to biological insight, by revealing model or error model misspecifications.

A second related risk is the failure to determine the parameter values that best fit the data, given a certain model structure. Determining the parameter values that best fit the data requires the optimization of the log-likelihood function over all parameter values (a measure of the discrepancy between model prediction and experimental data, as introduced below, in Section 1.3.2). The log-likelihood function commonly has multiple local minima, but it is often not known how many local minima exist. When an optimization algorithm returns a minimum, it is therefore not known whether this is a local or a global minimum. The two main types of optimization algorithms are stochastic and deterministic algorithms. Stochastic algorithms are usually computationally more expensive, but are less likely to return a local minimum than deterministic algorithms [283]. To mitigate the drawback of getting stuck at local minima, deterministic algorithms can be run many times with different initial parameter guesses. This approach, i.e. a deterministic optimization algorithm run many times with different initial parameter guesses, was proposed by Raue et al. in [283]. Raue et al. found that this approach was the most accurate and the fastest in a systematic comparison of different optimization algorithms, including twelve stochastic algorithms such as a standard evolutionary optimizer, an evolutionary optimizer with covariance matrix adaption (CMA-ES), and particle swarm optimization, and a hybrid scatter

search algorithm [283]. We will use this approach throughout this thesis and will provide more details on the implementation below (Section 1.3.2).

1.3.2 Parameter estimation

In this thesis, we will construct deterministic, mechanistic models. A classic framework to estimate the value of parameters in such cases, given a set of data and a model, is maximum likelihood estimation [189]. We first define the probability density function of the normal distribution $\mathcal{N}(\mu, \sigma^2)$:

$$f(x|\mu, \sigma^2) = \frac{1}{\sqrt{2\pi\sigma^2}} \exp\left(-\frac{(x-\mu)^2}{2\sigma^2}\right), \tag{1.1}$$

with μ the mean and σ the standard deviation. Consider a set of experimental data points $y_i(t_j)$, for observable i and time point j. We assume that each experimental data point contains normally distributed noise:

$$y_i(t_j) = \tilde{y}_i(t_j) + \epsilon_{i,j}, \tag{1.2}$$

with $\epsilon_{i,j} \sim \mathcal{N}(0, \sigma_{i,j}^2)$ and $\tilde{y}_i(t_j)$ the unknown value of the observable without noise. As noise might be relative to the value of the observable in some cases, the standard deviation of the noise $\sigma_{i,j}$ can be a function of $\tilde{y}_i$ or t_j, e.g. $\sigma_{i,j} = a_{i,j} + b_{i,j}\tilde{y}_i(t_j)$, with $a_{i,j}$ and $b_{i,j}$ constants. Given corresponding model simulation values $x_i(t_j, \boldsymbol{\theta})$, for observable i and time point j, and dependent on a model parameter vector $\boldsymbol{\theta}$, the likelihood function is defined as

$$\mathcal{L}(\boldsymbol{\theta}) = \prod_i \prod_j \frac{1}{\sqrt{2\pi\sigma_{i,j}^2}} \exp\left(-\frac{(y_i(t_j) - x_i(t_j, \boldsymbol{\theta}))^2}{2\sigma_{i,j}^2}\right), \tag{1.3}$$

with $\sigma_{i,j}$ the standard deviation of the noise of each data point. For known standard deviation values $\sigma_{i,j}$ (or $a_{i,j}; b_{i,j}$), maximizing the likelihood function with respect to $\boldsymbol{\theta}$ will give us the maximum likelihood parameter value estimates $\hat{\boldsymbol{\theta}}$ of the parameter vector $\boldsymbol{\theta}$. The likelihood of the observations is maximal when we parametrise our model with $\hat{\boldsymbol{\theta}}$. The values of the standard deviation $\sigma_{i,j}$ (or $a_{i,j}; b_{i,j}$) can also be estimated simultaneously with the model parameter value estimates $\hat{\boldsymbol{\theta}}$ [283]. Maximizing the likelihood is equivalent to minimizing the negative logarithm of the likelihood, which is usually done instead. The

negative logarithm of the likelihood, multiplied by -2 is given by:

$$\mathcal{LL}(\boldsymbol{\theta}) = -2\log\left(\mathcal{L}(\boldsymbol{\theta})\right) = \sum_i \sum_j \log 2\pi + \sum_i \sum_j \log \sigma_{i,j}^2 + \sum_i \sum_j \left(\frac{(y_i(t_j) - x_i(t_j, \boldsymbol{\theta}))^2}{\sigma_{i,j}^2} \right). \tag{1.4}$$

Minimizing $\mathcal{LL}(\boldsymbol{\theta})$ is non-trivial. First, it is computationally expensive. Raue et al. tested multiple optimization algorithms on a test model containing 115 parameters [283]. Each optimization algorithm required hundreds to thousands of function evaluations to converge to a minimum. Here, each function evaluation involved numerically solving the ODE model system. Second, as already mentioned in Section 1.3.1, the log-likelihood function commonly has multiple local minima. When an optimization algorithm returns a minimum, it is therefore not known whether this is a local or a global minimum. Throughout this thesis, to minimize $\mathcal{LL}(\boldsymbol{\theta})$, we will use a deterministic trust-region approach combined with a multi-start strategy, as implemented in the Matlab based modelling environment 'Data2Dynamics' [284] (see Section 1.3.1 above). A trust-region approach is a common technique for nonlinear optimization problems [237]. It is an iterative technique. We start with an intial guess, which is used as the starting point of the first step of the algorithm. At each step of the algorithm, the objective function that is minimised is approximated by a simple model such as a quadratic model around the starting point. This simple model is then solved exactly or approximately within a certain region, the trust-region, of the starting point. The point within the trust region at which the simple model takes on its minimum value is then substituted into the original objective function. If the original objective function at the proposed new point decreases by a sufficient amount compared to the starting point, the proposed point is accepted and the procedure is repeated, with the accepted point as the next starting point. When the objective function does not decrease enough, the proposed point is not accepted, the size of the trust region is decreased, and the next iteration is started with the same starting point as before. The algorithm stops when the objective function does not decrease any-more within tolerance, and there is exetensive theory that shows convergence to a local optimum under weak conditions [250, Chapter 4]. We use the function 'lsqnonlin' (trust-region reflective) for the Matlab Optimization Toolbox for all optimization problems in this thesis. This function is based on the method described in

[67]. The multi-start strategy we employ means that the optimization algorithm (the trust-region approach) is run independently multiple times with different initial guesses. The initial guesses are sampled using Latin hypercube sampling (LHS). For each parameter, a uniform sampling interval in log10 transformed parameter space is given. This interval is divided in N equally sized subintervals, with N the total number of initial guesses. Each subinterval is used to sample from once. The N sampled values are then assigned to the N initial guesses at random. LHS results in a better coverage of parameter space than random sampling [283]. We note that in Chapter 2, we will often only use 10 initial guesses when searching for an optimum. Given the number of model parameters (more than 5), we acknowledge that these 10 initial guesses correspond to a very coarse coverage of the different regions in parameter space. We will discuss in Section 2.10.5 why we nonetheless assume that the 10 initial guesses are sufficient to obtain an estimate of the global minimum for the specific type of model considered in Chapter 2. In general, we emphasize that many more initial guesses would be required for a sufficient coverage of parameter space, especially in the general setting.

We note we assume all parameter values in $\boldsymbol{\theta}$ are constant across the data set. Certain parameters can also be considered to be drawn from a probability distribution, as is done in a non-linear mixed effects approach [189]. This is for instance of interest when describing the variability of parameters for individuals within a population. Finally, we note that the minimization of $\mathcal{LL}(\boldsymbol{\theta})$ results in point estimates $\hat{\boldsymbol{\theta}}$ of the model parameter values. By applying Bayes's theorem, we obtain an expression for the posterior probability density function (PDF) of the parameters:

$$P(\boldsymbol{\theta}|y) = cL(y|\boldsymbol{\theta})P(\boldsymbol{\theta}), \tag{1.5}$$

with y denoting experimental data, $L(y|\boldsymbol{\theta})$ the likelihood function defined in equation (1.3), $P(\boldsymbol{\theta})$ the prior PDF of the model parameters, and c a normalizing constant such that the integral of $P(\boldsymbol{\theta}|y)$ is one. We note that for uniform parameter priors, the parameter posterior is proportional to the likelihood function $L(y|\boldsymbol{\theta})$ and then maximising the likelihood maximises the posterior, movitating the use of likelihood maximisation when minimal prior knowledge of the parameters is available. Markov chain Monte Carlo (MCMC) sampling

can be used to sample parameter values from the posterior probability distribution of parameters [282, 283]. We will not explore the parameter posterior distribution in this thesis.

1.3.3 Parameter identifiability

We can distinguish two types of parameter non-identifiability: structural and practical non-identifiability. Structural non-identifiability arises from the model structure and is independent from the experimental data. Structural non-identifiability arises when a relationship between model parameters exists, such that these model parameters can be varied while satisfying this relationship, without affecting the model observables. A simple example would be parameters a and b in the equation $\frac{\mathrm{d}x}{\mathrm{d}t} = abx$, for observable x. When a is multiplied by a factor u_a, we can choose $u_b = 1/u_a$ such that $u_a a u_b b x = abx$, and therefore, when the relationship $ab = C$ is satisfied, with C a constant, a change in a or b will not affect the value of x. Because $\mathcal{LL}(\boldsymbol{\theta})$ depends on the model output, structural non-identifiability corresponds to a manifold with constant $\mathcal{LL}(\boldsymbol{\theta})$ in parameter space. When no unique minimum of $\mathcal{LL}(\boldsymbol{\theta})$ with respect to θ_i exists, the parameter θ_i is structurally non-identifiable. Practical non-identifiability is dependent on the quality and amount of the experimental data. Following Raue et al., we define a practically non-identifiable parameter as "a parameter with a confidence region that is infinitely extended in increasing and/or decreasing direction of θ_i, although the likelihood has a unique minimum for this parameter" [281]. We will give an example of both structural and practical non-identifiability in Subsection 1.3.3.3. In this section, we will first introduce the Scaling Invariance Method as presented by Castro and De Boer to identify structurally non-identifiable parameters (Subsection 1.3.3.1). We will then introduce the Profile Likelihood Approach as presented by Raue et al. to identify both structurally and practically non-identifiable parameters. The Profile Likelihood Approach also returns confidence intervals for each parameter estimate.

1.3.3.1 The scaling invariance method

The Scaling Invariance Method by Castro and De Boer is a simple method that is sufficient to identify structurally non-identifiable parameters by considering invariances of the model

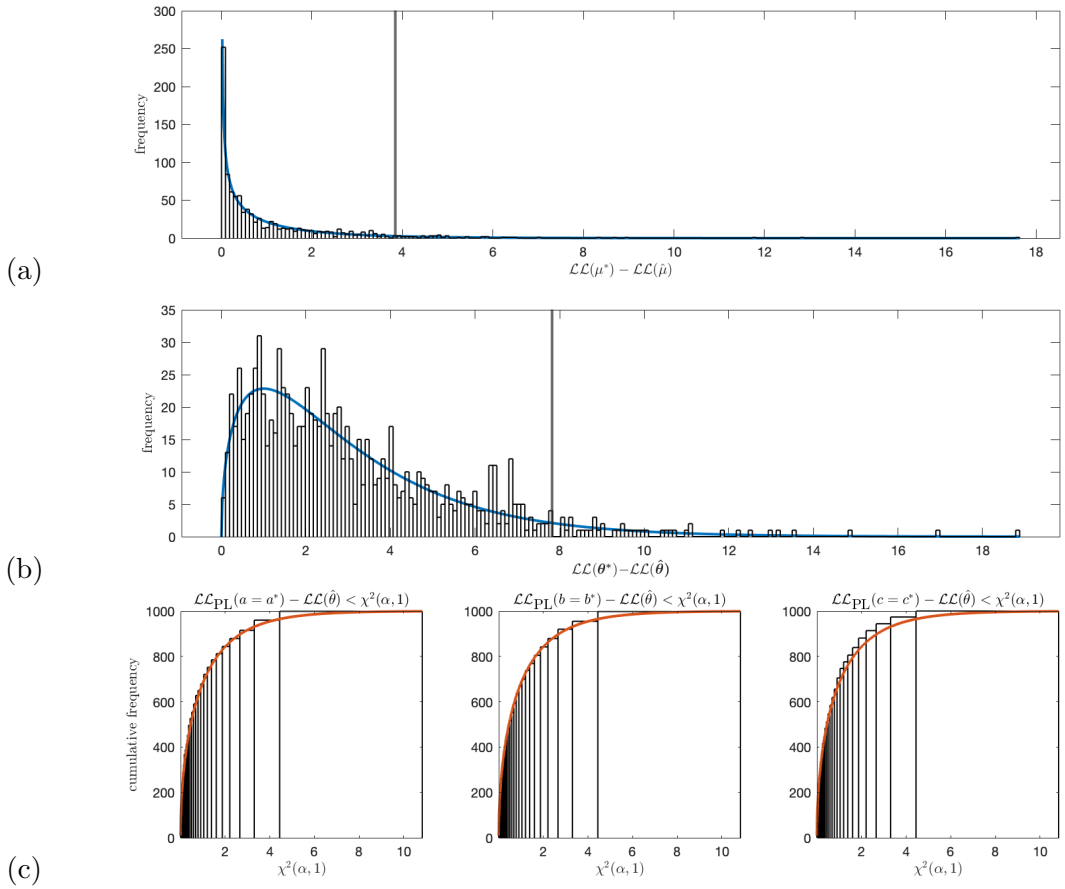


Figure 1.6: (a) The χ^2 distribution with one degree of freedom (blue) and a histogram of the values of $\mathcal{LL}(\mu^*) - \mathcal{LL}(\hat{\mu})$ for a thousand independent datasets, each consisting of ten samples drawn from $\mathcal{N}(0, 1)$, a standard normal distribution, where $\mu^* = 0$ and $\hat{\mu}$ are the true and estimated values of the mean. Assuming we know each dataset consists of ten samples drawn from $\mathcal{N}(\mu, 1)$, with known standard deviation $\sigma = 1$, we estimated the value of the mean μ by log-likelihood minimization independently for each of the thousand datasets. In 95% of all cases, the value of $\mathcal{LL}(\mu^*) - \mathcal{LL}(\hat{\mu})$ is smaller than $\chi^2(0.95, 1)$ (vertical grey line). (b) The χ^2 distribution with three degrees of freedom (blue) and a histogram of the values of $\mathcal{LL}(\boldsymbol{\theta}^*) - \mathcal{LL}(\hat{\boldsymbol{\theta}})$ for a thousand independent datasets, each consisting of ten samples drawn from a $\mathcal{N}(a, 1)$ distribution, ten samples drawn from a $\mathcal{N}(a + b, 1)$ distribution, and ten samples drawn from a $\mathcal{N}(a + b + c, 1)$ distribution, with $a = 10, b = 20, c = 30$. Assuming a known standard deviation $\sigma = 1$, we estimated the values of $\boldsymbol{\theta} = \{a, b, c\}$ by log-likelihood minimization independently for each of the thousand datasets. Here, we assume we know for each dataset that the first ten samples are drawn from a $\mathcal{N}(a, 1)$ distribution, the second ten samples from a $\mathcal{N}(a+b, 1)$ distribution, and the last ten samples drawn from a $\mathcal{N}(a + b + c, 1)$ distribution, and we estimated the values of a, b and c by log-likelihood minimization. In 95% of all cases, the value of $\mathcal{LL}(\boldsymbol{\theta}^*) - \mathcal{LL}(\hat{\boldsymbol{\theta}})$ is smaller than $\chi^2(0.95, 3)$ (vertical grey line). (c) The cumulative distribution function of χ^2 distribution with one degree of freedom (orange) and, for the same datasets as in (b), a cumulative histogram of the number of datasets for which $\mathcal{LL}_{\mathrm{PL}}(\theta_m = \theta_m^*) - \mathcal{LL}(\hat{\boldsymbol{\theta}}) < \chi^2(\alpha, 1)$, with $\theta_m = a$ (left), b (middle), and c (right).

output after application of a scaling transformation on its parameters [55]. We note that this method can only identify parameter non-identifiability due to scaling invariances. Other sources of (structural) parameter non-identifiability exist that are not detected by this method, for example those classified by discrete symmetries instead of scaling symmetries [346]. We now describe the method, assuming all variables x_i or their rate of change are measured, for at least one point in time with a value that is not zero. Given a system of differential equations

$$\frac{dx_i}{dt} = f_i(x_1, \ldots, x_n; \lambda_1, \ldots \lambda_m), \qquad i = 1, \ldots, n, \tag{1.6}$$

$$x_i(0) = x_{i,0}, \qquad i = 1, \ldots, n, \tag{1.7}$$

for n variables $x_i(t)$ and m model parameters λ_j. The method first decomposes the equations of a system of differential equations in a sum of linearly independent functions:

$$\frac{dx_i}{dt} = \sum_{k=1}^{M} f_{ik}(\tilde{x}_k, \tilde{\lambda}_k), \qquad i = 1, \ldots, n, \tag{1.8}$$

$$x_i(0) = x_{i,0}, \qquad i = 1, \ldots, n, \tag{1.9}$$

with $\tilde{x}_k$ and $\tilde{\lambda}_k$ the subset of variables and parameters included in f_{ik}. Each parameter λ_i is scaled by an unknown scaling factor u_{λ_i}. Each linearly independent function $f_{ik}(\tilde{x}_k, \tilde{\lambda}_k)$ is equated to its scaled version:

$$f_{ik}(\tilde{x}_k, \tilde{\lambda}_k) = f_{ik}(\tilde{x}_k, u_{\tilde{\lambda}_k}\tilde{\lambda}_k). \tag{1.10}$$

The equations (1.10) determine relationships between scaling factors that leave the system invariant. When it follows from equations (1.10) that $u_{\lambda_i} = 1$ for a certain scaling factor, no relationship between the corresponding parameter and other parameters is found by the method. Conversely, when it follows from equations (1.10) that u_{λ_i} need not be unity then λ_i is not structurally identifiable.

1.3.3.2 Non-observability

When a variable x_i in a system is not observed, i.e. there are no measurements of x_i or $\frac{dx_i}{dt}$ for a certain i available (or they are zero), the described method can be extended to non-identifiability of the variable x_i. In addition to the scaling factors u_{λ_k} for each parameter,

for each such x_i, $i = 1, \dots n$, we introduce a scaling factor u_{x_i} and equate each linearly independent function $f_{ik}(\tilde{x}_k, \tilde{\lambda}_k)$ to its scaled version as before. Because the scaled ODE for x_i is

$$\frac{du_{x_i}x_i}{dt} = u_{x_i}\frac{dx_i}{dt} = \sum_{k=1}^{M} f_{ik}(u_{\tilde{x}_k}\tilde{x}_k, u_{\tilde{\lambda}_k}\tilde{\lambda}_k),$$
$$u_{x_i}x_i(0) = u_{x_i}x_{i,0}, \tag{1.11}$$

we set:

$$f_{ik}(\tilde{x}_k, \tilde{\lambda}_k) = \frac{1}{u_{x_i}} f_{ik}(u_{\tilde{x}_k}\tilde{x}_k, u_{\tilde{\lambda}_k}\tilde{\lambda}_k). \tag{1.12}$$

We note that because $\frac{dx_i}{dt} = u_{x_i}\frac{dx_i}{dt}$, it follows that u_{x_i} has to be unity, i.e. $u_{x_i} = 1$, when non-zero measurements of x_i or $\frac{dx_i}{dt}$ are available. As above, if u_{x_i} need not be unity despite equation (1.12), then u_{x_i} is not a structurally identifiable variable.

1.3.3.3 The profile likelihood approach

We introduce the profile likelihood approach, which can be used to determine both structural and practical parameter un-identifiability. Andreas Raue et al. have proposed the following method to obtain confidence intervals for each parameter estimate using profile likelihoods [281]. Following Raue et al., we define log likelihood-based confidence regions as

$$\{\boldsymbol{\theta} | \mathcal{LL}(\boldsymbol{\theta}) - \mathcal{LL}(\hat{\boldsymbol{\theta}}) < \Delta_\alpha\}, \qquad \text{with } \Delta_\alpha = \chi^2(\alpha, df), \tag{1.13}$$

with Δ_α the α quantile of the χ^2 distribution with df degrees of freedom, where df is equal to the number of estimated parameters. To illustrate this, we generated a thousand independent datasets, each consisting of ten samples y_i, $i = 1, \dots 10$, drawn from $\mathcal{N}(0, 1)$, a standard normal distribution. Assuming we know each dataset consists of ten samples drawn from $\mathcal{N}(\mu, 1)$, with known standard deviation $\sigma = 1$, we estimated the value of the mean μ by log-likelihood minimization independently for each of the thousand datasets:

$$\hat{\mu} = \underset{\mu}{\operatorname{argmin}} \left(\mathcal{LL}(\mu)\right) =$$
$$\underset{\mu}{\operatorname{argmin}} \left(\sum_{i=1}^{10} \log 2\pi + \sum_{i=1}^{10} \log \sigma^2 + \sum_{i=1}^{10} \frac{(y_i - \mu)^2}{\sigma^2} \right) = \tag{1.14}$$
$$\underset{\mu}{\operatorname{argmin}} \left(\sum_{i=1}^{10} (y_i - \mu)^2 \right). \tag{1.15}$$

We show a histogram of the values of $\mathcal{LL}(\mu^*) - \mathcal{LL}(\hat{\mu})$, where $\mu^* = 0$ is the true value of the mean μ, and $\hat{\mu}$ the estimated the value of μ obtained by log-likelihood minimization (Figure 1.6 (a)). Note that the value of $\mathcal{LL}(\hat{\mu})$ will always be less or equal to $\mathcal{LL}(\mu^*)$. The value of $\mathcal{LL}(\mu^*) - \mathcal{LL}(\hat{\mu})$ gives us a measure of the amount of overfitting when using log-likelihood minimization for parameter estimation. We also show the expected χ^2 distribution with one degree of freedom (Figure 1.6 (a)). In 100α percent of all cases, the value of $\mathcal{LL}(\mu^*) - \mathcal{LL}(\hat{\mu})$ is smaller than $\chi^2(\alpha, 1)$ (e.g. indicated with a vertical grey line for $\alpha = 0.95$). When μ is assumed to be known, and the value of σ is estimated instead, a similar plot can be obtained (not shown). In a similar way, we generated a thousand data sets, each consisting of ten samples $y_{a,i}$ drawn from a $\mathcal{N}(a, 1)$ distribution, ten samples $y_{a,b,i}$ drawn from a $\mathcal{N}(a + b, 1)$ distribution, and ten samples $y_{a,b,c,i}$ drawn from a $\mathcal{N}(a + b + c, 1)$ distribution, with $a = 10, b = 20, c = 30$, $i = 1, \ldots, 10$. Again assuming the standard deviation $\sigma = 1$ is known, we estimated $\boldsymbol{\theta} = \{a, b, c\}$ by log-likelihood minimization independently for each of the thousand datasets. Here, we assume we know for each dataset that the first ten samples are drawn from a $\mathcal{N}(a, 1)$ distribution, the second ten samples from a $\mathcal{N}(a + b, 1)$ distribution, and the last ten samples drawn from a $\mathcal{N}(a + b + c, 1)$ distribution, and we estimated the values of a, b and c by log-likelihood minimization:

$$\hat{\boldsymbol{\theta}} = \underset{\boldsymbol{\theta}}{\operatorname{argmin}} \left(\mathcal{LL}(\boldsymbol{\theta})\right) = \underset{a,b,c}{\operatorname{argmin}} \left(\mathcal{LL}(a, b, c)\right)$$

$$= \underset{a,b,c}{\operatorname{argmin}} \left(\sum_{i=1}^{10} (y_{a,i} - a)^2 + \sum_{j=1}^{10} (y_{a,b,j} - a - b)^2 + \sum_{k=1}^{10} (y_{a,b,c,k} - a - b - c)^2 \right). \quad (1.16)$$

The resulting values of $\mathcal{LL}(\boldsymbol{\theta}^*) - \mathcal{LL}(\hat{\boldsymbol{\theta}})$, with $\boldsymbol{\theta}^* = \{10, 20, 30\}$ follow a χ^2 distribution with three degrees of freedom, as we estimated the values of three parameters this time (Figure 1.6 (b)). In order to obtain confidence intervals for the individual model parameters $\theta_m \in \boldsymbol{\theta}$, we will use profile likelihood based confidence intervals. We define the profile likelihood $\mathcal{LL}_{\mathrm{PL}}(\theta_m)$ as the minimal value of $\mathcal{LL}(\boldsymbol{\theta})$ with the value of the m'th parameter θ_m fixed:

$$\mathcal{LL}_{\mathrm{PL}}(\theta_m) = \min_{\tilde{\boldsymbol{\theta}}_m} \mathcal{LL}(\boldsymbol{\theta}), \quad (1.17)$$

with $\tilde{\boldsymbol{\theta}}_m = \{\theta_1, \ldots, \theta_{m-1}, \theta_{m+1}, \theta_N\}$. Starting from the maximum likelihood estimate $\hat{\boldsymbol{\theta}}$, one can now compute profile likelihood based confidence intervals for each individual parameter:

$$\{\theta_m | \mathcal{LL}_{\mathrm{PL}}(\theta_m) - \mathcal{LL}(\hat{\boldsymbol{\theta}}) < \Delta_\alpha\}, \qquad \text{with } \Delta_\alpha = \chi^2(\alpha, 1). \tag{1.18}$$

We illustrate this for the datasets used in the example with $\boldsymbol{\theta} = \{a, b, c\}$ above. For each of the thousand datasets, and each parameter $\theta_m \in \boldsymbol{\theta} = \{a, b, c\}$, we set θ_m to its true value θ_m^* and compute $\mathcal{LL}_{\mathrm{PL}}(\theta_m = \theta_m^*) - \mathcal{LL}(\hat{\boldsymbol{\theta}})$. We plot a cumulative histogram of the values of $\mathcal{LL}_{\mathrm{PL}}(\theta_m = \theta_m^*) - \mathcal{LL}(\hat{\boldsymbol{\theta}})$ and confirm it follows a $\chi^2(\alpha, 1)$ cumulative distribution function. In 100α percent of cases, $\mathcal{LL}_{\mathrm{PL}}(\theta_m = \theta_m^*) - \mathcal{LL}(\hat{\boldsymbol{\theta}})$ is smaller than $\chi^2(\alpha, 1)$ and the true value of the parameter of interest lies within the profile likelihood confidence interval with confidence level α (Figure 1.6 (c)).

In practice, to study local parameter identifiability, we will use profile likelihood plots. After obtaining maximum likelihood estimates $\hat{\theta}$, we vary the value of a model parameter θ_m and compute the corresponding values of $\mathcal{LL}_{\mathrm{PL}}(\theta_m) - \mathcal{LL}(\hat{\boldsymbol{\theta}})$. We plot $\mathcal{LL}_{\mathrm{PL}}(\theta_m) - \mathcal{LL}(\hat{\boldsymbol{\theta}})$ against the value of θ_m. The profile likelihood confidence interval is bounded by the value of $\Delta_\alpha = \chi^2(\alpha, 1)$. We recall that the true value of θ_m lies within a confidence region with confidence level α with probability α. Finite profile likelihood confidence intervals correspond to practical identifiable parameters. We show an example for one of the datasets used in the example with $\boldsymbol{\theta} = \{a, b, c\}$ above (Figure 1.7 (a)). These profile likelihood plots tell us that the true values of a, b and c lie within the intervals $\{a \mid 9.65 < a < 10.85\}$, $\{b \mid 18.97 < b < 20.69\}$, and $\{c \mid 29.03 < c < 30.74\}$ with probability $\alpha = 0.95$. We recall that the true values of a, b and c are 10, 20 and 30 respectively. Practically unidentifiable parameters result in infinite profile likelihood confidence intervals. We can not estimate their value at the given confidence level. Recall that in the example above, with $\boldsymbol{\theta} = \{a, b, c\}$, we generated datasets consisting of ten samples drawn from a $\mathcal{N}(a, 1)$ distribution, ten samples drawn from a $\mathcal{N}(a+b, 1)$ distribution, and ten samples drawn from a $\mathcal{N}(a+b+c, 1)$ distribution, with $a = 10, b = 20, c = 30$. All three parameters are identifiable. To illustrate a case of structural parameter unidentifiability, we generated a dataset consisting of ten samples $y_{a,b,i}$ drawn from a $\mathcal{N}(a + b, 1)$ distribution, and ten samples $y_{a,b,c,i}$ drawn from a

$\mathcal{N}(a+b+c,1)$ distribution, with $a=10, b=20, c=30$, $i=1,\ldots,10$. We again obtain estimates of a, b and c by log-likelihood minimization:

$$\hat{\boldsymbol{\theta}} = \underset{a,b,c}{\operatorname{argmin}} \left(\mathcal{LL}(a,b,c)\right)$$
$$= \underset{a,b,c}{\operatorname{argmin}} \left(\sum_{j=1}^{10} (y_{a,b,j} - a - b)^2 + \sum_{k=1}^{10} (y_{a,b,c,k} - a - b - c)^2 \right). \tag{1.19}$$

The profile likelihood plots for a and b are flat in this case, as both parameters are structural unidentifiable, noting this is a sufficient condition for practical unidentifiability as structural non-identifiability entail parameters can never be identified, even with perfect data (Figure 1.7 (b)). Finally, we give an example of practical non-identifiability. We generate a dataset consisting of ten samples $y_{a,i}$ drawn from a log normal $\mathcal{N}(\log_{10}(a),1)$ distribution, ten samples $y_{a,b,i}$ drawn from a $\mathcal{N}(\log_{10}(a+b),1)$ distribution, and ten samples $y_{a,b,c,i}$ drawn from a $\mathcal{N}(\log_{10}(a+b+c),1)$ distribution, with $a=10, b=20, c=30$, $i=1,\ldots,n$. We again obtain estimates of a, b and c by log-likelihood minimization:

$$\begin{aligned} \hat{\boldsymbol{\theta}} &= \underset{a,b,c}{\operatorname{argmin}} \left(\mathcal{LL}(a,b,c)\right) \qquad (1.20) \\ &= \underset{a,b,c}{\operatorname{argmin}} \left(y_a - \log_{10}(a))^2 + \sum_{j=1}^{10} (y_{a,b,j} - \log_{10}(a+b))^2 + \sum_{k=1}^{10} (y_{a,b,c,k} - \log_{10}(a+b+c))^2 \right). \end{aligned}$$

This time, the confidence intervals for both b and c are not bounded from below and therefore these parameters are practically unidentifiable for this data (Figure 1.8 (a)). We can resolve this practical unidentifiability by increasing the number of samples from three times 10 to three times a 100 (Figure 1.8 (b)).

The profile likelihood approach has been implemented in the Matlab based modelling environment 'Data2Dynamics', that we will use throughout this thesis [284].

An alternative to profile likelihoods is MCMC sampling. Using this approach, parameter values are sampled from the posterior probability distribution of parameters. This posterior distribution of parameters follows from Bayes' Theorem and equals the likelihood function (equation (1.3)), multiplied by the prior probability density function of the parameters, and normalized to become a probability distribution. When the prior probability density function is assumed to be uniform, the likelihood function is proportional to the posterior

(a)

(b)

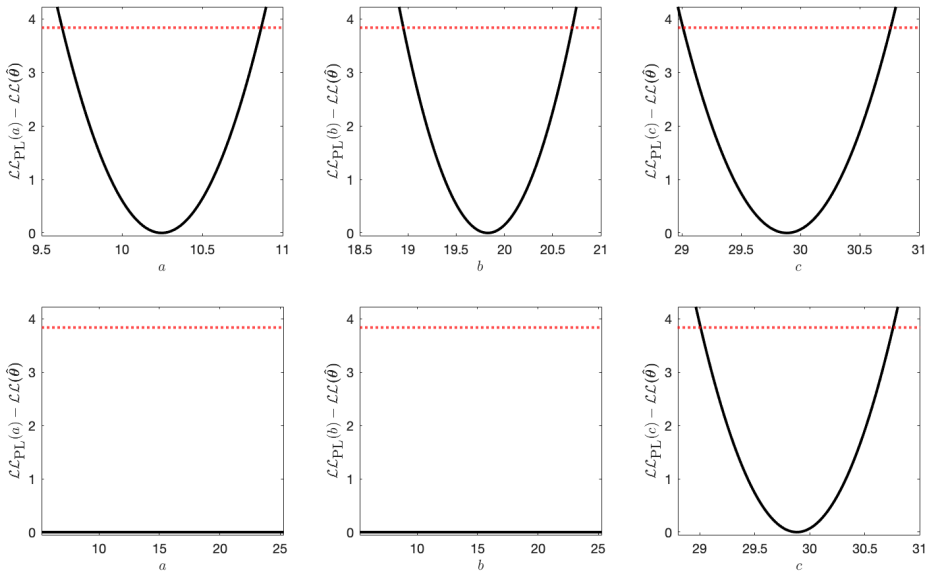


Figure 1.7: (a) Profile likelihood plots for identifiable parameters a, b and c. We generated a dataset consisting of ten samples drawn from a $\mathcal{N}(a, 1)$ distribution, ten samples drawn from a $\mathcal{N}(a+b, 1)$ distribution, and ten samples drawn from a $\mathcal{N}(a+b+c, 1)$ distribution, with $a = 10, b = 20, c = 30$. Assuming a known standard deviation $\sigma = 1$, we estimated the values of $\boldsymbol{\theta} = \{a, b, c\}$ by log-likelihood minimization, resulting in parameter estimates $\hat{\boldsymbol{\theta}}$. Here, we assume we know for each dataset that the first ten samples are drawn from a $\mathcal{N}(a, 1)$ distribution, the second ten samples from a $\mathcal{N}(a+b, 1)$ distribution, and the last ten samples drawn from a $\mathcal{N}(a+b+c, 1)$ distribution, and we estimated the values of a, b and c by log-likelihood minimization. For each parameter $\theta_m \in \{a, b, c\}$, we plot $\mathcal{LL}_{\mathrm{PL}}(\theta_m) - \mathcal{LL}(\hat{\boldsymbol{\theta}})$ against the value of θ_m. We also show the 95% confidence interval threshold (dashed, red). All three parameters are identifiable in this case. These profile likelihood plots tell us that the true values of a, b and c lie within the intervals $\{a \mid 9.65 < a < 10.85\}$, $\{b \mid 18.97 < b < 20.69\}$, and $\{c \mid 29.03 < c < 30.74\}$ with probability $\alpha = 0.95$. (b) Profile likelihood plots for structural unidentifiable parameters a and b, and identifiable c. We generated a dataset consisting of ten samples drawn from a $\mathcal{N}(a + b, 1)$ distribution, and ten samples drawn from a $\mathcal{N}(a + b + c, 1)$ distribution, with $a = 10, b = 20, c = 30$. Assuming a known standard deviation $\sigma = 1$, we estimated the values of $\boldsymbol{\theta} = \{a, b, c\}$ by log-likelihood minimization, resulting in parameter estimates $\hat{\boldsymbol{\theta}}$. Here, we assume we know for each dataset that the first ten samples are drawn from a $\mathcal{N}(a + b, 1)$ distribution, and the last ten samples drawn from a $\mathcal{N}(a+b+c, 1)$ distribution, and we estimated the values of a, b and c by log-likelihood minimization. For each parameter $\theta_m \in \{a, b, c\}$, we plot $\mathcal{LL}_{\mathrm{PL}}(\theta_m) - \mathcal{LL}(\hat{\boldsymbol{\theta}})$ against the value of θ_m. We also show the 95% confidence interval threshold $\Delta_{95\%} = \chi^2(95\%, 1)$ (dashed, red). The profile likelihood plots for a and b are flat in this case, as both parameters are unidentifiable.

(a)

(b)

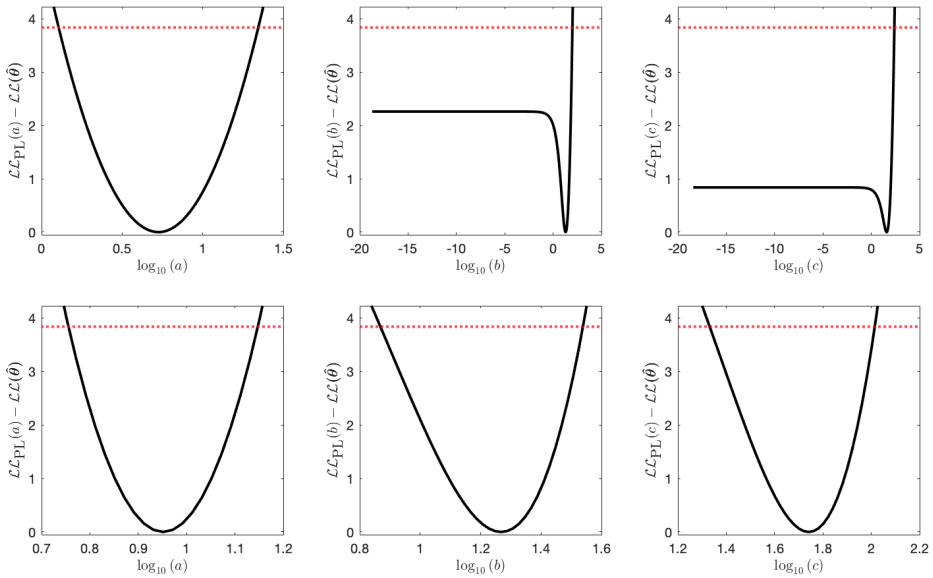


Figure 1.8: (a) Profile likelihood plots for practically unidentifiable parameters b and c, and identifiable a. We generated a dataset consisting of ten samples drawn from a $\mathcal{N}(\log_{10}(a), 1)$ distribution, ten samples drawn from a $\mathcal{N}(\log_{10}(a+b), 1)$ distribution, and ten samples drawn from a $\mathcal{N}(\log_{10}(a+b+c), 1)$ distribution, with $a = 10, b = 20, c = 30$. Assuming a known standard deviation $\sigma = 1$, we estimated the values of $\boldsymbol{\theta} = \{a, b, c\}$ by log-likelihood minimization, resulting in parameter estimates $\hat{\boldsymbol{\theta}}$. Here, we assume we know for each dataset that the first ten samples are drawn from a $\mathcal{N}((\log_{10}(a), 1)$ distribution, the second ten samples from a $\mathcal{N}((\log_{10}(a+b), 1)$ distribution, and the last ten samples drawn from a $\mathcal{N}((\log_{10}(a+b+c), 1)$ distribution, and we estimated the values of a, b and c by log-likelihood minimization. For each parameter $\theta_m \in \{a, b, c\}$, we plot $\mathcal{LL}_{\mathrm{PL}}(\theta_m) - \mathcal{LL}(\hat{\boldsymbol{\theta}})$ against the value of $\log_{10}(\theta_m)$. We also show the 95% confidence interval threshold $\Delta_{95\%} = \chi^2(95\%, 1)$ (dashed, red). The value of $\mathcal{LL}_{\mathrm{PL}}(\theta_m) - \mathcal{LL}(\hat{\boldsymbol{\theta}})$ reaches a plateau for decreasing $\log_{10}(b)$ and $\log_{10}(c)$ and never reaches the 95% confidence interval threshold $\Delta_{95\%} = \chi^2(95\%, 1)$. Therefore, both b and c are practically unidentifiable at the 95% confidence level. (b) Profile likelihood plots for identifiable parameters a, b and c. We generated a dataset consisting of hundred samples drawn from a $\mathcal{N}(\log_{10}(a), 1)$ distribution, hundred samples drawn from a $\mathcal{N}(\log_{10}(a+b), 1)$ distribution, and hundred samples drawn from a $\mathcal{N}(\log_{10}(a+b+c), 1)$ distribution, with $a = 10, b = 20, c = 30$. Assuming a known standard deviation $\sigma = 1$, we estimated the values of $\boldsymbol{\theta} = \{a, b, c\}$ by log-likelihood minimization, resulting in parameter estimates $\hat{\boldsymbol{\theta}}$. Here, we assume we know for each dataset that the first hundred samples are drawn from a $\mathcal{N}((\log_{10}(a), 1)$ distribution, the second hundred samples from a $\mathcal{N}((\log_{10}(a+b), 1)$ distribution, and the last hundred samples drawn from a $\mathcal{N}((\log_{10}(a+b+c), 1)$ distribution, and we estimated the values of a, b and c by log-likelihood minimization. For each parameter $\theta_m \in \{a, b, c\}$, we plot $\mathcal{LL}_{\mathrm{PL}}(\theta_m) - \mathcal{LL}(\hat{\boldsymbol{\theta}})$ against the value of $\log_{10}(\theta_m)$. We also show the 95% confidence interval threshold $\Delta_{95\%} = \chi^2(95\%, 1)$ (dashed, red). All three parameters are identifiable at the 95% confidence level in this case. The profile likelihood plots tell us that the true values of a, b and c lie within the intervals $\{a \mid 5.91 < a < 13.54\}$, $\{b \mid 7.73 < b < 33.73\}$, and $\{c \mid 21.95 < c < 100.32\}$ with probability $\alpha = 0.95$.

probability distribution and both methods (i.e. MCMC sampling and profile likelhoods) yield similar results when used to determine parameter identifiability [282, 283].

When a likelihood function is not available, such as for stochastic models, techniques such as approximate Bayesian computation (ABC) for parameter estimation could be used [335].

1.3.4 Parameter sensitivity analysis

Sensitivity analysis gives insight in how uncertainty in the value of the model parameters and initial conditions impacts the model simulations [213]. We will use the Extended Fourier Amplitude Sensitivity Test (eFAST) for sensitivity analysis, developed by Saltelli et al., and based on the Fourier Amplitude Sensitivity Test developed by Cukier et al. [73, 295]. We will use the Matlab based implementation by Marino et al. [213]. We will also closely follow the introduction to eFAST by Marino et al. in this section [213]. eFAST is a variance decomposition method using Fourier analysis. We first select the model output y we are interested in, e.g. one of the model variables at a specific point in time. The model output y will vary depending on the value of its input parameters x_i, $i = 1, \ldots$. We will express the value of each input parameter as the output of a sinusoidal function $x_i(z) = f_{\omega_{x_i}}(z)$ of $-\pi < z < \pi$, with frequency ω_{x_i}, where ω_{x_i} is an even integer. For parameter of interest p, a sinusoidal function $f_{\omega_p}(z)$ with even integer frequency ω_p is chosen and for all other model parameters $q, q \neq p$, a sinusoidal function $f_{\omega_q}(z)$ with even integer frequency ω_q, with $\omega_q < \omega_p/2$ is chosen. The corresponding ODE model outputs $y(z) = y(x_1(z), \ldots)$ can be expanded in a Fourier series:

$$y(z) = \sum_{j=-\infty}^{\infty} A_j \cos(jz) + B_j \sin(jz), \tag{1.21}$$

$$A_j = \frac{1}{2\pi} \int_{-\pi}^{\pi} y(z) \cos(jz) \mathrm{d}z, \tag{1.22}$$

$$B_j = \frac{1}{2\pi} \int_{-\pi}^{\pi} y(z) \sin(jz) \mathrm{d}z, \tag{1.23}$$

with $j \in \{-\infty, \ldots, -1, 0, 1, \ldots, \infty\}$, $-\pi < z < \pi$. By parity, we have $A_j = A_{-j}$ and $B_j = -B_{-j}$. Now N_s equally spaced sample points are chosen from the interval $-\pi < z < \pi$. Using the corresponding model output values $y(z_n) = y(x_1(z_n), \ldots)$, the contribution to the

model output variation by parameter p is estimated by:

$$s_p^2 = 2\sum_{j=1}^{M}(\hat{A}_{j\omega_p}^2 + \hat{B}_{j\omega_p}^2), \tag{1.24}$$

with the integer M the maximum number of harmonics of frequency ω_p that are considered, and $\hat{A}_j$ and $\hat{B}_j$ the estimated values of A_j and B_j using the N_s sample points, i.e.:

$$\hat{A}_j = \frac{1}{N_s}\sum_{n=1}^{N_s} y(z_n)\cos(jz_n), \tag{1.25}$$

$$\hat{B}_j = \frac{1}{N_s}\sum_{n=1}^{N_s} y(z_n)\sin(jz_n). \tag{1.26}$$

Similarly, the contribution to the model output variation by all complementary parameters q, $q \neq p$ is estimated by:

$$s_{cp}^2 = 2\sum_{j=1}^{\omega_p/2}(\hat{A}_j^2 + \hat{B}_j^2), \tag{1.27}$$

where we recall that all ω_q have been chosen such that $\omega_q < \omega_p/2$. The bound of M in the summation of equation (1.24) and $w_p/2$ in equation (1.27) ensure that interference at high modes, which is not intended, does not feature in these estimates. However these cutoffs are also a source of error in the algorithm, and hence the need for a dummy parameter as detailed below. The total sample variance $s_{p,total}$ of the model output is given by

$$s_{p,total}^2 = \sum_{n=1}^{N_s}\frac{(y(z_n) - \bar{y})}{(N_s - 1)}, \tag{1.28}$$

with N_s the number of samples, $y(z_n)$ the model output for each sample n, and $\bar{y}$ the average model output over the N_s samples. The sensitivity index for parameter p is then given by

$$S_p = \frac{s_p^2}{s_{p,total}^2}. \tag{1.29}$$

The total-order sensitivity index for parameter p is given by

$$S_{Tp} = 1 - \frac{s_{cp}^2}{s_{p,total}^2}. \tag{1.30}$$

The total-order sensitivity index gives a measure of the fraction of model output variance that is not explained by the other, complementary parameters. This fraction of the variance is a sum of the first order sensitivity index S_p and variance resulting form non-linear

interactions between p and the other parameters [213]. In Chapter 2, we will repeat the described procedure N_r times for each parameter of interest S_p. For each of the N_r repeats, a random phase shift is introduced in each of the sinusoidal functions $f_{\Omega_i}(s)$, $i = 1, \ldots,$ from which the parameter values are sampled. The reported sensitivity indices S_p and S_{Tp} are averages of the N_r different S_p and S_{Tp} returned. We will also include a dummy parameter that does not appear in the model equations and therefore acts as a negative control. The total number of function evaluations is N_s times N_r times N_p, with N_p the number of parameters plus 1, for the dummy parameter. The dummy parameter indicates the small size of algorithm artefact, such as interference between modes and a finite cut-off in equations (1.24) and (1.27).

1.3.5 Model selection

Several methods exist for model comparison, given a specific set of data. The standard method in biological sciences is the Akaike information criterium (AIC) [49]. The AIC is an asymptotically unbiased estimator of relative Kullback–Leibler information. Assume we have a set of j probability density functions $g_j(\mathbf{x}|\boldsymbol{\theta}_j)$, dependent on parameter sets $\boldsymbol{\theta}_j$. In this context, these probability density functions represent the set of models we would like to compare. Note that in this section, the functions $g_j(\mathbf{x}|\boldsymbol{\theta}_j)$ can define any probability distribution. Let further the probability density function $f(\mathbf{x})$ represent unknown 'reality'. Given a large set of observations y_i, $i \in \{1, 2, 3, \ldots\ N\}$ drawn independently from $f(\mathbf{x})$, we can compute maximum likelihood estimates $\hat{\boldsymbol{\theta}}_j$ for each model $g_j(\mathbf{x}|\boldsymbol{\theta}_j)$, by maximizing the logarithm of the likelihood function $\mathcal{L}(\boldsymbol{\theta}_j) = \prod_i g_j(y_i|\boldsymbol{\theta}_j)$, over $\boldsymbol{\theta}_j$:

$$\hat{\boldsymbol{\theta}}_j = \underset{\boldsymbol{\theta}_j}{\operatorname{argmax}} \log\left(\mathcal{L}(\boldsymbol{\theta}_j)\right) = \underset{\theta_\mathbf{j}}{\operatorname{argmax}} \sum_i \log\left(g_j(y_i|\boldsymbol{\theta}_j)\right). \tag{1.31}$$

As explained in [49, 50], the Kullback-Leibler information I for probability distributions $f(\mathbf{x})$ and $g_j(\mathbf{x}|\hat{\boldsymbol{\theta}}_j)$ is defined as

$$I(f, g_j) = \int f(\mathbf{x}) \log\left(\frac{f(\mathbf{x})}{g_j(\mathbf{x}|\hat{\boldsymbol{\theta}}_j)}\right) \mathrm{d}\mathbf{x} = \int f(\mathbf{x}) \log\left(f(\mathbf{x})\right) d\mathbf{x} - \int f(\mathbf{x}) \log\left(g_j(\mathbf{x}|\hat{\boldsymbol{\theta}}_j) \mathrm{d}\mathbf{x}\right). \tag{1.32}$$

I is the information lost when $g_j(\mathbf{x}|\hat{\boldsymbol{\theta}}_j)$ is used to approximate $f(\mathbf{x})$ [49, 50]. We can select the model that best represents reality by minimizing I over all models j. Note that

$\int f(\mathbf{x}) \log(f(\mathbf{x}))\mathrm{d}\mathbf{x}$ is independent of the model choice j, so to find the best model, we should maximize

$$K_j = \int f(\mathbf{x}) \log(g_j(\mathbf{x}|\hat{\boldsymbol{\theta}}_j))\mathrm{d}\mathbf{x} \tag{1.33}$$

over j. Using the set of samples y_i drawn from $f(\mathbf{x})$, a naive approximation of the integral is

$$K_j \approx \frac{1}{N}\sum_i \log(g_j(y_i|\hat{\boldsymbol{\theta}}_j)) = \frac{\log\left(\mathcal{L}(\hat{\boldsymbol{\theta}}_j)\right)}{N}. \tag{1.34}$$

However, this approximation is biased because the data has been used both for the estimation of the parameter values and for the approximation of the K_j. Akaike has shown that an asymptotically unbiased (i.e. unbiased for an increasing set of observations and fixed number of model parameters) estimator $\hat{K_j}$ of the expected relative Kullback-Leibler information is given by

$$\hat{K_j} = \frac{\log\left(\mathcal{L}(\hat{\boldsymbol{\theta}}_j)\right)}{N} - \frac{P_j}{N}, \tag{1.35}$$

with P_j the number of parameters of model j (see for a derivation [49]). Usually, this result is multiplied by $-2N$, resulting in the AIC value for model selection:

$$AIC_j = -2\log\left(\mathcal{L}(\hat{\boldsymbol{\theta}}_j)\right) + 2P_j. \tag{1.36}$$

When comparing a set of models, we select the model with the lowest AIC value.

1.3.6 Differential equations

We will use differential equations (DEs) throughout the thesis. In this section we will give some background information on DEs, and how we will solve them. We will only consider deterministic DEs. Ordinary differential equations (ODEs) describe the evolution of entities of interest with respect to an independent variable, usually time. Partial differential equations (PDEs) describe the evolution of entities of interest with respect to multiple independent variables, such as time and space, or time and age or size [92, 229, 347]. Some DEs can be solved analytically. Multiple methods exist to obtain numerical solutions of DEs, such as finite difference and finite element methods [329]. In this thesis, we will use finite difference methods to numerically solve the ODEs presented. Given the following initial

value problem (ODE with an initial condition):

$$\frac{dy(t)}{dt} = f(y(t), t), \qquad \text{with } y(t_0) = y_0, \tag{1.37}$$

where $y(t)$ describes the state of the entity of interest, and $f(y(t), t)$ a function describing the evolution of $y(t)$ over time. Following [329], we define a time interval of interest $[t_0, T]$ and divide the interval in mesh points $t_n = t_0 + nh, n = 0, 1, \ldots, N$, with $h = (T - t_0)/N$ and $N > 0$ an integer. We assume a unique solution $y(t_n)$ of the system of equations exists for each time point of interest t_n. We approximate $y(t_n)$ with y_n. The values y_n are calculated for $n = 0, 1, 2, \ldots, N$ using a finite difference method. The simplest finite difference method is the forward Euler method, that sets

$$y_{n+1} = y_n + hf(x_n, y_n), \qquad n = 0, 1, 2, \ldots, N. \tag{1.38}$$

Starting from $y = y_0$ at $t = t_0$, the values of y_n can be calculated. A Taylor series expansion of y around t_n gives

$$y(t_{n+1}) = y(t_n) + hf(t_n, y_n) + \frac{h^2}{2}\frac{\mathrm{d}^2 y}{\mathrm{d}t^2}(t_n) + \ldots, \tag{1.39}$$

We note that the Euler method is a linear extrapolation of the time derivative at t_n. Terms of order h^2 and higher are ignored. A more accurate method is the modified Euler method, given by

$$y_{n+1} = y_n + hf(t_n + \frac{1}{2}h, y_n + \frac{1}{2}hf(x_n, y_n)), \qquad n = 0, 1, 2, \ldots, N. \tag{1.40}$$

Following [329], we define the local truncation errors of both methods as:

$$T_n = \frac{y_{n+1} - y_n}{h} - \Phi(t_n, y(t_n); h), \tag{1.41}$$

with $\Phi(t_n, y(t_n); h) = f(t_n, y_n)$ and $\Phi(t_n, y(t_n); h) = f(t_n + \frac{1}{2}h, y_n + \frac{1}{2}hf(x_n, y_n))$ for Forward and modified Euler respectively. The global error of a method is defined as

$$e_n = y(t_n) - y_n. \tag{1.42}$$

It can be shown that the rate at which the global error e_n of the Euler method decays to zero when $h \to 0$ is of order $\mathcal{O}(h)$ and the rate at which the global error of the modified

Euler method decays to zero is of order $\mathcal{O}(h^2)$ (see [329, Chapter 12] for a derivation). This means that halving the step size h reduces the global error by a factor of about 2 and 4 for the Euler and modified Euler respectively. We note that the Euler method requires a single evaluation of $f(y(t), t)$ per time step. The modified Euler method requires two evaluations. More accurate methods exist, but involve more function evaluations. We refer to [329] for an overview of commonly used schemes. We will use the matlab ODE solver 'ODE45' to solve the ODEs in Chapters 2 and 3. ODE45 adapts the step size h based on an estimate of the size of the local truncation error using a 4'th and 5'th order method, where the order of a method corresponds to the rate at which the local truncation error decays as $h \to 0$.

In Chapter 4, we will use the method of characteristics to convert our PDE model into a system of ODEs, that we then solve using the modified Euler method. See [253] for a more detailed introduction on the method of characteristics. Specialising to a PDE of the form:

$$y_t(x,t) + f(x,t)y_x = g(x,y,t), \qquad -\infty < x < \infty, t > 0, \tag{1.43}$$

$$y(x,0) = y_0(x), -\infty < x < \infty, t = 0 \tag{1.44}$$

with $f(x,t)$, $g(x,y,t)$ known functions of $x, t \geq 0$, and $x, y, t \geq 0$. We can view $y(x,t)$ as the height of a surface above the x,t plane. When we trace out a path on the (x,t) plane, the corresponding value of $y(x,t)$ changes both because of changes in x and changes in t. We define the total derivative of $y(x,t)$ while following such a path over time as

$$\frac{\mathrm{d}y}{\mathrm{d}t} = y_x \frac{\mathrm{d}x}{\mathrm{d}t} + y_t. \tag{1.45}$$

Now, we consider a path on the x,t plane that satisfies

$$\frac{\mathrm{d}x}{\mathrm{d}t} = f(x,t). \tag{1.46}$$

When we move along this path, it follows that

$$\frac{\mathrm{d}y}{\mathrm{d}t} = y_x f(x,t) + y_t = g(x,y,t). \tag{1.47}$$

Therefore, the change in the height y is given by $g(x,y,t)$ when we move along the path. We start the path at the boundary of the (x,t) plane. We define the characteristic coordinate ξ as

$$x(\xi,0) = \xi, \qquad y(\xi,0) = y_0(\xi). \tag{1.48}$$

Hence, ξ is the value of x on the path at $t = 0$. The system of ODEs

$$\frac{\mathrm{d}x}{\mathrm{d}t} = f(x,t) \tag{1.49}$$

$$\frac{\mathrm{d}y}{\mathrm{d}t} = g(x,y,t), \tag{1.50}$$

$$x(0) = \xi, y(0) = y_0(\xi) \text{ at } t = 0, \tag{1.51}$$

traces out the solution curve along the path identified by ξ. Now, by varying ξ, we obtain a collection of curves that trace out the solution $y(x,t)$ of equations (1.43)-(1.44). These curves are called characteristic curves $(x(t;\xi), y(t;\xi))$, with ξ the characteristic coordinate that identifies the curve. The corresponding paths in the (x,t) plane are called characteristic projections.

Now we generalise to consider an example with a boundary condition at $x = 0$:

$$y_t(x,t) + f(x,t)y_x = g(x,y,t), \qquad x > 0, t > 0 \tag{1.52}$$

$$y(x,0) = 0, x > 0, t = 0 \tag{1.53}$$

$$y(0,t) = y_b(t), t > 0, x = 0 \tag{1.54}$$

with $f(x,t)$, $g(x,y,t)$ known functions of $x, t \geq 0$, and $x, y, t \geq 0$. This time, we also have characteristic curves starting at the boundary at $x = 0$. We define the characteristic coordinate τ as

$$y(0,\tau) = y_b(\tau). \tag{1.55}$$

The system of ODEs

$$\frac{\mathrm{d}x}{\mathrm{d}t} = f(x,t) \tag{1.56}$$

$$\frac{\mathrm{d}y}{\mathrm{d}t} = g(x,y,t), \tag{1.57}$$

$$x(\tau) = 0, y(\tau) = y_b(\tau) \text{ at } t = \tau, \tag{1.58}$$

traces out the solution of equations (1.52)-(1.54) along the paths identified by τ, that start at $x = 0$.

1.3.7 Alternative modelling techniques

. We give brief descriptions of discrete Boolean model and Graphical Gaussian models. These modelling methods are not used in the thesis, but we introduce them as they can be used for network reconstruction, relevant in the context of Chapter 2. We refer to the review by Markowetz and Spang for a more in depth review of the various modelling methods for network reconstruction [217].

A Boolean model or logical model consists of nodes with a binary value 0 or 1, and interactions between the nodes represented by directed edges. Each node represents an entity of interest, such as a particular gene or cytokine. When this entity is expressed above a certain threshold value, the node has value 1. Else, it has value 0. The Boolean model is updated in discrete time steps. The value of a node a at the next time-step t_{n+1} is determined by its Boolean update function. This function can have various forms, but is dependent on the values of all nodes at time t_n that influence node a via a directed edge. A simple Boolean update function is $a(t_{n+1}) = b(t_n)$ OR $c(t_n)$, for a model consisting of three nodes a, b and c, and with directed positive edges from b to a and from c to a. The value of a at time point t_{n+1} is 1 if b or c have value 1 at time point n. If both b and c are 0 at t_n, a is 0 at t_{n+1} [11].

A Graphical Gaussian model also consists of nodes representing the entities of interest, and edges representing interactions. Edges of a Graphical Gaussian model are undirected and self-edges are not allowed. In the context of cytokines, this method assumes the data of the production rate of P cytokines of interest follows a multivariate normal distribution $\boldsymbol{Y} \sim N(\boldsymbol{\mu}, \boldsymbol{\Sigma}^2)$, $\boldsymbol{Y} = (Y_1, \ldots, Y_P)$, with covariance matrix $\boldsymbol{\Sigma}$, with $\boldsymbol{\Sigma}$ invertible. Given n samples $\boldsymbol{y}^l = (y_1^l, \ldots, y_P^l)$, $l = 1, \ldots, n$ from $\boldsymbol{Y}$, we can calculate the sample covariance matrix S, with elements

$$s_{i,j} = \frac{1}{n} \sum_{l=1}^{n} (y_i^l - \bar{x_i})(y_j^l - \bar{y_j})^T, \tag{1.59}$$

with $\bar{y_i} = \frac{1}{n} \sum_{l=1}^{n} (y_i^l)$ the sample mean. The method assumes the sample covariance matrix S is invertible. We define the precision matrix $\Theta = \Sigma^{-1}$ as the inverse of the covariance matrix. We also define partial correlation coefficients between nodes i and j as $\psi_{i,j} = -\frac{\Theta_{i,j}}{\sqrt{\Theta_{i,i}\Theta_{j,j}}}$. A partial correlation coefficient gives a measure of the correlation between two

variables, after the removal, for both variables, of the linear relationship with all other variables (nodes) in the model. We define a saturated Graphical Gaussian model as a Graphical Gaussian model with all edge weights between nodes i and j, $i \neq j$ not equal to zero. The value of the sample partial correlation coefficients $\hat{\psi}_{i,j} = -\frac{\hat{\Theta}i,j}{\sqrt{\hat{\Theta}i,i\hat{\Theta}j,j}}$, with $\hat{\Theta} = S^{-1}$, corresponds to the edge weights in a saturated Graphical Gaussian Model. The number of edges in the Graphical Gaussian model can be reduced by applying a regularization method, such as the 'least absolute shrinkage and selection operator' (LASSO), that applies a penalty to the log likelihood function of the precision matrix [109]. The log likelihood function of the precision matrix Θ, given the data, is given by

$$\max_{\Theta} \left(\log \text{determinant}(\Theta) - \text{trace}(S\Theta)\right). \tag{1.60}$$

By differentiating with respect to Θ, it can be shown that $\hat{\Theta} = S^{-1} = \Omega$ is the maximum likelihood estimator of equation (1.60). Therefore, with no penalty, the full saturated Graphical Gaussian model is selected [354]. The LASSO penalized log likelihood function is given by:

$$\max_{\Theta} \left(\log \text{determinant}(\Theta) - \text{trace}(S\Theta) - \rho||\Theta||_1\right), \tag{1.61}$$

with the 1-norm of Θ, $||\Theta||_1$, the sum of the absolute values of the elements of Θ, and ρ a threshold value. The threshold value can be set to a range of values. For an increasing threshold, the maximum likelihood estimator of equation (1.61), $\hat{\Theta}$, will contain an increasing number of zero elements. Each additional zero element corresponds to a removed edge from the Graphical Gaussian model. Based on the value of the (non-penalized) log-likelihood function and the number of non-zero edge parameters for a range of different threshold values ρ, a model selection criterium such as the AIC (see Section 2.6) can be applied to select the optimal model that balances the model fit and data [96].

In Chapter 2, we will use an ODE based method for network selection. We have chosen an ODE approach over a discrete Boolean model as introduced above, as an ODE model allows a quantification of cytokine input levels and secretion rates on a continuous scale [220, 221, 238]. Furthermore, this type of model could easily be extended to incorporate more complicated (non-linear) interactions than currently considered, and can be used to analyse data at various points in time. The network inference method developed in

Chapter 2 requires data on the effects of the blockage of single cytokines on the system (interventional data). If such data is not available (i.e. if only observational data is available), a Graphical Gaussian model could be a suitable alternative. We note that data-based approaches, including Grapical Gaussian models, typically consider the correlation structure of the underlying dataset [217]. This makes them ill-suited for highly connected cytokine interaction data, where one cytokine"A" (e.g. non-inflammatory IL10) might down-regulate cytokine"B" (e.g. pro-inflammatory IL1) secretion (negative correlation), but cytokine B might simultaneously upregulate cytokine A secretion (positive correlation). Further, both positive and negative self-edges cannot be identified by correlation based methods, but can be by our ODE based method. Further details on our choice of our method over other, existing methods can be found in J.Jansen et al [164] (a manuscript on the network inference method described in Chapter 2, currently in review).

1.4 Thesis aims

We will combine mechanistic mathematical modelling with existing and novel experimental data to drive insight in the role of macrophages in inflammatory bowel disease (IBD) and related chronic inflammatory diseases, with a focus on cytokine signalling, antimicrobial activity and granuloma formation. Monocyte-derived macrophages play an important role in IBD. They produce all inflammatory cytokines that have been successfully targeted to treat IBD, including TNFα, IL-12/23, and IL-6. Furthermore, many common polymorphisms and Mendelian disorders that can present with IBD and other immune mediated inflammatory diseases are linked with important macrophage signalling pathways, such as defects in the NOD2 pathway. However, the complex molecular interactions within macrophages and the interactions of macrophages with their environment in the context of IBD are still poorly understood. Current key open questions include: in what ways can signalling pathways (including the mucosal cytokine network) be targeted to offer an effective therapy for different clinical subgroups of IBD; to what degree do hyper-inflammatory processes (gain of cytokine production) and immunodeficiency (loss of bacterial killing) intersect to produce inflammatory disease; and what factors and cellular processes drive granuloma formation in inflammatory bowel disease and other granulomatic disorders. Our three research chapters

will address various aspects of these questions. We will introduce the chapter aims in this section.

1.4.1 Chapter 2: cytokine interaction networks

TNFα has proven to be a very successful strategy in the treatment of inflammatory bowel disease and other immune mediated inflammatory diseases. The success of TNFα inhibition has inspired the development of several other anti-cytokine therapies. However, cytokine therapy is both disease and patient specific. A better understanding of cytokine functioning is key for the identification of cytokine (receptor)s as new therapeutic targets and of the context in which these targets should be used. The aim of Chapter 2 is two-fold. The first aim of the chapter is to study the impact of the cytokines TNFα, IL-1α, IL-1β, IL-6, and IFNγ on the regulation of IL-23 as captured in an existing flow cytometry dataset of stimulated human blood cells. We are interested in the regulation of IL-23, as the IL-23 driven Th17 pathway has been identified as an important therapeutic target, but is still poorly understood at a mechanistic level. We will develop a method to extract a minimal, weighted network from cytokine interaction data using a simple coupled ODE system and the Akaike information criterion for model selection, and apply our method to the experimental dataset. The development of this method is the second aim of this chapter. The method could be applied to other datasets involving cytokine signalling than the one studied in this chapter. The method enables us to study indirect cytokine interactions and to quantify the effects of cytokine inhibition. The extracted network can also be used to predict the combined effects of inhibiting various cytokines simultaneously. Our ODE approach is a novel method to extract cytokine networks. It requires data on the effects of the blockage of single cytokines on the system. We have chosen an ODE approach over for instance a discrete Boolean model, as an ODE model allows to quantify cytokine input levels and production rates on a continuous scale. Furthermore, this type of model could easily be extended to incorporate more complicated (non-linear) interactions than currently considered, if appropriate data would be available.

1.4.2 Chapter 3: bacterial handling

Mutations in the nucleotide-binding oligomerization domain-containing protein 2 (NOD2) gene is the strongest genetic risk factor for Crohn's disease (CD), one of the two main types of IBD. The role of NOD2 genetic defects in CD pathogenesis is still unclear. It has been proposed that the hyper-inflammatory phenotype observed in CD patients with genetic defects in the NOD2 pathway is caused by defective antibacterial activity. Further understanding of this aspect of CD pathology could point towards new treatment options, such as bacterial clearance inducing drugs. Apart from their effect on antibacterial activity, defects in the NOD2 pathway are also known to impair cytokine production. The main aim of Chapter 3 is to study the hypothesis that defects in the NOD2 pathway could drive a state of cytokine hyper-production as a result of a defect in antimicrobial activity, even in the presence of an impairment in cytokine production capability. We will use a combination of mathematical modelling, experimentation, and data from the literature to study this hypothesis. Experimental data for this chapter has been obtained by me, as part of this doctoral study, with the guidance of Sumeet Pandey, a post-doctoral fellow in Holm Uhlig's lab. To address the main aim of Chapter 3, we will (1) develop a mechanistic mathematical model to describe the level of infection of *in vitro* infected macrophages over time, as determined by an experimental killing assay, (2) investigate how additional microscopy data on the distribution of infection could falsify assumptions made in the construction of this mechanistic model, (3) include the relationship between cytokine concentration and bacterial load under control conditions in our mechanistic model, and (4), complement our study with data from the literature on the size of the effects of defects in the NOD2 pathway on both bacterial handling and cytokine production capability. We recall that bacterial handling is defined as intracellular bacterial killing. We will then determine if our experimental and mathematical framework, together with the data from the literature, suggests that defects in the NOD2 pathway could drive a state of cytokine hyper-production as a result of a defect in antimicrobial activity, even in the presence of an impairment of cytokine production capability. Although it has been proposed before that hyper-inflammation in subgroups of CD patients could be driven by bacterial handling defects, the balance be-

tween an impairment in bacterial handling and defects in cytokine production capability has not yet been studied. Our choice of methods to study this connection between NOD2 defects and hyper-inflammation, e.g. our combined approach of mathematical modelling with experimentation, is novel.

1.4.3 Chapter 4: granuloma formation

Granuloma are dynamic structures of clustered macrophages. Different types of granuloma can form in various parts of the body. Intestinal granuloma are a hallmark of inflammation in Crohn's disease and other inflammatory diseases of the gut, such as the immunodeficiency syndrome chronic granulomatous disease (CGD). Granuloma emerge in a pro-inflammatory cytokine environment when normal pathogen clearance mechanisms have failed. Their formation is a culmination of the disregulated cytokine and bacterial handling responses studied in Chapters 2 and 3. Many aspects of granuloma formation are poorly understood. The main aim of Chapter 4 is to develop a model of granuloma formation to study what factors and cellular processes drive granuloma formation in inflammatory bowel disease and other granulomatic diseases. As part of the main aim of the chapter, we will investigate the various model features, and verify the model against an agent-based model from the literature. We are particularly interested in macrophage fusion, that is thought to increase the ability of macrophages to handle high levels of pathogen load. As the distribution of infection is of special interest when considering the impact of fusion, we decided to use the pathogen load as an internal structuring variable in our model, i.e. the model considers the dynamics of pathogen load in a manner analogous to age structured models, to describe the granuloma size and distribution of infection over time. The secondary aim of the chapter is to use the developed model to conduct an initial study into the difference between the intestinal granuloma found in CD and in intestinal TB (iTB), and investigate the impact of macrophage fusion in this context. To address the aims of this chapter, we will (1) study the impact of the various model features, including macrophage recruitment, extra- and intracellular pathogen growth, pathogen killing by macrophages, and macrophage fusion, on the dynamics of the bacterial-load structured model, (2) compare our model dynamics compare with the dynamics of GranSim, an agent-based model from the literature, (4) determine in what

situations our model could be used instead of the much more complex agent-based model, (5) study the difference in the model dynamics when parametrised to represent granuloma found in CD and in iTB respectively, and (6) study the impact of macrophage fusion in this context. The use of pathogen load as an internal structuring variable is a novel approach in mechanistic granuloma modelling. This type of model is easier to analyse and less computationally expensive than existing agent-based models of granuloma formation. We will implement macrophage fusion as non-local source and sink terms in our model. The inclusion of terms of this specific form in a population structured model are of interest as they have not been studied before. Furthermore, fusion has not yet been considered in existing models of granuloma formation. Finally, no existing mathematical modelling studies have focussed explicitly on granulomas found in the gut.

1.5 Thesis structure

In **Chapter 2**, we develop a method to extract a minimal, weighted network from cytokine interaction data using a simple coupled ODE system and the Akaike information criterion (AIC) for model selection. We apply our method to extract a network of IL-23 regulation in the context of IBD. Cytokine production by monocytes of six cytokines that are relevant to IBD was measured by flow cytometry in the presence and absence of various cytokine (receptor) inhibitors. We infer possible direct cytokine interactions from the data by statistical analysis and enumerate all possible network configurations based on this initial set of network edges. Each network configuration can be represented by a system of ordinary differential equations and fitted to the experimental dataset. We rank the different network configurations based on their fit to the data, using the AIC. We repeat the network extraction process while considering a much larger set of network configurations consisting of all possible positive and negative interactions between all six cytokines, i.e. we do not constrain the possible edges to the statistically significant set of edges as we did before. We compare the optimal networks resulting from both approaches. Using the extracted networks we predict the effects of untested combinations of cytokine (receptor) inhibitors.

In **Chapter 3**, we study the immunodeficiency component of Crohn's disease caused by mutations in the NOD2 pathway using a combination of mathematical modelling, data

from the literature, and wet-lab experiments. We construct a model to describe the level of infection of *in vitro* infected macrophages over time, as determined by an experimental killing assay using macrophages form healthy donors. We then present a mathematical model that describes the distribution of infection over time, using an existing confocal microscopy dataset to parametrize the initial conditions of this model. Using experimental cytokine concentration data, we construct a mathematical model of the relationship between cytokine production and bacterial load over time. We study the effects of the introduction of bacterial handling defects on both the bacterial load and cytokine concentration simulations of this model. We will complement our study with data from the literature on the size of the effects of defects in the NOD2 pathway on both bacterial handling and cytokine production capability. We will then determine if our experimental and mathematical framework, together with the data from the literature on the the effects of mutations in the NOD2/XIAP/RIPK2 pathway, suggests that defects in the NOD2 pathway could drive a state of cytokine hyper-production as a result of a defect in antimicrobial activity, even in the presence of an impairment of cytokine production capability.

In **Chapter 4**, we develop a bacterial-load structured model of granuloma formation. We will study the impact of the various model features, including macrophage recruitment, extra- and intracellular pathogen growth, pathogen killing by macrophages, and macrophage fusion, on the dynamics of the model. We then compare our model with one of the agent-based models by the group of Denise Kirschner on granuloma formation in the lung. Finally, we parametrise our model to represent an *in vitro* model of CD and iTB type granuloma, and discuss their differences and the impact of fusion.

In **Chapter 5**, we summarize our thesis, discuss our contributions to the field, and point towards future work.

Chapter 2

Inference of an inflammatory cytokine interaction network

We develop a method to extract a minimal, weighted network from cytokine interaction data. We apply the method to extract a network of IL-23 regulation in the context of IBD. All data used for this extraction has been generated based on experiments conducted in the Uhlig lab, Oxford Gastroenterology Unit, by Dominik Aschenbrenner, Nuffield Department of Medicine, BRC Gastroenterology and Mucosal Immunology. The IL-23 regulation network has been included in the resulting publication by Dominik Aschenbrenner et al. [22]. The generation of the networks within this publication was my work, and this is detailed below more extensively than in [22], where summary results were presented. A manuscript on the network inference method described in this chapter is currently under review for publication.

2.1 Introduction

Inflammatory processes are tightly controlled by complex cytokine networks. The disregulation of cytokines is common to the wide array of immune mediated inflammatory diseases (IMIDS) such as inflammatory bowel disease (IBD), rheumatoid arthritis, atherosclerosis, and Alzheimer's disease.

Inhibition of the pro-inflammatory cytokine TNFα has proven to be a very successful strategy in the treatment of IBD and other IMIDS. The success of TNFα inhibition has inspired the development of several other anti-cytokine therapies, such as anti-IL6(R) and anti-p_{40}, the common subunit of IL-12 and IL-23 [249, 338]. Less promising are the inhibition of IFNγ and IL-13, which did not show efficacy in Crohn's disease (CD) and ulcerative colitis

(UC), the two main types of IBD, respectively [76, 286, 287]. The inhibition of IL-17A even aggravated CD, although it was effective in psoriasis and ankylosing spondylitis [27, 38, 156, 224]. Success of cytokine therapy is not only disease, but also patient specific, as up to 40% of CD patients do not respond to anti-TNFα therapy [32]. Secondary response rates are even lower and dosage often has to be increased in the patients that do respond [341]. As new anti-cytokine therapies are developed, it is critical to improve our understanding of the effects of the inhibition of one or more cytokines on the larger cytokine interaction network. Ultimately, this should facilitate patient-subgroup and disease-specific outcome predictions of each treatment, based on observed cytokine expression levels and other biomarkers.

In this chapter we will study six cytokines that are relevant in the context of IBD, i.e. TNFα, IL-1α, IL-1β, IL-6, IL-10, and IL-23. We will use an existing flow cytometry data set of their secretion by monocytes after peripheral blood mononuclear cell (PBMC) stimulation by bacteria derived lipopolysaccharide (LPS, recognized by the pathogen recognition receptor toll-like receptor 4 (TLR4)) in the presence and absence of anti IL10 receptor (aIL10R, an antibody that blocks IL-10 signalling through binding to the IL-10 receptor), and various other cytokines and cytokine (receptor) blocking antibodies (Figure 2.1). PBMCs are immune cells extracted from the whole blood. They consist mainly of lymphocytes, including T cells, B cells and natural killer (NK) cells, and monocytes, which are macrophage pre-cursors that are constantly recruited to the gut. In the context of this thesis we are particularly interested in monocytes and their progeny. They are major sources of (pro)inflammatory cytokines and chemokines, such as the ones included in the dataset central to this chapter (i.e. TNFα, IL-1α, IL-1β, IL-6, IL-10, and IL-23). They also play a key role in bacterial handling, which we will study in later chapters.

The stimulus LPS was chosen as it is a well-known and potent inducer of inflammatory cytokine secretion by monocytes [131]. The effect of blocking the signalling of the anti-inflammatory cytokine IL-10 is of interest, as IL-10 signalling defects cause a completely penetrant Mendelian form of IBD, and sequence variants in IL-10 have been associated with IBD risk [105, 126, 168]. Further, TNFα, IL-1, IL-6 and IL-23 are all important inflammatory mediators and (emerging) therapeutic targets in IBD and other IMIDs [110, 249]. We are especially interested in the regulation of IL-23, as the IL-23 driven Th17 pathway

has been identified as an important therapeutic target, but is still poorly understood at a mechanistic level [22, 341]. Mutations in the IL-23 receptor are protective in IBD, IL-23 deficient mice are protected from developing colitis, and blocking the p_{19} subunit of IL-23 has shown clinical improvement in several trials [22, 91, 100, 297, 340, 360].

The aim of this chapter is two-fold. Our first aim is to study the impact of the cytokines TNFα, IL-1α, IL-1β, IL-6, IL-10, and IFNγ on the regulation of IL-23 as captured in the dataset introduced above. We will develop a method to extract a minimal, weighted network from cytokine interaction data using a simple coupled ODE system and the Akaike information criterion (AIC) for model selection, and apply our method to the experimental dataset. The development of this method is the second aim of this chapter. The method could be applied to other datasets involving cytokine signalling than the one studied in this chapter. The developed method enables us to study direct and indirect cytokine interactions and to quantify the effects of cytokine inhibition. We will define direct and indirect interactions in Section 2.3. The extracted network and corresponding model can also be used to predict the combined effects of inhibiting various cytokines simultaneously.

We have chosen an ODE approach over for instance a discrete Boolean model, as an ODE model allows to quantify cytokine input levels and secretion rates on a continuous scale [220, 221, 238]. Furthermore, this type of model could easily be extended to incorporate more complicated (non-linear) interactions than currently considered, if appropriate data would be available. Our ODE approach is a novel method to extract cytokine networks. It requires data on the effects of the blockage of single cytokines on the system (interventional data). If such data is not available (i.e. if only observational data is available), other network inference methods may be used, such as Graphical Gaussian models or directed acyclic graphs (DAGs, also known as Bayesian networks) [99, 101, 212, 217, 238, 357]. Xue and collegues for instance, inferred an undirected signalling network of eight macrophage produced cytokines after LPS stimulation, using a Graphical Gaussian model based on significant partial correlation coefficients of all pair-wise cytokine interactions [358].

The chapter is structured as follows. We introduce the experimental data and extract a list of possible direct cytokine interactions using statistical analysis (Section 2.2). We model the data using systems of ordinary differential equations (Section 2.3), consider Structural

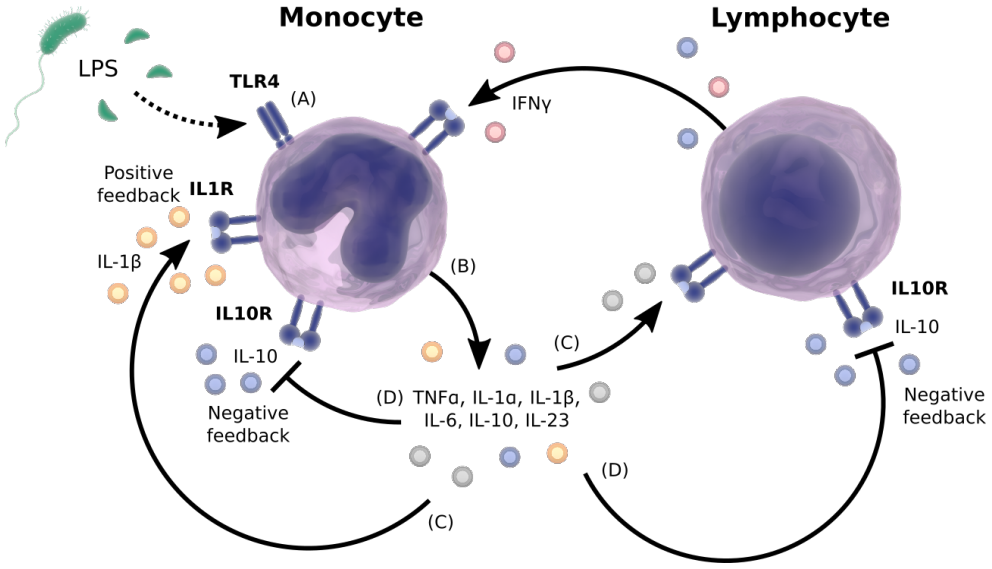


Figure 2.1: Graphical representation of the effect of LPS stimulation on the secretion of pro- and anti-inflammatory cytokines by PBMCs. The bacterial membrane component LPS is recognised by TLR4 proteins on the membrane of monocytes (A). Downstream signalling activates various transcription factors, most notably NF-κB, which in turn results in upregulated gene expression, production, and secretion of inflammatory cytokines, such as tumour necrosis factor alpha (TNFα), interleukin 1 alpha and beta (IL-1α/β), IL-6, IL-10 and IL-23 (B). Cytokines can act as stimuli themselves, either up-regulating (C) or down-regulating (D) further cytokine secretion of both monocytes and other cell types (e.g. lymphocytes) in a cytokine specific way, i.e. increased levels of a particular cytokine (e.g. IFNγ) could result in upregulated secretion of one cytokine (e.g. IL-23), while not affecting the secretion of another cytokine (e.g. IL-1β). We have shown IL-10 as an example of a cytokine having a negative feedback effect on further cytokine secretion, and IFNγ and IL-1β as examples of cytokines that have a positive feedback effect on further cytokine secretion.

parameter identifiability (Section 2.4), discuss model fitting (Section 2.5), and rank different network configurations using the AIC (Section 2.6). We introduce a second approach where we do not constrain the number of possible network interactions to the subset of edges resulting from the statistical analysis in Section 2.2, but instead consider all possible positive and negative interactions between all cytokines (Section 2.7). We consider practical parameter identifiability (Section 2.8) and explore parameter sensitivity for our selected model configuration (Section 2.9). We validate our approach using simulated data (Section 2.10). Using the extracted networks we predict the effects of untested combinations of cytokine (receptor) inhibitors (Section 2.11). Finally, in the appendix, we compare our method with

an existing method from the literature (Section 2.12). We end with a discussion (Section 2.12).

2.2 Data

All data presented in this chapter has been generated based on experiments conducted in the Uhlig lab, Oxford Gastroenterology Unit, by Dominik Aschenbrenner, Nuffield Department of Medicine, BRC Gastroenterology and Mucosal Immunology.

Fresh PBMCs were extracted from the blood of 17 healthy donors. The cells have been cultured for 16 hours with combinations of bacteria derived Lipopolysaccharide (LPS, recognized by the pathogen recognition receptor toll-like receptor 4 (TLR4, $200\,\mathrm{ng\,ml^{-1}}$) and aIL10R (an antibody that blocks IL-10 signalling through binding to the IL-10 receptor, $10\,\mu\mathrm{g\,ml^{-1}}$) in the presence of human recombinant granulocyte-macrophage colony-stimulating factor (GM-CSF), TNFα, IL-1β, IL-6, IL-10, IL-11, IL-12, IL-17A, IL-18, IL-23, IFNγ, or aGMCSF, aIFNγ, aIFNR1, aIL12, aIL19, aIL1α, aIL1β, aIL1R1, aIL24, aIL36g, aIL6R, aTNFα (with a $\equiv$ anti, R $\equiv$ receptor, and number of samples, $n \in \{3, \dots 17\}$, $10\,\mu\mathrm{g\,ml^{-1}}$). Not all antibodies were available at the time the experiments were performed. Further, some conditions (e.g. 'LPS + aIL36g') were excluded from later experiments, as they did not have a noticeable effect on the measured cytokine expression levels of the monocytes. Therefore, not all experimental conditions were measured for all 17 donors. All cells were intracellularly stained for TNFα, IL-1α, IL-1β, IL-6, IL-10, and the two subunits of IL-23, p_{19} and p_{40}. Using flow cytometry, one can determine the fluorescent intensity of the fluorescent dyes that were paired with the antibodies for the cytokines of interest. For each donor, in addition to the LPS stimulated samples, an unstimulated sample was available. As detailed below, several fluorescence dyes were used to detect the cells and cytokines of interest. For each fluorescent dye used, single stained bead controls were used to compensate for spectral overlaps. For each sample, the following gating strategy was used. First debris were excluded by gating on a forward versus side scatter area (FSC-A vs SSC-A) plot. Then single cells were selected by gating on a forward scatter height versus forward scatter area plot (FSC-A vs FSC-H). The viability dye eFluor 780 (Bioscience) was

used to label dead cells. This dye was excited by the red laser. Its emission was detected using a band pass filter of 750-810nm. By gating on eFluor 780 negative cells, dead cells were excluded. We then gated on CD14 positive cells, that were labelled using the Bv650 dye (excited by the violet laser, detected using a band pass filter of 650-670nm). We determined the percentage of cytokine expressing CD14+ cells and the mean fluorescence intensity of the cytokine expressing CD14+ cells for the cytokines of interest TNFα, IL-1α, IL-1β, IL-6, IL-10, and the two subunits of IL23, p_{19} and p_{40} as follows. We assume the vast majority of monocytes in the unstimulated samples do not express any of the cytokines of interest. For each donor, we set gating thresholds for the expression of TNFα, IL-1α, IL-1β, IL-6, IL-10, p_{19} and p_{40} using the unstimulated sample. TNFα was labelled using the Bv605 dye (excited by the violet laser, detected using a band pass filter of 600-620nm). IL-1α was labelled using the PE dye (excited by the green laser, detected using a band pass filter of 564-600nm). IL-1β was labelled using the FITC dye (excited by the blue laser, detected using a band pass filter of 505-525nm). IL-6 was labelled using the AF700 dye (excited by the red laser, detected using a band pass filter of 685-735nm). IL-10 was labelled using the Bv421 dye (excited by the violet laser, detected using a band pass filter of 425-475nm). p_{19} (one of the two subunits of IL23) was labelled using the eF660 dye (excited by the red laser, detected using a band pass filter of 663-677nm). p_{40} (one of the two subunits of IL23) was labelled using the Biot/STV-TxR dye (excited by the green laser, detected using a band pass filter of 600-620nm).

As explained above, for each donor and each cytokine, a fluorescence intensity threshold for cytokine expressing cells can be determined by assuming that the cytokine levels in unstimulated cells are negligible (Figure 2.2). After stimulation, the percentage of cells crossing this threshold gives a measure of cytokine expressing cells. This percentage of positive cells is usually used as a measure for cytokine expression in flow cytometry experiments [107]. However, the percentage of cytokine expressing cells does not contain any information about the amount of cytokines the cytokine expressing cells contain [302]. We therefore multiply the percentage (P) of monocytes expressing a cytokine with the mean fluorescence intensity (MFI) of the monocytes expressing that cytokine to obtain a measure

(PMFI, arbitrary units) of the amount of cytokine present within the monocytes. We emphasize we do not use the MFI of all monocytes, but only of the monocytes expressing the cytokine of interest. We have chosen to use PMFI instead of considering the fluor intensity of all monocytes, whether they express the cytokine or not, to exclude the observed random variation for very small cytokine expression levels (Figure 2.3). We show the average percentage change in PMFI after the addition of various stimuli (Table 2.1). For the remainder of this chapter, we will assume that the PMFI of each cytokine of interest is proportional to the cytokine secretion rate of that cytokine. Several assumptions underlie this assumption. First, we assume that monocytes are the major source of the cytokines of interest, in particular after LPS stimulation. Further, we assume each produced cytokine is secreted after a fixed, small amount of time and the intracellular cytokine concentration therefore scales with the cytokine secretion rate [302, 313], though in reality we recognise the PMFI may not scale linearly with the intracellular concentration of cytokine. During some processes, a simple relationship between cytokine production and secretion likely exists [242, 326]. For instance after LPS stimulation, RAW macrophages rapidly synthesize and secrete TNFα. Synthesized TNFα first appears in the Golgi complex, peaking 40 minutes after stimulation. All synthesized TNFα is subsequently secreted [314]. However, other cytokines, such as IL-1β and IL-18, are produced in an inactive form after TLR stimulation and require futher activation of the inflammasome for enzymatic cleavage and secretion [57]. Hence for these cytokines there is a complex relationship between intracellular cytokine levels and secretion due to need for enzymatic cleavage before release. Thus FACS is a good measure for some cytokines and has to be used with caution with others. Nonetheless, we note that FACS based measurements are a more accurate measure of protein secretion than RNA based measurements, as the correlation between mRNA and protein levels can be poor [208, 301]. We compare 'LPS' stimulated with unstimulated samples, 'LPS + x' with 'LPS' stimulated samples, 'LPS + aIL1β + x' with 'LPS + aIL1β' stimulated samples, 'LPS + aIL10R + x' with 'LPS + aIL10R' stimulated samples, and 'LPS + aIL10R + aIL1β + x' with 'LPS + aIL10R + aIL1β' stimulated samples, where x is an additional stimulus as indicated in the table. Red (blue) bold values indicate a significant positive (negative) effect of the added stimulus on the secretion of the cytokine of interest ($p < 0.05$, Wilcoxon test,

false discovery rate (FDR) corrected [34]). We note we only consider cytokine secretion by monocytes (live CD14+ cells), as the used stimulus LPS is recognized by monocytes. We assume that for our cytokines of interest (TNFα, IL-1α, IL-1β, IL-6, IL-10 and IL-23), the percentage of cytokine positive, CD14 negative cells (i.e. non-monocytes) after stimulation is negligible. This is confirmed for IL23 and IL10 after LPS and LPS+aIL10R stimulation in [22], Supplemental figure 3B.

Finally, we assume the concentration of cytokines in the supernatant builds up as cytokines are secreted over time.

We compare 'LPS' stimulated with unstimulated samples, 'LPS + x' with 'LPS' stimulated samples, 'LPS + aIL1β + x' with 'LPS + aIL1β' stimulated samples, 'LPS + aIL10R + x' with 'LPS + aIL10R' stimulated samples, and 'LPS + aIL10R + aIL1β + x' with 'LPS + aIL10R + aIL1β' stimulated samples, where x is an additional stimulus as indicated in the table. Red (blue) bold values indicate a significant positive (negative) effect of the added stimulus on the secretion of the cytokine of interest ($p< 0.05$, Wilcoxon test, FDR corrected [34]). We note we only consider cytokine secretion by monocytes (live CD14+ cells), as the used stimulus LPS is recognized by monocytes. We assume that for our cytokines of interest (TNFα, IL-1α, IL-1β, IL-6, IL-10 and IL-23), the percentage of cytokine positive, CD14 negative cells (i.e. non-monocytes) after stimulation is negligible. This is confirmed for IL23 and IL10 after LPS and LPS+aIL10R stimulation in [22], Supplemental figure 3B.

2.3 Model construction

Based on the statistical analysis of the flow cytometry dataset (Table 2.1) we constructed a network of possible direct cytokine interactions (Figure 2.4 and Table 2.2). We consider the effects of cytokine addition and cytokine (receptor) blockade of the six cytokines whose secretion rates were measured, i.e. TNFα, IL-1α, IL-1β, IL-6, IL-10 and IL-23. We also include the effects of IFNγ, as this was the only other cytokine included in Table 2.1 that had a significant effect on the secretion of IL-23. IFNγ is a cytokine produced by CD4+ and CD8+ T cells and NK cells during inflammation that can prime macrophages to produce inflammatory cytokines [240]. The total number of used data points is 1750. This number

Condition	TNF	IL-1α	IL-1β	IL-6	IL-10	IL-23 (p_{19})	IL-23 (p_{40})	n
LPS	**374%**	**42688%**	**18191%**	**17690%**	**7959%**	**2400%**	**573%**	17
aIL10R	0%	-6%	-8%	51%	64%	43%	-90%	13
LPS aGMCSF	-46%	**-25%**	**-20%**	**-19%**	5%	18%	12%	10
LPS aIFNγ	-19%	3%	-1%	6%	53%	100%	75%	10
LPS aIFNR1	-25%	19%	19%	11%	39%	77%	-38%	4
LPS aIL12	25%	3%	5%	-8%	25%	6%	4%	7
LPS aIL19	7%	-1%	1%	-2%	3%	9%	13%	7
LPS aIL1α	20%	**13%**	**12%**	13%	**37%**	60%	31%	13
LPS aIL1β	-24%	**-23%**	**-21%**	**-35%**	**-39%**	-73%	-74%	17
LPS aIL1R1	**-50%**	**-44%**	**-44%**	**-77%**	**-88%**	**-96%**	**-92%**	17
LPS aIL24	19%	21%	12%	7%	12%	81%	28%	9
LPS aIL36g	17%	9%	7%	1%	10%	24%	16%	3
LPS aIL6R	-15%	-3%	-7%	6%	16%	27%	10%	10
LPS aTNFα	10%	-9%	-18%	-4%	4%	**-65%**	-62%	10
LPS GM-CSF	76%	22%	16%	21%	19%	241%	297%	10
LPS IFNγ	**230%**	**27%**	5%	**43%**	-34%	**561%**	**468%**	14
LPS IL-10	**-82%**	**-104%**	**-101%**	**-111%**	**-112%**	**-158%**	-129%	10
LPS IL-11	-7%	-5%	-10%	-1%	-3%	-8%	-2%	8
LPS IL-12	**53%**	**40%**	**21%**	**49%**	15%	74%	-3%	9
LPS IL-17A	35%	9%	8%	12%	-12%	44%	-8%	4
LPS IL-18	12%	9%	1%	8%	9%	-17%	-3%	17
LPS IL-1β	6%	0%	3%	9%	5%	43%	-5%	10
LPS IL-23	0%	-2%	-6%	4%	-9%	0%	3%	8
LPS IL-6	-22%	**-12%**	**-22%**	-9%	**-22%**	-22%	14%	10
LPS TNFα	49%	3%	0%	11%	39%	31%	32%	10
LPS aIL10R	**803%**	**114%**	**74%**	**122%**	**129%**	**4681%**	**3381%**	17
LPS aIL1β aIL1α	7%	6%	2%	-2%	-4%	19%	74%	7
LPS aIL10R aGMCSF	7%	-6%	-6%	-7%	14%	28%	26%	10
LPS aIL10R aIFNγ	-35%	-1%	-4%	-4%	13%	17%	6%	10
LPS aIL10R aIFNR1	-32%	-1%	-19%	-30%	-59%	35%	119%	4
LPS aIL10R aIL12	10%	16%	10%	7%	28%	-4%	0%	7
LPS aIL10R aIL19	3%	1%	0%	-1%	-9%	3%	4%	7
LPS aIL10R aIL1α	25%	-1%	0%	-7%	-8%	0%	12%	13
LPS aIL10R aIL1β	-11%	**-20%**	**-15%**	**-22%**	**-34%**	**-38%**	**-37%**	17
LPS aIL10R aIL1R1	**-84%**	**-46%**	**-47%**	**-74%**	**-88%**	**-95%**	**-94%**	17
LPS aIL10R aIL24	**10%**	2%	5%	-1%	6%	14%	6%	9
LPS aIL10R aIL36g	1%	-2%	2%	-4%	-9%	-3%	-4%	3
LPS aIL10R aIL6R	13%	-2%	-3%	-1%	2%	15%	23%	10
LPS aIL10R aTNFα	51%	-2%	1%	-8%	6%	-15%	-9%	10
LPS aIL10R GM-CSF	19%	1%	-14%	-10%	-25%	16%	43%	10
LPS aIL10R IFNγ	**306%**	10%	-12%	14%	-31%	**182%**	**298%**	14
LPS aIL10R IL-11	12%	-11%	-20%	-13%	-15%	-16%	28%	8
LPS aIL10R IL-12	**48%**	**27%**	**18%**	**23%**	-5%	76%	58%	9
LPS aIL10R IL-17A	199%	6%	0%	-6%	-38%	40%	168%	4
LPS aIL10R IL-18	10%	0%	-8%	-4%	-9%	1%	20%	17
LPS aIL10R IL-1β	26%	4%	-5%	-4%	-15%	2%	26%	10
LPS aIL10R IL-23	32%	-4%	-12%	-9%	-23%	-9%	45%	8
LPS aIL10R IL-6	-7%	-5%	-23%	-16%	-22%	1%	30%	10
LPS aIL10R TNFα	35%	-2%	-14%	-10%	-8%	5%	33%	10
LPS aIL10R aIL1β aIL1α	-3%	-7%	-3%	**-18%**	**-18%**	**-31%**	**-18%**	7

Table 2.1: Summary of the healthy donor (n=3-17 healthy donors) flow cytometry data. We list the average percentage change after the addition of various stimuli of cytokine secretion, as measured by the MFI of the subset of cytokine expression cells, multiplied by the percentage of monocytes expressing that cytokine. We compare 'LPS' stimulated with unstimulated samples, 'LPS + x' with 'LPS' stimulated samples, 'LPS + aIL1β + x' with 'LPS + aIL1β' stimulated samples, 'LPS + aIL10R + x' with 'LPS + aIL10R' stimulated samples, and 'LPS + aIL10R + aIL1β + x' with 'LPS + aIL10R + aIL1β' stimulated samples, were x is an additional stimulus as indicated in the table. Red (blue) bold values indicate a significant positive (negative) effect of the added stimulus on the secretion of the cytokine of interest ($p< 0.05$, Wilcoxon test, FDR corrected [34]). This data is based on experiments conducted by Dominik Aschenbrenner, Nuffield Department of Medicine [22]. The cell populations have been gated using FlowJo by Dominik Aschenbrenner. I extracted the MFI of the various subsets from FlowJo and performed statistical analysis in R.

Condition	TNF	IL-1α	IL-1β	IL-6	IL-10	IL-23 (p_{19})	IL-23 (p_{40})
LPS aIFNγ	-	-	-	-	(☆)	-	-
LPS aIL1α	(☆)	☆(☆)	☆(☆)	-	☆☆	-	-
LPS aIL1β	(☆)	☆☆☆	☆☆☆	☆☆☆	☆☆☆	(☆)	(☆)
LPS aIL1R1	☆☆☆	☆☆☆	☆☆☆	☆☆☆	☆☆☆	☆☆	☆
LPS aIL6R	-	-	-	-	-	-	-
LPS aTNFα	-	(☆)	(☆)	-	-	☆	(☆)
LPS IFNγ	☆☆☆	☆	-	☆☆☆	-	☆☆	☆☆☆
LPS IL-10	☆	☆	☆	☆	☆	☆	-
LPS IL-1β	-	-	-	(☆)	-	-	-
LPS IL-23	-	-	-	-	-	-	-
LPS IL-6	-	☆(☆)	☆	(☆)	☆(☆)	-	-
LPS TNFα	-	-	-	-	-	-	-
LPS aIL10R	☆☆☆	☆☆☆	☆☆☆	☆☆☆	☆☆☆	☆☆☆	☆☆☆
LPS aIL1β aIL1α	-	-	-	-	-	-	-
LPS aIL10R aIFNγ	-	-	-	-	-	-	-
LPS aIL10R aIL1α	-	-	-	-	-	-	-
LPS aIL10R aIL1β	(★)	★★★	★★★	★★★	★★★	★★	★
LPS aIL10R aIL1R1	★★★	★★★	★★★	★★★	★★★	★★★	★★★
LPS aIL10R aIL6R	-	-	-	-	-	-	-
LPS aIL10R aTNFα	-	-	-	-	-	-	-
LPS aIL10R IFNγ	★★★	-	-	(★)	-	★★★	★★★
LPS aIL10R IL-1β	-	-	-	-	-	-	-
LPS aIL10R IL-23	-	-	-	-	-	-	-
LPS aIL10R IL-6	-	-	(★)	-	-	-	-
LPS aIL10R TNFα	-	-	-	-	-	-	-
LPS aIL10R aIL1β aIL1α	-	-	-	(★)	(★)	(★)	(★)

Table 2.2: The effects of the addition of human recombinant TNFα, IL-1β, IL-6, IL-10, IL-23, IFNγ, or aTNFα, aIL1α, aIL1β, aIL1R, aIL6R, aIFNγ, in the presence of LPS or LPS and aIL10R, on the frequency of cytokine (i.e. TNFα, IL-1α, IL-1β, IL-6, IL-10 or IL-23) producing live CD14+ cells multiplied by the mean fluor intensity of the respective cytokine producing cell population. Wilcoxon test against LPS stimulated samples: $^{☆}p\leq 0.05$, $^{☆☆}p\leq 0.01$, $^{☆☆☆}p\leq 0.001$, dashed arrows, and against LPS+aIL10R (LPS+aIL10R+aIL1-β) stimulated samples: $^{★}p\leq 0.05$, $^{★★}p\leq 0.01$, $^{★★★}p\leq 0.001$. Effects with p>0.05 after a FDR correction are shown in parenthesis [34]. Red (blue) values indicate a positive (negative) effect of the added stimulus on the secretion of the cytokine of interest. This data is based on experiments conducted by Dominik Aschenbrenner, Nuffield Department of Medicine [22]. The cell populations have been gated using FlowJo by Dominik Aschenbrenner. I extracted the MFI of the various subsets from FlowJo and performed statistical analysis in R.

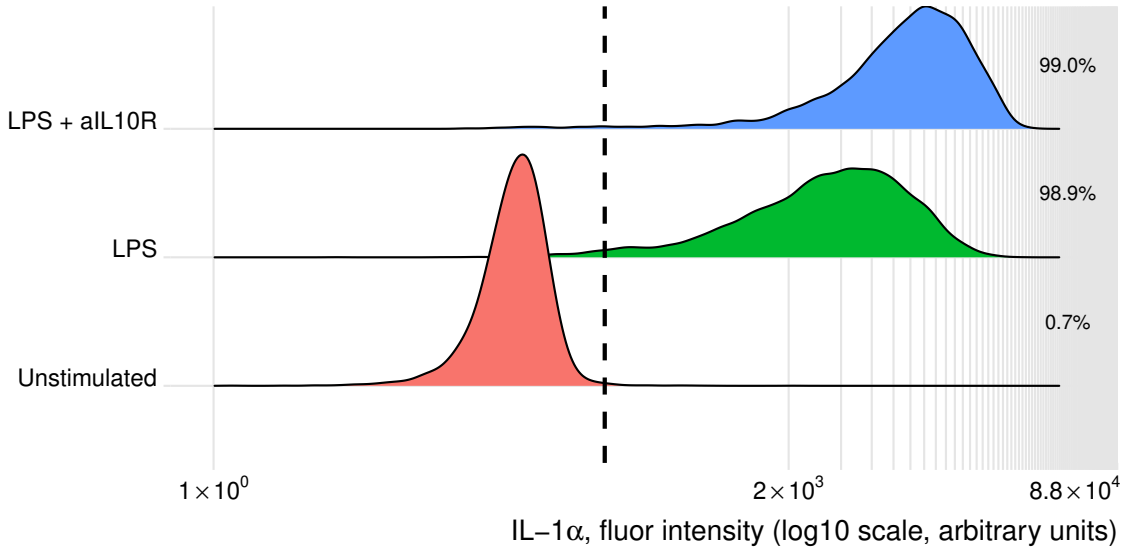


Figure 2.2: The fluor intensity for IL-1α of an 'unstimulated' (red), 'LPS stimulated' (green), and 'LPS + aIL10R' stimulated (blue) sample (healthy donor, live CD14+ cells). The percentages correspond to the percentage of live CD14+ cells with IL-1α expression above the threshold. The black dashed line indicates the threshold for IL-1α expression. The difference in percentage of IL-1α expressing cells between the 'LPS' and the 'LPS + aIL10R' is only 0.1%. The difference in mean fluor intensity (MFI) for all CD14+ cells is much larger. The MFI of IL-1α for all live CD14+ cells of the 'unstimulated', 'LPS stimulated' and 'LPS + aIL10R' stimulated samples is 56, 5047 and 11902 (arbitrary units) respectively.

breaks down as follows: for each of the six cytokines, we have 17 'LPS' samples, 13 'LPS + aIL1α' samples, 17 'LPS + aIL1β' samples, 17 'LPS + aIL1R' samples, 10 'LPS + aIL6R' samples, 10 'LPS + aTNFα' samples, 14 'LPS + IFNγ' samples, 10 'LPS + IL-10' samples, 10 'LPS + IL-1β' samples, 8 'LPS + IL-23' samples, 10 'LPS + IL-6' samples, 10 'LPS + TNFα' samples, 17 'LPS + aIL10R' samples, 7 'LPS + aIL1-α + aIL1-β' samples, 13 'LPS + aIL10R+ aIL1α' samples, 17 'LPS + aIL10R+ aIL1β' samples, 17 'LPS + aIL10R+ aIL1R' samples, 10 'LPS + aIL10R+ aIL6R' samples, 10 'LPS + aIL10R+ aTNFα' samples, 14 'LPS + aIL10R+IFNγ' samples, 10 'LPS + aIL10R+ IL-1β' samples, 8 'LPS + aIL10R+ IL-23' samples, 10 'LPS + aIL10R+ IL-6' samples, 10 'LPS + aIL10R+ TNFα' samples, and 7 'LPS + aIL10R+ aIL1-α + aIL1-β' samples (see also Table 2.1). This results in 296 times 6, for the number of cytokines, is 1776 samples. However, for 26 experiments, not a single IL23 expressing monocyte was observed (3/17 of the 'LPS' samples, 4/10 of the 'LPS + IL-10' samples, 4/7 'LPS + aIL1-α + aIL1-β' samples, 2/13 'LPS + aIL1-α' samples,

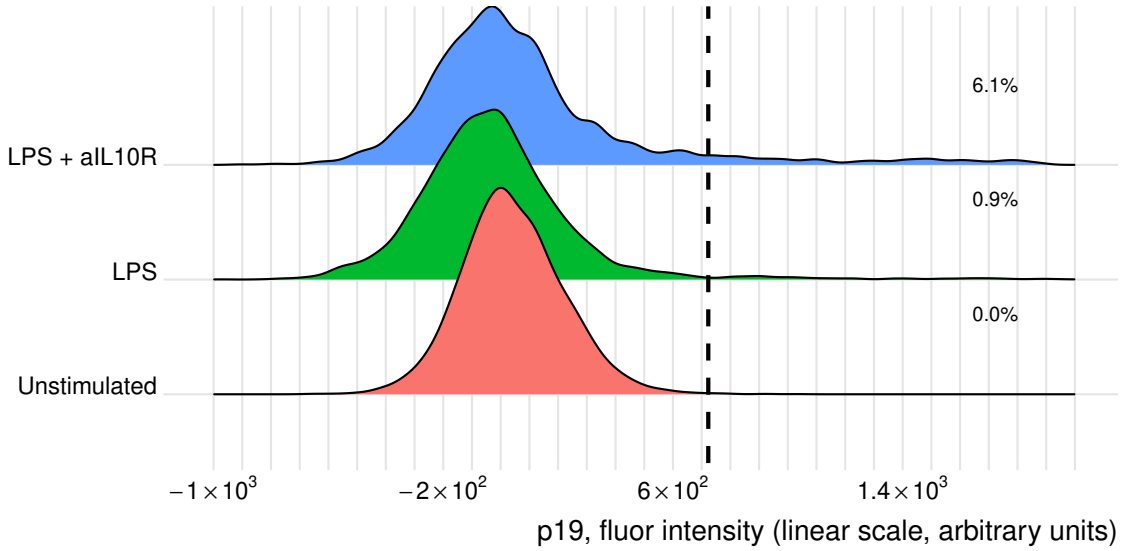


Figure 2.3: The fluor intensity for p_{19} of an 'unstimulated' (red), 'LPS stimulated' (green), and 'LPS + aIL10R' stimulated (blue) sample (healthy donor, live CD14+ cells). The percentages correspond to the percentage of live CD14+ cells with p_{19} expression above the threshold. The black dashed line indicates the threshold for p_{19} expression. While the percentage of p_{19} expressing live CD14+ cells increases after LPS stimulation (in comparison to unstimulated cells), the mean fluor intensity of p_{19} for all live CD14+ cells decreases from 41 to 9 (arbitrary units). Note we have shown the fluor intensity data on a linear scale in this figure, as a logarithmic scale is inappropriate for low fluor intensity signals, that can have a negative value due to instrument background correction [148, 261].

4/17 'LPS + aIL1-β' samples, 9/17 'LPS + aIL1R' samples). As we fit all datapoints on a log-transformed scale, we decided to exclude these samples from the dataset used for fitting. Thus, the total number of datapoints is 1750.

Starting from this initial network of potential direct interactions, our aim is to extract a minimal network that best balances model fit and complexity. We define the minimal network as the network configuration selected by the Akaike information criterion, this selects the network with the smallest number of edges, and thus complexity, whilst summarising the experimental data accurately. We modelled the cytokine dynamics via sets of coupled ODEs incorporating network configurations to provide a means of comparing the model fit of various network configurations. In particular, we aim to distinguish between direct and indirect interactions.

Definition 1 (direct interaction)**.** We define a direct cytokine interaction as a down- or upregulatory effect of the concentration of one cytokine (e.g. A) on the cytokine secretion

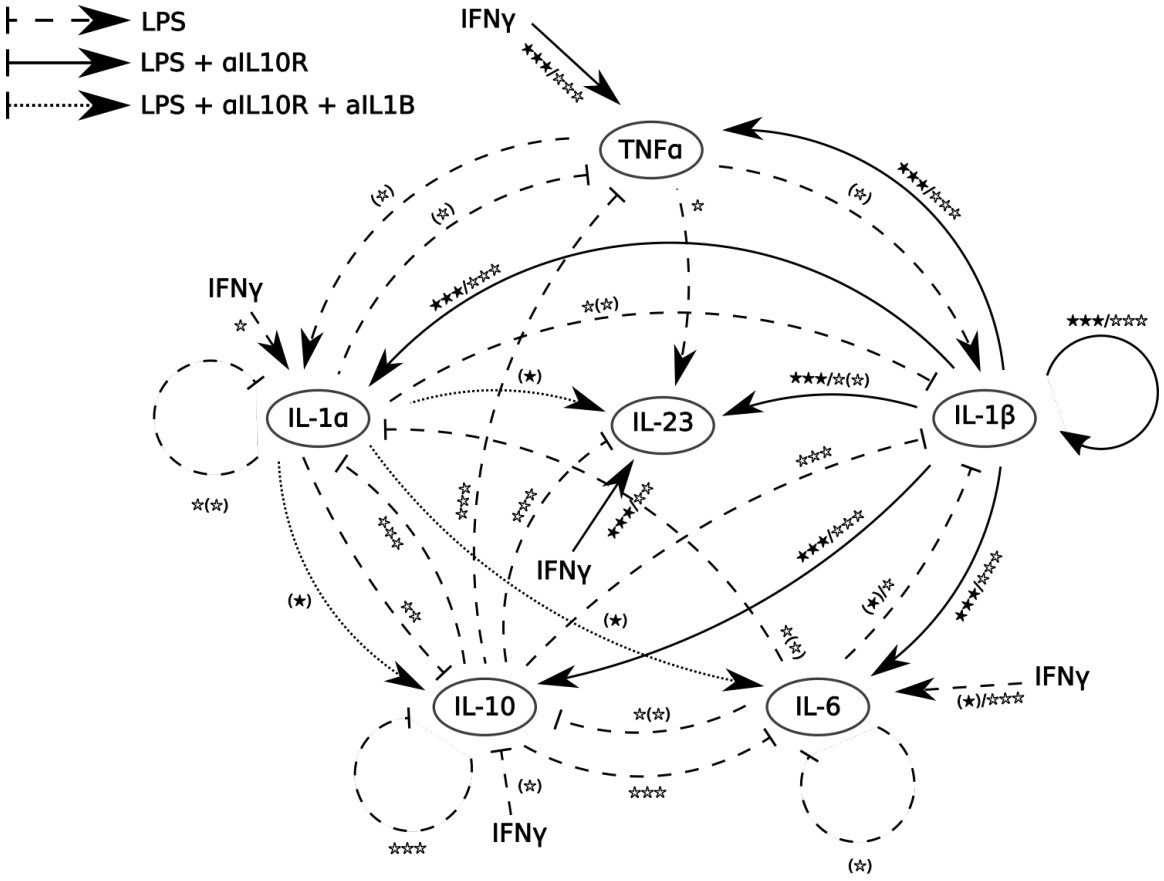


Figure 2.4: The effects of the addition of human recombinant TNFα, IL-1β, IL-6, IL-10, IL-23, IFNγ, or aTNFα, aIL1α, aIL1β, aIL1R, aIL6R, aIFNγ, in the presence of LPS or LPS and aIL10R, on the frequency of cytokine (i.e. TNFα, IL-1α, IL-1β, IL-6, IL-10 or IL-23) producing live CD14+ cells multiplied by the mean fluor intensity of the respective cytokine producing cell population. Wilcoxon test against LPS stimulated samples for the impact of the recorded experimental condition: *p$\leq$ 0.05, **p$\leq$ 0.01, ***p$\leq$ 0.001, dashed arrows, and against LPS+aIL10R (LPS+aIL10R+aIL1-β) stimulated samples: $^{\bigstar}$p$\leq$ 0.05, $^{\bigstar\bigstar}$p$\leq$ 0.01, $^{\bigstar\bigstar\bigstar}p\leq$ 0.001, solid arrows (dotted arrows). Effects with p$>$0.05 after a false discovery rate (FDR) correction are shown in parenthesis [34]. The information of this graph is also provided via Table 2.2.

rate of another cytokine (e.g. B), that is independent of the effects of the concentrations of other cytokines part of the studied network.

Definition 2 (indirect interaction)**.** We define an indirect cytokine interaction as a down- or upregulatory effect of the concentration of a cytokine (e.g. A) on the cytokine secretion rate of another cytokine (e.g. C), that is dependent of the effects of the concentrations of other cytokines part of the studied network.

We note that direct effects might be dependent on cytokines not present in the network. E.g. cytokine A might upregulate cytokine Z that in turn upregulates cytokine B. If the secretion rate of cytokine Z is not measured and cytokine Z is therefore not represented by a node in the network, the effect of A on B (via Z) is direct, according to above definition. Cytokine Z might for instance be produced by lymphocytes, while only monocyte produced cytokines were measured. Conversely, if cytokine Z is part of the network, the cytokine Z-dependent effect of A on B is indirect. Our model equations are of the form:

$$\frac{\mathrm{d}x_i}{\mathrm{d}t} = y_i(t) = s_i \prod_u (1 + \alpha_{u,i} x_u) \prod_v \left(\frac{1}{1 + \beta_{v,i} x_v} \right), \tag{2.1}$$

with $x_i(t)$ and $y_i(t)$ the time dependent concentration and secretion rate of cytokine i, s_i the size of the effect of LPS, and $\alpha_{u,i} \geq 0$ ($\beta_{v,i} \geq 0$) the size of the positive (negative) effect of cytokine u (v) on the secretion rate of cytokine i, $i \in \{\text{TNF}\alpha, \text{IL-1}\alpha, \text{IL-1}\beta, \text{IL-6}, \text{IL-10}, \text{IL-23}\}$ and $u, v \in \{\text{TNF}\alpha, \text{IL-1}\alpha, \text{IL-1}\beta, \text{IL-6}, \text{IL-10}, \text{IL-23}, \text{IFN}\gamma\}$. Similarly, $x_u(t)$ and $x_v(t)$ are the concentration of cytokine $u, v \in \{\text{TNF}\alpha, \text{IL-1}\alpha, \text{IL-1}\beta, \text{IL-6}, \text{IL-10}, \text{IL-23}\}$. We take the unit of time t in hours. The unit of cytokine concentration is arbitrary, as the fluorescence intensity measured by flow cytometry that was used to determine the cytokine secretion rate has arbitrary units. We note we do not have direct measurements of the cytokine concentration, but only measurements of the secretion rate of the various cytokines at $t = 16$h after stimulation. We set $x_{\text{IFN}\gamma} = 1$ when IFNγ was added at the start of the experiment and $x_{\text{IFN}\gamma} = 0$ otherwise. We do not trace the concentration of IFNγ over time, as the fluorescence intensity was not measured for this cytokine. IFNγ is thought to be predominantly produced by lymphocytes and not monocytes [111]. Further, we assume $x_i(0) = \gamma_i$ when cytokine i has been added at the start of the experiment, $i \in \{\text{TNF}\alpha,$

IL-1β, IL-6, IL-10, IL-23}. Else, we assume $x_i(0) = 0$. For convenience, we will replace TNFα, IL-1α, IL-1β, IL-6, IL-10, IL-23, IFNγ with the numbers 1, 2, 3, 4, 5, 6 and 7 respectively for all parameter indices. The form of equation (2.1) was taken to be as simple as possible. We have chosen a multiplicative model as this type of model is more suitable to describe cytokine dynamics than an additive model. In particular, multiplicative models are commonly found in the literature, e.g. [17, 83, 214, 244], and are based on the observation that the addition of a cytokine, e.g. IFNγ, can amplify the effects of a stimulatory agent, e.g. LPS or a bacterium, but can have no effect when added to monocytes in the absence of such a stimulatory agent (e.g. [113, Fig. 8B]). We can represent a specific network configuration with our model equations (2.1) by only considering the $\alpha_{u,i} \geq 0$ and $\beta_{v,i} \geq 0$ corresponding to the positive and negative network edges of that configuration and assuming all other $\alpha_{u,i}$ and $\beta_{v,i}$ are zero. For example, to represent the network configuration containing all 31 edges identified by statistical analysis (Figure 2.4, Table 2.2), we only consider the 31 $\alpha_{u,i} \geq 0$ and $\beta_{v,i} \geq 0$, and assume all other $\alpha_{u,i}$ and $\beta_{v,i}$ are zero. Note that whilst the secretion rate of a particular cytokine might decrease over time due to increasing inhibition, the simulated cytokine concentrations themselves are monotonously increasing as we did not include degradation or absorption terms (Equation (2.1)).

We assume that the secretion rate of the cytokines is so much higher than the degradation and absorption rates, that the latter can be ignored. We note that in an *in vivo* setting, cytokine clearance should not be ignored, as the serum half-lifes of in vivo administered cytokines can be in the order of several hours or even minutes [41], e.g. $6 - 60$ minutes for TNFα (in rats, [59]), < 30 minutes for IL-3 (in mice, [115]), ≈ 2 hours for IL-3 (in humans, [159]), 22.5 minutes for IL-2 (in humans, [39]), and 20 minutes - 4 hours for IL-10 (in humans, [8, 61, 158]), due to clearance processes such as filtration by the kidneys [15, 41, 279]. We assume cytokines in culture medium can be considered stable for the time course considered, as more than 90% of cytokines (IFNγ, IL-4, IL-5, IL-10, IL-12p$_{40}$) were recovered after four days of incubation in culture medium [169]. The PBMC might take up some of the cytokines during the time considered. However, we assume this amount is negligible. We note that *in vitro* PBMC cytokine concentration time courses of up to 80 hours after LPS stimulation indicate that after an initial increase in cytokine concentration,

the cytokine levels plateau [84]. We assume the plateau-phase indicates cytokines are no longer secreted, but are also not degraded or absorbed although we cannot rule out that after initial transients cytokines are absorbed and produced at exactly the same rate. We assume the cytokine levels do not influence the expression of cytokine receptors at the timescale considered and the number of cytokine receptors were no limiting factor for cytokine signalling. We note that in reality, cytokine receptors are known to be regulated by various factors. Type 1 interferons for instance upregulate IL10R expression on the surface of monocytes [201], while IL-4 downregulates TNF receptor surface expression [211]. We assume the cytokine/cytokine receptor blockade is 100% effective. The cytokine (receptor) blocking antibodies were all added at a concentration of 10 μg/ml. As the effectiveness of an antibody of neutralizing a cytokine is dependent on the concentration of that cytokine, we provide estimates of the concentration of the cytokines of interest in the IL23 dataset. Although no concentration data is available for the healthy donor FACS cytokine secretion dataset that we have used for the model fitting, we do have access to concentration data from a similar experiment where IBD patient cells were used, instead of healthy donor cells. The concentration of TNFα, IL1α and IL1β in the supernatant of PBMCs after 16h of LPS stimulation of 28 IBD patients is 5.8ng/ml, 0.7ng/ml, and 10.0ng/ml on average respectively. It has been reported that Infliximab, the TNFα blocking antibody used, neutralizes soluble TNFα at a concentration of 1 μg/ml, in a NF-κB reporter assay after addition of 50 ng/ml TNFα [343]. The IL-1α blocking antibody used (R&D; Cat.# AF-200-NA; polyclonal Goat IgG) neutralizes 0.05ng/ml IL-1α at a concentration of approximately 0.1μg/ml [65, 1]. The IL-1β blocking antibody used (R&D; Cat.# MAB201; clone: 8516) neutralizes 0.05ng/ml IL-1β at a concentration of approximately 0.001μg/ml [2, 65]. Hence, the ratio of added antibody and estimated concentration of cytokine is much higher than the ratio reported to be required for effective blockage. This strengthens our confidence in our assumption of 100% effectiveness of the cytokine blocking antibodies. We are not aware of estimates in the literature of the efficacy of anti IL-6 (Tocilizumab, Roche), anti-IL-10R (Biolegend; Cat.# 308807; clone: 3F9) or anti-IL-1R1 (R&D; Cat.# AF269; polyclonal Goat IgG) on the receptor blockage of monocytes specifically. However, we note that it has been reported that Tocilizumab, the IL6R blocking antibody used, blocked IL6 *in vitro* completely in immature

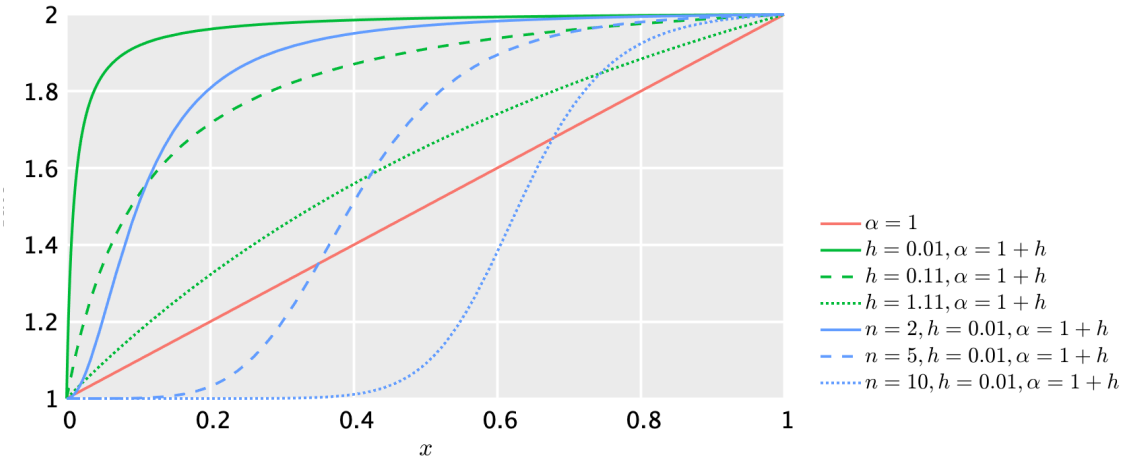


Figure 2.5: The secretion rate $p(x)$ of a cytokine as a function of cytokine concentration x, where $p(x) = (1 + \alpha x)$ (linear kinetics, red), $p(x) = \left(1 + \frac{\alpha x}{h+x}\right)$ (Michaelis-Menten kinetics, green), or $p(x) = \left(1 + \frac{\alpha x^n}{h+x^n}\right), n > 1$ (Hill kinetics, yellow). Note that $p(1) = 2$ for all curves. Except for the linear case (i.e. when $\alpha = 1$), none of the parameters are structurally identifiable.

monocyte derived DCs at a concentration of 5μg/ml (by determining the inhibition of IL6-induced pSTAT3 after 48h of LPS stimulation) [35].

2.4 Structural parameter identifiability

We apply the Scaling Invariance Method by Castro and de Boer to investigate the structural identifiability of our model parameters, to identify which parameters could or could not be uniquely identified given an arbitrarily large dataset [55]. We introduced this method in Section 1.3.3.1. Here, we apply the method to a general form of our N model equations (i.e. not specific to the IL23 data), given by:

$$\frac{\mathrm{d}x_i}{\mathrm{d}t} = s_i \prod_u (1 + \alpha_{u,i} x_u(t)) \prod_v \left(\frac{1}{1 + \beta_{v,i} x_v(t)}\right), \qquad i, u, v = 1, \ldots, N, \tag{2.2}$$

with $s_i > 0$ and $\alpha_{u,i}, \beta_{v,i} \geq 0$. Further, we assume $x_i(0) = \gamma_i$ when cytokine i has been added at the start of the experiment, or we assume $x_i(0) = 0$. We note that all model variables $x_i \geq 0$ are observable as we have non-zero measurements for $\frac{dx_i}{dt}$ for every x_i, $i = 1, \ldots n$ (see Section 1.3.3.2). We introduce scaling factors c_{s_i}, $c_{\alpha_{u,i}}$, $c_{\beta_{v,i}}$, c_{γ_i} for every model parameter $s_i, \alpha_{u,i}, \beta_{v,i}, \gamma_i$. We look for relationships between the scaling factors that leave the system

of equations (2.2) invariant. We initially assume $\alpha_{i,j}, \beta_{i,j} > 0$ for all $i, j \in \{1, \ldots, N\}$ and return the prospect of setting some of these values to zero, thus simplifying the dynamical system, later. We set the right-hand side of equations (2.2) equal to their scaled version, for every $i = 1, \ldots, N$:

$$\begin{aligned} & s_i \prod_u (1 + \alpha_{u,i} x_u) \prod_v \left(\frac{1}{1 + \beta_{v,i} x_v} \right) \\ = c_{s_i} s_i & \prod_u \left(1 + c_{\alpha_{u,i}} \alpha_{u,i} x_u\right) \prod_v \left(\frac{1}{1 + c_{\beta_{v,i}} \beta_{v,i} x_v} \right). \end{aligned} \tag{2.3}$$

We consider the case $N = 1$, with N the number of cytokines. Then,

$$\begin{aligned} & s_1 \left(1 + \alpha_{1,1} x_1\right) \left(\frac{1}{1 + \beta_{1,1} x_1} \right) \\ = c_{s_1} s_1 & \left(1 + c_{\alpha_{1,1}} \alpha_{1,1} x_1\right) \left(\frac{1}{1 + c_{\beta_{1,1}} \beta_{1,1} x_1} \right). \end{aligned} \tag{2.4}$$

Noting $s_1 > 0$ (and more generally $s_i > 0$), it follows that

$$\begin{aligned} & 1 + (\alpha_{1,1} + c_{\beta_{1,1}} \beta_{1,1}) x_1 + (\alpha_{1,1} c_{\beta_{1,1}} \beta_{1,1}) x_1^2 \\ = c_{s_1} & + (c_{\alpha_{1,1}} \alpha_{1,1} + \beta_{1,1}) x_1 + c_{\alpha_{1,1}} \alpha_{1,1} \beta_{1,1} x_1^2. \end{aligned} \tag{2.5}$$

Because $1, x_1, x_1^2$ are linearly independent, and $a_{1,1} > 0, \beta_{1,1} > 0$, it follows that

$$1 = c_{s_1}, \tag{2.6}$$

$$\alpha_{1,1} + c_{\beta_{1,1}} \beta_{1,1} = c_{\alpha_{1,1}} \alpha_{1,1} + \beta_{1,1}, \tag{2.7}$$

$$c_{\beta_{1,1}} = c_{\alpha_{1,1}}. \tag{2.8}$$

It follows that $c_{\alpha_{1,1}}(\beta_{1,1} - \alpha_{1,1}) = \beta_{1,1} - \alpha_{1,1}$, and therefore $c_{\beta_{1,1}} = c_{\alpha_{1,1}} = 1$ for $\alpha_{1,1} \neq \beta_{1,1}$. Therefore, s_1, $\alpha_{1,1}$, and $\beta_{1,1}$ are identifiable, provided that $\alpha_{1,1} \neq \beta_{1,1}$. When $\alpha_{1,1} = \beta_{1,1}$, $c_{\beta_{1,1}} = c_{\alpha_{1,1}}$ can take any value and $\alpha_{1,1} = \beta_{1,1}$ are structurally non-identifiable. We note that in this case, $\frac{\mathrm{d}x_1}{\mathrm{d}t} = s_1$, and the model has become independent of the value of $\alpha_{i,j} = \beta_{i,j}$. We consider the general case for $N > 1$ cytokines. If follows from equation (2.3) that for every $i = 1, \ldots, N$,

$$\begin{aligned} & \prod_{u=1}^{N} (1 + \alpha_{u,i} x_u) \prod_{v=1}^{N} \left(1 + c_{\beta_{v,i}} \beta_{v,i} x_v\right) \\ = c_{s_i} & \prod_{u=1}^{N} \left(1 + c_{\alpha_{u,i}} \alpha_{u,i} x_u\right) \prod_{v=1}^{N} (1 + \beta_{v,i} x_v). \end{aligned} \tag{2.9}$$

We rewrite equation (2.9) as

$$\left\{\prod_{u=1}^{N-1}\left(1+\alpha_{u,i}x_u\right)\left(1+c_{\beta_{u,i}}\beta_{u,i}x_u\right)\right\}\left(1+\alpha_{N,i}x_N\right)\left(1+c_{\beta_{N,i}}\beta_{N,i}x_N\right)$$
$$=c_{s_i}\left\{\prod_{u=1}^{N-1}\left(1+c_{\alpha_{u,i}}\alpha_{u,i}x_u\right)\left(1+\beta_{u,i}x_u\right)\right\}\left(1+c_{\alpha_{N,i}}\alpha_{N,i}x_N\right)\left(1+\beta_{N,i}x_N\right) \tag{2.10}$$

Suppose that the model gives structural identifiability for s_i, $\alpha_{j,i}$, and $\beta_{j,i}$ with $i,j \in \{1,2,\ldots,N-1\}$. We now show the model at level N is structurally identifiable to give the inductive step that shows the model for general N is structurally identifiable (if $\alpha_{i,j} \neq \beta_{i,j}$ for all i,j and $\alpha_{i,j},\beta_{i,j}$ positive for all i,j). To proceed note that for $i=N$, if follows from equation (2.10) that

$$\left\{\prod_{u=1}^{N-1}\left(1+\alpha_{u,N}x_u\right)\left(1+c_{\beta_{u,N}}\beta_{u,N}x_u\right)\right\}\left(1+\alpha_{N,N}x_N\right)\left(1+c_{\beta_{N,N}}\beta_{N,N}x_N\right)$$
$$=c_{s_N}\left\{\prod_{u=1}^{N-1}\left(1+c_{\alpha_{u,N}}\alpha_{u,N}x_u\right)\left(1+\beta_{u,N}x_u\right)\right\}\left(1+c_{\alpha_{N,N}}\alpha_{N,N}x_N\right)\left(1+\beta_{N,N}x_N\right) \tag{2.11}$$

Because x_N^0, x_N, x_N^2 are linearly independent we can look at the coefficient of x_N^0. Thus we have

$$\left\{\prod_{u=1}^{N-1}\left(1+\alpha_{u,N}x_u\right)\left(1+c_{\beta_{u,N}}\beta_{u,N}x_u\right)\right\}$$
$$=c_{s_N}\left\{\prod_{u=1}^{N-1}\left(1+c_{\alpha_{u,N}}\alpha_{u,N}x_u\right)\left(1+\beta_{u,N}x_u\right)\right\}. \tag{2.12}$$

Because $x_u^0, x_u, x_u^2, x_v, x_v^2$, $u \neq v, u, v \in \{1,\ldots,N-1\}$, are linearly independent, we have $c_{s_N}=1$, and

$$\alpha_{u,N}+c_{\beta_{u,N}}\beta_{u,N}=c_{\alpha_{u,N}}\alpha_{u,N}+\beta_{N,N} \tag{2.13}$$

$$c_{\alpha_{u,N}}=c_{\beta_{u,N}}, \qquad (\alpha_{u,N};\beta_{u,N}>0). \tag{2.14}$$

It follows that $c_{\alpha_{u,N}}=c_{\beta_{u,N}}=1$ for all $u \in \{1,\ldots,N-1\}$. Further, we now consider the coefficients of x_N and x_N^2 in equation (2.11). The scaling relation gives on noting $c_{s_N}=1$ from above,

$$\alpha_{N,N}+c_{\beta_{N,N}}\beta_{N,N}=c_{\alpha_{N,N}}\alpha_{N,N}+\beta_{N,N} \tag{2.15}$$

$$c_{\alpha_{N,N}}=c_{\beta_{N,N}}, \qquad (\alpha_{N,N};\beta_{N,N}>0). \tag{2.16}$$

Thus $c_{\alpha_{N,N}} = c_{\beta_{N,N}} = 1$ by similar reasoning to previously. It follows that

$$c_{s_N} = 1 = c_{\alpha_{i,N}} = c_{\beta_{i,N}}, \qquad i \in \{1, \ldots, N\}. \tag{2.17}$$

Letting $N \to j$ in the above, with $j \in \{1, \ldots, N-1\}$, the analogous result is immediately inherited and thus we have

$$c_{s_j} = 1 = c_{\alpha_{i,j}} = c_{\beta_{i,j}}, \qquad i, j \in \{1, \ldots, N\}, \tag{2.18}$$

proving the inductive step. Therefore, as in the case $N = 1$, we find that s_i, $\alpha_{N,i}$, and $\beta_{N,i}$ are identifiable, as $c_{s_i} = c_{\alpha_{N,i}} = c_{\beta_{N,i}} = 1$ when $\alpha_{N,i} \neq \beta_{N,i}$. Hence, we have the inductive step showing that for every cytokine $i \in \{1, 2, \ldots, N\}$, $s_i, \alpha_{j,i}$ and $\beta_{j,i}$ are identifiable for $j \in \{1, 2, \ldots, N\}$, provided that $\alpha_{j,i} \neq \beta_{j,i}$ and $\alpha_{i,j}, \beta_{i,j} > 0$. When $\alpha_{j,i} = \beta_{j,i}$, the positive and negative edge from j to i cancel out and this situation is indistinguishable from the case $\alpha_{j,i} = \beta_{j,i} = 0$. When $\alpha_{j,i} > 0$ and $\beta_{j,i} = 0$ we have the immediate generalisation of equation (2.15), so that $c_{\alpha_{j,i}}\alpha_{j,i} = \alpha_{j,i}$ and thus $\alpha_{j,i}$ is structurally identifiable with

$$\frac{\mathrm{d}x_i}{\mathrm{d}t} = s_i(1 + \alpha_{j,i})x_j \ldots. \tag{2.19}$$

Thus the model simplifies with no denominator term, and hence it is still structurally identifiable if we set $\beta_{j,i} = 0$ (or $\alpha_{j,i} = 0$) to simplify the model.

Finally, we consider the parameters $x_i(0) = \gamma_i$ $i = 1, \ldots, n$, each corresponding to the addition of a certain amount of cytokine i at the start of the experiment. When no edges from cytokine i to any of the other cytokines exist (i.e. $\alpha_{u,i} = \beta_{v,i} = 0$ for all $u, v = 1, \ldots, n$), the parameter γ_i is structurally non-identifiable, as the amount of added cytokine i does not influence the expression of any of the other cytokines in this case, i.e. the model for the other cytokines becomes independent of this parameter. We note that, in our studies below, we remove interactions (network edges), thus setting $\beta_{j,i}$ or $\alpha_{j,i}$ equal to zero only if either the interaction is not significant from the examination of the data, or we are examining whether a reduced network yields a better information criterion (which balances complexity against improved data fit). Thus we either estimate with $\alpha_{i,j}, \beta_{i,j} > 0$ or identically zero, with this binary decision not part of the parameter estimation. As setting $\alpha_{i,j}, \beta_{i,j}$ to zero induces a model simplification that still retains identifiability of the

remaining parameters we do not have difficulties from structural non-identifiability below, and we can set the non-identifiable parameters to zero without loss. This does not rule out the prospect of practical identifiability concerns and this is addressed later using profile likelihoods.

In summary, we identified two sources of structural non-identifiability in our model parameters. The first arises when both a positive and a negative edge from cytokine i to cytokine j exist with the same weight. In this case, the effect of the two edges cancels out and $\alpha_{i,j} = \beta_{i,j}$ is non-identifiable. As the model is independent of the value of $\alpha_{i,j} = \beta_{i,j}$ in this case, we can trivially resolve this non-identifiability by taking $\alpha_{i,j} = \beta_{i,j} = 0$. The second type of parameter non-identifiability arises when at the start of the experiment an amount is added of a cytokine (corresponding to the γ_i parameter) that has no effect on the expression of any of the cytokines. Again, the model for the interacting cytokines is independent of the value of this parameter. Apart from these two types of non-identifiability, which have no impact on network extraction or model prediction below as the model for the interacting cytokines is independent of the parameters once they are non-identifiable, all our model parameters are structurally identifiable, whenever $\frac{\mathrm{d}x_i}{\mathrm{d}t}$ is measured (at a non-zero value).

2.5 Model fitting

For each network configuration, we can fit the right hand-side of the system of equations (2.1) to our experimental dataset by log-likelihood minimization. Recall that we set all $\alpha_{u,i}$ and $\beta_{v,i}$ corresponding to non-existing edges to zero to represent a particular network configuration (Equation (2.1)). We will first introduce a normalized form of our experimental data. Recall that we take the mean fluor intensity (MFI) of all monocytes expressing a certain cytokine, multiplied by the percentage (P) of monocytes expressing that cytokine as a measure of cytokine secretion after sixteen hours of stimulation (PMFI):

$$\text{PMFI}_i = \text{MFI of monocytes expressing } i \times 100\% \times \frac{\#\text{ of monocytes expressing } i}{\text{total }\#\text{ of monocytes}}, \quad (2.20)$$

with i one of the cytokines. We have fluor intensity data for both subunits of IL-23, p_{19} and p_{40}. We have chosen to use the MFI of p_{19}, of the p_{19} and p_{40} double positive population

of monocytes, multiplied by the percentage of p_{19} and p_{40} double positive monocytes, as a measure of IL-23 secretion. In this section, we will use two tests for normality: the Kolmogorov-Smirnov test and the Shapiro-Wilk test [222, 310]. For both tests, the null hypothesis is that the data is sampled from a normal distribution. A p-value at less than a certain level (i.e. $p < 0.05$ or $p < 0.01$) indicates that the data significantly deviates from a normal distribution. The Shapiro-Wilk test statistic is given by:

$$W = \frac{(\sum_{i=1}^{n} a_i q_i)}{\sum_{i-1}^{n}(q_i - \bar{q})}, \tag{2.21}$$

for ordered samples $q_1 < q_2 < \ldots < q_n$, and with $\bar{q}$ the mean of all samples $q_1, \ldots, q_n$. Further, the coefficients a_i are calculated using the means, variances and covariances of the order statistics of sample size n of a standard normal distribution. For more details, we refer to [292]. The Shapiro-Wilk test statistic W can be interpreted as a measure of correlation between the ordered, sampled data and the expected values of the order statistics of samples drawn from a standard normal distribution. For each value of W, a corresponding p-value exists [292]. The Kolmogorov-Smirnov test statistic for normality is given by:

$$D = \max_{q}(|\hat{F}(q) - G(q)|), \tag{2.22}$$

with $\hat{F}(q)$ the empirical cumulative distribution function of the sample values and $G(q)$ the cumulative distribution function of a standard normal distribution. Because a standard normal distribution is used for comparison, we will standardise all sample values before applying the test (i.e. rescale them such that the sample mean is 0 and the sample variance is 1). For each value of D, a corresponding p-value exists [230].

For a large proportion of the studied conditions, the log 10 transformed PMFI data significantly deviated from a normal distribution (false discovery rate (fdr) corrected $p<0.05$ for both tests for normality). We therefore attempted to remove the non-normality by normalising the data. Ideally, we would have liked to normalise by dividing each sample by the sum of all studied experimental conditions. However, as not every experimental condition was measured for each donor, we chose to normalize by the 'LPS + aIL10R' condition, as this experimental condition was measured for all 17 donors. To clarify, for each donor, we normalized the sample PMFI value for each experimental condition by

dividing by the sample PMFI value of the 'LPS + aIL10R' condition for that particular donor and define the value of the experimentally measured, normalized secretion rate of cytokine i for data point j after 16 hours as:

$$\hat{y}_{i,j} = \frac{\text{PMFI}_i \text{ for data point } j}{\text{PMFI}_i \text{ for the same donor after 'LPS + aIL10R' stimulation}}. \tag{2.23}$$

As a result, none of the log 10 transformed datasets corresponding to each condition significantly deviated from a normal distribution any-more, as confirmed by both the Shapiro-Wilk test and Kolgomorov-Smirnov test (fdr corrected, $p > 0.05$ for both tests, excluding the 'LPS + aIL10R' condition that was used for normalization) (Figure 2.6).

Next, we assume each log 10 transformed measurement $\log_{10}(\hat{y}_{i,j})$ has a fixed, cytokine dependent measurement noise, rather than assuming a dependency of the noise on both the six cytokines and 26 conditions:

$$\log_{10}(\hat{y}_{i,j}) = \log_{10}(y_{i,j}) + \epsilon_i, \tag{2.24}$$

with $y_{i,j}$ and $\hat{y}_{i,j}$ (defined above in equation (2.23)) the value of the simulated and experimentally measured, normalized secretion rate of cytokine i for data point j after 16 hours, and $\epsilon_i \sim \mathcal{N}(0, \sigma_i^2)$. We thus assume a fixed standard deviation σ_i for each of the six cytokines, which we determined as follows. First, for each cytokine and each condition, we computed the residuals, i.e. the differences between each normalized log 10 transformed data point $\hat{y}_{i,j}$ and the mean of all log 10 transformed, normalized datapoints for that experimental condition and cytokine. We computed an estimate of the cytokine specific variance by dividing the square of these differences by the sample size minus one for each cytokine i, and computed the standard deviation as the square root of the variance. In Figure 2.7(a), we show plots of the residuals for each cytokine, together with a normal density function with parameters estimated from the data, excluding the 'LPS+aIL10R' condition that was used for normalization. For comparison, we show an example of the residuals of the log 10 transformed, non-normalised data for IL6 (Figure 2.7(b)). It is visibly clear that the distribution of the residuals of the normalised, log 10 transformed data approximates a normal distribution more closely than the bimodal distribution of the log 10 transformed non-normalised IL-6 data. However, using formal tests, we observe that the distribution of

the residuals for each of the six cytokines does not follow a normal distribution perfectly. In particular, the Shapiro-Wilk test indicates that the combined residuals for each cytokine (as shown in Figure 2.7) deviate from a normal distribution (fdr adjusted p-values all < 0.01), although the Kolgomorov-Smirnov test of normality does not reject normality of the combined data at that level (all p-values larger than 0.01 and for five of the six groups larger than 0.05).

We hypothesize that the standard deviation term σ may be condition dependent. Nevertheless, for the remainder of the chapter, we make a parsimonious assumption that each log 10 transformed measurement $\hat{y}_{i,j}$ has a fixed, cytokine dependent measurement noise. An experimental condition-dependent standard deviation term of the form $\sigma_{i,j}$ could be explored in future work.

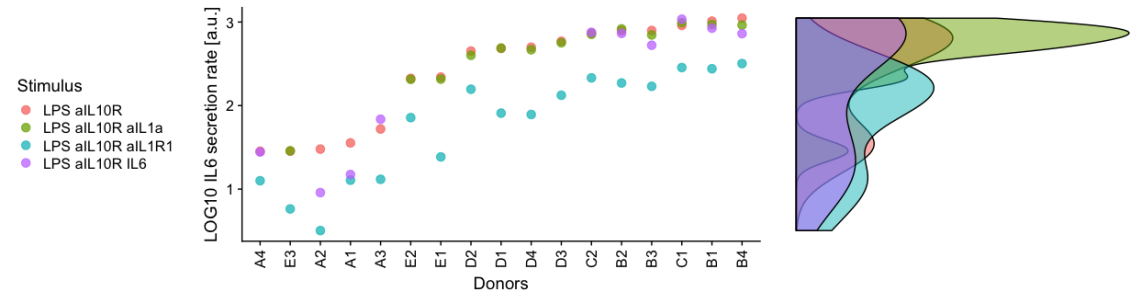
We can now fit the right hand-side of the system of equations (2.1), representing a particular network configuration, to each of our 1750 datapoints simultaneously, by minimizing $-2\log(\mathcal{L}(\boldsymbol{\theta}))$ over our parameter vector $\boldsymbol{\theta}$, where $\boldsymbol{\theta}$ contains the model parameters s_i and γ_i, and all $\alpha_{u,i}$, $\beta_{v,i}$ that are not fixed to zero for the network configuration of interest, and $\mathcal{L}(\boldsymbol{\theta})$ is the likelihood function:

$$\mathcal{L}(\boldsymbol{\theta}) = \prod_i \prod_j \frac{1}{\sqrt{2\pi\sigma_i^2}} \exp\left(-\frac{(\log_{10}(y_{i,j}) - \log_{10}(\hat{y}_{i,j}))^2}{2\sigma_i^2}\right), \tag{2.25}$$

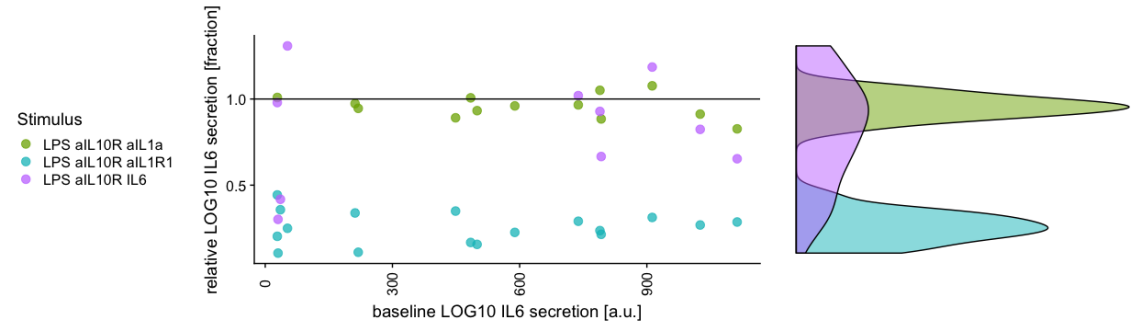
with $y_{i,j}$ and $\hat{y}_{i,j}$ (defined above in equation (2.23)) the value of the simulated and experimentally measured, normalized secretion rate of cytokine i for data point j after 16 hours, and σ_i the standard deviation of the log transformed measured secretion rate of cytokine i [283]. For each simulation corresponding to data point j, cytokine (receptor) blockades are simulated by setting the corresponding edge parameter ($\alpha_{u,i}/\beta_{v,i}$) to zero. We recall that cytokine additions are incorporated in the initial cytokine concentrations by setting $x_i(0) = \gamma_i$ when cytokine i has been added at the start of the experiment, and $x_i(0) = 0$ otherwise. We define the minimal distance as $D = \min_{\boldsymbol{\theta}} -2\log(\mathcal{L}(\boldsymbol{\theta}))$. We implemented the system of equations (2.1) in the Matlab based modelling environment 'Data2Dynamics' [284]. All fitting was executed in this environment, using a deterministic trust-region approach combined with a multi-start strategy (see for an introduction Section 1.3.2). To

clarify, we always used the trust-region approach with multi-start strategy to obtain estimates of D in this chapter. In Section 2.6.1, we will introduce a model selection algorithm that relies on the trust-region approach returning the global minimum for a given network configuration (and we comment further on its validation in Section 2.10.5 below). To obtain an estimate of D, we ran the trust-region algorithm multiple times, with different initial parameter value guesses, where each run returned the value of D after convergence of the algorithm to a local optimum. We select the smallest value of D from these estimates, assuming that this value represents a global minimum, i.e. the true value of D. The initial guesses for each parameter were sampled from a log-10 transformed uniform distribution with lower bound 10^{-10} and upper bound 10. When one of the estimated parameter values returned by the algorithm was equal to the upper bound, we increased the upper bound by a factor 1000 (i.e. multiplied by 10^3) and repeated the fitting procedure with the new bound. All parameter values $\alpha_{u,i}$ and $\beta_{v,i}$ corresponding to non-existing edges in the modelled network configuration were fixed to zero and not estimated. We used Latin-hypercube sampling to for our initial guesses. For all estimates of D presented in this chapter, we ran the deterministic trust-region algorithm with at least ten different initial guesses. Given the number of model parameters (more than 5), we acknowledge that these 10 initial guesses correspond to a very coarse coverage of the different regions in parameter space. We will discuss in Section 2.10.5 why we nonetheless have confidence (but not proof) that the 10 initial guesses are sufficient to obtain an estimate of the global minimum for the specific type of model we consider in this chapter. Generally, we emphasize that many many more initial guesses would be required for a sufficient coverage of parameter space, especially in the general setting.

We note that the dataset contains both data on IL-1α blockade, IL-1β blockade, IL-1α + IL-1β blockade, and their combined receptor (IL1R) blockade in the presence and absence of aIL10R. We observe that the IL1R receptor blockade has a larger effect than blocking the cytokines themselves, either separately or simultaneously (Figure 2.8). We hypothesize that the cytokine blockers to not neutralize all cytokines present in the supernatant, but that the IL1R blocker does effectively bind to all IL-1 receptors present. Our interaction model does not account for this, e.g. the simulated IL-10 and IL-23 secretion values for the



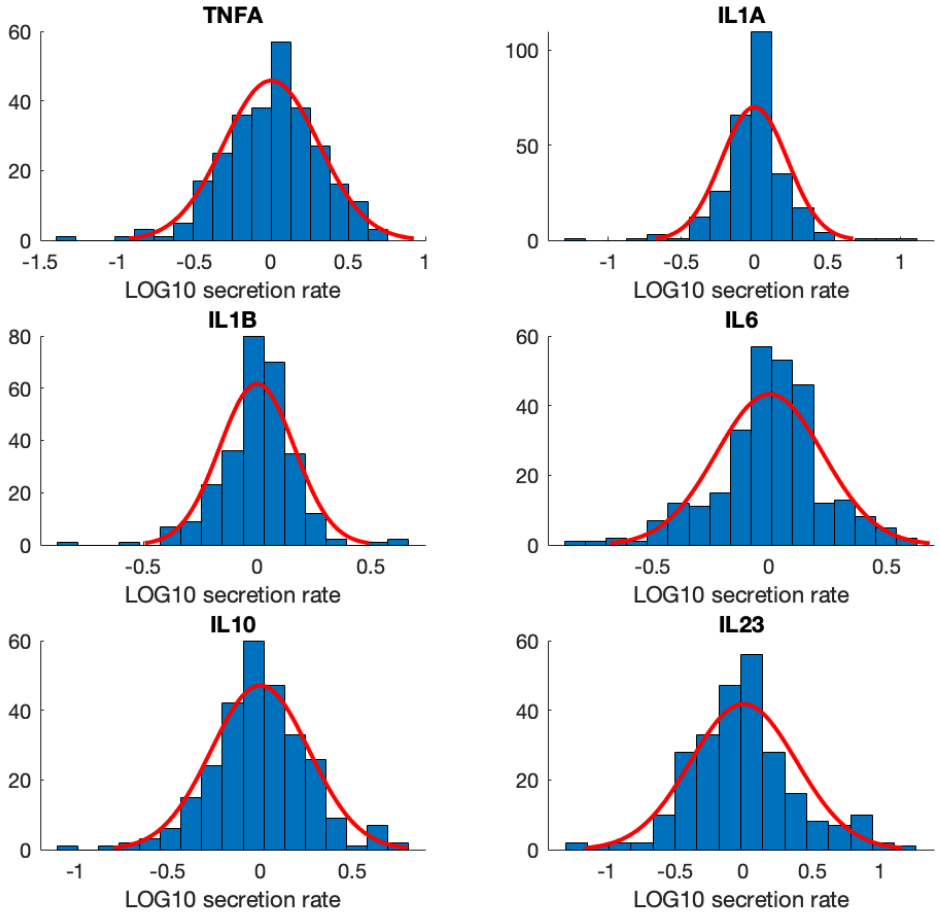
(**a**)



(**b**)

Figure 2.6: Example of the distribution of the data before (a), and after (b) normalization. The measured log transformed secretion rate of IL-6 after 1) 'LPS + aIL10R', 2)'LPS + aIL10R + aIL1α', 3) 'LPS + aIL10R + aIL1R' and 4) 'LPS + aIL10R + IL-6' stimulation is shown. Before normalization, for all four shown cases the data significantly deviates from a normal distribution (fdr corrected Shapiro-Wilk normality test and Kolmogorov-Smirnov test, $p<0.05$). After normalization, the data does not significantly deviate from a normal distribution any more.

(**a**) Normalised data



(**b**) Non-normalised data

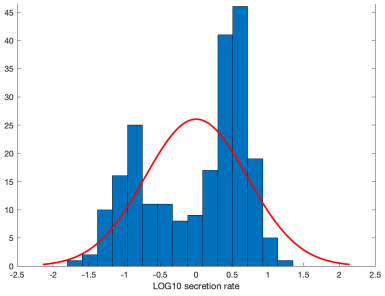


Figure 2.7: (a) Histogram of the residuals (i.e. difference from the group mean) for each cytokine. We define the residuals as the differences between the each log 10 transformed data point and the mean of all log 10 transformed measurements (for all donors) for that specific combination of added cytokines and cytokine (receptor) blockades. We excluded the 'LPS+aIL10R' condition that was used for normalization. We plot of a normal density function with parameters $\mu = 0$ and σ estimated from the log 10 transformed data in red. $\mu = 0$ is the mean of the residuals. σ was estimated as the sample standard deviation of the residuals. (b) Histogram of the residuals of the non-normalised log 10 transformed data for IL6. We plot a normal density function with parameters μ and σ estimated from the log 10 transformed data in red.

'aIL1α + aIL1β+aIL10R' and 'aIL1R+aIL10R' are equal. We could introduce parameters that correspond to the fraction of a cytokine that is neutralized after the addition of a cytokine blocker. For simplicity, and because the 'aIL1α + aIL1β+aIL10R' modulation was only measured for 7 out of 17 donors, we have chosen not to introduce such additional parameters.

The form of equation (2.1) was taken to be as simple as possible and more complicated forms are commonly found in the literature [17, 83, 214, 244, 349]. In particular, the saturation effects that are known to exist for increasing stimulus concentrations are commonly modelled using Michaelis-Menten or Hill functions. As our data includes only one time point and one secretion rate for each stimulus, including Michaelis-Menten/Hill kinetics would introduce unidentifiable parameters (Figure 2.5). We assume that the strength of each network edge can be represented by a single value $\alpha_{u,i}$ ($\beta_{v,i}$), that scales the size of the positive (negative) feedback of cytokine u (v) on the secretion rate of cytokine i. As saturation effects do exist in reality, we do not expect the model to accurately predict the secretion rate of the various cytokines for increasing/decreasing stimulus concentrations. If more time points, dose response curves, or degradation rates would be available, the equations could be extended accordingly. We will discuss (local) parameter identifiability for our model equations in Section 2.8.

Although the dataset used does not justify an extension of our simple model equations, the data does indicate the presence of saturation of the cytokine secretion rate. We observe for instance that in the presence of aIL10R, IL-1β secretion drives IL-23 secretion, as the blockade of IL-1β has a clear negative effect on IL-23 secretion. If IL-1β is added instead of blocked however, this does not have an impact on the level of IL-23 secretion at all (Table 2.1). A possible explanation is that under these conditions, the IL-1β concentrations have reached a level where further increase does not further increase IL-23 secretion, because the cells are already producing IL-23 at a maximum rate (i.e. the secretion rate of IL-23 is saturated). We recall we incorporated the addition of a cytokine i at the start of the experiment as a parameter representing the initial concentration of that cytokine γ_i. As the addition of IL-1β has no significant effect on the secretion of the other cytokines, the value of $\gamma_{\text{IL-1}\beta}$ is estimated to be almost zero. This is likely to be an underestimation of the

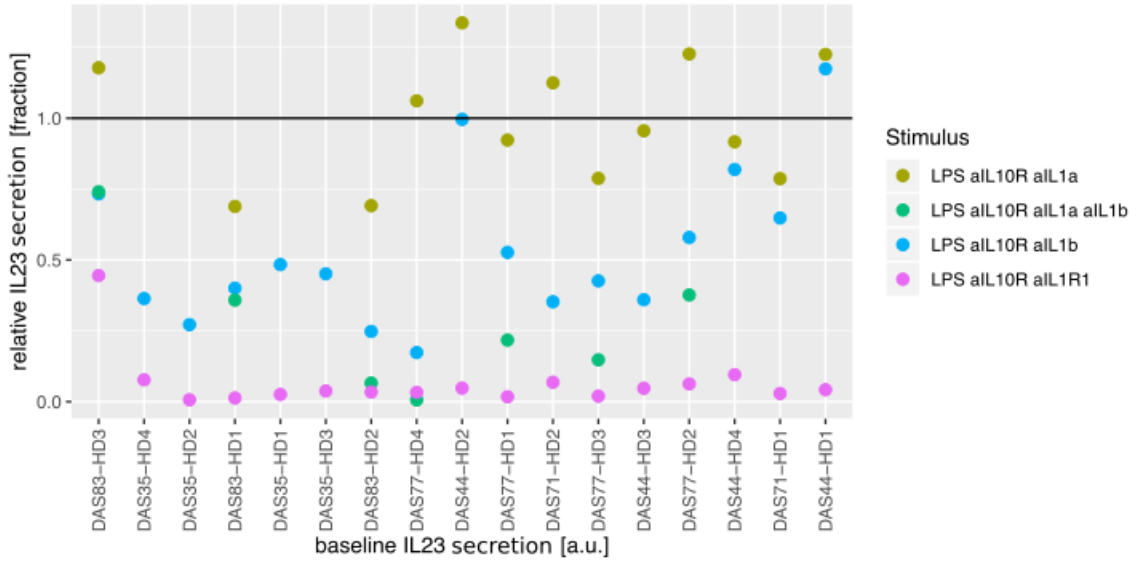


Figure 2.8: The measured log transformed secretion rate of IL-23 after 'LPS + aIL10R + aIL1α', 'LPS + aIL10R + aIL1β' , 'LPS + aIL10R + aIL1α + aIL1β', and 'LPS + aIL10R + aIL1R' stimulation, as a fraction of the measured log transformed secretion rate of IL-23 after 'LPS + aIL10R' stimulation (n=17 healthy donors). We observe that the IL1R receptor blockade has a larger effect than blocking the cytokines themselves, either separately or simultaneously.

true value of $\gamma_{\text{IL-1}\beta}$. More extensive experimental data (e.g. cytokine concentration data) would be needed to further explore this.

We emphasize that the extracted network provides us with an estimation of the size of the effects of the different cytokines at the secretion level observed after 16 hours of 200ng/ml LPS stimulation, because it was based on a data set corresponding to these conditions. We note that the cytokine network could look different for other stimulatory conditions. We could imagine for instance, that if less LPS was added to the system, the secretion levels of IL-1β would be lower, resulting in a reduced concentration of IL-1β which in turn would lead to less IL-23 secretion after 'LPS+aIL10R' stimulation. Because the monocytes would not be producing IL-23 at maximum capacity, adding IL-1β to the system might in this case significantly upregulate IL-23 secretion. Furthermore, the addition of another cytokine such as TNFα might also upregulate IL-23 secretion in this hypothetical situation. This reasoning illustrates that certain interactions might not be captured by the current data set due to saturation as discussed above. Again, more extensive experimental data would be needed to further explore this.

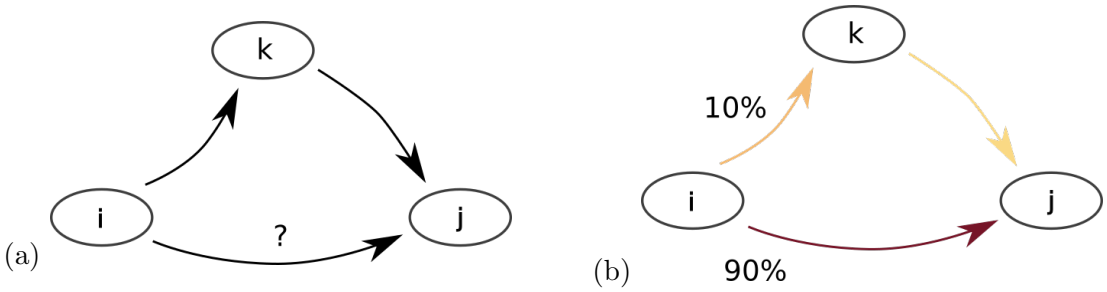


Figure 2.9: (a) When inhibition of cytokine i has a negative effect on the secretion rate of cytokine j, cytokine i might directly upregulate cytokine j secretion (edge labelled with a question mark). This effect could also be indirect, e.g. cytokine i upregulates cytokine k, which in turn upregulates cytokine j secretion. (b) The size of the direct upregulation effect of cytokine i on cytokine j is only a fraction of the total effect observed after blockade of the cytokine i receptor, as part of this effect is due to an indirect pathway (via cytokine k).

2.6 Model selection

Whilst the statistical analysis (Wilcoxon test, see Figure 2.4 and Table 2.2) resulted in a list of 31 pair-wise interactions, the mathematical model allows us to fit all interactions simultaneously to the 1750 data points. By comparing the model fit of different network configurations to the data, we will be able to distinguish between direct and indirect effects and determine the strength of the different interactions (Figure 2.9). We defined direct and indirect effects in Definitions 1 and 2 (Section 2.3).

Some of the edges present in the 31-edge network configuration might not be needed to describe the data, for instance because they represent indirect effects and no direct interactions represented by these edges exist in reality. The aim of this section is to identify the sub-configuration of the 31-edge network that best balances model fit and complexity. Starting from the 31 statistically significant direct cytokine interactions (Figure 2.4), there exist $\sum_{k=1}^{31} \binom{31}{k} = 2^{31} - 1$ distinct wiring possibilities of the network, each corresponding to a subnetwork of the original 31-edge network. In order to find the optimal fit, we will not have to consider these $2^{31} - 1$ possible network configurations explicitly, as we will discuss throughout this section.

2.6.1 Network selection algorithm

Let $\mathcal{O}$ be the set of N statistically significant edges, as identified in Table 2.2, Figure 2.4 for the dataset under consideration. We denote network configurations by subsets $S_i \subseteq \mathcal{O}$, with i a subscript corresponding to that specific configuration. When the number of edges n of a configuration is specified, we will also write S_i^n, with n the number of edges contained in the configuration, and i again a subscript corresponding to that specific configuration. As a clarifying example, consider a set of five statistically significant edges $\mathcal{O} = \{A, B, C, E, F\}$. The network configuration p consisting of edges C and E is a subset of $\mathcal{O}$, i.e. $S_p^2 = \{C, E\} \subset \{A, B, C, E, F\} = \mathcal{O}$. We recall that each network configuration S_i^n corresponds to a model. The model size n corresponds to the number of edges contained in S_i^n. Further, recall that the distance to the data for a given network configuration is defined by $D = \min_{\boldsymbol{\theta}} -2\log\left(\mathcal{L}(\boldsymbol{\theta})\right)$, with the likelihood function $\mathcal{L}(\boldsymbol{\theta})$ defined in Eq (2.25). We will refer to the minimum distance D to the data for a network configuration S_i as $D(S_i)$. We recall that S_i always refers to the set of an individual network, e.g. $S_i = \{A, B, C\}$, with A, B, and C edges.

Definition 3 (Optimal n-sized model S_{opt}^n)**.** We define the optimal model S_{opt}^n for a given network size n as the model with the lowest distance D to the data, out of all n-sized sub-configurations of $\mathcal{O}$, the set of N statistically significant edges.

Remark 1. When a smaller model is nested in a larger model, the distance between the experimental and simulated data of the smaller model has to be larger than or equal to the distance of the larger model. If S_i, S_j are two networks with S_i a subnetwork of S_j, then $D(S_i) \geq D(S_j)$. This is the case because we can construct S_j by adding edges to S_i. Each edge is represented by an edge parameter $\alpha_{u,v} \geq 0$ or $\beta_{u,v} \geq 0$ in the model. Removal of an edge is equivalent to the fixation of the corresponding edge parameter to zero. Hence, when searching for a minimal $D(S_j)$ over all model parameter values (≥ 0), this includes the case where the value of the edge parameters contained in S_j but not in S_i are all zero. The search space over all model parameters for a minimal $D(S_i)$ is therefore contained in the search space over all model parameters for a minimal $D(S_j)$. Therefore, $D(S_i) \geq D(S_j)$.

We note that the removal of some edges from a model network will have a larger effect on the model fit than the removal of others. The removal of an edge might be compensated for by indirect effects, or the parameter corresponding to the edge might have been very small to start with. We iteratively removed edges from the 31 edge network while minimizing the increase in D at each edge removal. This resulted in a list of initially selected networks for each network size, with the size of a network corresponding to its number of edges (Table 2.3). We define S^n_{init} as the initially selected network of size n using this process. Removal of an edge at each reduction in n was implemented by setting the corresponding edge parameter ($\alpha_{u,i}/\beta_{v,i}$) equal to zero. We define the weight of an edge in a particular network configuration as the value of $\alpha_{u,i}$ or $\beta_{v,i}$ for that network configuration. We also assigned colour-weights to each edge in each network configuration (Figure 2.10). We define the colour-weight of an edge for a particular network configuration, as the increase in D when the edge is removed from that configuration, divided by the increase in D when the edge with the largest increase in D for that configuration is removed from the configuration. We note that the edge with the lowest colour-weight for a particular network size n is not necessarily the edge that is removed to obtain the initially selected network size of size $n-1$. Removing an edge with a higher colour-weight might result in a better model fit, when the effects of this edge could be compensated for by other edges in the network.

Thus, now we will describe a procedure (Procedure Ω) that determines the optimal network configuration for a given model size n, $n = 1, \ldots, N$, with N the number of statistically significant edges, without having to consider every possible n sized sub-configuration individually. This is important, as the total number of possible network configurations quickly becomes prohibitively large for a growing number of edges. Before stating Procedure Ω, we introduce the concept of an essential (combination of) edge(s):

Definition 4 (Essential combination of edges)**.** We call a subset of edges within the initial configuration $S' \subseteq S^n_{init}$ essential if $D(\mathcal{O} \setminus S') \geq D(S^n_{init})$, where $\mathcal{O} \setminus S'$ is the model with all N statistically significant edges, except the edges contained in S'. We clarify that $\mathcal{O} \setminus S'$ refers to a single network configuration.

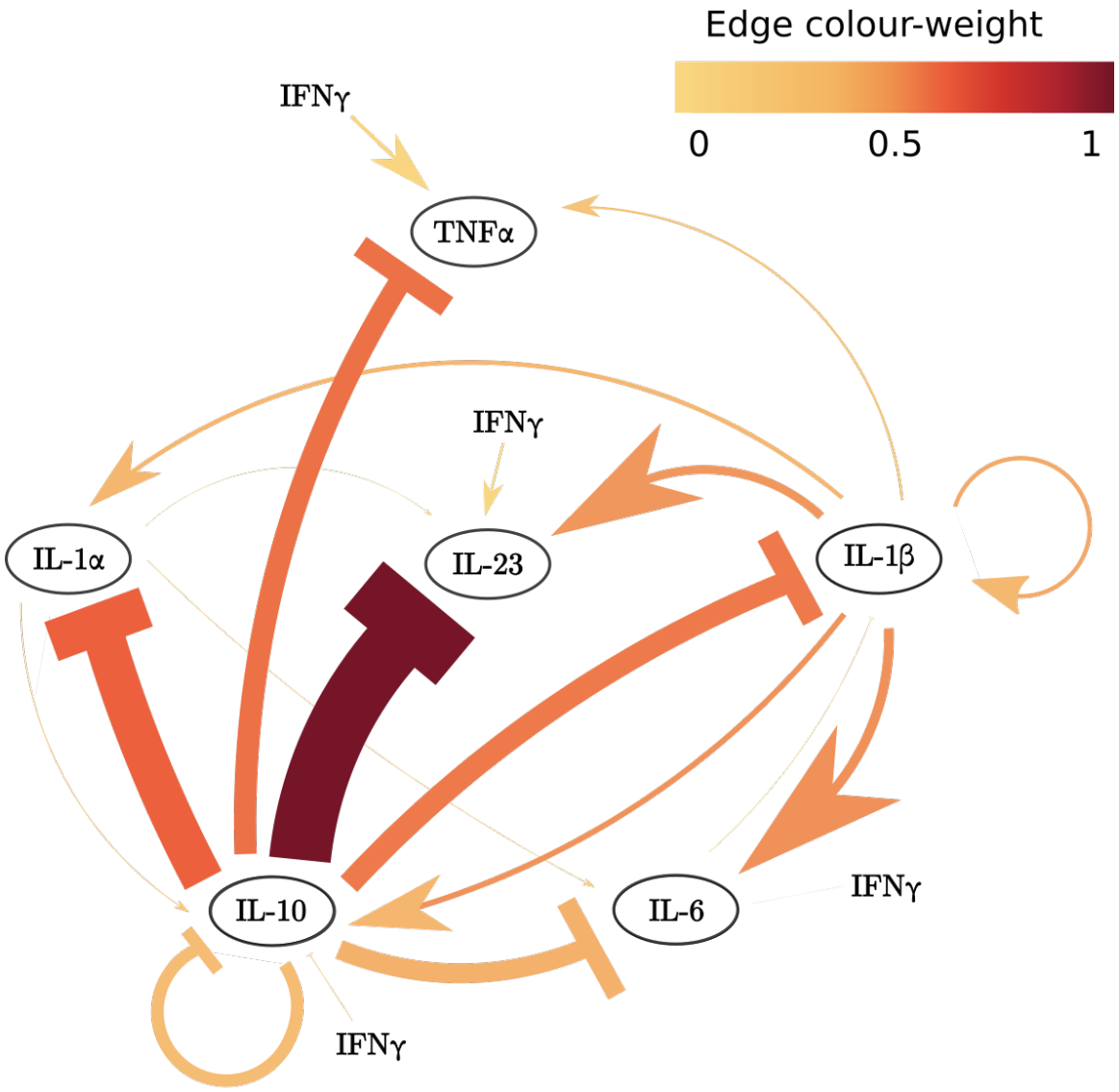


Figure 2.10: Graphical representation of the 20-edge model selected by the AIC using the constrained approach (Section 2.6). The concentration of TNFα, IL-1α, IL-1β, IL-6, IL-10 and IL-23 over time was described by a system of coupled ordinary differential equations. The AIC identifies the model including twenty edges as the optimal balance between model complexity and model fit, when only network configurations were considered including subsets of the 31 edges that were earlier identified by statistical analysis of the experimental dataset (Section 2.2). Edge widths are relative to the increase in fit obtained after addition of that edge, when starting from no edges and iteratively adding edges to the network. We define the colour-weight of an edge for a particular network configuration, as the increase in D when the edge is removed from that configuration, divided by the increase in D when the edge with the largest increase in D for that configuration is removed from the configuration. The edges of the twenty-edge model have been coloured based on their colour-weight. We do not show the effects of LPS, as LPS is present for all conditions and the data used for fitting is normalized per donor and cytokine.

Further, we note that any n-sized model configuration S^n can be written in the form $S^n = R \cup (S^n_{init} \setminus S')$, with $S' \subseteq S^n_{init}$ any subset of the initial configuration and $R \subseteq (\mathcal{O} \setminus S^n_{init})$ a network with the same number of edges as S' (i.e. $|S'| = |R|$). To clarify, this means that any n-sized model consists of l edges that are part of S^n_{init}, and $n - l$ edges that are not part of S^n_{init}, $l = 0, 1, \ldots, n$. Therefore,

Remark 2. If there exists an n-sized model S^n that fits the data better than S^n_{init}, it has to be of the form $S^n = R \cup (S^n_{init} \setminus S')$, with $S' \subseteq S^n_{init}$ any non-empty subset of the initial configuration and $R \subseteq (\mathcal{O} \setminus S^n_{init})$ a combination with the same number of edges as S' (i.e. $|S'| = |R|$).

Also,

Lemma 1. *If a combination of edges $S' \subseteq S^n_{init}$ is essential, no network configuration $W \subseteq (\mathcal{O} \setminus S')$ exists with a better fit to the data than S^n_{init}.*

Proof. Let S' be essential. It follows from the definition of an essential combination of edges that $D(\mathcal{O} \setminus S') \geq D(S^n_{init})$. It then follows from Remark 1 that $D(W) \geq D(\mathcal{O} \setminus S') \geq D(S^n_{init})$, with $W \subseteq (\mathcal{O} \setminus S')$. □

Lemma 2. *If a combination of edges $S' \subseteq S^n_{init}$ is essential, any combination of edges $S'' \subseteq S^n_{init}$ such that $S' \subseteq S''$ is also essential.*

Proof. Let $S' \subseteq S^n_{init} \subseteq \mathcal{O}$ be essential and let $S'' \subseteq S^n_{init} \subseteq \mathcal{O}$ such that $S' \subseteq S''$. Then, $(\mathcal{O} \setminus S'') \subseteq (\mathcal{O} \setminus S')$. It follows from Remark 1 that $D(\mathcal{O} \setminus S'') \geq D(\mathcal{O} \setminus S')$. It then follows from the definition of an essential combination of edges that $D(\mathcal{O} \setminus S'') \geq D(\mathcal{O} \setminus S') \geq D(S^n_{init})$. □

In Fig 2.11 we give a graphical overview of the key steps of Procedure Ω, for $n = 4$, and with $N = 16$ statistically significant edges.

Procedure $\mathbf{\Omega}$, to identify S^n_{opt} for a given model size n (as illustrated in Figure 2.11).

1: We start with the initial configuration S^n_{init}.
2: **for all** $S' \subseteq S^n_{init}$ **do** {We want to determine if an n-sized combination exists with a better fit to the data than S^n_{init}. It follows from Remark 2 that we can write all n-sized combinations in the form $R \cup (S^n_{init} \setminus S')$, with $R \subseteq (\mathcal{O} \setminus S^n_{init})$, with $|S'| = |R|$, and $S' \subseteq S^n_{init}$. Therefore, we need to check whether any subset of edges part of the initial model configuration $S' \subseteq S^n_{init}$ can be replaced by another combination of edges $R \subseteq (\mathcal{O} \setminus S^n_{init})$ (i.e. not part of the initial model configuration), with $|S'| = |R|$, such that $D(R \cup (S^n_{init} \setminus S')) < D(S^n_{init})$. If none of the S' can be replaced is such a way, it follows that $S^n_{init} = S^n_{opt}$. }
3: We check whether S' contains an essential (combination of) edges. If S' contains an essential (combination of) edges, S' is essential by Lemma 2. If S' is essential, it follows from Lemma 1 that no network configuration $W \subseteq (\mathcal{O} \setminus S')$ of size n exists with a better fit to the data than S^n_{init}. In particular, no $(R \cup (S^n_{init} \setminus S')) \subseteq (\mathcal{O} \setminus S')$ exists, with $R \subseteq (\mathcal{O} \setminus S^n_{init})$, with $|S'| = |R|$, such that $D(R \cup (S^n_{init} \setminus S')) < D(S^n_{init})$.
4: **if** S' is not essential **then** {We will replace S' by other combinations $R \subseteq (\mathcal{O} \setminus S')$, with $|R| = |S'|$. For all such R, we have to check whether $D(R \cup (S^n_{init} \setminus S')) < D(S^n_{init})$. If this is the case, we have found a model of size n that better fits the data than S^n_{init}.}
5: [Optional step specific to the IL23 dataset: compute $D(W \cup (S^n_{init} \setminus S')$, with $W = \{\beta_{44}, \beta_{42}, \beta_{23}, \beta_{45}, \alpha_{16}, \beta_{25}, \beta_{22}, \alpha_{13}, \alpha_{12}, \beta_{21}\}$, i.e. the ten edges listed in the last ten rows of Table 2.3)]. {We found that the inclusion of this line reduces the number of times D needs to be computed on line 7 of the algorithm in practice. }
6: **for all** $R \subseteq (\mathcal{O} \setminus S^n_{init})$, with $|R| = |S'|$ **do**
7: Consider all already computed values $D(Z_i)$ for edge configurations $Z_i \supseteq (R \cup (S^n_{init} \setminus S'))$, $i = 1, 2, \ldots$. Here, each Z_i is a single network configuration, where i indexes each such configuration that contains all edges within $(R \cup (S^n_{init} \setminus S'))$ and for which we already computed D. If any of these $D(Z_i)$ is larger than $D(S^n_{init})$, then $D(R \cup (S^n_{init} \setminus S')) \geq D(Z_i) \geq D(S^n_{init})$ and we therefore do not have to compute the value of $D(R \cup (S^n_{init} \setminus S'))$. Conversely, if we have not computed $D(Z_i)$ for a network configuration $Z_i \supseteq (R \cup (S^n_{init} \setminus S'))$ such that $D(Z_i) > D(S^n_{init})$, we compute the value of $D(R \cup (S^n_{init} \setminus S'))$.
8: **if** $D(R \cup (S^n_{init} \setminus S')) < D(S^n_{init})$ **then**
9: We have found a better fitting model of size n than S^n_{init}. We set $S^n_{init} = (R \cup (S^n_{init} \setminus S'))$ and repeat the algorithm.
10: **end if**
11: **end for**
12: **end if**
13: **end for**
14: Set $S^n_{opt} = S^n_{init}$ and return S^n_{opt}. {If none of the non-essential subsets $S' \subseteq S^n_{init}$ can be replaced by another combination of edges, such that we find a better fitting model of size n, it follows from Remark 2 that the initial configuration is the best fitting configuration of size n.}

After identifying the statistically significant edges and generating the list of initial configurations, we applied Procedure Ω to every network size $n \in \{2, \ldots, N-1\}$ to obtain a list with optimal network configurations for every model size. However, for the IL23 dataset, we did not find any network configurations that resulted in a better fit than the already found list of initially selected models for each model size n. We therefore conclude that each initially selected model is equal to a model with the best fit to the data for that particular network size. The application of Ω to every network size $n \in \{2, \ldots, N-1\}$ required the computation of D for $37,542$ different network configurations. We note that this number is dependent on the relative strength of the various interactions present in the dataset, and in particular on the number of essential edges. We recall that the total number of possible network configurations with 31 edges is $2^{31} - 1$. The fraction of the excluded number of network configurations is thus $(2^{31} - 1 - 37,542)/(2^{31} - 1)$, i.e. 99.9983% of all possible network configurations.

In order to identify the network configuration with an optimal balance between edge number and model fit, we used the Akaike information criterium (AIC) for model selection. The AIC can be computed as

$$\mathrm{AIC} = D + 2M, \tag{2.26}$$

with $D = \min_{\boldsymbol{\theta}} -2\log\left(\mathcal{L}(\boldsymbol{\theta})\right)$, $\mathcal{L}(\boldsymbol{\theta})$ the likelihood function as defined in equation (2.25), and M the number of model parameters (see Section 1.3.5). We recall that we always use a trust-region approach with multi-start strategy to obtain estimates of D in this chapter. We have rescaled all AIC values by subtracting the minimal AIC value found across all models.

We show a graphical summary of the colour-weighted 20 edge network identified by the AIC (Figure 2.10). The extracted network clearly indicates that in this inflammatory context, IL-23 is driven by IL-1β, and to a lesser extent by IFNγ, but not by TNFα. This supports the view of IL-1β as a promising target for those patients with high IL-23 levels that fail to respond to TNFα inhibition. The extracted network confirms the well-known negative feedback mechanism of IL-10 on cytokine expression. Our method predicts that the negative feedback of IL-10 on IL-23 is independent of the effect of IL-10 on the other

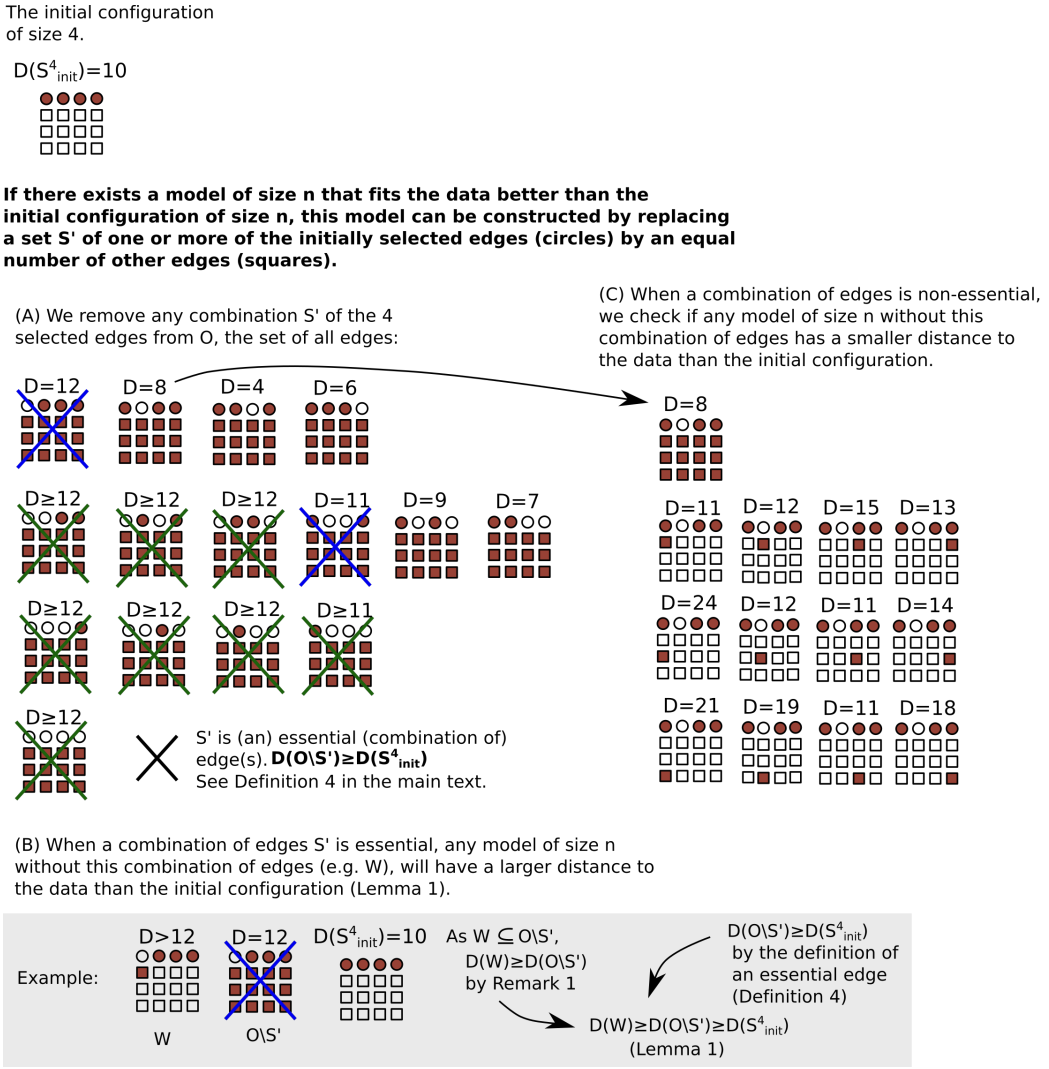


Figure 2.11: **Overview of Procedure Ω to find the optimal model (i.e. with the lowest distance D to the data) for a given model size n out of N statistically significant edges.** (A) We show an example for the initial configuration S^4_{init} of size 4 (circles) with 16 statistically significant edges (circles and squares). If there exists a model of size 4 that fits the data better than the initial configuration, this model can be constructed by replacing a set S' of one or more of the initially selected edges (circles) by an equal number of other edges (squares). We determine which of the 15 possible combinations of the 4 edges part of the initial configuration of size 4 are essential (blue and green crosses) Green crosses correspond to combinations S' that can be immediately deduced to be essential because they contain an essential subconfiguration S'' (Lemma 2). (B) We observe that if a subconfiguration S' of edges part of the initial configuration S^n_{init} is essential, this subconfiguration S' can not be replaced in the initial configuration S_{init} by any other combination of edges, e.g. R, with $|R| = |S'|$, in such a way that the resulting configuration $W = R \cup (S^n_{init} \setminus S')$ fits the data better than the initial configuration S_{init} (see grey insert). (C) If a subconfiguration S' is not essential, we check whether there exists another combination of edges, e.g. R, with $|R| = |S'|$, such that $R \cup (S^n_{init} \setminus S')$ fits the data better than the initial configuration S_{init}.

#	Edge	ΔD	ΔAIC	#	Edge	ΔD	ΔAIC
0	none	5234.5	5188.7	16	α_{25}	47.1	35.1
1	β_{56}	3794.2	3752.2	17	α_{24}	31.2	21.2
2	β_{52}	2829.2	2789.2	18	β_{43}	17.5	9.5
3	β_{53}	2298.9	2260.9	19	α_{26}	7.8	1.8
4	β_{51}	1779.1	1743.1	**20**	α_{74}	4.0	**0.0**
5	β_{54}	1321.2	1287.2	21	α_{72}	2.2	0.2
6	β_{55}	1028.1	996.1	22	β_{44}	0.9	0.9
7	α_{34}	802.4	772.4	23	β_{42}	0.2	2.2
8	α_{36}	603.5	575.5	24	β_{23}	0.0	4.0
9	α_{35}	469.2	443.2	25	β_{45}	0.0	6.0
10	α_{33}	370.1	346.1	26	α_{16}	0.0	8.0
11	α_{32}	269.1	247.1	27	β_{25}	0.0	10.0
12	α_{71}	185.1	165.1	28	β_{22}	0.0	12.0
13	α_{31}	132.9	114.9	29	α_{13}	0.0	14.0
14	α_{76}	86.2	70.2	30	α_{12}	0.0	16.0
15	β_{75}	67.9	53.9	**31**	β_{21}	**0.0**	18.0

Table 2.3: List of the 32 nested initially selected network configurations. Starting from no edges (all edges), we can iteratively add (remove) edges from the network while maximizing (minimizing) the decrease (increase) in distance D, with $D = \min_{\boldsymbol{\theta}} -2\log\left(\mathcal{L}(\boldsymbol{\theta})\right)$, between the model simulations and the data. We recall that we always use a trust-region approach with multi-start strategy to obtain estimates of D in this chapter. For each number of edges n, we list the model size n, the added (removed) edge, and the increase in D and AIC when compared to their minimal found values for network sizes 31 (blue) and 20 (red) respectively. $\mathcal{L}(\boldsymbol{\theta})$ and AIC are defined in equations (2.25) and (2.26) respectively.

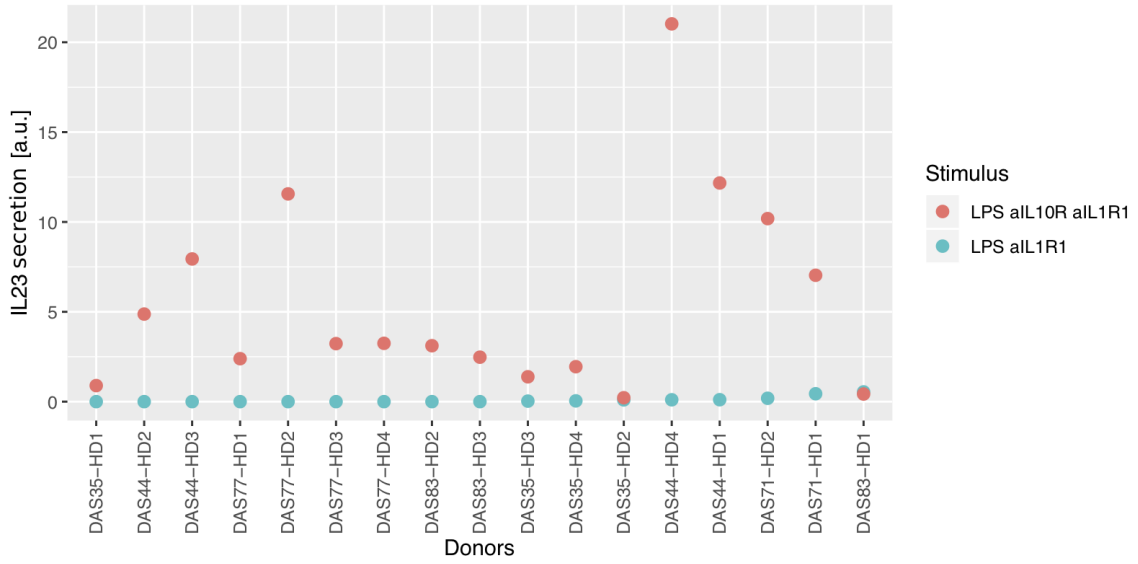


Figure 2.12: The measured log transformed secretion rate of IL-23 after 'LPS + aIL1R' and 'LPS + aIL10R + aIL1R' stimulation (n=17 healthy donors). The data confirms that IL-10 has a downregulatory effect on IL-23 secretion independent of IL-1.

studied cytokines (e.g. IL1β). This can also be directly inferred from the data (Figure 2.12). Further, we find that the positive regulation of IL23 by IL-1β is independent of the effect of IL-1β on the secretion of TNFα, IL-1α, IL-10 or IL-6. Finally, the experimentally observed up-regulation of IL-23 by IFNγ is not driven by the down-regulation of IL-10 by IFNγ.

2.7 Extended model

We repeat the iterative addition of edges, starting from a network with no edges, without restricting the set of possible edges to the list of statistically significant edges as we did before. Instead, we consider all 84 possible positive and negative interactions between all cytokines (i.e. a positive and a negative edge from each of the seven cytokines TNFα, IL-1α, IL-1β, IL-6, IL-10, IL-23 and IFNγ to each of the six cytokines TNFα, IL-1α, IL-1β, IL-6, IL-10, IL-23). We recall that we represent a positive (negative) edge from cytokine u (v) to cytokine i by a positive (negative) value of $\alpha_{u,i}$ ($\beta_{v,i}$) in our model equations (2.1). A positive edge corresponds to an up-regulatory effect and a negative edge corresponds to a down-regulatory effect. When an edge is absent from a specific network configuration, we

set the corresponding edge parameter ($\alpha_{u,i}/\beta_{v,i}$) to zero. In the extended model, we assume an edge is either positive or negative, i.e., when we have added a positive (negative) edge from one cytokine to another, we also remove the corresponding negative (positive) edge from the list of potential edges. We again generated a list of initially selected networks for each network size n, and computed the corresponding edge colour-weights (Table 2.4 and Figure 2.13). We recall that we used a trust-region approach with multi-start strategy to obtain estimates of D. While the constrained approach can only contain edges for which evidence exists in the data, the extended model might point towards potential edges that could be further tested experimentally.

The total number of possible network configurations is $\sum_{k=1}^{84} \binom{84}{k} = 2^{84} - 1 > 10^{25}$. Given the size of this number, we decided to not determine the minimal optimal network for each network size as we did before, but only consider the iteratively generated list of initially selected networks (Table 2.4)). We note that the model selected by the AIC from this list (the 'selected model') contains many more edges than in the constrained case (20 versus 29 edges). We note that the true optimal model in the extended case, corresponding to the network configuration that would be selected by the AIC if all possible network configurations were considered, is probably not part of the list of initially selected models. We expect that this optimal model contains less edges than the selected model. When we examine for instance the effects on the model fit of taking out each edge individually in the case of the found selected model in the extended case, we find that those effects are negligible for the majority of the edges, corresponding to a very small edge colour-weight in Figure 2.13. This model contains so many edges, that the removal of one edge can be compensated for by the other edges.

When comparing the outcome of the two approaches (Tables 2.3 and 2.4), we observe that for both approaches, down-regulatory effects of IL-10 and up-regulatory effects of IL-1β result in the largest increases in model fit. The most striking difference between the two approaches is the large effect on the model fit of the addition of an upregulatory edge from IL-23 to TNFα in the extended approach (compare Figures 2.10 and 2.13). This edge was not part of the set of 31 significant edges of the constrained approach, as the 'LPS+IL23' data did not show a significant difference from LPS in the statistical screening. It follows

from the data that IL-10 and IL-1β have negative and positive effects respectively on both TNFα and IL-23. We note that with the addition of a positive edge from IL-23 to TNFα, these effects can be incorporated in the network with three instead of four edges (i.e. IL-23 to TNFα replaces IL-10 to TNFα and IL-1β to TNFα). This explains why this IL-23 to TNFα edge is the third edge added to the extended model (Table 2.4).

When turning to the experimental data, we observe that the addition of IL-23 does not have an effect on TNFα secretion levels (Table 2.1). However, this does not necessarily mean that IL-23 does not have an effect on TNFα secretion, as the unexplored blockade of the IL-23(receptor) might still have an effect on TNFα secretion. We have seen this for instance in the case of IL-1β and IL-23: IL-1 receptor blockade decreases IL-23 secretion, but IL-23 secretion is not further increased when IL-1β is added, possibly due to saturation effects (Table 2.1, see Section 2.3).

2.8 Practical parameter identifiability

For a given model, we can investigate how accurately we can estimate the model parameter values given the data. The true values of all model parameters in $\boldsymbol{\theta}$ lie within a confidence region with confidence level α with probability α. Following Raue et al., we define an identifiable parameter θ_i as a parameter with a finite confidence interval for its estimate $\hat{\theta}_i$ [281]. We can distinguish two types of parameter non-identifiability: structural and practical non-identifiability. Structural non-identifiability arises from the model structure and is independent from the experimental data. We have investigated the structural identifiability of our model equations before, using the Scaling Invariance Method by Castro and de Boer (Section 2.4). In terms of log-likelihoods, when there is no unique minimum of $\mathcal{LL}(\boldsymbol{\theta})$ with respect to θ_i, the parameter θ_i is structurally non-identifiable. Practical non-identifiability is dependent on the quality and amount of the experimental data. Following Raue et al., we define a practically non-identifiable parameter as "a parameter with a confidence region that is infinitely extended in increasing and/or decreasing direction of θ_i, although the likelihood has a unique minimum for this parameter" [281]. We note that when a parameter is practically identifiable, it follows that this parameter is also structurally identifiable. We investigate the practical identifiability of the parameters of our model using the Profile

#	Edge	ΔD	ΔAIC	#	Edge	ΔD	ΔAIC
0	**none**	5501.3	5428.1	21	α_{22}	66.4	41.2
1	β_{56}	4061	3995.8	22	α_{12}	54.2	31
2	β_{52}	3096	3032.8	23	α_{24}	39.4	18.2
3	α_{61}	2505.4	2444.2	24	β_{51}	25.1	5.9
4	β_{53}	1975.5	1916.3	25	β_{42}	20.6	3.4
5	β_{54}	1537.7	1480.5	26	α_{72}	17.6	2.4
6	β_{55}	1255.2	1200	27	α_{75}	14.8	1.6
7	α_{36}	997.7	944.5	28	β_{14}	12.6	1.4
8	α_{34}	775.5	724.3	**29**	α_{74}	9.2	**0**
9	α_{35}	621.6	572.4	30	α_{31}	8	0.8
10	α_{76}	514.9	467.7	31	β_{15}	6.9	1.7
11	α_{33}	413.4	368.2	32	β_{16}	6.2	3
12	α_{32}	307	263.8	33	β_{41}	5.6	4.4
13	β_{66}	263.3	222.1	34	β_{11}	5.2	6
14	β_{65}	227.5	188.3	35	β_{44}	4.8	7.6
15	α_{64}	188.4	151.2	36	β_{45}	4.4	9.2
16	α_{25}	161.8	126.6	37	β_{46}	1.7	8.5
17	α_{26}	132.9	99.7	38	α_{73}	1	9.8
18	α_{71}	115.2	84	39	α_{21}	0.9	11.7
19	β_{62}	95.8	66.6	40	α_{23}	0.8	13.6
20	β_{43}	80.9	53.7	41	α_{13}	0.7	15.5
				42	β_{63}	**0**	16.8

Table 2.4: List of the 43 nested network configurations identified by the extended approach. Starting from no edges, we can iteratively add edges from the network while maximizing the decrease in distance D, with $D = \min_{\boldsymbol{\theta}} -2\log\left(\mathcal{L}(\boldsymbol{\theta})\right)$, between the model simulations and the data. We recall that we always use a trust-region approach with multi-start strategy to obtain estimates of D in this chapter. We consider all 84 possible positive and negative interactions between all cytokines. For each number of edges n, we list the model size n, the added (removed) edge, and the increase in D and AIC when compared to their minimal found values for network sizes 42 (blue) and 29 (red) respectively. $\mathcal{L}(\boldsymbol{\theta})$ and AIC are defined in equations (2.25) and (2.26) respectively.

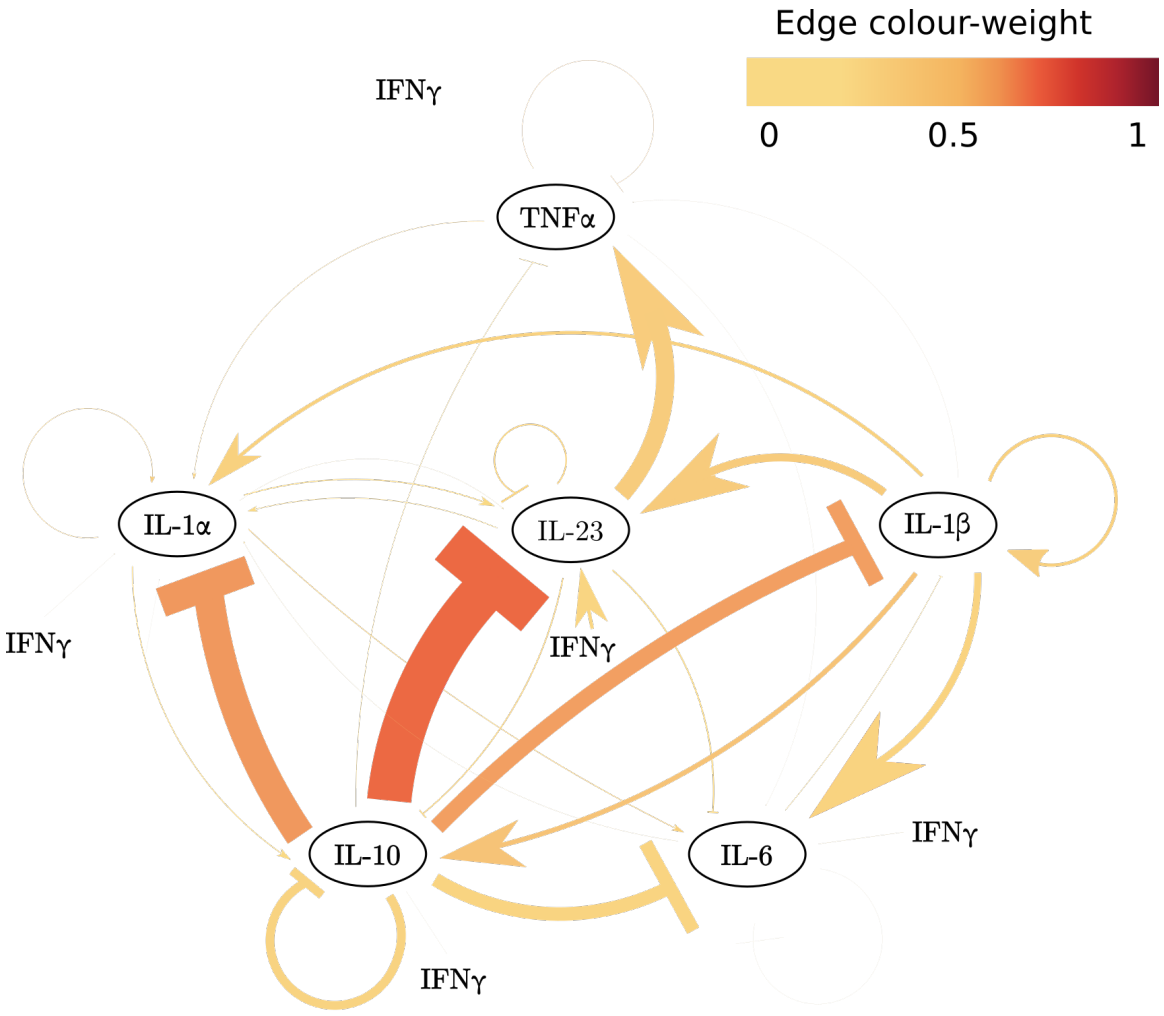
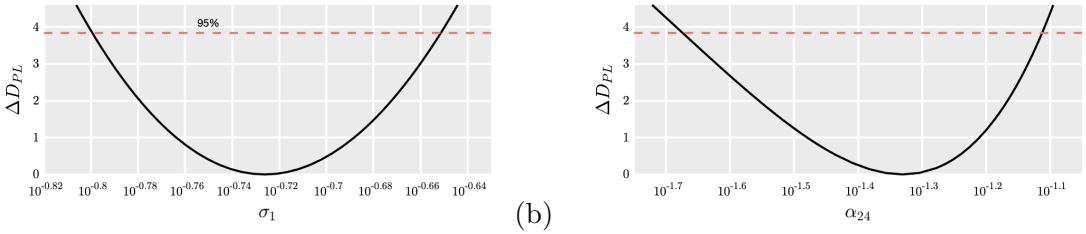


Figure 2.13: Graphical representation of the 29-edge model selected by the AIC using the extended approach (Section 2.7). The concentration of TNFα, IL-1α, IL-1β, IL-6, IL-10 and IL-23 over time was described by a system of coupled ordinary differential equations. The AIC identifies the model including twenty-nine edges as the optimal balance between model complexity and model fit, when the 43 nest selected network configurations were considered as listed in Table 2.4. Edge widths are relative to the increase in fit obtained after addition of that edge, when starting from no edges and iteratively adding edges to the network. We define the colour-weight of an edge for a particular network configuration, as the increase in D when the edge is removed from that configuration, divided by the increase in D when the edge with the largest increase in D for that configuration is removed from the configuration. The edges of the 29-edge model have been coloured based on their colour-weight. We do not show the effects of LPS, as LPS is present for all conditions and the data used for fitting is normalized per donor and cytokine.

Likelihood Approach [281]. We vary the value of each parameter $\theta_m \in \boldsymbol{\theta}$ over a broad range of values and compute for each value the increase in $D_{PL} = \min_{\tilde{\boldsymbol{\theta}}_m} -2\log\left(\mathcal{L}(\boldsymbol{\theta})\right)$, with $\tilde{\boldsymbol{\theta}}_m = \{\theta_1, \ldots, \theta_{m-1}, \theta_{m+1}, \theta_N\}$, i.e. for each fixed value of θ_m we find the minimal D_{PL} by fitting all other parameters to the data. This allows us to compute likelihood based parameter value confidence intervals for each parameter with threshold value ζ, the ζ quantile of the χ^2_1 distribution (See Section 1.3.3.3 for a discussion of this approach). Assuming a particular model describes the data sufficiently well, the true value of θ_m will lie within the ζ level confidence interval with probability ζ. Infinite confidence intervals in the parameter value space correspond to parameter non-identifiability. We will validate the coverage of the confidence intervals in Section 2.10.4. We recall the parameter vector $\boldsymbol{\theta}$ contains all model parameters σ_i, $\alpha_{u,i}$, $\beta_{v,i}$ and γ_i, where the six σ_i correspond to the LPS effect, the γ_i to the effects of the addition of individual cytokines at the start of the experiment, and each $\alpha_{u,i}$ and $\beta_{v,i}$ corresponds to a positive or negative network edge respectively. We note that when a certain positive (negative) edge from u (v) to i does not exist, we fix the corresponding parameter value $\alpha_{u,i}$ ($\beta_{v,i}$) to zero. These fixed parameters are not part of the vector of estimable parameters $\boldsymbol{\theta}$.

2.8.1 The 20-edge model

In this subsection, we will consider the practical parameter identifiability of the selected, 20-edge model. We will derive plausible intervals for each model parameter that we will use in Section 2.9 when we consider the sensitivity of the model output to the input parameters. The 20-edge selected model contains 31 fitted parameters. The parameters σ_1, σ_2, σ_3, σ_4, σ_5, σ_6, σ_7, γ_5, and the 19 edge parameters α_{24}, α_{25}, α_{26}, α_{31}, α_{32}, α_{33}, α_{34}, α_{35}, α_{36}, β_{51}, β_{52}, β_{53}, β_{54}, β_{55}, β_{56}, α_{71}, α_{74}, α_{75}, α_{76}, are practically identifiable up to the 95% confidence level. We show the profile likelihood plots of σ_1 (corresponding to the effect of LPS on TNFα) and α_{24} (corresponding to the positive effect of IL-1α on TNFα) as an example in Figure 2.14. These plots have been generated using the same Matlab environment 'Data2Dynamics' as we used before for model fitting and simulation [281, 284] (See Section 1.3.3). We now consider the practically non-identifiable parameters γ_3, γ_1, γ_6, γ_4, and β_{43} of the selected model.



(a) (b)

Figure 2.14: Example of two practically identifiable parameters. The increase in D_{PL} for various values σ_1 (left, corresponding to the effect of LPS on TNFα) and α_{24} (right, corresponding to the positive effect of IL1α on TNFα). For each value of σ_1 and α_{24}, all other parameter values were re-estimated using log-likelihood minimization. The 95% confidence interval threshold is shown as a red dashed line. This figure has been generated using the Matlab environment 'Data2Dynamics' [281, 284].

We show the profile likelihood plots for the parameters γ_3, γ_1, γ_6, and γ_4, corresponding to the effects of the addition of individual cytokines at the start of the experiment (Figure 2.15). We recall that we implement the addition of cytokine i at the start of the experiment as $x_i(0) = \gamma_i$, with $x_i(t)$ the concentration of cytokine i. We have to estimate the value of γ_i. We note that the confidence interval for γ_3 is unbounded from below and therefore practically non-identifiable. This parameter corresponds to the effect of the addition of IL1-β at the start of the experiment. We note that no significant difference in cytokine expression of the other cytokines was observed after addition of IL1-β (Table 2.1). Therefore, it is not surprising that the estimated value of γ_3 is so small. We can set γ_3 to zero without impacting the model fit. The profile likelihood profiles of γ_1 and γ_6, corresponding to the amount of added TNF-α and IL-23, are flat, corresponding to structural non-identifiable parameters. For this model configuration, γ_1 and γ_6 are structurally unidentifiable, because the selected model does not contain edges from TNFα or IL-23 to the other cytokines. Therefore, the addition of TNFα or IL-23 has no effect on the model fit (see Section 2.4). We can set the value of γ_1 and γ_6 to zero (or any other value) without impacting the model fit. The estimated value of γ_4, corresponding to the addition of IL-6, is very large. We note that in the selected model, IL-6 only has a negative effect on IL-1β, and no effect on the other cytokines. In line with this, the data indicates that the addition of IL-6 has a significant negative effect on the expression of IL-1β (Table 2.1). However, the blockade of the IL-6 receptor does not have a significant effect on the expression of IL-1β (Table 2.1). Although

not significant, we even observe slightly less IL-1β expression after the blockade of the IL-6 receptor. To accommodate this, the value of $\beta_{4,3}$, corresponding to the negative edge from IL-6 to IL-1β is estimated to have a very small value (i.e. less than 10^{-4}, Figure 2.16 (b)). The model simulations in the absence of the addition of IL-6 then correctly show almost no effect on the expression of IL-1β after blockade of the IL-6 receptor. When IL-6 is added, the expression of IL-1β goes down (Table 2.1). Because the estimated value of $\alpha_{4,3}$ is small, the estimated value of γ_4 needs to be very large for the model simulations to correctly show this experimentally observed negative effect on the expression of IL-1β after addition of IL-6. We note that a decrease of parameter $\beta_{4,3}$ can be compensated with an increase of parameter γ_4 (Figure 2.16). Therefore, the parameters γ_4 and $\beta_{4,3}$ are not practically identifiable.

For the sensitivity analysis in Section 2.9, we will vary all parameters within in plausible ranges. We can use the 95% confidence intervals of all practically identifiable parameters as a plausible upper and lower bound. To obtain a finite 95% confidence interval for γ_4 and $\beta_{4,3}$, we set an upper bound on γ_4 of 10^5. After setting this upper bound on γ_4, $\beta_{4,3}$ becomes identifiable and γ_4 is bounded rendering it practically identifiable (Figure 2.16(c)). We note we could resolve the practical non-identifiability experimentally by comparing the amount of IL-6 added at the start of the experiment to the concentration of IL-6 in the supernatant for one or more of the conditions. The amount of experimentally added IL6 for the 'LPS (+ aIL10R) + IL-6' stimulation condition was 10 μg/ml. Although no concentration data is available for this healthy donor dataset, we do have access to concentration data from a similar experiment from the same lab where IBD patient cells were used, instead of healthy donor cells. The concentration of IL-6 in the supernatant of PBMCs after 16h of LPS stimulation was 0.8 μg/ml on average (28 patients). The simulated control value of $x_4(16)$, corresponding to the dimensionless concentration of IL6 after 16 hours of LPS stimulation, has a simulated value of $10^{-0.8}$. We therefore assume the upper bound of 10^5 is many orders of magnitude larger than the true, unknown value of amount of added IL-6.

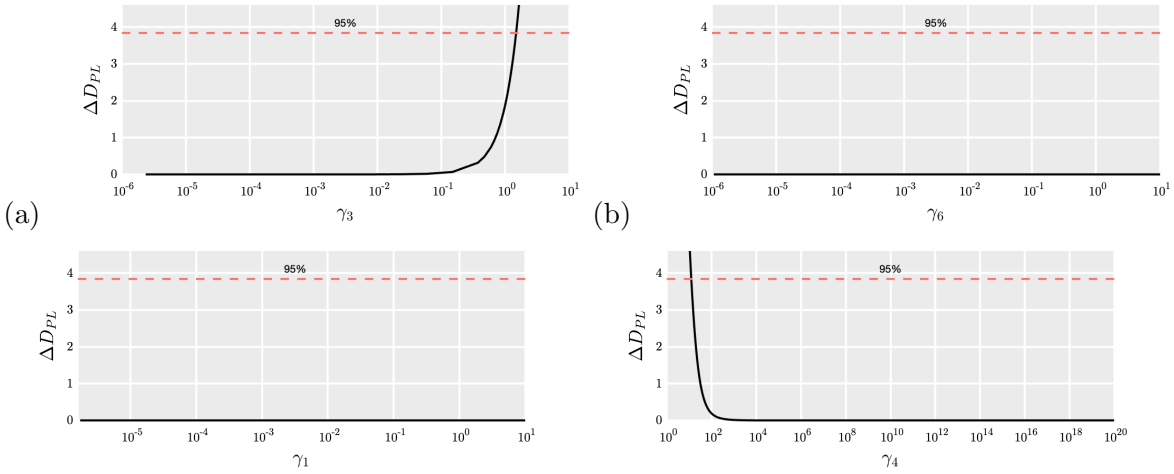


Figure 2.15: The increase in D_{PL} for various values of γ_3, γ_6, γ_1, γ_4, corresponding to the estimated amount of added IL-1β, IL-23, TNF-α and IL-6 respectively. For each value of γ_i, $i \in \{1, 3, 5, 6\}$, all other parameter values were re-estimated using log-likelihood minimization. The 95% confidence interval threshold is shown as a red dashed line. This figure has been generated using the Matlab environment 'Data2Dynamics' [281, 284].

2.8.2 Comparison between the selected 20-edge model and the 31-edge model

We set $\gamma_1 = \gamma_3 = \gamma_6 = 0$, and set an upper bound of 10^5 to the value of γ_4, such that all model parameters of the selected 20-edge model are practically identifiable. We note that fixing the parameters to these values has no effect on the quality of the model fit. We note that the addition of edges can cause a practically identifiable edge to become non-identifiable at a certain ζ level. For both the model containing all 31 statistically significant parameters, and the selected 20-edge model, we plot the increase in D_{PL} while varying the value of α_{74} (representing the positive effect of IFNγ on IL-6 secretion). Decreasing the number of parameters by taking out edges increases the level of identifiability of α_{74} from $\zeta = 0.19$ (31-edge model) to $\zeta = 0.05$ (20-edge model) (Figure 2.17). A parameter could also be practically non-identifiable because its estimated value is very small to start with. This is the case for the estimated values of α_{12}, α_{13}, α_{16}, β_{21}, β_{22}, β_{23}, β_{25}, β_{42}, β_{44} and β_{45} for the full, 31-edge model. We note none of the edges represented by these parameters are part of the selected 20-edge model. The value of D_{PL} does not reach the 95% confidence level when the estimated value of these parameters (for the 31-edge model configuration) is further reduced (e.g. Figure 2.18, solid lines). Even when we decrease the

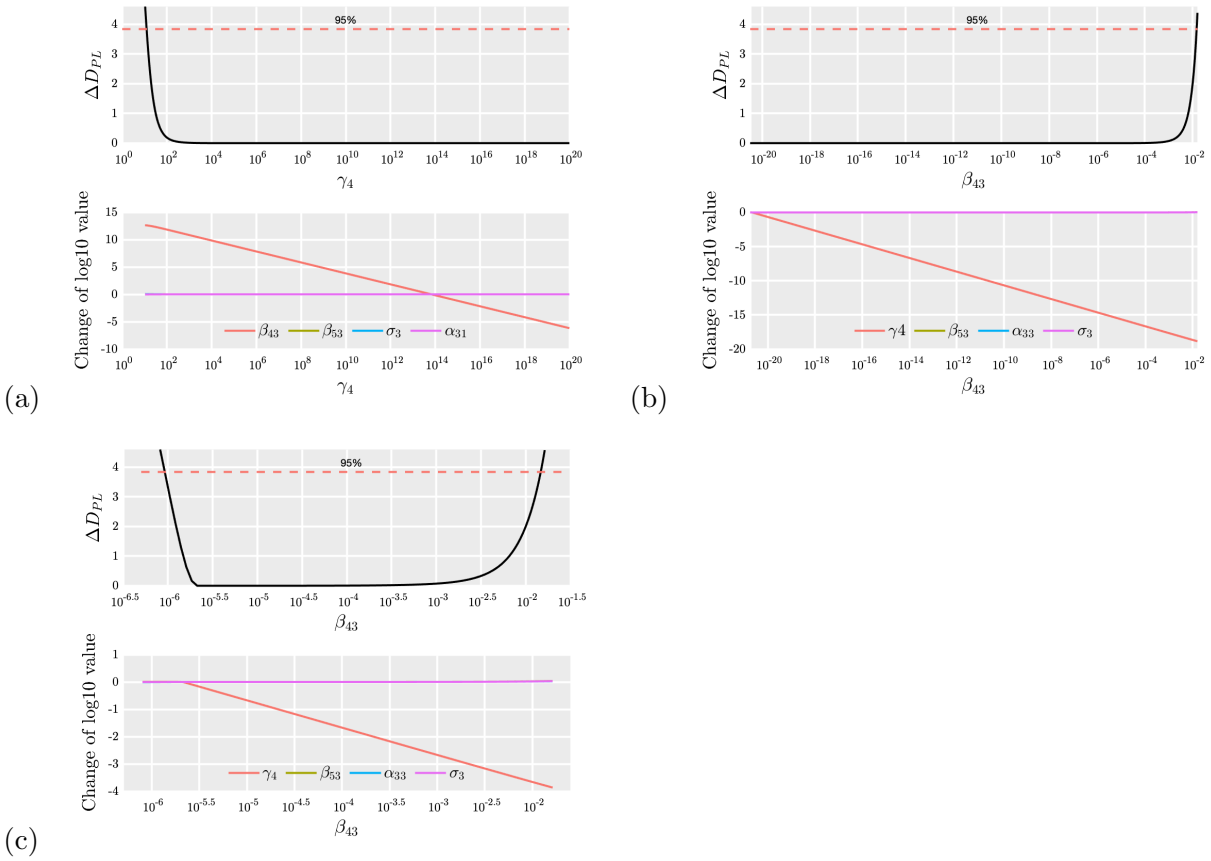


Figure 2.16: The increase in D_{PL} for various values of (a) γ_4 (top, corresponding to the amount of added IL-6) and (b) β_{43} (top, representing the negative effect of IL-6 on IL-1β secretion). For each value of γ_4 and β_{43}, all other parameter values were re-estimated using log-likelihood minimization. We show the changes in the estimated log10 transformed values of four of these parameters with respect to their original maximum likelihood estimate values, again for various values of γ_4 and β_{43} (a and b, bottom). The 95% confidence interval threshold is shown as a red dashed line (a and b, top).(c) We show the same plot for β_{43}, but with the upper bound of γ_4 to 10^5. After setting the upper bound of γ_4 to 10^5, β_{43} is identifiable up to the 95% confidence level. This figure has been generated using the Matlab environment 'Data2Dynamics' [281, 284].

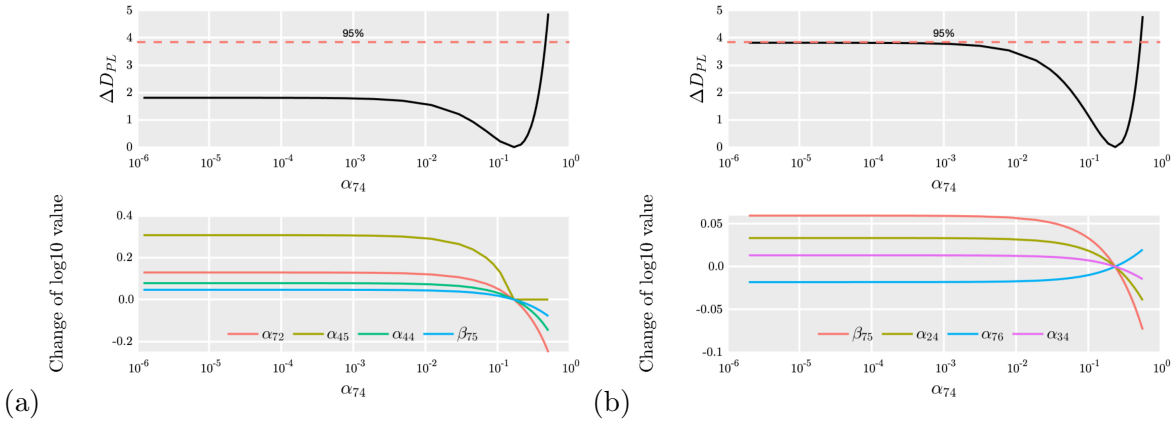


Figure 2.17: The increase in D_{PL} for various values of α_{74} (corresponding to a positive effect from IFN-γ to IL-6) (top). For each value of α_{74}, all other parameter values were re-estimated using log-likelihood minimization. We show the changes in the estimated log10 transformed values of four of these parameters with respect to their original maximum likelihood estimate values, again for various values of α_{74} (bottom). We show the changes in the estimated log10 transformed values of the four parameters with the largest increase for any value of α_{74} as an example, but note the values of the other model parameters were re-estimated for each value of α_{74} as well. The 95% confidence interval threshold is shown as a red dashed line (top). The effect of IFNγ on IL-6 that is represented by α_{74} is non-identifiable at the 95% level in the full 31 edge model (a). After removal of 11 edges, most notably α_{72} that was driving an indirect effect via IL-1α upregulation, α_{74} is identifiable up to the 95% confidence level (b). This figure has been generated using the Matlab environment 'Data2Dynamics' [281, 284].

value of one of these parameters while fixing all other parameters to their earlier estimated maximum likelihood values, the increase in $-2\log\mathcal{L}(\hat{\boldsymbol{\theta}})$ does not reach the 95% confidence level (Figure 2.18, dashed lines). There are two reasons these parameters are so small. First, the size of their effect is small, e.g. IL-6 addition decreases the average IL-10 secretion rate by only 22% (corresponding to edge β_{45}), whereas for instance IL-10 addition results in a decrease of 112% (Table 2.1). The second reason is that we use all data simultaneously when optimizing. Although IL-1α blockade seems to increase IL-1α, IL-1β, and IL-10 secretion (corresponding to edges β_{22}, β_{23} and β_{25} respectively), in the presence of IL-1β and/or aIL10R blockade, we observe the opposite effect (Table 2.1). As the model can not explain this conflicting information, the best fit is obtained by assuming the negative effects of IL-1α are negligible.

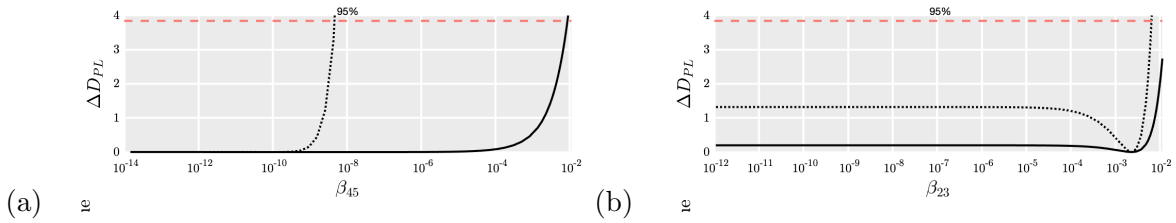


Figure 2.18: For the model configuration consisting of all 31 statistically significant edges, the increase in D_{PL} for various values of β_{45} (corresponding to a negative edge from IL-6 to IL-10) (a) and β_{23} (corresponding to a negative edge from IL-1α to IL-1β) (b) (solid lines). The increase in $-2\log\mathcal{L}(\hat{\boldsymbol{\theta}})$ while varying β_{45} and β_{23} and keeping all other parameters fixed to their estimated values $\hat{\boldsymbol{\theta}} = \underset{\boldsymbol{\theta}}{\operatorname{argmin}} -2\log\left(\mathcal{L}(\boldsymbol{\theta})\right)$ is shown as a black dotted line. The 95% confidence interval threshold is shown as a red dashed line. This figure has been generated using the Matlab environment 'Data2Dynamics' [281, 284].

2.9 Parameter sensitivity analysis

We examine the sensitivity of the selected 20-edge model simulations to changes in parameter values within plausible ranges. We will use the Extended Fourier Amplitude Sensitivity Test (eFAST) for sensitivity analysis, developed by Saltelli et al., and based on the Fourier Amplitude Sensitivity Test developed by Cukier et al. [73, 295] (Section 1.3.4). We will use the Matlab based implementation by Marino et al. [213]. We used the standard settings of the implementation by Marino et al. [213], i.e. 5 search curves and 65 samples per search curve for each run of eFAST, a frequency of 8 for the parameter of interest and a frequency of 1 for all other parameters. We also used a dummy parameter, to highlight when low sensitivities are below the threshold that may be reliably inferred from the algorithm.

We first need to determine the ranges that we will use to vary the model parameters within. We recall that the selected 20-edge model contains 31 fitted parameters. We recall that γ_i represents the amount of added cytokine i at the start of the experiment, for the experimental condition 'LPS + i'. We found that the parameters γ_1 and γ_6 are structurally non-identifiable and the parameter γ_3 is practically non-identifiable (see Section 2.8.1). We can set $\gamma_1 = \gamma_3 = \gamma_6 = 0$ without impacting the model fit. We will not consider γ_1, γ_3, or γ_6 for the sensitivity analysis and set $\gamma_1 = \gamma_3 = \gamma_6 = 0$. Further, we found that β_{43} and γ_4 are practically non-identifiable, corresponding to an infinite confidence interval at the 95% level (Figure 2.16(a) and (b)). We set an upper bound of 10^5 to the edge parameter β_{43}, such

that both β_{43} and γ_4 have finite confidence intervals at the 95% confidence level (Figure 2.16(c)). All other model parameters, including all 19 edge parameters of the selected model have finite confidence intervals at the 95% confidence level.

We vary all fitted model parameters (excluding γ_1, γ_3, or γ_6) on the range bounded by the 95% confidence level intervals. We sample uniformly from these ranges and compute the sensitivity and total order sensitivity indices for each model parameter. We take the cytokine secretion rates at $t = 16$ as our model output. We consider parameter sensitivity for the 'LPS' condition, and the conditions 'LPS+aIL-1α', 'LPS+aIL-1β', 'LPS+aIL1R','LPS+aIL10R', 'LPS+aIL-6', 'LPS+IL-10', 'LPS+IL-6', 'LPS+IFNγ' (Figures 2.19- 2.27). During eFAST, all parameters are varied simultaneously and the variance of the parameters and model output is considered (see Section 1.3.4 for an introduction of eFAST). The S_i gives a measure of the fraction of the variance that is explained by the variation of parameter i. The S_{it} gives a measure of the fraction of the variance that is not explained by the variation of the other parameters, i.e. $S_{it} = 1 - \sum_{j \neq i} S_j$. The difference between S_i and S_{it} therefore gives a measure of the fraction of the variance that can not be explained by the variation of individual parameters and corresponds to non-linear interactions between the model parameters. We note that the difference between S_i and S_{it} is generally small for our model parameters, indicating the size of non-linear interactions is small for our model.

We note that the parameters with the largest sensitivity coefficients S_i generally correspond to parameters that we would expect to have a large influence on the model output considered. For example, we consider the 'LPS' condition and IL-1α secretion rate at $t = 16$ (Figure 2.19, second column). In the selected model, edges from IL-10 and IL-1β to IL-1α exist. We would therefore expect that the corresponding edge parameter β_{52} and α_{32} would have the largest influence on the model output in this case (i.e. IL-1α secretion rate at $t = 16$), together with the stimulus parameter s_{IL-1A}. Indeed, the S_i of these three parameters are the largest in this case. We note the stimulus parameter s_{IL-10} has a large S_i as well. This is explained by the large effect of the amount of IL10 in the system on the expression of IL-1α (via the edge from IL-10 to IL-1α). When we consider the 'LPS + aIL10R' condition, as expected, the S_i from s_{IL-10} and β_{52} (corresponding to the edge from

IL-10 to IL-1α) is small (Figure 2.24). In general, the sensitivity results (Figures 2.19-2.27) highlight that across experimental conditions each cytokine is sensitive to its secretion parameter, s_i for cytokine i. Further each cytokine is sensitive to a relatively small number of edge weights, and thus other cytokines. In addition, except as expected in knock-out experimental conditions these dependencies are generally present across experimental conditions. The sensitivities are also associated with parameters that do not generate practical identifiability concerns, increasing confidence in the network selection process and biological conclusions drawn in this chapter, as the most sensitive parameters are constrained by the data.

2.10 Validation

We will validate our modelling approach introduced in this chapter using synthetic data. We will first introduce a general form of our modelling approach (Section 2.10.1). We will validate the statistical screening of edges and the AIC-based network model selection by considering four network motifs consisting of three nodes and two directed edges in the presence and absence of various cytokine (receptor) blockades (Fig 2.28) (Section 2.10.2). We will also explore the effects of the addition of individual cytokines (Section 2.10.3). We will verify the correct coverage of the parameter confidence intervals that we obtained using the Profile Likelihood approach (Section 2.10.4). Finally, we will present a validation of the optimisation strategy (Section 2.10.5).

2.10.1 General modelling approach

Based on a current experimental framework, such as the framework used to obtain the IL23 dataset used in this Chapter, our modelling approach requires an experimental dataset of cytokine secretion by *in vitro* stimulated immune cells in the presence and absence of various cytokine (receptor) inhibitors. Optionally, data on the addition of various cytokines and multiple timepoints can also be considered. We define an experimental condition as a specific combination of stimulus, cytokine (receptor) inhibitor, and added cytokine. For each condition, a measurement j should contain single values for the secretion rate of each

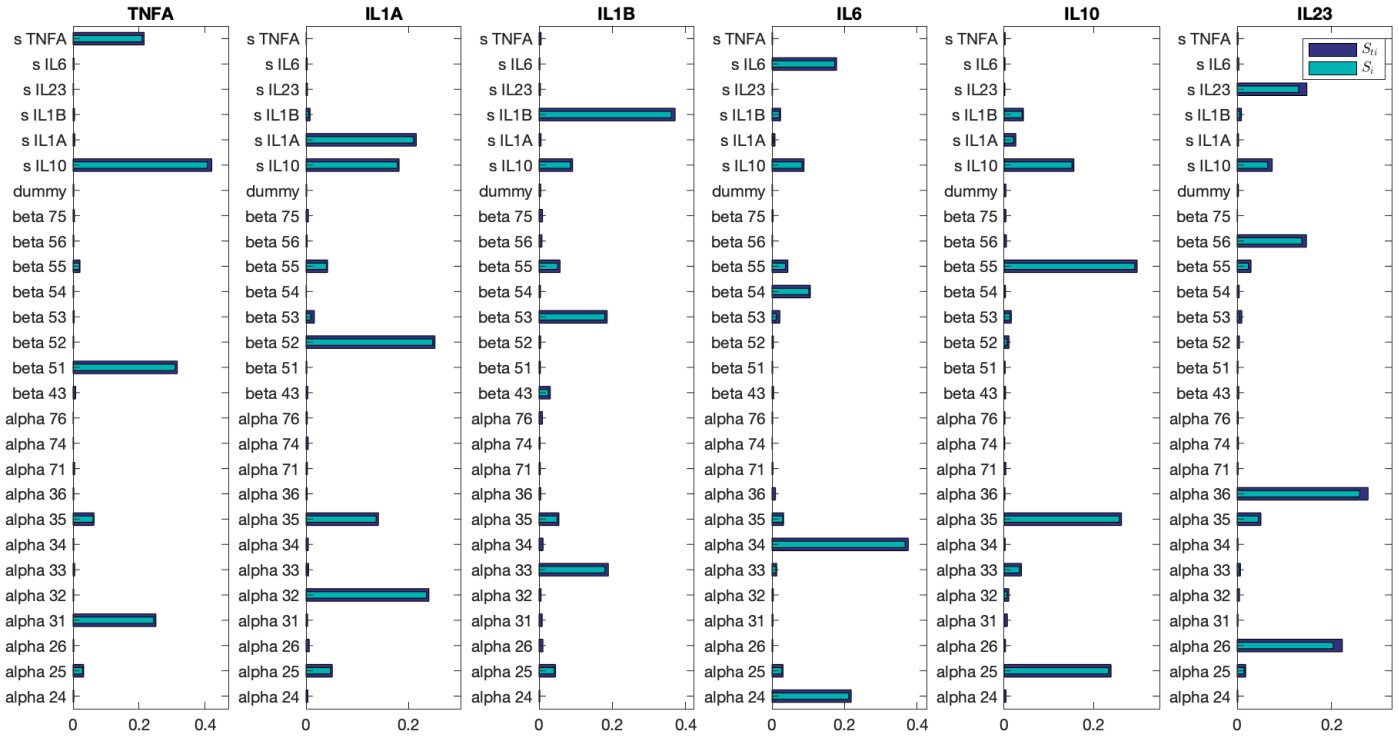


Figure 2.19: For the 'LPS' condition, eFAST parameter sensitivity analysis for the selected 20-edge model. As model outputs, we have chosen the cytokine secretion rate at $t = 16$ for every cytokine of interest (columns). We show both sensitivity S_i and total order sensitivity S_{ti} indices for each fitted model parameter and for a dummy parameter (rows).

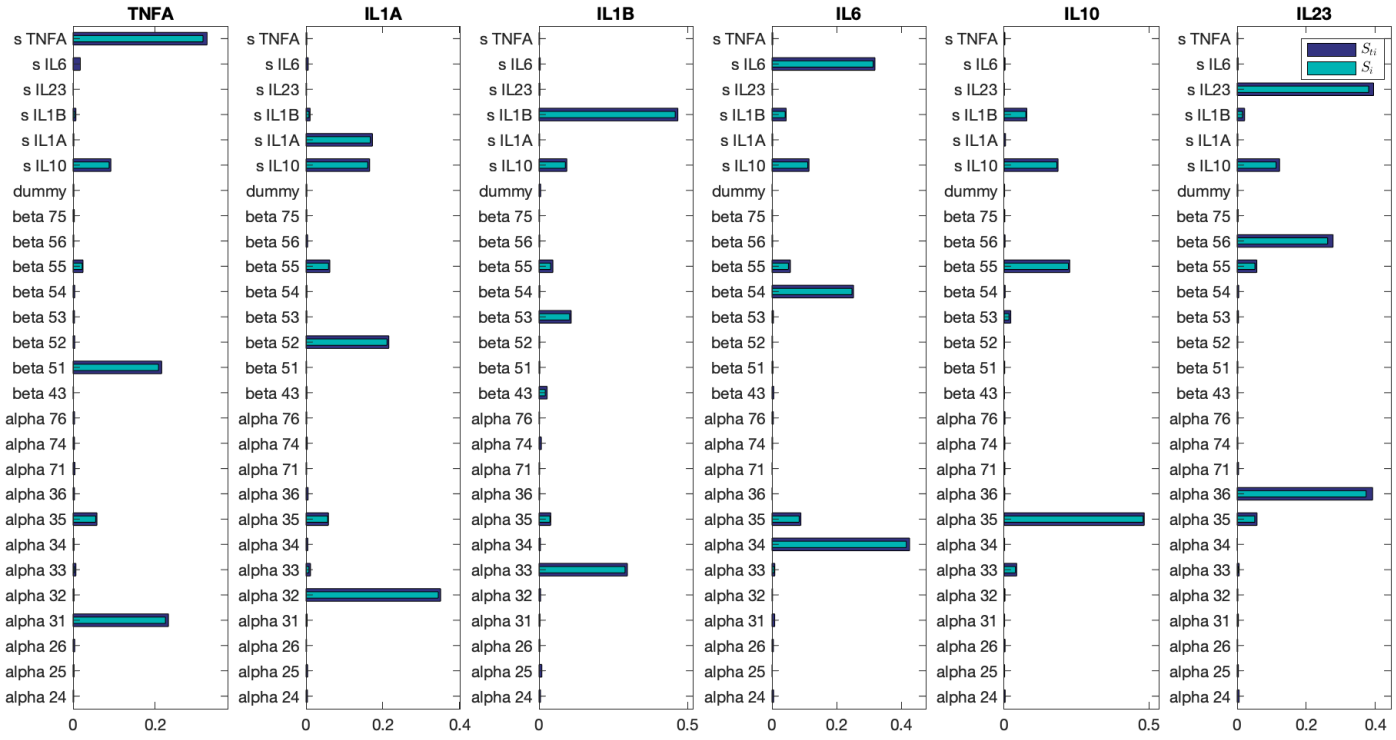


Figure 2.20: For the 'LPS+aIL1α' condition, eFAST parameter sensitivity analysis for the selected 20-edge model. As model outputs, we have chosen the cytokine secretion rate at $t = 16$ for every cytokine of interest (columns). We show both sensitivity S_i and total order sensitivity S_{ti} indices for each fitted model parameter and for a dummy parameter (rows).

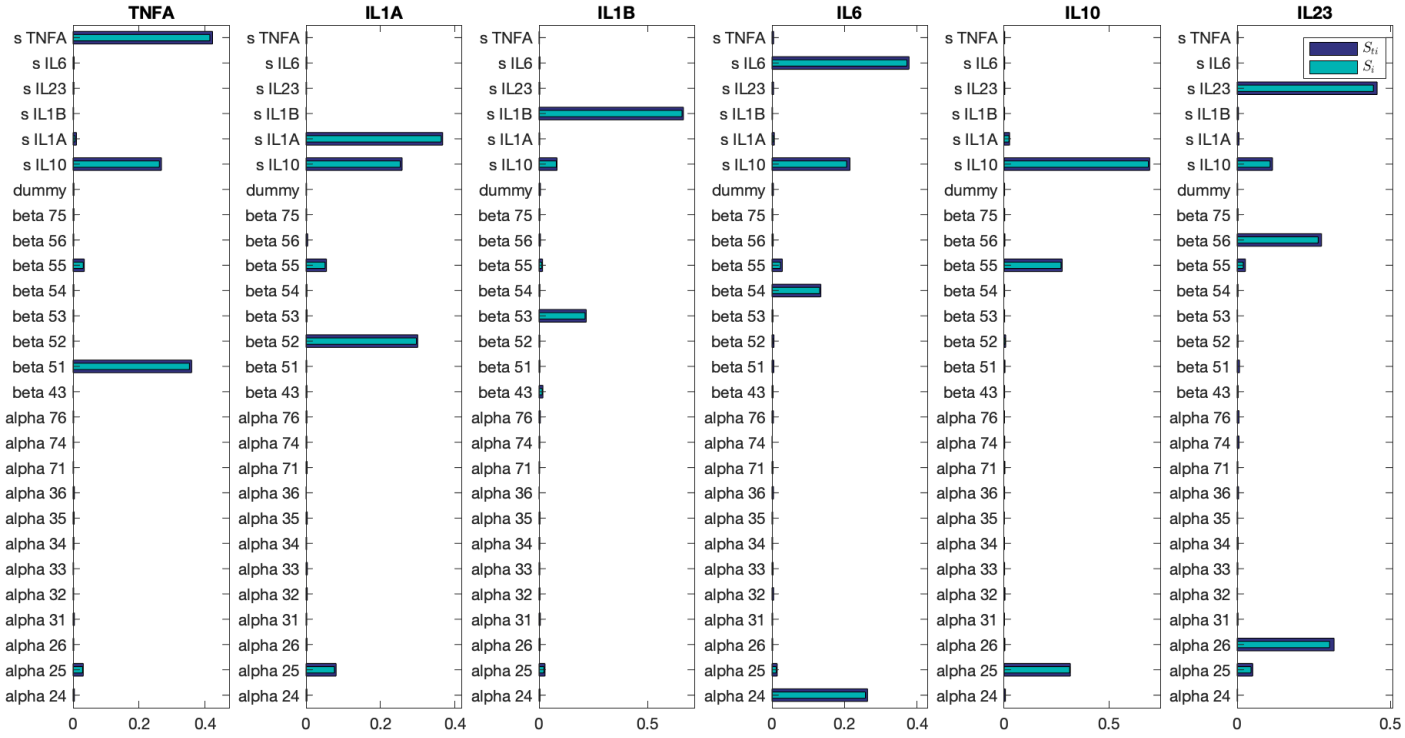


Figure 2.21: For the 'LPS+aIL-1β' condition, eFAST parameter sensitivity analysis for the selected 20-edge model. As model outputs, we have chosen the cytokine secretion rate at $t = 16$ for every cytokine of interest (columns). We show both sensitivity S_i and total order sensitivity S_{ti} indices for each fitted model parameter and for a dummy parameter (rows).

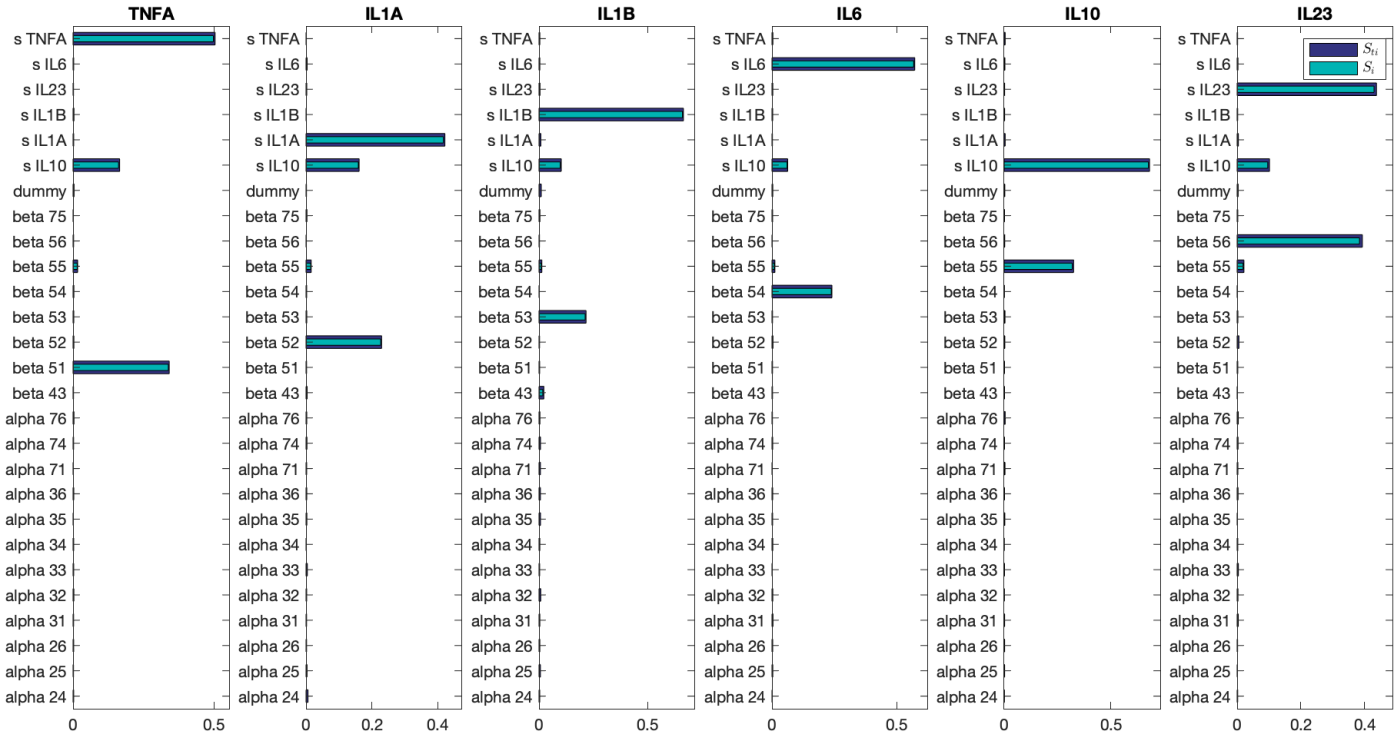


Figure 2.22: For the 'LPS+aIL1R' condition, eFAST parameter sensitivity analysis for the selected 20-edge model. As model outputs, we have chosen the cytokine secretion rate at $t = 16$ for every cytokine of interest (columns). We show both sensitivity S_i and total order sensitivity S_{ti} indices for each fitted model parameter and for a dummy parameter (rows).

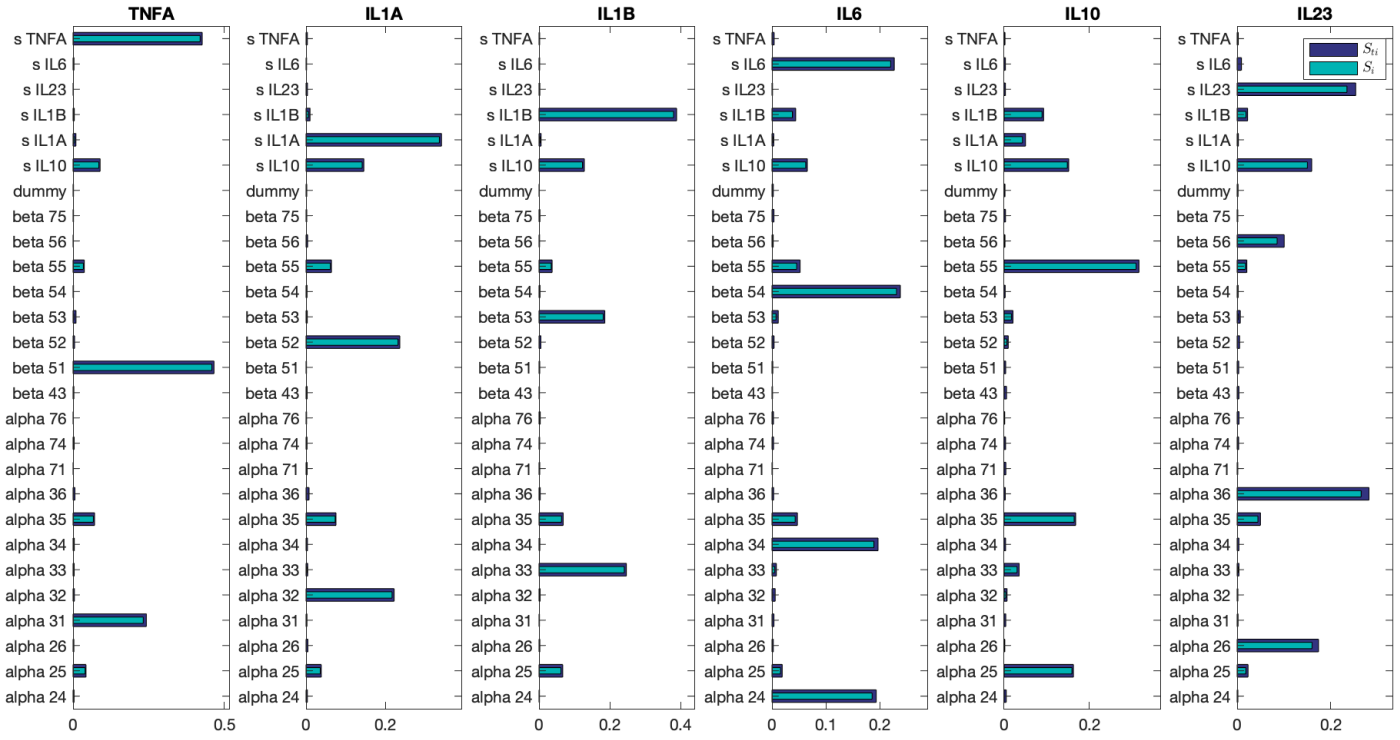


Figure 2.23: For the 'LPS+ aIL6R' condition, eFAST parameter sensitivity analysis for the selected 20-edge model. As model outputs, we have chosen the cytokine secretion rate at $t = 16$ for every cytokine of interest (columns). We show both sensitivity S_i and total order sensitivity S_{ti} indices for each fitted model parameter and for a dummy parameter (rows).

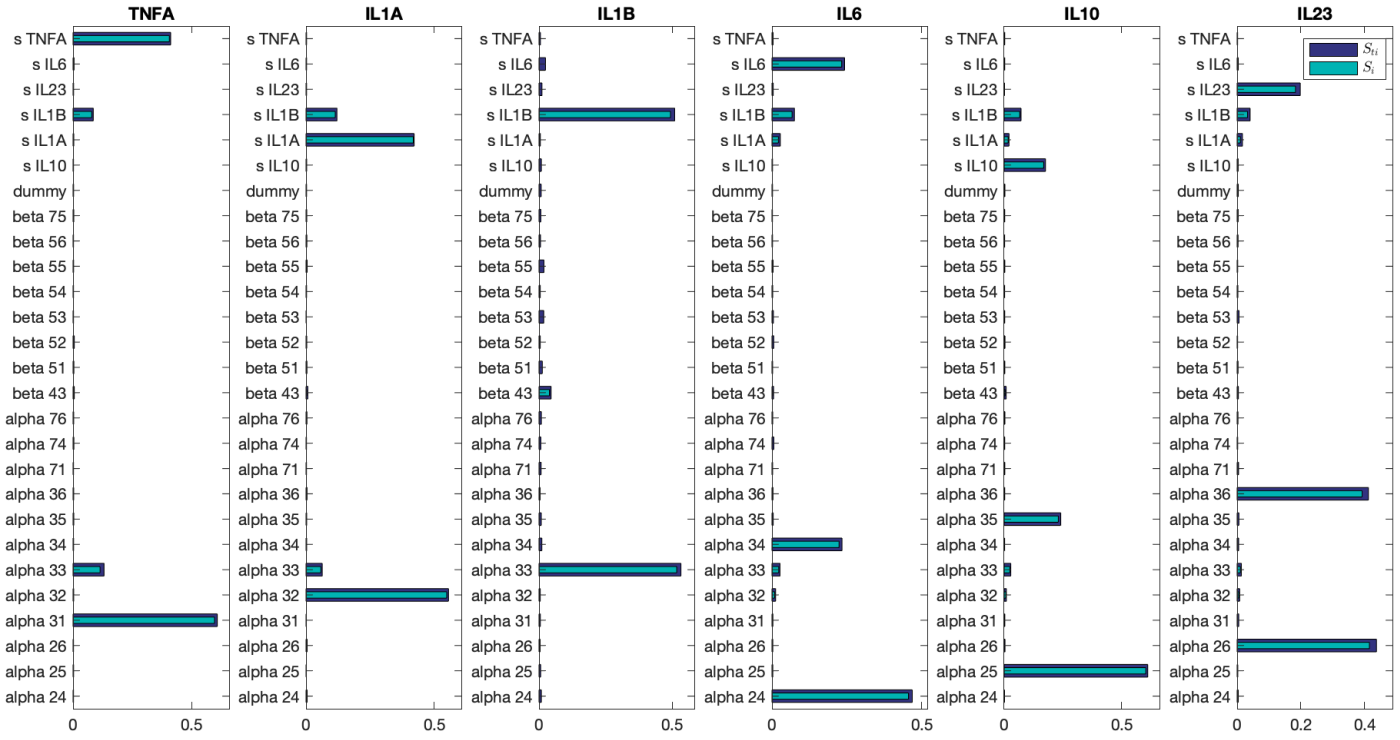


Figure 2.24: For the 'LPS + aIL10R' condition, eFAST parameter sensitivity analysis for the selected 20-edge model. As model outputs, we have chosen the cytokine secretion rate at $t = 16$ for every cytokine of interest (columns). We show both sensitivity S_i and total order sensitivity S_{ti} indices for each fitted model parameter and for a dummy parameter (rows).

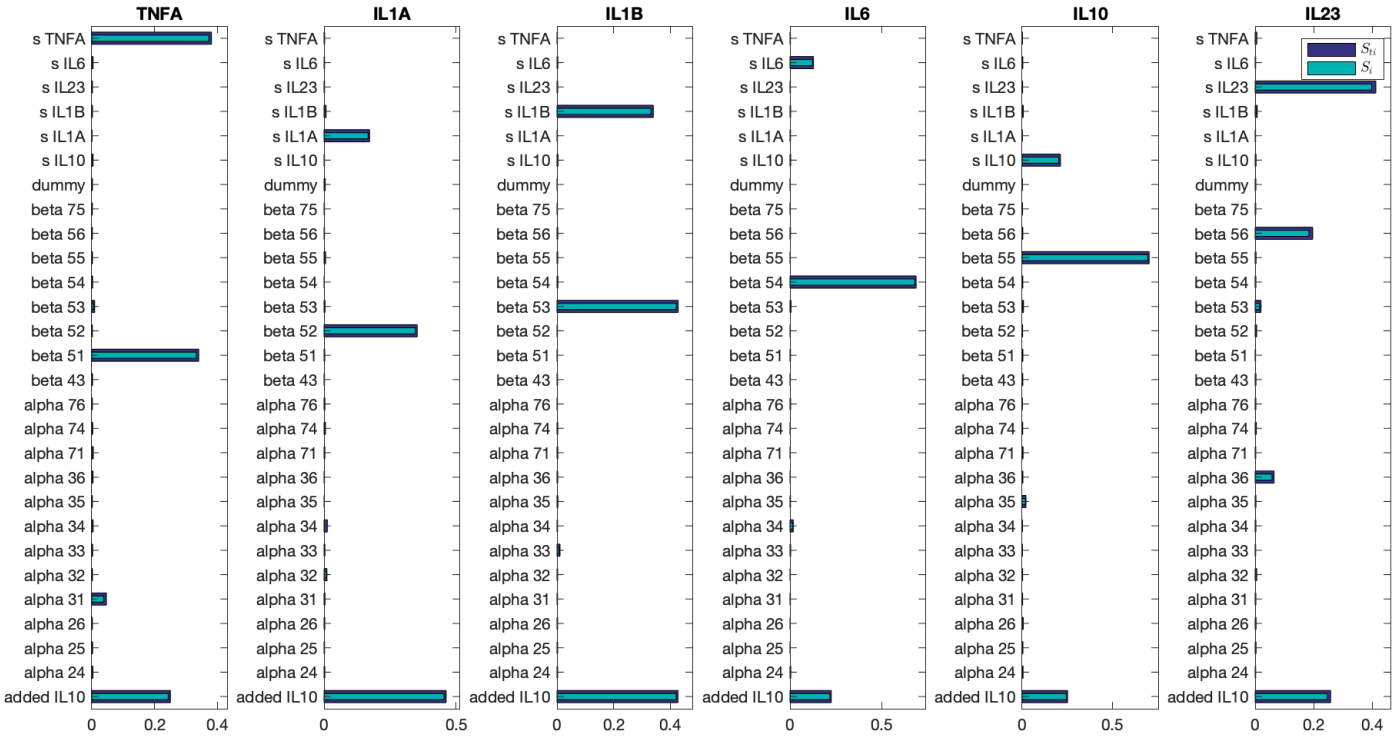


Figure 2.25: For the 'LPS + IL-6' condition, eFAST parameter sensitivity analysis for the selected 20-edge model.As model outputs, we have chosen the cytokine secretion rate at $t = 16$ for every cytokine of interest (columns). We show both sensitivity S_i and total order sensitivity S_{ti} indices for each fitted model parameter and for a dummy parameter (rows).

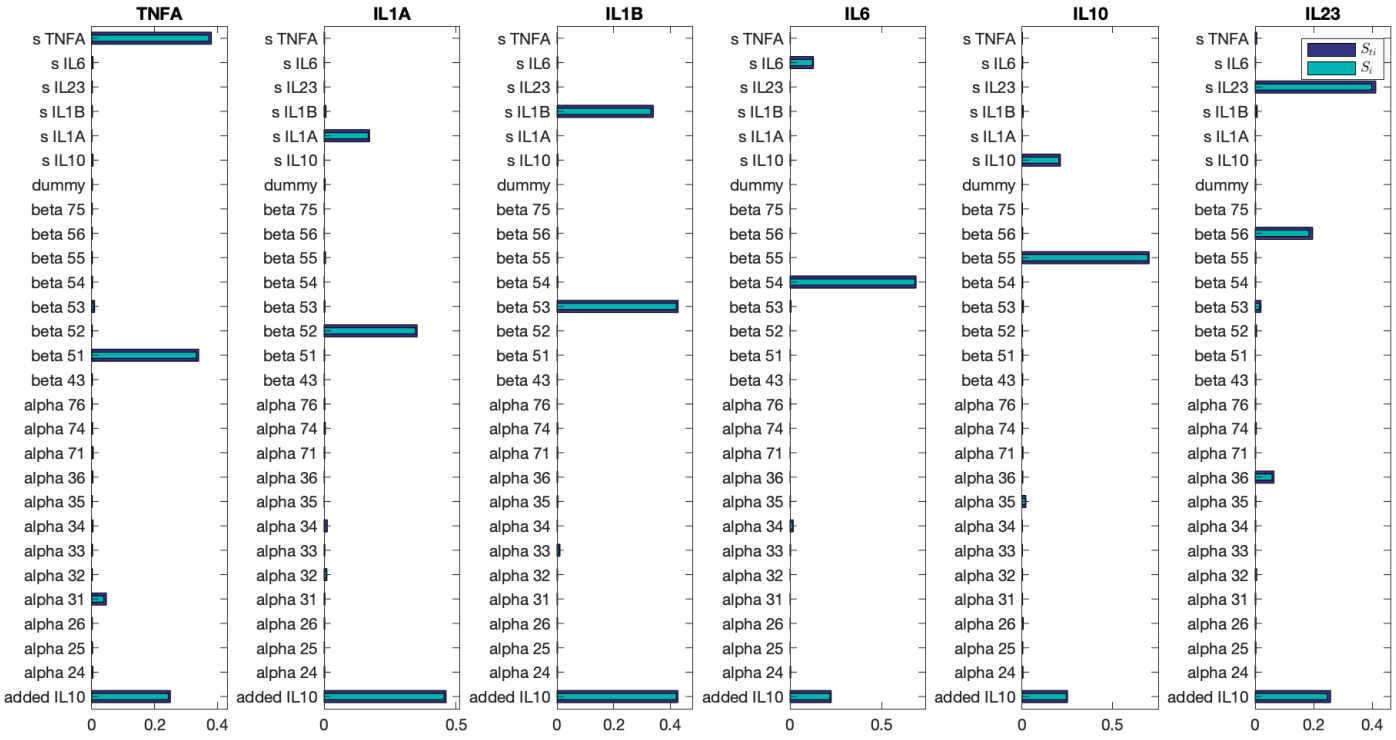


Figure 2.26: For the 'LPS+ IL-10' condition, eFAST parameter sensitivity analysis for the selected 20-edge model. As model outputs, we have chosen the cytokine secretion rate at $t = 16$ for every cytokine of interest (columns). We show both sensitivity S_i and total order sensitivity S_{ti} indices for each fitted model parameter and for a dummy parameter (rows).

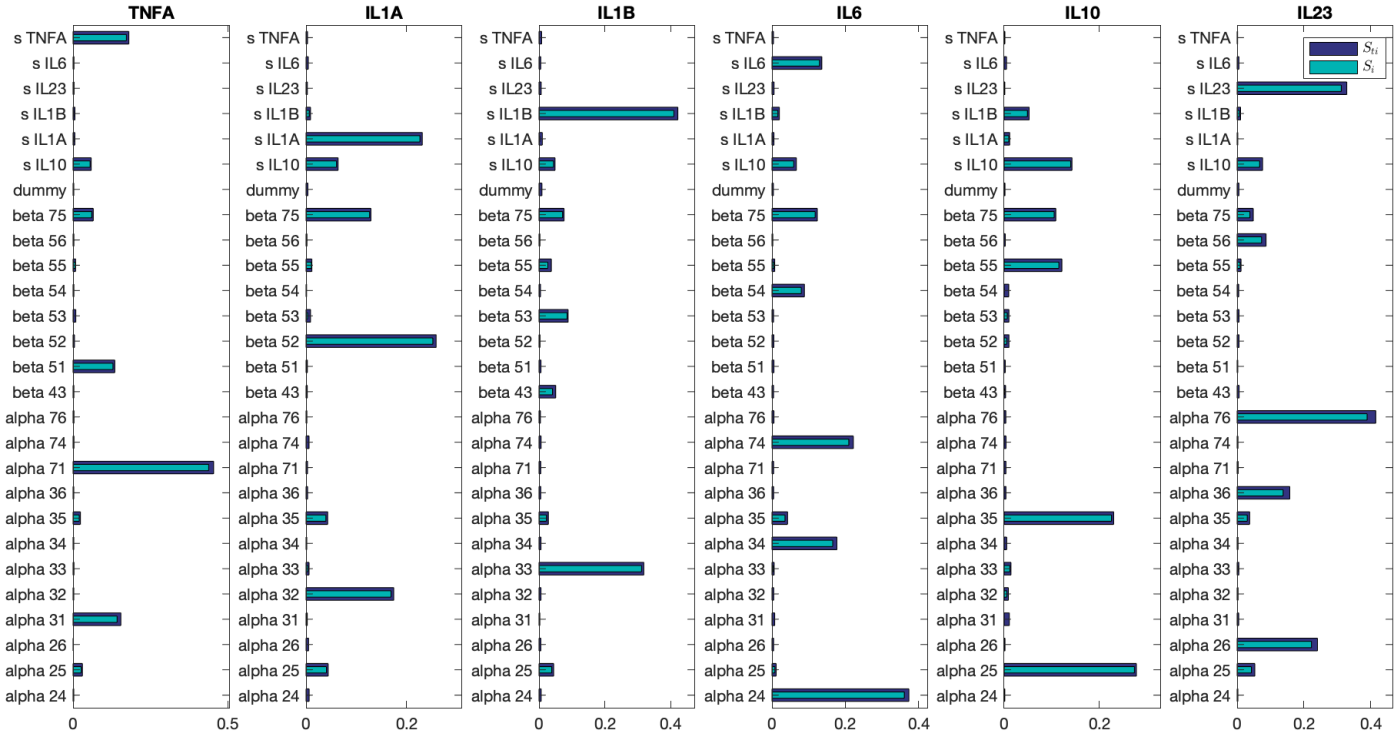


Figure 2.27: For the 'LPS + IFNγ' condition, eFAST parameter sensitivity analysis for the selected 20-edge model. As model outputs, we have chosen the cytokine secretion rate at $t = 16$ for every cytokine of interest (columns). We show both sensitivity S_i and total order sensitivity S_{ti} indices for each fitted model parameter and for a dummy parameter (rows).

cytokine of interest at a known moment in time. We assume we have multiple measurements for each condition, for instance corresponding to measurements obtained from cells from different donors, and the log 10 transformed measurements for each condition and each cytokine follow a normal distribution in the synthetic data or in real data (after a suitable scaling if need be). We further assume that the secretion rate of certain cytokines is dependent on the concentration of other cytokines.

As before, we can represent all cytokines and their interactions by a network. Each node in this network represents a cytokine and each directed edge an up- or down-regulatory effect from one cytokine on another. We introduce our general model equations:

$$\frac{\mathrm{d}x_i}{\mathrm{d}t} = y_i(t) = s_i \prod_u (1 + \alpha_{u,i} x_u(t)) \prod_v \left(\frac{1}{1 + \beta_{v,i} x_v(t)} \right), \qquad i, u, v = 1, \ldots, \tag{2.27}$$

with $x_i(t)$ and $y_i(t)$ the time dependent concentration and secretion rate of cytokine i, s_i the size of the effect of the stimulatory agent, and $\alpha_{u,i} \geq 0$ ($\beta_{v,i} \geq 0$) the size of the positive (negative) effect of cytokine u (v) on the secretion rate of cytokine i. Similarly, $x_u(t)$ and $x_v(t)$ are the concentrations of cytokine u, v. We take the unit of time t in hours. Further, we assume $x_i(0) = \gamma_i$ when cytokine i has been added at the start of the experiment. Else, we assume $x_i(0) = 0$. For a given number of cytokines, our model equations (2.1) can represent a specific network configuration, by fixing all $\alpha_{u,i}$, $\beta_{v,i}$ that do not correspond to an edge in this configuration to zero. The network edges correspond to all non-zero $\alpha_{u,i}$ and $\beta_{v,i}$. The weight of an edge is defined as the value of $\alpha_{u,i}$ or $\beta_{v,i}$.

The experimental cytokine secretion data of cytokine i for measurement j is given by $\hat{y}_{i,j}$. Each j has been obtained from a single donor and under a single stimulatory condition. For each network configuration, we can fit the right hand-side of the system of Eqs (2.1) to an experimental dataset by log-likelihood minimization, once normality of log10 transformed data has been tested for and confirmed when dealing with experiments. We minimise $-2\log(\mathcal{L}(\boldsymbol{\theta}))$ over our parameter vector $\boldsymbol{\theta}$, where $\boldsymbol{\theta}$ contains the model parameters s_i, and all $\alpha_{u,i}$, $\beta_{v,i}$ that are not fixed to zero for the network configuration of interest, and $\mathcal{L}(\boldsymbol{\theta})$ is the likelihood function:

$$\mathcal{L}(\boldsymbol{\theta}) = \prod_i \prod_j \frac{1}{\sqrt{2\pi\sigma_i^2}} \exp\left(-\frac{(\log_{10}(y_{i,j}) - \log_{10}(\hat{y}_{i,j}))^2}{2\sigma_i^2} \right), \tag{2.28}$$

with $y_{i,j}$ and $\hat{y}_{i,j}$ the value of the simulated and experimentally measured secretion rate of cytokine i for data point j, and σ_i the standard deviation of the log transformed measured secretion rate of cytokine i [283]. We assume a fixed standard deviation σ_i for each cytokine, that should be determined from the data for both real and noisy synthetic data

In order to identify the network configuration with an optimal balance between edge number and model fit, we use the Akaike information criterion (AIC) for model selection. The AIC value of a network configuration can be computed as

$$\text{AIC} = D + 2M, \tag{2.29}$$

with $D = \min_{\boldsymbol{\theta}} -2\log\left(\mathcal{L}(\boldsymbol{\theta})\right)$, $\mathcal{L}(\boldsymbol{\theta})$ the likelihood function as defined in Eq (2.25), and M the number of model parameters. We recall that each network edge is represented by one model parameter ($\alpha_{u,i}$ or $\beta_{v,i}$). Setting an edge to zero corresponds to the removal of a parameter from the model. We can rank network configurations by comparing their relative AIC values.

2.10.2 Four toy models

We consider for toy models. Each of the four motifs consists of two edges, and a third, spurious edge that might arise when a network is constructed based on statistical analysis (Fig 2.28, solid and dotted lines for the real and spurious edges respectively). We use our modelling approach to distinguish between real and spurious edges. For each of the four motifs, we generate synthetic datasets of cytokine secretion measurements for cytokines A, B, and C at a single point in time.

We generate synthetic data by simulating Eq (2.27). We assume our measurements are taken at $t = 16$h, and set the stimulus $s_i = 1$ for all $i \in \{A, B, C\}$. We further assume we have measurements for the stimulus alone, and the stimulus in the presence of a cytokine receptor blocker for each of the three cytokines. We assume no cytokines were added at the start of any of the experiments (see Section 2.10.3 for the case that cytokines were added). When no up- or down-regulatory edge between two cytokines exists in our constructed network, we set the corresponding parameter $\alpha_{u,i}$ or $\beta_{v,i}$ to zero. Else we set $\alpha_{u,i}$ or $\beta_{v,i}$ to 0.5. We assume we have 15 measurements for each experimental condition, for instance

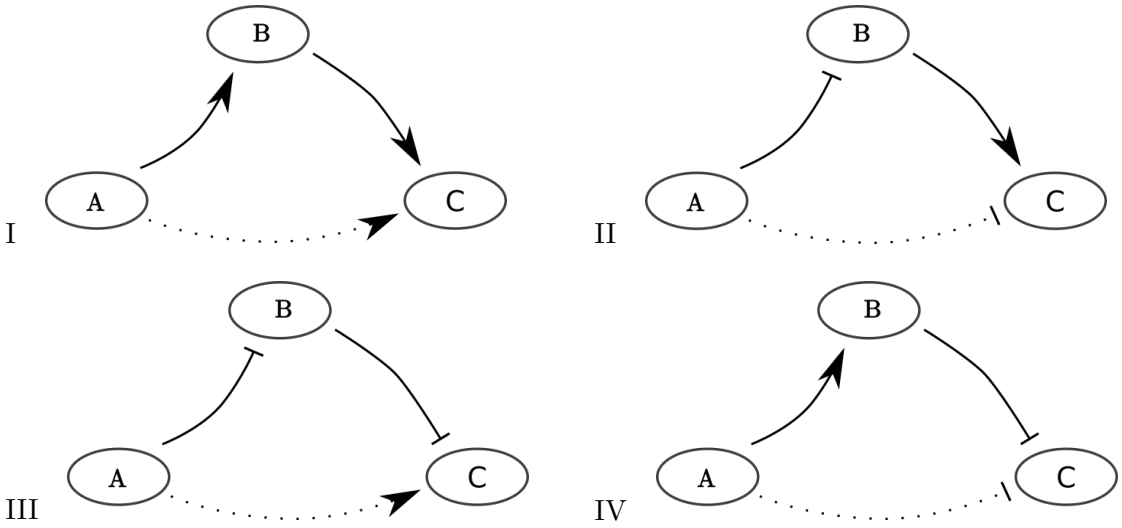


Figure 2.28: The four validation network motifs. Each motif consists of three cytokines and two directed edges. Inhibition of cytokine A has a negative (I and III) or positive (II and IV) effect on the secretion rate of cytokine C. However, this effect is indirect (via cytokine B), and the dotted edges between A and C do not exist.

corresponding to measurements obtained from 15 individual donors. We add normally-distributed noise with a standard deviation of 0.25 to all log10-transformed synthetic data points. This is multiplicative noise in terms of cytokine secretion rate, as justified previously. This level of noise is similar to the noise observed in the experimental IL23 dataset. We statistically analyse our synthetic data set. For each added cytokine blocker and each cytokine, we test whether the change is significant using a 2-sample t-test ($p \leq 0.05$, fdr corrected). We will consider a network edge from cytokine i to cytokine j statistically significant, when the change in secretion of cytokine j after the blockade of the cytokine i receptor is statistically significant.

We note that when we compute the distance D for a network configuration, we assume a known standard deviation σ_i for each cytokine i from the data. We determine σ_i from the data as follows. We compute the difference between each measurement and the mean of all measurements for that condition and cytokine, where each measurement corresponds to the log10 transformed secretion rate of one cytokine, condition, and donor. We compute the variance by normalizing the square of these differences by the sample size minus one for each cytokine and compute the standard deviation as the square root of the variance.

We generated 100 synthetic datasets for each of the four motifs shown in Fig 2.28. For each of the 400 datasets, the two edges used to generate the data were statistically significant ($p \leq 0.05$, fdr corrected). In 100%, 99%, 99%, and 100% of cases, the third, spurious edge was statistically significant as well for each of the four network motifs respectively ($p \leq 0.05$, fdr corrected). Further, in 32 of the 400 cases, one or more of the remaining fifteen edges (not including the three edges considered) was found to be statistically significant ($p \leq 0.05$, fdr corrected). When we increase the value of the two 'true' edge parameters $\alpha_{u,i}$ and/or $\beta_{v,i}$ from 0.5 to 0.75, in all 400 cases the third, spurious edge was found to be significant ($p \leq 0.05$, fdr corrected). Conversely, when we decrease the value of the 'true' edge parameters from 0.5 to 0.1, both 'true' edges are significant in only 93%, 70%, 59% and 93% of cases. In 28%, 14%, 13% and 29% of the 400 cases a spurious third edge was found to be significant in this case ($p \leq 0.05$, fdr corrected). All spurious results are anticipated to be small number effects, though such numbers of samplings reflect current experimental protocols, suggesting in practice sample sizes are not sufficient to extract very weak interactions. We will in the following only consider the case where the value of $\alpha_{u,i}$ and/or $\beta_{v,i}$ is set to 0.5.

For each of the four motifs, we estimate the model fit to each of the synthetic datasets (100 datasets per motif). We compute the model fit for the network extracted by statistical analysis and all sub-networks (by minimizing the log likelihood, with $D = -2\log(\mathcal{L})$ and the likelihood $\mathcal{L}$ defined in Eq (2.28) for a given number of edges). We then apply the AIC for model selection. We did not observe any false negatives, i.e. both 'true' edges used to generate the synthetic data were selected in all 400 cases. In 86%, 84%, 83%, and 88% of cases for each of the four motifs the AIC selected only the 'true', 2-edges, and in 8%, 9%, 12%, and 8% of cases a model including the spurious edge from cytokine A to cytokine C, i.e. A $\rightarrow$ C (test motifs I and III) or A $\dashv$ C (test motifs II and IV). We recall that in 32 of the 400 cases, spurious edges, other than the one from cytokine A to cytokine C were found to be significant. For these datasets, all sub-configurations including such significant edges were considered. Of these, in 25 cases, a model was selected by the AIC including one or more of such spurious edges. However, the weighting of the spurious edges included in selected model configurations was small (average edge weight < 0.05) compared to an average of 0.5

for the 'real' edges, highlighting that spurious edges are still subdominant in the predicted interactions and further emphasising that substantial interactions are extracted reliably, but weak interactions are subject to uncertainty given the extent of, and noise within, the data available in practice.

2.10.3 Cytokine addition

We repeat our analysis of the four test models, but this time consider the case that additional data is available, consisting of the addition of various cytokines to the system. We consider the same four test models, the same number of synthetic donors (15), and the same edge weight as before ($\alpha_{u,i} = \beta_{v,i} = 0.5$). We consider two additional experimental conditions, consisting of the addition of cytokine A and of cytokine B. For each condition, only a single cytokine is added, together with the stimulus. Hence, we have the following conditions: 'Stimulus', 'Stimulus + anti cytokine A', Stimulus + cytokine A', 'Stimulus + anti cytokine B', Stimulus + cytokine B', 'Stimulus + anti cytokine C', and 'Stimulus + cytokine C'. We recall that the addition of a cytokine i corresponds to setting the initial condition of that cytokine to $x_i(0) = \gamma_i$, with γ_i the initial concentration of the added cytokine. We generated 100 synthetic datasets as before, with $\gamma_A = 200$ and $\gamma_B = 200$ for all cytokines. For these value of γ_i, $i \in \{A, B\}$, the difference in cytokine j expression between the 'Stimulus' and 'Stimulus + cytokine i' conditions was statistically significant for all 'true edges' from i to j for all 400 synthetic test datasets. Further, the spurious edge from cytokine A to cytokine C was statistically significant in 399 cases. Still only considering the 'added cytokine data', in 36 of the 400 cases, spurious edges, other than the one from cytokine A to cytokine C were found to be significant. We recall that we found before that the difference in cytokine j expression between the 'Stimulus' and 'Stimulus + anti cytokine i' condition is statistically significant for all 'true edges' from i to j, and the spurious edge from cytokine A to cytokine C, for all 400 synthetic test datasets. When only considering the 'cytokine blockage data', in 32 of the 400 cases, spurious edges, other than the one from cytokine A to cytokine C were found to be significant (see Section 2.10.2). When we combine the 'cytokine blockage data' and 'added cytokine' data, we have 68 spurious edges other than the one from cytokine A to cytokine C that were found to be statistically significant, i.e. we find no overlap in

the spurious edges originating from the 'cytokine blockage data' and 'added cytokine data'. As before, for each of the four motifs, we estimate the model fit to each of the synthetic datasets (100 datasets per motif). We compute the model fit for the network extracted by statistical analysis (including all spurious edges originating from the 'cytokine blockage data' and 'added cytokine data') and all sub-networks (by minimizing the log likelihood, with $D = -2\log(\mathcal{L})$ and the likelihood $\mathcal{L}$ defined in Eq (2.28)) for a fixed number of edges. We then apply the AIC for model selection. Again, we did not observe any false negatives, i.e. both 'true' edges used to generate the synthetic data were selected in all 400 cases. In 87%, 84%, 83%, and 91% of cases for each of the four motifs the AIC selected only the 'true', 2-edges and in 10%, 3%, 9%, and 4% of cases a model including the spurious edge from cytokine A to cytokine C, i.e. A $\rightarrow$ C (test motifs I and III) or A $\dashv$ C (test motifs II and IV). In 22 cases, a model was selected by the AIC that included one or more spurious edges other than the one from cytokine A to cytokine C. We conclude that the number of times the true 2-edge model was selected increases when we consider the addition of cytokines. The total number and fraction of spurious edges that are selected decreases, and thus cytokine intervention data improves the reliability of the network extraction method. As before, the weighting of the spurious edges included in selected model configurations was small (average edge weight < 0.05) compared to an average of 0.5 for the 'real' edges.

Finally, we consider the addition of a fourth cytokine D to the system; see Figure 2.29. This mimics the addition of IFNγ in our experimental dataset. We implement the addition of cytokine D by multiplying the cytokine secretion rate $y_i(t)$ (eq (2.27)) with an additional term $(1 + \alpha_{D,i})$ $(\frac{1}{(1+\beta_{D,i})})$, where the value of $\alpha_{D,i}$ $(\beta_{D,i})$ corresponds to the edge width of the positive (negative) effect of the addition of cytokine D on cytokine i secretion. We will use test configuration IV in this case, and assume cytokine D positively (negatively) regulates cytokine A (B) (Figure 2.29). We generated 100 synthetic datasets as before, with $\alpha_{A,B} = \beta_{B,C} = 0.5$, $\alpha_{D,C} = \beta_{D,B} = 10^{0.5}$ and $\gamma_A = \gamma_B = 200$. For these parameter values, the 'true' edges corresponding to edge parameters $\alpha_{A,B}, \beta_{B,C}, \alpha_{D,C}, \beta_{D,B}$ were always statistically significant. The spurious negative edge from A to C was also statistically significant in all 100 cases. Further, in 18 of the 100 cases, spurious edges, other than the one from cytokine A to cytokine C were found to be significant. We applied

our method. Again, we did not observe any false negatives, i.e. all four 'true' edges used to generate the synthetic data were selected in all 100 cases. The AIC selected the true model in 92 out of 100 cases and in 3 out of 100 cases, a model including the spurious edge from cytokine A to cytokine C was selected. In 5 out of 100 cases, a spurious edge other than the spurious edge from cytokine A to cytokine C was selected. As before, the weighting of the spurious edges included in selected model configurations was small (average edge weight of 0.1) compared to an average of 0.5 for the 'real' edges $\alpha_{A,B}$ and $\beta_{B,C}$, and an average of $10^{0.5}$ for the 'real' edges $\alpha_{D,C}$ and $\beta_{D,B}$. We recall that for the same network configuration, in the absence of the addition of Cytokine D, the true, 2-edge network configuration was selected in 91 out of 100 cases and in 4 out of 100 cases, a model including the spurious edge from cytokine A to cytokine C was selected. In 5 out of 100 cases, a spurious edge other than the spurious edge from cytokine A to cytokine C was selected. Thus, the capability of the method in reducing the number of spurious edges is not substantially altered by the inclusion of synthetic data on the addition of cytokine D.

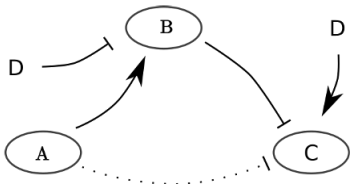


Figure 2.29: The validation network motif with added cytokine D. Inhibition of cytokine A has a positive effect on the secretion rate of cytokine C. However, this effect is indirect (via cytokine B), and the dotted edge between A and C does not exist.

2.10.4 Coverage of the confidence intervals

We considered local identifiability of the edge parameters for the selected 20-edge IL23 model using the Profile Likelihood Approach before, and obtained confidence intervals for each fitted model parameter (Section 2.8.1). Here, we will explicitly validate the coverage of such confidence intervals for the 'added cytokine D' test model (Figure 2.29). In particular, we will validate that the confidence intervals do indeed cover the range of predicted parameters at the required confidence level and the predicted parameter distribution is that of χ^2_1. We recall that using the profile likelihood approach, we can compute likelihood based parameter value confidence intervals for each parameter with threshold value ζ, the ζ quantile of the

χ^2_1 distribution. The true value of θ_m will lie within the ζ level confidence interval with probability ζ [281]. Infinite confidence intervals in the parameter value space correspond to practical parameter non-identifiability. For one of the synthetic datasets we generated before for the 'added cytokine D' test model, we calculated 99% parameter confidence intervals for each of the model parameters for the selected model. We show the profile likelihood plots in Figure 2.30. We recall that the log10-transformed values of the four edge parameters used to generate the synthetic data are $\log_{10} 0.5 = -0.301$ for $\alpha_{A,B}$ and $\beta_{B,C}$, and 0.5 for $\alpha_{D,C}$ and $\beta_{D,B}$. Further, the log10-transformed values of the three stimulus parameters used to generate the synthetic data are $\log_{10} 1 = 0$, and the log10-transformed values of the two 'added cytokine' parameters used to generate the synthetic data are $\log_{10} 200 = 2.3$. These values are contained in the 99% confidence intervals of all fitted parameters (Figure 2.30). We validated the coverage of the confidence intervals by calculating $D_{PL}(\theta^*_m) - D_{PL}(\hat{\theta}_m)$, for every edge parameter θ_m for 1000 independent datasets, with θ^*_m the true value of the parameter and $\hat{\theta}_m$ its estimated value. We plot the histograms of $D_{PL}(\theta^*_m) - D_{PL}(\hat{\theta}_m)$, where $D_{PL}(\hat{\theta}_m) = -2\log(\mathcal{L}(\hat{\boldsymbol{\theta}}))$, and confirm the histograms approximate a $\chi^2(\zeta, 1)$ distribution (Figure 31 (Cont.)).

2.10.5 Validation of the optimisation strategy

We recall that throughout this chapter, we used a trust-region approach with multi-start strategy to obtain estimates of D, the distance of the model simulations to the data. Here, we will validate this optimisation strategy. To obtain an estimate of D for a particular network configuration and dataset, we ran the trust-region algorithm 10 times, with different initial parameter value guesses, where each run returned the value of D after convergence of the algorithm to a local optimum. We selected the smallest value of D from these estimates, assuming that this value represents a global minimum, i.e. the true minimum value of D. The initial guesses for each parameter were sampled from a log-10 transformed uniform distribution with lower bound 10^{-10} and upper bound 10. When one of the estimated parameter values returned by the algorithm was equal to the upper bound, we increased the upper bound by a factor 1000 (i.e. multiplied by 10^3) and repeated the fitting procedure with the new bound. We repeated this procedure until none of the estimated parameter values

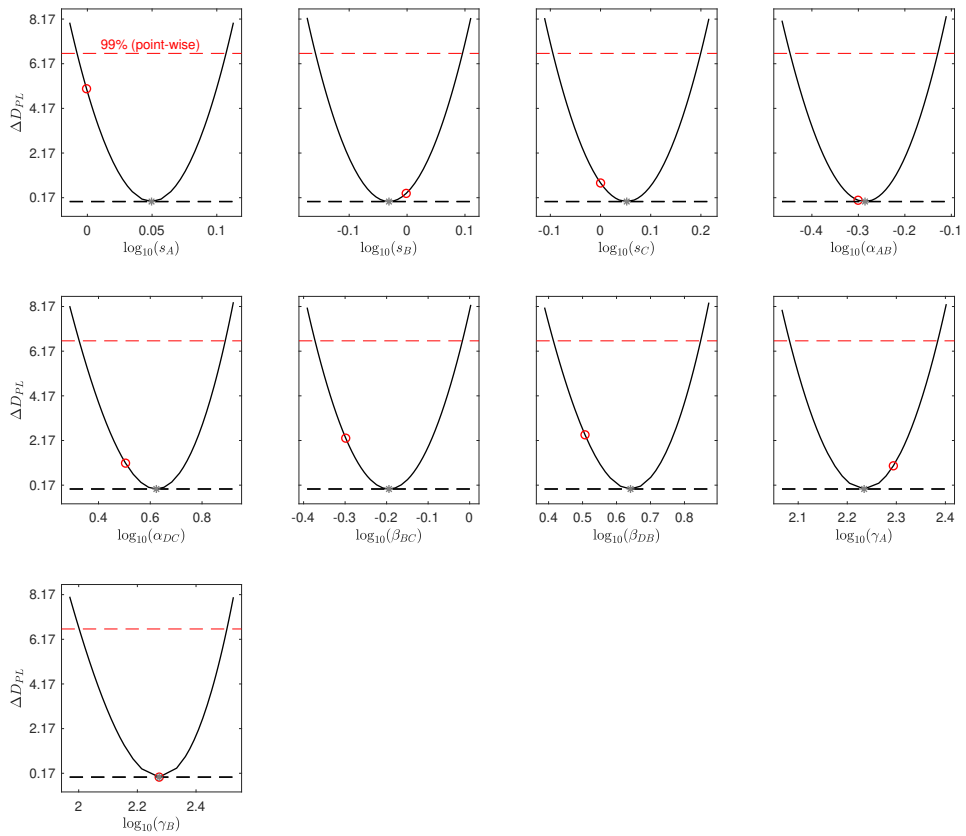


Figure 2.30: Profile likelihood plots for the fitted parameters of the selected 4-edge 'added cytokine D' validation model (Figure 2.29) for a synthetic dataset that was generated in the way described in the main text (Section 2.10.3). The parameter $\theta_m \in \boldsymbol{\theta}$ was varied over a broad range of values and for each fixed value of θ_m, the increase in $D_{PL}(\theta_m) = \min_{\tilde{\boldsymbol{\theta}}_m} -2\log\left(\mathcal{L}(\boldsymbol{\theta})\right)$ was computed, with $\mathcal{L}(\boldsymbol{\theta})$ the likelihood function as defined in Eq (2.25), and $\tilde{\boldsymbol{\theta}}_m = \{\theta_1, \ldots, \theta_{m-1}, \theta_{m+1}, \ldots, \theta_N\}$. The 99% confidence interval threshold is shown as a red dashed line. The parameter values used to generate the synthetic dataset are shown as red dots. The parameter values resulting in the minimal $D = \min_{\boldsymbol{\theta}} -2\log\left(\mathcal{L}(\boldsymbol{\theta})\right)$ are shown as grey stars. This figure has been generated using the Matlab environment 'Data2Dynamics' [281, 284].

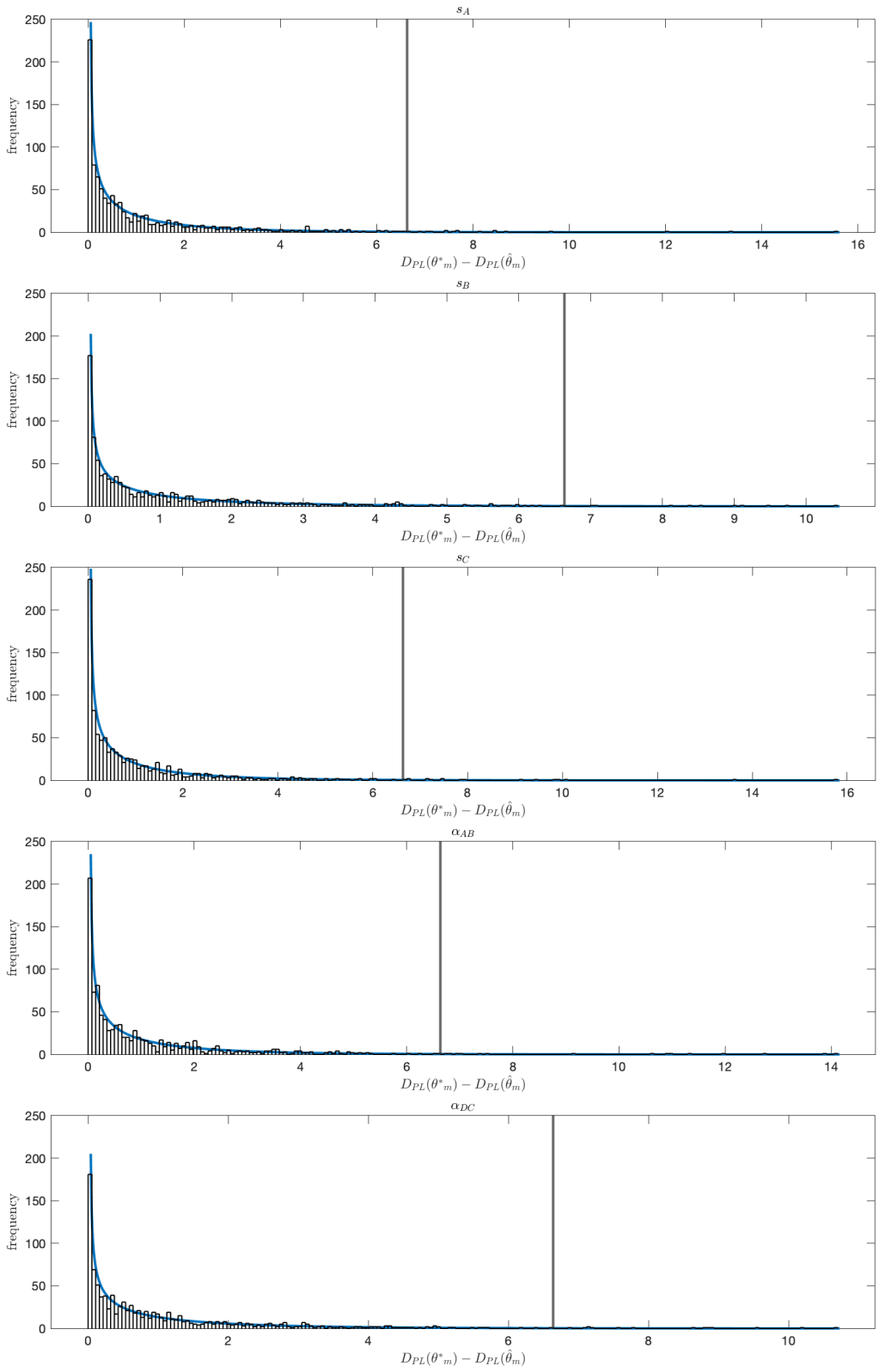


Figure 2.31: Validation of the coverage of the confidence intervals. Figure continues on next page.

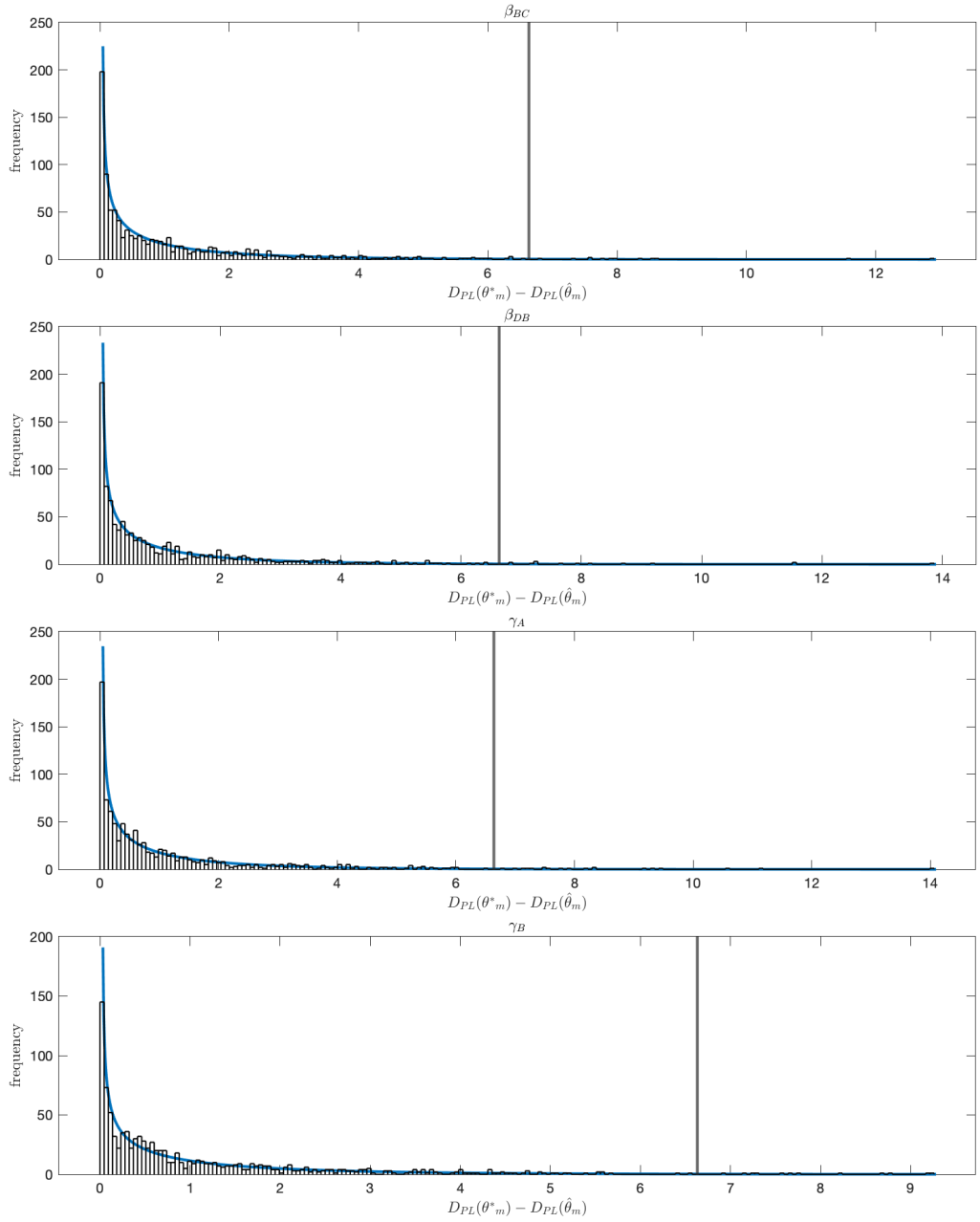


Figure 31 (Cont.): Validation of the coverage of the confidence intervals. The χ^2 distribution with one degree of freedom (blue) and, for a 1000 independent datasets, and for every edge parameter $\theta_m \in \boldsymbol{\theta}$ of the 4-edge 'added cytokine D' test model configuration, a histogram of the values of $D_{PL}(\theta^*_m) - D_{PL}(\hat{\theta}_m)$, with $D_{PL}(\theta_m) = \min_{\tilde{\boldsymbol{\theta}}_m} -2\log(\mathcal{L}(\boldsymbol{\theta}))$, $\tilde{\boldsymbol{\theta}}_m = \{\theta_1, \ldots, \theta_{m-1}, \theta_{m+1}, \ldots, \theta_N\}$. Here, θ^*_m is the true value of θ_m and $\hat{\theta}$ its estimated value by log-likelihood minimization, where the parameter for each plot is just above the plot, for example γ_B for the last plot. In 99% of all cases, the value of $D_{PL}(\theta^*_m) - D_{PL}(\hat{\theta}_m)$ is smaller than $\chi^2(0.99, 1)$ (vertical grey line).

returned by the algorithm were equal to the upper bound. Further, as discussed before, we set the upper bound of γ_4 to 10^5 to render it practically identifiable. We used Latin-hypercube sampling to sample the 10 initial guesses from parameter space. The number of free model parameters of the selected 20-edge IL23 model configuration is 31 (6 stimulus parameters s_i, 20 edge parameters $\alpha_{u,i}/\beta_{v,i}$, 5 added cytokine parameters γ_i. The full, 31-edge IL23 model contains 11 parameters more. Given the number of model parameters, we emphasize that the 10 initial guesses correspond to a very coarse coverage of the different regions in parameter space. The regular shape of all profile likelihood profiles of our three cytokine test model and selected 20 edge model (Sections 2.8.1 and 2.10.4) serve to motivate our assumption that the 10 initial guesses are nonetheless sufficient to obtain an estimate of the global minimum. To validate this assumption, we generated 1000 synthetic datasets by simulating the selected 20-edge model after sampling log-10 transformed parameters uniformly from the confidence intervals. We applied our optimisation strategy to each of the synthetic datasets, i.e. running the trust-region algorithm with 10 initial guesses sampled from a log-10 transformed uniform distribution with lower bound 10^{-10} and upper bound 10. In all 1000 cases, the true, global minimum was returned by the algorithm ($D < 10^{-7}$ for all cases). While we do not *prove* the global minimum is returned, the validation generates confidence that the global optimum is being found, for networks with a structure similar to that of the IL23 dataset.

2.11 Knock-outs

The construction of our model enables us to predict the effect of various untested combinations of cytokine (receptor) blockades on the system. We plot the simulated effects of many possible combinations of the experimentally tested modulations on TNFα, IL-1α, IL-1β, IL-6, IL-10, and IL-23. We plot the predictions of the two optimal models identified by the AIC for both our constrained and extended approach (Figures 32, 33, 34).

The dataset already contained multiple combinations of cytokine(receptor) blockades and no suggestions for additional experiments follow immediately from these model predictions (Figures 32, 33, 34). When our method would be applied to other, less extensive datasets, the model predictions of the combination of multiple blockades could be more

insightful. If for instance only data on the blockade of IL-10 and IL-1β had been measured, the model simulations of their combined effects would have been of interest in predicting the respective contribution of IL-10 and IL-1β to the regulation of IL-23.

2.12 Discussion

We have developed a method to extract a minimal, weighted network from cytokine interaction data using ordinary differential equations (ODEs) and the Akaike information criterion (AIC). By applying our method to a flow cytometry dataset containing cytokine secretion data by stimulated monocytes, we extracted a network of the regulation of IL-23, a key cytokine in inflammatory bowel disease pathogenesis. We first identified 31 statistically significant modulation effects of the blockade or addition of one cytokine on the secretion rate of another cytokine via statistical analysis. Based on this set of 31 directed edges, we explored the various different network configurations using subsets of edges by fitting the data to ODE models representing various network configurations. Model fitting for each network configuration of interest was implemented using a trust-region optimization approach, resulting in an estimate of the distance D between the model simulations and the data. We introduced an algorithm to efficiently determine the optimal subset of network edges for each given number of edges, without having to determine D (using the trust-region algorithm) for each possible network configuration explicitly. We defined the weight of an edge in a particular network configuration as the value of $\alpha_{u,i}$ or $\beta_{v,i}$ for that network configuration. We defined the colour-weight of an edge for a particular network configuration, as the increase in D when the edge is removed from that configuration, divided by the increase in D when the edge with the largest increase in D for that configuration is removed from the configuration. Building on the statistical analysis that resulted in a list of possible direct interactions, the ODE approach allows us to compare direct and indirect effects and adjust edge weights and colour-weights accordingly. We ranked the different network configurations balancing model fit and complexity, using the AIC for model selection. We considered structural and practical parameter identifiability and predicted the effects of untested combinations of cytokine (receptor) inhibitors. As a second, extended model approach we did not constrain the possible edges to the statistically significant set

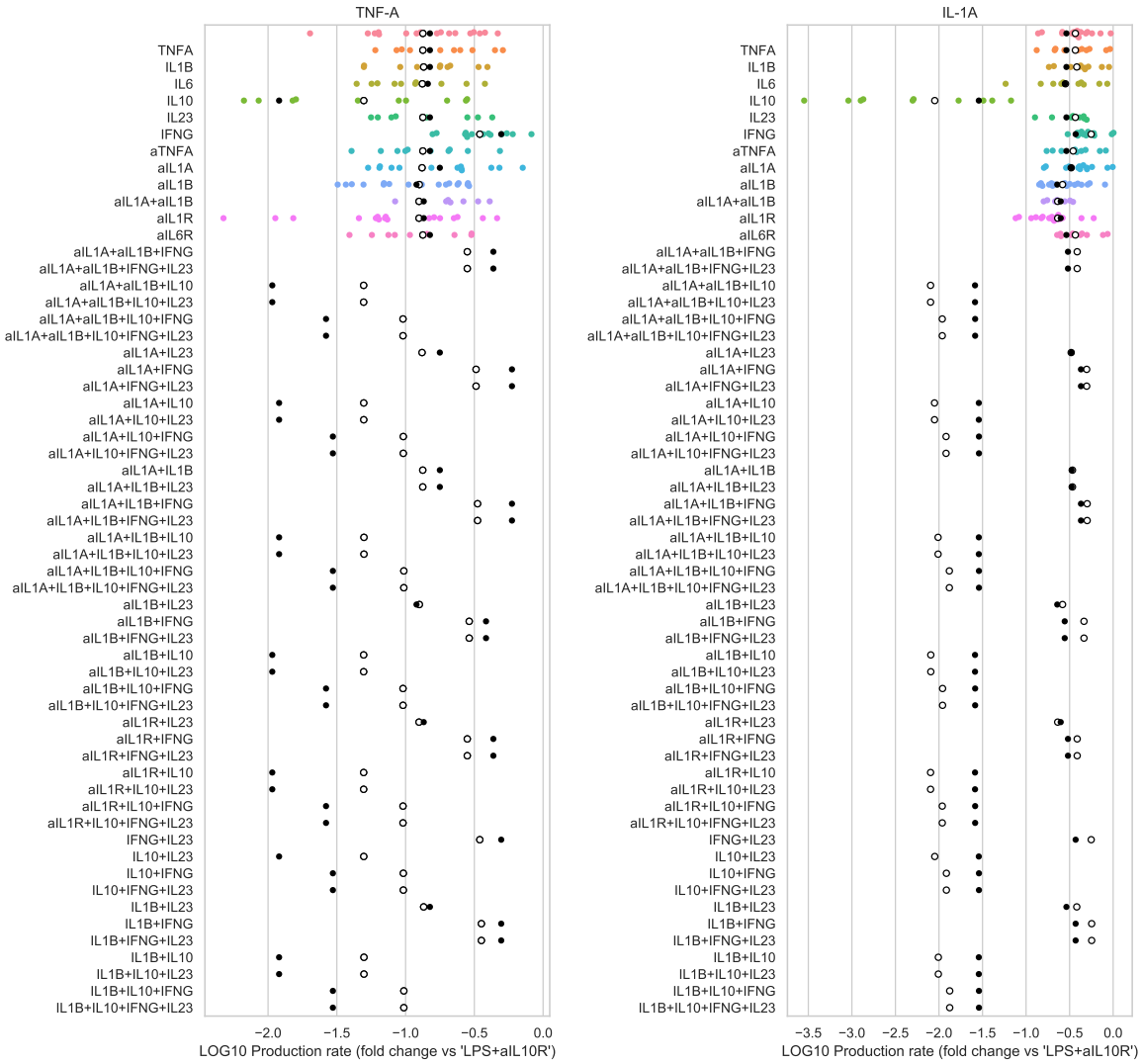


Figure 32: Simulated secretion rates of TNFα and IL-1α after addition of various combinations of cytokines and cytokine (receptor) blockades (Section 2.11). Experimental data points are plotted with coloured circles. Model predictions given by simulations generated via the optimal models as identified by the AIC resulting from our constrained (black) and extended (white, black borders) approach (see Section 2.7). (Figure continues on next page)

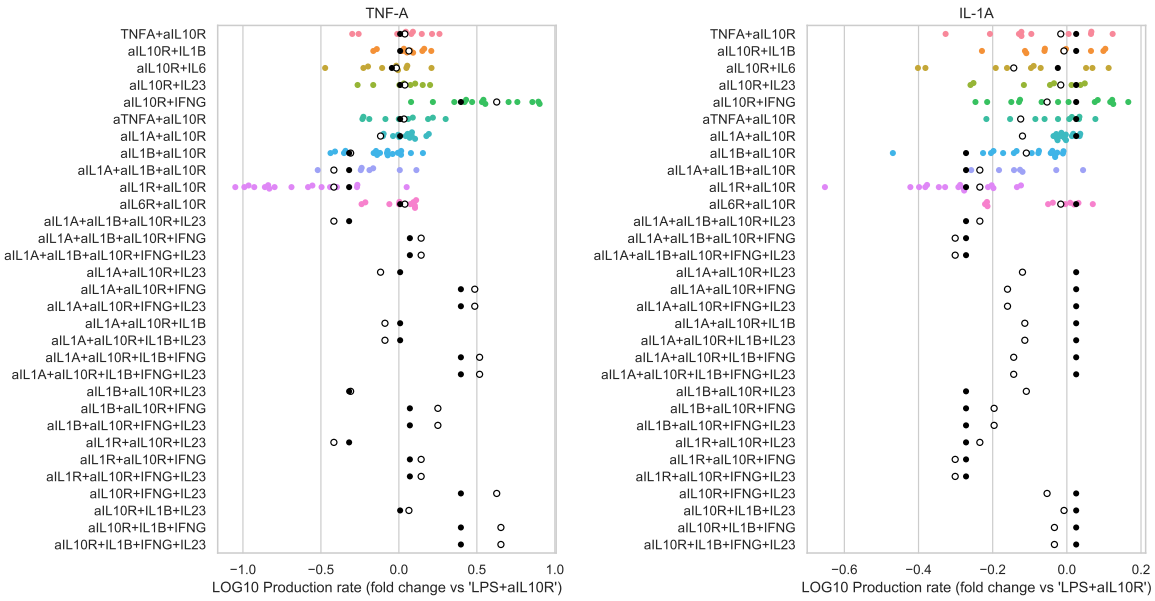


Figure 32: (Continued figure)

of edges, but instead explored networks based on all 84 possible cytokine interaction edges. We validated our method using synthetic datasets. We considered several test motifs. We observed that in ≈15% of the 400 synthetic datasets we studied, the models selected by the AIC contained one or more edges that were not part of the network configuration used to generate the synthetic datasets, though always with very low relative edge weights, where we defined the edge weight as the value of the corresponding edge parameter $\alpha_{u,i}$ or $\beta_{v,i}$. The edges used to generate the synthetic datasets were always part of the selected models. We conclude that our method generally selects network configurations that are equal or slightly larger than the 'real' network configurations with any such additions constituted by only very weakly interacting additional edges. We also validated the coverage of the confidence intervals (determined by the profile likelihood approach) of our model parameter values using synthetic data. Further, using a thousand synthetic datasets, we validated our optimisation strategy, i.e. the use of the trust-region algorithm, combined with 10 different initial guesses. In all 1000 cases, the true, global minimum was returned by the algorithm. While we do not *prove* the global minimum is returned, the validation generates confidence that the global optimum is being found. In the appendix, we compare our method with an existing method from the literature intended to reconstruct biological networks from

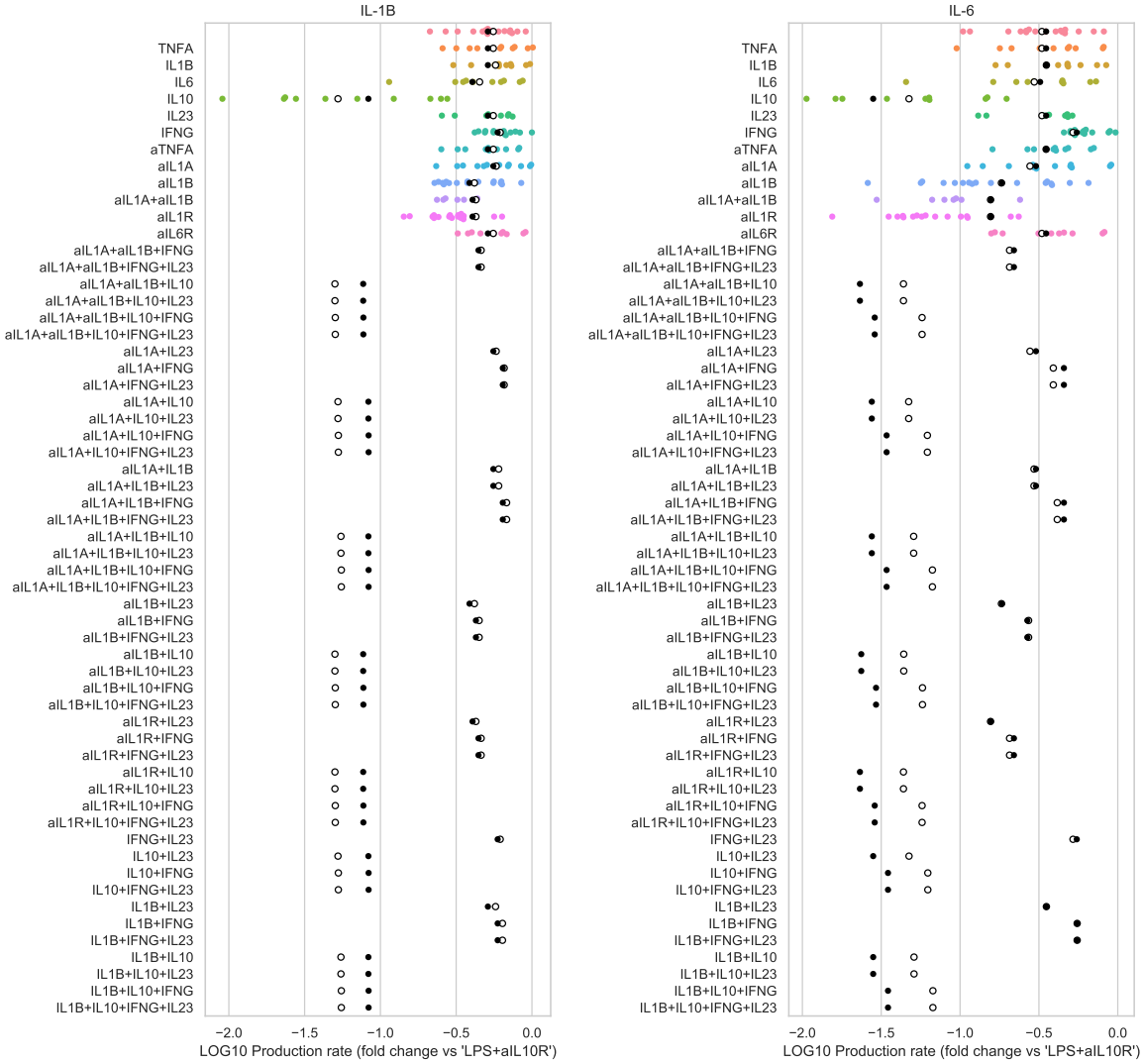


Figure 33: Simulated secretion rates of IL-1β and IL-6 after addition of various combinations of cytokines and cytokine (receptor) blockades (Section 2.11). Experimental data points are plotted with coloured circles. Model predictions given by simulations generated via the optimal models as identified by the AIC resulting from our constrained (black) and extended (white, black borders) approach(see Section 2.7). (Figure continues on next page)

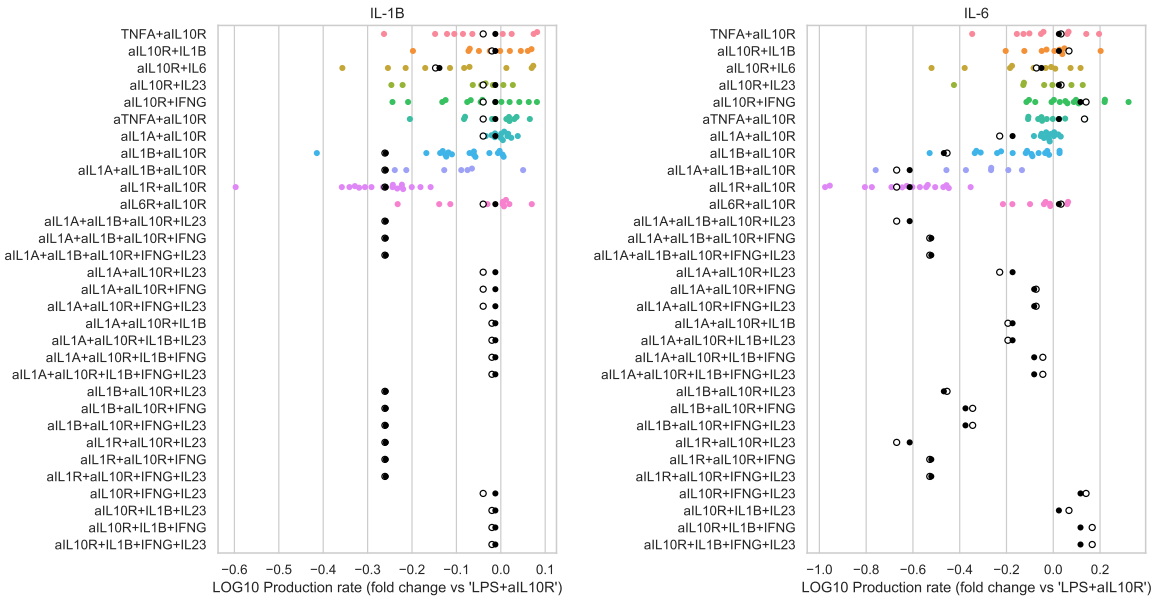


Figure 33: (Continued figure)

static interventional data: a method by Rice et al. that is based on conditional correlation analysis [291]. The most striking difference between the model extracted by the method of Rice et. al was the low weight and incorrect sign of the edge from IL-10 to IL-1β. Due to the positive correlation between the IL-1β and IL-10 for the 'LPS' sample, the method by Rice et al. was not able to correctly identify the the edge from IL-10 to IL-1β. We further note that the method by Rice et al. is not able to identify self-edges, such as commonly found in cytokine interaction networks [238, 358].

We applied our method to determine the roles of the cytokines TNFα, IL-1α, IL-1β, IL-6 and IFNγ in the regulation of IL-23. The IL-23 driven Th17 pathway has been identified as an important therapeutic target, but is still poorly understood at a mechanistic level [22, 341]. The optimal network we selected using the AIC clearly indicates that in this inflammatory context, IL-23 is driven by IL-1, and to a lesser extent by IFNγ, but not by TNFα. This supports the view of IL-1 as a promising target for those patients that fail to respond to TNFα inhibition. Another regulator of interest is IL-10. As the experimental data indicates that IL-10 downregulates both IL-23 and IL-1β, and IL-1β in turn upregulates IL-23, one might hypothesize that the observed downregulatory effect of IL-10 on IL-23 is IL-1β dependent: i.e. IL-10 might not have a direct effect on IL-23. How-

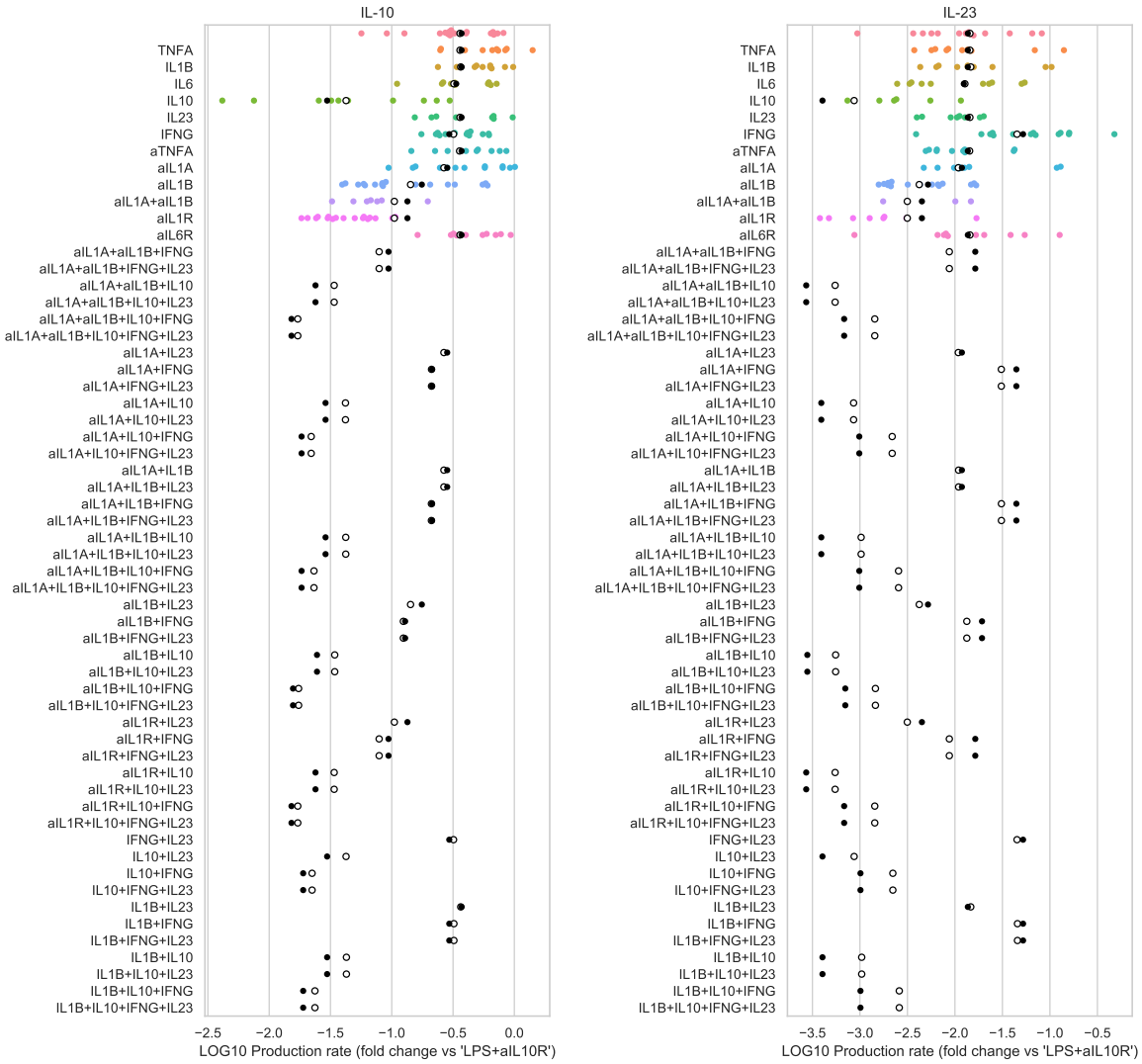


Figure 34: Simulated secretion rates of IL-10 and IL-23 after addition of various combinations of cytokines and cytokine (receptor) blockades (Section 2.11). Experimental data points are plotted with coloured circles. Model predictions given by simulations generated via the optimal models as identified by the AIC resulting from our constrained (black) and extended (white, black borders) approach(see Section 2.7). (Figure continues on next page)

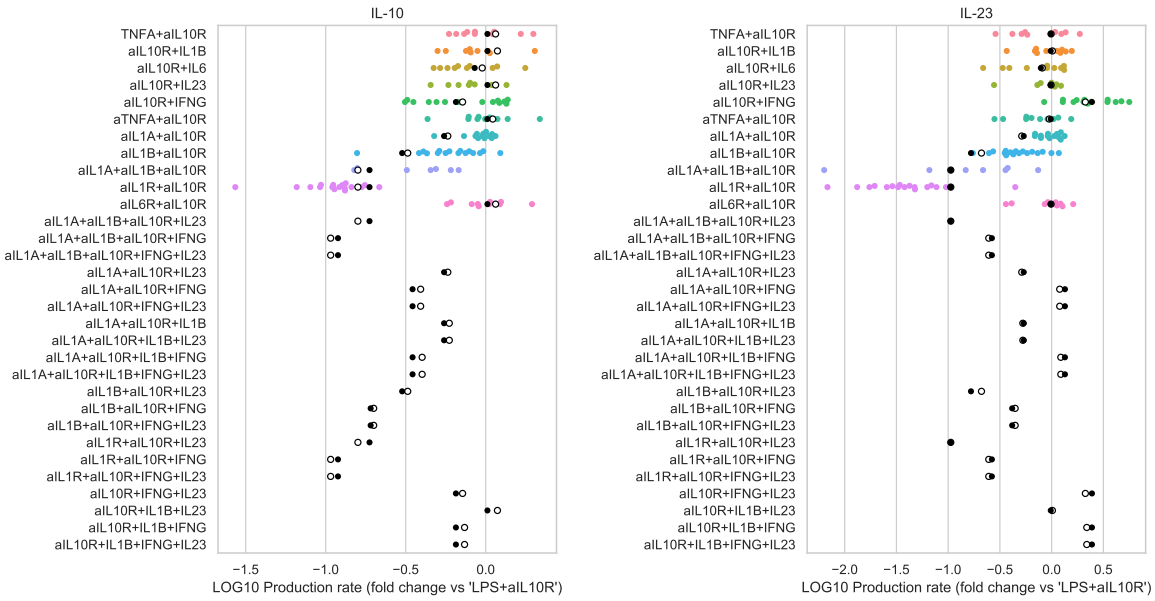


Figure 34: (Continued figure)

ever, the network clearly indicates that the downregulation by IL-10 of IL-23 is largely IL-1 independent. Thus, IL-23 is regulated by both IL-10 (negative effect) and IL-1 (positive effect). Furthermore, the extracted network indicates that the experimentally observed up-regulation of IL-23 by IFNγ is not pre-dominantly driven by the down-regulation of IL-10 by IFNγ. Finally, it is noted that the parameters with the largest sensitivity coincide with the parameters that we would expect to have the largest influence on the model outputs and also the high sensitivities are associated with parameters that do not generate practical identifiability, thus further increasing confidence in the network inference and subsequent conclusions.

A limitation of the current form of our modelling equations is the inability to account for the effects of saturation of the cytokine secretion rate. To incorporate these effects in the model, the effects of one cytokine on the secretion rate of another cytokine could be implemented as a saturating function of cytokine concentration (e.g. the positive effects of the concentration $x_i(t)$ of cytokine i on the secretion rate $y_j(t)$ of cytokine j could be given by $y_j(t) = \left(1 + \frac{\alpha x_i(t)}{h + x_i(t)}\right)$, with α the maximum secretion rate, and h the half-saturation constant). The dataset used does not justify an extension of the simple model equations we have chosen (see Section 2.3 on parameter identifiability issues). The addition of cytokines

in various concentrations within the experimental protocol would allow us to explore such saturation effects.

We have implemented LPS stimulation as a constant perturbation over time. We have chosen this implementation as it is the simplest form to capture the LPS effects in an ODE model. In reality, the response to LPS decays over time. We have not implemented this decay, as our dataset only contains a single time point (t = 16h). We similarly assume, with justification, that cytokines under the experimental conditions are not degraded over time. We use the ODE model as a tool to extract an optimal interaction network, based on the size of the modulating effects of the various cytokines that are (still) present after 16 hours of stimulation. Time-dependent data would be essential to study more complex cytokine dynamics over time.

We have used two approaches to extract our cytokine network: the constrained and the extended approach. For both the constrained and extended approach, we started with a model with no interactions and iteratively added edges that maximized the increase in model fit (as measured by the decrease in the distance D, obtained by trust-region optimization). For the initial, constrained approach, we subsequently confirmed that the resulting list of initial models for each model size were indeed the models with the best fit to the data (assuming that all estimates of D obtained by trust-region optimization were global minima). We did not do this for the extended approach, as the number of possible network configurations was prohibitively large. We have noted that the most striking difference between the two approaches is the large effect on the model fit of the addition of an upregulatory edge from IL-23 to TNFα in the extended approach. This edge was not part of the set of 31 significant edges of the constrained approach. Data on IL-23 (receptor) blockade was not included in the dataset. Although we can not exclude that the addition of IL-23 (receptor) blockade could have a negative effect on TNFα secretion levels by monocytes, we expect this to be unlikely, as monocytes do not express IL-23 receptors [62]. Any effect of IL-23 on monocyte cytokine secretion would therefore have to be indirect, e.g. IL-23 might upregulate a lymphocyte produced cytokine such as IFNγ that in turn causes up-regulation of TNFα by monocytes. This possibility could be explored by further experiments. We conclude that while the constrained approach can only contain edges for which evidence exists

in the data, the extended model can point towards potential edges that could be further tested experimentally, such as effects of IL-23 on other cytokines. We predicted the effects of untested combinations of cytokine (receptor) inhibitors using the extracted networks. The dataset already contained multiple combinations of cytokine(receptor) blockades and no suggestions for additional experiments followed immediately from the model predictions (Section 2.11).

In summary, we developed a method to extract a minimal, weighted network from cytokine interaction data using ordinary differential equations and the Akaike information criterion. This method enables us to distinguish direct from indirect effects of cytokine concentration on the secretion rate of other cytokines and determine the strength of the different cytokine interactions. By applying our method to an existing flow cytometry dataset, we extracted a network of the regulation of IL-23, a key cytokine in IBD. Our findings suggest that IL-1 is an important regulator of cytokine responses and a promising therapeutic target for IBD patient subgroups. In future work, we could expand our current dataset of interest by including the secretion of cytokines by other cell types present in the blood, e.g. IFNγ secretion by lymphocytes could be further explored. Finally, our method could be applied to other cytokine interaction data sets that include data on cytokine (receptor) blockades or cytokine additions.

Appendix: comparison with an existing method

We compare our method with an existing method from the literature intended to reconstruct biological networks: a method by Rice et al. that is based on conditional correlation analysis [291]. We have chosen a method that is designed to work with data including interventions, e.g. knock-outs, in the case of genes, or receptor blockades, in the case of cytokines. As noted before, when no interventional data is available, other methods, such as Gaussian graphical models could be used (introduced in Section 1.3.7), but these are not suitable here.

The method by Rice et al. is based on conditional correlation analysis [291]. The edge weight from cytokine u to cytokine v is determined based on the control data set and the data corresponding to the receptor blockade of cytokine u. First, the cytokine expression

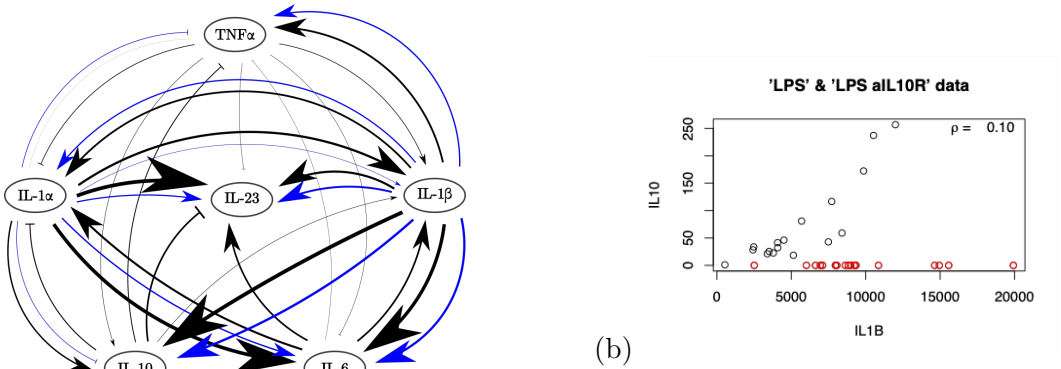
levels of cytokine u and v are standardised, such that the expression of each cytokine has zero mean and unit variance across both datasets. Then, the conditional correlation $\rho_{u,v}$ between cytokine u and v is defined as:

$$\rho_{u,v} = \sum_{j=1}^{J} y_u^j y_v^j, \tag{2.30}$$

with J the number of control samples plus the number of samples where cytokine u was blocked, and y_u^j, y_v^j the standardised (to have zero mean and unit variance) expression levels of cytokine u and v for sample j. The correlation coefficient $-1 \leq \rho_{u,v} \leq 1$ determines the weight of the edge from u to v. The sign of the correlation coefficient determines whether the edge is positive or negative.

We applied the method by Rice et al. to our IL23 dataset. We only considered the 'LPS', 'LPS+aIL1α', 'LPS+aIL1β', 'LPS+aIL1R', 'LPS+aIL6R', and 'LPS+aIL10R' conditions, as the method by Rice et al. is intended to be used on a dataset consisting of single cytokine (receptor) blockages only. We used the raw, non-normalised PMFI values. We show the resulting network in Figure 35(a). For IL-1α (IL-1β), we determined correlation coefficients using the 'LPS+aIL1α' ('LPS+aIL1β') data, shown in blue, and using the 'LPS+aIL1R' data, shown in black. We recall that edge weights identified by the method by Rice et al. correspond to the value of the corresponding correlation coefficient and the sign of an edge corresponds to the sign of this correlation coefficient. We note the method by Rice et al can not identify self-edges, though this is also required for the IL23 data, and in general. The most striking difference between the model extracted by the method by Rice et. al, except for the absence of self-edges, is the low weight of the edges from IL-10 to the other cytokines. We observe for instance that the weight of the edge from IL-10 to IL-1β is very small (i.e. $\rho_{\text{IL-10, IL-1}\beta} = 0.10$). This edge even has the wrong sign, as the effect of the blockage of the IL-10 receptor on the expression of IL-1β is positive (see Table 2.1). To investigate what happened, we plot the IL-1β expression versus the IL-10 expression for the 'LPS' condition and the 'LPS+aIL10R' condition, where we set the IL-10 expression to zero for the 'LPS+aIL10R' condition, following the approach by Rice et al. (Figure 35(b), 'LPS' samples in black, 'LPS+aIL10R' samples in red). We observe that the mean IL1β expression is larger in the presence of aIL10R, as expected. However, we note that the

correlation between IL-1β and IL-10 for the 'LPS' sample is positive, possibly because of the strong positive effect from IL-1β on IL-10 expression, or because there is an overall positive correlation between the level of cytokine expression due to LPS stimulation of the different cytokines for each donor. Due to the positive correlation between the IL-1β and IL-10 for the 'LPS' sample, the value of the correlation coefficient ρ of the 'LPS' and 'LPS+aIL10R' (of all shown sample points), is small, and has a positive sign (i.e. $\rho = 0.10$). Therefore, the edge weight from IL-10 to IL-1β is small as well, and has the wrong direction, indicating that Rice's algorithm, which is being applied outside of its intended scope, is not appropriately accommodating indirect or asymmetric cytokine interactions. In turn, this makes it unsuitable for network extraction in the context of the IL23 data and the objectives of this chapter. Due to the demonstrated unsuitability of the conditional correlation analysis to extract cytokine interactions, no biological conclusions should be drawn from this method and thus the biological conclusions made in this chapter are not altered by the conditional correlation analysis, nor is uncertainty added to them.



(a) (b)

Figure 35: (a) The IL23 network configuration selected by the conditional correlation analysis method by Rice et al [291]. Edge widths are proportional to the conditional correlation coefficients $\rho_{u,v}$, corresponding to an edge from cytokine u to v. Positive (negative) conditional correlation coefficients correspond to positive (negative) edges. For IL-1α (IL-1β), we determined correlation coefficients using the 'LPS+aIL1α' ('LPS+aIL1β') data, shown in blue, and using the 'LPS+aIL1R' data, shown in black. (b) The IL-1β expression versus the IL-10 expression for the 'LPS' condition and the 'LPS+aIL10R' condition, where we set the IL-10 expression to zero for the 'LPS+aIL10R' condition, following the approach by Rice et al. 'LPS' samples in black, 'LPS+aIL10R' samples in red.

Chapter 3

The balance between defective antibacterial activity and cytokine production impairment in driving Crohn's Disease pathogenesis

We study the immunodeficiency component of Crohn's disease using a combination of mathematical modelling, data from the literature, and wet-lab experiments. Experimental data for this study has been obtained by me, as part of this doctoral study, with the guidance of Sumeet Pandey, a post-doctoral fellow in Holm Uhlig's lab.

3.1 Introduction

Although Crohn's disease (CD), one of the two main types of inflammatory bowel disease (IBD), is characterised by a hyper-inflammatory phenotype, it has recently been hypothesized that in some patients CD could primarily be caused by an immunodeficiency in bacterial killing by the innate immune system [341]. This hypothesis is supported by genetic studies. Both common variants associated with an increased risk for CD such as NOD2 and ATG16L1, and rare monogenic mutations such as XIAP and NPC1 deficiencies cause antimicrobial activity defects. The resulting increased bacterial load might be the underlying trigger for long-term increased pro-inflammatory cytokine levels. Further understanding of this aspect of CD pathology could point towards new treatment options for patient subgroups, such as bacterial clearance inducing drugs.

Here, we focus on the NOD2/XIAP/RIPK2 pathway (Figure 1). Mutations in the

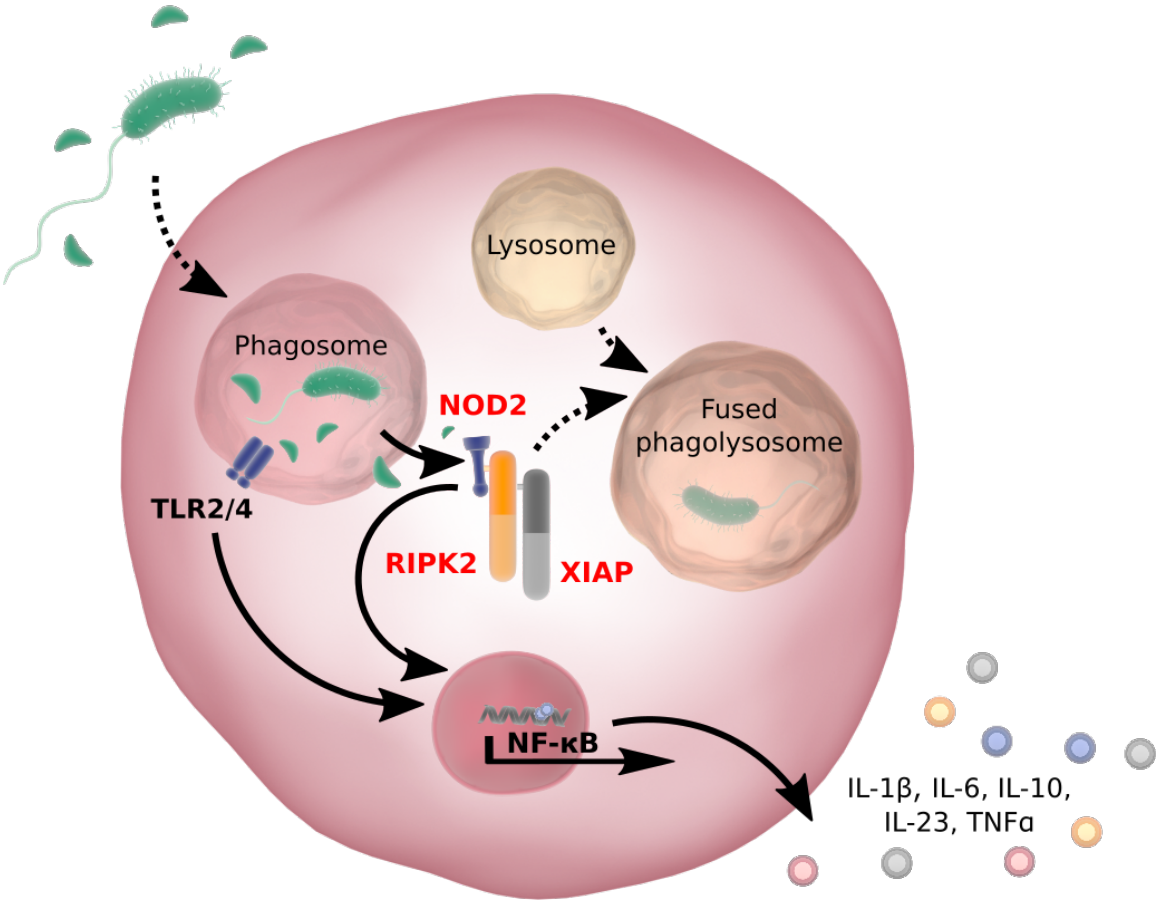


Figure 1: Schematic of the role of the NOD2 pathway in antimicrobial activity and cytokine production. After pathogen uptake, the NOD2-RIPK2-XIAP complex induces pathogen killing via autophagy and NF-κB mediated cytokine production (e.g. IL-1β, IL-6, IL-10, IL-23, TNFα). During autophagy, the pathogen containing vesicle (phagosome) fuses with a lysosome. The pathogen is then degradated. Other pathogen recognition receptors than NOD2, such as TLR2 and TLR4, also induce cytokine production. This figure has been inspired by the schematic in [306], Figure 7.

nucleotide-binding oligomerization domain-containing protein 2 (NOD2) gene is the strongest genetic risk factor for CD and X-linked inhibitor of apoptosis (XIAP) deficiency can cause a Mendelian type of IBD [324]. NOD2 is a pathogen recognition receptor that is highly expressed in monocytes and macrophages [336]. NOD2 stimulation by its ligand muramyl dipeptide (MDP), a bacterial cell wall component, induces cytokine production and enhances killing of pathogens by innate immune cells [6]. In accordance, macrophages from patients with a deficiency in the NOD2 pathway produce less pro-inflammatory cytokines than cells from healthy controls when stimulated with NOD2 ligand [306]. It seems therefore paradoxical that deficiencies in the NOD2 pathway trigger CD development with associated high levels of TNFα and other pro-inflammatory cytokines. The exact mechanism of NOD2 deficiency in CD pathogenesis is still unknown. Various mechanisms have been proposed. Most of these proposed mechanisms are independent of the effect of defects in the NOD2 pathway on antimicrobial activity. Examples include mechanisms dependent on deficiencies in antimicrobial peptide production, T cell activation, and cell recruitment (see Section 1.1.1.2). An initial reduction in cytokines might for instance impair immune cell recruitment and therefore impose a heightened risk of uncontrolled infection, accompanied by escalating pro-inflammatory cytokine levels (Scenario I, Figure 2) [176]. As mutations in the NOD2 pathway also cause a defect in the killing ability of innate immune cells, in an alternative scenario the observed hyper-inflammation in CD could be driven by the constantly increased bacterial load as a result of the NOD2 defect (Scenario II, Figure 3) [69, 306, 336]. We study the hypothesis of bacterial handling driven cytokine hyper-production, in the absence of immune cell recruitment (Scenario II), using a combination of mathematical modelling, wet-lab experiments, and data from the literature. We define bacterial handling as intracellular bacterial killing. Based on our wet-lab results, we construct a mathematical model that links bacterial load to cytokine production over time (1 to 25h post infection) in an *in vitro* system of *Salmonella* infected human monocyte-derived macrophages. We generate *in silico* model simulations of pathogen load and cytokine trajectories over time while varying the killing and cytokine production capability of the cells. We compare our model simulations with data from the literature on the size and timing of the effects of genetic defects in the NOD2 pathway on pathogen load and cytokine concentration.

3.1.1 Aims and objectives

The aim of this chapter is to study the hypothesis that defects in the NOD2 pathway could drive a state of cytokine hyper-production as a result of a defect in antimicrobial activity, even in the presence of an impairment in cytokine production capability, in the absence of other cell types (Scenario II). We will use a combination of mathematical modelling, experimentation, and data from the literature to study this hypothesis. Our research objectives are as follows: (1) to construct a mechanistic bacterial handling model that describes the level of infection of *in vitro* infected human macrophages from healthy donors over time; (2) to use a microscopy data set of the initial distribution of infection to generate model predictions that could falsify the assumptions made in the construction of the bacterial handling model; (3) to extend our bacterial handling model to describe the relationship between cytokine concentration and the level of infection of *in vitro* infected macrophages from healthy donors over time; (4) to investigate whether the introduction of an impairment in bacterial handling in this extended model can drive a state of cytokine hyper-production, even in the presence of an impairment of cytokine production capability; (5) to estimate the size of effects of defects in the NOD2 pathway on both bacterial handling and cytokine production capability from the literature; and finally, (6) to investigate if our experimental and mathematical framework, complemented with the data from the literature, suggests that defects in the NOD2 pathway could drive a state of cytokine hyper-production as a result of a defect in antimicrobial activity, even in the presence of an impairment of cytokine production capability.

3.1.2 Novelty

Although it has been proposed before that hyper-inflammation in subgroups of CD patients could be driven by bacterial handling defects, the balance between an impairment in bacterial handling and defects in cytokine production capability has not yet been studied. The possibility of bacterial handling driven hyperinflammation, even in the presence of an impairment in cytokine production capability, strengthens the hypothesis that the bacterial handling defect component of genetic defects in the NOD2 pathway can play a role in CD pathogenesis. This is important, as the role of NOD2 genetic defects in CD

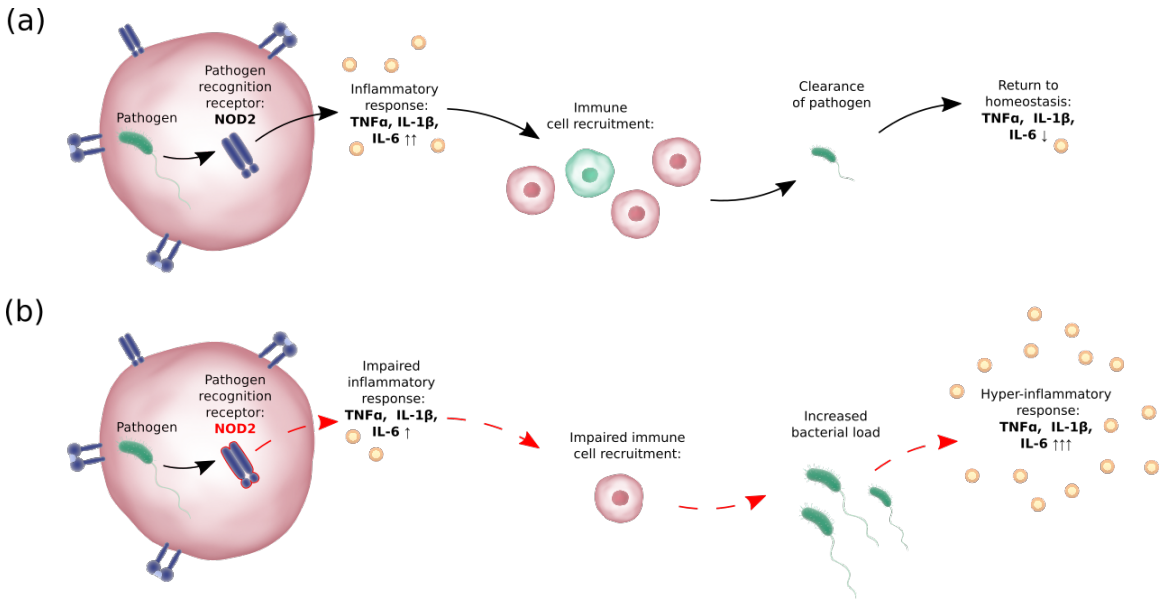


Figure 2: Scenario I. The exact mechanism of NOD2 deficiency in CD pathogenesis is still unknown. An initial reduction in cytokines might impair immune cell recruitment and therefore impose a heightened risk of uncontrolled infection, accompanied by escalating pro-inflammatory cytokine levels. Healthy (a), and impaired (b) version of this scenario.

pathogenesis is still unclear and other mechanisms have been proposed as well, including mechanisms that require cell recruitment (e.g. Scenario I above, we will not study this scenario). Another novelty of our study is our choice of methods, e.g. our combined approach of mathematical modelling with experimentation, to study the connection between NOD2 defects and hyper-inflammation. In contrast to most other studies that combine modelling and experimentation, we have chosen to work with primary human cells, as murine cells or immortalised cell lines do not recapitulate all features of human disease pathophysiology [165].

3.1.3 Structure

This chapter is structured as follows. We describe our methods (Section 3.2). We present our antimicrobial activity data and construct a mathematical model of the bacterial handling dynamics, linking initial bacterial numbers to the number of bacteria recovered at each point in time (Section 3.3.1). We present a mathematical model that describes the distribution of infection over time (Section 3.3.2). Using our experimental cytokine concentration data,

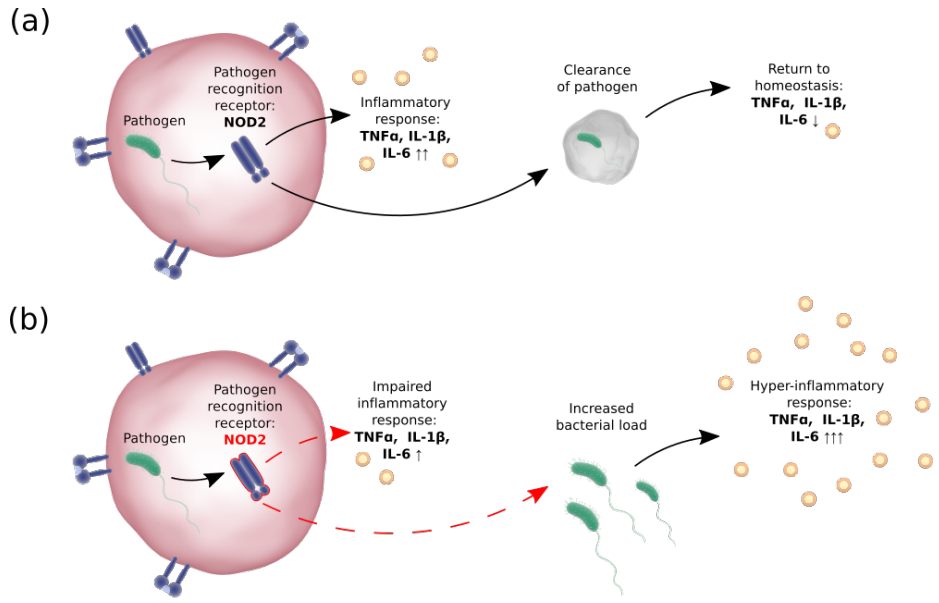


Figure 3: Scenario II. The observed hyper-inflammation in CD patients with a deficiency in the NOD2 pathway could be driven by the constantly increased bacterial load as a result of the NOD2 defect. Healthy (a), and impaired (b) version of this scenario.

we construct a mathematical model of the relationship between cytokine production and bacterial load (Section 3.3.3). We present our macrophage viability data (Section 3.3.6). We simulate the effects of bacterial handling defects on both the bacterial load and cytokine concentrations (Section 3.3.7). Using data from the literature, we study the effects of mutations in the NOD2/XIAP/RIPK2 pathway on our system. In particular, we use our integrated framework to examine whether the antimicrobial activity deficiency component to these mutations could on its own be sufficient to drive a state of cytokine hyper-production, as seen in disease phenotypes associated with such mutations (Section 3.3.9). We end with a discussion of our results (Section 3.4).

3.2 Methods

Unless otherwise stated, all wet-lab experiments were carried out by me (JEJ), as part of this doctoral study, with help and guidance from Sumeet Pandey, post-doctoral fellow in the Uhlig lab, Nuffield Department of Medicine. All other aspects of this chapter are my work.

3.2.1 Gentamicin protection assay

I determined the overall bacterial load over time with a Gentamicin protection assay. Peripheral Blood Mononuclear Cells (PBMCs) were supplied by the NHS blood bank as leukocyte cones and isolated by Ficoll gradient (Lymphoprep, Axis-Shield) centrifugation ($n = 8$ healthy donors). PBMCs consist mainly of lymphocytes, including T cells, B cells and natural killer (NK) cells, and monocytes, which are macrophage pre-cursors. The monocyte enriched fraction of the PBMCs was obtained by the adherence method (performed by Sumeet Pandey) followed by differentiation to monocyte-derived macrophages (MDM) over a period of 5 days in RPMI 1640 medium (Sigma) supplemented with 10% fetal calf serum (FCS, Sigma) and $100\,\mathrm{ng\,ml^{-1}}$ macrophage colony-stimulating factor (M-CSF, R&D). The gentamicin protection assay was performed using *Salmonella enterica serovar typhimurium* strain SL1344 (*Salmonella*) (kindly provided by Gordon Dougan, Sanger Institute, Cambridge, UK). Bacteria were grown overnight in lysogeny broth (LB, Sigma). Per well, 80,000 MDM were plated. For four donors (Donor A, B, C, and D), the MDM were infected at a multiplicity of infection (MOI), the number of bacteria added per macrophage, of 1,5, 10 or 20 for one hour, after which the antibiotic gentamicin ($100\,\mathrm{\mu g\,ml^{-1}}$, Gibco) was added to the dish. After the addition of gentamicin, no extracellular bacteria survive. The overall intracellular bacterial load per dish was quantified at various time points, by lysing all macrophages, plating them on lysogeny broth (LB) agar plates, and quantifying the number of colony forming units (CFUs) on the agar plate the following day (2 replicates per time point per donor). We assume that each colony represents one surviving intracellular bacterium [323]. We included a well with only bacteria and no macrophages. We repeated the experiment for four other donors (Donor E, F, G, and H), at an MOI of 10, but this time added three different modulations, mimicking various known bacterial handling defect inducing mutations. We added an IL-10 receptor blocking antibody (aIL10R, $10\,\mathrm{\mu g\,ml^{-1}}$, Biolegend; 3F9), the RIPK2 inhibitor Ponatinib (50 nM, Selleck Chemical), and the NPC1 (cholesterol sensor and transport) inhibitor U1866 ($2\,\mathrm{\mu g\,ml^{-1}}$, Sigma-Aldrich), that causes a lipid accumulation and a cellular phenotype resembling NPC1-Crohn's disease [306].

3.2.2 Protein level analysis

We determined the supernatant concentration of the cytokines TNFα, IFNγ, IL-1β, IL-6, IL-10, IL-8, IL-18 and IL-23 at various time points during the infection assay for Donor E, F, G, H, in the absence of modulations, by a Luminex assay. As a control, we measured the cytokine concentration in several dilutions of a mix of cytokines with known concentrations.

3.2.3 Viability assay

Apoptosis staining was performed on the MDM using a FITC Annexin V and propidium iodide (PI) apoptosis detection kit (BioLegend, Cat #640914). MDM (250,000 cells per condition) were left untreated, killed in a hot water bath, or infected with *Salmonella* for one hour (MOI= 20), after which the antibiotic gentamicin ($100\,\mu g\,ml^{-1}$, Gibco) was added, and their viability at $t = 25$h post infection was analysed by flow cytometry. Annexin V binds to phosphatidylserine that can be found on the external cell membrane of apoptotic cells. PI is a DNA and RNA binding dye that can penetrate necrotic cells.

3.2.4 Confocal microscopy

The confocal microscopy experiment and quantification of bacterial load using Fiji/ImageJ was performed by Athena Cavounidis, DPhil student in the Uhlig lab, Nuffield Department of Medicine. I (JEJ) determined the proportion of infected cells using Fiji/ImageJ. The confocal microscopy was performed using GFP expressing (NCTC 12023) *Salmonella enterica serovar typhimurium* (GFP-*Salmonella*). MDM (10,000) were seeded and infected for one hour at an MOI of 20 using GFP-*Salmonella Typhimurium* ($n = 7$ healthy donors). Gentamicin treatment ($100\,\mu g\,ml^{-1}$) in the presence of LysoTracker deep red (Thermo Fisher) and DAPI stain was performed for one hour. In particular note that LysoTracker deep red and DAPI stain were used to distinguish between macrophages. A macrophage nucleus was identified by a blue colour due to DAPI stain that labels DNA and the intracellular macrophage environment surrounding the nucleus was identified by LysoTracker deep red, a red fluorescent dye that labels acidic organelles in live cells, including lysosomes. Cells were fixed with 4% Pierce Formaldehyde (Thermo Fisher) for 10 minutes at 37° C prior to

sealing with vectashield (Vector labs). Images were acquired on a Zeiss LSM 880 microscope using a 63X/1.4 oil objective lens.

3.2.5 Mathematical modelling

We use ordinary differential equations (ODEs) to describe the bacterial load and cytokine concentration dynamics. We implemented our model equations in the Matlab based modelling environment 'Data2Dynamics' [284]. Minimization of the log likelihood function for parameter estimation and computation of profile likelihoods to study parameter identifiability were performed in this environment, using a deterministic trust-region approach combined with a multi-start strategy (see Sections 1.3.2 and 1.3.3). We estimated the parameters in Section 3.3.3 using a non-linear least squares approach with the Matlab function 'lsqnonlin'.

3.3 Results

3.3.1 Bacterial handling dynamics

We construct a mathematical model to describe the relationship between the number of bacteria per macrophage used for infection, and the bacterial load as determined by our gentamicin protection assay over time ((A) in Figure 4). We measure the bacterial load in CFU, the number of colony forming units. We assume that each colony represents one surviving intracellular bacterium [323]. We measure the time t in hours post infection and we only consider the time post the addition of the antibiotic gentamicin at $t = 1$h. We assume no extracellular pathogen survival occurs for $t > 1$h and therefore all of the bacteria are taken up by the macrophages before gentamicin addition. This was confirmed for $t > 2$h experimentally by the inclusion of a well containing only bacteria and no macrophages. No colony forming units were obtained from this well one hour after gentamicin addition. We note we do not know the size of the viable intra- or extracellular pathogen population during the first hour after gentamicin addition, as our first measurement was taken at $t = 2$h post infection. We therefore do not exclude the possibility that a fraction of the measured intracellular bacterial population at $t = 2$h post infection was taken up by the macrophages after gentamicin addition. However, we assume this fraction is sufficiently

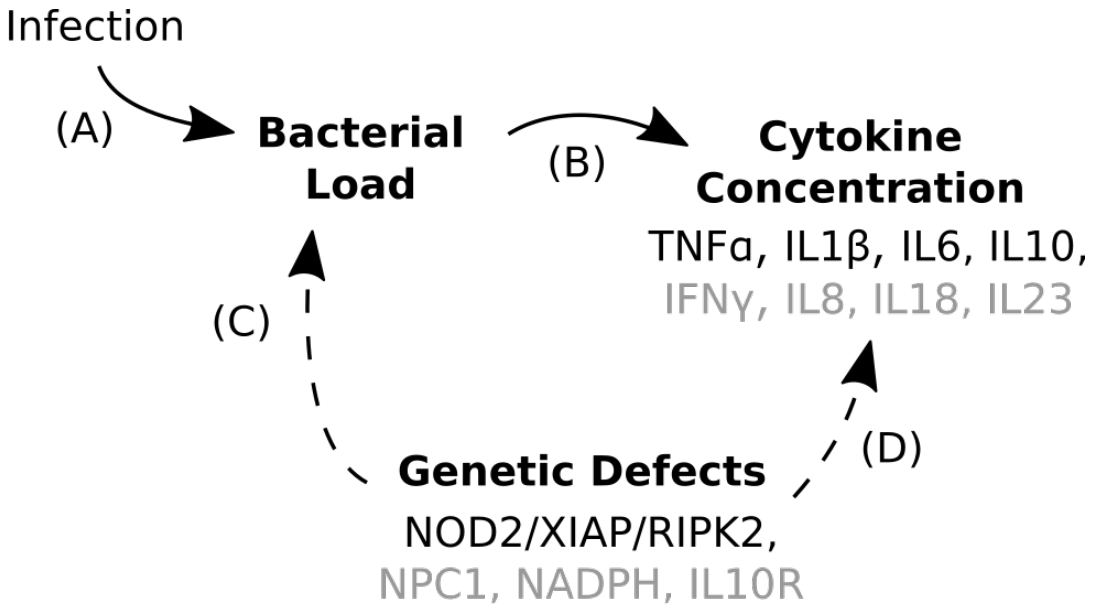


Figure 4: Overview of the modelled system of *Salmonella* infected macrophages. Using *in vitro* bacterial handling and cytokine concentration data, we have constructed a mathematical model describing the relationship between (A) multiplicity of infection (MOI) and bacterial load, and between (B) bacterial load and cytokine concentration over time. Introducing genetic mutations that are thought to play a role in CD (like) pathogenesis can have varying effects on cytokine concentration and bacterial handling, each with their own time-scale. Macrophages with such genetic defects can display altered cytokine levels independent of the bacterial load via (D), e.g. defects in IL-10 signalling cause an upregulation of pro-inflammatory cytokines such as IL-23 [22], but also dependent on the bacterial load (B) via (C), e.g. defects in NPC1 result in a heightened bacterial load due to impaired autophagy, the mechanism used by macrophages to kill and degrade pathogens [306]. We will focus on defects in the NOD2/XIAP/RIPK2 pathway and their effects on TNFα, IL-1β, IL-6, and IL-10 concentration (black). Defects in this pathway initially result in decreased cytokine production (D), which might be compensated for by an increased bacterial load driven cytokine production (B) via (C) at later points in time (Figure 1).

small compared to the number of bacteria taken up before the addition of gentamicin to justify our model assumption that no bacteria are taken up after gentamicin addition at $t = 1$h post infection and all timescales below are in units of hours unless otherwise stated. We will use the subscript *pop* for "population" when we assume a model parameter has the same value across all donors. Donor dependent parameters will be indicated with a subscript $i \in \{A, B, C, D, E, F, G, H\}$. When a parameter is introduced without a subscript, both donor dependent and independent forms will be explored. We track the overall intracellular bacterial load over time with the following ODE:

$$\frac{\mathrm{d}B_{i,j}}{\mathrm{d}t} = g_{pop}B_{i,j} - k(t)B_{i,j}, \tag{3.1}$$

with $B_{i,j}$ (in CFU) the number of bacteria for donor $i \in \{A, B, C, D, E, F, G, H\}$ and multiplicity of infection (MOI), i.e. the number of bacteria added per macrophage, $j \in \{1, 5, 10, 20\}$, t (in h) the time, g_{pop} the intracellular bacterial growth rate and $k(t)$ the time dependent macrophage killing rate. Both growth and killing are thus assumed to be proportional to the number of bacteria. We will initially consider a donor independent killing rate κ_{pop} which governs the scale of $k(t)$ as detailed below, and will later explore a donor dependent form (see Section 3.3.1.1). We assume the initial bacterial load is donor and MOI dependent. $B_{i,j}(t = 1\text{h}) = \sigma_i \frac{j}{10}$ is the initial bacterial load at $t = 1$h post infection (p.i.) for donor i with MOI j, where

$$\sigma_i \frac{j}{10}$$

is defined as the initial bacterial load at $t = 1$h post infection (p.i.) for donor i with MOI j. Due to the high donor-dependent variability of this type of data, scaled or normalised colony count data is commonly found in the literature [266, 273, 306]. We also assume that the uptake rate of bacteria by the macrophages before the addition of gentamicin scales linearly with MOI and fix the initial ratio of intracellular bacteria accordingly, i.e. for an MOI of 1, 5 and 20 the bacterial load at $t = 1$h p.i. is 0.1, 0.5, or 2 times the value observed for an MOI of 10 [26, 127]. We observe a slight increase in bacterial load at early time points (compare $t = 2$h and $t = 3$h for Donors C and D, Figure 7). Such an increase has been observed before in various similar killing assays using monocytes or their progeny, such as in [29, 154, 272, 218, 266], although other dynamics have been observed as well (see

Section 3.3.9). To capture the observation that the bacterial load seems to increase initially before decaying to zero, we let the killing rate k_{pop} increase over time. In particular, we have chosen $k_{pop}(t) = \kappa_{pop}(1 - e^{-\tau_{pop}(t-1)})$, with κ_{pop} the killing rate at late time and τ_{pop} a measure of the inverse time scale for macrophages to induce maximal rates of pathogen killing. Note that $k_{pop}(t = 1\text{h}) = 0\,\text{h}^{-1}$ and $k_{pop}(t) \to \kappa_{pop}$ as $t \to \infty$ for this choice of $k_{pop}(t)$. We assume that macrophages have a certain handling time before they can kill a pathogen: after a bacteria containing vesicle (phagosome) is formed, it fuses with a lysosome and is subsequently degraded [195].

We measured the bacterial load for eight healthy donors at various MOI, and at various points in time (see Section 3.2.1). We estimate the value of our parameter vector $\boldsymbol{\theta} = \{\sigma_A, \sigma_B, \sigma_C, \sigma_D, \sigma_E, \sigma_F, \sigma_G, \sigma_H, g_{pop}, \kappa_{pop}, \tau_{pop}, SD_{abs,pop}, SD_{rel,pop}\}$, where $SD_{abs,pop}$, $SD_{rel,pop}$ are scales of measurement error, as detailed below, by minimizing $\mathcal{LL}(\boldsymbol{\theta}) = -2\log\mathcal{L}(\boldsymbol{\theta})$, where $\mathcal{L}$ is the likelihood function:

$$\mathcal{L}(\boldsymbol{\theta}) = \prod_{i\in\{A,\ldots,H\}} \prod_{j\in\{1,5,10,20\}} \prod_{k\in\{2,\ldots,25\}} \frac{1}{\sqrt{2\pi(SD_{i,j,k})^2}} \exp\left(-\frac{(B_{i,j}(k) - \hat{B}_{i,j,}(k))^2}{2(SD_{i,j,k})^2}\right). \quad (3.2)$$

Here $B_{i,j}(k)$ and $\hat{B}_{i,j}(k)$ are the values of the simulated (using equation 3.1) and experimentally measured bacterial load respectively for donor $i \in \{A, B, C, D, E, F, G, H\}$, MOI $j \in \{1, 5, 10, 20\}$ and time point post infection $k \in \{2, 3, 4, 5, 6, 7, 8, 25\}$. The value of $\boldsymbol{\theta}$ is implicitly contained in the simulated bacterial loads $B_{i,j}(k)$. We estimate the standard deviation of the data $SD_{i,j,k}$ simultaneously with the data. We assume normally distributed measurement errors with both an absolute and a relative component: $SD_{i,j,k} = \sqrt{(SD_{abs,pop})^2 + (SD_{rel,pop})^2(B_{i,j}(k))^2}$. We have chosen this form, as we observe a larger absolute variation in colony forming units (CFU) for higher bacterial numbers, but ignoring the absolute part of the errors resulted in unrealistically small error estimates at $t = 25$h post infection (p.i.). Although the bacterial load decreases significantly over 25h, the vast majority of wells still contained some viable bacteria at our final time point.

Our data set does not allow us to determine the relative contribution of growth and killing on the change in bacterial load, resulting in structural parameter non-identifiability, identified by flat profile likelihood profiles using the profile likelihood approach (introduced in Section 1.3.3.3). We therefore assume that the doubling time of the bacteria is one

hour, i.e. g_{pop} =1.0 h^{-1}. We have based the estimation of this value on a bacterial growth analysis performed in the same lab for an earlier publication (Figure 5). After fixing g_{pop}, we confirmed all other model parameters had finite confidence intervals using the profile likelihood approach (Figure 6, the profile likelihood approach was introduced in Section 1.3.3.3). We recall we defined a practically identifiable parameter as one with a finite profile likelihood confidence interval for its estimate (Section 1.3.3.3, [281]). Therefore, after fixing g_{pop}, all free model parameters are practically identifiable according to above definition [283]. In addition, as practical identifiability concerns the ability to uniquely identify parameters given a limited set of real, noisy data, while structural identifiability concerns estimating parameters given sufficient amounts of perfect, noise-free data, we also have structural identifiability.

3.3.1.1 Comparison of donor dependent and independent parameter values

Apart from the scaling parameter σ_i, $i \in \{A, B, C, D, E, F, G, H\}$, we initially assumed that all parameter values are donor independent, i.e. we assumed the same value for κ_{pop} and τ_{pop} across all donors (solid lines in Figure 7). We explore donor dependent κ_i and τ_i, $i \in \{A, B, C, D, E, F, G, H\}$ (dashed lines in Figure 7). By introducing these donor dependent parameters in our parameter vector $\boldsymbol{\theta}$, we increase the total number of estimated parameters (by minimizing the log likelihood) from 12 to 26. We have decided to use population level κ_{pop} and τ_{pop}, as the donor dependent approach can introduce large variations in κ_i and τ_i between different donors that are not supported by the current data set. See for instance the large value for τ_B in Figure 7 (b). Taking a smaller, population value for τ mainly affects the simulated bacterial load before the first experimental point in time $t = 3$h and has therefore almost no effect on the model fit (Figure 7 (b)).

3.3.2 Macrophage distributions

In this section we will explore the time-dynamics of the distribution of the bacterial load. We note the system of equations introduced in this section will not be used in subsequent sections in this chapter. The aim of the section is to generate testable *in silico* model

Figure 5: Bacterial growth of *Salmonella* was assessed. The bacterial growth was determined as optical density (OD) at 595nm (n= 3 to 4 replicates). We fitted an exponential growth curve with growth parameter g_{pop} to the first five data points (using non-linear least squares). We exclude later time points when the growth is no longer exponential, possibly due to nutrient depletion or waste accumulation. The data was taken from an unpublished study by Pandey et al. on the role of neurotransmitter receptors on intrinsic antibacterial immunity.

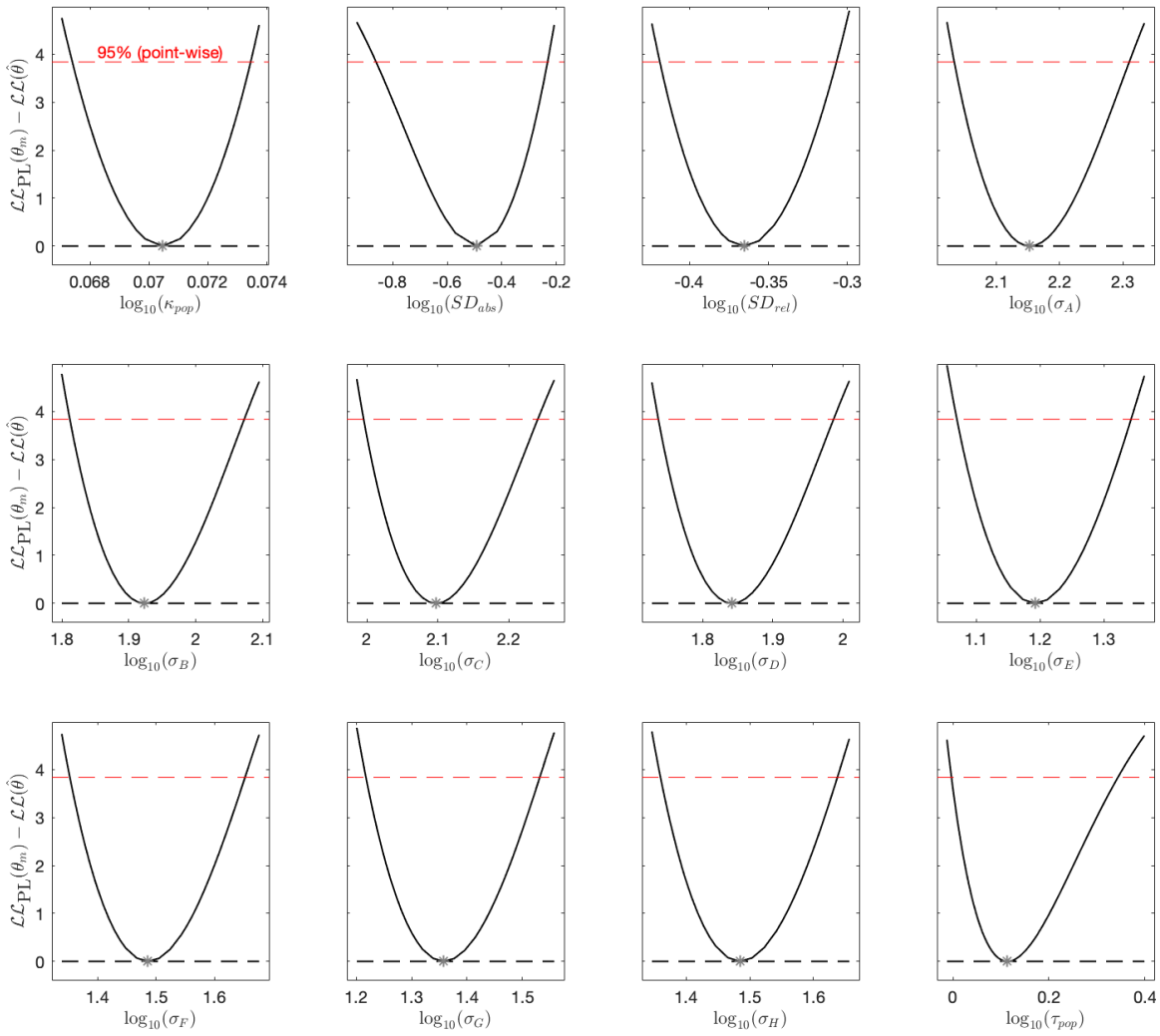


Figure 6: Profile likelihood plots for all parameters in $\boldsymbol{\theta}$ except g_{pop}, which we keep fixed. We estimated $\kappa_{pop}, \tau_{pop}, SD_{abs,pop}$ and $SD_{rel,pop}$ at the population level and took donor dependent values for σ_i for each donor $i \in \{A, B, C, D, E, F, G, H\}$. While fixing the mth parameter to the values as indicated on the x-axis, all other parameter values were estimated by minimizing the negative log likelihood: $\mathcal{LL}_{\mathrm{PL}}(\theta_m) = \min_{\theta_{n \neq m}} (\mathcal{LL}(\boldsymbol{\theta}))$, with $\mathcal{LL}(\boldsymbol{\theta}) = -2 \log (\mathcal{L}(\boldsymbol{\theta}))$ and $\mathcal{L}(\boldsymbol{\theta})$ the likelihood as defined in equation (3.2). Further, $\hat{\theta} = \underset{\boldsymbol{\theta}}{\operatorname{argmin}}(\mathcal{LL}(\boldsymbol{\theta}))$. We show the confidence interval threshold at the 95% level for individual parameters (i.e. point-wise confidence intervals, red dashed lines, see for more details Section 1.3.3). This plot has been generated with the Matlab based modelling environment 'Data2Dynamics' [284].

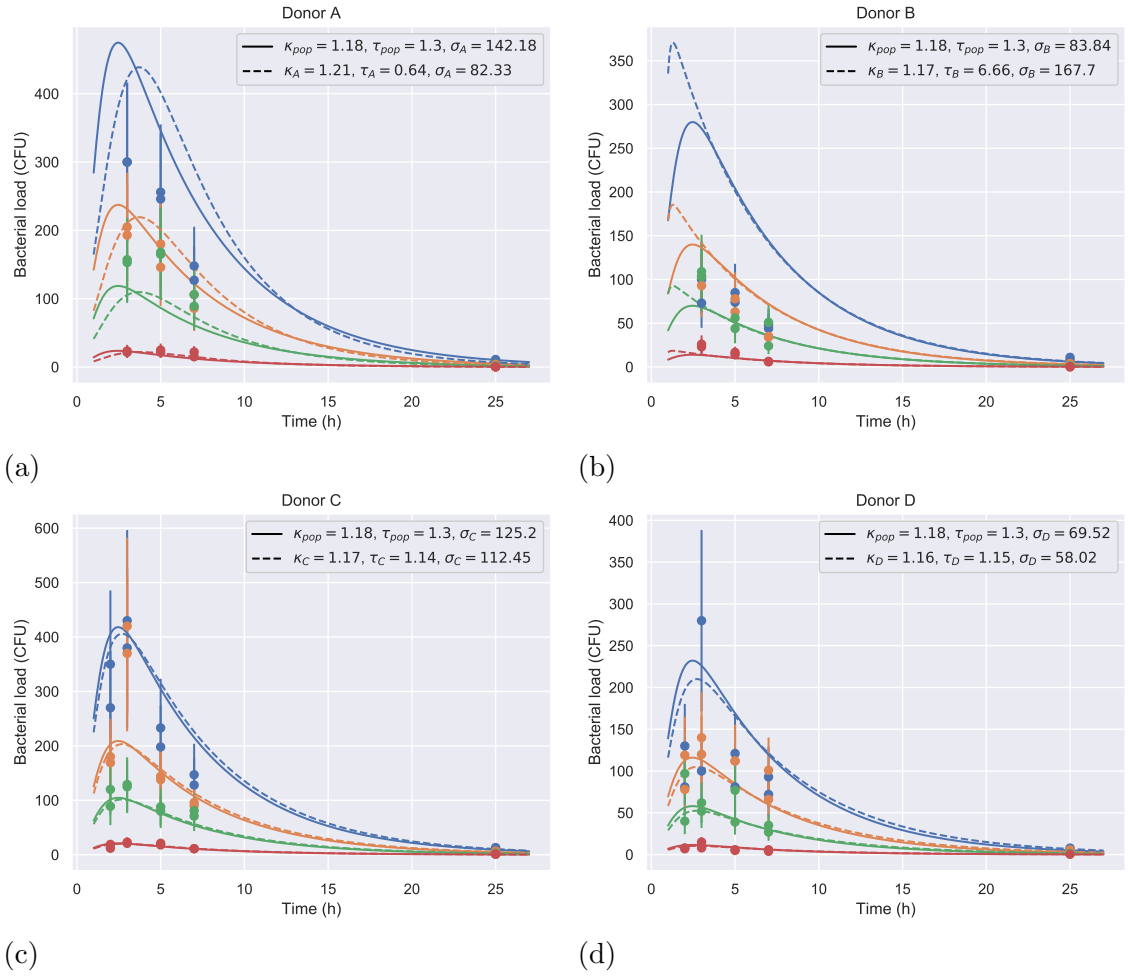


Figure 7: Experimental (round markers) and simulated (lines) data, for MOI=20 (blue), 10 (yellow), 5 (green) and 1 (red). We have taken g_{pop} =1.0 h^{-1} fixed and estimated κ, τ, $SD_{abs,pop}$, $SD_{rel,pop}$, and σ_i, with the latter denoting the initial bacterial load for an MOI of 10. We estimated σ_i independently for each donor, while estimating κ_{pop} and τ_{pop} at the population level (solid lines), and estimated κ_i, τ_i and σ_i for each donor independently (dashed lines). We only show plots for donors A, B, C and D, but we also used the control data of donors E, F, G, and H for parameter estimation.

predictions that have the potential to falsify several of our model assumptions, such as the assumption of exponential bacterial growth (as discussed in Section 3.4.2).

The number of intracellular bacteria per macrophage were quantified after one hour of *Salmonella* infection and an additional hour of gentamicin incubation using confocal microscopy ($n = 7$ healthy donors, Figures 8 and 9). We have combined the count data for all seven donors and binned it in eleven bins $n \in \{0, 1, 2, \ldots, 10+\}$. We fit several distributions to the experimental distribution. The simplest distribution, assuming that the chance of a macrophage taking up a bacterium at any given moment is equal for each macrophage and independent of earlier infection events, would be a Poisson distribution. In detail, let X be a random variable describing the number of observed intracellular bacteria in a macrophage. When X is a Poisson random variable with rate parameter $\lambda > 0$, the probability of observing x intracellular bacteria is

$$P(X = x) = \frac{\lambda^x e^{-\lambda}}{x!}, \tag{3.3}$$

for $x = 0, 1, 2, \ldots$ intracellular bacteria per macrophage. The expected number of intracellular bacteria per macrophage is $E(X) = \lambda$. Bacterial growth is ignored in this scenario. We estimate λ by minimizing the chi square value χ^2:

$$\chi^2 = \sum_n \frac{O_n - E_n}{E_n},$$

with O_n and E_n the observed and expected number of macrophages containing $n \in \{0, 1, 2, \ldots, 10+\}$ bacteria respectively. The chi square value is minimized for $\lambda = 2.3$, $\chi^2 = 452$. We observe that the Poisson distribution does not resemble the observed distribution very well: the estimated number of uninfected cells is too low (Figure 10 (b)). This is confirmed by a chi square goodness of fit test. If the observed distribution follows the hypothetical distribution, it approximates a chi-square distribution with $m - p - 1$ degrees of freedom, with m the number of bins, and p the number of parameters estimated when minimizing χ^2. One degree of freedom is lost as the sum of all counted macrophages is fixed: $\sum_n O_n = \sum_n E_n$ [235, Chapter 9.7]. As we have eleven bins and have estimated one parameter (λ), we have nine degrees of freedom in this case. The chance of obtaining the

experimentally observed distribution under a Poisson distribution with $\lambda = 2.3$ is negligibly small, as $\chi^2_9(0.1\%) = 21.5 \ll 452$.

We fit the observed distribution to a negative binomial distribution, again by minimizing χ^2. This is motivated by the assumption that infection events are Poisson distributed, but the infection rates of the macrophages are heterogeneous, and are gamma distributed, in which case the unconditional distribution of infection can be written as a negative binomial distribution (Figure 10 (c)). Let Z be a gamma distributed continuous random variable describing the rate of infection with parameters $\alpha > 0$ and $\beta > 0$ and probability mass function

$$P(Z = \zeta) = \frac{\beta^\alpha \zeta^{(\alpha-1)} e^{-\beta\zeta}}{\Gamma(\alpha)}, \tag{3.4}$$

with $\Gamma(\alpha)$ the Gamma function. The expected infection rate is $E(Z) = \frac{\alpha}{\beta}$ bacteria per macrophage per two hours. We let X be a random variable describing the number of observed intracellular bacteria in a macrophage as before. We assume that infection events are Poisson distributed, but the infection rates of the macrophages are heterogeneous, and are gamma distributed. The resulting negative binomial distribution has the following probability density function:

$$P(X = x) = \binom{x + r - 1}{x} q^r (1 - q)^x, \tag{3.5}$$

with parameters $r = \alpha$ and $q = \frac{1}{1+\beta}$. The expected number of infections is $\frac{rq}{1-q} = \frac{\alpha}{\beta}$. We note that an observed negative binomial distribution could alternatively be the result of population dependent bacterial growth after uptake (apparent contagion) [134]. As discussed in Section 3.4, it is theoretically not possible to distinguish between apparent contagion on one hand and existing macrophage heterogeneity on the other.

The negative binomial distribution fits the experimental data much better than the Poisson distribution: the chi square value is 11.2. As we have estimated two parameters in this case, we have $11 - 2 - 1 = 8$ degrees of freedom. As $\chi^2_8(10\%) = 13.4 > 11.2$, we can not reject the negative binomial distribution at the 10% level (Figure 10 (d)). Instead of assuming a continuous, Gamma distributed, heterogeneous macrophage infection rate, we also explored the possibility of multiple macrophage populations, each with their own, constant rate of infection. We again assume the infection events are Poisson distributed for

each independent macrophage population and ignore bacterial growth. This results in chi square values of 20.8, 7.8 and 7.7, and acceptance at the 0.4%, 17%, and 5.2% level for two, three, and four independent populations of macrophages, and 7, 5 and 3 degrees of freedom respectively (Figure 10 (e-j)). Note that we loose two degrees of freedom for the chi-square test for each additional population, as we estimate both the infection rates and the fraction of macrophages contained in each population.

We introduce a system of equations representing $N+1$ bacterial load dependent macrophage populations:

$$\begin{aligned}
\frac{\mathrm{d}M_0}{\mathrm{d}t} &= k(t)M_1, && (3.6)\\
\frac{\mathrm{d}M_1}{\mathrm{d}t} &= -gM_1 + 2k(t)M_2 - k(t)M_1, && (3.7)\\
\frac{\mathrm{d}M_n}{\mathrm{d}t} &= (n-1)gM_{n-1} - ngM_n + (n+1)k(t)M_{n+1} - nk(t)M_n, && (3.8)\\
\frac{\mathrm{d}M_{N+}}{\mathrm{d}t} &= (N-1)gM_{N-1} - Nk(t)M_{N+}, && (3.9)\\
B_{mean} &= \sum_n nM_n, && (3.10)\\
M &= \sum_n M_n = 1, && (3.11)
\end{aligned}$$

with M_n the fraction of the macrophage population containing n bacteria, and B_{mean} the mean bacterial load per macrophage. We again assume that the bacterial growth rate g_{pop} =1.0 h^{-1} is constant over time and that the killing rate $k(t) = \kappa_{pop}(1 - e^{-\tau_{pop}(t-1)})$ increases as t increases. We further assume that the killing rate becomes larger than the bacterial growth rate for some $t^* > 0$, i.e. we assume there exists a $t^* > 0$ such that $k(t) > g$ for all $t > t^*$. We observe that for this system:

$$\frac{\mathrm{d}B_{mean}}{\mathrm{d}t} = gB_{mean} - gNM_{N+} - kB_{mean}. \quad (3.12)$$

When compared to our original equation (3.1), we have averaged over the total number of macrophages, and we have introduced the extra term $-gNM_{N+}$. In Appendix B, we verify that when we let $N \to \infty$, this term will become arbitrarily small at finite time, for the parameter regime of interest, with $g/k(t) < 1$ for all t sufficiently large, as macrophage generation secures proportionally less bacteria, leading to geometric decay in M_n as n increases, which dominates the linear term N in NM_{N+}.

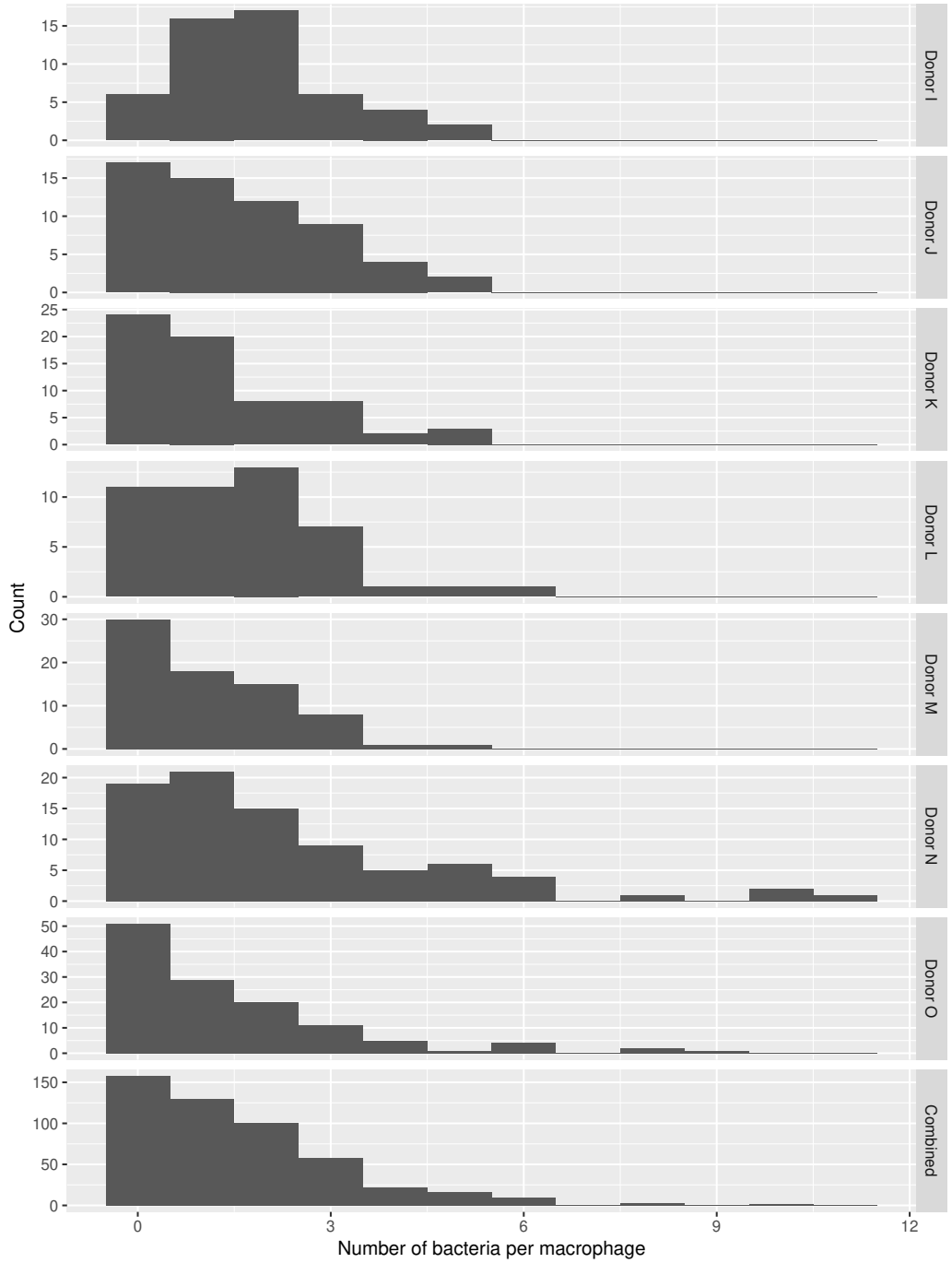
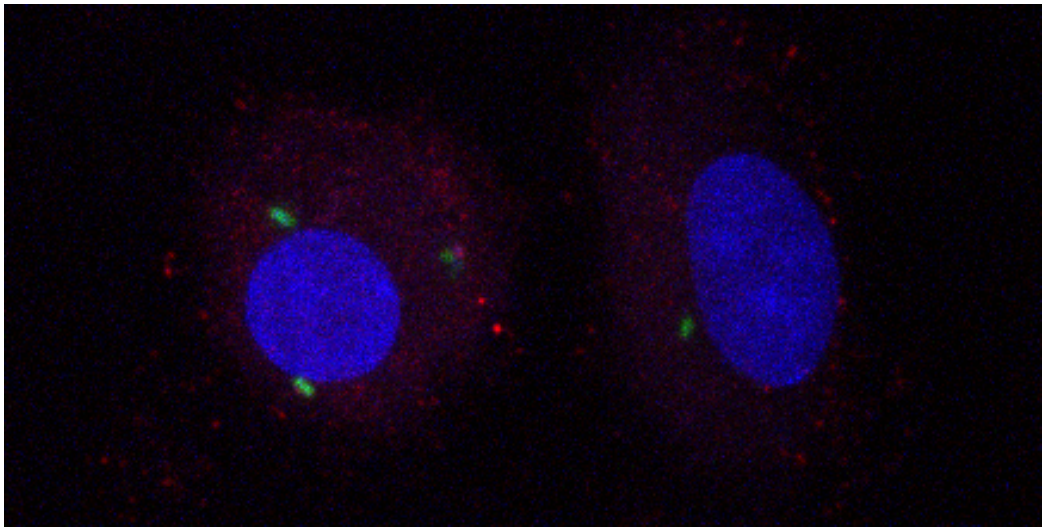
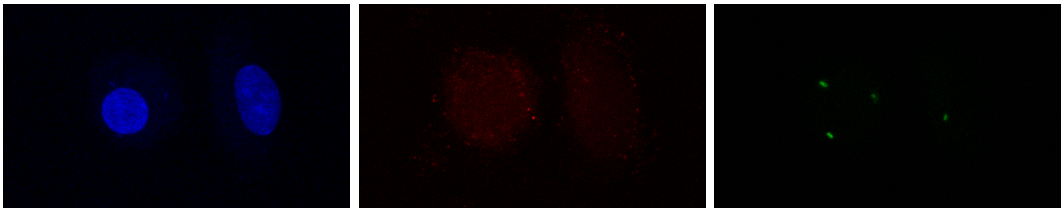


Figure 8: Number of GFP *Salmonella* per macrophage, as quantified by confocal microscopy (n=7 healthy donors). MDM were infected at an MOI of 20 for one hour and then incubated with gentamicin for an additional hour. We show the individual count data for Donor i, $i \in \{I, J, K, L, M, N, O\}$, and all data combined (lower row).



(a)



(b)

Figure 9: (a) Representative confocal image (maximum intensity projection) of two MDM infected with GFP *Salmonella*. MDM were infected at an MOI of 20 for one hour and then incubated with gentamicin for an additional hour. The left macrophage is infected with three, and the right macrophage with one GFP *Salmonella*. Cell nuclei are blue due to DNA staining with DAPI, acidic organelles within the macrophage are red due to staining with lysotracker and bacteria are green due to green fluorescent protein (GFP) expression. (b) The blue, red and green channels can be split to ease the quantification of the bacterial load.

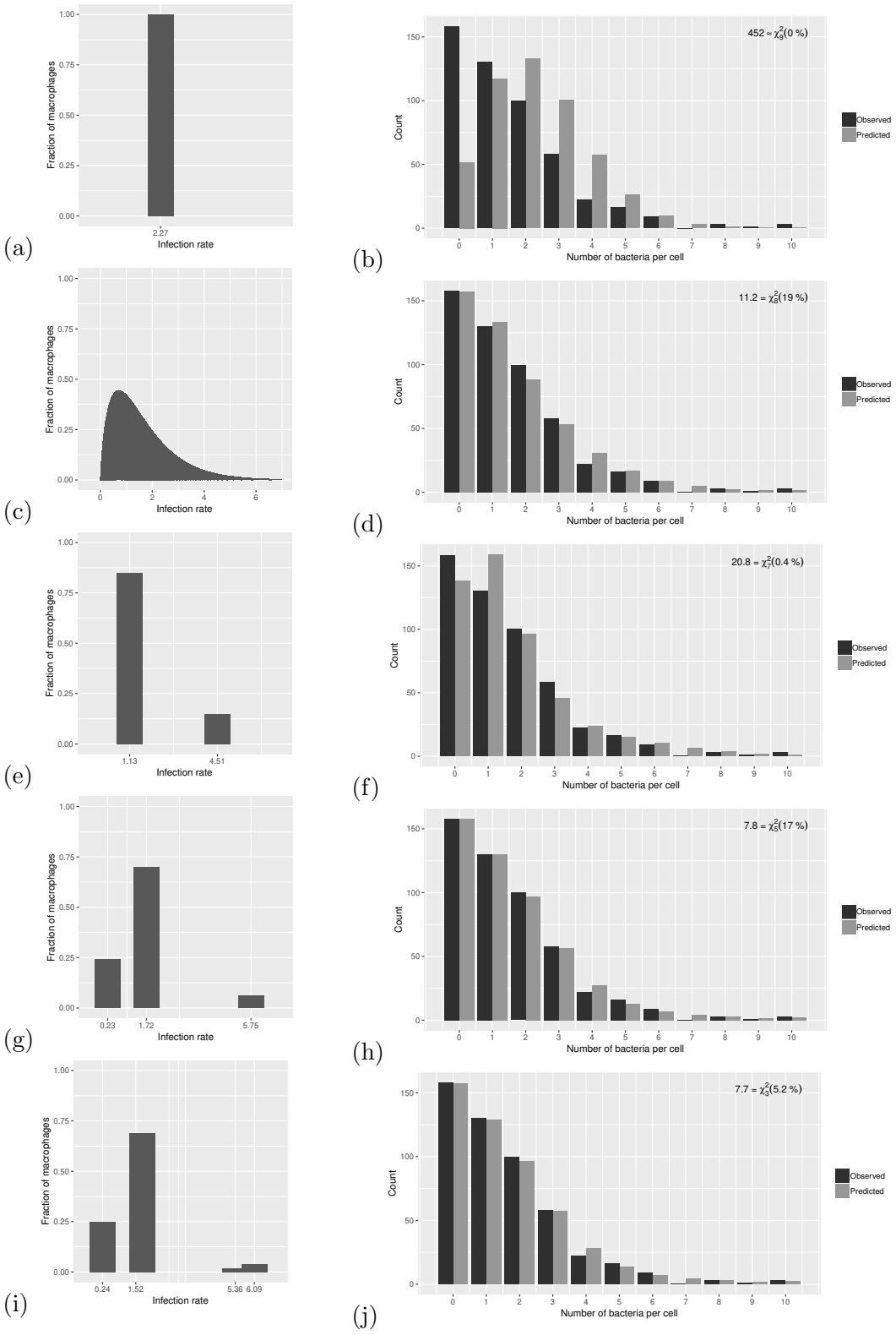


Figure 10: The estimated distribution of infection rates across cells (left) and distributions of infection (right, observations in dark grey, predictions in light grey), corresponding to a Poisson distribution (a,b), negative binomial distribution (c,d), and Poisson distribution with two (e,f), three (g,h), or four (i,j) distinct macrophage populations (each with their own rate of infection) respectively.

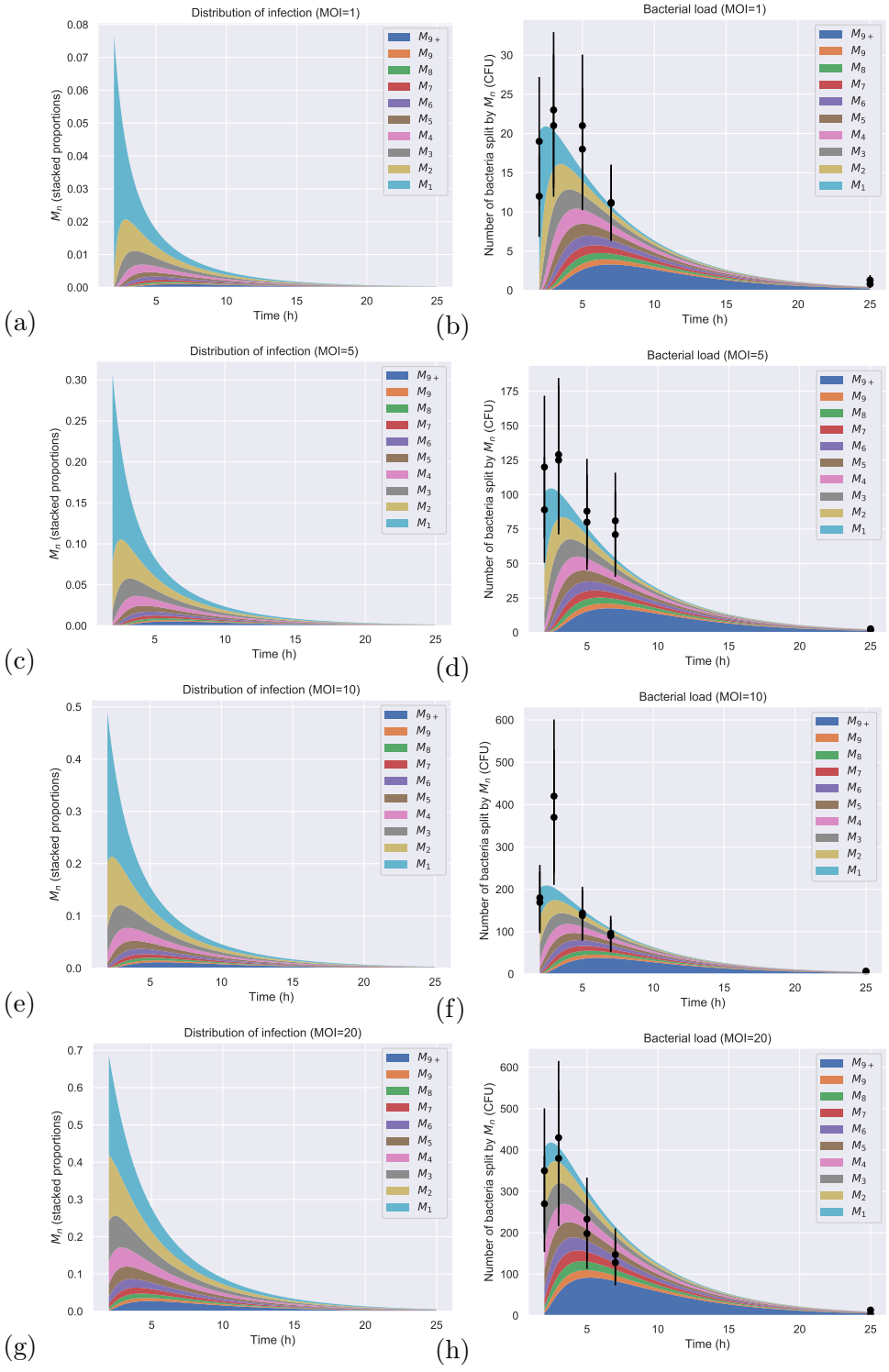


Figure 11: Simulated distributions of infection for donor C with system of equations (3.6). We use parameter values as estimated before (σ_C =125.2 CFU, g_{pop} =1.0 h^{-1}, κ_{pop} =1.2 h^{-1} and τ_{pop} =1.3 h^{-1}, see Figure 7, solid lines). We have taken $N = 100$. Note $\sum_i M_i = 1$, but we do not show M_0, the proportion of uninfected macrophages. (Legend continued on next page)

Figure 11: (Continued legend) As initial conditions (at $t = 2$h), we take the infection distributions obtained from the best negative binomial fit to the microscopy data, i.e. $r = 1.77$ and $q = 0.52$ for MOI=20 (equation (3.5)). Recall that the expected number of infections under a negative binomial distribution is $\frac{rq}{1-q}$. We assume the expected number of infections scales linearly with MOI. We therefore set q=$0.96, 0.81, 0.68$ for MOI=$1, 5, 10$ respectively. For the plots on the right hand side, we multiplied each fraction of the macrophage population M_n with its respective number of intracellular bacteria n, and with $\frac{B_{C,20}(t=2\text{h})}{B_{mean}(t=2\text{h}}$, where $B_{C,20}(t = 2\text{h})$ is the total number of bacteria at $t = 2$h for donor C at an MOI of 20 as simulated before (using equation (3.1)). This rescaling ensures the simulations of the total bacterial load match those in Figure 7, solid lines.

We plot as an example the simulated distributions of infection for donor C with $N = 100$ (Figure 11). We have also included a bar plot of the donor-independent predicted distribution of the infected macrophage population for MOI=20 at $t = 2, 6, 8, 18$h (Figure 12). The model simulations presented in Figures 11 and 12 are examples of testable model predictions. Subsequent experiments could challenge our *in silico* model assumptions by falsifying these model simulations. We assume, for instance, that bacteria will grow exponentially indefinitely. If the fraction of observed '9+' macrophages is much smaller than predicted, this could indicate that bacterial growth slows down over time, e.g. due to an increasingly hostile environment in the Salmonella-containing vacuole, or due to a lack of nutrients [53, 289]. Another possibility would be to observe a larger than predicted population of macrophages containing just one bacteria, as it has been observed that some bacteria enter a viable, dormant-like state after entering a macrophage [143].

3.3.3 Cytokine dynamics

In this section, we will return to our bacterial handling model (equation (3.1)) from Section 3.3.1. We will extend this bacterial handling model to describe the relationship between cytokine concentration and the level of infection of *in vitro* infected macrophages from healthy donors over time. Using a Luminex assay, we measured the supernatant concentration of IFNγ, IL-1β, IL-8, IL-10, IL-18, IL-23, and TNFα simultaneously with the bacterial load for donors E, F, G and H (Figure 13). We did not measure the cytokine concentration for donors A, B, C and D due to time constraints. All concentration data was measured for an MOI of 10. We note that in contrast to the former chapter, where we measured cy-

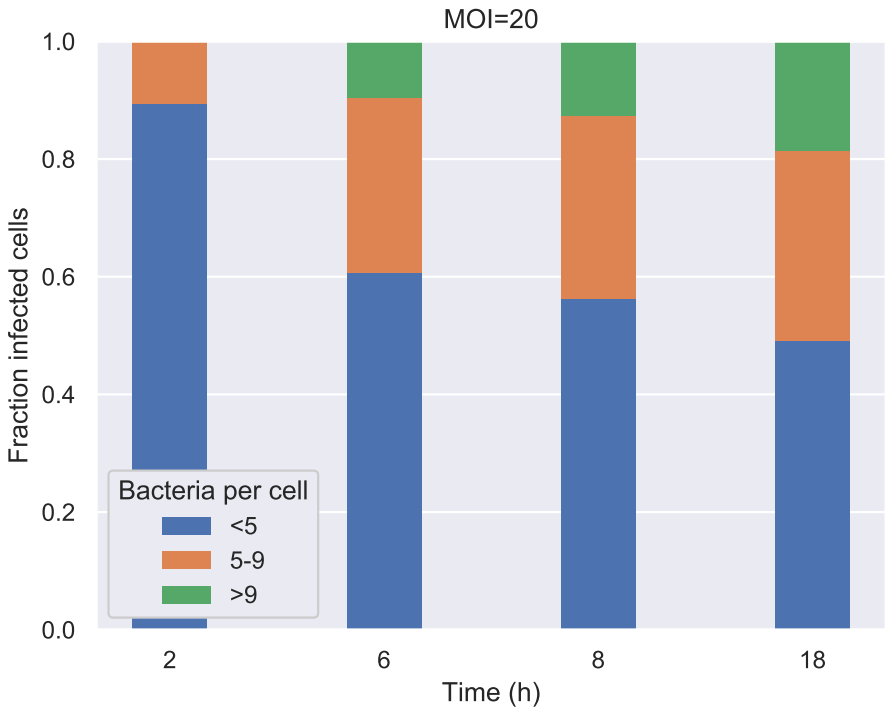


Figure 12: Measured (at $t = 2$h) and predicted (at $t = 6, 8, 18$h) distributions of the infected macrophage population for MOI=20. Simulated distributions of infection with system of equations (3.6), and parameter values estimated by minimising the log likelihood as before (g_{pop} =1.0 h^{-1}, κ_{pop} =1.2 h^{-1} and τ_{pop} =1.3 h^{-1}). We have taken $N = 100$. As initial conditions (at $t = 2$h, as the microscopy data was obtained at $t = 2$h post infection), we take the infection distributions obtained from the best negative binomial fit to the microscopy data, i.e. $r = 1.77$ and $q = 0.52$ (equation (3.5)).

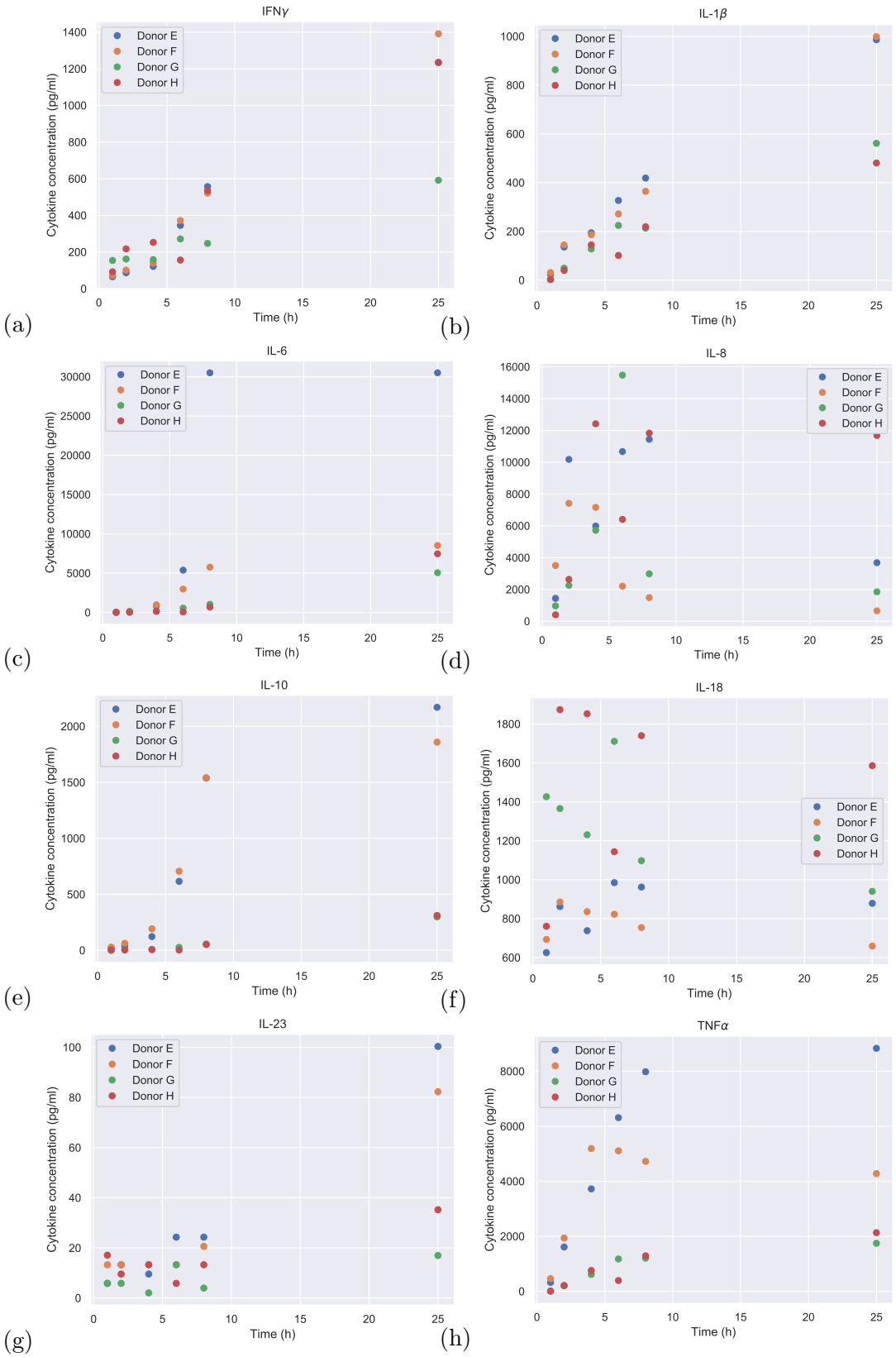


Figure 13: Supernatant cytokine concentrations at t=2, 3, 5, 7, 9, and 25h post infection for donor E, F, G, an H, with a multiplicity of infection of 10, as determined by a Luminex assay.

tokine production rates by flow cytometry, here we measured cytokine concentrations using a Luminex assay.

We observe that the cytokines IL-8 and IL-18 have a different dynamical profile from the other cytokines: their concentration is already high at early time points and is not monotonically increasing (Figure 13 (b), (f)). Their measured concentrations do not correlate highly with the other cytokines (Figure 14). As we are interested in cytokines whose production rate is sensitive to the size of the bacterial load at later time points, we have excluded IL-8 and IL-18 from our study. We have also excluded IL-23 because it is not secreted at high levels in our system (Figure 13 (g)). Only 7 out of the 24 measurements of the IL-23 were larger than the smallest concentration included in our standard curve measurements, i.e. the measurements of known cytokine concentration dilutions provided with the Luminex assay kit. Finally, we exclude IFNγ, because macrophages are not thought to produce large amounts of IFNγ [42, 341]. The measured IFNγ in our system might be a result of contamination with IFNγ producing lymphocytes (see Section 3.4).

We will use the subscript $l \in \{\text{IL-10}, \text{IL-1B}, \text{IL-6}, \text{TNFA}\}$ to indicate cytokines IL-10, IL-1β, IL-6 and TNFα respectively. For cytokine l, we assume that its production rate $f_{l,i}(B_i, t)$ is a donor dependent function of the current time and bacterial load:

$$\begin{aligned}
\frac{\mathrm{d}B_i}{\mathrm{d}t} &= g_{pop} B_i - \kappa_{pop}(1 - e^{-\tau_{pop}(t-1)})B_i, && (3.13)\\
\frac{\mathrm{d}C_{l,i}}{\mathrm{d}t} &= f_{l,i}(B_i, t), && (3.14)\\
B_i(t = 1\text{h}) &= \sigma_i, && (3.15)\\
C_{l,i}(t = 1\text{h}) &= 0, && (3.16)
\end{aligned}$$

with t (in h) the time, $B_i(t)$ (in CFU) the bacterial load and $C_{l,i}(t)$ (in pg ml^{-1}) the cytokine concentration for cytokine $l \in \{\text{IL-10}, \text{IL-1B}, \text{IL-6}, \text{TNFA}\}$ and donor $i \in \{E, F, G, H\}$ ((B) in Figure 4). As before, we use the subscript *pop* when we assume a model parameter has the same value across all donors. Donor dependent parameters are indicated with a subscript $i \in \{E, F, G, H\}$. The donor dependency of parameters introduced without subscript indicates that donor dependency will be specified for each simulation. Unless otherwise stated, we assume an MOI of 10 in this section, as all cytokine concentration data

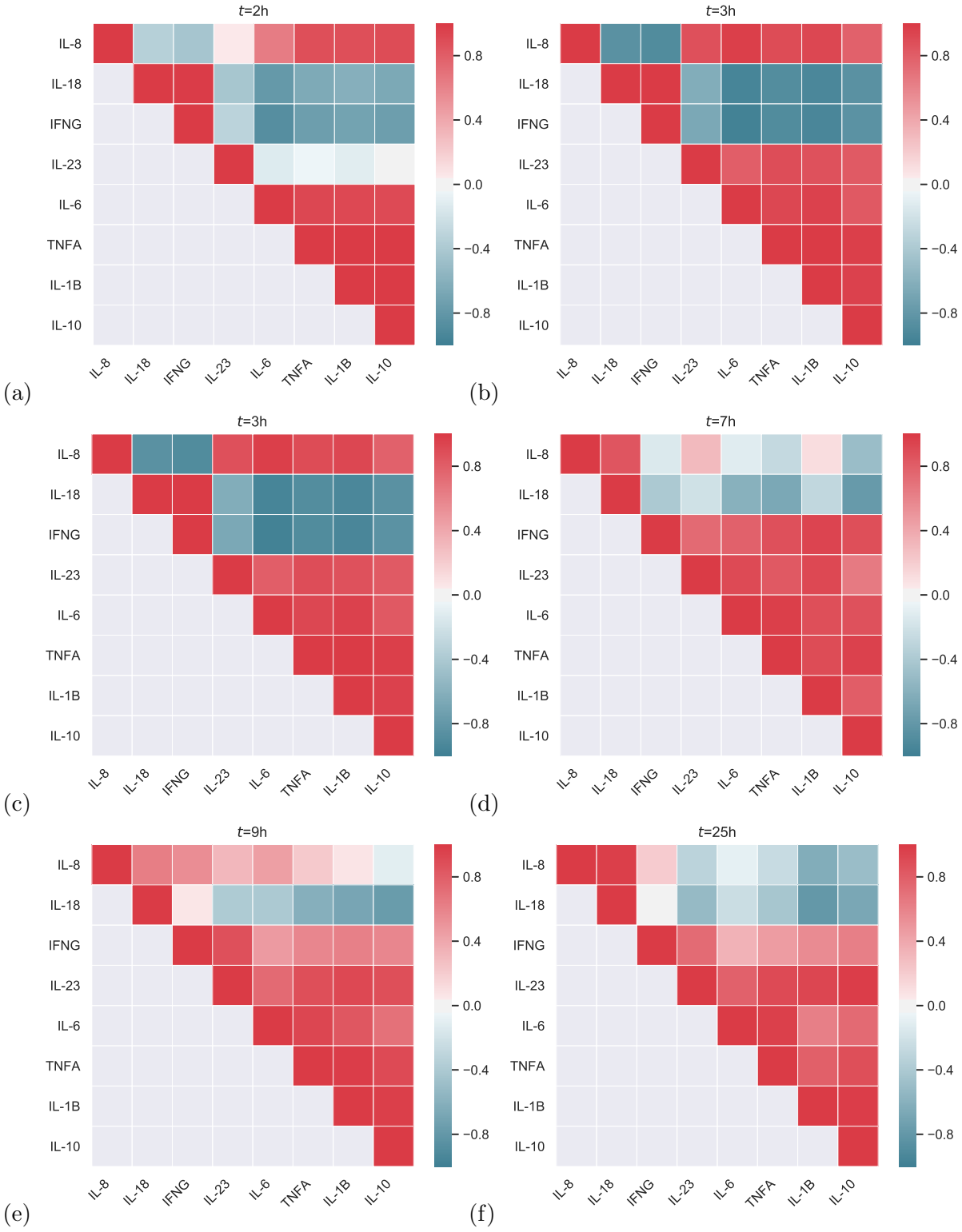


Figure 14: Upper triangular Pearson correlation matrices of the measured cytokine concentrations in Figure 13 at t=2, 3, 5, 7, 9, and 25h post infection. Colours correspond to the value of the Pearson correlation coefficient $r = \frac{(x-m_x)(y-m_y)}{\sqrt{\sum(x-m_x)^2 \sum(y-m_y)^2}}$, with m_x and m_y the means of the vectors containing concentration data of cytokine x and y.

was measured for an MOI of 10. The bacterial load equation (3.13) is equal to equation (3.1), with $k_{pop}(t) = \kappa_{pop}(1 - e^{-\tau_{pop}(t-1)})$ as before, and without the subscript j indicating the MOI, i.e. $B_i(t) = B_{i,10}(t)$. We use equation (3.13) to simulate the bacterial load, and not equation (3.12), as the extra term $-gNM_{N+}$ in equation (3.12) will become arbitrarily small at finite time for an exponentially decaying bacterial population. For all simulations throughout this section, we will assume that $g_{pop} = 1.0$ as before. We will further use the estimated values for σ_i, κ_{pop}, and τ_{pop} that we obtained via minimization of the log-likelihood (Figure 7, solid lines).

3.3.4 Further model assumptions

Although macrophages start being infected at $t = 0$h, the measured cytokine concentration after one hour of infection is very small for our cytokines of interest and we assume $C_{l,i}(t = 1\text{h}) = 0\,\text{pg}\,\text{ml}^{-1}$ (Figure 13).

The clearance rate of the various cytokines in our system is unknown. We assume that the production rate of the cytokines is much higher than the degradation and absorption rates, and that the latter can be ignored for the first 25h post infection. We assume that the production rate of the cytokines is so much higher than the degradation and absorption rates, that the latter can be ignored. We note that in an *in vivo* setting, cytokine clearance should not be ignored, as the local half-lifes of cytokines in vivo can be in the order of minutes, due to processes that include diffusion, enzymatic and non-enzymatic degradation or uptake via receptor mediated endocytosis into cytokine receptor positive cells [8, 90, 280]. We assume cytokines in culture medium can be considered stable for the time course considered, as more than 90% of cytokines (IFNγ, IL-4, IL-5, IL-10, IL-12p$_{40}$) were recovered after four days of incubation in culture medium [169]. The PBMC might take up some of the cytokines during the time considered. However, we assume this amount is negligible. We note that *in vitro* PBMC cytokine concentration time courses of up to 80 hours after LPS stimulation indicate that after an initial increase in cytokine concentration, the cytokine levels plateau [84]. We assume the plateau-phase indicates cytokines are no longer secreted, but are also not degraded or absorbed although we cannot rule out that after initial transients cytokines are absorbed and produced at exactly the

Cytokine	Increasing	Decreasing
IL-1β	[47], [119], [154], [218], [266]	
IL-6	[136], [154], [175]	
IL-10	[20], [7], [93], [136], [154], [119], [175], [218], [266], [273], [311], [317]	
TNFα	[20], [89], [119], [154], [167], [218], [268], [272], [273], [317], [327],	[175], [266]

Table 3.1: Instances in the literature of measured cytokine concentration trajectories over the first 24h of *in vitro* infection. Cell types used were either macrophage cell lines (THP-1, U937), primary human cells (PBMC, monocytes, MDM, monocyte derived dendritic cells), or murine cells (macrophages, dendritic cells). We have indicated whether the concentrations are still increasing or have started decreasing during this period of time.

same rate. Other studies mostly confirm these dynamics (i.e. the monotonically increasing or plateauing, but not decreasing, cytokine concentrations as observed by De Groote et al. [84]) during the first 24h of infection (Table 3.1). Because we have no information on the absorption rates of TNFα and the other cytokines in our system, and because the overall trend in the literature we decided to neglect the two studies reporting decreasing TNFα levels (Table 3.1, second column). At later time points, absorbance and degradation will become increasingly important, and after more than 24h, decreasing cytokine concentration levels have been observed [7, 93, 175, 272, 273, 334].

It is well known that cytokines can influence the production rates of other cytokines (see Chapter 2) [22, 141]. As we have no data on the blockade of the various cytokine receptors in our system, we will further ignore these feedback loops.

3.3.5 Further model developments

We now focus on the form of $f_{l,i}(B_i, t)$ (equation (3.14)). A simple form of $f_{l,i}$ would be a cytokine production rate proportional to B_i. However, many sources in the literature indicate that the production rate saturates for increasing bacterial load (Figure 15). We will therefore try

$$f_{l,i}(B_i) = p_{l,i}\frac{(B_i)^{q_l}}{(h_l)^{q_l} + (B_i)^{q_l}}, \tag{3.17}$$

with either $q_l = 1$ (Michaelis-Menten kinetics) or $q_l \neq 1$ (Hill kinetics), for each cytokine l. We will explore both donor-dependent ($h_{l,i}$ and $q_{l,i}$) and donor-independent ($h_{l,pop}$ and $q_{l,pop}$) forms of h_l and q_l. We assume $p_{l,i}$ is always donor dependent, as we observe a high variability in cytokine levels between donors (Figure 13).

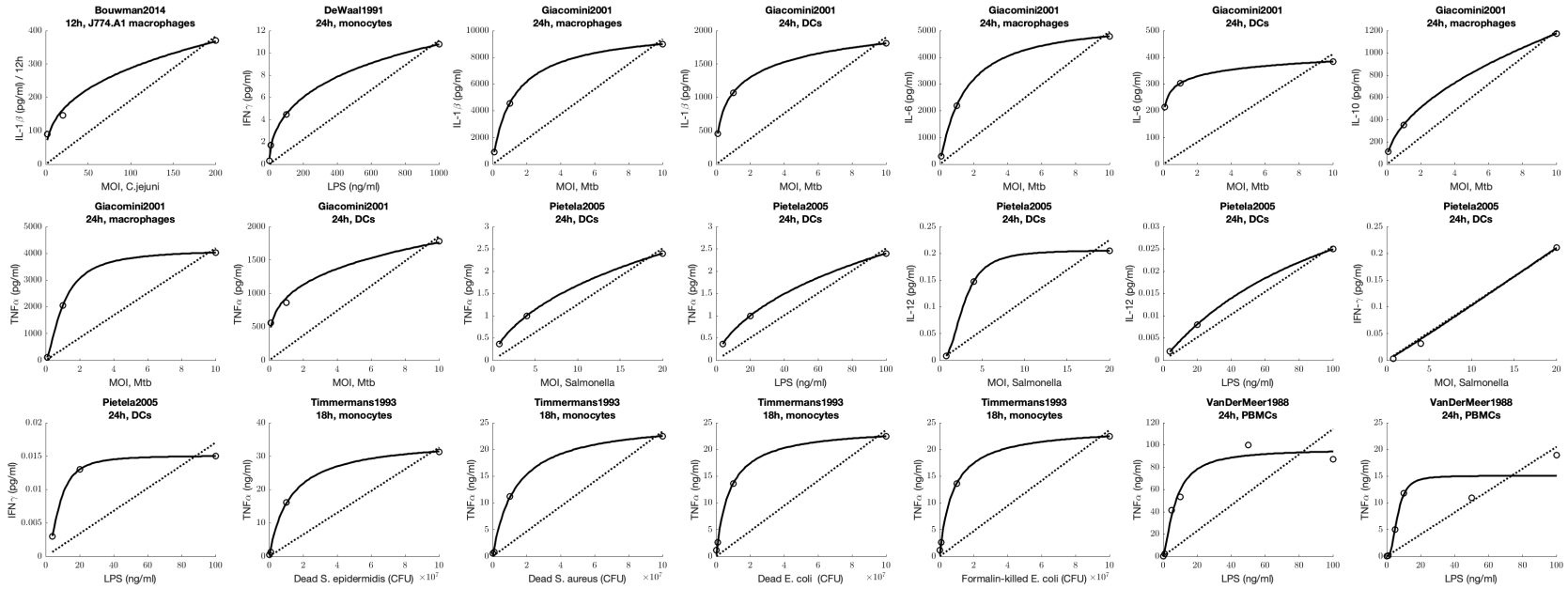


Figure 15: Sources in the literature indicate that the production rate saturates for increasing bacterial load. Cytokine concentration versus multiplicity of infection (MOI) or concentration of the bacterial cell-wall component LPS, a well-known inducer of cytokine production, at various time points. We show non-linear least squares fits to the data using linear (dashed lines, no saturation) and Hill kinetics (solid lines, saturation for an increasing bacterial load). All values were taken from the literature [7, 45, 119, 272, 334, 344]. We used Fiji to extract values from the figures in these references.

In order to determine the dependence of cytokine production on bacterial load, we fit a curve of the form

$$w_{l,i}(t) = \frac{a_{l,i}(t-1)^{n_l}}{b_l + (t-1)^{n_l}}, \qquad t \geq 1 \tag{3.18}$$

to each cytokine concentration trajectory data set, for donor dependent $a_{l,i}$, and donor-dependent $b_{l,i}$ and $n_{l,i}$ (using non-linear least squares, Figure 16 **(IL10.i.2)**, dashed lines, for IL-10). Throughout this section, we included plots for IL-10 in Figure 16. Similar plots for the other cytokines IL-1β, IL-6, and TNFα can be found in Appendix A, Figure 33. The plot labelling **(l.i.1-6)** of Figures 16 and 33 has three components, where $l \in \{$IL-10, IL-1B, IL-6, TNFA$\}$ corresponds to the cytokine, $i \in \{E, F, G, H\}$ to the donor, and the numbers 1-6 to the six different types of subplot as discussed below. We will first discuss the procedure used to generate all dashed lines in the described plots. We will then discuss the procedure used to generate all solid lines.

We plot the derivative of the curve, $w'_{l,i}(t)$ against time (Figure 16 **(l.i.3)**, dashed lines). We define $t^*_{l,i}$ as the last time point where either $w'_{l,i}(t)$ or $B_i(t)$ takes on its maximum value. As the initial cytokine production rate is small, we assume that at early time points, the cytokine production rate is not yet of the form (3.17). We assume that macrophages have a certain handling time after infection before they start producing cytokines. Like the killing rate, the cytokine production rate increases over time as the bacteria are recognized. For the form of equation (3.17), we are interested in the time when cytokine production is predominantly driven by the bacterial load and will therefore only consider time points greater than $t^*_{l,i}$. We define the parametric curve $\phi_{l,i}(B_i(t))$ by

$$B_i(t) = \sigma_i e^{\left((t-1)(g_{pop}-\kappa_{pop})+\frac{\kappa_{pop}}{\tau_{pop}}\left(1-e^{((1-t)\tau_{pop})}\right)\right)}, \tag{3.19}$$

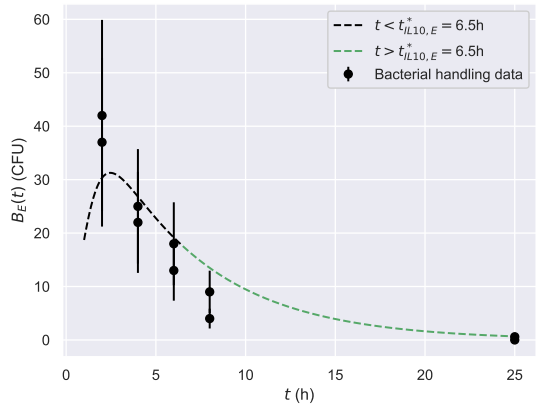
$$w'_{l,i}(t) = a_{l,i}\frac{n_l(t-1)^{n_l-1}}{b_l + (t-1)^{n_l}}\left(1 - \frac{(t-1)^{n_l}}{b_l + (t-1)^{n_l}}\right), \tag{3.20}$$

for $t > t^*_{l,i}$, where $B_i(t)$ is the solution of equation (3.13) with $B_i(t = 1\text{h}) = \sigma_i$, and $w'_{l,i}(t)$ is the derivative of equation (3.18). We plot this curve $\phi_{l,i}(B_i(t))$, i.e. we plot the fitted cytokine production rate $w'_{l,i}(t)$, against the bacterial load $B_i(t)$ as a parametric function of $t > t^*_{l,i}$ (Figure 16, **(l.i.4)**, green dashed lines). We recall that we have set $g_{pop} = 1.0$ as before, and further used the previously estimated values for σ_i, κ_{pop}, and τ_{pop} (obtained

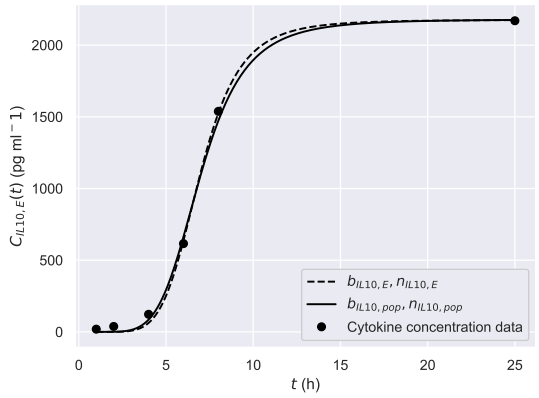
via minimization of the log-likelihood, Figure 7, solid lines). We estimate the parameters of equation (3.17), with donor dependent $p_{l,i}, q_{l,i}$ and $h_{l,i}$, by a non-linear least squares fit to this curve $\phi_{l,i}(B_i(t))$ (green, dashed), both for $q_{l,i} = 1$ and for $q_{l,i} \neq 1$ (Figure 16, **(l.i.4)**, orange and yellow dashed lines). Using the estimated parameter set, we then plot (3.14) against time (Figure 16, **(l.i.5)**, orange and yellow dashed lines). We modify equation (3.17), by introducing an additional parameter z_l, to incorporate the initial low production of cytokines:

$$\hat{f}_{l,i}(B_i, t) = (1 - e^{-z_l(t-1)}) f_{l,i}(B_i) = (1 - e^{-z_l(t-1)}) p_{l,i} \frac{(B_i)^{q_l}}{(h_l)^{q_l} + (B_i)^{q_l}}. \tag{3.21}$$

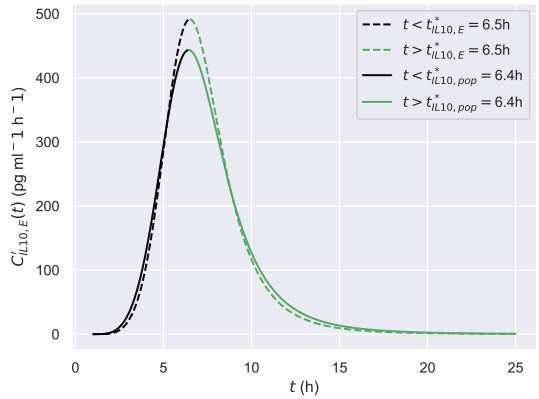
We estimate the value of $z_{l,i}$ while keeping all other parameters fixed, to obtain our final cytokine trajectory simulations (Figure 16, **(l.i.6)**, orange and yellow dashed lines). We do not vary any other parameter than $z_{l,i}$ by the time equation (3.21) is subject to fitting, as we are interested in the quality of our cytokine trajectory simulations, given the best fit of the cytokine production function $f_{l,i}$ to $\phi_{l,i}$, describing the dependence of the cytokine production rate on the bacterial load. The multiplication with $(1 - e^{-z_l(t-1)})$ incorporates the observation that there is an initial lag in cytokine production from the moment of infection.



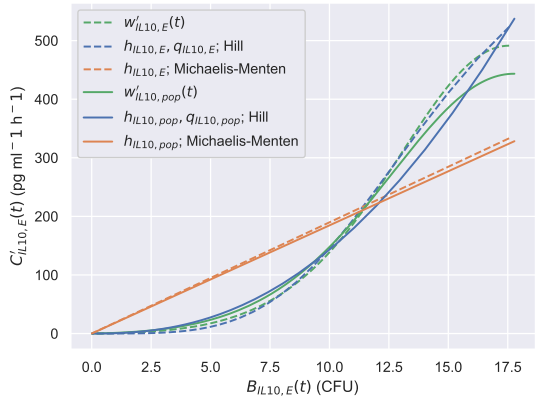
(IL10.E.1)



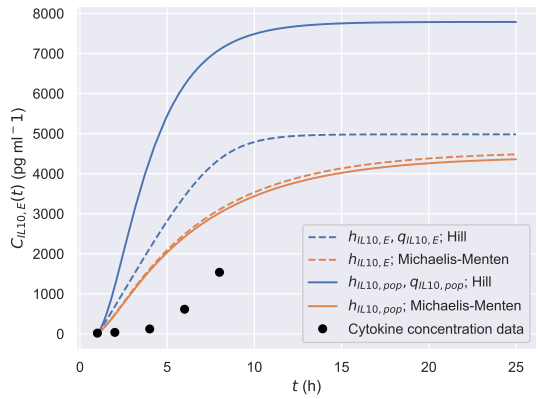
(IL10.E.2)



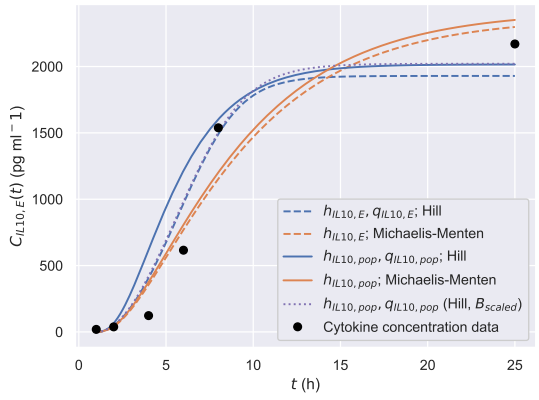
(IL10.E.3)



(IL10.E.4)

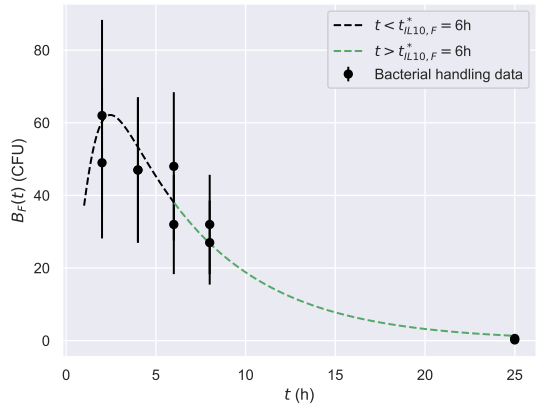


(IL10.E.5))

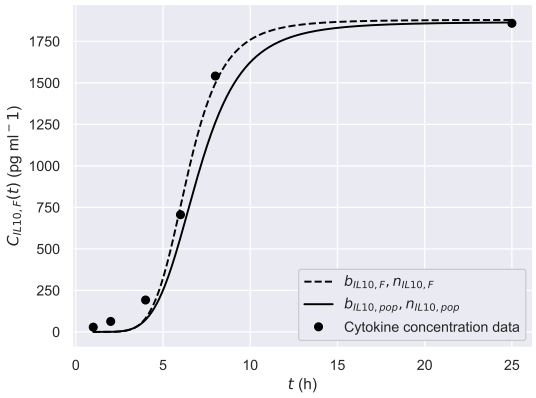


(IL10.E.6)

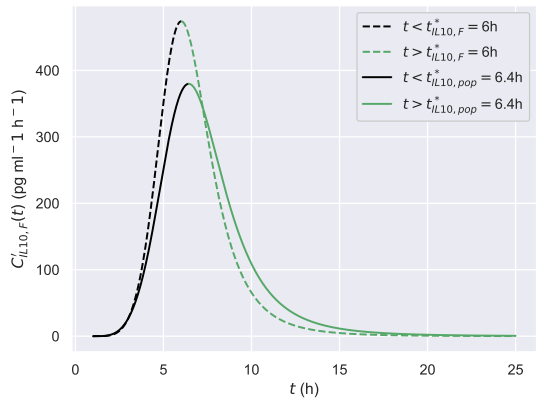
Figure 16: **(IL10.E.1-6)** Experimental data (black dots) and model simulations for IL-10 and Donor E. (Figure and legend continued on next page).



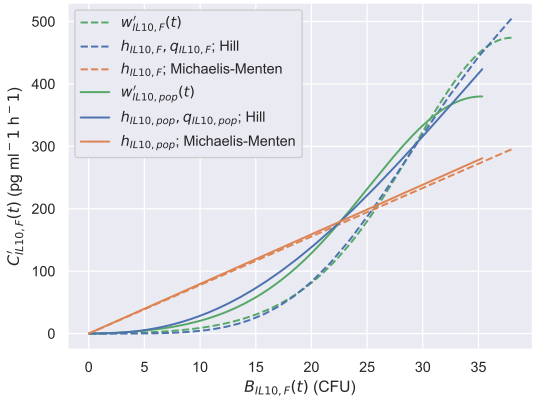
(IL10.F.1)



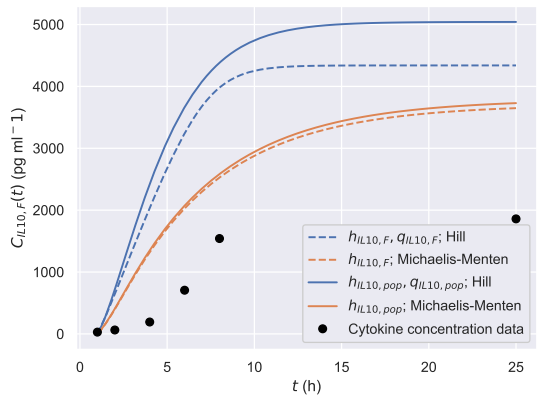
(IL10.F.2)



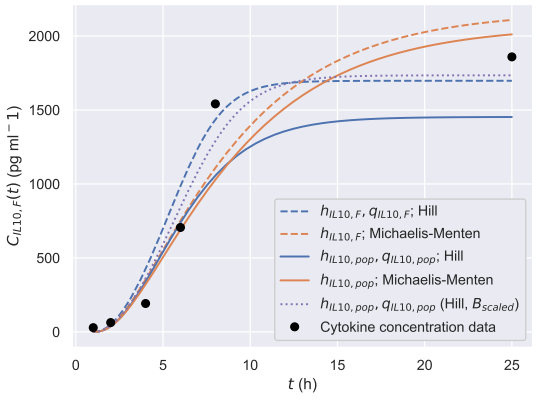
IL10.F.3)



(IL10.F.4)

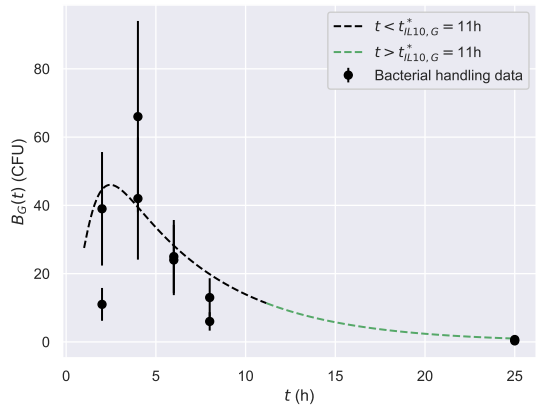


(IL10.F.5)

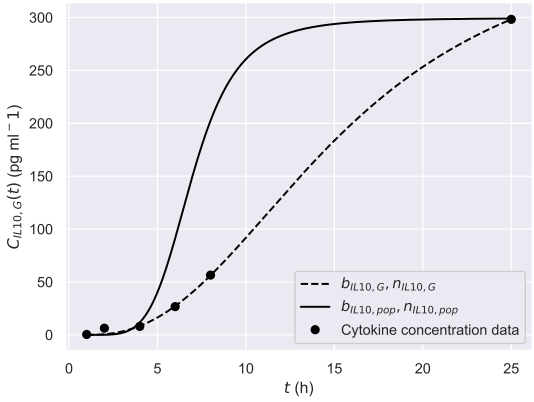


(IL10.F.6)

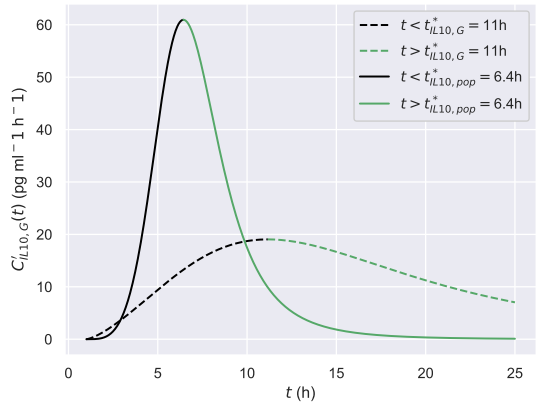
Figure 16: **(IL10.F.1-6)** Experimental data (black dots) and model simulations for IL-10 and Donor F. (Figure and legend continued on next page).



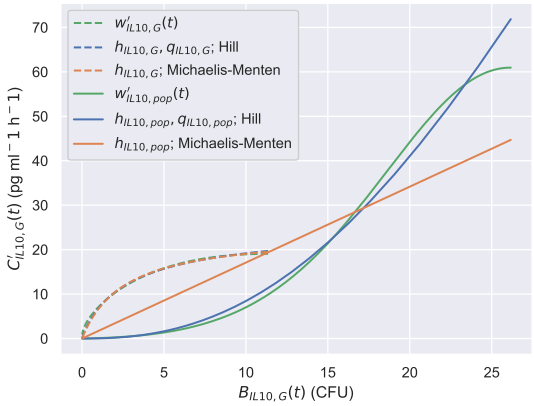
(IL10.G.1)



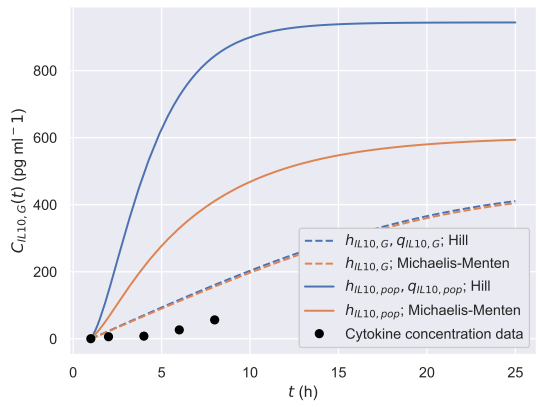
(IL10.G.2)



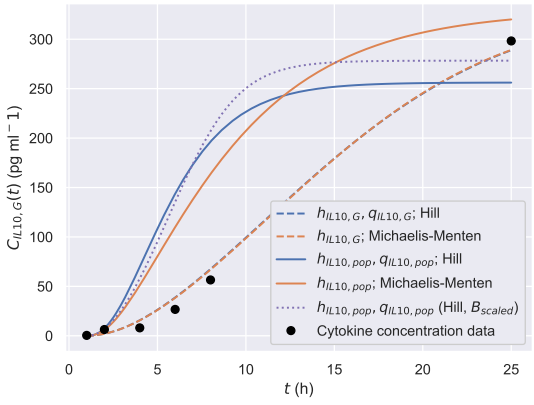
(IL10.G.3)



(IL10.G.4)

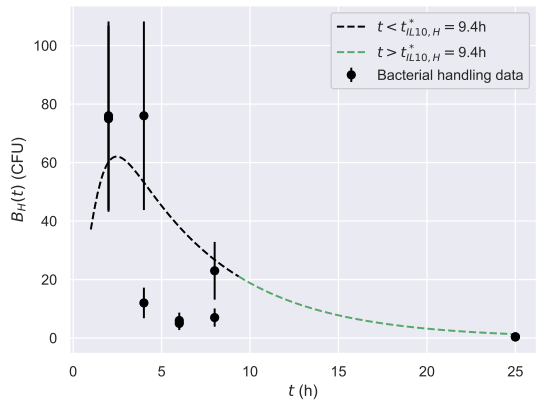


(IL10.G.5)

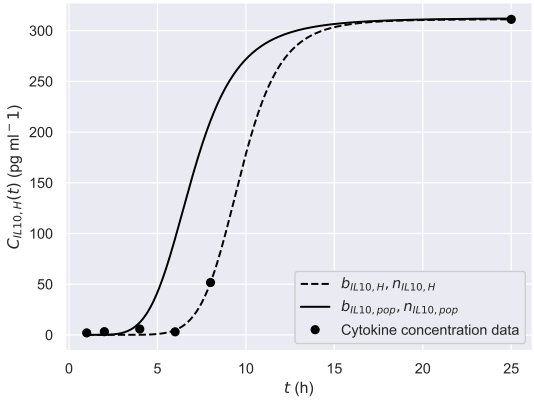


(IL10.G.6)

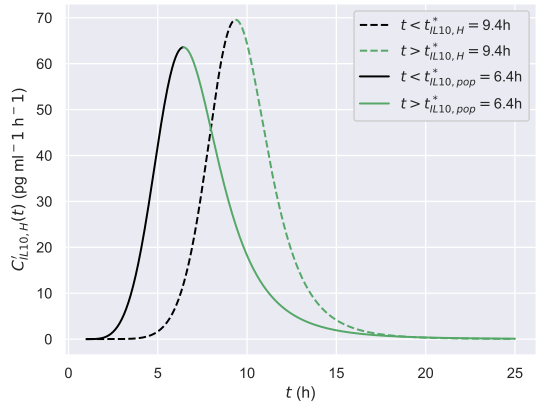
Figure 16: **(IL10.G.1-6)** Experimental data (black dots) and model simulations for IL-10 and Donor G. (Figure and legend continued on next page).



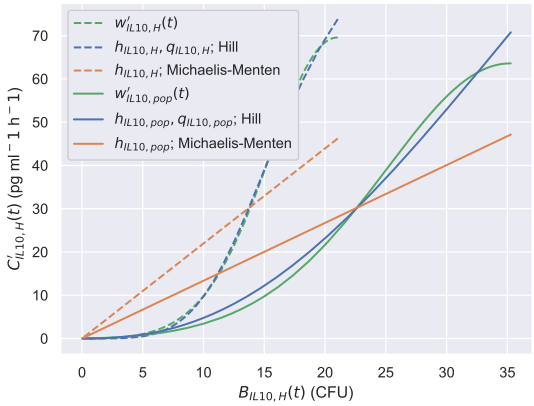
(IL10.H.1)



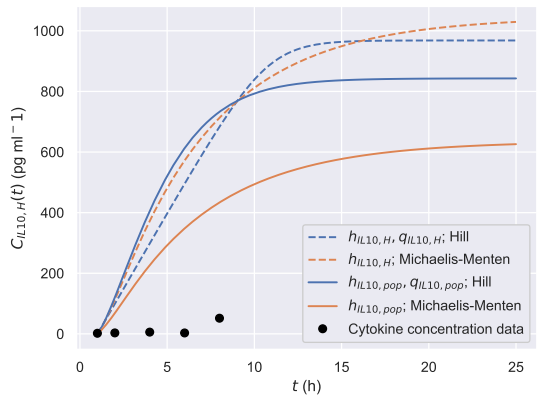
(IL10.H.2)



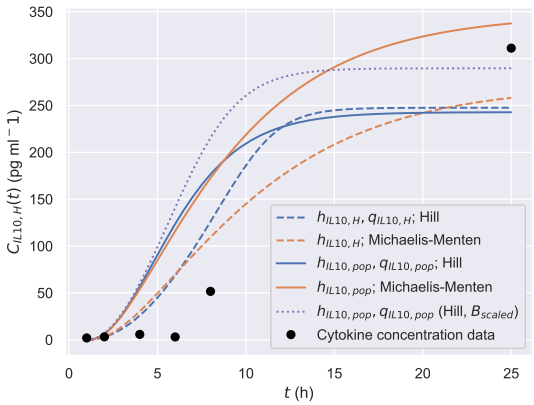
(IL10.H.3)



(IL10.H.4)



(IL10.H.5)



(IL10.H.6)

Figure 16: **(IL10.H.1-6)** Experimental data (black dots) and model simulations for IL-10 and Donor H. (Legend continued on next page).

Figure 16: Experimental data (black dots) and model simulations for IL-10 and MOI=10 (see Figure 33 for similar plots for the other cytokines IL-1B, IL-6, and TNFα) . Each subplot label **(I.i.1)** has three components, where $l \in$ {IL-10, IL-1B, IL-6, TNFA} corresponds to the cytokine, $i \in \{E, F, G, H\}$ to the donor, and the numbers 1-6 to the six different types of subplot as discussed below. **(IL-10.i.1)** Simulations of the bacterial load B_i (equation (3.13)) over time, with $g_{pop} = 1$ as before, and best fit parameters σ_i, τ_{pop}, and κ_{pop} (estimated by minimizing the negative log likelihood, see equation (3.2)). **(IL-10.i.2)** The curve $w_{l,i}(t) = \frac{a_{l,i}(t-1)^{n_{l,i}}}{b_{l,i}+(t-1)^{n_{l,i}}}$ (equation (3.18)) fitted to the cytokine concentration data (using non-linear least squares), and **(IL-10.i.3)** the derivative of $w_{l,i}(t)$, with donor-dependent (dashed lines), and independent (solid lines) values for $b_{l,i/pop}$ and $n_{l,i/pop}$, and $a_{l,i}$ always donor dependent. **(IL-10.i.4)** The parametric curve $\phi_{l,i}(B_i(t))$, i.e. $w'_{l,i}(t)$ against $B_i(t)$ (equations (3.19) and (3.20)), for $t > t^*_{l,i/pop}$, where $t^*_{l,i/pop}$ is defined as the latest time point where either $B_i(t)$ or $w'_{l,i}(t)$ takes on its maximum value, with donor-dependent (green, dashed lines), and independent (green, solid lines) values for $b_{l,i/pop}$, $n_{l,i/pop}$, and $t^*_{l,i/pop}$, and $a_{l,i}$ always donor dependent. The cytokine production rate $f_{l,i}(B_i) = p_{l,i}\frac{(B_i)^{q_l}}{(h_l)^{q_l}+(B_i)^{q_l}}$ (equation (3.17)) fitted to $\phi_{l,i}(B_i(t))$, both for $q_{l,i/pop} = 1$ (orange, a Michaelis-Menten type production rate) and for $q_{l,i/pop} \neq 1$ (blue, a Hill-type production rate), and both with donor-dependent (dashed lines), and independent (solid lines) values for $b_{l,i/pop}$, $n_{l,i/pop}$, $t^*_{l,i/pop}$, $h_{l,i/pop}$, and $q_{l,i/pop}$, and with σ_i, $a_{l,i}$, $p_{l,i}$, $g_{pop}, \tau_{pop}, \kappa_{pop}$ always donor (in)dependent (using non-linear least squares, while fixing the previously estimated parameters used to generate the simulations of $\phi_{l,i}(B_i(t))$). **(IL-10.i.5)** The cytokine concentration over time, with the cytokine production rate described by $f_{l,i}(B_i)$, and **(IL-10.i.6)** with the cytokine production rate described by $\hat{f}_{l,i}(B_i, t) = (1 - e^{-z_l(t-1)})f_{l,i}(B_i)$ (equation (3.21)), both for $q_{l,i/pop} = 1$ (orange, a Michaelis-Menten type production rate) and for $q_{l,i/pop} \neq 1$ (blue, a Hill-type production rate), and both with donor-dependent (dashed lines), and independent (solid lines) values for $b_{l,i/pop}$, $n_{l,i/pop}$, $t^*_{l,i/pop}$, $h_{l,i/pop}$, $q_{l,i/pop}$ and $z_{l,i/pop}$, and with σ_i, $a_{l,i}$, $p_{l,i}$, $g_{pop}, \tau_{pop}, \kappa_{pop}$ always donor (in)dependent. The values of $z_{l,i/pop}$ were estimated by fitting $\hat{f}_{l,i}(B_i, t)$ to the cytokine concentration data using non-linear least squares, while assuming all previously estimated parameters were fixed. The cytokine concentration over time, with the cytokine production rate described by $\hat{f}_{l,i}(B_{scaled})$ (equation (3.23)), for $q_{l,pop} \neq 1$, with donor-independent values for $b_{l,pop}$, $n_{l,pop}$, $t^*_{l,pop}$, $h_{l,pop}$, $q_{l,pop}$, $z_{l,pop}$, g_{pop}, τ_{pop}, and κ_{pop}, and with donor dependent $a_{l,i}$ and $p_{l,i}$ (dotted, purple line). As before, the values of $a_{l,i}$, $b_{l,pop}$, and $n_{l,pop}$ were estimated by fitting $w_{l,i}(t)$ to the cytokine concentration data using non-linear least squares. The values of $p_{l,i}$, $h_{l,pop}$, and $q_{l,pop}$ were estimated by fitting $f_{l,i}(B_i)$ to $\phi_{l,i}(B_i(t))$ using non-linear least squares. Legend continued on next page.

Figure 16: Continued legend. Finally, the values of $z_{l,i/pop}$, with the subscript i/pop referring either to the Donor i parameter or the population parameter, were estimated by fitting $\hat{f}_{l,i}(B_i, t)$ to the cytokine concentration data using non-linear least squares, while assuming all previously estimated parameters were fixed.

We are interested in the shape of the parametric curve $\phi_{l,i}(B_i(t))$, defined by equations (3.19) and (3.20). When the shape of the curve of $\phi_{l,i}(B_i)$ is sigmoid and not hyperbolic, the cytokine production rate (3.17) as a function of the bacterial load B_i should be described by Hill kinetics and not Michaelis-Menten kinetics. We assume $g_{pop} = 1\,\mathrm{h}^{-1}$ as before. The shape of $\phi_{l,i}(B_i)$ depends on parameters $\kappa_{pop}, \tau_{pop}, b_l$ and n_l. Varying σ_{pop} or $a_{l,i}$ only scales the curve $\phi_{l,i}(B_i)$, but has no effect on its shape (see equations (3.19) and (3.20)). We vary τ_{pop}, while adjusting κ_{pop} in such a way that the number of bacteria at $t = 25$h p.i. stays constant, in order to investigate what effect the shape of the bacterial load curve has on the shape of $\phi_{l,i}(B_i)$. We also varied n_l and adjusted b_l in such a way that $w'_{l,i}(t)$ takes on its maximum value at $t = 11$h (Figure 17, top to bottom). These plots show that the shape of $\phi_{l,i}(B_i)$ is primarily dependent on the saturation level of $w_{l,i}(t)$ at late time points. When the slope of $w_{l,i}(t)$ at late time points is nearly 0, (Figure 17, bottom row), $\phi_{l,i}(B_i)$ is sigmoid-shaped. These observations are not dependent on the value of $t^*_{l,i}$ (not shown).

We observe that the slope of $w_{l,i}(t)$ at late time points can be highly sensitive to the alteration of a single data point. Compare for instance the shape of $w_{\text{IL-10,G}}(t)$ for IL-10, donor G, with the other three donors (in Figure 16 **(IL10.i.2)**, dashed lines). The concentration for IL-10 at $t = 8$h p.i. is much lower for donor G than for the other donors, resulting in a differently shaped $w_{\text{IL-10},i}(t)$ and $\phi_{\text{IL-10},i}(B_i)$. In order to smooth out the effects of single data points, we have repeated the above parameter estimation procedure, but estimated $b_{l,pop}$, $n_{l,pop}$, $t^*_{l,pop}$, $h_{l,pop}$, $q_{l,pop}$ and $z_{l,pop}$ on the population level, while keeping σ_i, $a_{l,i}$, and $p_{l,i}$ donor-dependent and g_{pop}, κ_{pop} and τ_{pop} donor independent (Figure 16, solid lines).

We observe that the Hill and Michaelis-Menten curves visually produce quite similar fits (Figure 16, **(IL10.i.6)**). However, when we compare the fit of the two curves (Hill in blue, Michaelis-Menten in orange) to $\phi_{l,i}(B_i(t))$ (in green), the additional parameter of the Hill

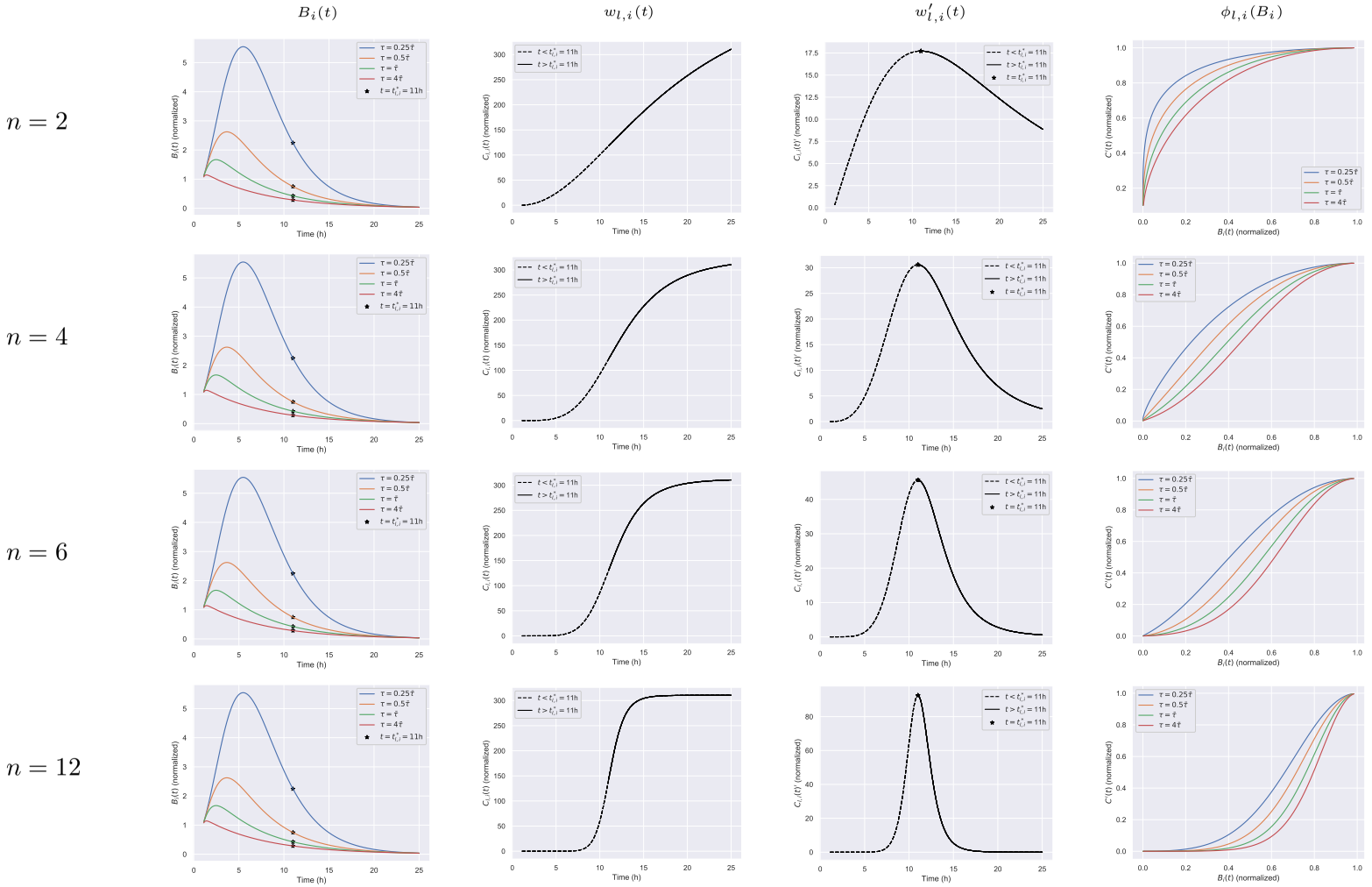


Figure 17: Exploration of the dependence of the shape of the parametric curve $\phi_{l,i}(B_i)$ on parameters $\kappa_{pop}, \tau_{pop}, b_{l,i}$ and $n_{l,i}$ (equations(3.19) and (3.20)). Parameter values initially used are $\sigma_i = 1$ CFU, $\kappa_{pop} = 1.2\,\mathrm{h}^{-1}$, $\tau_{pop} = 1.3\,\mathrm{h}^{-1}$, $a_{l,i} = 1$, $b_{l,i} = 9.7 \times 10^5$ and $n_{l,i} = 7.6$. We then vary the value of τ_{pop}, while adjusting the value of κ_{pop} in such a way that the number of bacteria at $t = 25$h post infection stays constant, in order to investigate what effect the shape of the bacterial load curve has on the shape of $\phi_{l,i}(B_i)$. We have taken τ_{pop} to be 0.25 (blue), 0.5 (yellow), 1 (green) or 4 (red) times its original value $\tau_{pop} = \bar{\tau}_{pop} = 1.3\,\mathrm{h}^{-1}$. We also varied $n_{l,i}$ and adjusted $b_{l,i}$ in such a way that the value of $t^*_{l,i} = 11$h stayed constant (top to bottom).

curve (in blue) clearly allows for a closer approximation of $\phi_{l,i}(B_i(t))$ (in green) (Figure 16, **(IL10.i.4)**). We will therefore assume Hill dynamics for the remainder of this chapter.

Finally, we introduce a normalised form of the bacterial load: $B_{scaled}(t = 1\text{h}) = 0.1, 0.5, 1, 2$ for an MOI of 1, 5, 10 or 20 respectively, such that $B_i(t) = \sigma_i B_{scaled}(t)$ (equation (3.13)). We recall that we defined $B_i(t = 1\text{h}) = \sigma_i$ as the initial bacterial load at $t = 1$h post infection (p.i.) for donor i with MOI 10. We re-estimate the values of the donor independent $b_{l,pop}$, $n_{l,pop}$, $t^*_{l,pop}$, $h_{l,pop}$, $q_{l,pop}$ and $z_{l,pop}$, and donor dependent $a_{l,i}$ and $p_{l,i}$, where $l \in \{\text{IL-10, IL-1B, IL-6, TNFA}\}$ corresponds to the cytokine and $i \in \{E, F, G, H\}$ to the donor as before (Figure 16, **(IL10.i.6)** dotted purple lines). We will refer to this set of estimated parameter values with a tilde (~). Briefly, to obtain these parameter values, we have set $g_{pop} = 1.0$ as before, and further used the previously estimated values for σ_i, κ_{pop}, and τ_{pop} to simulate B_{scaled} (obtained via minimization of the log-likelihood, Figure 7, solid lines). The values of $a_{l,i}$, $b_{l,pop}$, and $n_{l,pop}$ were estimated by fitting $w_{l,i}(t)$ to the cytokine concentration data using non-linear least squares. The values of $p_{l,i}$, $h_{l,pop}$, and $q_{l,pop}$ were then estimated by fitting $f_{l,i}(B_i)$ to $\phi_{l,i}(B_i(t))$ using non-linear least squares. Finally, the values of $z_{l,i/pop}$ were estimated by fitting $\hat{f}_{l,i}(B_i, t)$ to the cytokine concentration data using non-linear least squares, while assuming all previously estimated parameters were fixed. Normalised bacterial load data is commonly found in the literature and the normalisation of B_i does not have a large impact on our simulations (Figure 16 **(IL10.i.6)**, compare solid blue and dotted purple lines). We define an averaged form for the cytokine concentration, by replacing the donor dependent maximum production rate $p_{l,i}$ by an averaged maximum production rate $p_{l,avg}$, with value $\tilde{p}_{l,avg} = \frac{1}{N}\sum_i \tilde{p}_{l,i}$, with $N = 4$ the number of donors. Our model equations are then given by:

$$\frac{\mathrm{d}B_{scaled}}{\mathrm{d}t} = g_{pop}B_{scaled} - \kappa_{pop}(1 - e^{-\tau_{pop}(t-1)})B_{scaled}, \tag{3.22}$$

$$\frac{\mathrm{d}C_{l,avg}}{\mathrm{d}t} = p_{l,avg}(1 - e^{-z_{l,pop}(t-1)})\frac{(B_{scaled})^{q_{l,pop}}}{(h_{l,pop})^{q_{l,pop}} + (B_{scaled})^{q_{l,pop}}}, \tag{3.23}$$

with $t \geq 1$h post infection, $B_{scaled}(t = 1\text{h}) = 0.1, 0.5, 1, 2$ for an MOI of 1, 5, 10 or 20

respectively, and $C_{l,avg}(t = 1\text{h}) = 0\,\text{pg}\,\text{ml}^{-1}$, for cytokine l. Solving equation (3.22) gives:

$$B_{scaled}(t) = B_{scaled}(t = 1\text{h}) e^{\left((t-1)(g_{pop}-\kappa_{pop})+\frac{\kappa_{pop}}{\tau_{pop}}\left(1-e^{((1-t)\tau_{pop})}\right)\right)}, \tag{3.24}$$

$$C_{l,avg}(t) = p_{l,avg} \int_0^t (1 - e^{-z_{l,pop}(t-1)}) \frac{(B_{scaled})^{q_{l,pop}}}{(h_{l,pop})^{q_{l,pop}} + (B_{scaled})^{q_{l,pop}}} dt, \tag{3.25}$$

for $t \geq 1\text{h}$. We have listed all parameter values that we estimated (referred to with a tilde) that are needed to simulate the donor independent bacterial load B_{scaled} and averaged cytokine concentrations $C_{l,avg}(t)$ over time in Table 3.2. Note that the parameter p_l only scales the cytokine concentration. We will use the obtained parameter values from Table 3.2 and equations (3.22) and (3.23) to explore the dependency of cytokine production on bacterial load in later sections.

3.3.6 Macrophage viability

When a macrophage dies during the gentamicin protection assay, the gentamicin will kill any intracellular bacteria present in the macrophage. The low numbers of intracellular bacteria observed at 25h after infection could therefore in theory be explained by the existence of a large population of dead macrophages. Moreover, *Salmonella*-induced cell death can result in the release of pro-inflammatory cytokines such as IL-1β and IL-18 [128]. In our model equations (3.22) and (3.23), we ignored the cell-death dependent reduction of bacterial load and increase of cytokine release. In order to confirm the underlying hypothesis that most macrophages were still alive 25h after infection, we performed a viability assay by flow cytometry (Figure 18). We compared uninfected macrophages with infected macrophages, and have included macrophages killed in a hot water bath as a positive control. We only observed a small decrease in the percentage of viable cells justifying why the effects of cell death on our system have been neglected.

3.3.7 Handling defects versus hyper-inflammation

In this section, we will investigate whether the introduction of an impairment in bacterial handling in our model framework (equations (3.22) and (3.23)) can drive a state of cytokine hyper-production, even in the presence of an impairment of cytokine production capability. We will use the estimated, donor-independent set of parameter values $\tilde{\boldsymbol{\Xi}}$ introduced in

Parameter	Description	Value
$\tilde{g}_{pop}$	bacterial growth rate	$1.0\,\mathrm{h}^{-1}$
$\tilde{\kappa}_{pop}$	maximal bacterial killing rate	$1.2\,\mathrm{h}^{-1}$
$\tilde{\tau}_{pop}$	scaling of killing rate at early time points	$1.3\,\mathrm{h}^{-1}$
$\tilde{p}_{\mathrm{IL-10},avg}$	averaged maximal production rate for IL-10	$3.81 \times 10^2\,\mathrm{pg\,ml}^{-1}\,\mathrm{h}^{-1}$
$\tilde{h}_{\mathrm{IL\text{-}10},pop}$	saturation constant for IL-10	0.78
$\tilde{q}_{\mathrm{IL\text{-}10},pop}$	Hill coefficient for IL-10	3.4
$\tilde{z}_{\mathrm{IL\text{-}10},pop}$	scaling of IL-10 production rate at early time points	0.17
$\tilde{p}_{\mathrm{IL-1}\beta,avg}$	averaged maximal production rate for IL-1β	$1.5 \times 10^3\,\mathrm{pg\,ml}^{-1}\,\mathrm{h}^{-1}$
$\tilde{h}_{\mathrm{IL\text{-}1}\beta,pop}$	saturation constant for IL-1β	2.0×10^8
$\tilde{q}_{\mathrm{IL\text{-}1}\beta,pop}$	Hill coefficient for IL-1β	0.19
$\tilde{z}_{\mathrm{IL\text{-}1}\beta,pop}$	scaling of IL-1β production rate at early time points	30
$\tilde{p}_{\mathrm{IL-6},avg}$	averaged maximal production rate for IL-6	$5.9 \times 10^3\,\mathrm{pg\,ml}^{-1}\,\mathrm{h}^{-1}$
$\tilde{h}_{\mathrm{IL\text{-}6},pop}$	saturation constant for IL-6	0.74
$\tilde{q}_{\mathrm{IL\text{-}6},pop}$	Hill coefficient for IL-6	6.2
$\tilde{z}_{\mathrm{IL\text{-}6},pop}$	scaling of IL-6 production rate at early time points	0.10
$\tilde{p}_{\mathrm{TNF}\alpha,avg}$	averaged maximal production rate for TNFα	$2 \times 10^6\,\mathrm{pg\,ml}^{-1}\,\mathrm{h}^{-1}$
$\tilde{h}_{\mathrm{TNF}\alpha,pop}$	saturation constant for TNFα	43
$\tilde{q}_{\mathrm{TNF}\alpha,pop}$	Hill coefficient for TNFα	2.4
$\tilde{z}_{\mathrm{TNF}\alpha,pop}$	scaling of TNFα production rate at early time points	30

Table 3.2: The estimated, donor-independent set of parameter values $\tilde{\boldsymbol{\Xi}}$, that can be used to simulate equations (3.22) and (3.23). We assume $g_{pop} = 1.0$ as before (3.3.1). The values of the other parameters used in the normalized bacterial handling equation $\frac{\mathrm{d}B_{scaled}}{\mathrm{d}t} = g_{pop}B_{scaled} - \kappa_{pop}(1 - e^{-\tau_{pop}(t-1)})B_{scaled}$ were estimated, with $B(t = 1\mathrm{h}) = 0.1, 0.5, 1, 2$ for an MOI of 1, 5, 10 or 20 respectively (equation (3.22), by minimizing the log likelihood, using data from all eight donors $i \in \{A, B, C, D, E, F, G, H\}$). Multiplying B_{scaled} with the donor dependent scaling factors σ_i, $i \in \{A, B, C, D, E, F, G, H\}$ returns donor specific values of bacterial load, i.e. $B_i = \sigma_i B_{scaled}$ (Figure 7, solid lines, and Figures 16 and 33 **(l,i,1)**). The values of $a_{l,i}$, $b_{l,pop}$, and $n_{l,pop}$ were estimated by fitting $w_{l,i}(t)$ to the cytokine concentration data using non-linear least squares. The values of $p_{l,i}$, $h_{l,pop}$, and $q_{l,pop}$ were then estimated by fitting $f_{l,i}(B_i)$ to $\phi_{l,i}(B_i(t))$ using non-linear least squares. The values of $z_{l,i/pop}$ were estimated by fitting $\hat{f}_{l,i}(B_i, t)$ to the cytokine concentration data using non-linear least squares, while assuming all previously estimated parameters were fixed. Finally, we define the averaged maximum production rate $p_{l,avg}$, with value $\tilde{p}_{l,avg} = \frac{1}{N}\sum_i \tilde{p}_{l,i}$, with $N = 4$ the number of donors. See the main text for full details on the fitting procedure. All control experimental bacterial load data and cytokine concentration presented in this chapter was used to obtained these estimates.

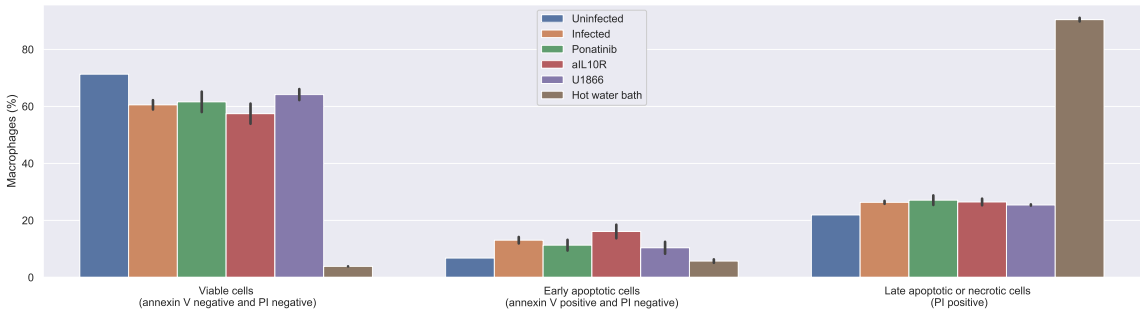


Figure 18: The percentage of live, early apoptotic, and late apoptotic/necrotic macrophages at 25h post infection (MOI=10), compared to uninfected macrophages and macrophages killed in a hot water bath. The vast majority of both infected and uninfected macrophages is still alive at this time point. The presence of an IL-10 receptor antibody, Ponatinib, and U1866 during infection do noticeably affect cell viability in this assay. Abbreviation: PI, propidium iodide.

Section 3.3.3 as our control parameter values (Table 3.2). Simulations of equations (3.22) and (3.23)) parametrised with $\tilde{\mathbf{\Xi}}$ represent the bacterial handling and cytokine concentration dynamics of healthy donors. We represent a bacterial handling defect by adjusting the value of the macrophage killing rate κ_{pop}. We assume that for our pathway of interest (i.e. the NOD2/XIAP/RIPK2 pathway), the values of both the bacterial growth rate g_{pop} and the time delay in killing τ_{pop} are unaffected. We note that for other defects, it might be appropriate to alter the values of these two parameters too. One could think for instance of a defect that delays the fusion of the *Salmonella* containing vesicle with a lysosome, which could be represented by a decrease in the value of τ_{pop} [260]. As defects in the NOD2/XIAP/RIPK2 pathway are known to impair cytokine production after stimulation of the pathogen recognition receptor NOD2, we simulate varying degrees of cytokine production impairment by varying the values of the cytokine production parameters $p_{l,avg}$ (Figure 20) [306]. We simulated our model equations (3.22)-(3.23), with parameter values taken from Table 3.2. We assume that the delay in cytokine production, as represented by $z_{l,pop}$, and the shape of the curve $\phi_{l,pop}$, as determined by $h_{l,pop}$ and $q_{l,pop}$, are not affected by the defect. We only vary $p_{l,avg}$, and not $z_{l,pop}$, $h_{l,pop}$ or $q_{l,pop}$, as we assume the cytokine production defect is driven by an impairment in pathogen recognition, resulting in an impaired cytokine secretion response. We assume the impairment in pathogen recognition does not affect the time it takes to start cytokine production (which would alter

$z_{l,pop}$), or the underlying process driving the saturation level of cytokine production (which would alter $h_{l,pop}$ and $q_{l,pop}$). We note that a combination of decreased values of κ_{pop} and $p_{l,avg}$ can result in lower levels of certain cytokines compared to control (dashed lines, using the parameters values $\tilde{\mathbf{\Xi}}$ from Table 3.2 as control) at early time points, and higher levels due to an increased bacterial load at later time points (Figure 20, cytokines IL-6, IL-10 and TNFα). Thus, our system is capable of producing a state of increased cytokine levels during infection, in the presence of an impairment of cytokine production capability. We observed that not only the levels of the pro-inflammatory cytokines, but also the level of IL-10, the most well-known anti-inflammatory cytokine, increases for an increasing bacterial load. IL-10 is essential for the down-regulation of pro-inflammatory immune responses [126, 236]. During the initial 25h post infection, we found IL-10 levels to correlate highly with the pro-inflammatory cytokines TNFα, IL-1β, and IL-23 (Figure 14). In line with this, the absolute levels of IL-10 in inflamed tissue and blood of CD patients were found to be higher than in healthy donors [25, 184]. We will therefore use the term 'hyper-production' rather than 'hyper-inflammation' to describe the state where the simulated or measured cytokine concentration is higher for a certain modulation than under control conditions.

We show the parameter regime for which we observe such a state of cytokine hyper-production for various MOI, when we simulated our model equations (3.22)-(3.23), with parameter values taken from Table 3.2 (Figure 21-23 for MOI= $1, 10, 25$ respectively). We observe that the range of parameters where the cytokine concentrations are larger than control (i.e. the area of the coloured regions in the heat maps), IL-10, and to a lesser extent IL-6 are sensitive to changes in MOI within the range examined. We further observe for IL-10 and IL-6 that bacterial load driven cytokine hyper production occurs more slowly, i.e. at a later point in time, for increasing MOI. This phenomenon can be explained by comparing the different shapes of $f_{l,scaled}(B_{scaled})$ (Figure 24). For MOI= 25, IL-1β and IL-10 and early time, the cytokine production rate is insensitive to bacterial handling defects, as it has saturated (green triangles), i.e. the amount of cytokines produced is not sensitive to a defect in killing for this level of bacterial load. Only when the bacterial load has decreased enough over time, bacterial load driven hyper-production will occur.

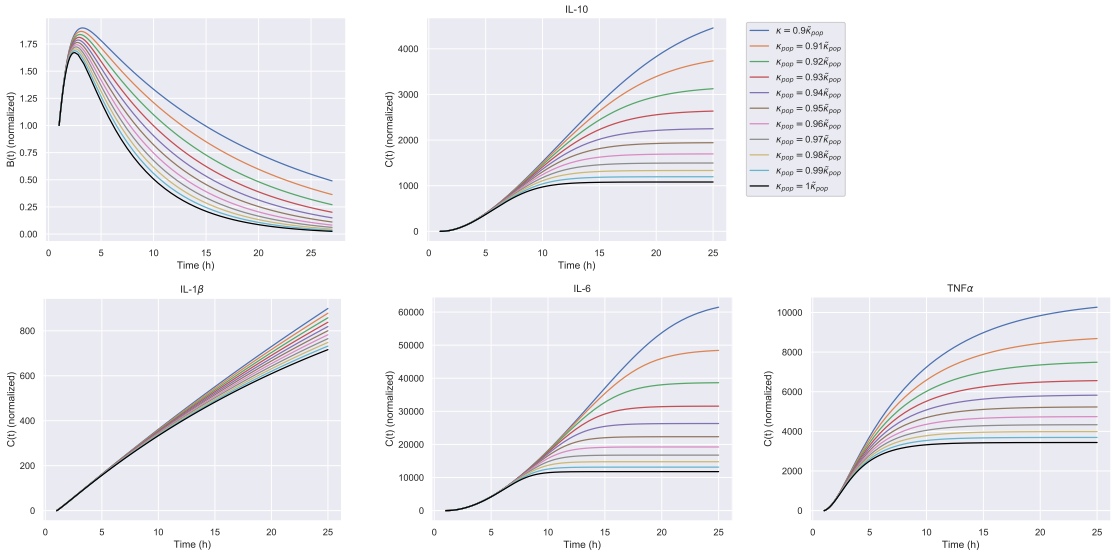


Figure 19: Exploration of the dependence of the simulated cytokine trajectories and bacterial load on the value of the killing parameter κ_{pop} (equations (3.22) and (3.23)). We have taken the estimated values obtained from our estimated, donor-independent set of parameter values $\tilde{\boldsymbol{\Xi}}$ (Table 3.2) to simulate the cytokine trajectories for MOI=10. We varied κ_{pop} by multiplying the estimated value $\tilde{\kappa}_{pop}$ by various factors between 0.9 and 1.

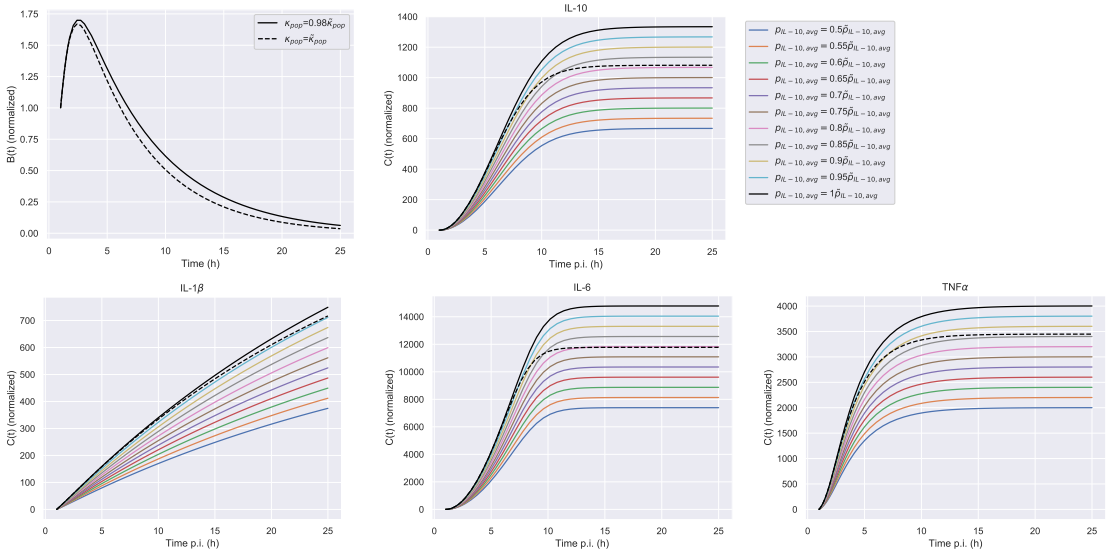


Figure 20: Exploration of the dependence of the simulated cytokine trajectories and bacterial load on the value of the cytokine production parameters $p_{l,avg}$ (equations (3.22) and (3.23)). We have taken the estimated values obtained from our estimated, donor-independent set of parameter values $\tilde{\boldsymbol{\Xi}}$ (Table 3.2) to simulate the cytokine trajectories for MOI=10 (dashed black lines), and also multiplied the estimated value $\tilde{\kappa}_{pop}$ by 0.98 to mimic a bacterial handling defect (solid black lines). We varied the overall production rate $p_{l,pop}$ for each cytokine l by multiplying $\tilde{p}_{avg}$ by various factors between 0.5 and 1, with $\kappa_{pop} = 0.98\tilde{\kappa}_{pop}$ (solid coloured lines).

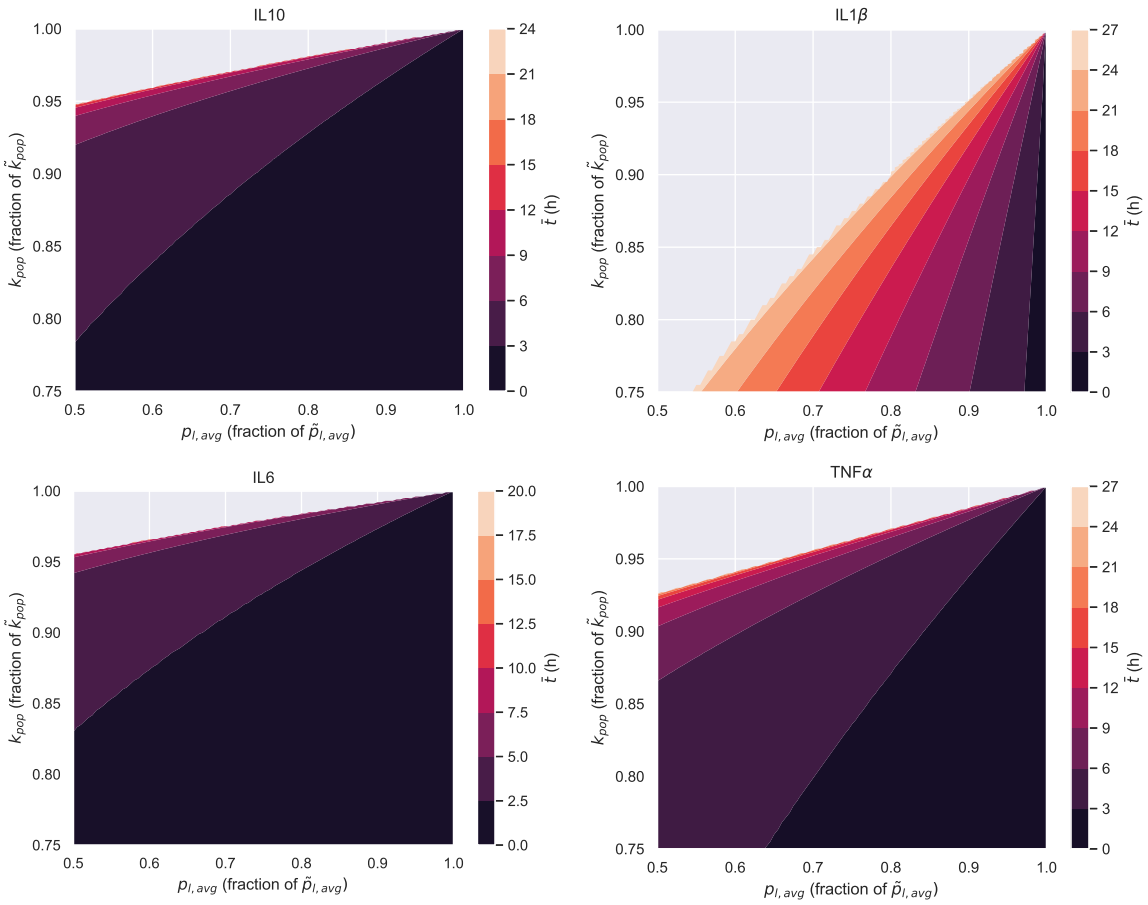


Figure 21: With MOI=1, heat maps for the value of the first instance in time $\bar{t}$ where the simulated cytokine concentration for the altered values of κ_{pop} and $p_{l,avg}$ obtains a higher value than the simulated cytokine concentration for the original values $\tilde{\kappa}_{pop}$ and $\tilde{p}_{l,avg}$ (equations (3.22) and (3.23)). No colour indicates that the simulate cytokine concentration for the altered values never reaches the level of the simulated cytokine concentration for the original values. The original values represent the healthy control data and the altered values represent bacterial handling defects. We have taken the estimated values obtained from $\tilde{\boldsymbol{\Xi}}$ (Table 3.2) to simulate the cytokine trajectories for MOI=1 (the original values). We multiplied the estimated value $\tilde{\kappa}_{pop}$ by a factor varying between 0.75 and 1, and multiplied the estimated values $\tilde{p}_{l,avg}$ by by a factor varying between 0.5 and 1 (the altered values).

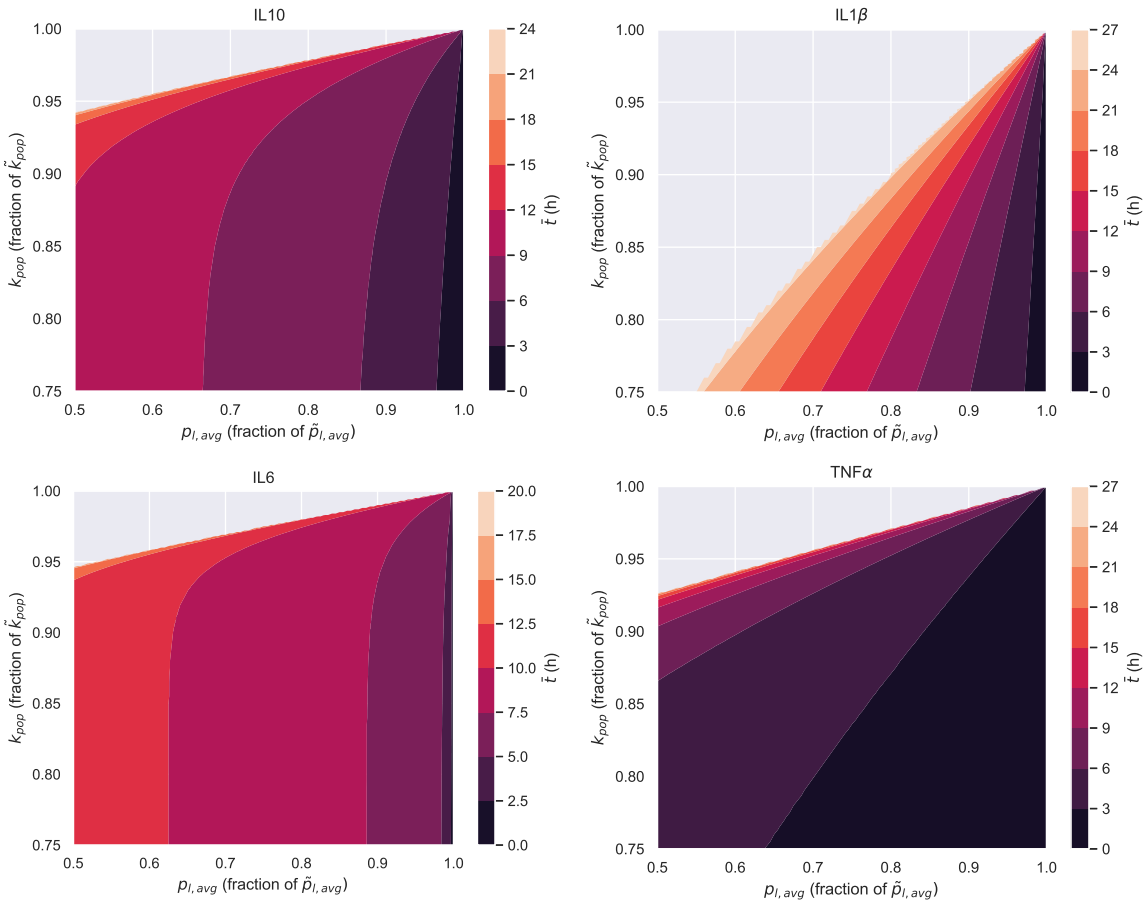


Figure 22: With MOI=10, heat maps for the value of the first instance in time $\bar{t}$ where the simulated cytokine concentration for the altered values of κ_{pop} and $p_{l,avg}$ obtains a higher value than the simulated cytokine concentration for the original values $\tilde{\kappa}_{pop}$ and $\tilde{p}_{l,avg}$ (equations (3.22) and (3.23)). No colour indicates that the simulate cytokine concentration for the altered values never reaches the level of the simulated cytokine concentration for the original values. The original values represent the healthy control data and the altered values represent bacterial handling defects. We have taken the estimated values obtained from $\tilde{\boldsymbol{\Xi}}$ (Table 3.2) to simulate the cytokine trajectories for MOI=10 (the original values). We multiplied the estimated value $\tilde{\kappa}_{pop}$ by a factor varying between 0.75 and 1, and multiplied the estimated values $\tilde{p}_{l,avg}$ by by a factor varying between 0.5 and 1 (the altered values).

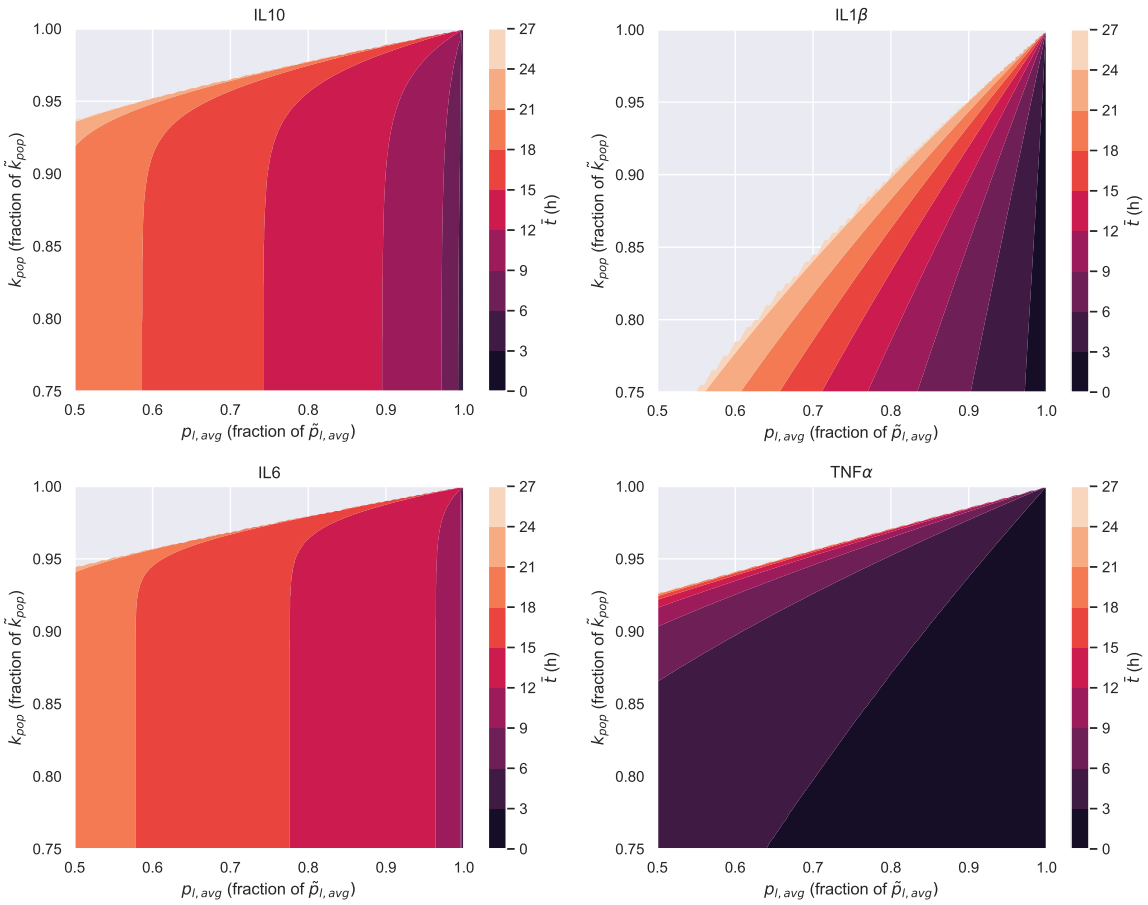


Figure 23: With MOI=25, heat maps for the value of the first instance in time $\bar{t}$ where the simulated cytokine concentration for the altered values of κ_{pop} and $p_{l,avg}$ obtains a higher value than the simulated cytokine concentration for the original values $\tilde{\kappa}_{pop}$ and $\tilde{p}_{l,avg}$ (equations (3.22) and (3.23)). No colour indicates that the simulate cytokine concentration for the altered values never reaches the level of the simulated cytokine concentration for the original values. The original values represent the healthy control data and the altered values represent bacterial handling defects. We have taken the estimated values obtained from $\tilde{\boldsymbol{\Xi}}$ (Table 3.2) to simulate the cytokine trajectories for MOI=25 (the original values). We multiplied the estimated value $\tilde{\kappa}_{pop}$ by a factor varying between 0.75 and 1, and multiplied the estimated values $\tilde{p}_{l,avg}$ by by a factor varying between 0.5 and 1 (the altered values).

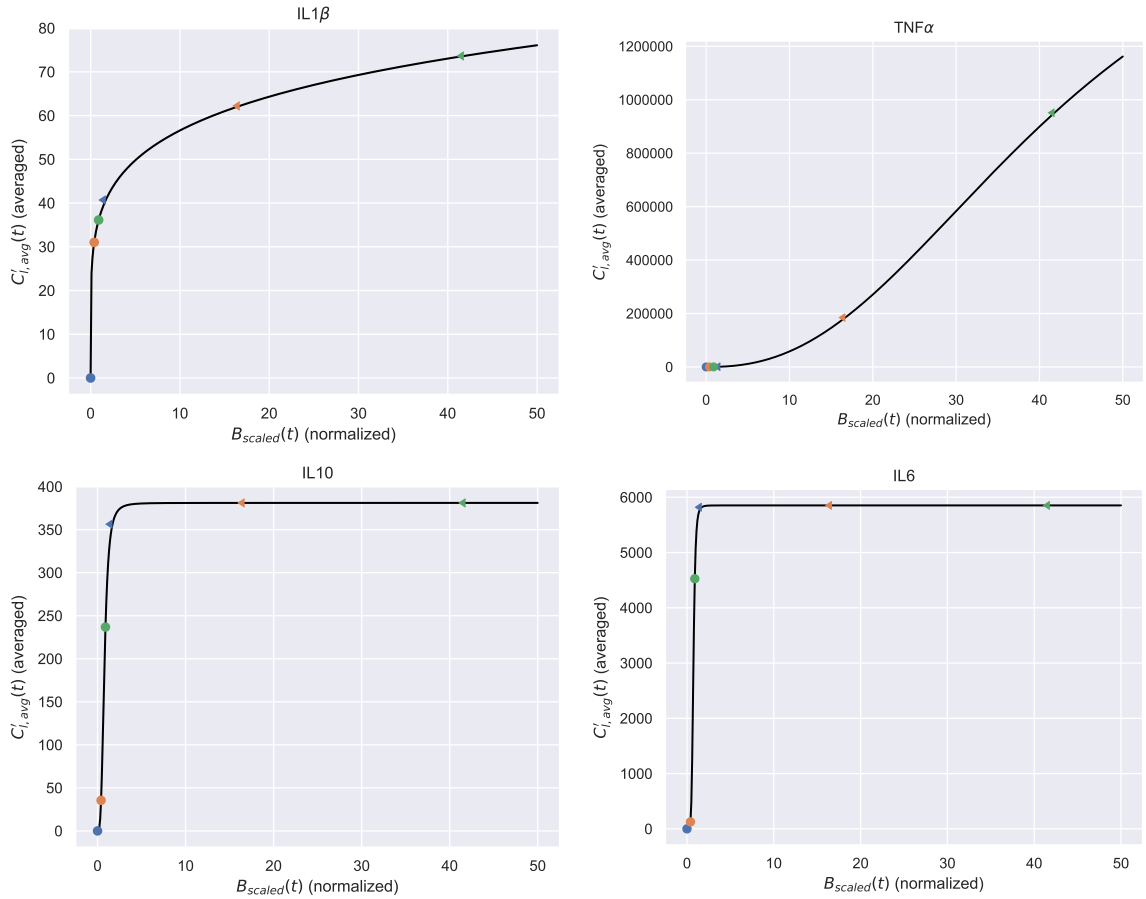


Figure 24: The Hill curves $f_l(B_{scaled}) = p_{l,avg}\frac{(B_{scaled})^{q_{l,pop}}}{(h_{l,pop})^{q_{l,pop}}+(B_{scaled})^{q_{l,pop}}}$ (equation (3.17)), with parameter values taken from $\tilde{\boldsymbol{\Xi}}$ (Table 3.2). We show the maximum (triangles) and minimum (circles) simulated scaled bacterial load from $t = 1 - 25$h for MOI= 1 (blue), 10 (yellow), and 25 (green) (using equation (3.22)).

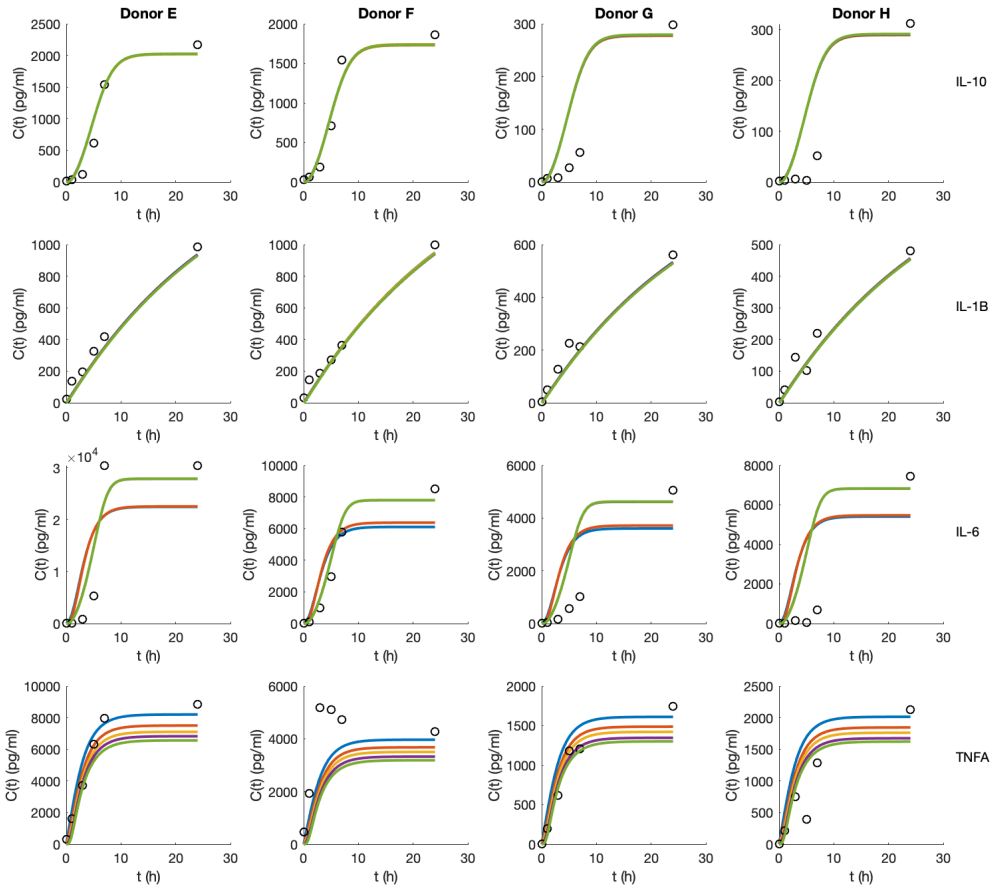


Figure 25: For $g = 0.1$ (blue), $g = 0.5$ (red), $g = 1$ (yellow), $g = 2$ (purple), or $g = 5$ (green), simulations of the cytokine concentration over time, with the cytokine production rate described by $\hat{f}_{l,i}(B_i, t) = (1 - e^{-z_l(t-1)}) f_{l,i}(B_i)$ (equation (3.21)), with donor-independent values for $b_{l,pop}$, $n_{l,pop}$, $t^*_{l,pop}$, $h_{l,pop}$, $q_{l,pop}$, $z_{l,pop}$, g_{pop}, τ_{pop}, and κ_{pop}, and with donor dependent $a_{l,i}$ and $p_{l,i}$. We note the blue, red and yellow and green curves are overlapping for IL-10 (first row) and IL-1B (second row). For IL-6 (third row) and TNFα (fourth row), separate curves can be distinguished, though the global behaviour is almost the same for two orders of magnitude of variation in g_{pop}. The values of $p_{l,i}$, $h_{l,pop}$, and $q_{l,pop}$ were estimated by fitting $f_{l,i}(B_i)$ to $\phi_{l,i}(B_i(t))$ (equation (3.17), and equations (3.19)-(3.20)) using non-linear least squares. Finally, the values of $z_{l,i/pop}$ were estimated by fitting $\hat{f}_{l,i}(B_i, t)$ to the cytokine concentration data using non-linear least squares, while assuming all previously estimated parameters were fixed. We also show the experimental cytokine concentrations data (black circles).

3.3.8 Exploration of the effects of varying the bacterial growth rate

We have studied the impact of numerous model parameters, including the kill rate κ_{pop}, when examining handling defects. Here, we also consider the growth rate g, which we have previously fixed via $g_{pop} = 1$ per hour, since the bacterial handling equation (3.1) becomes practically non-identifiable when g_{pop}, κ_{pop} and τ_{pop} are all free parameters to be learned. When we fix the value of g_{pop}, all parameters of equation (3.1) are practically identifiable (see Section 3.3.1). We now explore the effects of assuming a different value of g_{pop} on downstream inferences. We will explore $g_{pop} = 0.1, 0.5, 1, 2$ and 5. For each of these values of g_{pop}, we estimate corresponding values of σ_i, $i = \{A, B, C, D, E, F, G, H\}$, κ_{pop} and τ_{pop} by log-likelihood minimization as before (Figure 7). Because g_{pop} is practically non-identifiable, it has essentially no-impact on the quality of the fit of equation (3.1) to the bacterial handling data. We re-estimated our baseline set of model parameters (Table 3.2) following exactly the same procedure as before (See Section 3.3.3), but with $g_{pop} = 0.1, 0.5, 1, 2$ and 5. We observe that varying g_{pop} has little influence on impact on the quality of the fit to the cytokine concentration data (Figure 25). For each considered value of g_{pop}, we also show similar plots as in Figure 20, to explore the dependency of the simulated cytokine trajectories and bacterial load on the value of the cytokine production parameters $p_{l,avg}$ (Figures 26-29). In these figures, we multiplied the estimated value of κ_{pop} by 0.98 to mimic a bacterial handling defect (solid black lines). We varied the overall production rate $p_{l,pop}$ for each cytokine l by multiplying $\tilde{p}_{avg}$ by various factors between 0.5 and 1, while we set the value of κ_{pop} to 0.98 times the estimated value of κ_{pop}. We observe that the impact of setting the value of κ_{pop} to 98% of its estimated value on the bacterial load is larger for a larger value of g_{pop}. The values of κ_{pop} for $g_{pop} = 0.1, 0.5, 1, 2$ and 5 are $\kappa_{pop} = 0.28, 0.68, 1.2, 2.2$ and 5.2 respectively. The ratio between the estimated values of κ_{pop} and the value of g_{pop} becomes smaller for an increasing g_{pop} (i.e $\kappa_{pop}/g_{pop} = 2.8, 1.4, 1.2, 1.1, 1.0$ for $g_{pop} = 0.1, 0.5, 1, 2$ and 5 respectively). We recall we are interested in bacterial load-driven cytokine hyperproduction, i.e. an increased level of cytokines in the presence of a bacterial handling defect. Because the impact of setting the value of κ_{pop} to 98% of its estimated value on the bacterial load is larger for a larger value of g_{pop}, we observe that the range adjusted values of the population

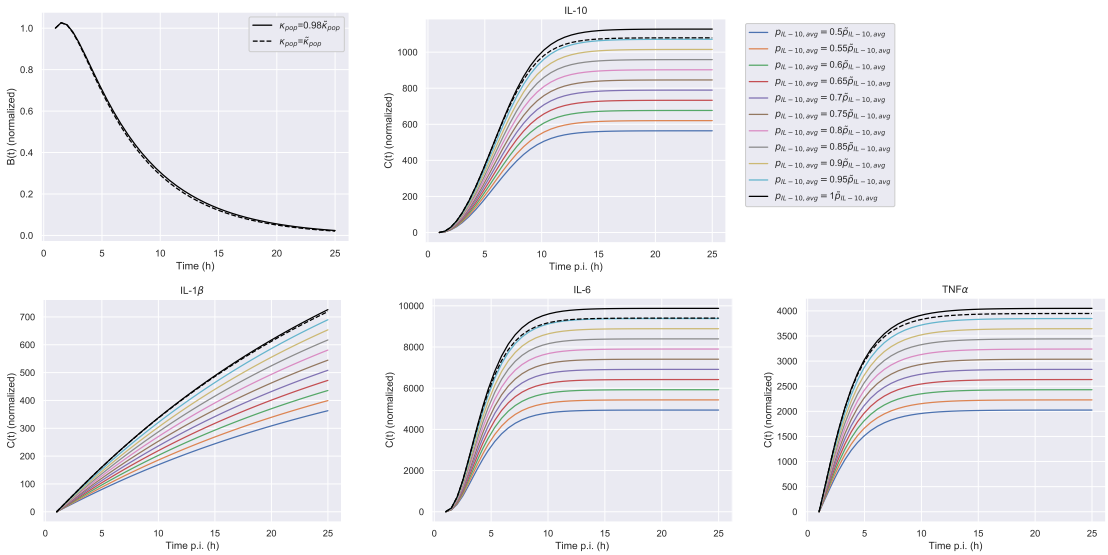


Figure 26: For $g_{pop} = 0.1$, exploration of the dependence of the simulated cytokine trajectories and bacterial load on the value of the cytokine production parameters $p_{l,avg}$ (equations (3.22) and (3.23)). We have taken the estimated values obtained as detailed in the main text (Section 3.3.8), to simulate the cytokine trajectories for MOI=10 (dashed black lines), and also multiplied the estimated value of κ_{pop} by 0.98 to mimic a bacterial handling defect (solid black lines). We varied the overall production rate $p_{l,pop}$ for each cytokine l by multiplying $\tilde{p}_{avg}$ by various factors between 0.5 and 1, while we set the value of κ_{pop} to 0.98 times the estimated value of κ_{pop} (solid coloured lines).

production rate of cytokine l, $p_{l,pop}$, for which we observe bacterial load driven cytokine hyperproduction increases for an increasing value of g_{pop}.

3.3.9 Literature comparison

The aim of this section is to estimate the size of effects of defects in the NOD2 pathway on both bacterial handling and cytokine production capability from the literature. We have set up an *in silico* model system (equations (3.22) and (3.23)) that is capable of displaying bacterial handling defect-driven hyper-production of cytokines for certain values of κ_{pop} and $p_{l,avg}$, i.e. we observed in Figure (20) that the control cytokine concentrations (dotted black lines, parameter values taken from our estimated, donor-independent set of parameter values $\tilde{\boldsymbol{\Xi}}$, e.g. $\kappa_{pop} = \tilde{\kappa}_{pop}$ and $p_{l,avg} = \tilde{p}_{l,avg}$, Table 3.2), can be smaller than the cytokine concentrations in the presence of both a defect in bacterial handling and an impairment in cytokine production capability (coloured solid lines, the values of both κ_{pop} and $p_{l,avg}$ smaller than $\tilde{\kappa}_{pop}$ and $\tilde{p}_{l,avg}$ respectively) (see Section 3.3.7). We searched the

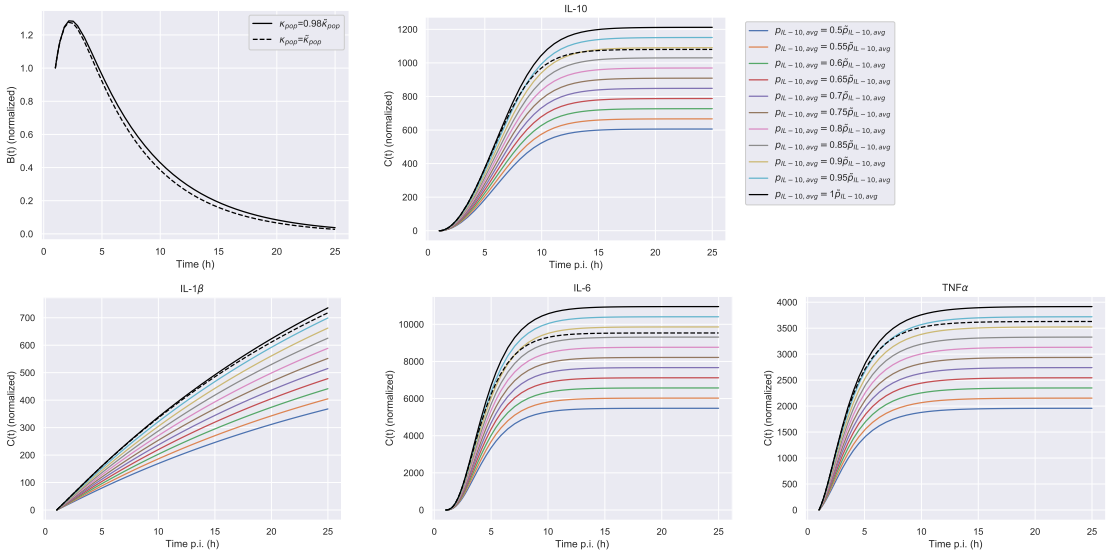


Figure 27: For $g_{pop} = 0.5$, exploration of the dependence of the simulated cytokine trajectories and bacterial load on the value of the cytokine production parameters $p_{l,avg}$ (equations (3.22) and (3.23)). We have taken the estimated values obtained as detailed in the main text (Section 3.3.8), to simulate the cytokine trajectories for MOI=10 (dashed black lines), and also multiplied the estimated value of κ_{pop} by 0.98 to mimic a bacterial handling defect (solid black lines). We varied the overall production rate $p_{l,pop}$ for each cytokine l by multiplying $\tilde{p}_{avg}$ by various factors between 0.5 and 1, while we set the value of κ_{pop} to 0.98 times the estimated value of κ_{pop} (solid coloured lines).

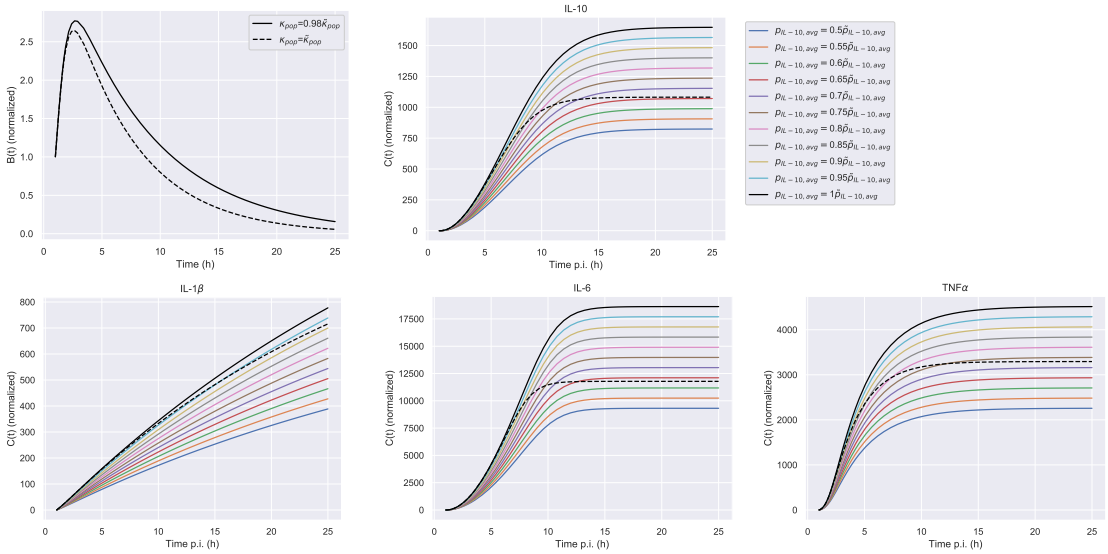


Figure 28: For $g_{pop} = 2$, exploration of the dependence of the simulated cytokine trajectories and bacterial load on the value of the cytokine production parameters $p_{l,avg}$ (equations (3.22) and (3.23)). We have taken the estimated values obtained as detailed in the main text (Section 3.3.8), to simulate the cytokine trajectories for MOI=10 (dashed black lines), and also multiplied the estimated value of κ_{pop} by 0.98 to mimic a bacterial handling defect (solid black lines). We varied the overall production rate $p_{l,pop}$ for each cytokine l by multiplying $\tilde{p}_{avg}$ by various factors between 0.5 and 1, while we set the value of κ_{pop} to 0.98 times the estimated value of κ_{pop} (solid coloured lines).

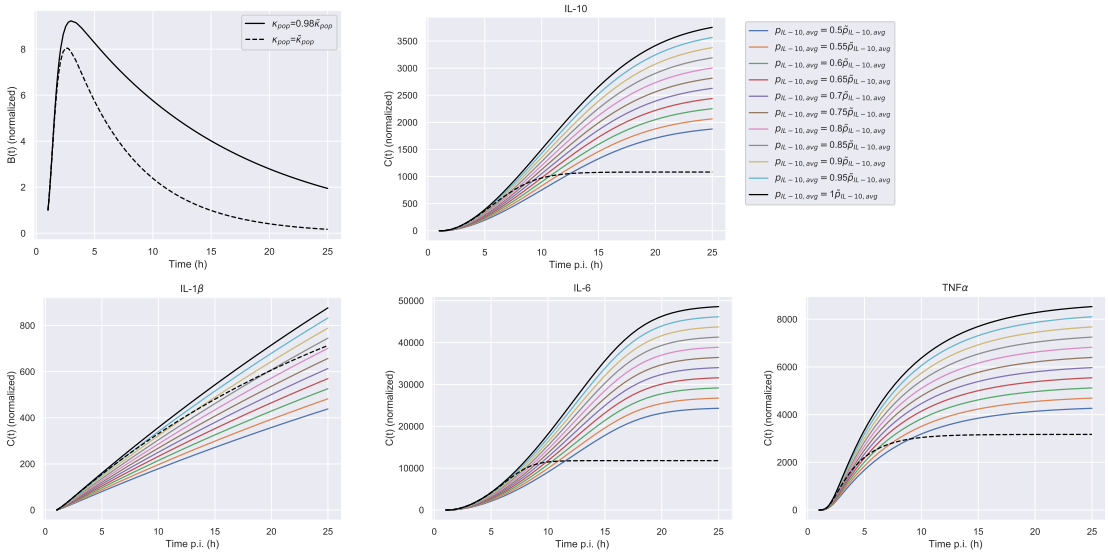


Figure 29: For $g_{pop} = 5$, exploration of the dependence of the simulated cytokine trajectories and bacterial load on the value of the cytokine production parameters $p_{l,avg}$ (equations (3.22) and (3.23)). We have taken the estimated values obtained as detailed in the main text (Section 3.3.8), to simulate the cytokine trajectories for MOI=10 (dashed black lines), and also multiplied the estimated value of κ_{pop} by 0.98 to mimic a bacterial handling defect (solid black lines). We varied the overall production rate $p_{l,pop}$ for each cytokine l by multiplying $\tilde{p}_{avg}$ by various factors between 0.5 and 1, while we set the value of κ_{pop} to 0.98 times the estimated value of κ_{pop} (solid coloured lines).

	First author	Year	Cell type	Modulation	Bacterial species	MOI	Gentamicin	Time point(s) post infection	CFU (% of control)
[29]	Bauler	2008	Unactivated murine bone marrow derived macrophages	XIAP+/y vs XIAP-/y	L. monocytogenes	1	0.5h	1, 3, 5, 11h	ns
[29]	Bauler	2008	Murine bone marrow derived macrophages activated with LPS and IFNγ	XIAP+/y vs XIAP-/y	L. monocytogenes	10	0.5h	0.5, 2, 6, 10h	ns
[29]	Bauler	2008	Murine peritoneal macrophages	XIAP+/y vs XIAP-/y	L. monocytogenes	10	0.5h	0.5, 2, 5, 8h	ns
[69]	Cooney	2009	Monocyte derived dendritic cells (GM-CSF + IL4)	WT vs 1007sinsC	AIEC	25	1h	1.17, 2, 3h	98.1, 157.8, 343.5
[69]	Cooney	2009	Monocyte derived dendritic cells (GM-CSF + IL4)	WT vs R702W or G908R	AIEC	25	1h	1.17, 2, 3h	100.0, 142.2, 434.8
[266]	Peeters	2007	Monocytes	WT vs NOD2 R702W, G908R, and het 1007fsinsC	AIEC	10	2h	2, 3, 6, 26h	ns
[306]	Schwerd	2016	MDM (M-CSF)	WT vs NOD2 hom 1007fsinsC	AIEC	10	1h	3h	101.6
[306]	Schwerd	2016	MDM (M-CSF)	WT vs NOD2 hom 1007fsinsC	*S. typhimurium*	10	1h	3h	100.8
[306]	Schwerd	2016	MDM (M-CSF)	WT + MDP vs NOD2 hom 1007fsinsC + MDP	AIEC	10	1h	3h	171.6
[306]	Schwerd	2016	MDM (M-CSF)	WT + MDP vs NOD2 hom 1007fsinsC + MDP	*S. typhimurium*	10	1h	3h	148.8
[306]	Schwerd	2016	MDM (M-CSF)	HC vs XIAP y/-	*S. typhimurium*	10	1h	3h	100
[306]	Schwerd	2016	MDM (M-CSF)	HC + MDP vs XIAP y/- + MDP	*S. typhimurium*	10	1h	3h	175.2
[306]	Schwerd	2016	MDM (M-CSF)	WT vs RIPK2-ponatinib	AIEC	10	1h	3h	115.2
[306]	Schwerd	2016	MDM (M-CSF)	WT vs RIPK2-ponatinib	*S. typhimurium*	10	1h	3h	124.2
[306]	Schwerd	2016	MDM (M-CSF)	WT + MDP vs RIPK2-ponatinib + MDP	AIEC	10	1h	3h	180.2
[306]	Schwerd	2016	MDM (M-CSF)	WT + MDP vs RIPK2-ponatinib + MDP	*S. typhimurium*	10	1h	3h	198.8
[306]	Schwerd	2016	MDM (M-CSF)	WT vs XIAP-Cp-21a	AIEC	10	1h	3h	96.1
[306]	Schwerd	2016	MDM (M-CSF)	WT vs XIAP-Cp-21a	*S. typhimurium*	10	1h	3h	93.8
[306]	Schwerd	2016	MDM (M-CSF)	WT + MDP vs XIAP-Cp-21a + MDP	AIEC	10	1h	3h	182.4
[306]	Schwerd	2016	MDM (M-CSF)	WT + MDP vs XIAP-Cp-21a + MDP	*S. typhimurium*	10	1h	3h	161.9
[187]	Lapaquette	2012	Murine peritoneal macrophages	WT vs NOD2-/-	AIEC	20	0.3h	4, 8h	162.5, 197.1

Table 3.3: Summary of literature data on the effects of various defects in the NOD2/XIAP/RIPK2 pathway on the bacterial load of macrophages, dendritic cells or monocytes after infection with a gram-negative pathogen. Cytokines added during cell differentiation are listed in parenthesis. The drugs ponatinib and Cp-21a inhibit RIPK2 and XIAP respectively, and 1007fsinsC, R702W, and G908R are CD-associated NOD2 polymorphisms. Abbreviations: WT, wild type; hom, homozygous; het, heterozygous; MDM, monocyte derived macrophage; M-CSF, macrophage colony-stimulating factor; GM-CSF, granulocyte-macrophage colony-stimulating factor; CFU, colony forming units; MOI, multiplicity of infection.

literature for killing assay and cytokine concentration data in the presence of mutations in the NOD2/XIAP/RIPK2 pathway. We constrained our search to data on monocytes, or monocyte progeny (e.g. macrophages and dendritic cells), infected by gram-negative bacteria. We summarize our findings of the literature on the effects of various defects in the NOD2/XIAP/RIPK2 pathway on the bacterial load in Table 3.3.

The killing assay data from the studies listed in Table 3.3 have been generated by different labs under various experimental conditions. We note that the time course of bacterial load is highly dependent on the cell and pathogen type used, and on other experimental conditions. In the literature, a wide variety of time courses can be found for killing assays using monocytes or their progeny (e.g. [29, 154, 218, 266, 272] for dynamics similar to the ones we observed for our experimental set-up, i.e. an initial increase followed by a decrease in bacterial load, [20, 29, 130, 162, 167, 272, 305, 327] for a continuous decrease, [162, 188, 259, 268, 305] for a continuous increase, and [325] for a stable bacterial load). When we use the data from the different studies listed in Table 3.3 to estimate the size of typical bacterial handling defects, we will therefore also re-estimate the model parameter values for the control set-up when appropriate. As before, we assume that a defect in bacterial handling can be represented by a lowered value of κ_{pop}, and a defect in cytokine production by a decreased value of $p_{l,avg}$ (Section 3.3.7). We will thus keep all other parameters fixed when estimating the effects of defects in the NOD2 pathway on bacterial handling and cytokine production.

Of the five literature studies listed, the experiments by Schwerd et. al most closely resemble our used experimental system, as they were performed in the same lab and the same macrophage differentiation protocol and killing assay protocol were used [306]. Monocyte derived macrophages (MDM) were infected with *Salmonella* or adherent-invasive *Escherichia coli* (AIEC) and the bacterial load was measured at a single point in time ($t = 3$h post infection). The modulations studied include the addition of the RIPK2 inhibitor Ponatinib, and the addition of the XIAP inhibitor Cp-21a to MDM from healthy controls. Further, MDM from inflammatory bowel disease (IBD) patients carrying homozygous NOD2 variants, and MDM from XIAP-deficient males were used, as the XIAP gene is found on the X-chromosome. For the various modulations described in this study, we estimate the altered

value of the killing rate κ_{pop} using the observed percentage increase or decrease in bacterial load at $t = 3$h post infection, while fixing all other parameter values to our set of estimated parameter values $\tilde{\boldsymbol{\Xi}}$ (Table 3.2). We fixed all other parameters to this control set, as no data is available on the time course of the control bacterial load or cytokine production. We note that in the study by Schwerd et al., both *Salmonella* and adherent-invasive *Escherichia coli* (AIEC) were used as a model pathogen. As our set of estimated parameter values $\tilde{\boldsymbol{\Xi}}$ are based on data from *Salmonella* experiments, and not AIEC, we only used the *Salmonella* data from Schwerd et al. (Figure 30). As the experimental conditions were equal to our own experiments for the *Salmonella* data, we assume our set of estimated model parameter values $\tilde{\boldsymbol{\Xi}}$ will be suitable to describe the *Salmonella* infection dynamics of Schwerd et al.

We note that the addition of MDP, the ligand of NOD2, increases the bacterial handling capability of control macrophages (Figure 30). The smallest estimated value of κ_{pop} is $\kappa_{pop} = 0.87\tilde{\kappa}_{pop}$ for *Salmonella* infection, after addition of the RIPK2 inhibitor Ponatinib, and with $\tilde{\kappa}_{pop}$ the previously estimated value of κ_{pop} in the absence of modulations (Table 3.2, Figure 30, brown line). We observe that greater differences are found when comparing the various modulations in the presence of MDP. In the case of *Salmonella* infection, the estimated value of κ_{pop} after Ponatinib and MDP addition is for instance $0.89/1.28 = 0.70$ times the estimated value of κ_{pop} for MDP addition alone (Figure 30, blue and pink lines). The cytokines simulations in Figure 30 have been created under the assumption that the various modulations do not have a direct effect on the cytokine production ability of the MDM, i.e. we assume that $p_{l,scaled}$ is fixed for all modulations. Schwerd et al. measured however, that MDM stimulated with the bacterial cell wall component MDP, the ligand of NOD2, showed an impaired TNFα production in the presence of modulations in the NOD2/XIAP/RIPK2 pathway [306]. No quantitative measurements of the size of the cytokine production impairment during infection were reported. Depending on the size of the impairment in cytokine production, represented by the decrease of the value of $p_{l,scaled}$, hyper-production of the various cytokines might or might not be observed for each modulation (Figure 22).

In Cooney et al. dendritic cells were infected with AIEC at an MOI of 25 [69]. The bacterial load in dendritic cells expressing wild type and Crohn's disease associated suscep-

tibility variants in NOD2 (1007fsinsC, R702W or G908R) were compared at $t = 1.17, 2, 3$h post infection. The bacterial load in this data set is continuously decreasing over time. In our own experimental results we observed an initial increase in bacterial load. The difference in bacterial handling dynamics found in [69] and in our own data might be a result of the cell type or type of pathogen used. Because a time course of (donor dependent) bacterial load was available, we re-estimated the values of σ_i, τ_{pop} and two values for κ_{pop}, for the wild-type case and for cells expressing Crohn's disease-variant NOD2, with $B_i(t = 1\text{h}) = 2.5\sigma_i$ (equation (3.13), by minimizing the log-likelihood, see equation (3.2)). We will indicate these estimated values for the wild-type case with a hat ($\hat{\sigma}_i, \hat{\tau}_{pop}$ and $\hat{\kappa}_{pop}$). As before, we have fixed the growth rate g_{pop}. We use $g_{pop} = 0.36$, based on a growth rate analysis for AIEC found in a study by Demarre et al. ([87], text S1, maximum doubling time of 50 minutes). We express the estimated value of the altered κ_{pop} for cells expressing Crohn's disease-variant NOD2 as a fraction of the estimated wild-type value of κ_{pop}. We observe more pronounced bacterial handling defects, i.e. a smaller value of κ_{pop} relative to the control value $\hat{\kappa}_{pop}$ in the presence of a mutation, than in the case of Schwerd et al. (Figure 31) [306]. The simulations shown in Figure 31 form another example of the observed range of change in killing capability and the possible corresponding effect on cytokine concentrations typically observed for mutations in the NOD2 pathway.

We do not show the bacterial handling data by Bauler et al., as no significant difference in bacterial handling dynamics was found between XIAP+/y and XIAP-/y cells (Table 3.3) [29]. Similarly, in Peeters et al., no significant difference in bacterial handling was observed between monocytes obtained from patients expressing wild type NOD2 and patients with NOD2 polymorphisms during an AIEC infection. However, in Peeters et. al, the concentrations of IL-10, IL-1β and IL-6 were significantly lower at $t = 8$h post infection in the presence of a mutation [266]. The concentrations of IL-10, IL-1β and IL-6 were at $52\%, 64\%$, and 67% of their respective control values [266]. As these values have been obtained in the absence of an impairment in bacterial handling (as no significant effect on the bacterial load was observed), they give an indication of the possible size of the effects of defects in NOD2 on cytokine production capabilities. The studies by Bauler et al. and Peeters et al. also tell us that defects in the NOD2 pathway do not impair bacterial handling in all cases.

We already observed in the study by Schwerd et al. that the size of the observed bacterial handling defect is dependent on the specific mutation. While no significant difference in bacterial handling dynamics was found between XIAP+/y and XIAP-/y cells, differences of up to 198.8% (number of colonies, wild type + MDP versus RIPK2-ponatinib + MDP) were found for other mutations (Table 3.3). Apart from the mutation, the cell type and pathogen used might also influence the size of the bacterial handling defect.

Finally, in Lapaquette et al., both bacterial load and cytokine concentration (TNFα and IL-6) in murine peritoneal wild type and NOD2 knock-out macrophages infected with AIEC was measured [187]. Increased bacterial load at $t = 4$ and 8h post infection was observed in NOD2 knock-out cells (Figure 32, blue and black dots). Interestingly, the experimentally measured concentration of TNFα and IL-6 was also found to be increased in NOD2 knock-out cells ($t = 4$h). We would expect that the TNFα and IL-6 production in NOD2 deficient cells is initially impaired. The observed increase in cytokine production at $t = 4$h p.i. might be driven by an increased bacterial load due to the bacterial handling defect, in line with our hypothesis. As multiple time points are available for the bacterial load, we re-estimate values for σ_i, τ_{pop} and two values for κ_{pop}, for the knock-out and control cells respectively, based on the bacterial handling data from [187] (using equation (3.13) for $B_i(t)$, by minimizing the log-likelihood, see equation (3.2)). We indicate these estimated values with a breve ($\breve{\sigma}_i, \breve{\tau}_{pop}$ and $\breve{\kappa}_{pop}$). Recall that $B_i(t) = \sigma_i B_{scaled}(t)$. As in the case of Cooney et al., we use $g_{pop} = 0.36$, based on a growth rate analysis for AIEC found in a study by Demarre et al. ([87], text S1, maximum doubling time of 50 minutes). In Figure 32 we show simulations of B_{scaled}, with $B_{scaled}(t = 1\text{h}) = 2$, corresponding to the MOI of 20 (equation (3.22)). Note that we rescaled the experimental data by dividing by $\breve{\sigma}_i$ (black and blue dots). As no time series data was available for the cytokine trajectories, we can parametrise our cytokine concentration equations for the study by Lapaquette et. al. We note that the parameter values we estimated before ($\tilde{p}_{l,avg}, \tilde{h}_{l,pop}, \tilde{q}_{l,pop}$ and $\tilde{z}_{l,pop}$) have been estimated using data from a different cell type (murine versus human macrophages) and a different type of pathogen (AIEC versus *Salmonella*) than the data from Lapaquette et al. They are therefore not suitable to generate any simulations of the cytokine trajectories for the study by Lapaquette et. al. The estimated decrease in the value of $\breve{\kappa}_{pop}$ for the NOD2 knock-out

cells for the study by Lapaquette et al. compared to control is $\kappa_{pop} = 0.79\check{\kappa}_{pop}$ (Figure 32). For this size of defect, for MOI= 25, we would expect to observe cytokine driven hyper-production in our own experimental system for all four measured cytokines, even in the presence of a large impairment in cytokine production capability (i.e. $p_{l,avg} = 0.5\tilde{p}_{l,avg}$, see Figure 23). This is in line with the data by Lapaquette et al, where such hyper-production was observed at $t = 4$h for both TNFα (1.9 times higher concentration than control) and IL-6 (1.44 times higher concentration than control). We conclude that the observed hyper-production in the data from the study by Lapaquette et. al could be explained by bacterial load driven hyper production.

3.4 Discussion

We studied the effects of defects in the NOD2 pathway on cytokine production by infected human macrophages using a combination of mathematical modelling, wet-lab experiments and literature data. The role of NOD2 genetic defects in CD pathogenesis is still unclear. It has been proposed that the hyper-inflammatory phenotype observed in CD patients with genetic defects in the NOD2 pathway is caused by defective antibacterial activity. Apart from their effect on antibacterial activity, defects in the NOD2 pathway are also known to impair cytokine production. The aim of this chapter was to study the hypothesis that defects in the NOD2 pathway could drive a state of cytokine hyper-production as a result of a defect in antimicrobial activity, even in the presence of an impairment in cytokine production capability. Further understanding of this aspect of CD pathology could point towards new treatment options, such as bacterial clearance inducing drugs.

We constructed a mechanistic bacterial handling model that describes the level of infection of *in vitro* infected human macrophages from healthy donors over time (Section 3.3.1). We assumed exponential bacterial growth and a killing rate that increases over time. We used a microscopy data set of the initial distribution of infection to generate model predictions that could falsify our assumption of exponential growth in the absence of macrophage killing (Section 3.3.2). We extended our bacterial handling model to describe the relationship between cytokine concentration and the level of infection of *in vitro* infected macrophages from healthy donors over time (Section 3.3.3)). In our modelling system, a

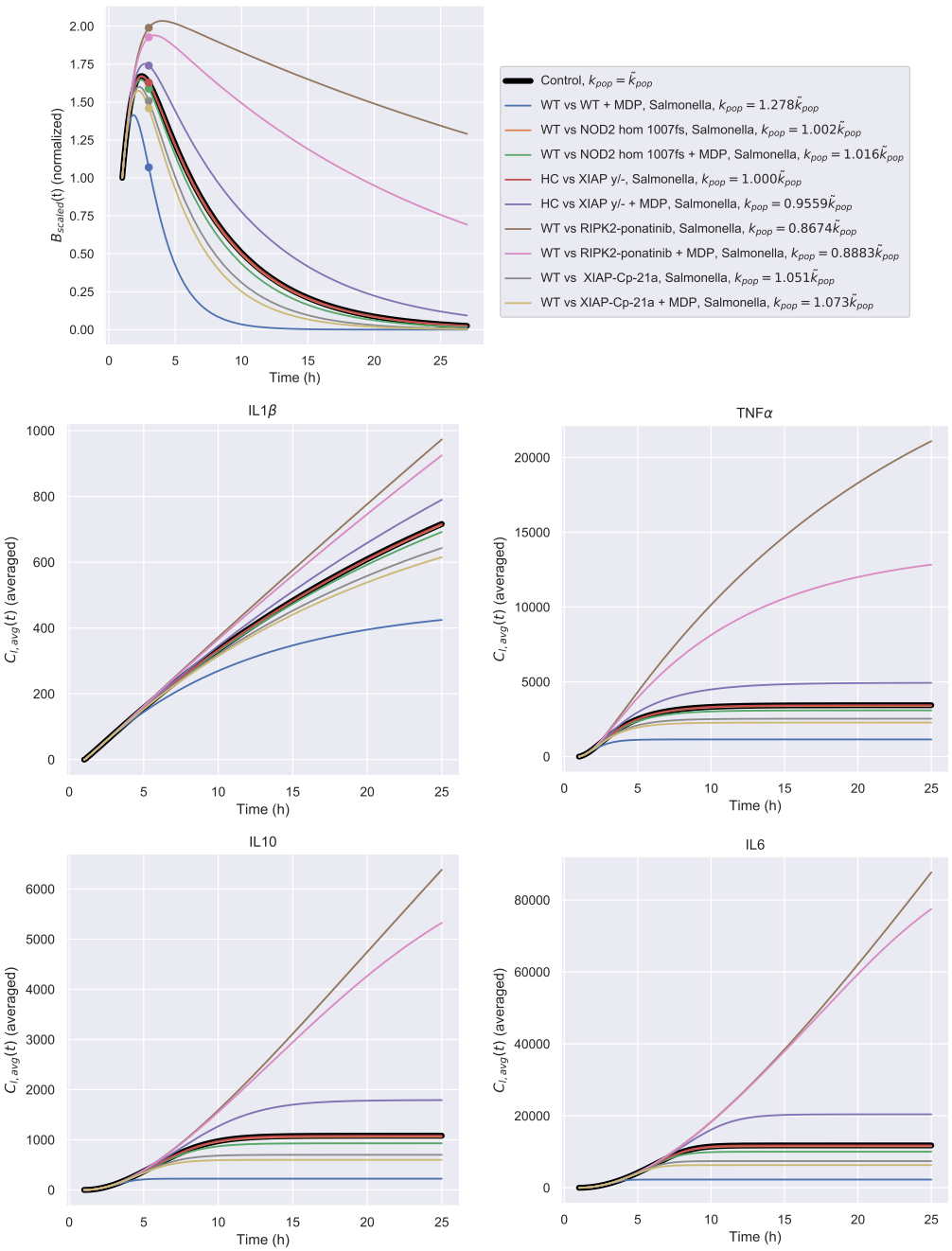


Figure 30: Experimental data (dots) and simulations (lines) of the bacterial load (B_{scaled}) and cytokine concentrations ($C_{l,avg}$) over time (equations (3.22) and (3.23)), for MDM infected with *Salmonella* at an MOI of 10, with various values of κ_{pop} estimated using the modulation data obtained from the publication by Schwerd et. al (see Table 3.3, using non-linear least squares), and all other parameter values as in Table 3.2 [306]. In the legend, we present the estimated values of κ_{pop} for the various modulations as the fraction of the estimated value of $\kappa_{pop} = \tilde{\kappa}_{pop}$ under control conditions (Table 3.2). Note that the simulations of cytokine concentration in this figure have been created under the assumption that the various modulations do not have a direct effect on the cytokine production ability of the MDM, i.e. we assume that $p_{l,avg}$ is fixed for all modulations.

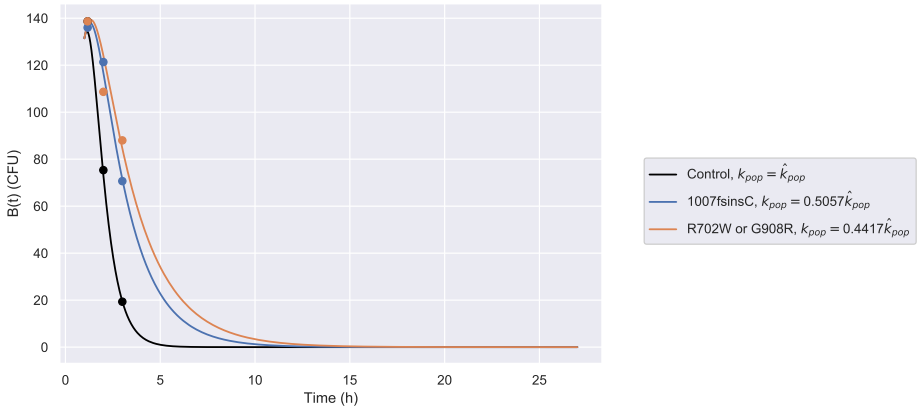


Figure 31: Experimental data (dots) and simulations (lines) of the bacterial load ($B_i(t)$, equation (3.13)) over time, for monocyte derived dendritic cells (MDDC) infected with adherent-invasive *Escherichia coli* (AIEC) at an MOI of 25, with the value of σ_i, τ_{pop} and three different values of κ_{pop} estimated using the control and modulation data obtained from the publication by Cooney et al. (see Table 3.3, by minimizing the log likelihood), and $g_{pop} = 0.36$ [69]. In the legend, we present the estimated values of κ_{pop} for the two modulations as the fraction of the estimated value of $\kappa_{pop} = \hat{\kappa}_{pop}$ under control conditions, where $\hat{\kappa}_{pop}$ is estimated from fitting the data from the study by Cooney et al. [69].

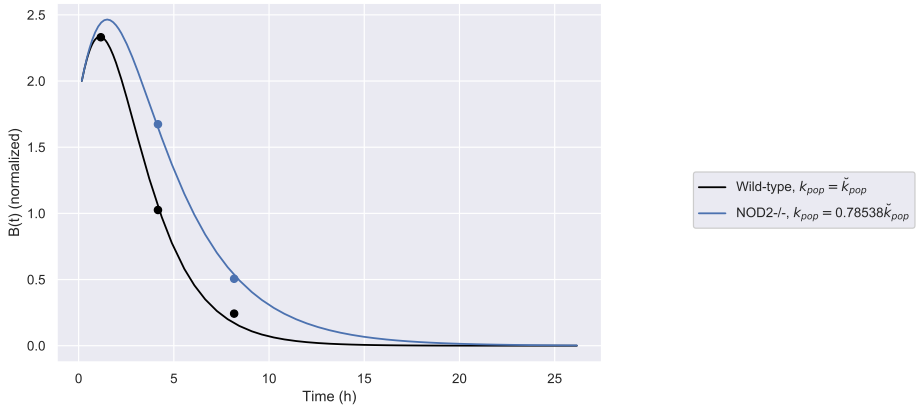


Figure 32: Experimental data (dots) and simulations (lines) of the bacterial load B_{scaled} (equation (3.13), with $B_{scaled}(t) = \frac{B_i(t)}{\sigma_i}$), for murine peritoneal macrophages infected with adherent-invasive *Escherichia coli* (AIEC) at an MOI of 20, with σ_i, τ_{pop} and two different κ_{pop} estimated using the control and NOD2-/- data obtained from the publication by Lapaquette et al. (see Table 3.3, by minimizing the log likelihood), and $g_{pop} = 0.36$ (black and blue lines). In the legend, we present the estimated values of κ_{pop} for the NOD2-/- cells as the fraction of the estimated value of $\kappa_{pop} = \breve{\kappa}_{pop}$ for the wild-type cells. Here, $\breve{\kappa}_{pop}$ has been estimated using the data obtained from the publication by Lapaquette et al. [187]

higher load of infection drives increased cytokine production. Cytokine production rates saturate for an increasing bacterial load. We determined in which cases the introduction of an impairment in bacterial handling in this extended model would drive a state of cytokine hyper-production, even in the presence of an impairment of cytokine production capability (Section 3.3.7). We represented impairments in bacterial handling and cytokine production by decreasing the parameter values of the killing parameter κ and cytokine production parameter p_l, with l the cytokine, compared to their estimated values for healthy controls. Finally, we estimated the size of effects of defects in the NOD2 pathway on both bacterial handling and cytokine production capability found in the literature (Section 3.3.9). We found that our experimental and mathematical framework, complemented with this data from the literature, suggests that defects in the NOD2 pathway could drive a state of cytokine hyper-production as a result of a defect in antimicrobial activity, even in the presence of an impairment in cytokine production capability. We will discuss the above results sections in the light of this main conclusion. We will end with a summary and possible future directions.

3.4.1 Bacterial handling dynamics

The aim of Section 3.3.1 was to construct a mechanistic bacterial handling model that describes the level of infection of *in vitro* infected human macrophages. We infected human monocyte derived macrophages (MDMs) from healthy controls with the model pathogen *Salmonella* and measured bacterial load over time ($t = 1 - 25$h post infection). We work with primary human cells, rather than murine cells or immortalized cell lines, as we assume them to be more relevant for studying human IBD pathogenesis [165]. We used blood derived MDM from healthy donors as they are much easier to obtain than gut resident macrophages. In most tissues, the resident macrophage population is self-renewing and has a tissue-specific phenotype [123]. In contrast, monocytes are assumed to be constantly recruited to the gut. We therefore assume MDM are a good substitute for tissue resident macrophages in the gut. We have chosen to study macrophages rather than other cell types such as epithelial cells or fibroblasts, as the NOD2 receptor, our receptor of interest, is primarily expressed in macrophages [336].

We use ordinary differential equations (ODEs) to describe the bacterial load and cytokine concentration dynamics. We assume unlimited exponential pathogen growth and an initial killing rate of zero. The killing rate quickly increases over time, resulting in almost no bacteria at $t = 25$h post infection. As the number of bacteria we use to infect our system with is relatively low, we assume that a lack of nutrients does not limit the pathogen growth rate in our system. We could test our assumption of exponential growth by tracking the number of bacteria on an individual cell level over time, for instance by confocal microscopy. Further, we note that we could also consider a bacterial growth rate that decreases over time after uptake, i.e. $g(t) = \gamma e^{-\tau(t-1)}$, instead of a killing rate that increases over time. The bacterial growth rate might for instance decrease because of the increasingly hostile environment within the Salmonella-containing vacuole. One could investigate the contribution of growth to the bacterial numbers by infecting macrophages with a pathogen that is unable to replicate intra-cellularly.

We have chosen to work with a relatively low load of infection, as we assume that this is the situation most closely resembling the *in vivo* human gut environment, where very few pathogens cross the epithelial barrier under non-inflamed conditions. Furthermore, when increasing the bacterial load, the occurrence of high macrophage death could start to influence the reliability of the gentamicin protection assay as a measure of infection burden.

3.4.2 Distribution of infection

Multiple assumptions were made when constructing our bacterial handling model in Section 3.3.1. The aim of Section 3.3.2 was to explore ways in which various of the assumptions of our bacterial handling model could be falsified, such as the assumption of unlimited bacterial growth.

Using existing microscopy data, we first studied the initial distribution of *Salmonella* infected MDM. We found that the initial distribution of infection resembles a negative binomial distribution ($11.2 = \chi^2_8(19\%)$) much more than a Poisson distribution ($452 = \chi^2_9(0\%)$). We therefore hypothesize that infection events are Poisson distributed, but the infection rates of the macrophages are heterogeneous, and are gamma distributed, in which case the unconditional distribution of infection can be written as a negative binomial distribution.

We note that a negative binomial distribution could also be obtained by assuming bacterial growth after uptake (apparent contagion), as the microscopy data was captured after an hour of infection [134]. Finally, we note that intracellular *Salmonella* could alter the phenotype of their host macrophage, making it more or less susceptible to further infection events (true contagion). This was explored by Julia Gog and collegues in a study on *Salmonella* infection in mouse macrophages [127]. Based on our microscopy data, it is theoretically not possible to distinguish between contagion on one side and existing macrophage heterogeneity on the other, as both result in a negative binomial distribution, but our studies are insensitive to such subleties [134].

We split the single bacterial handling equation (3.1) into a model of coupled equations that describes the distribution of infection over time (equations (3.6)). We assume the initial distribution of infection is negative binomial distributed and estimate the parameter values of this distribution using the microscopy data. We used this system to generate simulations of the macrophage distribution over time (Figures 11 and 12). We included these simulations in this study as they produced testable model predictions. Subsequent experiments could challenge our *in silico* model assumptions by falsifying these model simulations. We assume, for instance, that bacteria will grow exponentially indefinitely. If the fraction of observed '9+' macrophages is much smaller than predicted, this could indicate that bacterial growth slows down over time, e.g. due to an increasingly hostile environment in the Salmonella-containing vacuole, or due to a lack of nutrients [53, 289]. Another possibility would be to observe a larger than predicted population of macrophages containing just one bacteria. It has been observed that some bacteria enter a viable, dormant-like state after entering a macrophage [143]. It remains an open question whether the inability of some bacteria to replicate intracellularly is driven by pathogen heterogeneity or by macrophage heterogeneity [294, 309].

3.4.3 Cytokine dynamics

The aim of Section 3.3.3 was to extended our bacterial handling model (Section 3.3.1) to describe the relationship between cytokine concentration and the level of infection of *in vitro* infected macrophages from healthy donors over time. We measured the supernatant

concentration of TNFα, IFNγ, IL-1β, IL-8, IL-10, IL-18 and IL-23 simultaneously with the bacterial load (Figure 13). The pro-inflammatory cytokines TNFα, IFNγ, IL-1β, IL-18 and IL-23, the anti-inflammatory cytokine IL-10, and IL-6, that can have both pro- and anti-inflammatory effects, are all thought be important in the pathogenesis and progression of IBD [110, 249, 290, 341]. For instance, IL-8 is an important immune cell recruiting factor, secreted by macrophages after pathogen recognition [293, 362]. As with the bacterial load data, the specific cytokine profiles are both pathogen and cell type specific [318]. *S. typhimurium* for instance induces secretion of IL-1β and IL-8 by MDM, but adherent invasive *Escherichia coli* does not [141].

Macrophages are well known producers of all measured cytokines, except for IFNγ, which we excluded from our mathematical modelling study [42, 341]. Although IFNγ production by macrophages has been observed in some experimental setups, this could be the result of contamination with small amounts of lymphocytes, the cells that are classicly seen as IFNγ producers [42]. We do not exclude the possibility that the observed IFNγ measured in our system is produced by contamination with lymphocytes that were not removed during the monocyte isolation phase of the experiments.

We also excluded IL-8 and IL-18 from our mathematical modelling study, as they have a different dynamical profile from the other cytokines. We have further excluded IL-23 because its secretion level in our system is very low (Figure 13). Only 7 out of the 24 measurements of the IL-23 were larger than the smallest concentration included in our standard curve measurements, i.e. the measurements of known cytokine concentration dilutions provided with the Luminex assay kit. When studying the effects of certain modulations, such as an IL-10 receptor blocking antibody, IL-23 might be expressed at higher level, whereupon it could be of interest to include the IL-23 dynamics in our mathematical model [22]. Similarly, if we would study the effects of cell recruitment, the chemokine IL-8 could be of interest, as it is an important immune cell recruiting factor [293, 362].

We used our experimental cytokine concentration data and bacterial load data to mathematically model the dynamics of IL-1β, IL-10, IL-6, and TNFα. We used the single equation (3.1) introduced in Section 3.3.1 to describe the bacterial load, and not the system of equations (3.6) describing the distribution of infection over time, as the extra term introduced

in the system of equations from Section 3.3.2 is negligible for finite bacterial populations and the arbitrary parameter, N, large. We assume cytokine production is an increasing function of bacterial load. This is confirmed by the literature. It has also been reported in the literature that cytokine production saturates for increasing initial load of infection (Figure 15). We only measured the cytokine concentration for one multiplicity of infection (MOI, the initial ratio of macrophages and bacteria). As the bacterial load changes over time during the experiment, we were able to estimate the dependence of cytokine production on bacterial load. In order to improve our parameter estimates, we could repeat our experiments for higher MOI. This would allow us to determine more accurately at what level of infection the cytokine production levels start to saturate. Further, we have not considered the contribution of dead bacteria on cytokine concentration. A proportion of the measured cytokine concentration might be induced by dead bacteria. This could be investigated by repeating each experiment with varying numbers of heat-killed bacteria.

3.4.4 Handling defects

The aim of Section 3.3.7 was to determine in which cases the introduction of an impairment in bacterial handling in our system would drive a state of cytokine hyper-production, even in the presence of an impairment in cytokine production capability. We considered our model system as presented in Section 3.3.3 (equations (3.22) and (3.23), with parameter values as in Table 3.2, obtained by fitting to our experimental healthy control killing and cytokine concentration data). We investigated the effects of varying κ_{pop} and $p_{l,avg}$ on our system (compared to the healthy control baseline values as listed in Table 3.2), representing genetic defects in the NOD2/XIAP/RIPK2 pathway that both affect the bacterial handling capability (via κ_{pop}) and cytokine production ability (via $p_{l,avg}$) of the cells (Figures 19, 20) [69, 306, 336]. Here, the subscript l denotes the cytokine. Bacterial load drives cytokine production in our *in silico* model. Increasing the bacterial load by decreasing the value of the killing parameter κ_{pop} therefore increases cytokine concentration. If the increase in bacterial load is large enough, we observe increased cytokine concentrations in the presence of genetic defects, even when the cytokine production ability is impaired (represented by a decreased value of $p_{l,avg}$). We showed the parameter regime where this bacterial-load driven

cytokine hyper-production occurs for different multiplicities of infection (MOIs) (Figures 21-23, coloured regions). In addition we considered the impact of varying bacterial growth rates g_{pop}. In particular we observed an insensitivity across a large range (Figure 25). We did also observe that for an increasing g_{pop}, cytokine hyperproduction emerged for more severe impairments in cytokine production rates (Figures 26-29).

Originally, we aimed to experimentally measure the effects of various inhibitors of proteins in the NOD2/XIAP/RIPK2 and other macrophage pathways that play a role in bacterial handling as a next step. We added three different modulations ($n = 4$ donors) to our experimental set-up, mimicking various known bacterial handling defect inducing mutations (Section 3.2). Because of the high variability of the effects of the various inhibitors on the measured bacterial load, this modulation data was not considered to be sufficiently reliable and reproducible. Instead, we compared our *in silico* model estimates to data from the literature on defects in the NOD2/XIAP/RIPK2 pathway (Section 3.3.9) [69, 187, 266, 306].

3.4.5 Literature data

The aim of Section 3.3.9 was to estimate the size of effects of defects in the NOD2 pathway on both bacterial handling and cytokine production capability found in the literature. We parametrised our bacterial handling model with data from papers by Schwerd et al., Cooney et al., and Lapaquette et al. for both healthy control and modulated conditions (see Figures 30, 31, and 32) [69, 187, 306]. This allowed us to estimate the size of the decrease of the value of κ_{pop} when comparing healthy control data with modulated data from cells with various defects in the NOD2 pathway. In the study by Peeters et al., the size of the decrease in cytokine production ability (IL-10, IL-1β and IL-6) of cells from patients with NOD2 polymorphisms was measured [266].

The estimated sizes of the decrease in κ and p_l for various modulations in the NOD2 pathway are rough estimates, and we note the high variability between studies for these type of experiments. We observed that defects in the NOD2 pathway do not even impair bacterial handling in all cases (e.g. the studies by Bauler et al. and Peeters et al. [29, 266]). The size of the bacterial handling impairment is dependent on the specific mutation, and possible on the cell type and pathogen used in the experiment. Still, we can compare the

range of values of κ_{pop} and $p_{l,avg}$ found. Even though the value of $p_{l,avg}$ might be halved in the presence of some defects, our model system suggests that the negative effects on the cytokine concentration can be compensated by decreasing the value of κ_{pop} (as explored in Section 3.3.7). This is in accordance with data from the study by Lapaquette et al., who measured the bacterial load and cytokine production simultaneously in NOD2 knock out cells, and observed both an increased bacterial load and increased cytokine concentration levels [187]. Hence we are led to our main conclusion: modelling and parameter estimation highlight that, in terms of mechanisms and overall scales observed in experimental systems, it is plausible for bacterial handling driven cytokine hyper-production to occur with these type of defects.

3.4.6 Summary and future work

In this chapter, we studied the immunodeficiency component of Crohn's disease using a combination of mathematical modelling and wet-lab experiments. Our main conclusion is that our experimental and mathematical framework, complemented with data from the literature, suggests that defects in the NOD2 pathway could drive a state of cytokine hyper-production as a result of a defect in antimicrobial activity, even in the presence of an impairment in cytokine production capability.

More robust, quantitative estimates of the dependence of the cytokine production on bacterial load could be obtained by repeating our experiments and measure the cytokine concentration for varying multiplicities of infection (MOI). Further, the predicted bacterial load driven hyper production of cytokines could be experimentally tested by investigating various modulations in the NOD2/XIAP/RIPK2 pathway. The modelling framework suggests that such hyper production will be more pronounced for lower MOI, as the cytokine production rate becomes saturated for high numbers of bacteria (Figure 24). This is relevant, as the number of bacteria a macrophage encounters in the gut will be typically low.

Apart from experiments required for further model testing, we could additionally extend our integrated framework in various ways. Within the current set-up, we could investigate the effects of pro-inflammatory cell death on the levels of cytokines. We infected

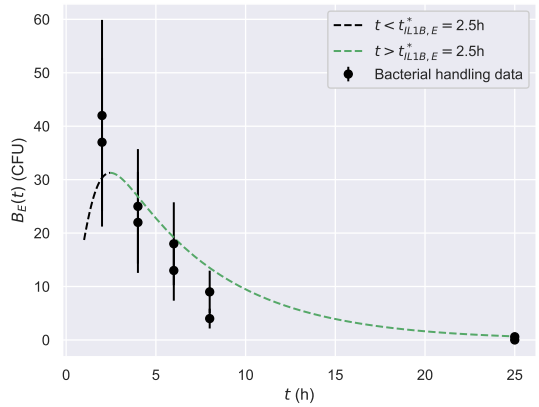
macrophages with *Salmonella* grown overnight and observed negligible cell death. For instance, when *Salmonella* bacteria are added in an earlier growth phase, they can induce a rapid inflammatory macrophage cell death called pyroptosis [103, 128, 205].

Using our integrated framework, we could also study other mutations of interest, such as mutations in NPC1, IL-10R, and NADPH. NCP1 mutations can cause Crohn's like disease, and IL-10 signalling defects cause a completely penetrant Mendelian form of IBD [126, 306]. Mutations in NADPH oxidase can lead to the immunodeficiency syndrome chronic granulomatous disease (CGD) [228]. CGD is characterized by uncontrolled inflammation, often accompanied with granuloma formation [108]. Up to 40% of CGD patients develop Crohn's disease-like intestinal inflammation [304]. Although each of these mutations is associated with both bacterial handling defects and increased cytokine levels, similar to the studied NOD2/XIAP/RIPK2 pathway, the size and time scale of these effects are specific to each mutation. Defects in the IL-10 receptor might for instance result in a delayed increase of pro-inflammatory cytokines such as IL-23, as IL-10 mediated inhibition of cytokine production in the absence of mutations only starts several hours after infection. Other defects might not have a direct effect on cytokine production at all, e.g. an increase in pro-inflammatory cytokines during infection in the presence of mutations in the NCP1 and NCP2 genes might be solely due to an impairment in bacterial clearance.

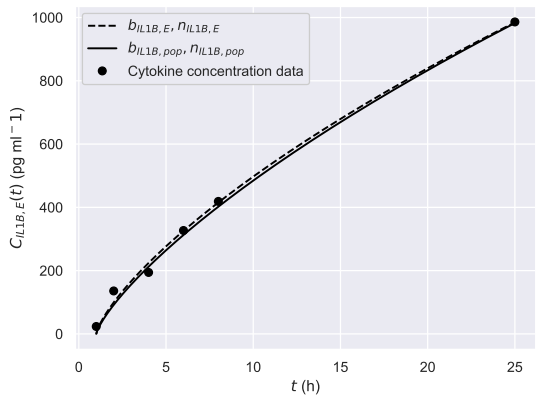
We could also study the contribution of the various pathogen recognizing receptors, such as TLR4, NLRC4 and NOD2, to the overall cytokine production in response to infection [128]. In order to do this, we could compare the cytokine profiles of full bacteria, as we have studied here, with isolated bacterial components, such as LPS, *Salmonella* flagellin and MDP, to activate TLR4, NLRC4 inflammasome and NOD2 signalling respectively. Alternatively, we could block various toll like and nod like receptors while studying *Salmonella* infection. Addition of heat-killed bacteria would allow us to distinguish between a pro-inflammatory response to dead and live bacteria. Further, blocking various (combinations of) cytokines and their receptors, would allow us to determine the feedback effects of cytokines on each others production rates and on the bacterial killing rate. The production of IFNγ might for instance be purely driven by the presence of other cytokines, and not by the bacterial load directly. Finally, though perhaps aspirational, we could extend our

set-up and study the effects of cell recruitment and interaction with other cells types, such as neutrophils and fibroblasts.

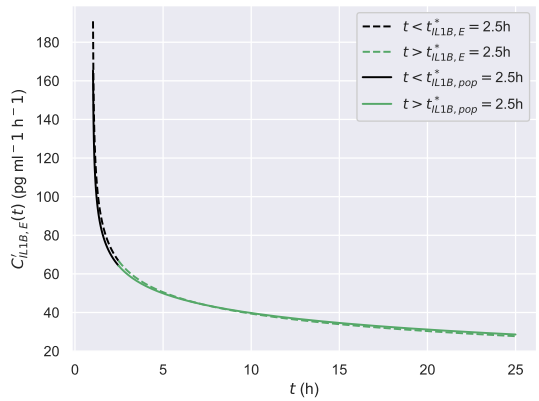
Appendix A



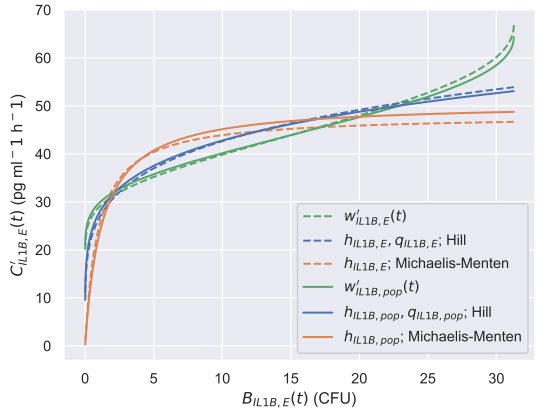
(IL1B.E.1)



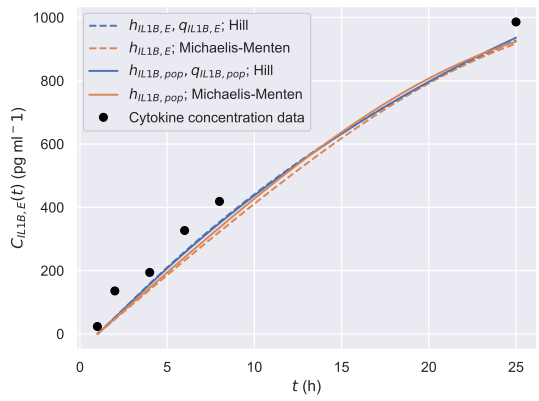
(IL1B.E.2)



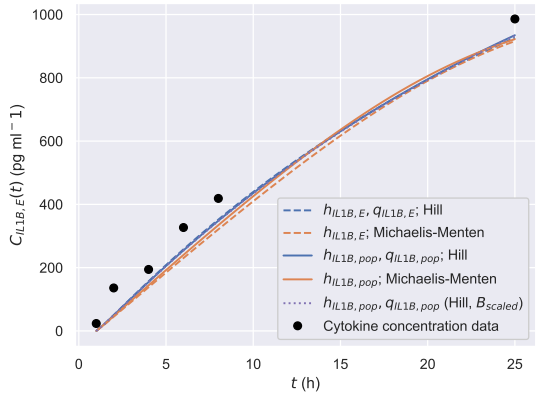
(IL1B.E.3)



(IL1B.E.4)

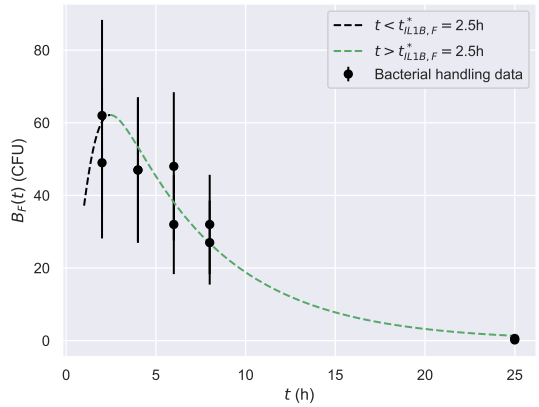


(IL1B.E.5)

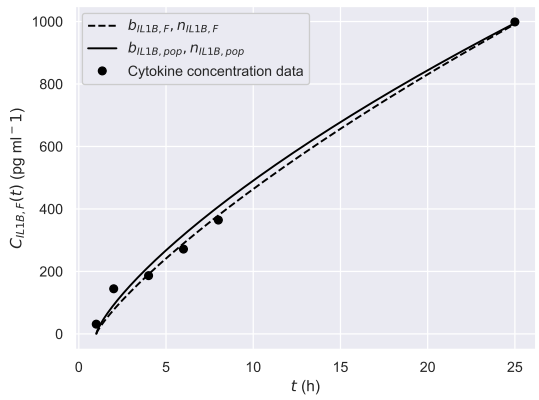


(IL1B.E.6)

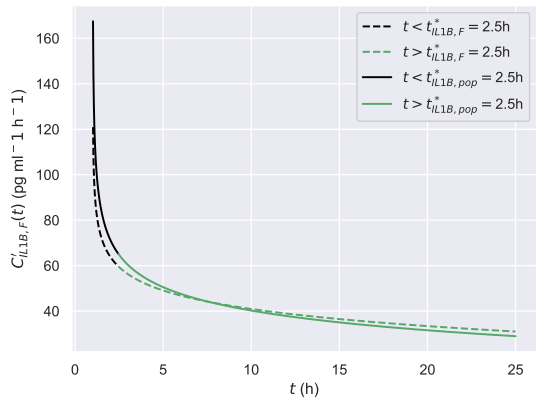
Figure 33: **(IL1B.E.1-6)** Experimental data (black dots) and model simulations for IL-1β and Donor E, see Section 3.3.3. (Figure and legend continued on next page).



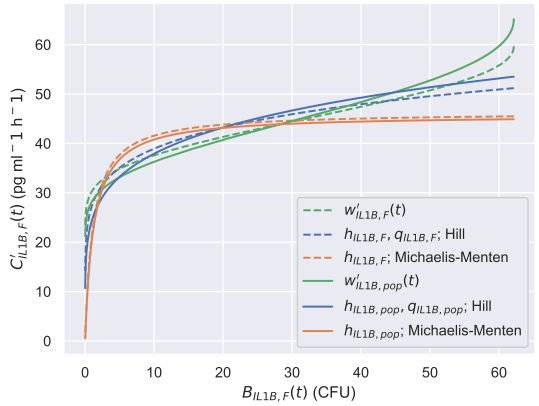
(IL1B.F.1)



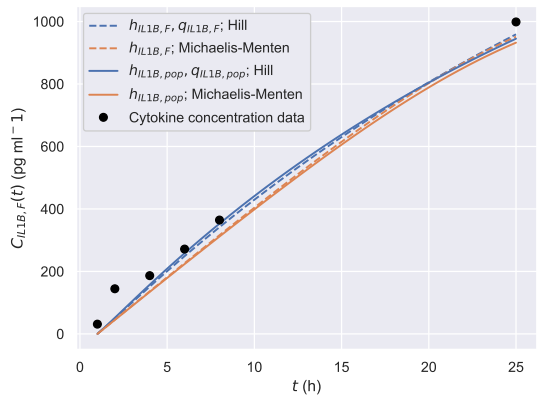
(IL1B.F.2)



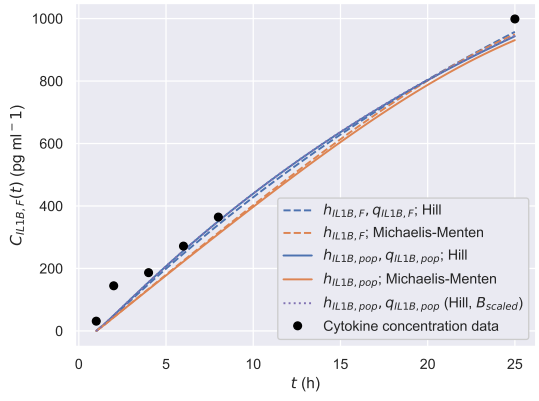
(IL1B.F.3)



(IL1B.F.4)

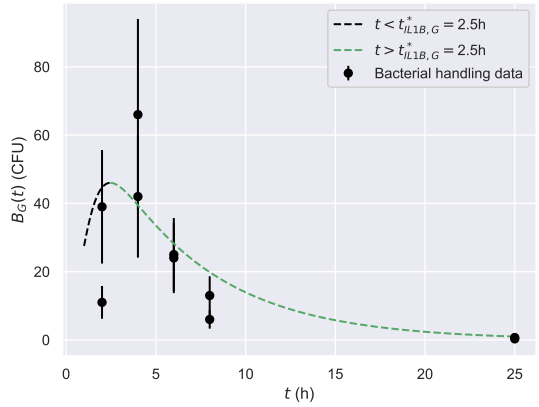


(IL1B.F.5)

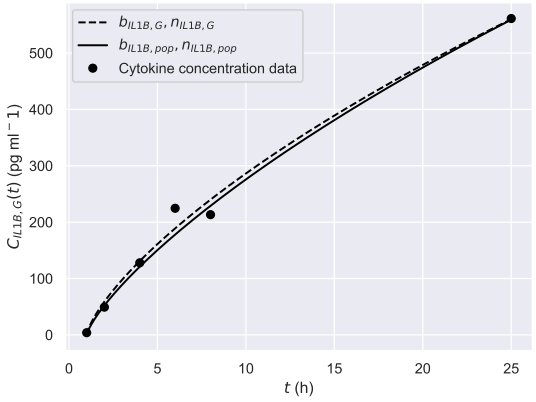


(IL1B.F.6)

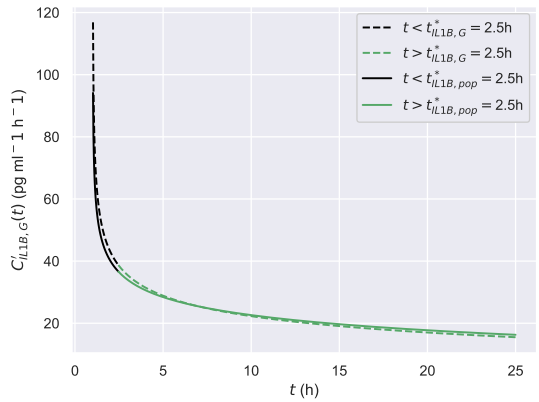
Figure 33: **(IL1B.F.1-6)** Experimental data (black dots) and model simulations for IL-1β and Donor F, see Section 3.3.3. (Figure and legend continued on next page).



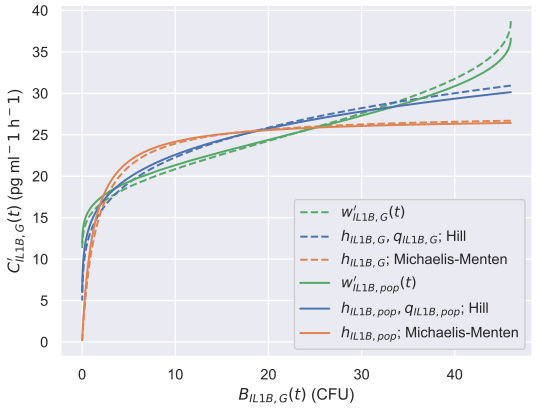
(IL1B.G.1)



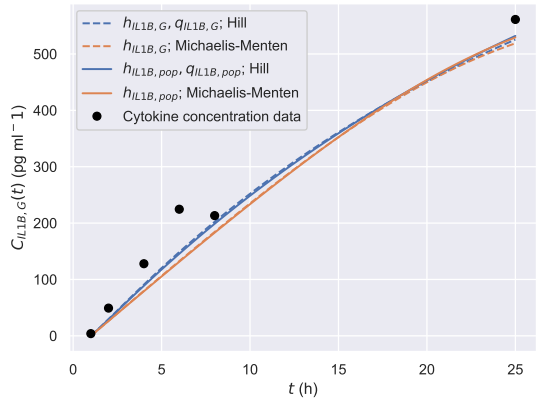
(IL1B.G.2)



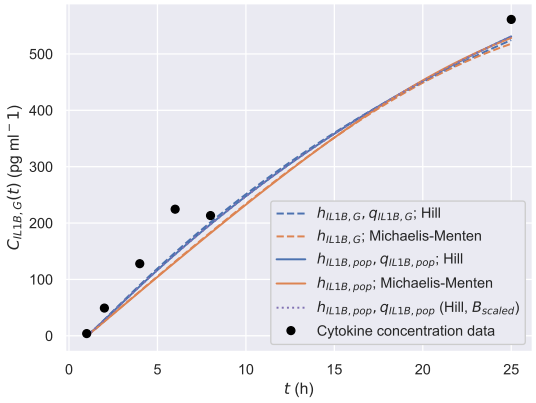
(IL1B.G.3)



(IL1B.G.4)

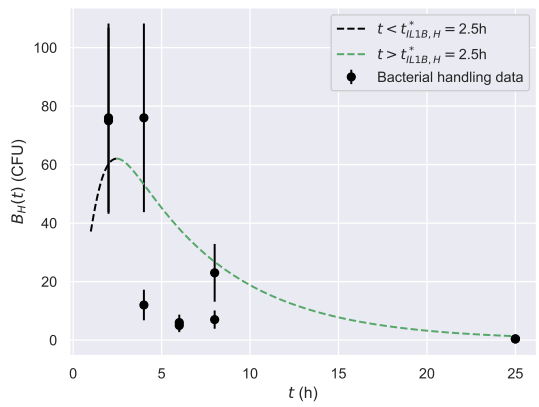


(IL1B.G.5)

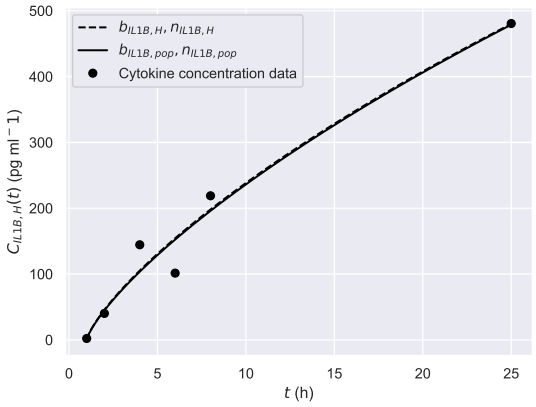


(IL1B.G.6)

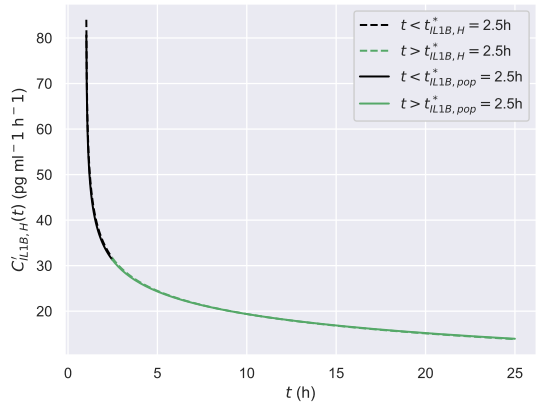
Figure 33: **(IL1B.G.1-6)** Experimental data (black dots) and model simulations for IL-1β and Donor G, see Section 3.3.3. (Figure and legend continued on next page).



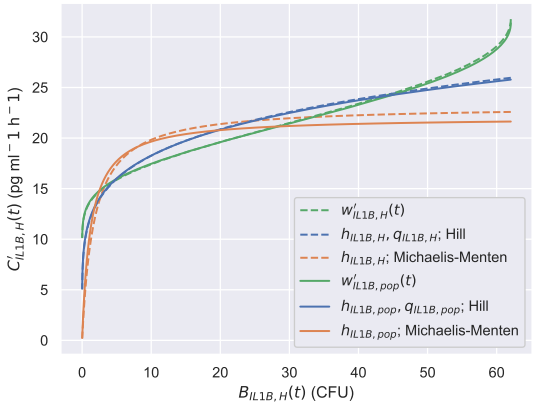
(IL1B.H.1)



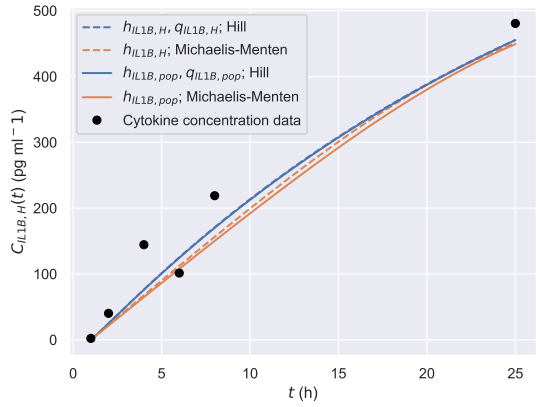
(IL1B.H.2)



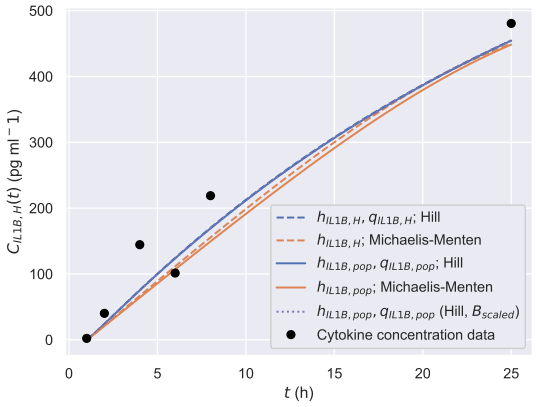
(IL1B.H.3)



(IL1B.H.4)

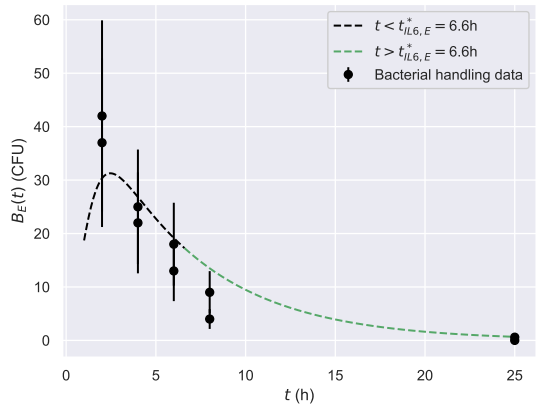


(IL1B.H.5)

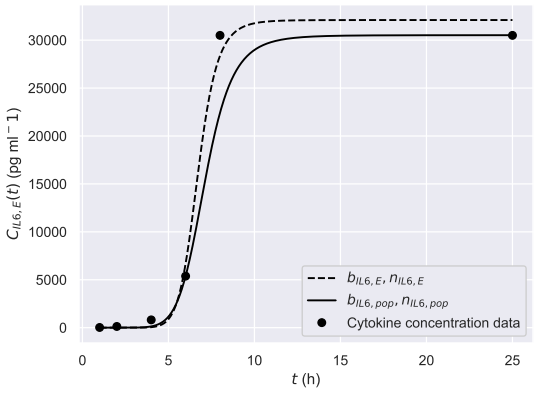


(IL1B.H.6)

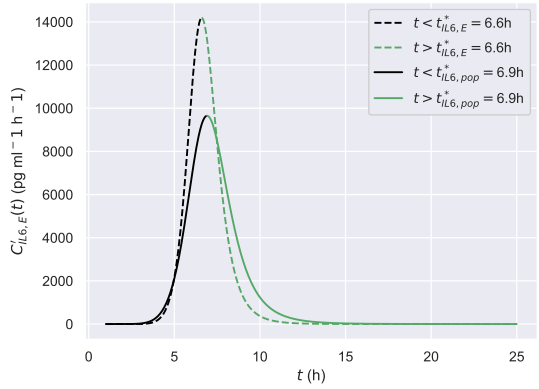
Figure 33: **(IL1B.H.1-6)** Experimental data (black dots) and model simulations for IL-1β and Donor H, see Section 3.3.3. (Legend continued on next page).



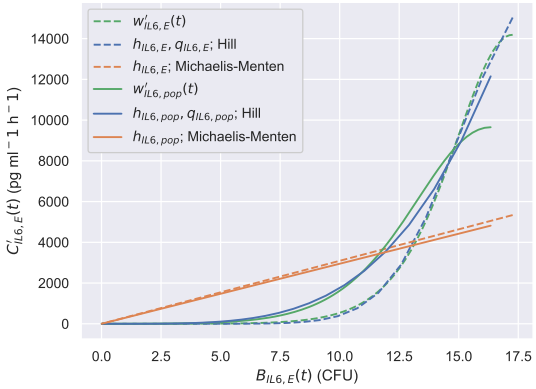
(IL6.E.1)



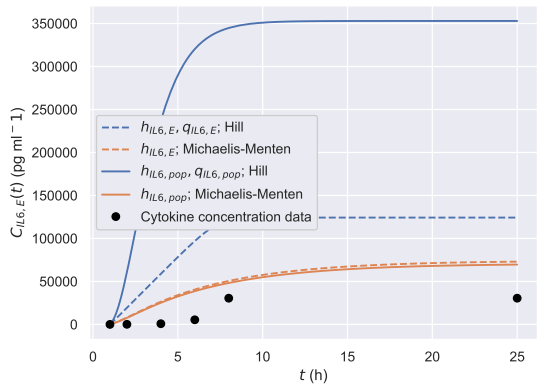
(L6.E.2)



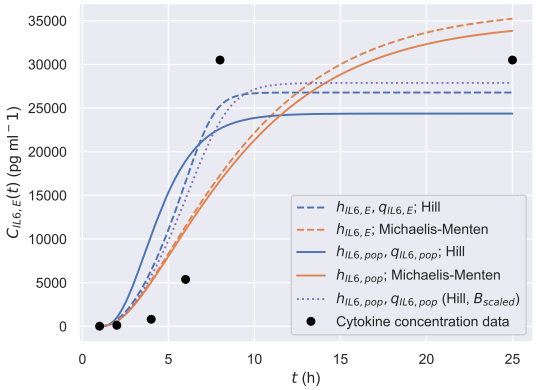
(L6.E.3)



(L6.E.4)

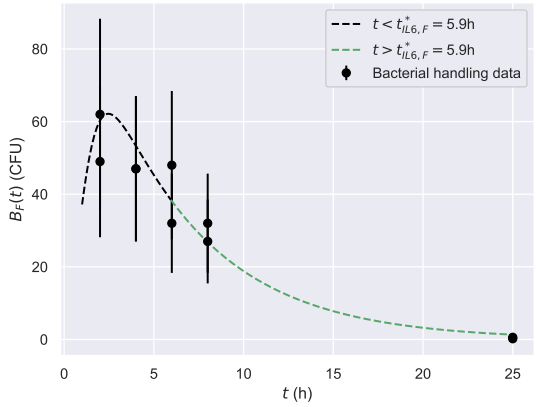


(L6.E.5)

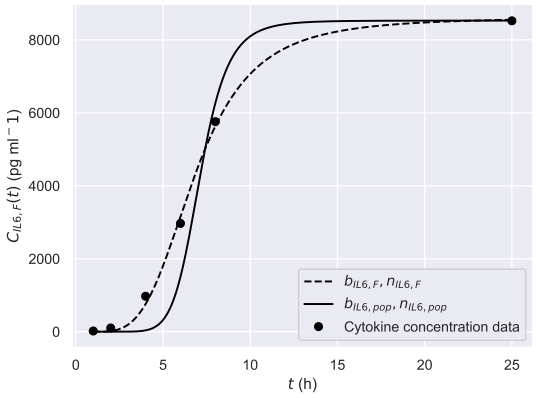


(L6.E.6)

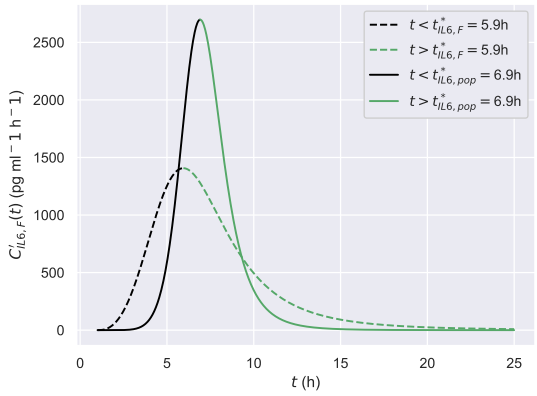
Figure 33: **(L6.E.1-6)** Experimental data (black dots) and model simulations for IL-6 and Donor E, see Section 3.3.3. (Figure and legend continued on next page).



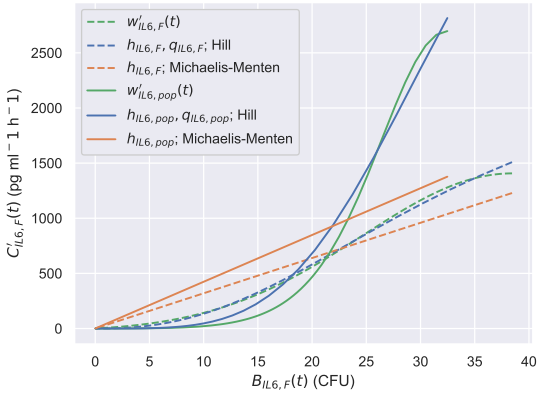
(IL6.F.1)



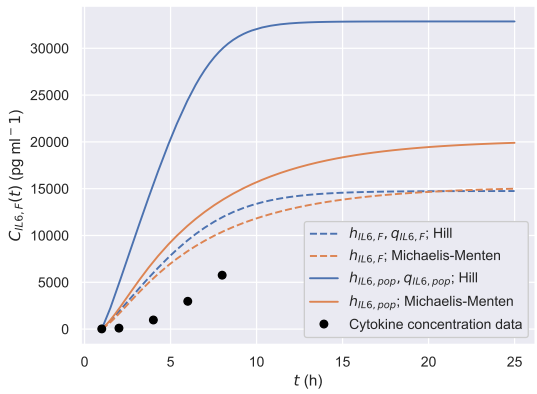
(IL6.F.2)



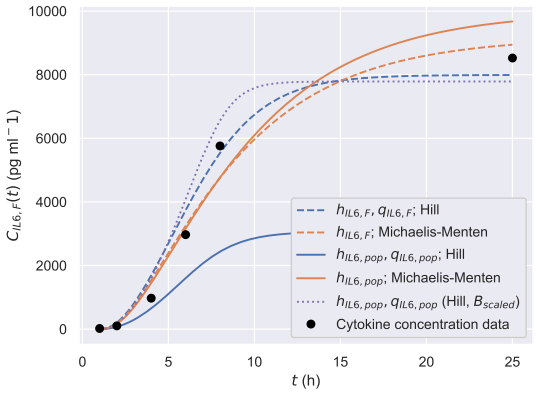
(IL6.F.3)



(IL6.F.4)

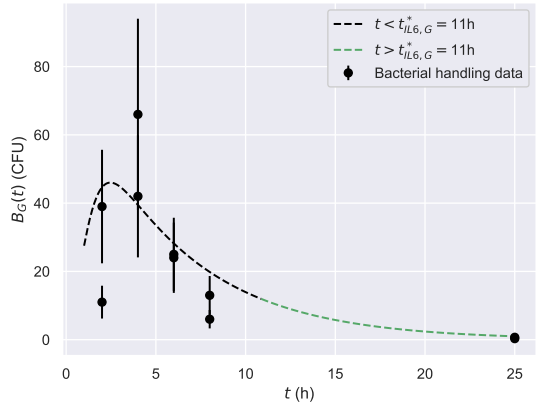


(IL6.F.5)

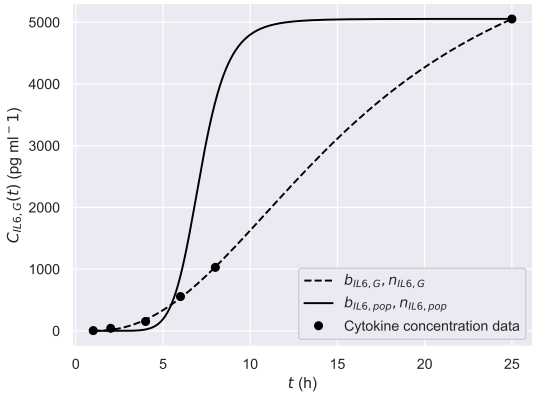


(IL6.F.6)

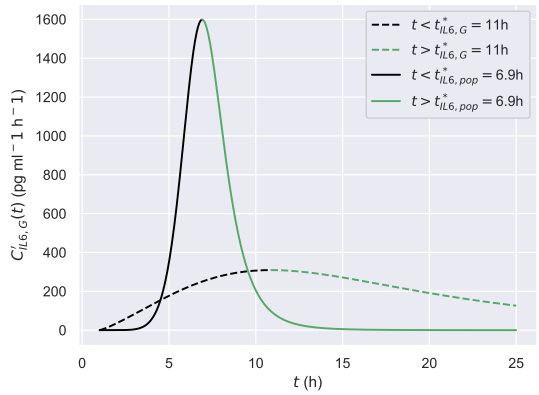
Figure 33: **(IL6.F.1-6)** Experimental data (black dots) and model simulations for IL-6 and Donor F, see Section 3.3.3. (Figure and legend continued on next page).



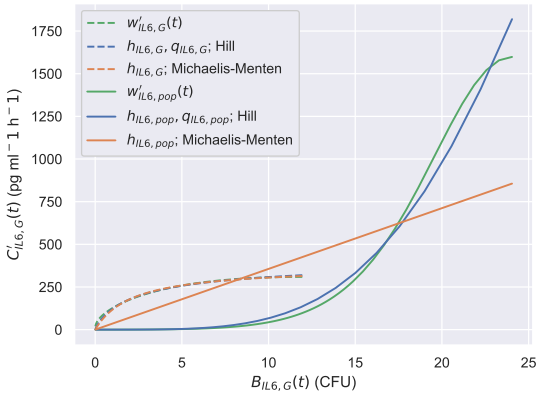
(IL6.G.1)



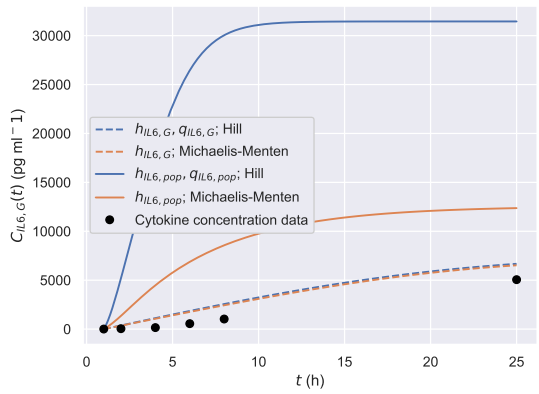
(IL6.G.2)



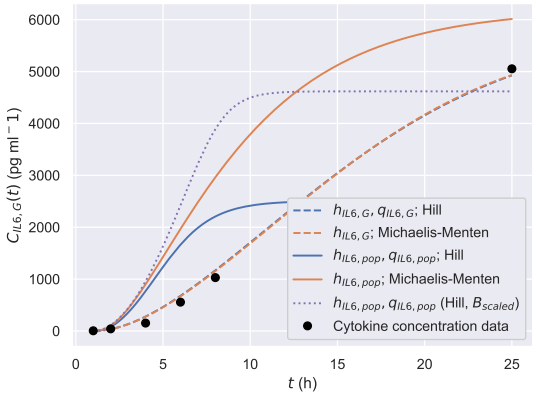
(IL6.G.3)



(IL6.G.4)

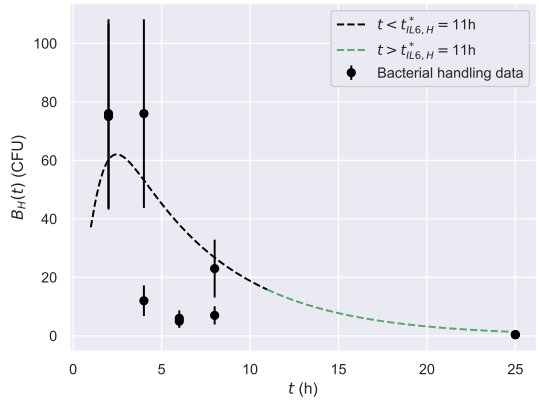


(IL6.G.5)

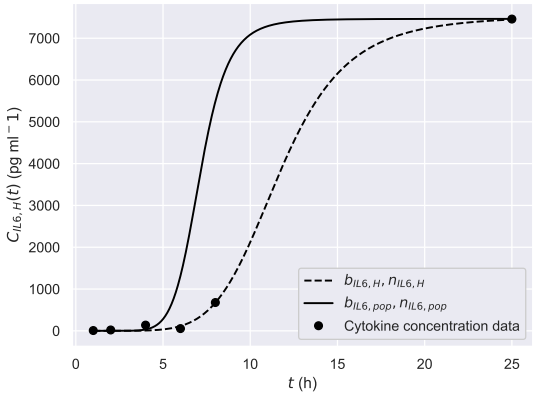


(IL6.G.6)

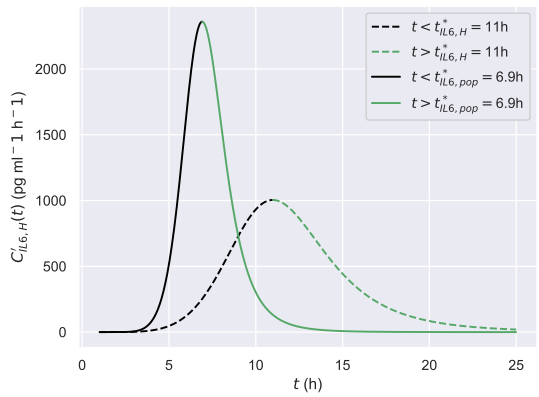
Figure 33: **(IL6.G.1-6)** Experimental data (black dots) and model simulations for IL-6 and Donor G, see Section 3.3.3. (Figure and legend continued on next page).



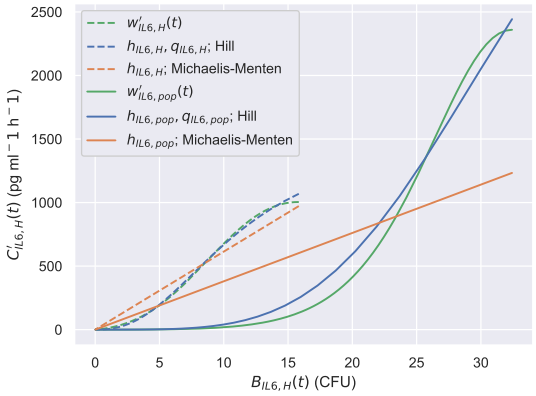
(IL6.H.1)



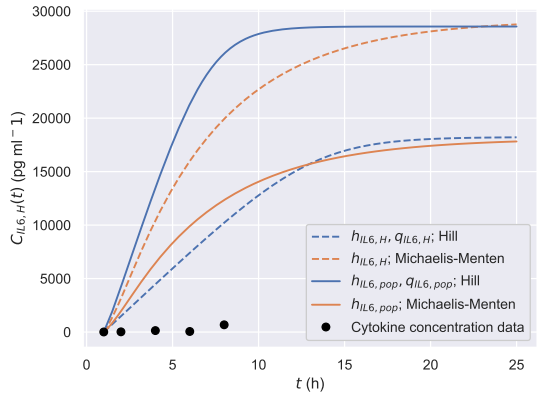
(IL6.H.2)



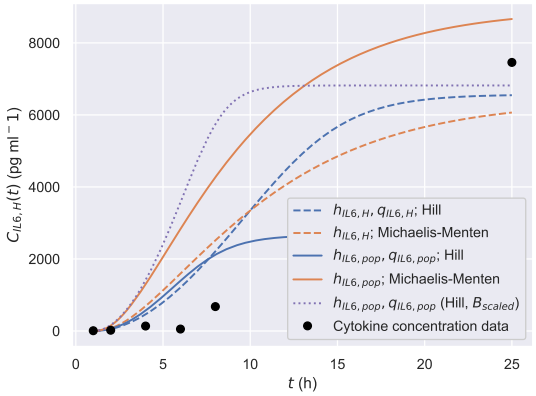
(IL6.H.3)



(IL6.H.4)

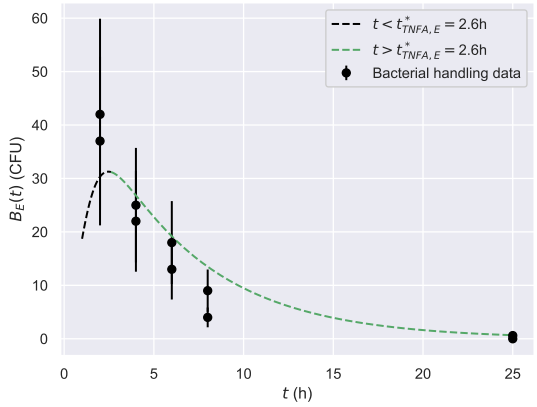


(IL6.H.5)

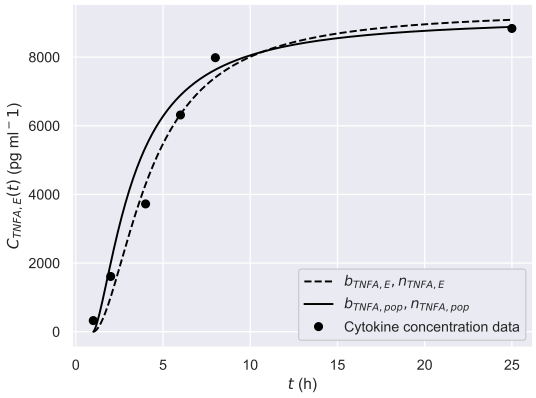


(IL6.H.6)

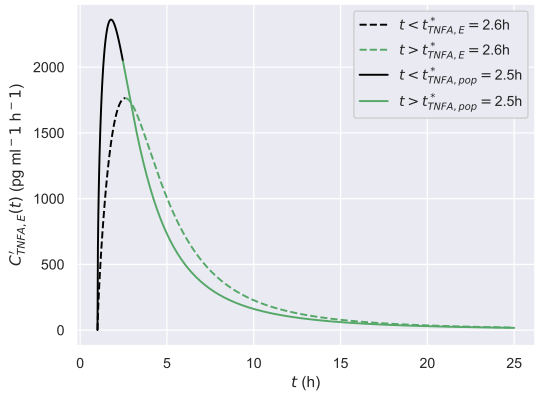
Figure 33: **(IL6.H.1-6)** Experimental data (black dots) and model simulations for IL-6 and Donor H, see Section 3.3.3. (Legend continued on next page).



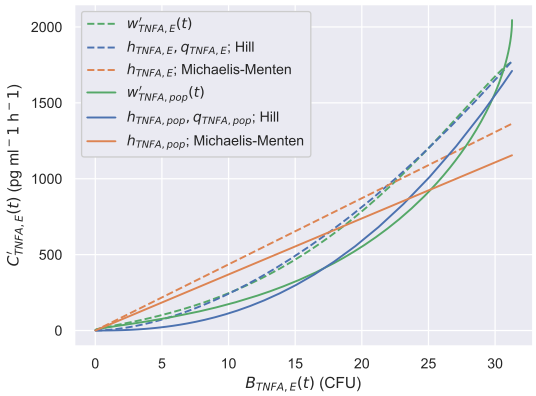
(TNFA.E.1)



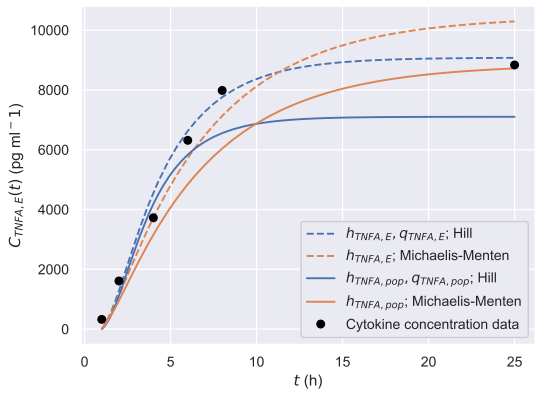
(TNFA.E.2)



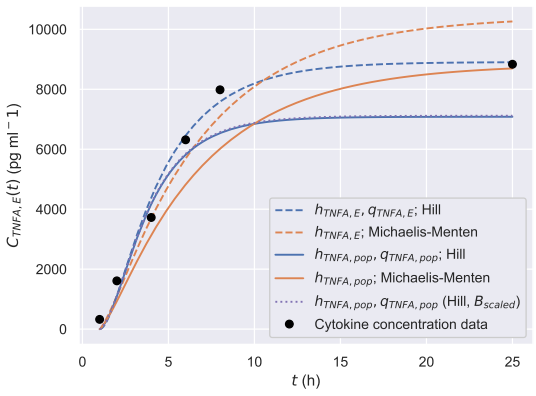
(TNFA.E.3)



(TNFA.E.4)

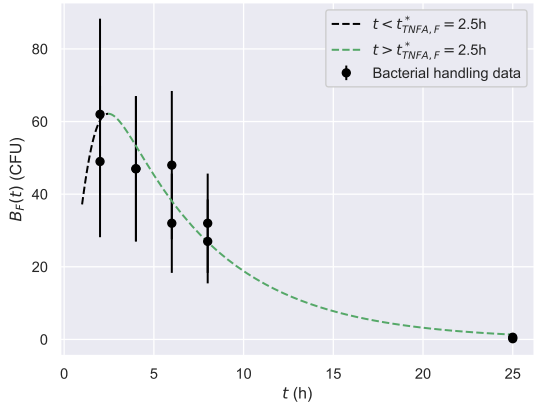


(TNFA.E.5)

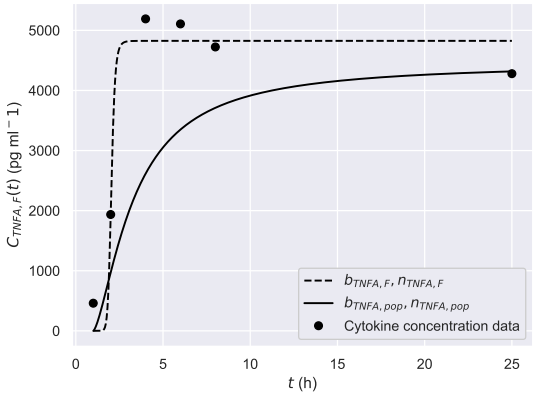


(TNFA.E.6)

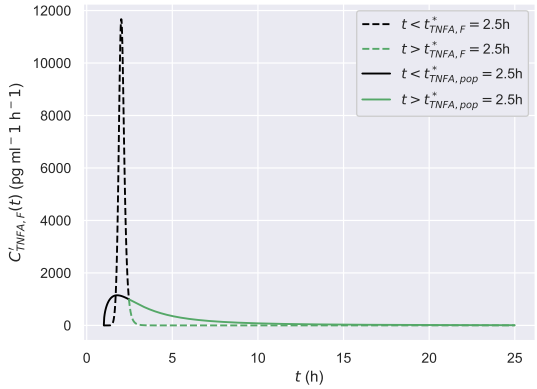
Figure 33: **(TNFA.E.1-6)** Experimental data (black dots) and model simulations for TNFα and Donor E, see Section 3.3.3. (Figure and legend continued on next page).



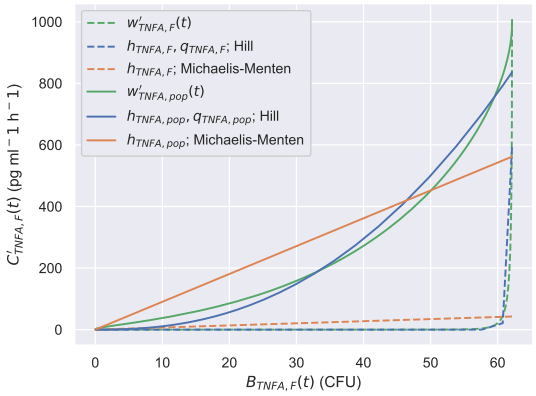
(TNFA.F.1)



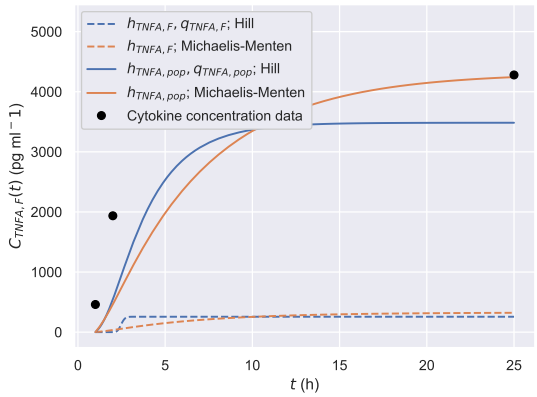
(TNFA.F.2)



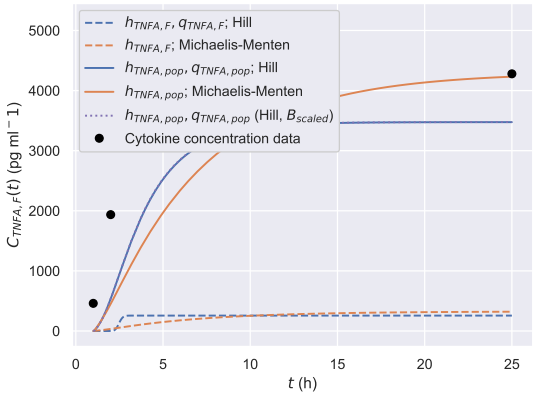
(TNFA.F.3)



(TNFA.F.4)

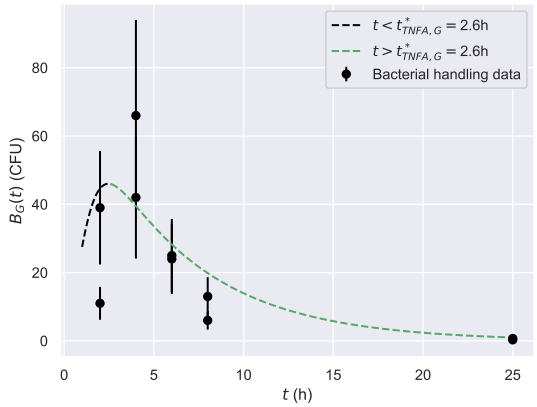


(TNFA.F.5)

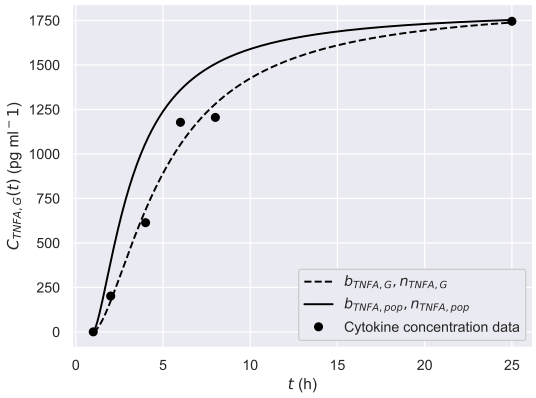


(TNFA.F.6)

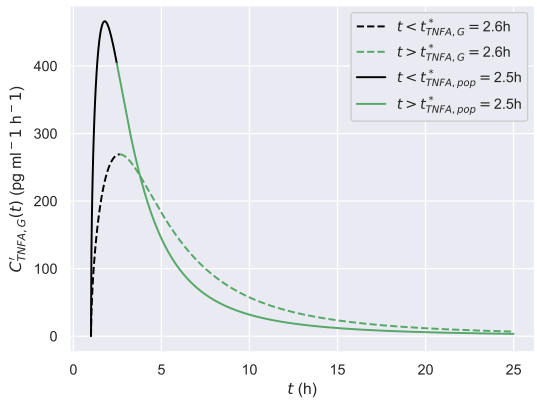
Figure 33: **(TNFA.F.1-6)** Experimental data (black dots) and model simulations for TNFα and Donor F, see Section 3.3.3. (Figure and legend continued on next page).



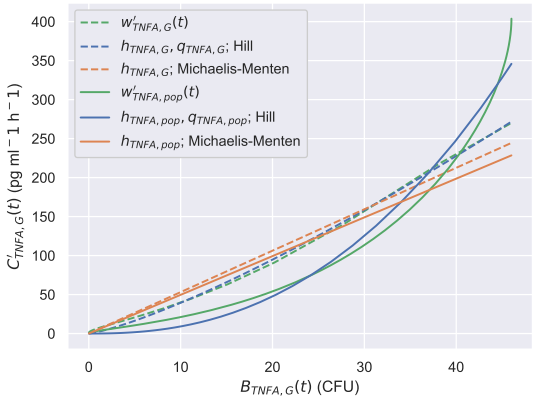
(TNFA.G.1)



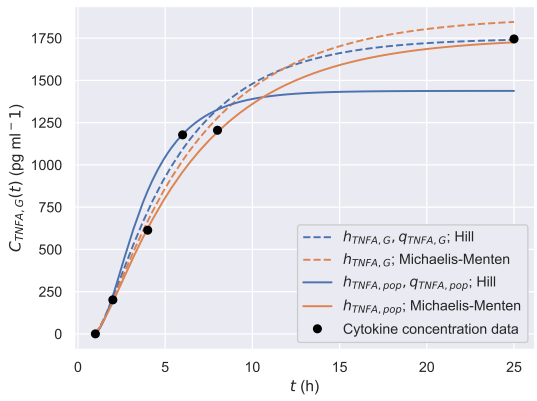
(TNFA.G.2)



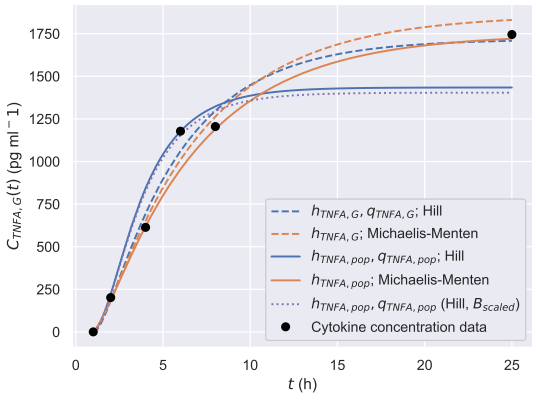
(TNFA.G.3)



(TNFA.G.4)

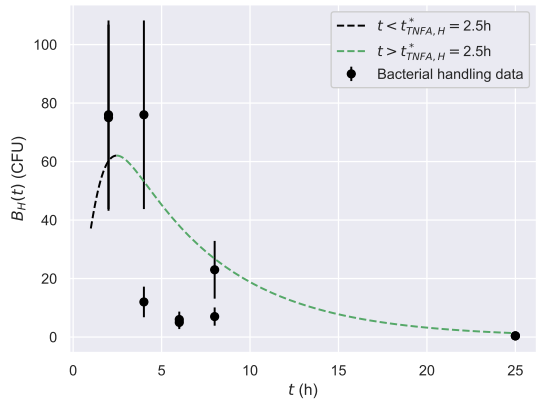


(TNFA.G.5)

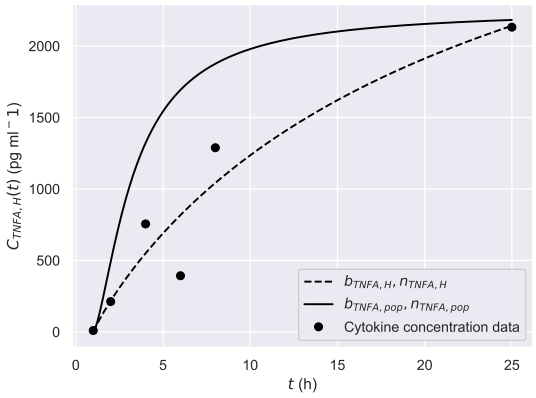


(TNFA.G.6)

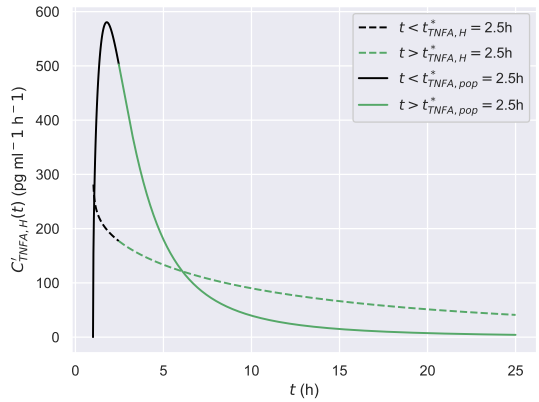
Figure 33: **(TNFA.G.1-6)** Experimental data (black dots) and model simulations for TNFα and Donor G, see Section 3.3.3. (Figure and legend continued on next page).



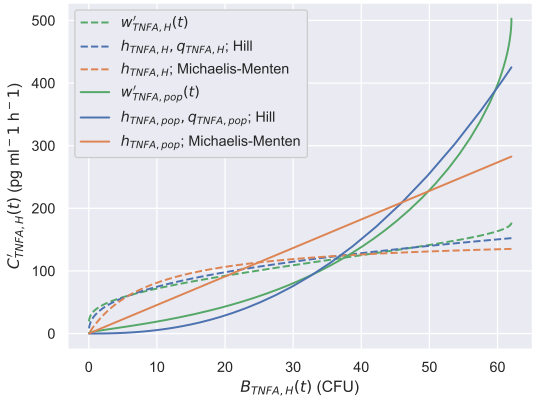
(TNFA.H.1)



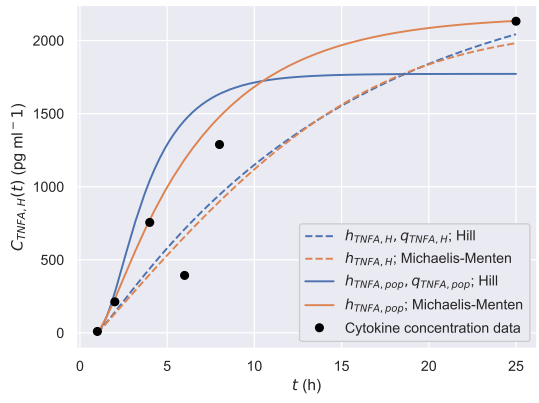
(TNFA.H.2)



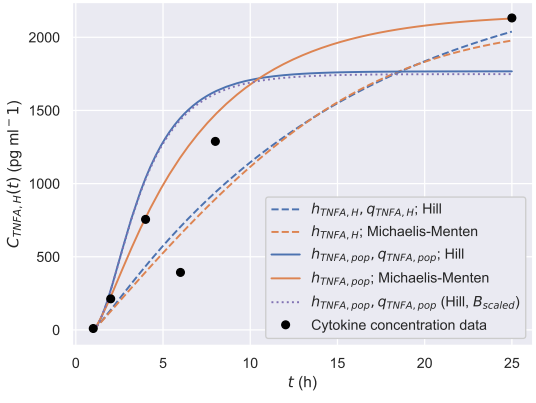
(TNFA.H.3)



(TNFA.H.4)



(TNFA.H.5)



(TNFA.H.6)

Figure 33: **(TNFA.H.1-6)** Experimental data (black dots) and model simulations for TNFα and Donor H, see Section 3.3.3. (Legend continued on next page).

Figure 33: Experimental data (black dots) and model simulations for cytokine $l \in \{$IL-1B, IL-6, TNFA$\}$ and MOI=10 (see for similar plots for IL-10 Figure 33, Section 3.3.3). Each subplot label **(I.i.1)** has three components, where $l \in \{$IL-10, IL-1B, IL-6, TNFA$\}$ corresponds to the cytokine, $i \in \{E, F, G, H\}$ to the donor, and the numbers 1-6 to the six different types of subplot as discussed below. Simulations of the bacterial load B_i (equation (3.13)) over time, with $g_{pop} = 1$ as before, and best fit parameters σ_i, τ_{pop}, and κ_{pop} (estimated by minimizing the negative log likelihood, see equation (3.2)). **(l.i.2)** The curve $w_{l,i}(t) = \frac{a_{l,i}(t-1)^{n_{l,i}}}{b_{l,i}+(t-1)^{n_{l,i}}}$ (equation (3.18)) fitted to the cytokine concentration data (using non-linear least squares), and **(l.i.3)** the derivative of $w_{l,i}(t)$, with donor-dependent (dashed lines), and independent (solid lines) values for $b_{l,i/pop}$ and $n_{l,i/pop}$, and $a_{l,i}$ always donor dependent. **(l.i.4)** The parametric curve $\phi_{l,i}(B_i(t))$, i.e. $w'_{l,i}(t)$ against $B_i(t)$ (equations (3.19) and (3.20)), for $t > t^*_{l,i/pop}$, where $t^*_{l,i/pop}$ is defined as the latest time point where either $B_i(t)$ or $w'_{l,i}(t)$ takes on its maximum value, with donor-dependent (green, dashed lines), and independent (green, solid lines) values for $b_{l,i/pop}$, $n_{l,i/pop}$, and $t^*_{l,i/pop}$, and $a_{l,i}$ always donor dependent. The cytokine production rate $f_{l,i}(B_i) = p_{l,i}\frac{(B_i)^{q_l}}{(h_l)^{q_l}+(B_i)^{q_l}}$ (equation (3.17)) fitted to $\phi_{l,i}(B_i(t))$, both for $q_{l,i/pop} = 1$ (orange, a Michaelis-Menten type production rate) and for $q_{l,i/pop} \neq 1$ (blue, a Hill-type production rate), and both with donor-dependent (dashed lines), and independent (solid lines) values for $b_{l,i/pop}$, $n_{l,i/pop}$, $t^*_{l,i/pop}$, $h_{l,i/pop}$, and $q_{l,i/pop}$, and with σ_i, $a_{l,i}$, $p_{l,i}$, $g_{pop}, \tau_{pop}, \kappa_{pop}$ always donor (in)dependent (using non-linear least squares, while fixing the previously estimated parameters used to generate the simulations of $\phi_{l,i}(B_i(t))$). **(l.i.5)** The cytokine concentration over time, with the cytokine production rate described by $f_{l,i}(B_i)$, and **(l.i.6)** with the cytokine production rate described by $\hat{f}_{l,i}(B_i, t) = (1 - e^{-z_l(t-1)})f_{l,i}(B_i)$ (equation (3.21)), both for $q_{l,i/pop} = 1$ (orange, a Michaelis-Menten type production rate) and for $q_{l,i/pop} \neq 1$ (blue, a Hill-type production rate), and both with donor-dependent (dashed lines), and independent (solid lines) values for $b_{l,i/pop}$, $n_{l,i/pop}$, $t^*_{l,i/pop}$, $h_{l,i/pop}$, $q_{l,i/pop}$ and $z_{l,i/pop}$, and with σ_i, $a_{l,i}$, $p_{l,i}$, $g_{pop}, \tau_{pop}, \kappa_{pop}$ always donor (in)dependent. The values of $z_{l,i/pop}$ were estimated by fitting $\hat{f}_{l,i}(B_i, t)$ to the cytokine concentration data using non-linear least squares, while assuming all previously estimated parameters were fixed. The cytokine concentration over time, with the cytokine production rate described by $\hat{f}_{l,i}(B_{scaled})$ (equation (3.23)), for $q_{l,pop} \neq 1$, with donor-independent values for $b_{l,pop}$, $n_{l,pop}$, $t^*_{l,pop}$, $h_{l,pop}$, $q_{l,pop}$, $z_{l,pop}$, g_{pop}, τ_{pop}, and κ_{pop}, and with donor dependent $a_{l,i}$ and $p_{l,i}$ (dotted, purple line). As before, the values of $a_{l,i}$, $b_{l,pop}$, and $n_{l,pop}$ were estimated by fitting $w_{l,i}(t)$ to the cytokine concentration data using non-linear least squares. The values of $p_{l,i}$, $h_{l,pop}$, and $q_{l,pop}$ were estimated by fitting $f_{l,i}(B_i)$ to $\phi_{l,i}(B_i(t))$ using non-linear least squares. Finally, the values of $z_{l,i/pop}$ were estimated by fitting $\hat{f}_{l,i}(B_i, t)$ to the cytokine concentration data using non-linear least squares, while assuming all previously estimated parameters were fixed.

Appendix B

We verify that when we let $N \to \infty$, M_{N+} goes to zero faster than N goes to infinity in equation (3.12), which was given by:

$$\frac{\mathrm{d}B_{mean}}{\mathrm{d}t} = gB_{mean} - gNM_{N+} - kB_{mean}.$$

We recall we assumed that the killing rate becomes larger than the bacterial growth rate for some $t^* > 0$, i.e. we assume there exists a $t^* > 0$ such that $k(t) > g$ for all $t > t^*$. We define

$$R_m = -mgM_m + (m+1)k(t)M_{m+1}, \qquad m \in \{0, \ldots, N-2\}, \tag{3.26}$$

$$R_{N-1} = -(N-1)gM_{N-1} + Nk(t)M_{N+}, \tag{3.27}$$

and rewrite equations (3.6)-(3.9) as:

$$\begin{aligned}
\frac{\mathrm{d}M_r}{\mathrm{d}t} &= R_r - R_{r-1}, \qquad m \in \{0, \ldots, N-2\}, && (3.28)\\
&\vdots \\
\frac{\mathrm{d}M_{N-2}}{\mathrm{d}t} &= R_{N-2} - R_{N-3}, && (3.29)\\
\frac{\mathrm{d}M_{N-1}}{\mathrm{d}t} &= R_{N-1} - R_{N-2}, \\
\frac{\mathrm{d}M_{N+}}{\mathrm{d}t} &= R_{N-1}.
\end{aligned}$$

We have

$$\frac{\mathrm{d}M_{N+}}{\mathrm{d}t} = (N-1)gM_{N-1} - Nk(t)M_{N+}. \tag{3.30}$$

With $\kappa(t) = \int_0^t k(s)\mathrm{d}s$, we can write:

$$\frac{\mathrm{d}}{\mathrm{d}t}(e^{N\kappa(t)}M_{N+}) = (N-1)ge^{N\kappa(t)}M_{N-1}. \tag{3.31}$$

It follows that

$$M_{N+} = M_{N+}(0)e^{-N\kappa(t)} + (N-1)g\int_0^t e^{(-N\kappa(t)+N\kappa(s))}M_{N-1}(s)\mathrm{d}s, \tag{3.32}$$

where we note that the first term on the right hand side of equation (3.32), $M_{N+}(0)e^{-N\kappa(t)}$, becomes exponentially small after finite time for $N \gg 1$. We further note that the second

term on the right hand side of equation (3.32) is a Laplace integral, i.e. an integral of the form

$$I(N) = \int_a^b f(s) e^{N\phi(s)} \mathrm{d}s, \tag{3.33}$$

with in this case $a = 0$, $b = t$, $f(s) = M_{N-1}(s)$, and $\phi(s) = -\kappa(t) + \kappa(s)$ [33, p. 258]. We will use Laplace's method to obtain the asymptotic behaviour of $I(N)$ as $N \to \infty$. We refer to [33, p. 261-272] for an introduction of Laplace's method. For a large value of N, we note that

$$e^{(-N\kappa(t)+N\kappa(s))} = e^{(-N\int_s^t k(p)\mathrm{d}p)} \tag{3.34}$$

is 1 for $s = t$ and small when $s < t - \mathrm{ord}(\frac{1}{N})$. We expand both $f(s)$ and $\phi(s)$ around t. The first two terms of the expansion of $\phi(s)$ around t are given by

$$\phi(s) = -\kappa(t) + \kappa(s) \approx -\kappa(t) + \kappa(t) + (s-t)\kappa'(t) = (s-t)\kappa'(t) = (s-t)k(t). \tag{3.35}$$

For $N \gg 1$, and $t \gg 1/N$, it follows that

$$I(N) = \int_0^t e^{(-N\kappa(t)+N\kappa(s))} M_{N-1}(s)\mathrm{d}s \tag{3.36}$$

$$\approx \left(M_{N-1}(t) \int_0^t e^{(N(s-t)k(t))} \mathrm{d}s \right) \{1 + \ldots\} \tag{3.37}$$

$$= \frac{M_{N-1}(t)}{Nk(t)} \left[1 + \mathcal{O}\left(\frac{1}{N}\right) \right], \tag{3.38}$$

where we have used that

$$\int_0^t e^{(-N(t-s)k(t))} \mathrm{d}s = \frac{1}{Nk(t)} [1 - e^{-Ntk(t)}]. \tag{3.39}$$

We note that $e^{-Ntk(t)}$ is exponentially small for $N \gg 1$, and $t \gg 1/N$. Inserting equation (3.38) into equation (3.32) gives

$$M_{N+} = \frac{N-1}{N} \frac{gM_{N-1}}{k(t)} \left[1 + \mathcal{O}\left(\frac{1}{N}\right) \right]. \tag{3.40}$$

Inserting equation (3.40) into equation (3.27) gives

$$R_{N-1} = -(N-1)gM_{N-1} + (N-1)gM_{N-1} \left[1 + \mathcal{O}\left(\frac{1}{N}\right) \right], \tag{3.41}$$

$$= (N-1)gM_{N-1} \left[\mathcal{O}\left(\frac{1}{N}\right) \right]. \tag{3.42}$$

It follows that:

$$R_{N-1} = (N-1)gM_{N-1}\mathcal{O}\left(\frac{1}{N}\right) =: (N-1)k(t)M_{N-1}h_{N-1}(t), \tag{3.43}$$

with $h_{N-1}(t) \sim \mathcal{O}\left(\frac{1}{N}\right)$. It follows that:

$$\frac{\mathrm{d}M_{N-1}}{\mathrm{d}t} = R_{N-1} - R_{N-2} =$$
$$(N-2)gM_{N-2} - (N-1)k(t)M_{N-1}(1-h_{N-1}(t)). \tag{3.44}$$

Then,

$$\frac{\mathrm{d}}{\mathrm{d}t}(e^{(N-1)K_{N-1}(t)}M_{N-1}) = (N-2)gM_{N-2}e^{(N-1)K_{N-1}(t)}, \tag{3.45}$$

with

$$K_{N-1}(t) = \kappa(t) - \int_0^t k(\bar{t})h_{N-1}(\bar{t})\mathrm{d}\bar{t} \sim \kappa(t) - \mathcal{O}\left(\frac{1}{N}\right). \tag{3.46}$$

Then, as previously,

$$M_{N-1}(t) = M_{N-1}(0)e^{-(N-1)K_{N-1}(t)}$$
$$+(N-2)g\int_0^t e^{(-(N-1)K_{N-1}(t)+(N-1)K_{N-1}(s))}M_{N-2}(s)\mathrm{d}s. \tag{3.47}$$

Using Laplace's method as before, it follows that, for $N \gg 1$, $t \gg 1/N$,

$$M_{N-1} = \frac{N-2}{N-1}\frac{g}{k(t)[1-h_{N-1}(t)]}M_{N-2}\left(1+\mathcal{O}\left(\frac{1}{N-1}\right)\right) =$$
$$\frac{N-2}{N-1}\frac{g}{k(t)}M_{N-2}\left(1+\mathcal{O}\left(\frac{1}{N}\right)\right), \tag{3.48}$$

noting $h_{N-1}(t) \sim \mathcal{O}\left(\frac{1}{N}\right) \sim \mathcal{O}\left(\frac{1}{N-1}\right)$. Now suppose

$$M_{N-r} = \frac{N-(r+1)}{N-r}\frac{g}{k(t)}M_{N-(r+1)}\left(1+\mathcal{O}\left(\frac{1}{N}\right)\right), \tag{3.49}$$

noting $\frac{1}{N-r} \sim \mathrm{ord}\left(\frac{1}{N}\right)$ for $r < N/2$ for example. Equation (3.49) is true for $r = 1$, as above (equation (3.48)). We also have

$$\frac{\mathrm{d}M_{N-(r+1)}}{\mathrm{d}t} = (N-(r+1))gM_{N-(r+1)(t)})\mathcal{O}\left(\frac{1}{N}\right) - R_{N-(r+2)} =$$
$$(N-(r+1))k(t)M_{N-(r+1)h_{N-(r+1)}(t)} - R_{N-(r+2)} =$$
$$(N-(r+2))gM_{N-(r+2)} - (N-(r+1))k(t)M_{N-(r+1)}(1-h_{N-(r+1)}(t)), \tag{3.50}$$
$$\tag{3.51}$$

with $h_{N-(r+1)}(t) \sim \mathcal{O}\left(\frac{1}{N}\right)$. As above,

$$M_{N-(r+1)}(t) =$$

$$M_{N-(r+1)}(0)e^{-(N-(r+1))K_{N-(r+1)}}$$

$$+(N-(r+2))g\int_0^t e^{(-(N-(r+1))K_{N-(r+1)}(t)+(N-(r+1))K_{N-(r+1)}(s))}M_{N-(r+2)}(s)\mathrm{d}s, \quad (3.52)$$

with

$$K_{N-(r+1)}(t) = \kappa(t) - \int_0^t k(\bar{t})h_{N-(r+1)}(\bar{t})\mathrm{d}\bar{t} \sim \kappa(t) - \mathcal{O}\left(\frac{1}{N}\right). \quad (3.53)$$

Using Laplace's method as before, it follows that, for $N \gg 1$, $t \gg 1/N$,

$$M_{N-(r+1)}(t) = \frac{N-(r+2)}{N-(r+1)}\frac{g}{k(t)}M_{N-(r+2)}\left(1+\mathcal{O}\left(\frac{1}{N}\right)\right), \quad (3.54)$$

proving the inductive step, providing $N-(r+2) \sim \mathrm{ord}\,(N)$, which holds when $r < N/2$. Hence,

$$M_{N+} = \left(\frac{(N-1)}{N}\right)\left(\frac{g}{k(t)}\right)M_{N-1}\left(1+\mathcal{O}\left(\frac{1}{N}\right)\right) =$$

$$\left(\frac{N-1}{N}\right)\left(\frac{N-2}{N-1}\right)\cdots\left(\frac{N-(s-1)}{N-(s-2)}\right)\left(\frac{N-s}{N-(s-1)}\right)\left(\frac{g}{k(t)}\right)^s M_{N-s}\left(1+\mathcal{O}\left(\frac{1}{N}\right)\right)^s =$$

$$\frac{N-s}{N}\left(\frac{g}{k(t)}\right)^s M_{N-s}\left(1+\mathcal{O}\left(\frac{1}{N}\right)\right)^s, \quad (3.55)$$

providing $s < N/2$. Let s be the smallest integer larger than $\sqrt{N}$, then $s \ll N/2$, $s > \sqrt{N}$ by definition, and $s \leq \sqrt{N}+1$. We can bound $\left(1+\mathcal{O}\left(\frac{1}{N}\right)\right)^s$ by $\left(1+\frac{a}{N}\right)^s$ for some a of $\mathcal{O}(1)$. As $\log(1+x) < x$ for all $x > 0$, we have

$$\left(1+\mathcal{O}\left(\frac{1}{N}\right)\right)^s < \left(1+\frac{a}{N}\right)^s =$$

$$e^{s\log 1+a/N} < e^{sa/N} \approx e^{a/\sqrt{N}} \approx 1+\mathcal{O}\left(\frac{1}{\sqrt{N}}\right) < 2. \quad (3.56)$$

Further, because we assumed there exists a t^* such that $\frac{g}{k(t)} < 1$ for all $t > t^*$, we have $\log\left(g/k(t)\right) = -\beta < 0$ for all $t > t^*$. Then

$$\left(\frac{g}{k(t)}\right)^{\sqrt{N}} = e^{-\beta\sqrt{N}}. \quad (3.57)$$

It follows from equations (3.55)-(3.57), and $M_{N-s} \leq \sum_n M_n = 1$, that

$$NM_{N+1} < 2N\left(\frac{g}{k}\right)^{\sqrt{N}} = 2Ne^{-\beta\sqrt{N}} \to 0, \qquad \text{as } N \to \infty. \quad (3.58)$$

Hence, we have confirmed that M_N+ goes to zero geometrically as N increases, and thus much faster than N goes to infinity.

Chapter 4

A bacterial load-structured model of granuloma formation

After having studied the role of macrophages in inflammatory bowel disease (IBD) at the signalling (Chapter 2) and cellular scale (Chapter 3), we will now focus on granuloma formation. Granuloma formation is of special interest as it involves both impaired bacterial clearance and inflammatory cytokine production in macrophages, the focus of our former two chapters. We develop a bacterial-load structured model and conduct an initial study comparing CD and intestinal Mycobacterium tuberculosis granuloma. We also consider the impact of fusion in this context.

4.1 Introduction

Granuloma are dynamic structures of clustered macrophages and sometimes other immune cells, thought to form as a response to persistent stimuli, such as pathogens or foreign bodies that could not be cleared effectively by individual macrophages. Granuloma have a protective function by restricting pathogen spread, but can also facilitate long-term intracellular pathogen survival [257]. Various types of granuloma can form in different parts of the body. *Mycobacterium tuberculosis* (TB) granuloma in the lung for instance consist of several T cell subsets and multiple populations of differentiated macrophages, such as epithelioid macrophages and foam cells. TB granuloma do often contain a necrotic core, consisting of dead macrophages that burst due to intracellular bacterial overload [288]. Granuloma in response to a foreign body such as silica particles or tattoo pigments in the skin or lymph nodes do not contain T cells and are usually not necrotic [257]. The intestinal

granuloma found in the immunodeficiency syndrome chronic granulomatous disease (CGD) are generally large, non necrotic and often do not contain living infectious agents (anymore) [185, 298, 299]. The time-scale of granuloma degradation might therefore be much larger than that of bacterial clearance in CGD. The granuloma associated with Crohn's disease (CD) are still poorly understood. One of the causative species of CD granuloma might be adherent-invasive *Escherichia coli* (AIEC), a bacterial species highly associated with CD [79, 225]. Other pathogens implicated in CD granuloma formation include *Listeria monocytogenes* and *Streptococcus* spp. [203].

In the context of this thesis, we are primarily concerned with granuloma found in the gut, such as CD and intestinal *Mycobacterium tuberculosis* (TB) granuloma. Although most commonly observed in the lung, TB can be found in other organs too, such as the joints, bone, meninges or the gastrointestinal tract [80]. Intestinal TB (iTB) is mainly prevalent in the developing world [12]. Distinguishing iTB from Crohn's disease (CD) is difficult and misdiagnosis can have severe consequences [174]. The incidence rise of CD in the developing world comes with an increased the risk of misdiagnosis. Both diseases can present with granuloma, with different features that can help distinguish between the two [278]. Granuloma displaying necrosis (also called caseation) are unique to iTB and a decisive criterion in iTB diagnosis. Further, iTB granuloma are generally larger than CD granuloma (diameter approximately twice as large) [278]. It is known that adaptive immunity plays an important role in TB. Macrophages activated by T cell produced IFNγ are much more effective in killing *Mycobacterium tuberculosis* [288]. In line with this, iTB granuloma are usually surrounded by a cuff of lymphocytes (e.g. T cells), but this is not the case for CD [12, 198, 332]. This suggests that macrophage mediated killing of the causative agents in CD granuloma is less dependent on adaptive immunity than in iTB granuloma.

In this chapter we construct a mechanistic model to study what factors and cellular processes drive granuloma formation. Our model is applicable to all granuloma formed in response to an intracellular pathogen, such as *Mycobacterium tuberculosis*, *Salmonella* or *E. coli* [177, 210, 225, 270]. We note that as our model does not consider adaptive immune responses or spatial heterogeneity, it is not suitable to describe granuloma dynamics depending on such features. We represent granuloma formation with a model that considers the

dynamics of pathogen load in a manner analogous to age structured models, to describe the granuloma size and distribution of infection over time. Due to the structure of our model, we do not consider granuloma formation in response to a larger agent, such as a parasitic worm, egg or medical implant. Similarly, the model is not suitable to study granuloma without a known antigenic trigger, such as sarcoid granuloma [257]. Our bacterial-load structured model has been inspired by a lipid structured model of macrophages in a study on the formation of atherosclerotic plaques, and by the larger body of literature on age and size-structured models [74, 75, 104, 229]. The use of pathogen load as an internal structuring variable is a novel approach in mechanistic granuloma modelling. The distribution of infection is of special interest, as the net growth rate of the bacteria, but also cell signalling and macrophage death, might be dependent on the bacterial load of the macrophage. We note that the internal structuring variable (e.g. age or size) of modelled entities (e.g. individuals or cells) in structured population models is usually assumed to be increasing over time [18]. In our model, the bacterial load of a macrophage can also decrease due to intra-cellular pathogen killing.

Several other types of mathematical models studying granuloma dynamics can be found in the literature, including ABMs [177], a spatial partial differential equation (PDE) model [137] and a Petri net model [10].

A key feature of macrophages within a granuloma is their ability to fuse, resulting in MGC formation [145]. Fused macrophages might be better at degrading large particles [190, 239, 245, 257, 300]. We have implemented cell fusion as non-local source and sink terms in our model. The inclusion of terms of this specific form in a population structured model are of interest as they have not been studied before. Furthermore, fusion has not yet been considered in existing models of granuloma formation (e.g. the agent-based models by the group of Denise Kirschner [177]).

We will verify our model against one of the agent-based models developed by the group of Denise Kirschner [63]. The comparison with the agent-based model allows us to investigate our model behaviour within a biologically realistic parameter range. Furthermore, we investigate to what extent our model could replicate the dynamics of the much more complex agent-based model.

We parametrise our model to represent an *in vitro* model suitable to test model predictions in future studies. We will base our model parametrisation on an *in vitro* model developed by the group of Frédéric Altare [190, 225, 269, 275, 276]. We will use this parametrisation to conduct an initial study into the difference between the granuloma found in CD and in intestinal TB (iTB), and investigate the impact of fusion in this context.

4.1.1 Aims, research questions, and novelty

The main aim of this chapter is to develop a model of granuloma formation. As part of this aim, we will investigate the various model features, and verify the model against an agent-based model from the literature. The secondary aim of the chapter is to use our model to conduct an initial study into the difference between the intestinal granuloma found in CD and in intestinal TB (iTB), and investigate the impact of macrophage fusion in this context. Our research questions are as follows: what is the impact of the various model features, including macrophage recruitment, extra- and intracellular pathogen growth, pathogen killing by macrophages, and macrophage fusion, on the dynamics of the bacterial-load structured model; how do our model dynamics compare to the dynamics of GranSim, an agent-based model from the literature; and in what situations could our model be used instead of the much more complex agent-based model; what is the difference in the model dynamics when parametrised to represent granuloma found in CD and in iTB respectively; and what is the impact of macrophage fusion in this context?

The use of pathogen load as an internal structuring variable is a novel approach in mechanistic granuloma modelling. Our model is easier to analyse and less computationally expensive than existing agent-based models of granuloma formation. We have implemented cell fusion as non-local source and sink terms in our model. The inclusion of terms of this specific form in a population structured model are of interest as they have not been studied before. Furthermore, fusion has not yet been considered in existing models of granuloma formation. Finally, no existing mathematical modelling studies have focussed explicitly on granulomas found in the gut.

4.1.2 Structure

The chapter is structured as follows. We first introduce our model. We will then describe how our model equations can be related to underlying stochastic interactions between bacteria and individual macrophages. We will study how varying the model parameters results in different model outcomes. We then compare our model with one of the agent-based models by the group of Denise Kirschner on granuloma formation in the lung. Finally, we parametrise our model to represent an *in vitro* model of CD and iTB type granuloma, and discuss their differences and the impact of fusion. We end with a discussion.

4.2 Model statement

In this section, we will introduce our model equations that describe the granuloma size and distribution of infection, and the population of extracellular bacteria over time. We assume a granuloma consists of a macrophages, each with a certain bacterial load. We will not consider other cells types. When the level of infection within a macrophage reaches a certain level, the macrophage bursts and releases its bacterial contents to the extracellular environment. The total mass of the granuloma is given by $G(t)$ and the total bacterial load of the granuloma is given by $B(t)$. We will introduce expressions for $G(t)$ and $B(t)$ below. Units of mass used are the average mass of a bacterium (β) and macrophage (μ). Units of time used are 10 minutes (θ). For each macrophage within the granuloma, we define the level of infection b as the ratio of bacterial mass to macrophage mass, with units β/μ. We will use b as an internal structuring variable. We let b range from 0 (no infection) to b_{burst}, the bacterial mass density at which a macrophage bursts due to infection overload. We note we have chosen to describe the total granuloma size in terms of mass, rather than macrophage numbers. Given we assume each macrophage has the same mass ($\tilde{\mu}$), then $G(t)/\tilde{\mu}$ gives the total number of macrophages within the granuloma. The reason why we have chosen to use macrophage mass rather than numbers to describe the granuloma size is that it enables the constraint of mass conversation during the process of fusion to be readily captured. Briefly, in our model, when two macrophages of mass μ with bacterial load b_1 and b_2 fuse, they produce a single macrophage of mass 2μ with bacterial load $(b_1+b_2)/2$. Hence, macrophage

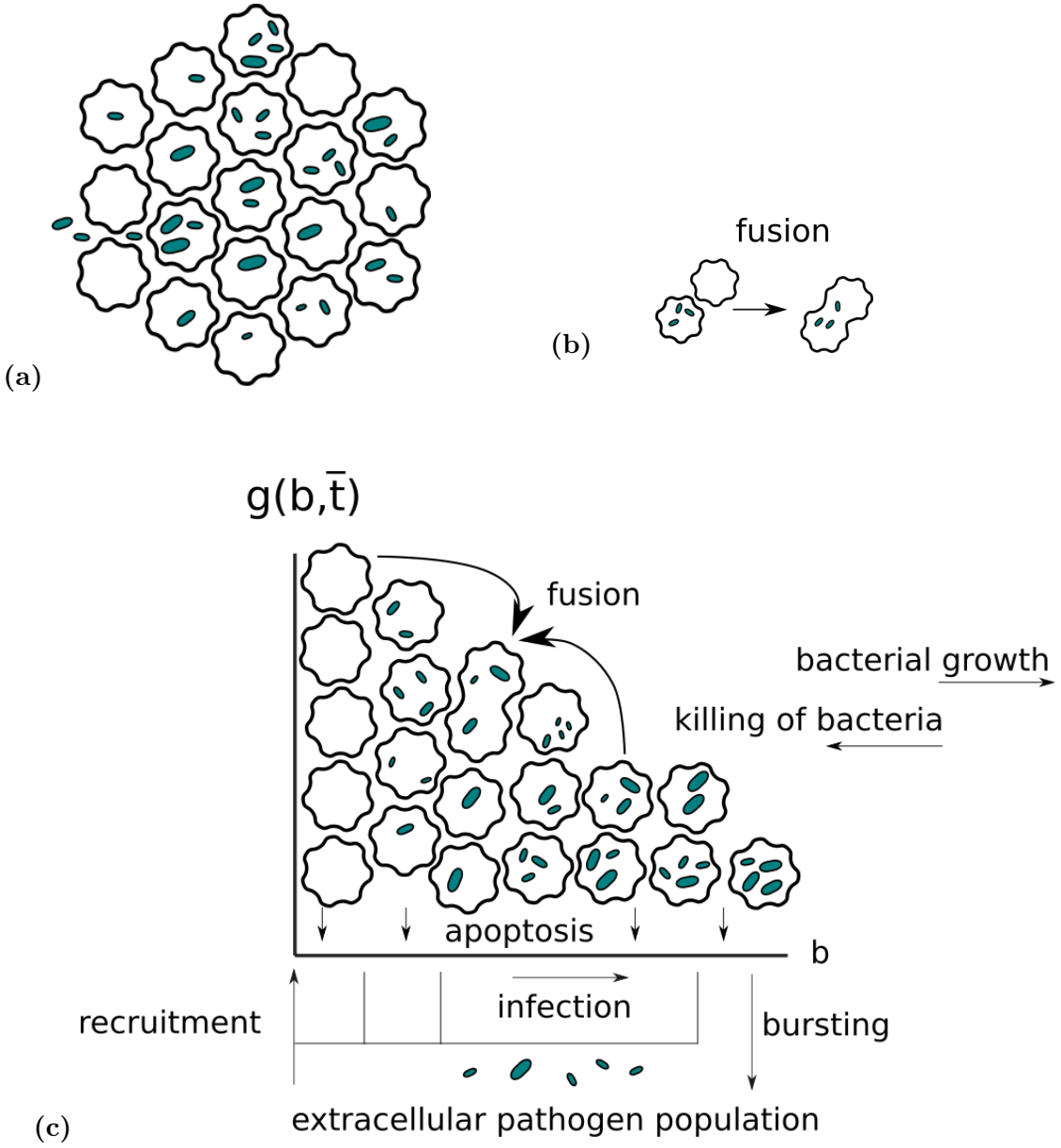


Figure 1: **(a)** A graphical representation of the spatial structure of a granuloma (cross section), consisting of macrophages (white), and bacteria (green). **(b)** Fusion events do not alter mass or bacterial load of the total granuloma. **(c)** A graphical summary of our bacterial load structured model for a fixed moment in time $t = \bar{t}$, with the bacterial mass density b on the horizontal axis and $g(b, \bar{t})$ on the vertical axis. Arrows indicate various model features that alter $g(b, t)$ over time. The model assumes a continuous distribution of bacterial load. We show individual macrophages for illustrative purposes. Space is not considered in our model.

fusion has no impact on the total granuloma size G (described in terms of macrophage mass) or total load of infection B (described in terms of bacterial mass). We note that if we would have used macrophage numbers to describe the granuloma size instead, the granuloma size would have shrunk every time two macrophages fuse. Proceeding, note we also describe the level of infection b as a ratio of bacterial mass to macrophage mass, rather than the absolute value of bacterial mass within each macrophage. The underlying motivation here is that a larger macrophage contains more lysosomes and other cell organelles used for particle clearance. Therefore, we assume the clearance capability of a certain amount of particle or pathogen mass is proportional to the mass of each macrophage. As observed above, macrophage fusion of two equal mass macrophages with bacterial load b_1 and b_2 will entail the level of infection of the resulting macrophage to $(b_1 + b_2)/2$ under these assumptions. Finally, note we have chosen to describe the total pathogen (or non-living particle) load in terms of mass, rather than pathogen (or particle) numbers. An underlying motivation is that we assume that the ability of a macrophage to clear a specific bacteria (or non-living particle) is proportional to the mass of this bacteria (or particle) relative to the macrophage mass, and that the specific number of bacteria (or particles) is less relevant. Finally, we assume the bacterial mass of a growing population of bacteria may be treated as continuous, requiring relatively large numbers of sufficiently small bacteria.

We now introduce our model equations. For Δb sufficiently small, let $g(b,t)\Delta b + \mathrm{o}(\Delta b)$ denote the mass of macrophages in the granuloma for which b is in the interval $[b, b+\Delta b]$. Then, the total mass of the granuloma is given by

$$G(t) = \int_0^{b_{\text{burst}}} g(b,t)db. \tag{4.1}$$

The total mass of all bacteria within the granuloma is given by

$$B(t) = \int_0^{b_{\text{burst}}} bg(b,t)db. \tag{4.2}$$

The dimensional model is given by

$$\frac{\partial g(b,t)}{\partial t} + \frac{\partial}{\partial b}\left\{g(b,t)[Z(b,t) + uE(t)]\right\} = \\ - A(g(b,t)) - F(g(b,t)) + F'(g(b,t)), \qquad \text{for } t > 0, b \in (0, b_{\text{burst}}), \tag{4.3}$$

$$g(b,0) = 0, \qquad \text{for } b > 0, \tag{4.4}$$

$$g(0,t) = R(E(t), B(t)), \qquad \text{for } t \geq 0, \tag{4.5}$$

$$\frac{\mathrm{d}E(t)}{\mathrm{d}t} = \Xi(E(t)) + b_{\text{burst}} g(b_{\text{burst}}, t)[Z(b_{\text{burst}}, t) + uE(t)] - uE(t)G(t), \tag{4.6}$$

$$E(0) = E_0, \tag{4.7}$$

with $E(t)$ the extracellular bacterial load, $Z(b,t)$ the local rate of change in bacterial mass density per unit macrophage mass due to bacterial growth and killing by the macrophages and $uE(t)$ the rate of bacterial uptake per unit mass of the macrophages (phagocytosis). Further, $A(g(b,t))$ describes the rate of macrophage apoptosis and $F(g(b,t))$ and $F'(g(b,t))$ macrophage fusion, which are non-local, non-linear functionals of $g(b,t)$ that capture the dynamics of fusion. $\Xi(E)$ is the rate of extracellular bacterial growth and $R(E(t), B(t))$ represents cell recruitment. We will discuss the type of this boundary condition (i.e. a Dirichlet instead of Neumann boundary condition) in Section 4.2.1. No infected macrophages are present at $t = 0$, so that $B(0) = G(0) = 0$ and $E(0) = E_0 > 0$ is the initial extracellular bacterial load. Macrophages burst due to bacterial overload at $b = b_{\text{burst}}$ bacteria per macrophage. We will only consider forms of $Z(b,t)$ such that $[Z(b_{\text{burst}}, t) + uE(t)] \geq 0$ and $Z(0,t) = 0$ for all $t > 0$. The condition $[Z(b_{\text{burst}}, t) + uE(t)] \geq 0$ for all t ensures that macrophages that have burst do not re-enter the granuloma. The condition $Z(0,t) = 0$ for all t ensures that no macrophages will ever attain a negative bacterial load. We further note that because $g(b,0) = 0$ for all $b > 0$, but $g(0,0) = R(E(0), B(0))$, we have a discontinuity at $t = 0, b = 0$, and along the associated characteristic passing through $(0,0)$ (except in the trivial case $R(E(0), B(0)) = 0$). Note that hyperbolic PDEs support discontinuities (shocks), so that the model is well-posed. We note that the assumption that macrophages burst once bacteria mass hits a fixed proportion of macrophage mass is a simplification. In reality macrophages burst at varying levels of bacterial infection. The distribution of the load at which a *Francisella tularensis* infected macrophage bursts was studied in [53, 120]. We have chosen a fixed bacterial load at which a macrophage bursts for simplicity, and because the agent-based model GranSim we later compare our model to, also assumes a fixed bacterial load at which a macrophage bursts [63]. We show a graphical summary of our model in Figure 1(a). We do not consider space in our model (Figure 1(b)). The units

	Units	Description
b	β/μ	Bacterial mass density
b_{burst}	β/μ	Bacterial mass density at which a macrophage bursts
p	β/μ	Intracellular carrying capacity
q	β/μ	Killing saturation constant
$g(b,t)$	μ^2/β	Macrophage mass divided by bacterial mass density
R	μ^2/β	Recruitment term
c	μ^2/β	Constant recruitment parameter
$G(t)$	μ	Total macrophage mass within granuloma
$B(t)$	β	Total intracellular bacterial load
$E(t)$	β	Total extracellular bacterial load
E_0	β	Initial extracellular bacterial loads
ψ	β	Extracellular carrying capacity
$\Xi(E)$	β/θ	Extracellular growth term
$Z(b,t)$	$\beta/(\mu\theta)$	Intracellular growth and killing term
$k(t)$	$\beta/(\mu\theta)$	Killing term
κ	$\beta/(\mu\theta)$	Maximum killing rate
$F(g)$	$\mu^2/(\beta\theta)$	Fusion sink term
$F'(g)$	$\mu^2/(\beta\theta)$	Fusion source term
$A(g)$	$\mu^2/(\beta\theta)$	Apoptosis term
α	$1/\theta$	Apoptosis rate
λ	$1/\theta$	Maximum intracellular growth rate
ζ	$1/\theta$	Maximum extracellular growth rate
η	$1/(\mu\theta)$	Fusion rate
u	$1/(\mu\theta)$	Uptake rate
w	μ^2/β^2	Recruitment rate parameter
v	$1/\beta$	Intracellular bacterial load driven recruitment parameter

Table 4.1: Units and a description of all model variables, parameters and functionals, with β the average mass of a bacterium, μ the average mass of a recruited macrophage, and θ ten minutes.

of all model variables and parameters are listed in Table 4.1. We recall that units of mass used are the average mass of a bacterium (β) and recruited macrophage (μ). Units of time used are 10 minutes (θ).

We will discuss the biological terms, $R(E(t), B(t)), Z(b,t), \Xi(E), A(g(b,t)), F(g(b,t))$ and $F'(g(b,t))$ in turn.

4.2.1 Recruitment: $R(E(t), B(t))$

We consider the growth of the granuloma due to cell recruitment. Integrating equation (4.3) with respect to b gives an expression for the total granuloma size over time:

$$\frac{\mathrm{d}G(t)}{\mathrm{d}t} = uR(E(t), B(t))E(t) - g(b_{\text{burst}}, t)\left[Z(b_{\text{burst}}, t) + uE(t)\right] - \int_0^{b_{\text{burst}}} A(g(b,t)) - F(g(b,t)) + F'(g(b,t))db, \quad (4.8)$$

with u the uptake rate per unit of macrophage mass (with units $1/(\mu\theta)$). Thus, the growth rate of $G(t)$ due to recruitment is given by $uR(E(t), B(t))E(t)$. We can interpret $uR(E(t), B(t))$ as the mass of freshly recruited macrophages infected per unit of time per unit mass of extracellular bacterium. We will discuss the form of $R(E(t), B(t))$. Firstly, it is proportional to $E(t)$, as motivated by the following. The presence of the extracellular bacterial population $E(t)$ is sensed by pathogen recognition receptors (PRRs) and triggers pro-inflammatory cytokine secretion. This in turn leads to recruitment of macrophage precursors (monocytes) from the blood. We assume all monocytes turn into macrophages after recruitment. We further assume that the inflammatory recruitment response (e.g. the amount of cytokine secretion) is amplified by the intracellular bacterial load $B(t)$, as intracellular bacteria increase macrophage activation. We will therefore assume that the mass of freshly recruited macrophages infected per unit of time per extracellular bacterium is given by:

$$uR := uwE(t)(1 + vB(t)), \quad (4.9)$$

where the constants $w \geq 0$ and $v \geq 0$ scale the respective contribution of $E(t)$ and $B(t)$ to the recruitment term. Note that all recruited macrophages are uninfected. Finally, we note that the Dirichlet boundary condition, $g(0, t) = R(E(t), B(t))$ at $b = 0$, is required for macrophage mass balance when we integrate equation (4.3) with respect to b. This is the reason we have imposed a Dirichlet, rather than a Neumann boundary condition at $b = 0$ in our model equations (4.3)-(4.7).

4.2.2 Bacterial growth: $Z(b,t)$ and $\Xi(E)$

We assume saturating extracellular bacterial growth, i.e. the bacterial load will not grow indefinitely, for instance due to a lack of resources, and this is modelled via logistic saturation [53]. The intra-cellular killing is also assumed to saturate for increasing bacterial load and is modelled by saturation kinetics [229]. $Z(b,t)$ and $\Xi(E)$ are then given by:

$$Z(b,t) := \lambda b\left(1-\frac{b}{p}\right)-b\left(\frac{k(t)}{q+b}\right), \tag{4.10}$$

$$\Xi(E) := \zeta E\left(1-\frac{E}{\psi}\right). \tag{4.11}$$

In particular the time dependence in the intracellular kiling term, $k(t)$, models various levels of macrophage activation. Intracellular killing might for instance be amplified after an adaptive immune response has been initiated, such as the case in *Mycobacterium tuberculosis* infection [288]. We also observe increasing killing rates on a shorter time span (hours instead of weeks), such as in *in vitro* infection studies of *E. Coli*, and our own *Salmonella* infection experiments [87] (see Chapter 3). When k is time-independent in a model simulation, we will use $k := \kappa$.

4.2.3 Apoptosis: $A(g(b,t))$

We take the apoptosis rate of the macrophages, denoted α below, constant and independent of the bacterial load,

$$A := \alpha g(b,t). \tag{4.12}$$

During apoptosis, the intracellular bacteria contained within that macrophage die as well. Apoptotic cell death can therefore prevent the survival and spread of intracellular pathogens [247]. In contrast, during necrotic death due to bacterial overload at $b = b_{\text{burst}}$, the intracellular bacteria spread [31].

4.2.4 Fusion: $F(g(b,t))$ and $F'(g(b,t))$

Fusion will lead to redistribution of the bacterial load by diluting the bacterial load per unit macrophage mass of the most laden macrophages. To consider fusion, we use a law of mass action for the fusion of a macrophage with internal pathogen mass b per unit macrophage mass. This may fuse with other macrophages. Noting the well-mixed spatially homogeneous

assumption, and the law of mass action, the number of macrophages it can potentially fuse with, of internal pathogen mass per unit macrophage mass in the interval $[b', b' + \Delta b']$, is given by $g(b', t)\Delta b'$. Thus the reaction (see also Figure 1(c))

$$b + b'_* \xrightarrow{\eta} \frac{b + b'_*}{2}, \tag{4.13}$$

with $b'_* \in [b', b' + \Delta b']$, the law of mass action loss of macrophages with internal pathogen mass per unit macrophage is given by

$$\eta g(b, t)g(b', t)\Delta b' + o(\Delta b'). \tag{4.14}$$

Noting η is assumed to be constant, summing such terms across all intervals required for a partition of $b' \in [0, b_{\text{burst}}]$, and taking standard integration limits, gives

$$F(g(b, t)) = \eta \int_0^{b_{\text{burst}}} g(b, t)g(b', t)db' = \eta g(b, t)G(t). \tag{4.15}$$

The fusion source term F' is given by:

$$F'(g(\bar{b}, t)) = 2\eta \int_{\max(0, 2\bar{b} - b_{\text{burst}})}^{\min(2\bar{b}, b_{\text{burst}})} g(2\bar{b} - b', t)g(b', t)db', \tag{4.16}$$

where the integrand in equation (4.16) can be deduced from the observation that when $b = 2\bar{b} - b'$, we have $\bar{b} = (b + b')/2$ so that $\bar{b}$ is the bacterial mass of the fused macrophage, with the limits following from the constraint $b = 2\bar{b} - b' \in (0, b_{\text{burst}})$. We note that F and F' balance each other out, as required by mass conservation, when we integrate equation (4.3) with respect to b, noting the change of limits depicted in Figure 2:

$$\begin{aligned}\int_0^{b_{\text{burst}}} F'(\bar{b}, t)d\bar{b} = \\ 2\eta \int_0^{b_{\text{burst}}} \int_{\frac{1}{2}b'}^{\frac{1}{2}b_{\text{burst}} + \frac{1}{2}b'} g(2\bar{b} - b', t)g(b', t)d\bar{b}db' = \\ \eta \int_0^{b_{\text{burst}}} \int_0^{b_{\text{burst}}} g(\tilde{b}, t)g(b', t)d\tilde{b}db' = \\ \int_0^{b_{\text{burst}}} F(b, t)db,\end{aligned} \tag{4.17}$$

with $\tilde{b} = 2\bar{b} - b'$ and F and F' defined in equations (4.15) and (4.16) respectively. Similarly, we can multiply equation (4.3) with b and then integrate with respect to b to confirm

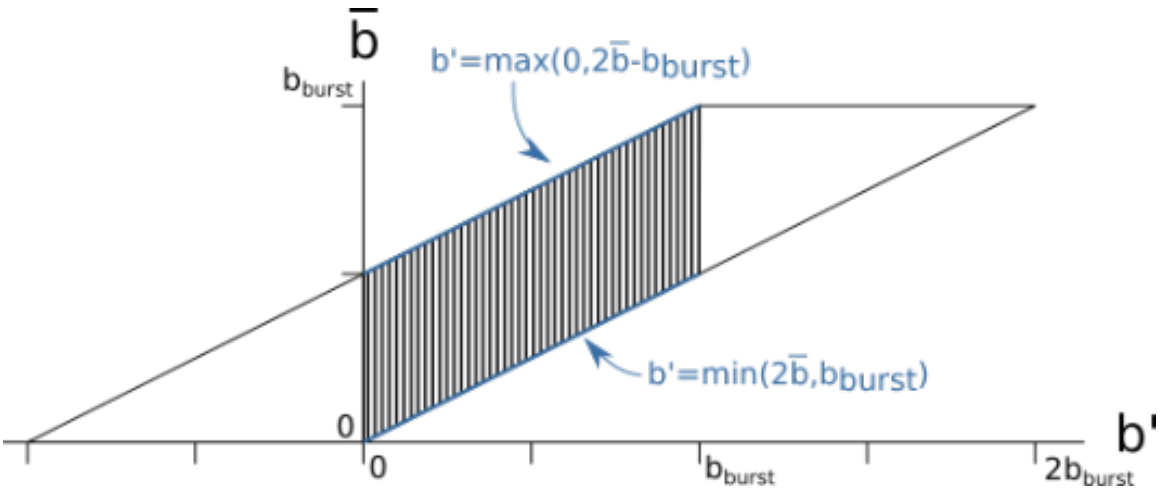


Figure 2: The integration domain of $\int_0^{b_{\text{burst}}} F'(\bar{b},t)d\bar{b} = 2\eta \int_0^{b_{\text{burst}}} \int_{\max(0,2\bar{b}-b_{\text{burst}})}^{\min(2\bar{b},b_{\text{burst}})} g(2\bar{b}-b',t)g(b',t)db'd\bar{b}$ (striped surface).

pathogen mass is conserved during fusion:

$$\int_0^{b_{\text{burst}}} bF'(\bar{b},t)d\bar{b} = \frac{\eta}{2}\int_0^{b_{\text{burst}}}\int_0^{b_{\text{burst}}} b'g(\tilde{b},t)g(b',t)d\tilde{b}db' + \frac{\eta}{2}\int_0^{b_{\text{burst}}}\int_0^{b_{\text{burst}}} \tilde{b}g(\tilde{b},t)g(b',t)d\tilde{b}db' = \int_0^{b_{\text{burst}}} bF(b,t)db, \quad (4.18)$$

again with $\tilde{b} = 2\bar{b} - b'$.

4.2.5 Full system

The full system is given by

$$\frac{\partial g(b,t)}{\partial t} + \frac{\partial}{\partial b}\left\{g(b,t)\left[\lambda b\left(1-\frac{b}{p}\right) - b\left(\frac{k(t)}{q+b}\right) + uE(t)\right]\right\} = -\alpha g(b,t) - \eta g(b,t)G(t) + 2\eta\int_{\max(0,2b-b_{\text{burst}})}^{\min(2b,b_{\text{burst}})} g(2b-b',t)g(b',t)db', \quad (4.19)$$

$$\frac{\mathrm{d}E(t)}{\mathrm{d}t} = \zeta E(t)\left(1-\frac{E(t)}{\psi}\right) + b_{\text{burst}}g(b_{\text{burst}},t)\left[\lambda b_{\text{burst}}\left(1-\frac{b_{\text{burst}}}{p}\right) - b_{\text{burst}}\left(\frac{k(t)}{q+b_{\text{burst}}}\right) + uE(t)\right] - uE(t)G(t), \quad (4.20)$$

$$g(b,0) = 0, \qquad b > 0, \tag{4.21}$$

$$g(0,t) = wE(t)(1+vB(t)), \tag{4.22}$$

$$E(0) = E_0, \tag{4.23}$$

with the dimensions of all variables and parameters listed in Table 4.1.

Integrating equation (4.19) with respect to b gives an expression for the total granuloma size over time:

$$\begin{aligned}\frac{\mathrm{d}G(t)}{\mathrm{d}t} &= uw(1+vB(t))E^2(t) \\ &\quad - g(b_{\text{burst}},t)\left[\lambda b_{\text{burst}}\left(1-\frac{b_{\text{burst}}}{p}\right) - b_{\text{burst}}\left(\frac{k(t)}{q+b_{\text{burst}}}\right) + uE(t)\right] \\ &\quad - \alpha G(t).\end{aligned} \tag{4.24}$$

Similarly, integrating equation (4.19) after multiplying by b gives us an expression for the total intracellular bacterial load over time:

$$\begin{aligned}\frac{\mathrm{d}B(t)}{\mathrm{d}t} &= \int_0^{b_{\text{burst}}} g(b,t)\left[\lambda b\left(1-\frac{b}{p}\right) - b\left(\frac{k(t)}{q+b}\right) + uE(t)\right]db - \alpha B(t) \\ &\quad - b_{\text{burst}}g(b_{\text{burst}},t)\left[\lambda b_{\text{burst}}\left(1-\frac{b_{\text{burst}}}{p}\right) - b_{\text{burst}}\left(\frac{k(t)}{q+b_{\text{burst}}}\right) + uE(t)\right].\end{aligned} \tag{4.25}$$

Note that the killing of bacteria by macrophages lowers the total intracellular bacterial load, but not the total granuloma size. Macrophages are only removed from the granuloma via bursting or apoptosis.

4.2.6 Characteristics

We will use a characteristic based method to solve our system (4.19)-(4.23). The method of characteristics was introduced in Section 1.3.6. We recall that in Section 1.3.6 we introduced the example problem (equations (1.52)-(1.54)):

$$g_t(b,t) + Q(b,t)g_b = W(b,g,t), \qquad b>0, t>0 \tag{4.26}$$

$$g(b,0) = 0, \qquad b>0, t=0 \tag{4.27}$$

$$g(0,t) = g_{\text{boundary}}(t), \qquad t>0, b=0 \tag{4.28}$$

with $Q(b,t)$, $W(b,g,t)$ known functions of $b,t \geq 0$, and $b,g,t \geq 0$. With $t^\star$ parametrising the boundary data, and thus labelling each characteristic arising from equation (4.28), the system of ODEs

$$\frac{\mathrm{d}b}{\mathrm{d}t} = Q(b,t) \tag{4.29}$$

$$\frac{\mathrm{d}g}{\mathrm{d}t} = W(b,g,t), \tag{4.30}$$

$$b(t^\star) = 0, g(t^\star) = g_{\text{boundary}}(t^\star) \text{ at } t = t^\star, \tag{4.31}$$

traces out the solution of equations (4.26)-(4.28) along the paths identified by $t^\star$. Similarly, with $b^\star$ parametrising the initial condition, and thus labelling each characteristic arising from equation (4.27), the system of ODEs

$$\frac{\mathrm{d}b}{\mathrm{d}t} = Q(b,t) \tag{4.32}$$

$$\frac{\mathrm{d}g}{\mathrm{d}t} = W(b,g,t), \tag{4.33}$$

$$b(0) = b^\star, g(0) = 0 \text{ at } t = 0, \tag{4.34}$$

traces out the solution of equations (4.26)-(4.28) along the paths identified by $b^\star$. We note our system (4.19)-(4.23) is of the form (4.26)-(4.28), with

$$Q(b,t) = \lambda b\left(1 - \frac{b}{p}\right) - b\left(\frac{k(t)}{q+b}\right) + uE(t), \tag{4.35}$$

$$W(b,g,t) = g(b,t)\left(\lambda - \frac{2\lambda b}{p} - \frac{k(t)q}{(q+b)^2}\right) - \alpha g(b,t) - F(g(b,t)) + F'(g(b,t)), \tag{4.36}$$

$$g_{\text{boundary}}(t) = wE(t)(1 + vB(t)), \tag{4.37}$$

with $F(g(b,t))$ and $F'(g(b,t))$ as in equations (4.15) and (4.16), and further $E(t), B(t)$ and $G(t)$ as in equations (4.20), (4.24), and (4.25), on use of

$$\frac{\partial}{\partial b}\left[\lambda b\left(1 - \frac{b}{p}\right) - b\left(\frac{k(t)}{q+b}\right) + uE(t)\right] = \lambda - \frac{2\lambda b}{p} - \frac{k(t)q}{(q+b)^2}. \tag{4.38}$$

We will write $b(t;t^\star)$ and $g(t;t^\star)$ for the solution of our system (4.19)-(4.23) along the characteristic curve identified by $t^\star$, and $b(t;b^\star)$ and $g(t;b^\star)$ for the solution of our system

(4.19)-(4.23) along the characteristic curve identified by $b^\star$. Then, the system of ODEs

$$\frac{\mathrm{d}b(t;t^\star)}{\mathrm{d}t} = \lambda b(t;t^\star)\left(1-\frac{b(t;t^\star)}{p}\right) - b(t;t^\star)\left(\frac{k(t)}{q+b(t;t^\star)}\right) + uE(t), \tag{4.39}$$

$$\begin{aligned}\frac{\mathrm{d}g(t;t^\star)}{\mathrm{d}t} &= g(t;t^\star)\left(\lambda - \frac{2\lambda b(t;t^\star)}{p} - \frac{k(t)q}{(q+b(t;t^\star))^2}\right)\\ &\quad - \alpha g(t;t^\star) - F(g(t;t^\star)) + F'(g(t;t^\star)),\end{aligned} \tag{4.40}$$

$$\frac{\mathrm{d}b(t;b^\star)}{\mathrm{d}t} = \lambda b(t;b^\star)\left(1-\frac{b(t;b^\star)}{p}\right) - b(t;b^\star)\left(\frac{k(t)}{q+b(t;b^\star)}\right) + uE(t), \tag{4.41}$$

$$\begin{aligned}\frac{\mathrm{d}g(t;b^\star)}{\mathrm{d}t} &= g(t;b^\star)\left(\lambda - \frac{2\lambda b(t;b^\star)}{p} - \frac{k(t)q}{(q+b(t;b^\star))^2}\right)\\ &\quad - \alpha g(t;b^\star) - F(g(t;b^\star)) + F'(g(t;b^\star)),\end{aligned} \tag{4.42}$$

$$\begin{aligned}\frac{\mathrm{d}E(t)}{\mathrm{d}t} &= \zeta E(t)\left(1-\frac{E(t)}{\psi}\right)\\ &\quad + b_{\mathrm{burst}} g(t;t^{\star\star})\left[\lambda b_{\mathrm{burst}}\left(1-\frac{b_{\mathrm{burst}}}{p}\right) - b_{\mathrm{burst}}\left(\frac{k(t)}{q+b_{\mathrm{burst}}}\right) + uE(t)\right]\\ &\quad - uE(t)G(t),\end{aligned} \tag{4.43}$$

$$b(t^\star;t^\star) = 0,$$

$$g(t^\star;t^\star) = wE(t^\star)(1+vB(t^\star)), \tag{4.44}$$

$$b(0;b^\star) = b^\star,$$

$$g(0;b^\star) = 0, \tag{4.45}$$

$$E(0) = 0, \tag{4.46}$$

traces out the solution of our system (4.19)-(4.23) along characteristic curves identified by $t^\star$ and $b^\star$. We note that for characteristic curves identified by $b^\star$ that arise from the initial condition $g(b,0) = 0$ for all $b > 0$, we have $g(t,b^\star) = 0$ for all $t \geq 0$. We therefore have $g(b,t) = 0$ for all (b,t) that are not part of one of the characteristic curves $t^\star$. We define $t^{\star\star}$ as the characteristic coordinate such that $b(t;t^{\star\star}) = b_{\mathrm{burst}}$. If no such coordinate exists, $g(t;t^{\star\star}) = 0$. Further, we note that the condition $[Z(b_{\mathrm{burst}},t) + uE(t)] \geq 0$ for all t (see Section 4.2) ensures that we can ignore characteristic curves from the moment that $b(t;t^\star) > b_{\mathrm{burst}}$, i.e. when macrophages burst. The condition $[Z(b_{\mathrm{burst}},t) + uE(t)] \geq 0$ for all t ensures that $b(t;t^\star) \geq 0$ for all $t, t^\star$, i.e. none of the characteristic curves will ever become negative. We will elaborate on how we implemented the fusion terms $F(g(t;t^\star))$ and $F'(g(t;t^\star))$ numerically in Section 4.4.2. We need to ensure characteristic curves do not

cross in the (b,t) plane else $g(b,t)$ becomes multivalued and a unique well-defined solution thus does not exist. Using τ to parametrise characteristic curves via

$$\frac{\mathrm{d}t}{\mathrm{d}\tau} = 1, \qquad \frac{\mathrm{d}b}{\mathrm{d}\tau} = Q(b,t), \tag{4.47}$$

we have either

$$\text{(i)} \qquad t = \tau + t^{\star}, \qquad \frac{\mathrm{d}t}{\mathrm{d}\tau} = 1, \qquad \frac{\mathrm{d}b}{\mathrm{d}\tau} = Q(b, t^{\star} + \tau),$$

for equations (4.29)-(4.31), or

$$\text{(ii)} \qquad t = \tau, \qquad \frac{\mathrm{d}t}{\mathrm{d}\tau} = 1, \qquad \frac{\mathrm{d}b}{\mathrm{d}\tau} = Q(b, \tau),$$

for equations (4.32)-(4.34), with suitable initial conditions (that include b^* for case (ii)) and with $Q(b,t)$ differentiable. From the theory of phase planes [125], integral paths of

$$\frac{\mathrm{d}t}{\mathrm{d}\tau}, \qquad \frac{\mathrm{d}b}{\mathrm{d}\tau}$$

will only intersect in the (b,t) phase plane only at equilibrium points, that is where $\frac{\mathrm{d}t}{\mathrm{d}\tau} = \frac{\mathrm{d}b}{\mathrm{d}\tau} = 0$. However, that will never happen for (i) or (ii) and hence characteristic curves will never cross for both equations (4.29)-(4.31) and equations (4.32)-(4.34).

4.3 System-size expansion

To increase the interpretability of our bacterial-load structured PDE model equations introduced in the previous Section, we will describe how our model equations can be related to underlying stochastic interactions between bacteria and individual macrophages. We will follow the approach as presented in PhD thesis Chapter 5 by Thomas Woolley [356]. We will relate the chemical master equation, a stochastic model, to a deterministic ODE model by an approach developed by Van Kampen [171, Chapter 10]. This ODE model is constructed as a b-discretised version of our PDE model, with b the bacterial mass density, such that the PDE model can be obtained from the ODE model in the continuum limit.

4.3.1 Background

In this subsection we introduce the method developed by Van Kampen [171]. We closely follow the approach presented by Thomas Woolley's PhD thesis [356, p.70-77]. See also [95, supplemental methods], for a presentation similar to [356, p.70-77]. Let $(S_1, \dots S_K)$ be K species. Following [356], we will present each species as an interacting entity for the remainder of this subsection. When we apply the method to derive our PDE model (Subsection 4.3.2), we will take macrophages with varying levels of infection, and quantities of extracellular bacteria as our species of interest. The K species undergo $(R_1, \dots, R_J)$ reactions. An example of such a reaction is

$$S_1 + S_2 \xrightarrow{\kappa} S_3, \tag{4.48}$$

where both S_1 and S_2 disappear and one of S_3 is created. The coefficient κ is the probability rate constant of the reaction. For a reaction R_j, it is defined as

Definition 5. $\kappa_j dt$ = the probability that a randomly chosen set of R_j reactant molecules will undergo the R_j^{th} reaction in the next infinitesimal interval $[t, t + dt)$.

Let $U_i(t)$ be the integer random variable of number of individual species S_i, and $\boldsymbol{U}(t) = (U_1(t), \dots U_K(t))$ the state vector of the system at time t. The stoichiometric vector $\boldsymbol{\nu}_j = (\nu_{1j}, \dots, \nu_{K_j})$ is the state change vector of reaction R_j. Let $\boldsymbol{u}$ be a realisation of $\boldsymbol{U}$. If the system is in state $\boldsymbol{u}$, and reaction R_j occurs, the system changes to state $\boldsymbol{u} + \boldsymbol{\nu}_j$. We define the propensity function $a_j(\boldsymbol{u})$ such that

Definition 6. $a_j(\boldsymbol{u})dt$ = the probability, given $\boldsymbol{U} = \boldsymbol{u}$, that one R_j reaction will occur in the next infinitesimal interval $[t, t + dt)$.

We also need the following assumption [121]:

Assumption 1. The probability of more than one reaction occurring in the system in the interval $[t, t + dt)$ is $o(dt)$.

We can now derive the chemical master equation, which describes the rate of change of the probability of being in a certain state $\boldsymbol{u}$. First, we define $P(\boldsymbol{u}, t+dt)$ as the probability of

being in state $\boldsymbol{u}$ at time $t+dt$. This probability $P(\boldsymbol{u}, t+dt)$ is equal to the probability $P(\boldsymbol{u}, t)$ times the probability that no reaction occurs in the interval $[t + dt)$, plus the probability of being in a state one reaction R_j away from $\boldsymbol{u}$ at time t times the probability of that reaction occurring in the interval $[t + dt)$:

$$P(\boldsymbol{u}, t + dt) = P(\boldsymbol{u}, t) \left(1 - \sum_{j=1}^{J} a_j(\boldsymbol{u}) dt \right) + \sum_{j=1}^{J} P(\boldsymbol{u} - \boldsymbol{v_j}, t) a_j(\boldsymbol{u} - \boldsymbol{v}_j) dt + o(dt). \quad (4.49)$$

Rearranging and taking $dt \to 0$ results in the chemical master equation:

$$\frac{\partial P(\boldsymbol{u}, t)}{\partial t} = \sum_{j=1}^{J} [P(\boldsymbol{u} - \boldsymbol{v_j}, t) a_j(\boldsymbol{u} - \boldsymbol{v}_j) - P(\boldsymbol{u}, t) a_j(\boldsymbol{u})]. \quad (4.50)$$

We now define a new random variable, η_i (which is of order one as $\Omega \to \infty$), through the relation

$$U_i = \phi_i \Omega + \eta_i \sqrt{\Omega}, \quad (4.51)$$

where we set the system size parameter Ω to the mean value of the initial values $U_i(0)$, $i = 1, \ldots, K$. ϕ_i is the expected ratio of the population at time t to the initial population and is a dimensionless 'macroscopic' variable. Let $\boldsymbol{\phi} = (\phi_1, \ldots, \phi_K)$ and $\boldsymbol{\eta} = (\eta_1, \ldots, \eta_K)$. We note that

$$\lim_{\Omega \to \infty} \frac{\boldsymbol{U}}{\Omega} = \boldsymbol{\phi}, \quad (4.52)$$

therefore, as the size of the system (Ω) grows, individual interactions become less important and the population can be treated as a continuum. We will now first introduce a macroscopic rate $\alpha_j(\boldsymbol{\phi})$ for each reaction R_j and relate the macroscopic rates to the microscopic propensity functions $a_j(\boldsymbol{u})$ defined before (Definition 6). We will then take a van Kampen expansion of the master equation (4.50). In the thermodynamic limit of large system size (i.e. when we let Ω grow), we will see that the master equation decomposes in a deterministic part, describing the mean-field dynamics of the reacting species in terms of the evolution of $\boldsymbol{\phi}$ over time, and lower order stochastic fluctuations around the mean-field dynamics.

The microscopic propensity function has the form $a_j(\boldsymbol{u}) = \kappa_j h_j(\boldsymbol{u})$, where $h_j(\boldsymbol{u})$ is the number of distinct combinations of R_j reactants available in state $\boldsymbol{u}$ and the probability

rate constant κ_j has been defined above (Definition 5). As an example, we consider the following reaction R_j:

$$S_{j1} + S_{j2} \xrightarrow{\kappa_j} S_{j3}, \tag{4.53}$$

The microscopic propensity is given by $a_j(\boldsymbol{u}) = \kappa_j u_{j1} u_{j2}$. For each reaction R_j, we introduce a macroscopic rate $\alpha_j(\boldsymbol{\phi})$. The macroscopic rates $\alpha_j(\boldsymbol{\phi})$ are chosen in such a way that the $\boldsymbol{\phi}$ are solutions of

$$\frac{d\phi_i}{dt} = \sum_{j=1}^{J} \alpha_j(\boldsymbol{\phi}) \nu_{ij}. \tag{4.54}$$

Equation (4.54) describes the expected evolution of the system over time. Hence, applying the principle of mass balance, we find that the macroscopic rate $\alpha_j(\boldsymbol{\phi}) = \kappa_j \phi_{j1} \phi_{j2} \Omega$ [171, 356]. Here, the Ω is a scaling factor needed as each ϕ_i is expressed as a ratio of the population to the initial population, with $\phi(0) = \frac{U(0)}{\Omega}$. In general, for a reaction

$$S_{j1} + \ldots + nS_{jq} + \cdots + S_{jp} \xrightarrow{\kappa_j} S_i, \tag{4.55}$$

with p different species, the microscopic propensity rate is given by

$$a_j(\boldsymbol{u}) = \kappa_j u_{j1} \ldots u_{jq}(u_{jq} - 1) \ldots (u_{jq} - (n-1)) \ldots u_{jp}, \tag{4.56}$$

as we need to take into account that reactions must occur between distinct particles. The macroscopic rate is given by [171, 356]

$$\alpha_j(\boldsymbol{\phi}) = \kappa_j \phi_{j1} \ldots \phi_{jp}^n \ldots \phi_{jp} \Omega^{p-1}. \tag{4.57}$$

We note the scaling factor Ω^{p-1}, obtained as we multiply ϕ_j by Ω for each reactive species, multiply by κ_j, and then divide by Ω to retrieve the rate of change of ϕ_i resulting from reaction j.

We can expand the microscopic propensity function $a_j(\boldsymbol{u})$ around $\alpha_j(\boldsymbol{\phi})$:

$$\frac{a_j(\boldsymbol{u})}{\Omega} = \frac{a_j(\boldsymbol{\phi}\Omega + \boldsymbol{\eta}\sqrt{\Omega})}{\Omega} = \alpha_j(\boldsymbol{\phi}) + \frac{1}{\sqrt{\Omega}} \sum_{i=1}^{K} \eta_i \frac{\partial \alpha_j(\boldsymbol{\phi})}{\partial \phi_i} + \mathcal{O}(1/\Omega). \tag{4.58}$$

We note that the difference between $a_j(\boldsymbol{\phi}\Omega + \boldsymbol{\eta}\sqrt{\Omega})/\Omega$ and $\alpha_j(\boldsymbol{\phi} + \frac{\eta}{\sqrt{\Omega}})$ is of the order of single molecules, and is absorbed in the term $\mathcal{O}(1/\Omega)$. In a similar way we find:

$$\frac{a_j(\boldsymbol{u} - \boldsymbol{\nu_j})}{\Omega} = \frac{a_j(\boldsymbol{\phi}\Omega + \boldsymbol{\eta}\sqrt{\Omega} - \boldsymbol{\nu_j})}{\Omega} = \alpha_j(\boldsymbol{\phi}) + \frac{1}{\sqrt{\Omega}} \sum_{i=1}^{K} \eta_i \frac{\partial \alpha_j(\boldsymbol{\phi})}{\partial \phi_i} + \mathcal{O}(1/\Omega). \tag{4.59}$$

In order to expand the master equation, we first transform the function $P(\boldsymbol{U},t)$ into a new function Π that depends on η:

$$P(\boldsymbol{U},t) = \Pi(\boldsymbol{\eta},t) = \Pi((\eta_i,\ldots,\eta_K),t) \tag{4.60}$$

We differentiate Π with respect to time, while keeping the number of molecules fixed (i.e. $\frac{\partial U_i}{\partial t} = 0$, as the time derivative of the master equation (4.50) is taken with constant $\mathbf{U}$ [171, p.245]):

$$\frac{\partial P(\boldsymbol{U},t)}{\partial t} = \frac{\partial \Pi(\boldsymbol{\eta},t)}{\partial t} + \sum_{i=1}^{K} \frac{\mathrm{d}\eta_i}{\mathrm{d}t}\frac{\partial \Pi(\boldsymbol{\eta},t)}{\partial \eta_i} = \frac{\partial \Pi(\boldsymbol{\eta},t)}{\partial t} - \sqrt{\Omega}\sum_{i=1}^{K} \frac{\mathrm{d}\phi_i}{\mathrm{d}t}\frac{\partial \Pi(\boldsymbol{\eta},t)}{\partial \eta_i}. \tag{4.61}$$

We also expand $P(\boldsymbol{u}-\boldsymbol{v_j},t) = \Pi(\eta - \frac{\boldsymbol{\nu_j}}{\sqrt{\Omega}})$ around η:

$$\Pi\left(\eta - \frac{\boldsymbol{\nu_j}}{\sqrt{\Omega}}\right) = \Pi(\boldsymbol{\eta}) - \frac{1}{\sqrt{\Omega}}\sum_{i=1}^{K} \boldsymbol{\nu_{i,j}}\frac{\partial \Pi(\boldsymbol{\eta})}{\partial \eta_i} + \frac{1}{2\Omega}\sum_{i=1}^{K}\sum_{l=1}^{K} \boldsymbol{\nu_{i,j}}\boldsymbol{\nu_{l,j}}\frac{\partial^2 \Pi(\boldsymbol{\eta})}{\partial \eta_i \partial \eta_l} + \mathcal{O}\left(\frac{1}{\Omega^{3/2}}\right). \tag{4.62}$$

We insert equations (4.58), (4.59), (4.61), and (4.62) into the master equation (4.50), neglecting terms of order $1/\sqrt{\Omega}$:

$$\frac{\partial \Pi(\boldsymbol{\eta},t)}{\partial t} - \sqrt{\Omega}\sum_{i=1}^{K} \frac{\mathrm{d}\phi_i}{\mathrm{d}t}\frac{\partial \Pi(\boldsymbol{\eta},t)}{\partial \eta_i} = \sum_{j=1}^{J}\left(-\sqrt{\Omega}\sum_{i=1}^{K} \boldsymbol{\nu_{i,j}}\frac{\partial \Pi(\boldsymbol{\eta})}{\partial \eta_i} + \frac{1}{2}\sum_{i=1}^{K}\sum_{l=1}^{K} \boldsymbol{\nu_{i,j}}\boldsymbol{\nu_{l,j}}\frac{\partial^2 \Pi(\boldsymbol{\eta})}{\partial \eta_i \partial \eta_l}\right)\left(\alpha_j(\boldsymbol{\phi}) + \frac{1}{\sqrt{\Omega}}\sum_{i=1}^{K}\eta_i\frac{\partial \alpha_j(\boldsymbol{\phi})}{\partial \phi_i}\right). \tag{4.63}$$

Collecting leading order terms, of order $\sqrt{\Omega}$, returns the macroscopic equation:

$$\sum_{i=1}^{K} \frac{\mathrm{d}\phi_i}{\mathrm{d}t}\frac{\partial \Pi(\boldsymbol{\eta},t)}{\partial \eta_i} = \sum_{i=1}^{K}\sum_{j=1}^{J} \alpha_j(\boldsymbol{\phi})\boldsymbol{\nu_{i,j}}\frac{\partial \Pi(\boldsymbol{\eta})}{\partial \eta_i}, \tag{4.64}$$

which is satisfied by the definition of $\alpha_j(\boldsymbol{\phi})$, equation (4.54). The ODE system (4.54) describes the mean-field dynamics of the system. In the thermodynamic limit of large system size, or equivalently the limit of weak noise, i.e. when the system size parameter Ω is large, we can ignore the lower order terms of (4.63) that describe the stochastic fluctuations

around the deterministic mean-field dynamics. By setting $\phi_i\Omega = X_i$, with X_i the expected number of molecules in the limit of weak noise, we can rescale equation (4.54) as

$$\frac{dX_i}{dt} = \sum_{j=1}^{J} \Omega\alpha_j(\boldsymbol{\phi})\nu_{ij}, \tag{4.65}$$

with $\alpha_j(\boldsymbol{\phi})\Omega = \kappa_j\phi_{j1}\dots\phi_{jp}^n\dots\phi_{jp}\Omega^p = \kappa_j X_{j1}\dots X_{jp}^n\dots X_{jp}$ for reaction R_j (equation (4.55)) as before.

4.3.2 Derivation of the bacterial-load structured model

Let $(S_1,\dots S_N)$ be N species. Species S_i represents a macrophage with bacterial mass density b (i.e. bacterial mass per macrophage, expressed in units β) in the interval $\left((i-1)\frac{b_{\text{burst}}}{N}, i\frac{b_{\text{burst}}}{N}\right]$, $i = 1,\dots,N$, with $N \gg 1, \frac{b_{\text{burst}}}{N} \ll b_{\text{burst}}$, where $b = b_{\text{burst}}$ is the bacterial mass density that causes bursting of the macrophage. Also, let $\Delta b = \frac{b_{\text{burst}}}{N}$. Let $(X_1,\dots X_N)$ be the number of macrophages of species $(S_1,\dots,S_N)$. Let X_0 be the number of macrophages with no bacterial mass, corresponding to species S_0. Let S_B be another species, of mass Δb, representing extracellular bacteria and Y be the total number of the species S_B. When a macrophage bursts, it therefore releases N such quantities. To ease the comparison with our PDE model equations, we have chosen to describe the total pathogen (or non-living particle) load in terms of mass, rather than pathogen (or particle) numbers. In our PDE model, the total pathogen load is also described in terms of bacterial mass. However we note that for the stochastic reactions introduced below, we assume discrete bacteria, each with a fixed mass Δb, so that species S_i would represent a macrophage containing i bacteria and N bacteria would be released when a macrophage bursts.

We define the following reactions, where reaction rates are indicated with star-superscripted variables which may be functions of other variables:

i Intracellular growth: $S_i \xrightarrow{r_i^*} S_{i+1} \qquad i \in \{1,\dots,N-1\}$

ii Bursting due to growth: $S_N \xrightarrow{r_N^*} NS_B$

iii Uptake of bacteria: $S_i + S_B \xrightarrow{u^*} S_{i+1} \qquad i \in \{0,\dots,N-1\}$

iv Bursting due to uptake: $S_N + S_B \xrightarrow{u^*} NS_B$

v Killing of bacteria: $S_i \xrightarrow{\kappa_i^*} S_{i-1} \qquad i \in \{2, \ldots, N\}$

vi Apoptosis of macrophage: $S_i \xrightarrow{\alpha^*} \emptyset \qquad i \in \{1, \ldots, N\}$

vii Extracellular growth: $\emptyset \xrightarrow{\zeta^*} S_B$

viii Bacterial redistribution:

$$S_i + S_j \xrightarrow{\eta^*} 2S_{(i+j)/2} \qquad i, j \in \{1, \ldots, N\}, \text{ for } i + j \text{ even}$$

$$S_i + S_j \xrightarrow{\eta^*} S_{(i+j+1)/2} + S_{(i+j-1)/2} \qquad i, j \in \{1, \ldots, N\}, \text{ for } i + j \text{ odd}$$

We represent fusion by a bacterial redistribution reaction (viii). Like the fusion term in the bacterial-load structured PDE model, the redistribution reaction averages the bacterial load of two macrophages. It can be viewed as a process of fusion and immediate splitting. The splitting assumption is necessary to ensure no macrophage mass or pathogen mass is lost due to fusion. When $(i + j)$ is even, we split into two macrophages with an equal, averaged bacterial load. When $(i + j)$ is odd, we assume two macrophages are created, one of $S_{(i+j+1)/2}$ and one of $S_{(i+j-1)/2}$, to ensure conservation of bacterial mass. We note that in the bacterial-load structured PDE model, we assume macrophages of equal mass fuse to produce a macrophage of double the mass and do not track the individual numbers of macrophages in the model. We briefly note that reactions that induce no change, such as reaction (viii) for $i = j$ can be excluded from, or included within, the reaction scheme, according to the detailed cell level interactions that are considered, with no change in the resulting continuum model we will derive below (equations (4.79)-(4.83)).

By applying the law of mass action, we can write down the following system of ODEs:

$$
\begin{aligned}
X_0 &= X_0(X_i, Y), && (4.66)\\
\frac{\mathrm{d}X_1}{\mathrm{dt}} &= u^*X_0Y - u^*X_1Y + \kappa_2^*X_2 - r_1^*X_1 - \alpha^*X_1 - 2\eta^*X_1\sum_{j=1}^{N} X_j \\
&\quad +2\eta^*X_1X_1 + \eta^*\left(X_2X_1 + X_1X_2\right), && (4.67)\\
\frac{\mathrm{d}X_i}{\mathrm{dt}} &= u^*X_{i-1}Y - u^*X_iY + \kappa_{i+1}^*X_{i+1} - \kappa_i^*X_i + r_{i-1}^*X_{i-1} - r_i^*X_i - \alpha^*X_i \\
&\quad -2\eta^*X_i\sum_{j=1}^{N} X_j + 2\eta^*\sum_{j=\max(1,2i-N)}^{j=\min(2i-1,N)} X_{2i-j}X_j \\
&\quad +\eta^*\sum_{j=\max(0,2i-N)}^{j=\min(2i-1,N-1)} X_{2i-j}X_{j+1} \\
&\quad +\eta^*\sum_{j=\max(2,2i-N)}^{j=\min(2i-1,N+1)} X_{2i-j}X_{j-1}, && (4.68)\\
\frac{\mathrm{d}X_N}{\mathrm{dt}} &= u^*X_{N-1}Y - u^*X_NY - \kappa_N^*X_N + r_{N-1}^*X_{N-1} - r_N^*X_N - \alpha^*X_N \\
&\quad -2\eta^*X_N\sum_{j=1}^{N} X_j \\
&\quad +2\eta^*X_NX_N + \eta^*\left(X_NX_{N-1} + X_{N-1}X_N\right), && (4.69)\\
\frac{\mathrm{d}Y}{\mathrm{dt}} &= \zeta^* - Y\sum_{j=0}^{j=N} X_ju^* + NX_N(r_N^* + u^*Y), && (4.70)
\end{aligned}
$$

with initial conditions $X_i(0) = X_{i,0}, Y(0) = Y_0$, and $X_0 = X_0(X_i; Y)$ denotes that the pathogen free macrophage mass is given by a prescribed function of the "infected" macrophage and extracellular masses. As was described in the previous Subsection 4.3.1 (see equation (4.65)), this ODE system (4.66)-(4.70) arises as the weak noise limit, or equivalently in the thermodynamic limit of large system size, of the system defined by reactions (i)-(viii).

We will now show how our PDE equations can be recovered in the continuum limit from the system of equations (4.66)-(4.70). By the mean value theorem, we can choose $b_i^* \in \left((i-1)\frac{b_{\mathrm{burst}}}{N}, i\frac{b_{\mathrm{burst}}}{N}\right]$ such that $\tilde{\mu}X_i(t) = g(b_i^*, t)\Delta b$, for $i = 1, \ldots, N$, with $g(b,t)$ the macrophage mass density for bacterial mass density b, and $\tilde{\mu}$ is the average weight of a macrophage. Because we express macrophage weight in the same quantity, $\tilde{\mu}$ becomes unity and we will therefore refrain from referring to this scale factor in the remainder of the text. We let $E(t) = Y(t)\Delta b$, $r_i^* = \frac{1}{\Delta b}r(b_i^*) = \frac{1}{\Delta b}\lambda b_i^*\left(1 - \frac{b_i^*}{p}\right)$, $u^* = u$, $\zeta^*\Delta b = \zeta E\left(1 - \frac{E}{\psi}\right)$,

$\alpha^* = \alpha$, $\eta^* = \frac{\eta}{2}$, $\kappa_i^* = \frac{1}{\Delta b}\kappa(b_i^*) = \frac{1}{\Delta b} b_i^* \frac{k(t)}{q+b_i^*}$, with $k(b_i^*) = 0$ for $i > N$ and $i = 1$, as we assume that infected macrophages can not become uninfected again. Further, let $b_0^* = 0$, $g(b_0^*, t) = g(0, t) = \frac{X_0}{\Delta b}$, and $g(b_i^*, t) = \frac{X_i}{\Delta b}$. We obtain

$$\begin{aligned}
\frac{\mathrm{d}g(b_i^*,t)}{\mathrm{dt}} &= \frac{\left(g(b_{i-1}^*,t) - g(b_i^*,t)\right) uE}{\Delta b} + \frac{\kappa(b_{i+1}^*)g(b_{i+1}^*,t) - \kappa(b_i^*)g(b_i^*,t)}{\Delta b} \\
&\quad + \frac{r(b_{i-1}^*)g(b_{i-1}^*,t) - r(b_i^*)g(b_i^*,t)}{\Delta b} - \alpha g(b_i^*,t) \\
&\quad - \eta g(b_i^*,t) \sum_{j=1}^{N} g(b_j^*,t)\Delta b + \eta \sum_{j=\max(1,2i-N)}^{j=\min(2i-1,N)} g(b_{2i-j}^*,t) g(b_j^*,t)\Delta b \\
&\quad + \frac{\eta}{2} \sum_{j=\max(0,2i-N)}^{j=\min(2i-1,N-1)} g(b_{2i-j}^*,t) g(b_{j+1}^*,t)\Delta b \\
&\quad + \frac{\eta}{2} \sum_{j=\max(2,2i-N)}^{j=\min(2i-1,N+1)} g(b_{2i-j}^*,t) g(b_{j-1}^*,t)\Delta b, \qquad (4.71) \\
\frac{\mathrm{d}E}{\mathrm{dt}} &= \zeta E\left(1 - \frac{E}{\psi}\right) \\
&\quad - uE \sum_{j=0}^{N} g(b_j^*,t)\Delta b + b_{\mathrm{burst}} g(b_N^*,t)\left[\lambda b_N^*\left(1 - \frac{b_N^*}{p}\right) + uE\right], \qquad (4.72)
\end{aligned}$$

for $i = 1, \ldots N$. For consistency, we set $g(b_i^*, t) = 0$ for $i > N$, as all macrophages burst at $b = b_{\mathrm{burst}}$, but note that the value of $g(b_i^*, t)$ for $i > N$ does not feed back into the system as we assumed $k(b_i^*) = 0$ for $i > N$. Take $N \to \infty$ and $\Delta b \to 0$, with $N\Delta b \equiv b_{\mathrm{burst}}$, then

$$\frac{X_i(t)}{\Delta b} = g(b_i^*, t) \to g(i\Delta b, t), \qquad (4.73)$$

where the points $i\Delta b$ become a continuum. With the aid of equation (4.73), it follows that

$$\sum_{j=1}^{N} g(b_j^*,t)\Delta b \to \int_0^{b_{\mathrm{burst}}} g(b,t)db = G(t), \qquad (4.74)$$

$$\sum_{j=1}^{N} b_j^* g(b_j^*,t)\Delta b \to \int_0^{b_{\mathrm{burst}}} bg(b,t)db = B(t), \qquad (4.75)$$

on taking standard integration limits. Similarly,

$$\sum_{j=\max(1,2i-N)}^{j=\min(2i-1,N)} g(b^*_{2i-j},t)g(b^*_j,t)\Delta b \to \int_{\max(0,2b-b_{\rm burst})}^{\min(2b,b_{\rm burst})} g(2b-b',t)g(b',t)db', \quad (4.76)$$

$$\sum_{j=\max(0,2i-N)}^{j=\min(2i-1,N-1)} g(b^*_{2i-j},t)g(b^*_{j+1},t)\Delta b \to \int_{\max(0,2b-b_{\rm burst})}^{\min(2b,b_{\rm burst})} g(2b-b',t)g(b',t)db', \quad (4.77)$$

$$\sum_{j=\max(2,2i-N)}^{j=\min(2i-1,N+1)} g(b^*_{2i-j},t)g(b^*_{j-1},t)\Delta b \to \int_{\max(0,2b-b_{\rm burst})}^{\min(2b,b_{\rm burst})} g(2b-b',t)g(b',t)db'. \quad (4.78)$$

Therefore, by taking $N \to \infty$ and $\Delta b \to 0$, with $N\Delta b \equiv b_{\rm burst}$, we retrieve our PDE model equations:

$$\frac{\partial g(b,t)}{\partial t} + \frac{\partial}{\partial b}\left\{g(b,t)\left[\lambda b\left(1-\frac{b}{p}\right) - b\left(\frac{k(t)}{q+b}\right) + uE(t)\right]\right\} = - \alpha g(b,t) - \eta g(b,t)G(t) + 2\eta \int_{\max(0,2b-b_{\rm burst})}^{\min(2b,b_{\rm burst})} g(2b-b',t)g(b',t)db', \quad (4.79)$$

$$\frac{{\rm d}E(t)}{{\rm d}t} = \zeta E(t)\left(1-\frac{E(t)}{\psi}\right) + b_{\rm burst}g(b_{\rm burst},t)\left[\lambda b_{\rm burst}\left(1-\frac{b_{\rm burst}}{p}\right) - b_{\rm burst}\left(\frac{k(t)}{q+b_{\rm burst}}\right) + uE(t)\right] - uE(t)G(t), \quad (4.80)$$

with $k(t) = 0$ for $b \geq b_{\rm burst}$. We close the system by setting

$$g(b,0) = 0, \qquad b > 0, \quad (4.81)$$

$$g(0,t) = wE(t)(1+vB(t)), \quad (4.82)$$

$$E(0) = E_0, \quad (4.83)$$

which also can be deduced from analogous discrete analogies if required. The units of all model variables and parameters are as before and are listed in Table 4.1.

4.4 Model exploration

4.4.1 Non-dimensionalisation

In this section, we will use a non-dimensionalised version of our continuum model, by taking:

$$b = b_{\text{burst}}\hat{b}, \qquad t = \frac{b_{\text{burst}}}{uE_0}\hat{t}, \qquad g = \frac{E_0}{b_{\text{burst}}^2}\hat{g}, \qquad B = E_0\hat{B}, \tag{4.84}$$

$$G = \frac{E_0}{b_{\text{burst}}}\hat{G}, \qquad E = E_0\hat{E}, \qquad v = \frac{1}{E_0}\hat{v}, \qquad w = \frac{1}{b_{\text{burst}}^2}\hat{w}, \tag{4.85}$$

$$\lambda = \frac{uE_0}{b_{\text{burst}}}\hat{\lambda}, \qquad p = b_{\text{burst}}\hat{p}, \qquad q = b_{\text{burst}}\hat{q}, \qquad \kappa = uE_0\hat{\kappa}, \tag{4.86}$$

$$\alpha = \frac{uE_0}{b_{\text{burst}}}\hat{\alpha}, \qquad \eta = u\hat{\eta}, \qquad \zeta = \frac{uE_0}{b_{\text{burst}}}\hat{\zeta}, \qquad \psi = E_0\hat{\psi}. \tag{4.87}$$

We will drop the hats for ease of notation. We will assume $k := \kappa$ is constant throughout the section. The non-dimensionalised system is then given by:

$$\begin{aligned}\frac{\partial g(b,t)}{\partial t} + \frac{\partial\left(g(b,t)\left[\lambda b\left(1-\frac{b}{p}\right) - b\left(\frac{\kappa}{q+b}\right) + E(t)\right]\right)}{\partial b} = \\ - \alpha g(b,t) \\ - \eta g(b,t)G(t) + 2\eta\int_{\max(0,2b-1)}^{\min(2b,1)} g(2b-b',t)g(b',t)db',\end{aligned} \tag{4.88}$$

$$\begin{aligned}\frac{\mathrm{d}E(t)}{\mathrm{d}t} = \\ \zeta E(t)\left(1-\frac{E(t)}{\psi}\right) + g(1,t)\left[\lambda\left(1-\frac{1}{p}\right) - \left(\frac{k(t)}{q+1}\right) + E(t)\right] - E(t)G(t),\end{aligned} \tag{4.89}$$

$$g(b,0) = 0, \qquad b > 0, \tag{4.90}$$

$$g(0,t) = wE(t)(1+vB(t)), \tag{4.91}$$

$$E(0) = 1, \tag{4.92}$$

with

$$G(t) = \int_0^1 g(b,t)db, \tag{4.93}$$

$$B(t) = \int_0^1 bg(b,t)db. \tag{4.94}$$

One reason we non-dimensionalised is that the dimensionless model has less model parameters than the original model. In addition, we chose to scale b with b_{burst} such that b ranges from 0 to 1, while we chose to scale E with E_0 so that we start with a unit of extracellular bacterial mass at $t = 0$. We further chose to scale t by $\frac{b_{\text{burst}}}{uE_0}$, with u the uptake rate per

unit of macrophage mass, since this scaling removes u from equation (4.19). In addition, while we explore the effects of setting the other model parameters (e.g. $\alpha, \eta, k, \lambda, \zeta$) to zero in future sections; we will always assume $u \neq 0$ and hence the use of u in the scaling rather than any of the other remaining model parameters. A minor disadvantage of this choice of non-dimensionalisation is the difficulty in interpreting the resulting scales, though it is a simple matter to reinstate dimensions if or when required. Nonetheless the timescale, $\frac{b_{\text{burst}}}{uE_0}$, is the scale of the burst time at least initially, if the cell uptake of bacteria dominates the other intracellular dynamics, facilitating interpretation.

4.4.2 Numerical solutions

Various methods have been used to numerically solve structured population models [4, 19, 216, 364]. We will use a characteristics based method to numerically solve our system (4.19)-(4.23), as also discussed in Section 4.2.6. The discontinuity in the solution of our system, i.e. $g(b, 0) = 0$ for all $b > 0$, but $g(0, 0) = w$, makes this method preferable over finite difference schemes [215]. At every time step, we add a characteristic curve at $b = 0$. We track b and g over time for each of the characteristic curves. We use the modified Euler method to solve the ODEs and numerically checked the convergence of our method (see Appendix A). We compute the total granuloma size G and bacterial load B at each time step using the composite trapezium rule (Figure 3), i.e. $G \approx \sum_i \Delta_i g_i$ and $B \approx \sum_i \Delta_i g_i b_i$, with g_i, b_i the value of g and b for characteristic i, $i = 1, \dots N$ at the fixed time point of interest. Here, the width Δ_i associated with each characteristic i is defined by $\Delta_i = c_i^u - c_i^l$, with $c_i^l = b_i - \frac{b_i - b_{i-1}}{2}$, $c_i^u = b_i + \frac{b_{i+1} - b_i}{2}$, $i = 2, \dots N$, and $c_1^l = b_1$, $c_N^u = b_N$, with all evaluations at the fixed time point. Characteristics for which $b_i > b_{\text{burst}}$ are discarded, as macrophages cease to exist after bursting. When the characteristic curves start crossing $b = b_{\text{burst}}$, i.e. macrophages start bursting, we add an additional characteristic curve i with $b_i = b_{\text{burst}}$ and g_i a linear interpolation of the two characteristic curves with the largest bacterial burden $b < b_{\text{burst}}$ at that point in time. This ensures the full integration domain is used when computing G and B (Figure 3). We note that for an increasing killing rate $k(t)$, the gradient of a characteristic (i.e. $\frac{db}{dt}$) can become negative. This corresponds to a negative bacterial growth rate due to macrophage killing. The bacterial load will never become negative, as

$Z(0,t) = 0$. Further, we will not consider cases where characteristics have negative gradient at $b = 1$, as macrophages cease to exist after bursting. As the gradient of the characteristics is independent of g, characteristics will never cross (see Section 1.3.6 for more details).

We compute the increase F'_k and decrease F_k due to fusion at each time step for each characteristic k, $k = 1 \dots N$ as follows (in particular, consult Figure 4, to consider line 7):

1: $F_{1\dots N} \leftarrow \mathbf{0}$
2: $F'_{1\dots N} \leftarrow \mathbf{0}$
3: **for** $i = 1$ to N **do**
4: **for** $j = 1$ to N **do**
5: $F_i \leftarrow F_i + \eta g_i g_j \Delta_j$
6: **for** $k = 1$ to N **do**
7: $F'_k \leftarrow F'_k + \eta g_i \Delta_i g_j \Delta_j \frac{length\left([c_k^l, c_k^u] \cap \left[\frac{c_i^l + c_j^l}{2}, \frac{c_i^u + c_j^u}{2} \right] \right)}{\frac{\Delta_i + \Delta_j}{2}}$
8: **end for**
9: **end for**
10: **end for**
11: **for** $k = 1$ to N **do**
12: $F'_k \leftarrow \frac{F'_k}{\Delta_k}$
13: **end for**

We tested this discrete implementation for a unit step function (Appendix A, Figure 22 (b)). We recall that fusion does not affect the total macrophage or pathogen mass. We confirm that our discrete implementation does conserve macrophage mass:

$$\sum_i F_i \Delta_i = \sum_i \left(\sum_j -\eta g_i g_j \Delta_j \right) \Delta_i = -\eta \left(\sum_i \Delta_i g_i \right)^2, \tag{4.95}$$

and also

$$\sum_i F'_i \Delta_i = \sum_i \left(\sum_j \eta g_i \Delta_i g_j \Delta_j \underbrace{\left(\sum_k \frac{length\left([c_k^l, c_k^u] \cap \left[\frac{c_i^l + c_j^l}{2}, \frac{c_i^u + c_j^u}{2} \right] \right)}{\frac{\Delta_i + \Delta_j}{2}} \right)}_{=1} \right)$$
$$= \eta \left(\sum_i \Delta_i g_i \right)^2, \tag{4.96}$$

where the equality in the sum over k arises as the intervals $[c_k^l, c_k^u]$ are a partition of the domain, and the size of $\left[\frac{c_i^l + c_j^l}{2}, \frac{c_i^u + c_j^u}{2} \right]$ is equal to that of $\frac{\Delta_i + \Delta_j}{2}$. In a similar way is can be shown that the total bacterial mass is still conserved in the discretised numerical scheme during fusion.

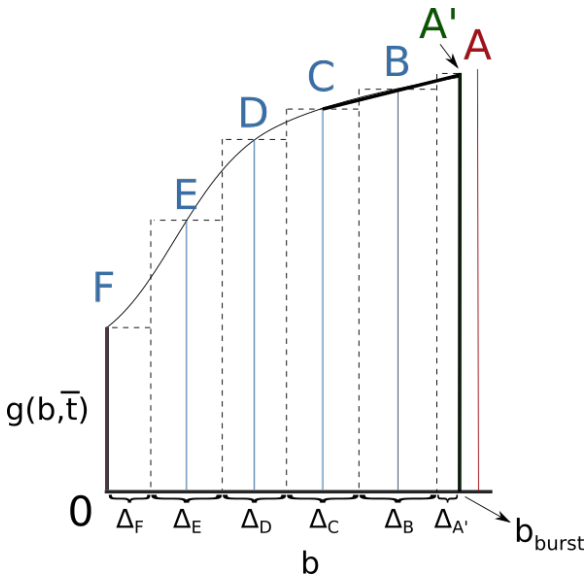


Figure 3: We use the composite trapezium rule to approximate the total granuloma mass G and total bacterial mass B at each time point $t = \bar{t}$, i.e. $G \approx \sum_i \Delta_i g_i$ and $B \approx \sum_i \Delta_i g_i b_i$, with g_i, b_i the value of g and b for characteristic i, $i = 1, \dots N$ at the time point of interest (blue lines in the figure). We show the bacterial mass density b on the horizontal axis and $g(b, \bar{t})$ on the vertical axis, with $t = \bar{t}$ fixed. The width Δ_i associated with each characteristic i is defined by $\Delta_i = c_i^u - c_i^l$, with $c_i^u = b_i + \frac{b_{i+1} - b_i}{2}$, $c_i^l = b_i - \frac{b_i - b_{i-1}}{2}$, $i = 2, \dots N$, and $c_1^l = b_1$, $c_N^u = b_N$. Characteristics for which $b > b_{\text{burst}}$ are discarded, as macrophages cease to exist after bursting (A, in red). From the moment the first characteristic is discarded, we add an additional characteristic at $b = b_{\text{burst}}$ (A′, in green) at every time point, with $g(b_{\text{burst}})$ computed by linear interpolation of the two characteristics with the largest bacterial burden $b < b_{\text{burst}}$ at that point in time (B and C, in blue).

4.4.3 Silica beads

The aim of this subsection is to study a simplified case of our model. The behaviour of this simplified model will serve as a benchmark when studying the effects of the addition of various model components in future sections. In this section, we set $\alpha = \eta = \lambda = \kappa = \zeta = 0$, i.e. we assume there is no apoptosis, macrophage fusion, bacterial growth, or killing of bacteria. Because we assume no killing or growth, we can view $E(t)$ as a non-living substance, such as silica particles, tattoo pigments, or latex beads [296].

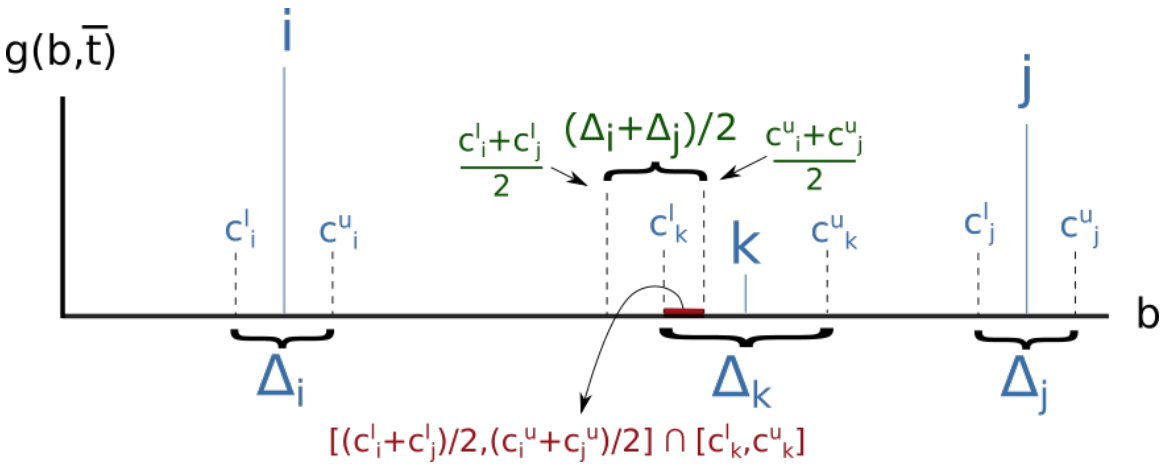


Figure 4: For each two characteristic curves i and j we compute their contribution to the increase in the value g_k of each characteristic curve k due to fusion. We show the bacterial mass density b on the horizontal axis and $g(b,\bar{t})$ on the vertical axis, with $t=\bar{t}$ fixed. The width Δ_i associated with each characteristic i is defined by $\Delta_i = c_i^u - c_i^l$, with $c_i^u = b_i + \frac{b_{i+1}-b_i}{2}$, $c_i^l = b_i - \frac{b_i - b_{i-1}}{2}$, $i = 2,\dots N$, and $c_1^l = b_1$, $c_N^u = b_N$. When two macrophages with a bacterial load within the intervals $[c_i^l, c_i^u]$ and $[c_j^l, c_j^u]$ fuse, the bacterial load of the fused macrophage lies within the interval $[\frac{c_i^l+c_j^l}{2}, \frac{c_i^u+c_j^u}{2}]$ (green). We determine the increase in g_k using the overlap between $[\frac{c_i^l+c_j^l}{2}, \frac{c_i^u+c_j^u}{2}]$ and $[c_k^l, c_k^u]$ (red), the values of g_i and g_j, and the interval widths Δ_i, Δ_j and Δ_k (see main text for full details).

The non-dimensionalised silica particle dynamics are described by:

$$\frac{\partial g(b,t)}{\partial t} + E(t)\frac{\partial g(b,t)}{\partial b} = 0, \qquad t>0, b\in(0,1), \tag{4.97}$$

$$\frac{\mathrm{d}E(t)}{\mathrm{d}t} = [g(1,t) - G(t)]E(t), \qquad t>0, \tag{4.98}$$

$$g(b,0) = 0, \qquad b\in(0,1), \tag{4.99}$$

$$g(0,t) = R, \qquad t>0, \tag{4.100}$$

$$E(0) = 1, \tag{4.101}$$

with

$$G(t) = \int_0^1 g(b,t)db, \tag{4.102}$$

$$B(t) = \int_0^1 bg(b,t)db. \tag{4.103}$$

The recruitment term R is defined by $R = wE(t)(1+vB(t))$. We will also consider a simplified case with constant recruitment $R=c$ in Section 4.4.3.1.

At $t = 0$ fresh macrophages start being recruited as a result of a dimensionless unit of foreign substance E. The total number of foreign particles in the system is constant:

$$\frac{dB}{dt} = [G(t) - g(1,t)]E(t) = -\frac{dE}{dt}. \tag{4.104}$$

This equality follows directly from equations (4.98) and (4.25), with $\alpha = \lambda = \kappa = 0$. The characteristic curves that trace out the solution satisfy:

$$b(t;t^\star) = \int_{t^\star}^{t} E(t')dt', \qquad \text{for } t > t^\star, \tag{4.105}$$

where each characteristic curve is identified by the characteristic coordinate $t^\star$, with $g(t^\star) = R(t^\star)$ (see Figure 5) (as introduced in Section 4.2.6). Equation (4.105) and $g(t^\star) = R(t^\star)$ follow from equations (4.39)-(4.40), with $\lambda = k = \alpha = F(g) = F'(g) = 0$ and $u = 1$. Equivalently $g(t^\star) = R(t^\star)$ follows immediately from the invariance of g along a characteristic by equation (4.97). We note that

$$\frac{dG}{dt} = [R(t) - g(1,t)]E(t), \tag{4.106}$$

and we can write

$$\frac{dE}{dt} = -E(t)\int_0^t [R(t') - g(1,t')]E(t')dt' + g(1,t)E(t). \tag{4.107}$$

4.4.3.1 Constant recruitment

We simplify our model by replacing the recruitment term $R = wE(t)(1 + vB(t))$ by a constant $R = c > 0$. This represents a case where the foreign material taken up by the macrophages does not trigger an inflammatory response. Granuloma formation is driven by the baseline macrophages levels present at the site of foreign antigen presence. Recall that the granuloma growth rate before non-dimensionalisation is given by uRE (equation (4.24)). With $R = c$ constant, the granuloma growth rate is proportional to the extracellular particles present. In this case the solution is completely determined by the gradient $(\frac{db}{dt})$ of the leading characteristic curve $b(t;0)$ (Figure 6). We recall that $b(t;t^\star)$, with $t^\star = 0$, is defined in equation (4.105) as

$$b(t;0) = \int_0^t E(t')dt', \qquad \text{for } t > 0. \tag{4.108}$$

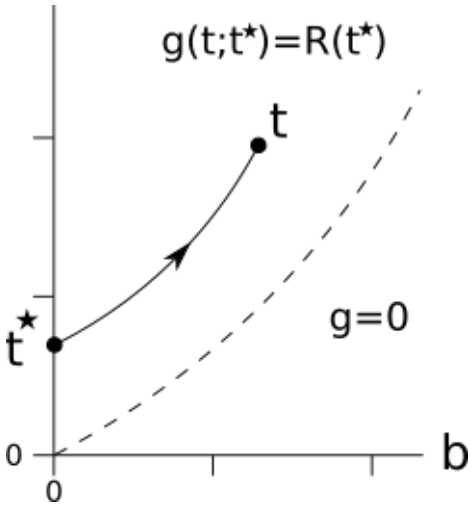
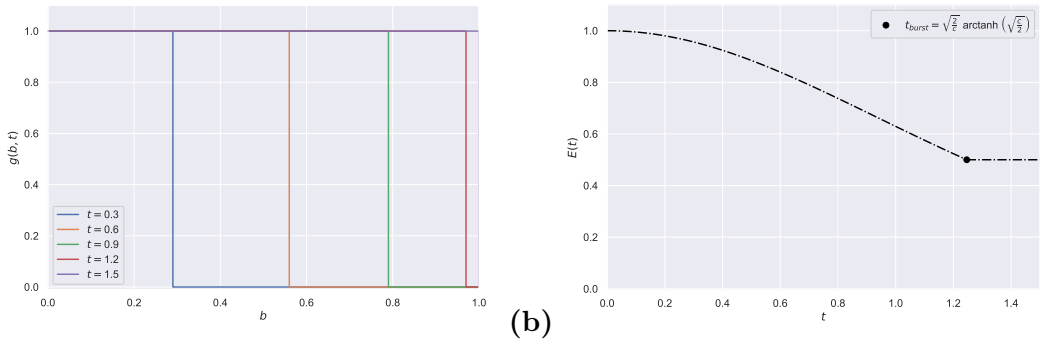


Figure 5: For each characteristic coordinate $t^\star$, a characteristic curve is defined with $g(t^\star) = R(t^\star)$, $b(t^\star; t^\star) = 0$ at $t = t^\star$, and $b(t; t^\star)$ defined in equation (4.105) for all $t > t^\star$. On characteristic curves emerging from $t = 0, b > 0$, we have the trivial dynamics that $g = 0$, inherited from the condition $g(b, 0) = 0$.



(a) **(b)**

Figure 6: Constant recruitment, Section 4.4.3.1. **(a)** The distribution of $g(b, t)$ for various t. **(b)** $E(t)$ against time. We have taken $R = c = 1$.

We define t_{burst} as the point in time that this curve $b(t;0)$ hits the right boundary, $b = 1$:

$$b(t_{\text{burst}};0) = \int_0^{t_{\text{burst}}} E(t')dt' = 1. \tag{4.109}$$

This is the moment the first macrophage bursts. For all $t > t_{\text{burst}}$, $\frac{dG}{dt} = \frac{dE}{dt} = \frac{dB}{dt} = 0$, as the rate of uptake of foreign substance is balanced by the rate of release of foreign substance due to bursting. We emphasize that $t^\star$ is different from t_{burst}. We recall that we defined characteristic coordinate $t^\star$ as the characteristic coordinate that identifies each characteristic curve and that $t^\star = 0$ for the leading characteristic curve $b(t;0)$ (see Section 4.2.6). We defined t_{burst} as the point in time that the leading characteristic curve $b(t;0)$ hits the right boundary, $b = 1$. The solution is given by

$$g(b,t) = \begin{cases} 0, & \text{for } \int_0^t E(t')dt' < b \leq 1, \quad (4.110) \\ c, & \text{for } 0 \leq b \leq \int_0^t E(t')dt'. \quad (4.111) \end{cases}$$

Because $g(1,t) = 0$ for $t < t_{\text{burst}}$, differentiating equation (4.107) gives for $t < t_{\text{burst}}$:

$$\frac{d^2E}{dt^2} = \left(\frac{dE}{dt}\right)^2 \frac{1}{E} - cE^2, \tag{4.112}$$

with $E(0) = 1$ and $E'(0) = 0$. The solution is

$$E(t) = 1 - \tanh^2\left(\sqrt{\frac{c}{2}}t\right) = 1 - \left(\frac{2}{1+e^{-\sqrt{2c}t}} - 1\right)^2, \tag{4.113}$$

with integral

$$\int_0^t E(t')dt' = \sqrt{\frac{2}{c}}\tanh\left(\sqrt{\frac{c}{2}}t\right) < \sqrt{\frac{2}{c}}. \tag{4.114}$$

When $c < 2$, the leading characteristic will reach the right boundary ($b = 1$) at

$$t_{\text{burst}} = \sqrt{\frac{2}{c}}\text{arctanh}\left(\sqrt{\frac{c}{2}}\right). \tag{4.115}$$

We recall that from that moment onwards, the rate of uptake of foreign substance is balanced by the rate of release of foreign substance due to bursting. The final amount of extracellular foreign substance is given by

$$E(t_{\text{burst}}) = 1 - c/2. \tag{4.116}$$

When $c > 2$, the mass of recruited macrophages per unit of time is large enough to take up all extracellular substance before the first macrophage bursts. The gradient ($\frac{db}{dt}$) of the leading characteristic goes to zero before it reaches the right hand side boundary ($b = 1$), demonstrating necrosis versus non-necrosis for different values of recruitment.

4.4.3.2 Non-constant recruitment

We return to our original recruitment term $R(t) = wE(t)(1 + vB(t))$. In a similar way to the constant recruitment case, the recruitment $R(t)$ needs to be sufficient to ensure uptake of all foreign material. When the mass of foreign material is too high compared to the mass of recruited macrophages, macrophages will become necrotic and burst (at $b = 1$).

We define G^*, B^*, E^*, $g(b)^*$ as the late time, steady state granuloma size, intracellular, and extracellular particle load and macrophage mass density with bacterial load content b respectively. When bursting occurs, the value of $E^* = 1 - B^* > 0$ can by found by first setting equations (4.104) and (4.106) to zero:

$$g(1)^* = wE^*(1 + vB^*) = G^*. \tag{4.117}$$

Because for constant B^* and $E^* > 0$, we have $g(b)^* = g(1)^*$ for all $0 \leq b \leq 1$ and therefore $G^* = 2B^*$, it follows that

$$E^* = \begin{cases} \dfrac{2}{w+2}, & \text{for } v = 0, \quad (4.118) \\ \dfrac{(2 + w + vw) - \sqrt{(2 + w + vw)^2 - 8vw}}{2vw}, & \text{for } v > 0. \quad (4.119) \end{cases}$$

When all extracellular material is taken up before the first macrophage bursts, $E^* = 0$.

We show a heat-map for E^* against the value of w and v (Figure 7(a)). We also show three case examples for (i) $v = 0, w = 2$, (ii) $v = 4, w = 2$, and (iii) $v = 2, w = 0.1$. The first two cases examples are necrotic, and representative of the dynamics for $v = 0$ and $v > 0$ respectively, the third one is non-necrotic. We observe oscillatory dynamics when $v = 0$ (case i), and damped dynamics when $v > 0$ (case ii).

4.4.3.3 Fusion

After having explored the dynamics of a simplified version of our model in the case of constant (Section 4.4.3.1) and non-constant (Section 4.4.3.2) recruitment, we will explore the effects of introducing various model features in this section and following sections. In this section, we consider fusion events. These are of special interest, as they have not been considered in previous modelling studies. Macrophages are thought to fuse when single macrophages can not effectively degrade their intracellular load. Fusion results in the

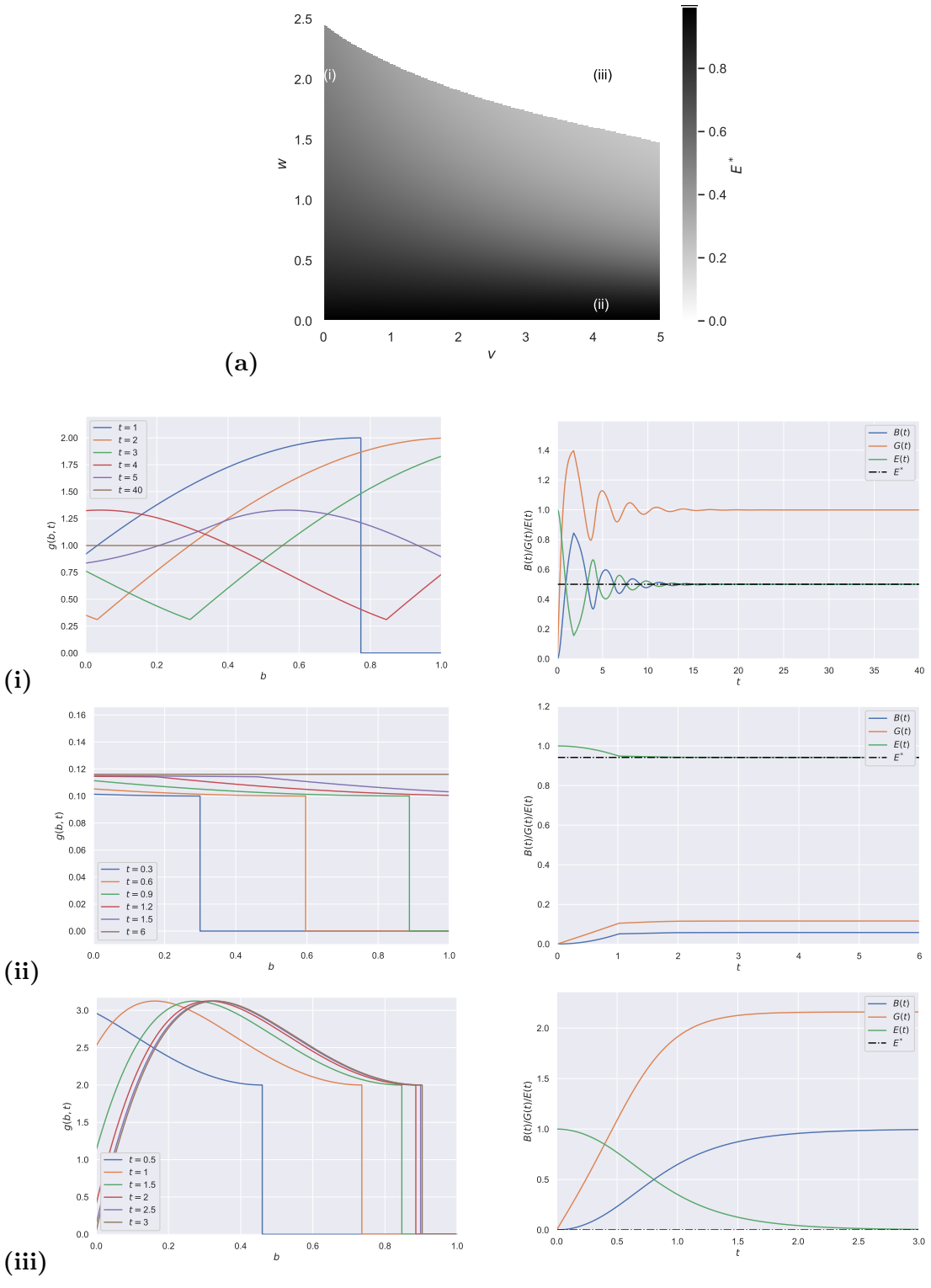


Figure 7: Non-constant recruitment, Section 4.4.3.2. **(a)** A heat-map for the steady state extracellular material concentration E^* against the value of w and v. The distribution of $g(b,t)$ for various t (left) and B, G and E against time (right) for **(i)** $v = 0, w = 2$, **(ii)** $v = 4, w = 0.1$, and **(iii)** $v = 4, w = 2$. The labels **(i)**, **(ii)**, and **(iii)** correspond to the heat-map labels in **(a)**. We did not consider macrophage apoptosis, fusion, killing, or bacterial growth: $\alpha = \eta = \lambda = \kappa = \zeta = 0$.

formation of multi-nucleated giant cells (MGCs). MGCs were first described in tuberculosis infection over 150 years ago and are a key characteristic of granulamotous infections [145]. MCGs are found in all types of granuloma, including granuloma induced by pathogens and granuloma induced by non-living particles [257]. Fused macrophages might be better at degrading large particles [257]. Experimental evidence on macrophage fusion and the role of fusion in the degradation of large particles can for instance be found in [190, 239, 245, 300]. Although fusion is thought to be the dominating mechanism of MGC formation, we note that more recent studies indicate that modified cell division might also be a mechanism of MGC formation relevant in inflammatory granulomas [147, 257]. We again distinguish between necrotic and non-necrotic granuloma, where necrosis is represented by bursting macrophages. As before, we ignore apoptosis, intra- and extra-cellular pathogen growth and killing by macrophages. We use cases (i) and (iii) from Section 4.4.3.2 (Figure 7) as an example of a necrotic and non-necrotic granuloma respectively. Non-necrotic macrophages may fuse, which alters the distribution of particles within the granuloma, but has no effect on the total granuloma size (G) or particle load (B) (Figure 8(iii)). All foreign material is eventually taken up in the absence of necrosis.

Increasing the value of the fusion parameter η in the necrotic case has a negative effect on the steady state values $E^* > 0$ and G^* and a positive effect on B^* (Figure 8(i)). In steady state with $E^* > 0$ the macrophage mass lost to bursting should be balanced by the mass gained by infection of uninfected macrophages: $g(1)^* = wE^*(1 + vB^*)$ (integrating Equation (4.88) with respect to b and setting $\frac{dG}{dt} = 0$, with $\alpha = 0$). Without fusion, we observed that the steady state distribution of foreign material within the granuloma is uniform (Figure 7(i), $t = 40$). When fusion is introduced (with $\eta = 0.35$), a non-uniformly distributed solution exists and an increased mass of foreign material can be held by the granuloma, resulting in a decreased E^* (Figure 8(i) top row and a close up including the trajectory of a single characteristic in (a)). When the value of the fusion parameter η is further increased, all foreign material is taken up over time (Figure 8((i) bottom row and (b)).

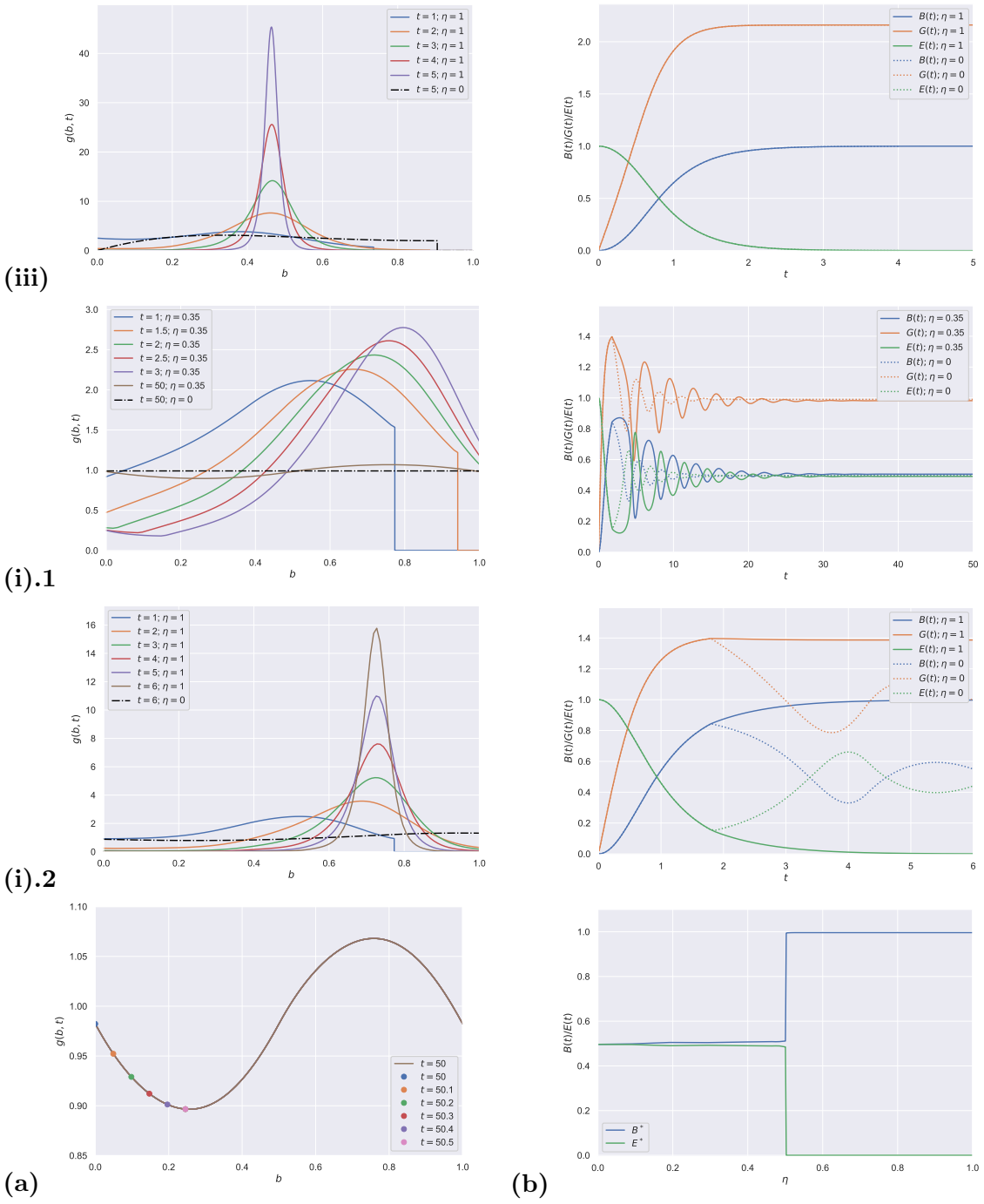


Figure 8: Fusion, Section 4.4.3.3. The distribution of $g(b,t)$ for various t (left) and B, G and E against time (right) for **(iii)** $v = 4, w = 2$, $\eta \in \{0,1\}$ and **(i).1** $v = 0, w = 2$, $\eta = \{0, 0.35\}$ and **(i).2** $v = 0, w = 2$, $\eta = \{0,1\}$. **(a)** The same as **(i).1** (left hand-side figure), but only the distribution of $g(b,t)$ at $t = 50$ (brown line) is shown, with $v = 0, w = 2, \eta = 0.35$. The trajectory of a single characteristic $g(b,t;t^\star = 50)$ is shown for various points in time (coloured dots). **(b)** The value of E^* and B^* against increasing values of η, with $v = 0, w = 2$. We observe a sharp transition between the two steady states with a non zero and zero sized extracellular pathogen population. The labels **(iii)** and **(i)** correspond to the heat-map labels in Figure 7 **(a)**, with values of v and w as already listed in this caption. We did not consider macrophage apoptosis, killing, or bacterial growth: $\alpha = \lambda = \kappa = \zeta = 0$.

4.4.4 Pathogens

4.4.4.1 Extracellular growth

We consider extracellular pathogen growth $\Xi(E) = \zeta E\left(1-\frac{E}{\psi}\right)$, $\zeta > 0$ (see Equation (4.11)). We are concerned with pathogens that can grow outside macrophages, but do not replicate intra-cellularly (λ=0). We also ignore fusion (η=0) apoptosis (α=0) and intracellular killing (κ=0). We assume $\psi > E_0 = 1$, i.e. the carrying capacity of the extra cellular pathogen population is larger than the initial mass of the extracellular population. We first ignore the intracellular component of the recruitment, i.e. set $v = 0$. When $w > 0$ is small enough, bursting occurs for $\zeta = 0$ (see Figure 7(a), grey, $E^* > 0$, where the asterisk refers to the steady state extracellular bacterial load as before). In this case, for any $\zeta > 0$, $E^* = \psi$. We recall that in steady state with $E^* > 0$ the macrophage mass lost to bursting is balanced by the mass gained by infection of uninfected macrophages: $g(1)^* = wE^*$ (integrating Equation (4.88) with respect to b and setting $\frac{dG}{dt} = 0$, with $\eta = \alpha = v = 0$). For $E^* = \psi > 0$ we have $g(b)^* = g(1)^*$ for all $0 \leq b \leq 1$ in this case. Therefore $g(1)^* = G^* = 2B^*$ and $B^* = \frac{w\psi}{2}$ (Figure 9(a), with $v = 0, w = 2, \zeta = 1, \psi = 2$). When bursting does not occur for $\zeta = 0$ (see Figure 7(a), white, $E^* = 0$), sufficiently fast extracellular growth can nonetheless drive E^* to ψ (Figure 9(b), with $v = 0, w = 2.5, \zeta = 1, \psi = 2$). We consider $v > 0$ and look for steady states for E and B. Setting $\Xi(E) = 0$ gives $E^* = 0$ or $E^* = \psi$. It follows from $g(1)^* = wE^*(1 + vB^*)$ and $G^* = 2B^*$ that $B^* = \frac{w\psi}{2-vw\psi}$ when $E^* = \psi$. This expression for B^* becomes negative for $vw\psi > 2$. We observe that $E^* = 0$ in such cases (Figure 9(c), with $v = 0.3, w = 2.2, \zeta = 1, \psi = 5$). When $vw\psi < 2$, we sometimes observe oscillatory behaviour (Figure 9(d), with $v = 0.3, w = 2.2, \psi = 2$ and $\zeta = 1$). When ζ is sufficiently large, $E^* = \psi$ in this case (Figure 9**(d)**, with $v = 0.3, w = 2.2, \psi = 2$ and $\zeta = 10$). We do not consider the observed oscillatory behaviour that drives E to zero a relevant model feature within the scope of our project. While the observed oscillatory behaviour of the model may be an interesting mathematical feature for future study, the required parameters do not fall within the parameter regimes that are relevant for granuloma when we compare to the agent based model GranSim. Hence, it does not fall within the scope of our study, comparing this continuum model to GranSim, in the context of Crohn's

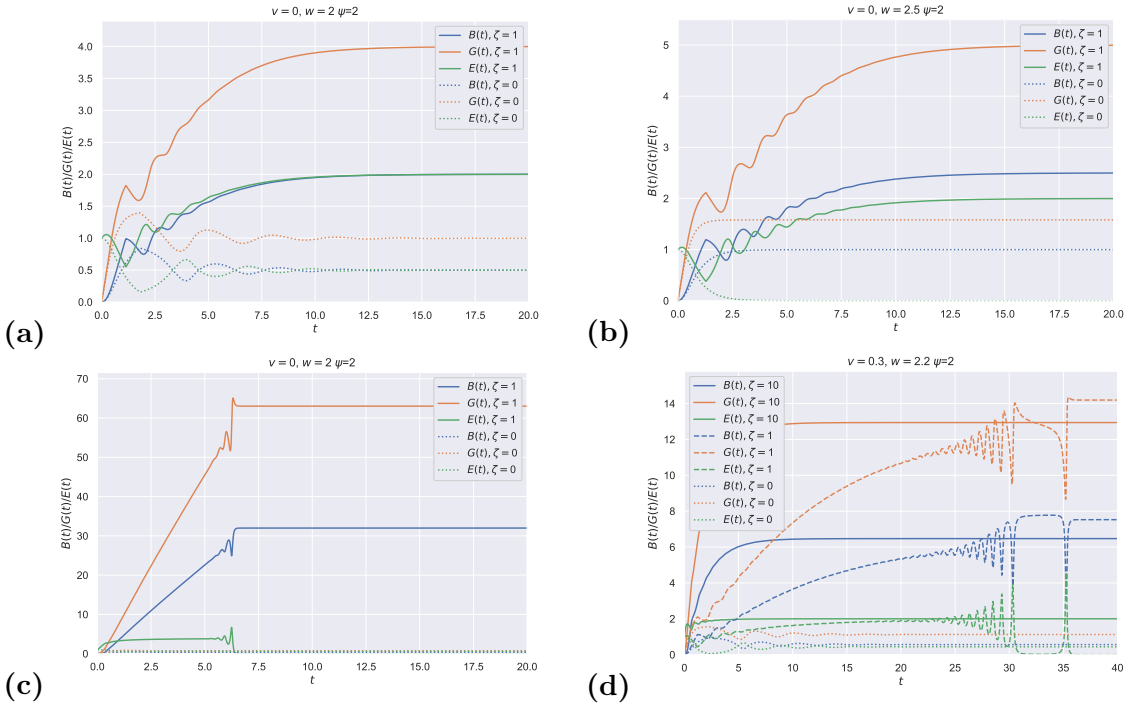


Figure 9: Extracellular growth, Section 4.4.4.1. B, G and E against time for **a)** $v = 0, w = 2, \zeta \in \{0, 1\}, \psi = 2$, **(b)** $v = 0, w = 2.5, \zeta \in \{0, 1\}, \psi = 2$, **c)** $v = 0.3, w = 2.2, \zeta \in \{0, 1\}, \psi = 5$, **(d)** $v = 0.3, w = 2.2, \psi = 2$, with $\zeta = 0$ (dotted lines), $\zeta = 1$ (dashed lines) and $\zeta = 10$ (solid lines). We did not consider macrophage apoptosis, fusion, killing, or intracellular bacterial growth: $\alpha = \eta = \lambda = \kappa = 0$.

disease and intestinal TB granuloma. Hence such features are not pursued below.

4.4.4.2 Intracellular growth and killing

We consider intra-cellular growth and killing in the absence of extra-cellular growth. Recall that the intra-cellular growth and killing term is given by $Z(b,t) = \lambda b\left(1 - \frac{b}{p}\right) - b\left(\frac{k(t)}{q+b}\right)$. In this section we only consider constant $k(t) = \kappa$. We first consider the case without killing (κ=0). We distinguish $p < 1$ and $p > 1$, with 1 the non-dimensional bursting load (Figure 10, solid (A) and dashed (B) blue lines respectively). In the former case, bacteria do not induce necrosis, even when the bacterial load is high. In contrast, in the necrotic case, pathogens keep growing until the macrophage bursts. We show an example of both cases (Figure 11).

We consider killing. For increasing $\kappa > 0$, the bacterial load of a macrophage can now decrease due to intra-cellular pathogen killing. Although characteristic curves in our model

can have a negative gradient (i.e. decreasing b over time as a result of killing), we recall that b will never become negative because $Z(0,t) = 0$. As macrophages cease to exist when their bacterial load exceeds 1, we will not consider cases where characteristic curves have a negative gradient at the right boundary $b = 1$. The zeros of $Z(b,t)$ are given by

$$b_0^\dagger = 0, \tag{4.120}$$

$$b_1^\dagger = \frac{\lambda(q-p) - \sqrt{\lambda^2 p^2 + \lambda^2 q^2 - 4\kappa\lambda q + 2\lambda^2 pq}}{2\lambda}, \tag{4.121}$$

$$b_2^\dagger = \frac{\lambda(q-p) + \sqrt{\lambda^2 p^2 + \lambda^2 q^2 - 4\kappa\lambda q + 2\lambda^2 pq}}{2\lambda}. \tag{4.122}$$

We can distinguish three cases (Figure 10, orange and green lines). In the case **(C)** (Figure 10, solid orange line), $b_2^\dagger$ does not lie between zero and one. When the recruitment is large enough, no macrophage will reach a bacterial load larger than $b_1^\dagger$ before all extra-cellular pathogens are taken up. The infection is cleared over time (Figure 12 **(C).1**). We recall that killing of pathogens by macrophages decreases their bacterial load, but has no impact on the total granuloma size $G(t) = \int_0^1 g(b,t)db$. Only bursting and apoptosis can decrease $G(t)$. For each characteristic, as b moves to zero due to killing, $g(b,t)$ increases over time as the total area $G(b,t) = \int_0^1 g(b,t)db$ is not affected by killing. In Figure 12 **(C).1** (left) and elsewhere where killing drives characteristics to the left boundary $b = 0$, we decided to limit the range of $g(b,t)$ on the y-axis for visibility reasons. When recruitment is insufficient, a pathogen outbreak will occur (Figure 12 **(C).2**). In the case **(D)** (Figure 10, dashed orange line), both $b_1^\dagger$ and $b_2^\dagger$ have values between zero and one. When recruitment is large enough, the infection will be cleared over time in a similar way as before. For smaller recruitment, all characteristics will move to $b = 0$ or $b = b_2^\dagger$ over time (Figure 12 **(D)**). When $b_0^\dagger$ is the only zero of $Z(b)$ in the interval $[0,1]$ (Figure 10, green line), the macrophages kill the pathogens they take up and the total bacterial load will decrease over time (Figure 12 **(E)**).

As a final example, we show how the introduction of fusion can help clear infection in a case such as **(D)**, i.e. both $b_1^\dagger$ and $b_2^\dagger$ have values between zero and one (Figure 10). We observed that without fusion, all characteristics will move to $b = 0$ or $b = b_2^\dagger$ over time. This corresponds to a situation where some macrophages have such a high bacterial load (i.e. $b_1^\dagger < b < b_2^\dagger$) that they can not clear it. With sufficient fusion, the bacterial load of the

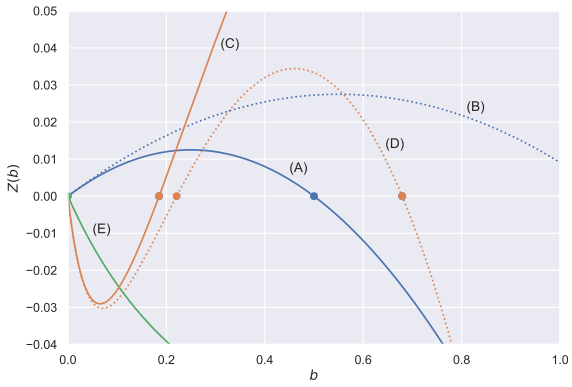


Figure 10: The intra-cellular growth and killing $Z(b) = \lambda b\left(1 - \frac{b}{p}\right) - b\left(\frac{\kappa}{q+b}\right)$ against b for **(A)** $\lambda = 0.1, p = 0.5, \kappa = 0$ (solid blue), **(B)** $\lambda = 0.1, p = 1.1, \kappa = 0$ (dashed blue), **(C)** $\lambda = 0.8, p = 1.5, \kappa = 0.2, q = 0.1$ (solid orange), **(D)** $\lambda = 0.8, p = 1, \kappa = 0.2, q = 0.1$ (dashed orange), and **(E)** $\lambda = 0.1, p = 2, \kappa = 0.2, q = 0.5$ (solid green).

most laden macrophages gets diluted to a level (i.e. $0 < b < b_1^\dagger$) where the macrophages are able to clear their intracellular load again (Figure 13).

4.5 Model verification against an agent-based model

The aim of this section is to compare our model dynamics compare to the dynamics of GranSim, an agent-based model of *Mycobacterium tuberculosis* (TB) induced granuloma formation in the lung developed by the group of Denise Kirschner. GranSim was published in 2003 and has since been continuously updated and validated against human and animal experimental data [63, 98, 285, 307]. The comparison with GranSim allows us to investigate our model behaviour within a biologically realistic parameter range. Furthermore, it is of interest to see to what extent our much simpler model could qualitatively replicate the dynamics of GranSim. Although GranSim contains many more features than our model, it does not consider macrophage fusion. For our comparison, we will derive fixed values for our model parameters, whereas the GranSim parameter equivalents are often dynamically changing. Because of the large discrepancies in structure between the two models, all comparisons are for qualitative purposes only. Throughout this section, we will use the dimensional version of our model. As before, units used are the average mass of a bacterium (β) and recruited macrophage (μ). Units of time used are 10 minutes (θ) and days (days).

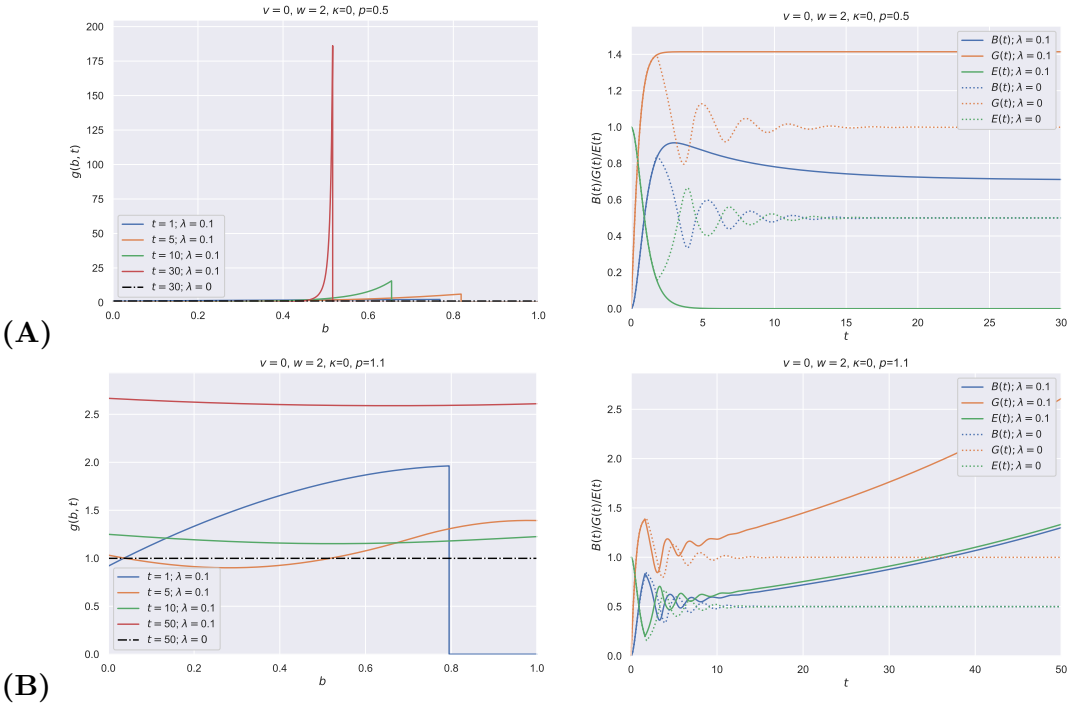


Figure 11: Intracellular growth, Section 4.4.4.2. The distribution of $g(b,t)$ for various t (left) and B, G and E against time (right) for **(A)** $p = 0.5 < 1$, and **(B)** $p = 1.1 > 1$, both with $v = 0, w = 2$, and λ as indicated in the legend. The labels **(A)** and **(B)** correspond to the labels in Figure 10, with values of λ and p as already listed in this caption. We did not consider macrophage apoptosis, fusion, killing, or extracellular bacterial growth: $\alpha = \eta = \kappa = \zeta = 0$.

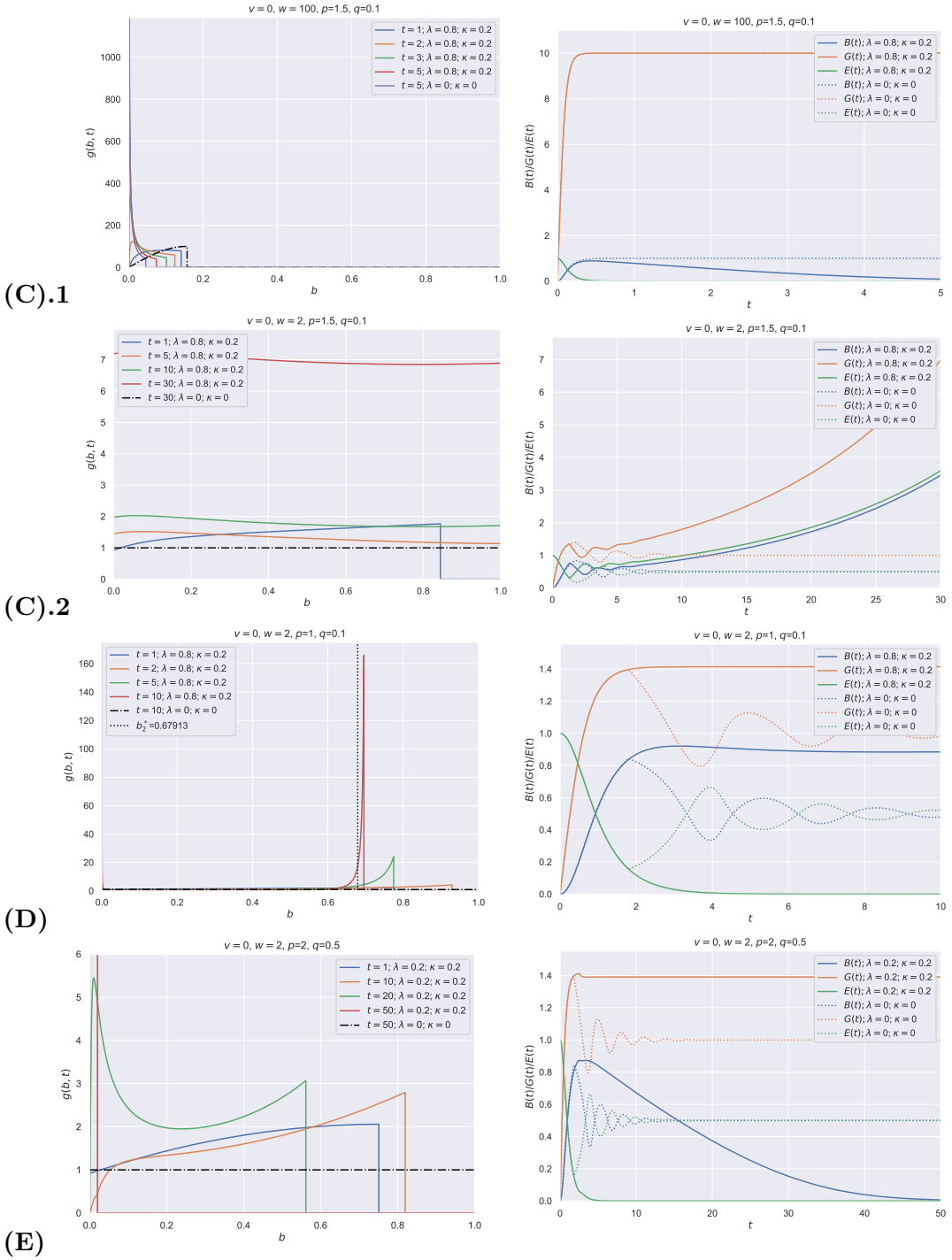


Figure 12: Killing and growth, Section 4.4.4.2. The distribution of $g(b,t)$ for various t (left) and B, G and E against time (right) for **(C).1** $v = 0, w = 100$, and **(C).2** $v = 0, w = 2$, both with $p = 1.5, q = 0.1$, for **(D)**, with $v = 0, w = 2, p = 1, q = 0.1$, and for **(E)**, with $v = 0, w = 2, p = 2, q = 0.5$ and κ and λ as indicated in the legend. The labels **(C)**, **(D)** and **(E)** correspond to the labels in Figure 10, with values of λ, κ, p and q as already listed in this caption. We did not consider macrophage apoptosis, fusion, or extracellular bacterial growth: $\alpha = \eta = \zeta = 0$.

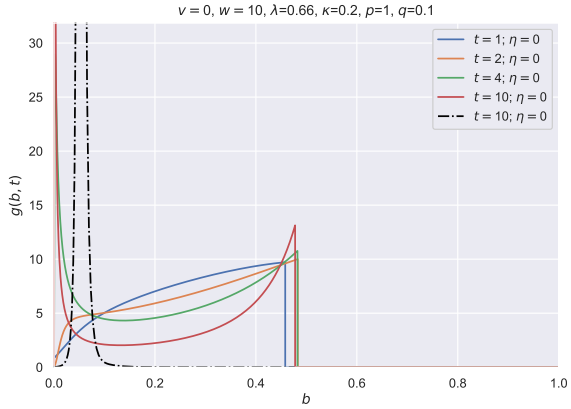
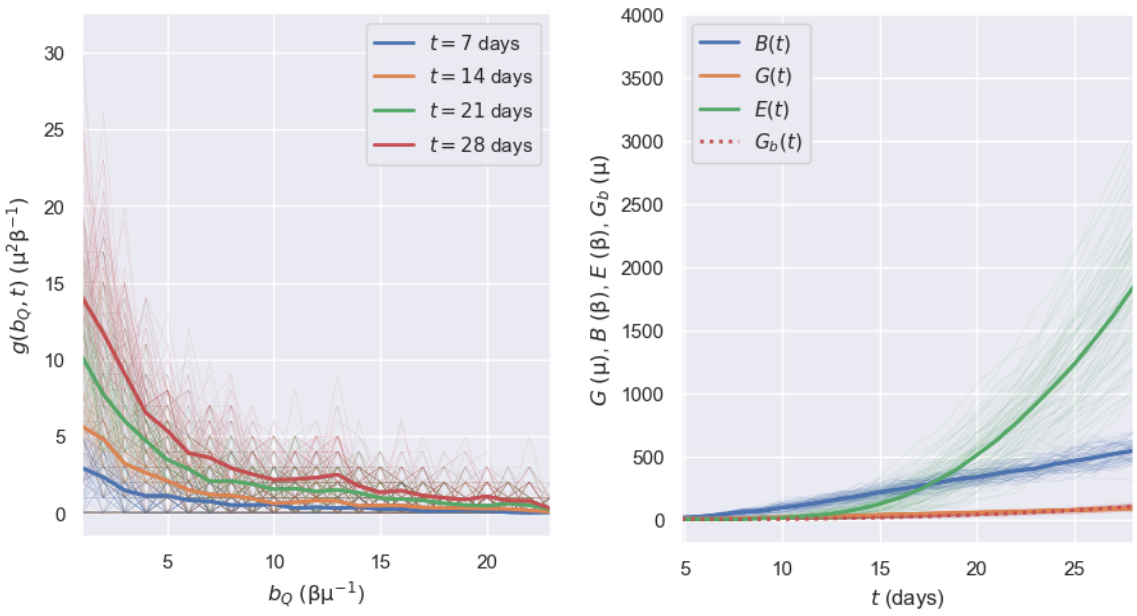


Figure 13: Fusion can help clear infection by diluting the bacterial load of the most laden macrophages. Distribution of $g(b,t)$ for various t, with $\eta \in \{0,5\}, v = 0, w = 10, \lambda = 0.66, \kappa = 0.2, p = 1, q = 0.1$. We did not consider macrophage apoptosis or extracellular bacterial growth: $\alpha = \zeta = 0$.

In GranSim, bacterial and macrophage populations are tracked by numbers. We convert numbers to mass by assuming each GranSim macrophage and bacteria has average mass.

We use the 2-dimensional GranSim model executable, parameterised with the GranSim 'baseline containment' parameter set, that can be downloaded from the Kirschner lab webpage (`malthus.micro.med.umich.edu/MSM/GRviz/`, accessed on 17 June 2020). This iteration of the model is based on the model by Cilfone et al. [63]. GranSim simulations using the 'baseline containment' parameter set result in a stable bacterial load at 200 days post infection, and organized granuloma with features comparable to experimentally observed granuloma [63]. Agents in this version of GranSim are T cells and macrophages. Each of the micro-compartments on the GranSim grid can contain a maximum of one macrophage and two T cells. Micro-compartments also contain a continuous amount of intra- and extracellular bacteria, and of various cytokines. Adaptive immunity plays an important role in TB. Macrophages activated by T cell produced IFNγ are much more effective in killing *Mycobacterium tuberculosis* [288]. In GranSim, T cells are introduced in the model after 28 days, the time that it takes for the adaptive immune system to activate (see [64], value derived from a non-human primate model of TB infection [199]). GranSim T_γ cells can activate macrophages via IFNγ where-after the macrophages gain the ability to kill intracellular bacteria. We note that although our model does not contain T cells, we could still include T



(a) **(b)**

Figure 14: Results of a 100 individual simulations of GranSim (thin lines) and their average (bold lines), using the 'baseline containment' parameter set. **(a)** The discrete distribution of the number of infected macrophages $g(b_Q, t)$, with $b_Q \in \{1, 2, 3 \ldots 23\}$ $\beta\mu^{-1}$ the intracellular bacterial load, rounded to the nearest positive integer, for $t = 7, 14, 21, 28$ days. **(b)** The total number of intracellular bacteria (B), the total number of macrophages containing bacteria (G), the total number of extracellular bacteria (E), and the cumulative mass of macrophages that have burst (G_b) over time.

cell mediated killing implicitly, by letting the killing rate $k(t)$ increase over time. However, in this section we will only run our simulations for the first 28 days of infection, when no T cells are present. No intracellular killing takes place during this time. In GranSim, intracellular bacteria grow exponentially and extracellular bacteria grow logistically. Macrophages burst when their intracellular bacterial load reaches 23 $\beta\mu^{-1}$ and release their intracellular bacterial burden to the environment.

We ran the GranSim executable 108 times times with the default 100 by 100 grid size and 10 minute interval time-step, and discarded the 8 simulations where the infection was cleared during the first 28 days. We show the 100 individual and averaged distribution of infection for $t = 10, 14, 21, 28$ days, and 100 individual and averaged trajectories for the first 28 days of infection of the total number of macrophages containing bacteria (G), the total number of extracellular bacteria (E), the total number of intracellular bacteria (B),

and the cumulative number of macrophages that have burst (G_b) over time (Figure 14). We will compare these simulations with simulations of our own model.

In GranSim, all model simulations start at $t = 0$ days with a single infected macrophage. The bacterium within this macrophage grows until the macrophage bursts, at $\bar{t} = 4.85$ days. As our model initially does not contain any infected macrophages, we start our model simulations at $\bar{t}$ days, with an initial extracellular bacterial load $E(\bar{t}) = b_{\text{burst}} = 23\ \beta\mu^{-1}$, and $G(\bar{t}) = 0\ \mu$.

We set the value of the bursting size and the intra-cellular growth rate in our model to the corresponding values of GranSim's 'baseline containment' parameter set ($b_{\text{burst}} = 23\ \beta\mu^{-1}$ and $\lambda = 4.5 \times 10^{-3}\ \theta^{-1}$ respectively). Following GranSim, we assume exponential intracellular growth, by letting our intracellular carrying capacity parameter $p \to \infty$. We set the fusion parameter $\eta = 0\ \mu^{-1}\theta^{-1}$, as fusion is not implemented in GranSim. We set $\kappa = 0\ \beta\mu^{-1}\theta^{-1}$, as no intracellular killing takes place during the first 28 days of infection. We will discuss our remaining model parameters ($\alpha, u, v, w, \zeta, \psi$).

We estimate the apoptosis rate α, the fraction of infected macrophages that die due to apoptosis per unit of time. Apoptosis in GranSim is dependent on the micro-compartment specific concentration of the cytokine TNF. When a GranSim infected macrophage dies by TNF induced apoptosis, its intracellular bacterial load disappears as well. We have made the same assumption (see Equation (4.19)). We show the number of GranSim infected macrophages that died due to TNF induced apoptosis as a fraction of the total number of infected macrophages per one day interval (Figure 15 **(a)**). We estimate α by averaging this fraction for the final 14 days of infection ($t = 14 - 28$ days), and dividing it by 144, the number of 10 minute intervals per day. We only use the final 14 days of infection, as α is approximately constant during this time, but not before. We note we could have also explored an increasing, non-constant form of α, inspired by the GranSim dynamics. We have chosen to use a constant α for simplicity. We will explore the effects of setting $\alpha = 0\ \theta^{-1}$ later in this section. In GranSim, macrophages secrete various cytokines in response to infection, that in turn recruit more macrophages from the blood. The recruited macrophages can take up extracellular bacteria. Our model does not contain explicit equations for cytokine concentrations, but we assume that the number of recruited macrophages infected per unit

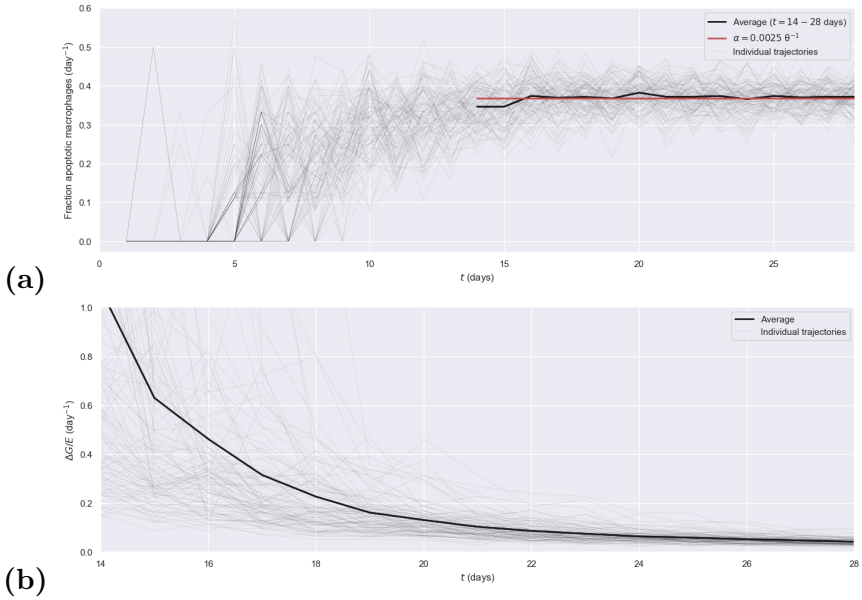


Figure 15: Results of a 100 individual simulations of GranSim (thin black lines) and their average (bold black lines). **(a)** Plot of $\frac{G_{apop}(t)}{G_{apop(t)}+G(t)}$ against time (days), i.e. the number of GranSim infected macrophages that died due to TNF induced apoptosis during the past day $G_{apop}(t)$, divided by the sum of this number and the total number of infected macrophages at that point in time $G(t)$, calculated for each day. **(b)** Plot of the increase in total number of GranSim infected macrophages $\Delta G(t) = G(t) - G(t-1)$, divided by the total extracellular load $E(t)$, and calculated for each day. The 'baseline containment' parameter set was used.

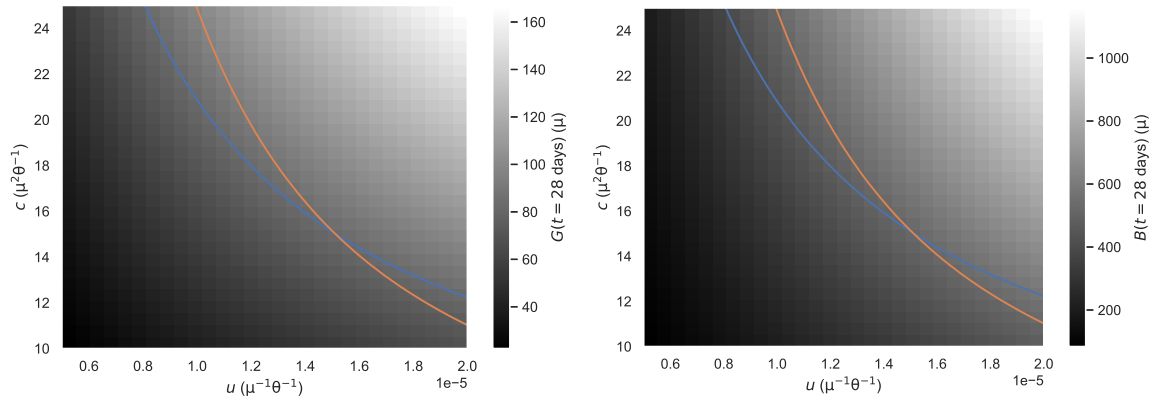


Figure 16: Heatmaps of our model simulations, showing the granuloma size G **(a)**, and bacterial load B **(b)** at $t = 28$ days for varying c and u, and ζ adjusted such that $E(t = 28 \text{ days}) = 1.8 \times 10^3\ \beta$, the average extracellular bacterial load in GranSim after 28 days of infection. Contour plots of $G(t = 28 \text{ days}) = 85\ \mu$ (blue) and $B(t = 28 \text{ days}) = 5.4 \times 10^2\ \beta$ (orange), the average granuloma size and intracellular bacterial load in GranSim after 28 days of infection. Parameter values are $\lambda = 4.5 \times 10^{-3}\ \theta^{-1}$, $b_{\text{burst}} = 23\ \beta\mu^{-1}$, $E(\bar{t}) = 23\ \beta$, $\alpha = 2.5 \times 10^{-3}\ \theta^{-1}$, $\psi = 1.14 \times 10^6\ \beta$, $\kappa = 0\ \beta\mu^{-1}\theta^{-1}$, $\eta = 0\ \mu^{-1}\theta^{-1}$.

of time per extracellular bacteria ($uR(t)$, equation (4.9)) is an increasing function of the intracellular and extracellular load: $uR(t) = uwE(1 + vB)$. We show the increase in total number of GranSim infected macrophages per day, divided by the total extracellular load E (Figure 15 **(b)**). We note that this amount, which corresponds to the term $uR(t)$ in our model, decreases over time, i.e. the chance of an extracellular bacteria to be taken up by an uninfected GranSim macrophage decreases over time. As both E and B increase over time, our original form of $R(t) = wE(1 + vB)$ is not suitable to describe such recruitment dynamics. We will assume $R(t) = c$ instead, with c a constant. We note we could have also explored a decreasing, non-constant form of c to mimic the GranSim dynamics. We have chosen a constant c for simplicity. We will explore a range of values for c.

The number of bacteria taken up per unit of time uEG in our model is dependent on the extracellular bacterial load E, but independent of the bacterial load of each macrophage. In GranSim, uptake decreases for an increasing intracellular bacterial load and macrophages containing more than eleven bacteria do not take up any bacteria at all. Further, a macrophage in GranSim can at most take up a single bacterium every ten minutes, and only if such a bacterium is present in the Moore neighbourhood of the macrophage. Instead of assuming a non-constant, bacterial load-dependent form of u to mimic the GranSim dynamics, we keep u constant for simplicity. We will explore a range of values for u.

In GranSim, the extracellular carrying capacity is 114β for each of the 10,000 grid micro-compartments. We set the extracellular carrying capacity parameter $\psi = 114 \times 10^4$ β, corresponding to the maximal GranSim bacterial load. We will discuss the effects of increasing the value of ψ for both models later in this section. The extracellular bacterial growth rate in GranSim is 0.0025 θ^{-1}. We have chosen not to set the bacterial growth rate parameter ζ to this number, but instead to adjust its value such that the extracellular bacterial load $E(t = 28 \text{ days}) = 1.8 \times 10^3$ β, the average extracellular bacterial load in GranSim after 28 days of infection. We adjust ζ, because we implicitly incorporate the effects of the capability of GranSim macrophages to kill extra-cellular bacteria. In our model, we assume bacteria can only be killed after internalization. The GranSim extracellular killing results in a lower net extracellular bacterial growth rate. We note that extra-cellular killing by GranSim is dependent on the total number of macrophages present, but also on the

accessibility of the extracellular bacteria, as GranSim macrophages can only kill bacteria present in the Moore neighbourhood of the macrophage, where the Moore neighbourhood is defined as the micro-compartment containing the macrophage, and the eight surrounding micro-compartments.

We re-emphasize that we simplified the GranSim dynamics extensively, by trying to capture the temporal GranSim dynamics in fixed parameter values, such as for ζ, α and c; hence, as previously stated, any comparisons we make are for qualitative purposes only.

We varied c and u and adjusted ζ such that $E(t = 28 \text{ days}) = 1.8 \times 10^3$ β, the average extracellular bacterial load in GranSim after 28 days of infection (Figure 14). We show heat maps for G and B at $t = 28$ days and indicate where $G(t = 28 \text{ days}) = 85$ μ (blue) and $B(t = 28 \text{ days}) = 5.4 \times 10^2$ β (orange), the average granuloma size and intracellular bacterial load in GranSim after 28 days of infection (Figure 16). We plot the distribution of infection and trajectories of B, G, E, and G_b for $c = 17$ $\mu^2\beta^{-1}$, $u = 1.1 \times 10^{-5}$ $\mu^{-1}\theta^{-1}$, $\zeta = 1.3 \times 10^{-3}$ θ^{-1}, the point of intersection of the blue and orange lines (Figure 17).

We can now address the main aim of this section: to compare the dynamics of GranSim to our model dynamics. We will compare the average dynamics of GranSim parametrised with the set of 'baseline containment' parameter values as shown in Figure 14 with our model dynamics as shown in Figure 17. We note that for these simulations of our model, we have chosen values for c, u and ζ such that the size of the extracellular bacterial load, intracellular bacterial load, and granuloma size G at 28 days of infection of our model simulations match those of the GranSim simulations. We have also set the initial size of these three entities in our model to values corresponding to the GranSim initial conditions. It is therefore not surprising that our model trajectories of B, G and E (Figure 17 (b)) resemble the corresponding GranSim trajectories (Figure 14 (b)). We are interested to explore the key similarities and differences between our model and GranSim for our chosen parametrisation. First, we observe that for this parametrisation of our model, the distribution of bacterial load resembles the GranSim dynamics (Figures 14 (a) and 17 (a)). Further, the number of burst macrophages over time G_b resemble the GranSim dynamics (Figures 14 (b) and 17 (b), red lines). The effects of removing the apoptosis feature on our model dynamics also resemble the effects of removing this feature on the GranSim dynamics (Figure 18).

Further increasing the value of the extracellular bacterial carrying capacity ψ does not impact our model dynamics notably, as the value of $\psi = 1.14 \times 10^6$ β was already much higher than the extracellular bacterial load at any point in time. We are effectively assuming exponential bacterial growth. Similarly, increasing the maximal number of bacteria per micro-compartment in GranSim from 114 to 1×10^6 β, does not have a significant impact on the granuloma size G and the bacterial load size B after 28 days of infection (average increase of 0.8% and 1% respectively, $N = 100$ simulations, 2 sample t-test, $p>0.05$). However, this increase in the extracellular bacterial load does significantly increase the total GranSim extracellular bacterial population after 28 days of infection by 198% ($N = 100$ simulations, 2 sample t-test, $p<0.05$). Due to the spatial structure of GranSim, the additional extracellular bacteria are not accessible to macrophages. In highly infected areas, macrophages were already taking up bacteria at their maximum rate before the carrying capacity was increased. Furthermore, GranSim contains necrotic micro-compartments that are inaccessible to macrophages. In contrast, the growth rate of the granuloma in our model (number of macrophages per unit of time) is proportional to the total extracellular bacterial load. We will discuss the implications of this difference in the discussion (Section 4.7)

Finally, we note that multiple GranSim features remain that have no equivalent in our model. For instance, in both GranSim and our model, macrophages can die due to apoptosis or bursting. The intracellular bacterial load dies within the macrophage during apoptosis, but becomes extracellular after bursting. In GranSim, a third type of cell death exists. During this spontaneous death due to age macrophages release their intracellular bacterial load to the environment. This type of cell death is rare compared to TNF induced apoptosis (After 28 days, on average 11 and 625 macrophages have died due to age and TNF induced apoptosis respectively, $N = 100$ simulations, average granuloma size $G(t = 28 \text{ days}) = 85$ μ). We ignored cell death due to age in our model comparisons, as no corresponding feature in our model exists. Other differences that we did not consider include the explicit inclusion of various cytokines, the explicit inclusion of an uninfected macrophage population, and of course the spatial structure of GranSim. Each micro-compartment can only be occupied by one macrophage and at later time points (starting after 19 days of infection), macrophage movement is further restricted by inaccessible necrotic micro-compartments. We note that

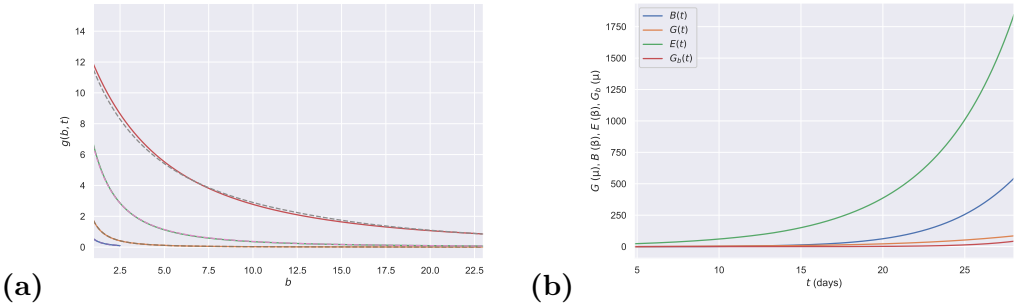


Figure 17: Simulations of our model, for comparison with GranSim, for t from $t = \bar{t} = 4.85$ to $t = 28$ days. **(a)** The distribution of the number of infected macrophages $g(b, t)$, for $t = 7, 14, 21$, and 28 days. **(b)** Plots of the total number of intracellular bacteria (B), the total number of macrophages containing bacteria (G), the total number of extracellular bacteria (E), and the cumulative number of macrophages that have burst (G_b) over time. Parameter values are $\lambda = 4.5 \times 10^{-3}\ \theta^{-1}$, $b_{\text{burst}} = 23\ \beta\mu^{-1}$, $E(\bar{t}) = 23\ \beta$, $\alpha = 2.5 \times 10^{-3}\ \theta^{-1}$, $\psi = 1.14 \times 10^{6}\ \beta$, $\kappa = 0\ \beta\mu^{-1}\theta^{-1}$, $\eta = 0\ \mu^{-1}\theta^{-1}$, $c = 17\ \mu^{2}\beta^{-1}$, $u = 1.1 \times 10^{-5}\ \mu^{-1}\ \theta^{-1}$, $\zeta = 1.3 \times 10^{-3}\ \theta^{-1}$, with these choices as motivated in the main text.

the multiple differences between GranSim and our model have been accounted for implicitly when we simulated our model with the values $c = 17\ \mu^{2}\beta^{-1}, u = 1.1 \times 10^{-5}\ \mu^{-1}\ \theta^{-1}, \zeta = 1.3 \times 10^{-3}\ \theta^{-1}$, as these were based on GranSim 'baseline' cell number simulations at $t = 28$ days.

4.5.1 The impact of fusion

Finally, we consider the effects of fusion. We recall that GranSim does not consider cell fusion. We will use the same model parameters as before, when we compared our model with GranSim (Figure 17). However, this time we will explore a positive value of the fusion rate parameter η. Macrophages become multi-nucleated giant cells (MGCs) after fusion. We estimate the level of fusion on an *in vitro* model of human peripheral blood mononuclear cell (PBMC) granuloma formation developed by the group of Frédéric Altare [190]. On average, after 10 days of infection, 1.5 small multi-nucleated cells (4.5 nuclei on average) and 7 large multi-nucleated cells (20 nuclei on average) were observed per granuloma in this model [190]. Assuming each additional nucleus corresponds to a fusion event, we can determine the fusion rate per granuloma. As our fusion parameter considers fusion per macrophage, we divide the obtained rate by the averaged simulated Granuloma size G over ten days of infection. This results in $\eta = 1.5 \times 10^{-5}\ \mu^{-1}\theta^{-1}$. We show our model simulations with

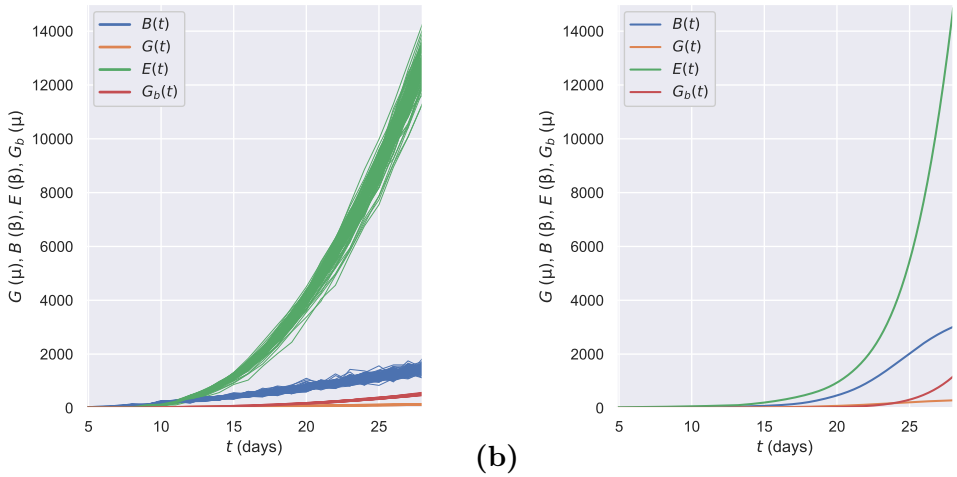


Figure 18: The effects of removing the apoptosis feature on our model dynamics resemble the effects of removing this feature on the GranSim dynamics. Simulations of GranSim **(a)** and our model **(b)**, shown for t from $t = \bar{t} = 4.85$ to $t = 28$ days, without TNF induced apoptosis. Plots of the total number of intracellular bacteria (B), the total number of macrophages containing bacteria (G), the total number of extracellular bacteria (E), and the cumulative number of macrophages that have burst (G_b) over time. For GranSim, the 'baseline containment' parameter set was used, but without TNF induced apoptosis. Parameter values used for our model are $\lambda = 4.5 \times 10^{-3}\ \theta^{-1}$, $b_{\text{burst}} = 23\ \beta\mu^{-1}$, $E(\bar{t}) = 23\ \beta$, $\alpha = 0\ \theta^{-1}$, $\psi = 1.14 \times 10^{6}\ \beta$, $\kappa = 0\ \beta\mu^{-1}\theta^{-1}$, $\eta = 0\ \mu^{-1}\theta^{-1}$, $c = 17\ \mu^{2}\beta^{-1}$, $u = 1.1 \times 10^{-5}\ \mu^{-1}\ \theta^{-1}$, $\zeta = 1.3 \times 10^{-3}\ \theta^{-1}$, with these choices as motivated in the main text.

$\eta = 0\ \mu^{-1}\theta^{-1}$ and with $\eta = 1.5 \times 10^{-5}\ \mu^{-1}\theta^{-1}$ (Figure 19). We observe that the effects of fusion are negligible for our estimated level of fusion.

4.6 Differentiating between Crohn's disease and intestinal tuberculosis

The aim of this section is to use our model to compare an *in vitro* TB induced model with an adherent-invasive *Escherichia coli* (AIEC) induced model by choosing a suitable parameter set for both. We will also discuss the impact of fusion in this context. We base our parametrisation on an *in vitro* model of human peripheral blood mononuclear cell (PBMC) granuloma formation developed by the group of Frédéric Altare [190, 225, 269, 275, 276]. We have chose this specific *in vitro* system, as it would be a suitable system to test model predictions in future work (see Section 4.7). The TB and AIEC induced granuloma are representative of granuloma found in intestinal TB (iTB) and Crohn's disease

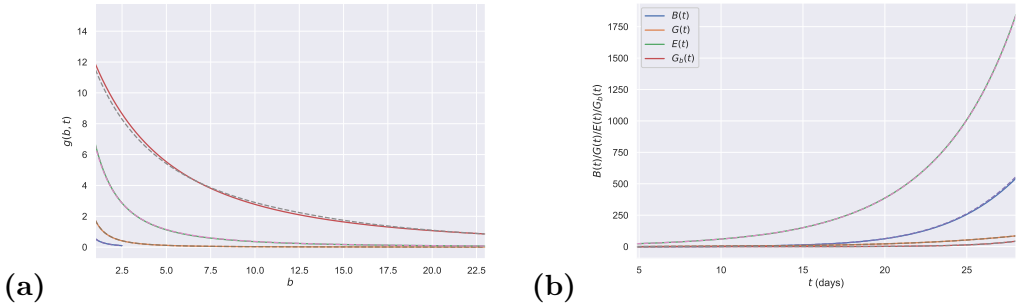


Figure 19: Simulations of our model, for comparison with GranSim, with ($\eta = 1.5 \times 10^{-5}$ $\mu^{-1}\theta^{-1}$, dashed lines), and without ($\eta = 0$ $\mu^{-1}\theta^{-1}$, solid lines) fusion, for t from $t = \bar{t} = 4.85$ to $t = 28$ days. **(a)** The distribution of the number of infected macrophages $g(b, t)$, for $t = 7, 14, 21$, and 28 days. **(b)** Plots of the total number of intracellular bacteria (B), the total number of macrophages containing bacteria (G), the total number of extracellular bacteria (E), and the cumulative number of macrophages that have burst (G_b) over time. Parameter values are $\lambda = 4.5 \times 10^{-3}$ θ^{-1}, $b_{\text{burst}} = 23$ $\beta\mu^{-1}$, $E(\bar{t}) = 23$ β, $\alpha = 2.5 \times 10^{-3}$ θ^{-1}, $\psi = 1.14 \times 10^{6}$ β, $\kappa = 0$ $\beta\mu^{-1}\theta^{-1}$, $c = 17$ $\mu^{2}\beta^{-1}$, $u = 1.1 \times 10^{-5}$ μ^{-1} θ^{-1}, $\zeta = 1.3 \times 10^{-3}$ θ^{-1}, with these choices as motivated in the main text.

(CD) respectively. The two diseases are difficult to tell apart and the type of granuloma associated with CD and iTB are one of the few differentiating characteristics [12]. Because of the uncertainty in the model parameter values, all simulations in this section are for qualitative purposes only.

For the iTB granuloma simulation, we set the intra- and extracellular growth rates, extracellular carrying capacity, bacterial uptake rate, bursting size and TNF driven apoptosis rate to the same values as before, when we compared our model to GranSim (Table 4.2). We have chosen to use the same parameter values, as very little quantitative data of iTB granuloma formation can be found in the literature. Additionally, recruited monocyte-derived macrophages, and not tissue resident macrophages, are thought to be the main source of lung TB granuloma formation [129]. We therefore assume that the human monocytes used in the *in vitro* PBMC model are similar enough to their counterparts in the *in vivo* human lung to justify the same parameter values. We run our simulation for 21 days, the maximum time span used by the study of *in vitro* PBMC granuloma formation from the Altare group [190]. We also intially assume no fusion takes place (i.e. $\eta = 0$ $\mu^{-1}\theta^{-1}$). The effects of fusion will be explored later in this section. We assume the initial number of extracellular bacteria and number of macrophages available to take up extracellular bacteria are different

from before, when we assumed an *in vivo* lung environment, and adjusted our corresponding model parameters accordingly. The PBMC in the *in vitro* setup are infected with a multiplicity of infection of 1 TB for every 1000 PBMC [190]. Assuming 5% of the PBMC are monocytes, this results in 1 TB for every 50 monocytes [172]. The mean size of an *in vitro* granuloma at the final measured time point after 21 days of infection is 5500 cells, 825 (15%) of which are monocytes [190]. We therefore assume an initial bacterial load of $E_0 = \frac{825}{50} = 16.5\ \beta$ for a typical *in vitro* granoluma. We adjust the value of the constant recruitment parameter c such that the normalized distance between our simulated granuloma size and the mean granuloma size numbers at $t = 7, 14, 21$ days after TB infection is minimal (resulting in $c = 557.2\ \mu^2\beta^{-1}$, experimental data from [190]). We have taken $R(t) = c$ constant, as in the former section, assuming the rate at which an extracellular bacteria is taken up by an uninfected macrophage $uR(t)$ stays constant over time. An $R(t)$ of the form $R(t) = vE(1 + wB)$ is not suitable, as it assumes monocytes are recruited from the blood in response to secreted cytokines. Finally, we consider the effects of fusion. We recall that on average, after 10 days of infection, 1.5 small multi-nucleated cells (4.5 nuclei on average) and 7 large multi-nucleated cells (20 nuclei on average) were observed per granuloma [190]. Assuming each additional nucleus corresponds to a fusion event, we can determine the fusion rate per granuloma as before. We recall that as our fusion parameter considers fusion per macrophage, we divide the obtained rate by the averaged simulated Granuloma size G over ten days of infection. This results in $\eta = 1.5 \times 10^{-5}\ \mu^{-1}\theta^{-1}$. We show model simulations over ten days with $\eta = 0\ \mu^{-1}\theta^{-1}$ and with $\eta = 1.5 \times 10^{-5}\ \mu^{-1}\theta^{-1}$ (Figure 20).

For CD, the agent inciting granuloma formation remains elusive [257]. One of the causative species of CD granuloma might be adherent-invasive *Escherichia coli* (AIEC), that has been shown to induce granulomas *in vitro* by the Altare group [203, 225]. We will generate simulations of an AIEC granuloma that was induced *in vitro* using the same procedure as the TB granuloma just described. As the same cell type was used, and since no further information on the difference in rate of uptake is available, we assume the recruitment and infection rates for the AIEC case are similiar to the TB case (i.e. we take u and c as before). We run our simulation for 9 days, the maximum time span used by the

study of *in vitro* AIEC granuloma formation [225]. Multinucleated cells are rarely found in *in vivo* CD granuloma. Consistent with this, and in contrast to the TB case, less than one multinucleated cell per granuloma after 9 days of infection was observed in the *in vitro* system [225]. We therefore assume fusion is negligible and set the fusion parameter $\eta = 0$ $\mu^{-1}\theta^{-1}$. We note that this finding is in accordance with a study using endoscopic biopsy data, where multi-nucleated giant cells (MGCs) were only found in iTB granuloma, but not in CD granuloma [359].

In contrast to many other intracellular pathogens including TB, AIEC does not induce apoptosis in human macrophages [124, 247]. We have therefore taken $\alpha = 0$. No evidence of necrosis due to bursting has been reported and viable macrophages with up to 50 intracellular AIEC have been observed [87]. We therefore set the bursting size for AIEC infected macrophages very high (1000 bacteria), and set the intracellular carrying capacity for AIEC LF82 $p = 50$. AIEC has a much higher growth rate than *Mycobacterium tuberculosis* (TB). Exact rates depend on various factors, such as experimental conditions, cell type and bacterial strain. A time course of *in vitro* infection study of AIEC in the macrophage cell line THP-1 can be found in a study by Demarre et. al [87]. A simple mechanistic model of the time course of infection was constructed in this study. We will use their estimate of an initial intracellular doubling time for AIEC of approximately 4.8 hours [87]. Similar doubling times for this AIEC strain (LF82) have been reported for other cell types (3.85 and 3.7 hours, measured in human monocyte derived macrophages and J774-A1 cells [124]). In contrast, the intracellular doubling time for TB is approximately 26 hours [63, 262]. Following Demarre et. al, we assume a lag phase of 8.2 hours post infection with no bacterial growth or killing, i.e. we define $\lambda = k = 0$ for $t < 8.2$h, and a doubling time of 4.8h for $t > 8.2$h [87]. We will discuss the form of k for $t > 8.2$h below. As all bacteria are assumed to be taken up before they start replicating, we ignore extracellular bacterial growth (i.e. ζ=0 θ^{-1}). This is consistent with the *in vitro* results, where the antibiotic gentamicin was added after all extracellular bacteria were taken up [225]. After an initial net increase in bacterial load after infection, the intracellular AIEC population starts decreasing due to intracellular killing [87, 124]. We therefore take $k(t)$ of the form $k(t) = \kappa_{max}(1 - e^{-\tau t})$ for $t > 8.2$h and $k(t) = 0$ for $t < 8.2$h. We note the form of $k(t)$ and our assumption of

exponential intracellular bacterial growth is similar to our model of *in vitro Salmonella* infection (see Chapter 3). A range of initial bacterial loads was explored in the *in vitro* study of AIEC induced granuloma formation [225]. Even at a multiplicity of infection (MOI) as low as 1 TB for every 10,000 PBMC, intracellular bacteria were still observed after 9 days of infection for this MOI [225]. This is of interest as this low MOI is consistent with conditions found in the gut. We will assume an MOI of 30, the MOI used in a study by Demarre et. al [87]. As we assume a 1500 times higher MOI than in the TB case, we set $E_0 = 2.5 \times 10^4$ at 1500 times the value used before. We take $\tau = 1.7 \times 10^{-2}\ \theta^{-1}$, so that the time at which the intracellular bacterial load is at its maximum (at $t = 19$ hours post infection) matches the observations by Demarre et. al, while keeping all other parameters fixed [87]. As no quantitative data on the intracellular bacterial load over time for *in vitro* AIEC granuloma exists, we will not estimate values for κ_{max} and q, the level of infection at which killing takes on half its maximum value (see Equation (4.10)). We show an example for $\kappa_{max} = 1.31\ \beta\mu^{-1}\theta^{-1}$ and $q = 50\ \beta\mu^{-1}$ (Figure 21). At these values, the surviving intracellular bacterial population after 9 days of infection is 29% of its size after 2 hours of infection, corresponding to the decrease in bacteria measured by confocal microscopy for MOI=100 ([225], third figure. We measured the decrease in number of green pixels, corresponding to GFP positive bacteria in Fiji, see Appendix B). A summary of the parameter estimates may be found in Table 4.2. We observe that the AIEC granuloma size initially increases until all bacteria are taken up and then stays constant over time (Figure 21). In contrast, the TB granuloma keeps growing (Figure 20). In the AIEC case, no extracellular bacterial growth is assumed, because macrophages in the gut will only encounter very few bacteria at a time and no large extracellular population drives granuloma growth [225]. Hence, it is not a surprise that the model prediction in this case is that the extracellular bacterial population gets completely taken up. In contrast, in *in vitro* TB granuloma, bacteria are encountered in between macrophages [269]. A non-zero extracellular bacterial load in the TB case is therefore realistic. We note that in our simulations the AIEC granuloma is much larger than the TB granuloma, while *in vivo* TB granuloma are usually found to be larger. The difference in size can be explained by the much higher initial bacterial load for the simulated AIEC granuloma. Because the simulated TB granuloma keep growing

Par.	Units	TB	AIEC	Description
b_{burst}	$\beta\mu^{-1}$	23	1000	Bacterial load when a macrophage bursts
E_0	β	16.5	2.5×10^4	Initial bacterial load
κ_{max}	$\beta\mu^{-1}\theta^{-1}$	0	0 for $t < 8.2$h, 1.31 for $t > 8.2$h	Maximum killing rate
τ	$\beta\mu^{-1}\theta^{-1}$	-	1.7×10^{-2}	Delay in killing
q	$\beta\mu^{-1}$	-	50	Bacterial load at which the killing rate takes on half its maximum value
α	$1/\theta$	2.5×10^{-3}	0	Apoptosis rate macrophages (TNF induced)
λ	θ^{-1}	4.5×10^{-3}	0 for $t < 8.2$h, 2.4×10^{-2} for $t > 8.2$h	Intracellular bacterial growth rate
ζ	θ^{-1}	1.3×10^{-3}	1.5×10^{-1}	Extracellular bacterial growth rate
η	$\mu^{-1}\theta^{-1}$	1.5×10^{-5}	0	Fusion rate.
c	$\mu^2\beta^{-1}$	557	557	Recruitment
u	$\mu^{-1}\theta^{-1}$	1.1×10^{-5}	1.1×10^{-5}	Uptake rate
ψ	β	1.14×10^6	1.14×10^6	Extracellular carrying capacity
p	β	∞	∞	Intracellular carrying capacity

Table 4.2: Parameter values taken to simulate TB and AIEC induced *in vitro* granuloma models. Units of all model parameters are listed as well, with $\theta = 10$ minutes β = average mass of a bacteria and μ = average mass of a macrophage.

over time, and the AIEC granuloma do not, the simulated TB granuloma will eventually outgrow the CD granuloma, though this is beyond the timescales we have considered, as we do not consider adaptive immune events. Finally, we note that fusion in this *in vitro* model does not seem to play a large role in the granuloma dynamics. We found the number of fusion events for the AIEC granuloma to be negligible. For the TB granuloma, fusion slightly decreased the the number of burst macrophages and reduced necrosis in this way (Figure 20, compare dashed and solid lines). An increase of the fusion rate could magnify this effect.

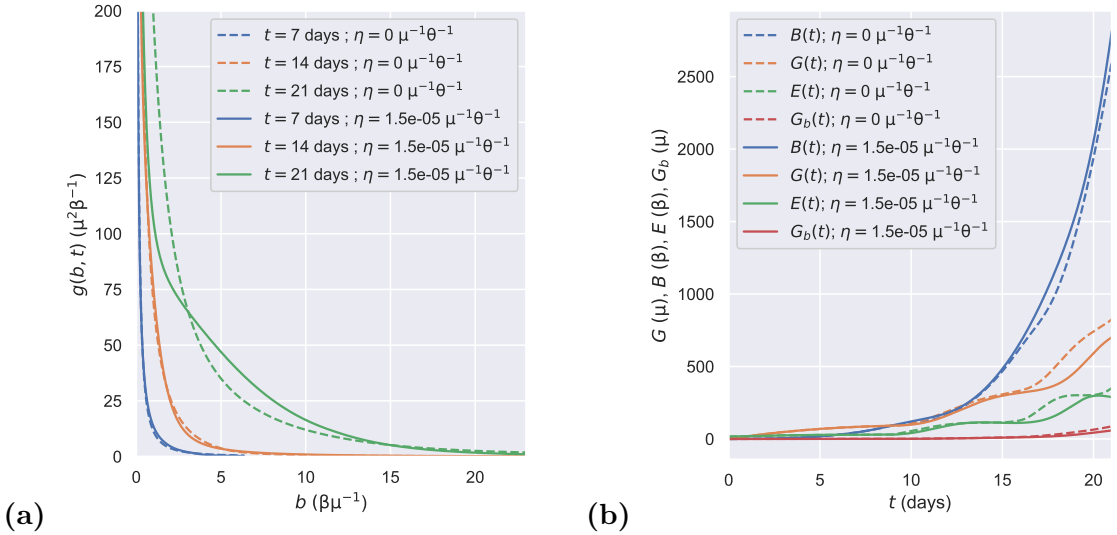


Figure 20: Simulations of our model, parametrised to represent an *in vitro* TB granuloma, from $t = 0$ to $t = 21$ days. **(a)** The distribution of the number of infected macrophages $g(b, t)$, for $t = 7, 14$ and 21 days. **(b)** The total number of intracellular bacteria (B), the total number of macrophages containing bacteria (G), the total number of extracellular bacteria (E), and the cumulative number of macrophages that have burst (G_b) over time. We have taken $\eta = 0\ \mu^{-1}\theta^{-1}$ (dashed lines) or $\eta = 1.5 \times 10^{-5}\ \mu^{-1}\theta^{-1}$ (solid lines) and all other parameters as in Table 4.2, column TB.

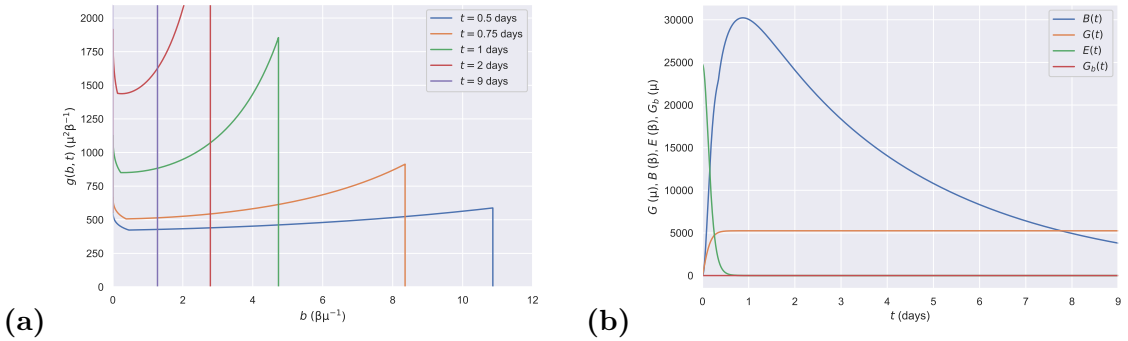


Figure 21: Simulations of our model, parametrised to represent an *in vitro* AIEC granuloma, from $t = 0$ to $t = 9$ days. **(a)** The distribution of the number of infected macrophages $g(b, t)$, for $t = 0.5, 0.75, 1, 2$ and 9 days. **(b)** The total number of intracellular bacteria (B), the total number of macrophages containing bacteria (G), the total number of extracellular bacteria (E), and the cumulative number of macrophages that have burst (G_b) over time. We have taken all parameters as in Table 4.2, column AIEC.

4.7 Discussion

We developed and studied a bacterial-load structured model of granuloma formation by macrophage aggregation that tracks the granuloma size, intracellular bacterial load, extracellular bacterial load, and bacterial load distribution within the granuloma over time. Model features include intracellular and extracellular bacterial growth, intracellular bacterial killing by macrophages, macrophage recruitment, infection, fusion, apoptosis, and bursting due to bacterial overload. Apoptosis is a form of regulated cell death that contibutes to infection containment, as the intracellular bacteria contained within an apoptotic macrophage die as well [247]. In contrast, during necrotic death due to bacterial overload and consecutive bursting, the intracellular bacteria spread [31].

Cell fusion is a key feature of granuloma formation, resulting in multi-nucleated cells that are thought to be better at degrading particles [145, 190, 239, 245, 257, 300]. We have included macrophage fusion as non-linear and non-local source and sink terms in our model. When two macrophages fuse, they produce a macrophage with their averaged bacterial load and combined mass. Fusion conserves both macrophage and bacterial mass. Terms of this specific type have not been studied before, although related size-structured models of coagulation and fragmentation processes do exist [345]. In size-structured models, the total number, not mass, of modelled entities is considered. During coagulation in size-structured models, modelled entities are combined, while during fragmentation they break up, resulting in an increase and decrease in average model entity size. Coagulation and fragmentation decrease and increase the total number of modelled entities respectively. We can view our fusion terms as a process of coagulation and simultaneous fragmentation into two equal parts. Note that this type of process in a size-structured model would conserve the total number of particles, just as macrophage mass is conserved in our model during fusion. Fusion is additionally of interest as it has not yet been considered in existing, other types of mathematical models of granuloma formation, such as the agent-based models by the group of Denise Kirschner [177].

We studied how changes in parameters correspond to various types of granuloma found in the body. We first considered a granuloma of non-living substance, such as silica particles,

tattoo pigments, or latex beads [296]. Assuming constant recruitment allowed us to explore an analytically tractable simplified version of the model.

We observed that the recruitment needs to be sufficient to ensure uptake of all foreign material and to avoid necrosis. When the mass of foreign material is too high compared to the mass of recruited macrophages, macrophages will become necrotic and burst. Necrosis has been observed *in vivo* for excessive silica particle concentrations [114, 312]. In an *in vitro* model of nano-particle induced granuloma formation, repeated cycles of phagocytosis and cell death accompanied by particle release were also observed [296].

Still only considering non-living particles, we observed the total particle load and granuloma size were only affected by the introduction of fusion in necrotic granuloma, but not in non-necrotic systems. In a necrotic granuloma, increasing the fusion rate increases the mass of foreign material that a granuloma can hold. In non-necrotic granuloma, fusion does not affect the extracellular particle load of granuloma size, but does affect the distribution of infection as macrophages continue to fuse over time. Such continued fusion events were for instance observed in an *in vitro* human PBMC granuloma model induced by *N. brasiliensis* larvae [308]. After 14 days the majority of macrophages had fused, and cells contained over a 100 nuclei each. We mention this study as an example of continued fusion by macrophages, though we also note that our model is not suitable to describe the dynamics of an *N. brasiliensis* larva induced granuloma, as we are concerned with intracellular pathogens.

We considered extracellular pathogen growth. The extracellular pathogen population will grow to its carrying capacity, unless the macrophage recruitment rate is sufficiently high relative to the extracellular growth rate. We also observed oscillatory behaviour that drives the extracellular pathogen population to zero for a certain parameter regime observed when we include a dependency of the macrophage recruitment on the intracellular bacterial load. We do not consider this oscillatory behaviour that drives E to zero a relevant model feature within the scope of our project. We note the oscillations are not present within the parameter regime studied in the GranSim comparison, and the intestinal granuloma simulations. The oscillations could be explored in future work.

We considered intracellular bacterial growth and death and explored the effects of varying the various model parameters related to these processes. When the intracellular carrying capacity of bacteria is smaller than the intracellular bacterial load required for a macrophage to burst, bacteria do not induce necrosis, even when the bacterial load is high. This is for instance observed in *Mycobacterium leprae* induced granuloma, consisting of macrophages with an average load of 120 pathogens [135, 186, 288]. In contrast, in the necrotic case, pathogens keep growing until the macrophage bursts. In TB infected mice, the cytolytic burst size lies between 20-40 pathogens per macrophage [288].

We considered killing. Contrary to most applications of age-structured models, we allow the bacterial load to decrease over time due to killing. However, bacterial load can never become negative and we do not consider biologically irrelevant case where burst macrophages reincarnate. As expected, killing can clear infection over time. Due to the form of our growth and killing equation, a special case exists where macrophages can effectively clear their bacterial load up to a certain threshold of infection. After passing this threshold, their load either grows to carrying capacity, or the macrophage bursts, depending on the parameter set used. The introduction of fusion can dilute the bacterial load of the most laden macrophages. Macrophages with a bacterial load beyond the threshold up until which they are able to clear their bacterial load, can fuse with macrophages with a lower bacterial load, resulting in an increased capability of the granuloma to clear bacteria.

We compared our model with the agent-based model GranSim developed by the group of Denise Kirschner [63]. The comparison with the agent-based model allowed us to investigate our model behaviour within a biologically realistic parameter range. Furthermore, we investigated to what extent our much simpler model could replicate the dynamics of GranSim. We note that any comparisons we make between our model and GranSim are for qualitative purposes only, as GranSim is a much more complex model. Multiple GranSim model features do not have an equivalent in our model and we ignored the spatial structure of GranSim. We further tried to estimate fixed parameter values for our model, such as for ζ, α and c, while in GranSim, these values typically change over time. We only compare simulations up to 28 days of infection, the moment T cells are introduced in GranSim. We do not compare the models after the adaptive immunity has been activated, as our model

does not contain T cells. We choose a set of parameter values to approximate the GranSim extracellular bacterial load E, intracellular bacterial load B, and granuloma size G at $t = 28$ days. The simulations for E, B and G at earlier time points using this parameter set are similar to the GranSim trajectories. Moreover, the number of burst macrophages over time, the distribution of bacterial load, and the effects of the removal of apoptosis resemble the GranSim dynamics. The removal of TNF induced apoptosis has a large impact on the level of infection, suggesting a critical role for apoptosis in infection containment for this parametrisation of the model [247]. We did note a difference in the effects of increasing the extracellular carrying capacity. Increasing the GranSim extracellular carrying capacity almost tripled the total extracellular bacterial load, but had no significant effect on the granuloma size after 28 days of infection. Due to the spatial structure of GranSim, the additional extracellular bacteria are not accessible to macrophages. In highly infected areas, macrophages were already taking up bacteria at their maximum rate before the carrying capacity was increased. Furthermore, GranSim contains necrotic micro-compartments that are inaccessible to macrophages. In contrast, the growth rate of the granuloma in our model (number of macrophages per unit of time) is proportional to the total extracellular bacterial load. We conclude that our model is not suitable in its current form to account for walled off bacteria. We could introduce a compartment of inaccessible extracellular bacteria in our model to more closely approach the GranSim model. When inaccessibility of bacteria is less relevant, for instance when the extracellular pathogen population is small, or when studying the initial stages of granuloma formation, our current model could be used.

Finally, we simulated an *in vitro* intestinal granuloma model. These simulations were inspired by an *in vitro* model of human peripheral blood mononuclear cell (PBMC) granuloma formation developed by the group of Frédéric Altare [225, 275]. We choose to simulate an *in vitro* model of granuloma formation, to give an impression of how our model could be integrated with experimental data in future work. A combination of an *in vitro* granuloma model such as developed by the group of Altare, combined with a mathematical model, could drive biological insight in the many unknowns of CD granuloma formation. We note that testing model predictions using an *in vitro* model is more feasible than in the corresponding *in vivo* setting in the human gut. We choose the *in vitro* model developed

by the group of Altare over other *in vitro* granuloma models as it is especially suitable to study intestinal granuloma by using primary human blood cells. As monocyte-derived macrophages are constantly recruited to the gut, the cell type used is the most appropriate choice in this setting [123]. In contrast to blood monocytes, tissue-resident gut macrophages are poor at participating in a granulomatous reaction *in vitro* [97]. We compared the *in silico* model simulations of an *in vitro* TB induced model with an AIEC induced model, where we assume these *in vitro* granuloma are representative of intestinal TB (iTB) and CD granuloma respectively. This is of interest as iTB and CD are difficult to tell apart and the type of granuloma associated with CD and iTB are one of their few differentiating characteristics [12]. While macrophages can kill AIEC, we assumed they can not kill TB in the absence of an adaptive immune response during the first days post infection [63]. We further assumed no macrophages burst during an AIEC infection and AIEC do not induce apoptosis [87, 124, 247]. We only implemented fusion for the TB granuloma, as the cell fusion rate was negligible in the *in vitro* AIEC study [225]. In the case of TB, the inclusion of a fusion term did not have a large impact on our model simulations.

4.7.1 Summary and conclusions

Granuloma formation is of special interest as it involves both impaired bacterial clearance and inflammatory cytokine production in macrophages, the focus of our former two chapters. We are particularly interested in cell fusion, that is thought to increase the ability of macrophages to handle high levels of pathogen load. Because of the dependency of the proposed effects of fusion on bacterial load, we developed a bacterial-load structured model of granuloma formation, which was the main aim of this chapter. In the context of this thesis, we are primarily concerned with granuloma found in the gut, such as CD and intestinal *Mycobacterium tuberculosis* (TB) granuloma. We have therefore parametrised our model to represent such granuloma and conduct an initial study into the difference between the granuloma found in CD and in intestinal TB (iTB), while explicitly considering the impact of fusion in this context. This was the secondary aim of this chapter.

As part of the main aim of this chapter to develop a bacterial-load structured model, we investigated the various model features, including cell fusion, and verified our model

against one of the agent-based models developed by the group of Denise Kirschner [63]. Our model simulations of the bacterial load and granuloma size for the first 28 days of granuloma formation were in qualitative agreement with the the agent-based model results. In contrast to the agent-based model, our model is not capable to account for the effects of walled-off extracellular bacteria, as found in long-lived, necrotic tuberculosis granuloma. Our model does not feature a spatial component. Only when pathogen inaccessibility is less relevant should our simpler model be used. Our model is easier to analyse and less computationally expensive than the agent-based model. It also includes macrophage fusion as a model feature.

The second aim of this chapter was to conduct an intitial study into the difference between the granuloma found in CD and in intestinal TB (iTB), while explicitly considering the impact of fusion in this context. We parametrised our model to represent an *in vitro* model of human peripheral blood mononuclear cell (PBMC) granuloma formation developed by the group of Frédéric Altare [225, 275]. In contrast to the CD type granuloma, the TB granuloma kept growing over the simulated time span. An important, albeit negative, result is that in the *in vitro* set-up we studied, fusion is not predicted to have a big impact on the model dynamics for the parameters associated with an *in vitro* AIEC study. However, more generally fusion can significantly alter the granuloma dynamics to enhance the clearance of infection.

The use of pathogen load as an internal structuring variable is a novel approach in mechanistic granuloma modelling. We have implemented cell fusion as non-local source and sink terms in our model. The inclusion of terms of this specific form in a population structured model are of interest as they have not been studied before. Furthermore, fusion has not yet been considered in existing models of granuloma formation. Finally, no existing mathematical modelling studies have focussed explicitly on granulomas found in the gut.

In future work, a controlled *in vitro* environment could be used to refine our parameter estimates and test our model predictions. One could for instance study the dependency of the rate of bacterial uptake and fusion on the bacterial load per macrophage. We have assumed a constant uptake and fusion rate per macrophage. Other areas of interest include the effects of fusion, bursting and apoptosis on the granuloma size, level of infection,

and distribution of bacteria within the granuloma. Macrophages from individuals with an immunodeficiency in bacterial handling capability are at risk of developing granulomatous disease. Studying the dependency of macrophage killing ability on bacterial load per macrophage is therefore particularly relevant. Finally, the role of the various cytokines important in granuloma formation and cell fusion such as IL-4 or IL-13 is an area of interest [86, 223, 232, 239, 257]. A combined experimental and modelling set-up explicitly considering macrophage fusion inducing cytokines could be used to further study this component of granuloma dynamics.

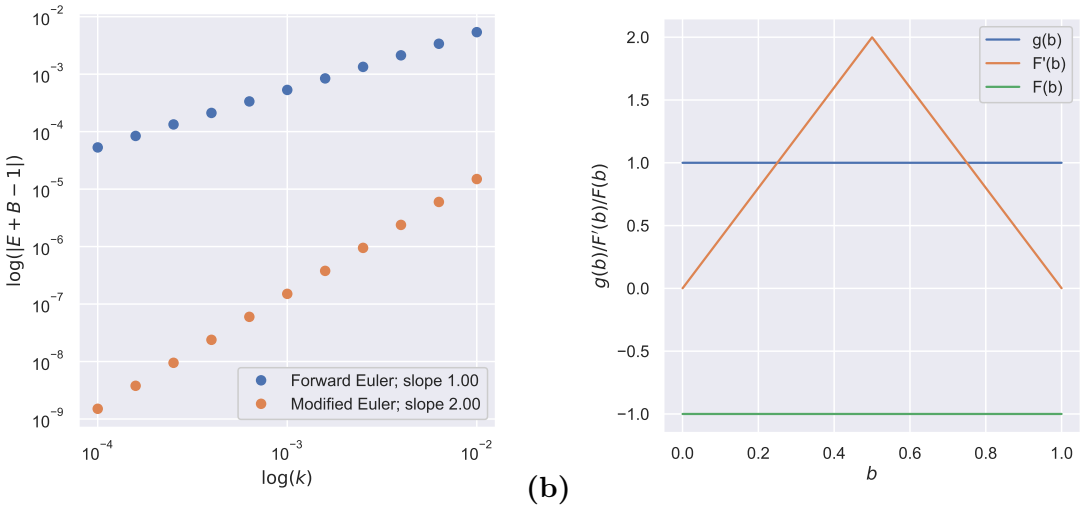
Appendix A

We test the convergence of our modified Euler method. We use the non-dimensionalised version of our system. We set $\alpha = \eta = \lambda = \kappa = v = 0$, and $w = 2$. Because we assume no killing, growth, or apoptosis takes place, the total mass of particles in our system is constant over time: $B(t) + E(t) = 1$. We plot the difference between this known particle mass and the numerical approximation of particle mass at $t = 1$ against the time step size k, both for the forward Euler and modified Euler method on a log-log scale. As expected, the slope of the two graphs is 1.00 and 2.00 for the forward and modified Euler method respectively (Figure 22 (a)).

We have tested our implementation of the fusion source term. For a unit step function $g(b) = 1$, for $0 < b < 1$ and $g(b) = 0$ otherwise, the fusion source term as defined in equation (4.16) is constant in time and has solution $F'(b) = \eta 4b$ for $0 < b < 0.5$ and $F'(b) = \eta(4-4b)$ for $0.5 < b < 1$. The fusion sink term as defined in equation (4.15) has solution $F(b) = -\eta$ for this choice of $g(b)$. We confirmed our numerical implementation of both the fusion source and sink term satisfied this form (Figure 22 (b)).

Appendix B

We determined the decrease in bacteria from 2 h to 9 days after infection in the study by Meconi et al. [225]. We loaded the two figures showing the GFP expression at 2 h and 9 days of infection in Fiji (middle subfigures of [225], third figure). We split the images to their



(a) **(b)**

Figure 22: (a) Log-log plot of the difference between the analytical particle mass and our numerical approximation of the particle mass for both the forward (blue) and modified (orange) Euler method against the time step size k, at $t = 1$, with $\alpha = \eta = \lambda = \kappa = v = 0$, and $w = 2$. (b) The unit step function $g(b) = 1$, for $0 < b < 1$ and $g(b) = 0$ otherwise, (blue) and the fusion source $F'(b)$ (orange) and sink $F(b)$ (green) for this choice of $g(b)$, with $\eta = 1$.

respective red, green and blue components using the menu command 'Image/Color/Split Channels', and measured the number of green pixels, using the menu commands 'Image/Set Threshold/Auto', 'Analyze/Set Measurements...', where we ticked the boxes 'Area' and 'Limit to threshold', and 'Analyze/Measure'. As both figures contain the same number of pixels, the decrease in number of green pixels is a measurement of the decrease in bacterial load.

Chapter 5

Discussion

We summarize the key findings of the thesis and reflect on how our work has contributed to our understanding of macrophages in inflammatory bowel disease, and to the wider field of systems biology. We discuss future directions of our work. We finish with a perspective on the role of mechanistic modelling in biological science, including immunology.

5.1 Thesis summary

We have developed simple mechanistic mathematical models to study key open questions in the context of macrophage functioning in inflammatory bowel disease (IBD), a complex, multi-factorial, and chronic immune mediated disease. We focussed on cytokine signalling (Chapter 2), bacterial handling (Chapter 3), and granuloma formation (Chapter 4). Macrophages play an important role in IBD, but many aspects of their functioning remain poorly understood. The study of **cytokine networks** is important for the identification of cytokine (receptor)s as new therapeutic targets and of the context in which these targets should be used. Common genetic variants associated with IBD risk, such as *NOD2* and *ATG16L1* polymorphisms point towards an important role for impaired **bacterial handling** in Crohn's Disease, one of the two major types of IBD. Dynamic, **granulomatous structures** are a hallmark of intestinal inflammation. They emerge in a pro-inflammatory cytokine environment when normal pathogen clearance mechanisms have failed. Their formation is a culmination of the dis-regulated cytokine and bacterial handling responses studied in the earlier chapters.

5.1.1 Introduction

In Chapter 1, we gave an overview of macrophage biology and mathematical modelling of macrophages in inflammation. We also highlighted two studies that successfully combined modelling with experimentation in the context of macrophage functioning in inflammation, and more generally have argued before that such an approach can drive novel mechanistic insights (Jansen et. al, [165]).

5.1.2 Correlation does not imply causation: inference of an inflammatory cytokine network

In Chapter 2, we aimed to gain mechanistic understanding in the regulation of IL-23, a key cytokine in IBD, by developing a method to extract a minimal, weighted cytokine interaction network from experimental data.

Inflammatory processes are tightly controlled by complex cytokine networks. Inhibition of the pro-inflammatory cytokine TNFα has proven to be a very successful strategy in the treatment of inflammatory bowel disease and other immune mediated inflammatory diseases. The success of TNFα inhibition has inspired the development of several other anti-cytokine therapies. However, cytokine therapy is both disease and patient specific. A better understanding of cytokine functioning is key for the identification of cytokine (receptor)s as new therapeutic targets and of the context in which these targets should be used.

In light of this, we developed a method to extract a minimal, weighted network from cytokine interaction data using a simple coupled ODE system and the Akaike information criterion (AIC) for model selection. We also validated the method with synthetic data, examining its structural and practical identifiability together with its sensitivity to demonstrate objective network extraction where a gold standard was present. We applied the method to extract a network of IL-23 regulation in the context of IBD, using an experimental flow cytometry dataset. Statistical analysis of the dataset containing cytokine production data by stimulated monocytes identified 31 statistically significant modulation effects of the blockade or addition of one cytokine on the production rate of another cytokine. Based on this set of 31 edges, we explored the various different network configurations using subsets

of edges by fitting the data to ODE models representing the various network configurations. In contrast to the statistical analysis that resulted in a list of possible direct interactions, the ODE approach allows us to compare direct and indirect effects and adjust edge weights accordingly. We assigned weights to each edge in each network configuration, by computing the increase in distance between the simulated and experimental data when the corresponding edge parameter was set to zero, and all other parameters were kept the same. We ranked the different network configurations based on model fit and complexity, using the AIC for model selection. We introduced a second approach where we do not constrain the number of possible network interactions to the subset of edges resulting from the statistical analysis, but instead considered all possible positive and negative interactions between all cytokines. We investigated parameter identifiability and predicted the effects of untested combinations of cytokine (receptor) inhibitors.

5.1.2.1 Biological importance

The aim of the model was to investigate which cytokines are important in the regulation of IL-23, a key cytokine in IBD pathogenesis. A transcriptional signature IL-23 producing inflammatory monocytes has been found to be predictive of anti-TNFα therapy resistance [22]. The model clearly indicates that in this inflammatory context, IL-23 is driven by IL-1β production, but not by TNFα production. Further, the model finds that the positive regulation of IL-23 by IL-1β is independent of the effect of IL-1β on the production of TNFα, IL-1α, IL-10 or IL-6. This supports the view of IL-1β as a promising target for those patients that fail to respond to TNFα inhibition. The model also shows that the negative feedback of IL-10 on IL-23 is independent of the effect of IL-10 on the other studied cytokines (TNFα, IL-1α, IL-1β, and IL-6). Finally, the observed up-regulation of IL-23 by IFNγ is not driven by the down-regulation of IL-10 by IFNγ. This suggests IFNγ works as a direct amplifier of IL-23 production.

5.1.2.2 Connection to the wider systems biology field

Multiple network inference methods exist, such as information theoretic or Bayesian modeling approaches [99, 101, 212, 238]. Xue and collegues for instance, inferred an undirected

signalling network of eight macrophage produced cytokines after LPS stimulation, using a Graphical Gaussian model (GGM) based on significant partial correlation coefficients of all pair-wise cytokine interactions [357]. Our dataset however was richer than the datasets commonly deployed for network inference using such methods. As quantitative effects of the addition or blockage of single cytokines on the system were known, we were able to model networks with directed, weighted edges that are either positive or negative. The model selection procedure further allowed us to differentiate between causation and correlation. We could remove edges between cytokines with correlated production rates when that correlation was found to be driven by other cytokines in the network. The developed method underlying our model could be applied to any similar type of dataset. The resulting extracted networks could be used to generate model predictions of untested (combinations of) cytokine (receptor) inhibitors. Such predictions could be tested to validate the network. Furthermore, the type of model (ODE based) could easily be extended to incorporate more complicated (non-linear) interactions, if appropriate data would be available. In contrast, such dynamic cytokine interactions could not be captured by the static, data-driven approaches as found in [99, 357].

5.1.3 Getting it just right: the balance between immunodeficiency and hyper-inflammation

In Chapter 3, we studied the immunodeficiency component of Crohn's disease using a combination of mathematical modelling and wet-lab experiments.

Although CD is characterised by a hyper-inflammatory phenotype, it has recently been hypothesized that CD could primarily be caused by an immunodeficiency in bacterial killing by the innate immune system [341]. This hypothesis is supported by genetic studies. Further understanding of this aspect of CD pathology could point towards new treatment options, such as bacterial clearance inducing drugs. We focussed on the NOD2/XIAP/RIPK2 pathway. Mutations in the nucleotide-binding oligomerization domain-containing protein 2 (NOD2) gene is the strongest genetic risk factor for CD and X-linked Inhibitor of Apoptosis (XIAP) deficiency can cause a Mendelian type of IBD [324]. NOD2 is a pathogen recognition receptor that is highly expressed in monocytes and macrophages [336]. NOD2

stimulation by its ligand muramyl dipeptide (MDP), a bacterial cell wall component, induces cytokine production and enhances killing of pathogens by innate immune cells [6]. In accordance, macrophages from patients with a deficiency in the NOD2 pathway produce less pro-inflammatory cytokines than cells from healthy controls when stimulated with NOD2 ligand [306]. It seems therefore paradoxical that deficiencies in the NOD2 pathway trigger CD development with associated high levels of TNFα and other pro-inflammatory cytokines.

We studied the hypothesis that the observed high levels of pro-inflammatory cytokines are driven by an increased bacterial load caused by the killing deficiency component of NOD2 defects. In particular, we hypothesised that other mechanisms associated with NOD2 deficiency, such as impaired immune cell recruitment, are not required to explain the inflammatory phenotype. We used a combination of wet-lab experiments, mathematical modelling, and data from the literature to study this hypothesis. For this chapter, I (JEJ) obtained experimental data myself, as part of this doctoral study, with the guidance of Sumeet Pandey, a post-doctoral fellow in Holm Uhlig's lab. Based on our wet-lab results, I constructed a mathematical model that links bacterial load to cytokine production over time (25h) in an *in vitro* system of *Salmonella* infected human monocyte-derived macrophages, thus generating *in silico* model simulations of pathogen load and cytokine trajectories (IL-1β, IL-6, IL-10, TNFα) over time while varying the killing and cytokine production capability of the cells. The model simulations were compared with data from the literature on the size and timing of the effects of genetic defects in the NOD2 pathway on pathogen load and cytokine concentration. In particular, literature data was used to determine estimates of typical changes in the values of our killing capability and cytokine production capability parameters, corresponding to mutations in the NOD2 pathway.

5.1.3.1 Biological importance

The aim of the model was to investigate whether bacterial handling driven cytokine hyperproduction fits in a simple framework of infected macrophages, in the absence of cell recruitment or other cell types. We concluded that our system is indeed capable of producing a state of increased cytokine levels during infection, even in the presence of an impairment

of cytokine production capability, and that the data from the literature did fit within this framework. This is in accordance with data from a study by Lapaquette et al., who measured the bacterial load and cytokine production simultaneously in NOD2 knock out cells, and observed both an increased bacterial load and increased cytokine concentration levels [187].

Further, we studied the initial distribution of infection using an existing confocal microscopy data set. We found that the initial distribution of infection follows a negative binomial distribution, and not a Poisson distribution. We therefore hypothesize that infection events are Poisson distributed, but the infection rates of the macrophages are heterogeneous, and are gamma distributed, in which case the unconditional distribution of infection can be written as a negative binomial distribution. This relates to the key open question on the role of macrophage heterogeneity in disease dynamics and will be further discussed in Section 5.2.

5.1.3.2 Connection to the wider systems biology field

Of our three research chapters, this chapter most closely reflects our argument for mechanistic model driven experimentation (Section 5.1.1).

Many mechanistic modelling efforts on macrophages in inflammation have been disconnected from wet-lab experimentation. We have previously provided an overview of such studies [165]. We found that when mechanistic modelling studies were complemented by wet-lab experimentation, the vast majority of associated experimental systems consisted of mouse models, murine or other animal/human immortalised cell lines. However, animal models and cell lines do not recapitulate all features of human disease pathophysiology and response to drug exposure [82, 363]. We have set an example by choosing to work with primary human cells.

The aims of this project were such that I (JEJ) could generate the experimental data needed myself. This created the opportunity to gain insight into the nature of wet-lab data collection. Such understanding is useful in the collaborative effort that this type of modelling should be. However it has also highlighted the challenges. Working with primary human cells entails less experimental control and thus higher signal-to-noise ratios, whereas

modelling demands low ratios: the tension in these mutually exclusive demands in turn emphasizes the need for experimental experience, to reduce noise, and higher modelling and data skills to manage the noise objectively. More generally therefore the challenges observed in this project further highlight the need for interdisciplinary training to interface wet and dry lab studies.

5.1.4 The whole is more than it parts: a bacterial load-structured model of granuloma formation

In Chapter 4, we studied what factors and cellular processes drive granuloma formation in Crohn's disease and other granulomatic disorders. The study of granuloma formation involves both the pro-inflammatory cytokine responses and the bacterial handling defects we studied in the preceding chapters. We developed a continuum model for the bacterial loaded structure of a granuloma forming via macrophage aggregation. The model tracks the granuloma size, intracellular bacterial load, extracellular bacterial load, and bacterial load distribution within the granuloma over time. It was also demonstrated how this model may be related to a discrete analogue to motivate the use of a continuum framework. Model features include intracellular and extracellular bacterial growth, intracellular bacterial killing by macrophages, macrophage recruitment, infection, fusion, apoptosis, and bursting due to bacterial overload. Our model is applicable to all granuloma formed in response to an intracellular pathogen, such as *Mycobacterium tuberculosis*, *Salmonella* or *E. coli* [177, 210, 225, 270]. However, as our model does not consider adaptive immune responses or spatial heterogeneity, it is not suitable to describe granuloma dynamics dependent on such features.

We studied how varying the model parameters resulted in different model dynamics, and how this relates to known granuloma phenotypes. We compared our model model dynamics with one of the agent-based models developed by the group of Denise Kirschner [63]. This comparison allowed us to investigate our model behaviour within a biologically realistic parameter range. Furthermore, we investigated to what extent our model could replicate the dynamics of the much more complex agent-based model. Our model simulations of the total extracellular load, intracellular load, total granuloma size and intracellular bacterial

distribution were comparable to the GranSim trajectories. Moreover, the number of burst macrophages over time and the effects of the removal of apoptosis resemble the GranSim dynamics. In contrast to the agent-based model, our model is not capable of accounting for the effects of walled-off extracellular bacteria, as found in long-lived, necrotic tuberculosis granuloma.

Finally, we parametrised of our model to represent an *in vitro* granuloma model that could be used in future work to test model predictions in a controlled *in vitro* environment. This parametrisation was inspired by an *in vitro* model of human peripheral blood mononuclear cell (PBMC) granuloma formation developed by the group of Frédéric Altare [225, 275]. We conducted an initial study into the difference between the granuloma found in CD and in intestinal TB (iTB), while explicitly considering the impact of fusion in this context.

5.1.4.1 Biological importance

In contrast to the former chapters, the construction of the model presented in this chapter was not guided by wet-lab data. All model features included have been based on evidence present in the literature. The primary aim of the chapter was to provide a knowledge constrained framework of our current understanding of features important in granuloma formation. One of such features of macrophages within a granuloma is their ability to fuse, resulting in multinucleated giant cell formation (MGC) [145]. Fused macrophages might be better at degrading large particles [190, 239, 245, 257, 300]. Fusion has not yet been considered in existing models of granuloma formation.

The current presented framework provided the following qualitative predictions of granuloma dynamics. We first considered a simplified version of our model, considering no apoptosis, intracellular killing or growth, or extracellular growth. This corresponds to a granuloma induced by non-living substance, such as silica particles, tattoo pigments, or latex beads. The simplified model predicts that when the mass of foreign antigen is too high compared to the mass of recruited macrophages, macrophages will become necrotic and burst. Sufficient recruitment is therefore important to avoid necrosis. In our model, increasing the fusion rate increases the mass of foreign material that a granuloma can hold

and can consequently decrease the number of macrophages dying due to bacterial overload. In non-necrotic granuloma, the model predicts that fusion does not affect the extracellular bacterial load of granuloma size, but does affect the distribution of infection as macrophages continue to fuse over time. After the introduction of killing and growth, we observed a special case exists where macrophages can effectively clear their bacterial load up to a certain threshold of infection. After passing this threshold, their load either grows to carrying capacity, or they burst, depending on the parameter set used. The introduction of fusion can dilute the bacterial load of the most laden macrophages in this case. Macrophages with a bacterial load beyond the threshold can fuse with macrophages with a lower bacterial load, resulting in an increased capability of the granuloma to clear bacteria. We will discuss potential experiments to test our model predictions in Section 5.2.

The second aim of the chapter was to conduct an initial study into the difference between the granuloma found in CD and in intestinal TB (iTB), by choosing suitable parametrisations of our model. In contrast to the CD type granuloma, the iTB granuloma kept growing over the simulated time span. In the *in vitro* set-up we studied for experimental models of CD and iTB granulomas, fusion does not seem to have a big impact on the model dynamics.

5.1.4.2 Connection to the wider systems biology field

The use of pathogen load as an internal structuring variable is a novel approach in mechanistic granuloma modelling. The distribution of infection is of special interest, as the net growth rate of the bacteria, but also cell signalling and macrophage death, could be dependent on the bacterial load of the macrophage. We have chosen a bacterial-load structured model over an agent-based model, as it is both faster to simulate and easier to analyse the various model features. We have implemented cell fusion as non-local source and sink terms in our model. The inclusion of terms of this specific form in a population structured model are of interest as they have not been studied before, especially in regard to the impact of fusion.

5.2 Future work

In Chapters 2 and 3, we presented ODE based models of cytokine interaction dynamics and bacterial handling dynamics in human macrophages respectively. The form of the equations in Chapter 2 was taken to be as simple as possible. In future work, the equations could be extended by including data containing more time points, or dose response curves. Of particular interest are the inclusion of Hill coeficients that are larger than one, as these type of equations allow for multiple steady states, together with bistable, excitable, hysteresis, and oscillatory dynamics [209]. An interesting example can be found in [58], where hysteresis and oscillations of the concentrations of TNFα as observed during corneal allograft rejection of rabbits were studied. The study of bistability and hysteresis in the context of inflammation is important, as it is a concept that is clinically very relevant: excessive immune cell recruitment and cytokine production (e.g. flare-ups in IBD) can lead to a persistent state of inflammation. The method underlying the cytokine signalling model of Chapter 2 could also be applied to other datasets involving cytokine signalling.

We could use the experimental gentamicin protection assay set-up as presented in Chapter 3 to carry out additional experiments in parallel with model development. First, we would repeat our experiments and measure the cytokine concentration for varying multiplicities of infection (MOI). This would allow us to generate more robust, quantitative estimates of the dependence of the cytokine production on bacterial load.

Further, we could study the effects of various inhibitors of proteins in the NOD2/XIAP/RIPK2 pathway, to investigate if we indeed observe bacterial handling driven cytokine hyper-production as predicted by our model. The modelling framework suggests that such hyper-production will be more pronounced for lower MOI, as the cytokine production rate becomes saturated for high numbers of bacteria. This is relevant, as the number of bacteria a macrophage encounters in the gut will be typically low. We could also investigate the effects of other mutations of interest because of their role in bacterial handling, such as mutations in NPC1, IL10R, and NADPH. We could again measure bacterial load and cytokine concentration over time and quantify the contribution and timing of the resulting bacterial handling defect on cytokine hyper-production for each.

We could integrate our ODE model describing the bacterial handling dynamics from Chapter 2 with our ODE model on cytokine interactions from Chapter 3. Experimentally blocking various (combinations of) cytokines and their receptors would allow us to determine the feedback effects of cytokines on each others production rates and on the bacterial killing rate. The model could then be used to predict the quantitative effects of perturbations of the system (e.g. (combinations of) genetic defects or cytokine receptor blockades) on cytokine levels and bacterial load over time. We could also study the contribution of the various pathogen recognizing receptors, such as TLR4, NLRC4 and NOD2, to the overall cytokine production in response to infection [128]. In order to do this, the cytokine profiles of full bacteria could be compared with isolated bacterial components, such as LPS, *Salmonella* flagellin and MDP, to activate TLR4, NLRC4 inflammasome and NOD2 signalling respectively. The model would then provide a framework that can predict cytokine levels for any combination of bacteria or bacteria component levels. Finally, we could extend our experimental set-up and study the effects of cell recruitment (in a two well system), or study the effects of the addition of neutrophils or fibroblasts. For each of these additional studies, the resulting model predictions should be used for model testing and validation by further experiments.

In Chapter 4, we presented a bacterial-load structured partial differential equation (PDE) model to study the dynamics of granuloma formation. We used the bacterial load as an internal structuring variable, as we assume that the distribution of infection within the granuloma has important consequences for its dynamics. In future work, this model could be complemented by an *in vitro* system to study granuloma formation. One could use non living particles such as latex micro-beads as a granuloma inducing agent. Determination of the distribution of infection over time by microscopy experiments could be used to parametrise such a model. The model could be used to predict the effects of fusion or increased phagocytosis on the granuloma dynamics, including granuloma size, the occurrence of necrosis, and the distribution of infection. Similarly, the effects of bacterial growth and macrophage killing ability could be studied by the addition of various types of bacteria.

Macrophages from individuals with an immunodeficiency in bacterial handling capability are at risk of developing granulomatous disease. Studying the dependency of macrophage

killing ability on bacterial load per macrophage and overall granuloma dynamics is therefore particularly relevant. The role of the various cytokines important in granuloma formation and cell fusion is another area of interest. A combined experimental and modelling set-up explicitly considering macrophage fusion inducing cytokines such as IL-4 or IL-13 would allow us to further study this component of granuloma dynamics. Finally, a key open question is what role macrophage heterogeneity plays in disease. We already observed in our bacterial handling study (Chapter 3) that the uptake rate of bacteria is not uniform across the macrophage population. Our PDE model incorporates macrophage heterogeneity in killing ability due to differences in bacterial load. We could extend the model to study other sources of heterogeneity, such as macrophage activation and corresponding killing ability, by the inclusion of additional state variables in our model.

5.3 Challenges of mechanistic model driven experimentation

A key theme of this discussion has been how mechanistic modelling can feed back into experimental biology. This approach comes with challenges. Firstly, it is important for a modeller to gain insight in the biological field of interest, to identify relevant research questions. Understanding the state of the art of the field can be challenging on its own. However, the key challenge is to identify where a model could drive insight beyond what the experiments and standard statistical data analysis techniques of static data can tell. Often, this lies in presenting a rapid means of asking "what if" questions, isolating mechanisms to examine their individual effect, and providing a conceptual framework. In turn, this allows rapid hypothesis generation and theoretical testing to identify furhter experiments, especially in light of biological complexity and non-linearity. However, in attempting to realise such ambitions, it is important to recognise the weaknesses of models, which are idealisations and thus ultimately "wrong" but nonetheless often useful. It is also important to recognise the timescales involved and that the iterative cycle currently extends beyond a single DPhil. Thus there is a need to build upon existing modelling frameworks, which will in turn require systematic and reproducible standards for research software, though such needs have only recently been recognised and motivates developments in this area, such as a new Doctoral Training Centre focussed on reproducible and sustainable practices [3]. A

second challenge is an understanding of the nature of wet-lab data collection. Biological data collection often comes with high signal-to-noise ratios, whereas modelling demands low ratios. For the second research chapter, I generated the experimental data that was required for my study. However, acquiring the required wet-lab based skills takes time, whilst experimental experience reduces noise. Therefore, in practice, a collaboration between a modeller and experienced experimentalist might in many cases be preferable in complex multi-disciplinary science.

5.4 Perspective on mechanistic modelling

Models should be as simple as possible. Adding unnecessary complexity is unhelpful in obtaining insight in the essence of the problem at stake and increases the prospect of a lack of identifiability and a loss of predictive capability as well as increases the risk of unfounded claims. Further, in order to go beyond speculation and contribute to biology, any modelling effort should be interdisciplinary. Good models can shape our understanding of biology, or make quantitative predictions. Some do both. Models are needed as intuition alone is not sufficient to predict the dynamics of complex, nonlinear non-local interactions in biological systems. Many examples of useful mechanistic models in mathematical biology exist, including areas such as heart, brain and tumour modelling [13, 81, 118, 241, 315, 337]. Within immunology, mechanistic mathematical models have provided important insights in HIV dynamics and T cell functioning [70, 71, 82, 117].

Over the past decade, the development of high-throughput experimental methods in biomedical research has made it possible to obtain increasingly rich data from relevant human cells and tissues. Bioinformatics tools and machine learning are used to organize and analyse these integrated datasets. This novel availability of organized data has created both an opportunity and need for the construction of mechanistic models tightly integrated with experimental approaches.

With above considerations in mind, in this thesis we aimed to develop simple mechanistic mathematical models to study key open questions in the context of macrophage functioning in inflammatory bowel disease (IBD), a complex, multi-factorial, and chronic immune mediated disease. Macrophages play an important role in IBD, but many aspects

of their functioning remain poorly understood. The key open questions we were concerned with are: in what ways can signalling pathways (including the mucosal cytokine network) be targeted to offer an effective therapy for different clinical subgroups of IBD; to what degree do hyper-inflammatory processes (gain of cytokine production) and immunodeficiency (loss of bacterial killing) intersect to produce inflammatory disease; and what factors and cellular processes drive granuloma formation in inflammatory bowel disease and other granulomatic disorders? Aspects of these questions have been addressed in this thesis. Many open questions on macrophage functioning remain. They provide opportunity for future study by a synergistic approach of wet-lab experiments, data analytics, and mechanistic mathematical modelling.

Bibliography

[1] *https://www.rndsystems.com/products/human-il-1alpha-il-1f1-antibody_af-200-na*. Accessed on 10-06-2021.

[2] *https://www.rndsystems.com/products/human-il-1beta-il-1f2-antibody-8516_mab201*. Accessed on 10-06-2021.

[3] *https://www.sabsr3.ox.ac.uk*. Accessed on 27-07-2021.

[4] L. M. Abia, O. Angulo, and J. C. López-Marcos, *Size-structured population dynamics models and their numerical solutions*, Discrete and Continuous Dynamical Systems - Series B, 4 (2004), pp. 1203–1222.

[5] C. Abraham and J. H. Cho, *Functional consequences of NOD2 (CARD15) mutations*, Inflammatory Bowel Diseases, 12 (2006), pp. 641–650.

[6] ——, *Inflammatory bowel disease*, New England Journal of Medicine, 361 (2009), pp. 2066–2078.

[7] J. Abrams, C. G. Figdor, R. De Waal Malefyt, B. Bennett, and J. E. De Vries, *Interleukin 10 (IL-10) inhibits cytokine synthesis by human monocytes: An autoregulatory role of IL-10 produced by monocytes*, Journal of Experimental Medicine, 174 (1991), pp. 1209–1220.

[8] O. Adachi, A. Nakano, O. Sato, S. Kawamoto, H. Tahara, N. Toyoda, E. Yamato, A. Matsumori, K. Tabayashi, and J. Miyazaki, *Gene tranfer of Fc-fusion cytokine by in vivo electroporation: Application to gene therapy for viral myocarditis*, Gene Therapy, 9 (2002), pp. 577–583.

[9] M. Adler, A. Mayo, X. Zhou, R. A. Franklin, J. B. Jacox, R. Medzhitov, and U. Alon, *Endocytosis as a stabilizing mechanism for tissue homeostasis*, Proceedings of the National Academy of Sciences, 115 (2018), pp. e1926–e1935.

[10] L. Albergante, J. Timmis, L. Beattie, and P. M. Kaye, *A Petri net model of granulomatous inflammation: implications for IL-10 mediated control of Leishmania donovani infection*, PLoS Computational Biology, 9 (2013), p. e1003334.

[11] R. Albert and J. Thakar, *Boolean modeling: A logic-based dynamic approach for understanding signaling and regulatory networks and for making useful predictions*, Wiley Interdisciplinary Reviews: Systems Biology and Medicine, 6 (2014), pp. 353–369.

[12] M. A. Almadi, S. Ghosh, and A. M. Aljebreen, *Differentiating intestinal tuberculosis from crohn's disease: a diagnostic challenge*, American Journal of Gastroenterology, 104 (2009), pp. 1003–1012.

[13] P. M. Altrock, L. L. Liu, and F. Michor, *The mathematics of cancer: integrating quantitative models*, Nature Reviews Cancer, 15 (2015), pp. 730–745.

[14] A. N. Ananthakrishnan, *Epidemiology and risk factors for IBD*, Nature Reviews Gastroenterology and Hepatology, 12 (2015), pp. 205–217.

[15] S. R. Andersen, L. J. Lambrecht, S. K. Swan, D. L. Cutler, E. Radwanski, M. B. Affrime, and J. J. Garaud, *Disposition of recombinant human interleukin-10 in subjects with various degrees of renal function*, Journal of Clinical Pharmacology, 39 (1999), pp. 1015–1020.

[16] C. A. Anderson, G. Boucher, C. W. Lees, A. Franke, M. D'Amato, K. D. Taylor, J. C. Lee, P. Goyette, M. Imielinski, A. Latiano, C. Lagacé, R. Scott, L. Amininejad, S. Bumpstead, L. Baidoo, R. N. Baldassano, M. Barclay, T. M. Bayless, S. Brand, C. Büning, J. F. Colombel, L. A. Denson, M. De Vos, M. Dubinsky, C. Edwards, D. Ellinghaus, R. S. Fehrmann, J. A. Floyd, T. Florin, D. Franchimont, L. Franke,

M. Georges, J. Glas, N. L. Glazer, S. L. Guthery, T. Haritunians, N. K. Hayward, J. P. Hugot, G. Jobin, D. Laukens, I. Lawrance, M. Lémann, A. Levine, C. Libioulle, E. Louis, D. P. McGovern, M. Milla, G. W. Montgomery, K. I. Morley, C. Mowat, A. Ng, W. Newman, R. A. Ophoff, L. Papi, O. Palmieri, L. Peyrin-Biroulet, J. Panés, A. Phillips, N. J. Prescott, D. D. Proctor, R. Roberts, R. Russell, P. Rutgeerts, J. Sanderson, M. Sans, P. Schumm, F. Seibold, Y. Sharma, L. A. Simms, M. Seielstad, A. H. Steinhart, S. R. Targan, L. H. Van Den Berg, M. Vatn, H. Verspaget, T. Walters, C. Wijmenga, D. C. Wilson, H. J. Westra, R. J. Xavier, Z. Z. Zhao, C. Y. Ponsioen, V. Andersen, L. Torkvist, M. Gazouli, N. P. Anagnou, T. H. Karlsen, L. Kupcinskas, J. Sventoraityte, J. C. Mansfield, S. Kugathasan, M. S. Silverberg, J. Halfvarson, J. I. Rotter, C. G. Mathew, A. M. Griffiths, R. Gearry, T. Ahmad, S. R. Brant, M. Chamaillard, J. Satsangi, J. H. Cho, S. Schreiber, M. J. Daly, J. C. Barrett, M. Parkes, V. Annese, H. Hakonarson, G. Radford-Smith, R. H. Duerr, S. Vermeire, R. K. Weersma, and J. D. Rioux, *Meta-analysis identifies 29 additional ulcerative colitis risk loci, increasing the number of confirmed associations to 47*, Nature Genetics, 43 (2011), pp. 246–252.

[17] W. D. Anderson, H. K. Makadia, A. D. Greenhalgh, J. S. Schwaber, S. David, and R. Vadigepalli, *Computational modeling of cytokine signaling in microglia*, Molecular BioSystems, 11 (2015), pp. 3332–3346.

[18] O. Angulo and J. C. López-Marcos, *Numerical integration of autonomous and non-autonomous non-linear size-structured population models*, in Mathematical Biosciences, vol. 177-178, 2002, pp. 39–71.

[19] ——, *Numerical integration of fully nonlinear size-structured population models*, Applied Numerical Mathematics, 50 (2004), pp. 291–327.

[20] T. Arai, K. Hiromatsu, H. Nishimura, Y. Kimura, N. Kobayashi, H. Ishida, Y. Nimura, and Y. Yoshikai, *Endogenous interleukin 10 prevents apoptosis in*

macrophages during salmonella infection, Biochemical and Biophysical Research Communications, 213 (1995), pp. 600–607.

[21] I. Arnott, D. Barker, S. Bloom, F. Cummings, J. Dalrymple, and J. Eaden, *IBD standards: standards for the healthcare of people who have inflammatory bowel disease (IBD), 2013 update*, The IBD Standards Group, (2013), pp. 1–32.

[22] D. Aschenbrenner, M. Quaranta, S. Banerjee, N. Ilott, J. Jansen, B. Steere, Y.-H. Chen, S. Ho, K. Cox, C. V. Arancibia-Cárcamo, M. Coles, E. Gaffney, S. P. Travis, L. Denson, S. Kugathasan, J. Schmitz, F. Powrie, S. N. Sansom, and H. H. Uhlig, *Deconvolution of monocyte responses in inflammatory bowel disease reveals an IL-1 cytokine network that regulates IL-23 in genetic and acquired IL-10 resistance*, Gut, (2020).

[23] R. Atreya, J. Mudter, S. Finotto, J. Müllberg, T. Jostock, S. Wirtz, M. Schütz, B. Bartsch, M. Holtmann, C. Becker, D. Strand, J. Czaja, J. F. Schlaak, H. A. Lehr, F. Autschbach, G. Schürmann, N. Nishimoto, K. Yoshizaki, H. Ito, T. Kishimoto, P. R. Galle, S. Rose-John, and M. F. Neurath, *Blockade of interleukin 6 trans signaling suppresses T-cell resistance against apoptosis in chronic intestinal inflammation: Evidence in Crohn disease and experimental colitis in vivo*, Nature Medicine, 6 (2000), pp. 583–588.

[24] R. Atreya, M. Zimmer, B. Bartsch, M. J. Waldner, I. Atreya, H. Neumann, K. Hildner, A. Hoffman, R. Kiesslich, A. D. Rink, T. T. Rau, S. Rosejohn, H. Kessler, J. Schmidt, and M. F. Neurath, *Antibodies against tumor necrosis factor (TNF) induce T-cell apoptosis in patients with inflammatory bowel diseases via TNF receptor 2 and intestinal CD14+ macrophages*, Gastroenterology, 141 (2011), pp. 2026–2038.

[25] F. Autschbach, J. Braunstein, B. Helmke, I. Zuna, G. Schürmann, Z. I. Niemir, R. Wallich, H. F. Otto, and S. C. Meuer, *In situ expression of interleukin-10 in noninflamed human gut and in inflammatory bowel disease*, American Journal of Pathology, 153 (1998), pp. 121–130.

[26] I. Avalos Vizcarra, V. Hosseini, P. Kollmannsberger, S. Meier, S. S. Weber, M. Arnoldini, M. Ackermann, and V. Vogel, *How type 1 fimbriae help Escherichia coli to evade extracellular antibiotics*, Scientific Reports, 6 (2016), pp. 1–13.

[27] D. Baeten, X. Baraliakos, J. Braun, J. Sieper, P. Emery, D. Van Der Heijde, I. McInnes, J. M. Van Laar, R. Landewé, P. Wordsworth, J. Wollenhaupt, H. Kellner, J. Paramarta, J. Wei, A. Brachat, S. Bek, D. Laurent, Y. Li, Y. A. Wang, A. P. Bertolino, S. Gsteiger, A. M. Wright, and W. Hueber, *Anti-interleukin-17A monoclonal antibody secukinumab in treatment of ankylosing spondylitis: A randomised, double-blind, placebo-controlled trial*, The Lancet, 382 (2013), pp. 1705–1713.

[28] J. K. Baillie, E. Arner, C. Daub, M. De Hoon, M. Itoh, H. Kawaji, T. Lassmann, P. Carninci, A. R. Forrest, Y. Hayashizaki, G. J. Faulkner, C. A. Wells, M. Rehli, P. Pavli, K. M. Summers, and D. A. Hume, *Analysis of the human monocyte-derived macrophage transcriptome and response to lipopolysaccharide provides new insights into genetic aetiology of inflammatory bowel disease*, PLoS Genetics, 13 (2017), p. e1006641.

[29] L. D. Bauler, C. S. Duckett, and M. X. O'Riordan, *XIAP regulates cytosol-specific innate immunity to listeria infection*, PLoS Pathogens, 4 (2008), p. e1000142.

[30] L. Beattie, A. Sawtell, J. Mann, T. C. Frame, B. Teal, F. de Labastida Rivera, N. Brown, K. Walwyn-Brown, J. W. Moore, S. MacDonald, E. K. Lim, J. E. Dalton, C. R. Engwerda, K. P. MacDonald, and P. M. Kaye, *Bone marrow-derived and resident liver macrophages display unique transcriptomic signatures but similar biological functions*, Journal of Hepatology, 65 (2016), pp. 758–768.

[31] S. M. Behar, C. J. Martin, M. G. Booty, T. Nishimura, X. Zhao, H. X. Gan, M. Divangahi, and H. G. Remold, *Apoptosis is an innate defense function*

of macrophages against Mycobacterium tuberculosis, Mucosal Immunology, 4 (2011), pp. 279–287.

[32] S. Ben-Horin, U. Kopylov, and Y. Chowers, *Optimizing anti-TNF treatments in inflammatory bowel disease*, Autoimmunity Reviews, 13 (2014), pp. 24–30.

[33] C. M. Bender and S. A. Orszag, *Advanced mathematical methods for scientists and engineers I : asymptotic methods and perturbation theory*, Springer, New York, 1999.

[34] Y. Benjamini and Y. Hochberg, *Controlling the false discovery rate: a practical and powerful approach to multiple testing*, Journal of the Royal Statistical Society: Series B (Methodological), 57 (1995), pp. 289–300.

[35] B. C. Betts, E. T. St Angelo, M. Kennedy, and J. W. Young, *Anti-IL6-receptor-alpha (tocilizumab) does not inhibit human monocyte-derived dendritic cell maturation or alloreactive T-cell responses*, Blood, 118 (2011), pp. 5340–5343.

[36] C. R. Beuzón, S. P. Salcedo, and D. W. Holden, *Growth and killing of a Salmonella enterica serovar Typhimurium sifA mutant strain in the cytosol of different host cell lines*, Microbiology, 148 (2002), pp. 2705–2715.

[37] M. E. Bianchi, *DAMPs, PAMPs and alarmins: all we need to know about danger*, Journal of Leukocyte Biology, 81 (2006), pp. 1–5.

[38] J. Bilsborough, S. R. Targan, and S. B. Snapper, *Therapeutic targets in inflammatory bowel disease: current and future*, The American Journal of Gastroenterology Supplements, 3 (2016), pp. 27–37.

[39] C. Bindon, M. Czerniecki, P. Ruell, A. Edwards, W. H. McCarthy, R. Harris, and P. Hersey, *Clearance rates and systemic effects of intravenously administered interleukin 2 (IL-2) containing preparations in human subjects*, British Journal of Cancer 1983 47:1, 47 (1983), pp. 123–133.

[40] A. Biswas, Y. J. Liu, L. Hao, A. Mizoguchi, N. H. Salzman, C. L. Bevins, and K. S. Kobayashi, *Induction and rescue of Nod2-dependent Th1-driven granulomatous inflammation of the ileum*, Proceedings of the National Academy of Sciences of the United States of America, 107 (2010), pp. 14739–14744.

[41] V. Bocci, *Interleukins*, Clinical Pharmacokinetics, 21 (1991), pp. 274–284.

[42] C. Bogdan and U. Schleicher, *Production of interferon-γ by myeloid cells - fact or fancy?*, Trends in Immunology, 27 (2006), pp. 282–290.

[43] K. R. Bortoluci and R. Medzhitov, *Control of infection by pyroptosis and autophagy: Role of TLR and NLR*, Cellular and Molecular Life Sciences, 67 (2010), pp. 1643–1651.

[44] C. Boutros, A. Tarhini, E. Routier, O. Lambotte, F. L. Ladurie, F. Carbonnel, H. Izzeddine, A. Marabelle, S. Champiat, A. Berdelou, E. Lanoy, M. Texier, C. Libenciuc, A. M. Eggermont, J. C. Soria, C. Mateus, and C. Robert, *Safety profiles of anti-CTLA-4 and anti-PD-1 antibodies alone and in combination*, Nature Reviews Clinical Oncology, 13 (2016), pp. 473–486.

[45] L. I. Bouwman, M. R. de Zoete, N. M. C. Bleumink-Pluym, R. A. Flavell, and J. P. M. van Putten, *Inflammasome activation by Campylobacter jejuni*, The Journal of Immunology, 193 (2014), pp. 4548–4557.

[46] E. A. Boyle, Y. I. Li, and J. K. Pritchard, *An expanded view of complex traits: from polygenic to omnigenic*, Cell, 169 (2017), pp. 1177–1186.

[47] P. Broz, K. Newton, M. Lamkanfi, S. Mariathasan, V. M. Dixit, and D. M. Monack, *Redundant roles for inflammasome receptors NLRP3 and NLRC4 in host defense against Salmonella*, Journal of Experimental Medicine, 207 (2010), pp. 1745–1755.

[48] J. H. Brumell, A. J. Perrin, D. L. Goosney, and B. B. Finlay, *Microbial pathogenesis: new niches for Salmonella*, Current Biology, 12 (2002), pp. 15–17.

[49] K. P. Burnham and D. R. Anderson, *Model selection and multimodel inference: a practical information-theoretic approach*, New York, London: Springer, 2nd ed., 2002.

[50] ——, *Multimodel inference: Understanding AIC and BIC in model selection*, Sociological Methods and Research, 33 (2004), pp. 261–304.

[51] A. B. Caldwell, H. A. Birnbaum, Z. Cheng, A. Hoffmann, and J. D. Vargas, *Network dynamics determine the autocrine and paracrine signaling functions of TNF*, Genes and Development, 28 (2014), pp. 2120–2133.

[52] S. W. Canna, C. Girard, L. Malle, A. de Jesus, N. Romberg, J. Kelsen, L. F. Surrey, P. Russo, A. Sleight, E. Schiffrin, C. Gabay, R. Goldbach-Mansky, and E. M. Behrens, *Life-threatening NLRC4-associated hyperinflammation successfully treated with IL-18 inhibition*, Journal of Allergy and Clinical Immunology, 139 (2017), pp. 1698–1701.

[53] J. Carruthers, M. López-García, J. J. Gillard, T. R. Laws, G. Lythe, and C. Molina-París, *A novel stochastic multi-scale model of Francisella tularensis infection to predict risk of infection in a laboratory*, Frontiers in Microbiology, 9 (2018), p. 1165.

[54] S. Castanheira and F. García-del Portillo, *Salmonella populations inside host cells*, Frontiers in Cellular and Infection Microbiology, 7 (2017), p. 432.

[55] M. Castro and R. J. de Boer, *Testing structural identifiability by a simple scaling method*, PLoS Computational Biology, 16 (2020), p. e1008248.

[56] M. Cemma, S. Grinstein, and J. H. Brumell, *Autophagy proteins are not universally required for phagosome maturation*, Autophagy, 12 (2016), pp. 1440–1446.

[57] A. H. Chan and K. Schroder, *Cytokines Focus: Inflammasome signaling and regulation of interleukin-1 family cytokines*, The Journal of Experimental Medicine, 217 (2020).

[58] C. C. Chan, J. Stark, and A. J. George, *Analysis of cytokine dynamics in corneal allograft rejection*, Proceedings of the Royal Society B: Biological Sciences, 266 (1999), pp. 2217–2223.

[59] X. Chen, D. C. DuBois, R. R. Almon, and W. J. Jusko, *Characterization and Interspecies Scaling of rhTNF-α Pharmacokinetics with Minimal Physiologically Based Pharmacokinetic Models*, Drug Metabolism and Disposition, 45 (2017), p. 798.

[60] Z. Cheng, B. Taylor, D. R. Ourthiague, and A. Hoffmann, *Distinct single-cell signaling characteristics are conferred by the MyD88 and TRIF pathways during TLR4 activation*, Science Signaling, 8 (2015), pp. 1–13.

[61] A. E. Chernoff, E. V. Granowitz, L. Shapiro, E. Vannier, G. Lonnemann, J. B. Angel, J. S. Kennedy, A. R. Rabson, S. M. Wolff, and C. A. Dinarello, *A randomized, controlled trial of IL-10 in humans. Inhibition of inflammatory cytokine production and immune responses.*, Journal of immunology, 154 (1995), pp. 5492–5499.

[62] G. Chognard, L. Bellemare, A. N. Pelletier, M. C. Dominguez-Punaro, C. Beauchamp, M. J. Guyon, G. Charron, N. Morin, D. Sivanesan, V. Kuchroo, R. Xavier, S. W. Michnick, S. Chemtob, J. D. Rioux, and S. Lesage, *The dichotomous pattern of IL-12R and IL-23R expression elucidates the role of IL-12 and IL-23 in inflammation*, PLoS ONE, 9 (2014), p. e89092.

[63] N. A. Cilfone, C. R. Perry, D. E. Kirschner, and J. J. Linderman, *Multi-scale modeling predicts a balance of tumor necrosis factor-α and interleukin-10 controls the granuloma environment during Mycobacterium tuberculosis infection*, PLoS ONE, 8 (2013), p. e68680.

[64] N. A. Cilfone, E. Pienaar, G. M. Thurber, D. E. Kirschner, and J. J. Linderman, *Systems pharmacology approach toward the design of inhaled formulations of rifampicin and isoniazid for treatment of tuberculosis*, CPT: Pharmacometrics and Systems Pharmacology, 4 (2015), pp. 193–203.

[65] M. J. Clemens, A. J. H. Gearing, and A. G. Morris, *Lymphokines and interferons : a practical approach*, Practical approach series, IRL Press, Oxford, 1987.

[66] M. Coccia, O. J. Harrison, C. Schiering, M. J. Asquith, B. Becher, F. Powrie, and K. J. Maloy, *IL-1β mediates chronic intestinal inflammation by promoting the accumulation of IL-17A secreting innate lymphoid cells and CD4 + Th17 cells*, Journal of Experimental Medicine, 209 (2012), pp. 1595–1609.

[67] T. F. Coleman and Y. Li, *An interior trust region approach for nonlinear minimization subject to bounds*, SIAM Journal on Optimization, 6 (1996), pp. 418–445.

[68] J. F. Colombel, P. Rutgeerts, H. Malchow, M. Jacyna, O. H. Nielsen, J. Rask-Madsen, S. Van Deventer, A. Ferguson, P. Desreumaux, A. Forbes, K. Geboes, L. Melani, and M. Cohard, *Interleukin 10 (Tenovil) in the prevention of postoperative recurrence of Crohn's disease*, Gut, 49 (2001), pp. 42–46.

[69] R. Cooney, J. Baker, O. Brain, B. Danis, T. Pichulik, P. Allan, D. J. Ferguson, B. J. Campbell, D. Jewell, and A. Simmons, *NOD2 stimulation induces autophagy in dendritic cells influencing bacterial handling and antigen presentation*, Nature Medicine, 16 (2010), pp. 90–97.

[70] L. N. Cooper, *Theory of an immune system retrovirus*, Proceedings of the National Academy of Sciences of the United States of America, 83 (1986), pp. 9159–9163.

[71] D. J. Covert and D. Kirschner, *Revisiting early models of the host-pathogen interactions in HIV infection*, Comments on Theoretical Biology, 5 (2000), pp. 383–411.

[72] M. R. Cronan, R. W. Beerman, A. F. Rosenberg, J. W. Saelens, M. G. Johnson, S. H. Oehlers, D. M. Sisk, K. L. Jurcic Smith, N. A. Medvitz, S. E. Miller, L. A. Trinh, S. E. Fraser, J. F. Madden, J. Turner, J. E. Stout, S. Lee, and D. M. Tobin, *Macrophage Epithelial Reprogramming Underlies*

Mycobacterial Granuloma Formation and Promotes Infection, Immunity, 45 (2016), pp. 861–876.

[73] R. I. Cukier, C. M. Fortuin, K. E. Shuler, A. G. Petschek, and J. H. Schaibly, *Study of the sensitivity of coupled reaction systems to uncertainties in rate coefficients. I Theory*, Journal of Chemical Physics, 59 (1973), pp. 3873–3878.

[74] J. M. Cushing, *A size-structured model for cannibalism*, Theoretical Population Biology, 42 (1992), pp. 347–361.

[75] ——, *An introduction to structured population dynamics*, Society for Industrial and Applied Mathematics, 1998.

[76] S. Danese, J. Rudziński, W. Brandt, J. L. Dupas, L. Peyrin-Biroulet, Y. Bouhnik, D. Kleczkowski, P. Uebel, M. Lukas, M. Knutsson, F. Erlandsson, M. B. Hansen, and S. Keshav, *Tralokinumab for moderate-to-severe UC: A randomised, double-blind, placebo-controlled, phase IIa study*, Gut, 64 (2015), pp. 243–249.

[77] S. Danese, S. Vermeire, P. Hellstern, R. Panaccione, G. Rogler, G. Fraser, A. Kohn, P. Desreumaux, R. W. Leong, G. M. Comer, F. Cataldi, A. Banerjee, M. K. Maguire, C. Li, N. Rath, J. Beebe, and S. Schreiber, *Randomised trial and open-label extension study of an anti-interleukin-6 antibody in Crohn's disease (ANDANTE I and II)*, Gut, 68 (2019), pp. 40–48.

[78] A. M. Dannenberg and G. A. W. Rook, *Pathogenesis of Pulmonary Tuberculosis: an Interplay of Tissue-Damaging and Macrophage-Activating Immune Responses-Dual Mechanisms That Control Bacillary Multiplication*, in Tuberculosis, ASM Press, apr 2014, pp. 459–483.

[79] A. Darfeuille-Michaud, J. Boudeau, P. Bulois, C. Neut, A. L. Glasser, N. Barnich, M. A. Bringer, A. Swidsinski, L. Beaugerie, and J. F. Colombel, *High prevalence of adherent-invasive Escherichia coli associated with ileal mucosa in Crohn's disease*, Gastroenterology, 127 (2004), pp. 412–421.

[80] A. Dasgupta, N. Singh, and A. Bhatia, *Abdominal tuberculosis: a histopathological study with special reference to intestinal perforation and mesenteric vasculopathy*, Journal of Laboratory Physicians, 1 (2009), pp. 56–61.

[81] M. R. Davies, K. Wang, G. R. Mirams, A. Caruso, D. Noble, A. Walz, T. Lavé, F. Schuler, T. Singer, and L. Polonchuk, *Recent developments in using mechanistic cardiac modelling for drug safety evaluation*, Drug Discovery Today, 21 (2016), pp. 924–938.

[82] M. M. Davis, C. M. Tato, and D. Furman, *Systems immunology: just getting started*, Nature Immunology, 18 (2017), pp. 725–732.

[83] J. Day, A. Friedman, and L. L. S. Schlesinger, *Modeling the immune rheostat of macrophages in the lung in response to infection*, Proceedings of the National Academy of Sciences of the United States of America, 106 (2009), pp. 11246–11251.

[84] D. De Groote, P. F. Zangerle, Y. Gevaert, M. F. Fassotte, Y. Beguin, F. Noizat-Pirenne, J. Pirenne, R. Gathy, M. Lopez, I. Dehart, D. Igot, M. Baudrihaye, D. Delacroix, and P. Franchimont, *Direct stimulation of cytokines (IL-1β, TNF-α, IL-6, IL-2, IFN-γ and GM-CSF) in whole blood. I. Comparison with isolated PBMC stimulation*, Cytokine, 4 (1992), pp. 239–248.

[85] K. M. De Lange, L. Moutsianas, J. C. Lee, C. A. Lamb, Y. Luo, N. A. Kennedy, L. Jostins, D. L. Rice, J. Gutierrez-Achury, S. G. Ji, G. Heap, E. R. Nimmo, C. Edwards, P. Henderson, C. Mowat, J. Sanderson, J. Satsangi, A. Simmons, D. C. Wilson, M. Tremelling, A. Hart, C. G. Mathew, W. G. Newman, M. Parkes, C. W. Lees, H. Uhlig, C. Hawkey, N. J. Prescott, T. Ahmad, J. C. Mansfield, C. A. Anderson, and J. C. Barrett, *Genome-wide association study implicates immune activation of multiple integrin genes in inflammatory bowel disease*, Nature Genetics, 49 (2017), pp. 256–261.

[86] K. M. DeFife, C. R. Jenney, A. K. McNally, E. Colton, and J. M. Anderson, *Interleukin-13 induces human monocyte/macrophage fusion and macrophage*

mannose receptor expression., Journal of immunology (Baltimore, Md. : 1950), 158 (1997), pp. 3385–3390.

[87] G. Demarre, V. Prudent, H. Schenk, E. Rousseau, M. A. Bringer, N. Barnich, G. T. Van Nhieu, S. Rimsky, S. De Monte, and O. Espéli, *The Crohn's disease-Associated Escherichia coli strain LF82 relies on SOS and stringent responses to survive, multiply and tolerate antibiotics within macrophages*, PLoS Pathogens, 15 (2019), p. e1008123.

[88] E. Domínguez-Hüttinger, N. J. Boon, T. B. Clarke, and R. J. Tanaka, *Mathematical modeling of Streptococcus pneumoniae colonization, invasive infection and treatment*, Frontiers in Physiology, 8 (2017), p. 115.

[89] R. P. Donnelly, S. L. Freeman, and M. P. Hayes, *Inhibition of IL-10 expression by IFN-gamma up-regulates transcription of TNF-alpha in human monocytes*, Journal of Immunology, 155 (1995), pp. 1420–147.

[90] J. H. Donohue and S. A. Rosenberg, *The fate of interleukin-2 after in vivo administration.*, The Journal of Immunology, 130 (1983), pp. 2203–2208.

[91] R. H. Duerr, K. D. Taylor, S. R. Brant, J. D. Rioux, M. S. Silverberg, M. J. Daly, A. H. Steinhart, C. Abraham, M. Regueiro, A. Griffiths, T. Dassopoulos, A. Bitton, H. Yang, S. Targan, L. W. Datta, E. O. Kistner, L. P. Schumm, A. T. Lee, P. K. Gregersen, M. M. Barmada, J. I. Rotter, D. L. Nicolae, and J. H. Cho, *A genome-wide association study identifies IL23R as an inflammatory bowel disease gene*, Science, 314 (2006), pp. 1461–1463.

[92] R. Eftimie, J. J. Gillard, and D. A. Cantrell, *Mathematical models for immunology: current state of the art and future research directions*, Bulletin of Mathematical Biology, 78 (2016), pp. 2091–2134.

[93] P. Ekman, M. Saarinen, Q. He, C. Gripenberg-Lerche, A. Grönberg, H. Arvilommi, and K. Granfors, *HLA-B27-transfected (Salmonella Permissive) and HLA-A2-transfected (Salmonella Nonpermissive) human monocytic U937 cells*

differ in their production of cytokines, Infection and Immunity, 70 (2002), pp. 1609–1614.

[94] A. M. Elaiw, *Global properties of a class of HIV models*, Nonlinear Analysis: Real World Applications, 11 (2010), pp. 2253–2263.

[95] J. Elf and M. Ehrenberg, *Fast evaluation of fluctuations in biochemical networks with the linear noise approximation*, Genome Research, 13 (2003), pp. 2475–2484.

[96] S. Epskamp, M. Rhemtulla, and D. Borsboom, *Generalized Network Psychometrics: Combining Network and Latent Variable Models*, Psychometrika, 82 (2017), pp. 904–927.

[97] S. Fais and F. Pallone, *Inability of normal human intestinal macrophages to form multinucleated giant cells in response to cytokines*, Gut, 37 (1995), pp. 798–801.

[98] M. Fallahi-Sichani, M. El-Kebir, S. Marino, D. E. Kirschner, and J. J. Linderman, *Multiscale computational modeling reveals a critical role for TNF-α receptor 1 dynamics in tuberculosis granuloma formation*, The Journal of Immunology, 186 (2011), pp. 3472–3483.

[99] F. Farhangmehr, M. R. Maurya, D. M. Tartakovsky, and S. Subramaniam, *Information theoretic approach to complex biological network reconstruction: Application to cytokine release in RAW 264.7 macrophages*, BMC Systems Biology, 8 (2014), p. 77.

[100] B. G. Feagan, W. J. Sandborn, G. D'Haens, J. Panés, A. Kaser, M. Ferrante, E. Louis, D. Franchimont, O. Dewit, U. Seidler, K. J. Kim, M. F. Neurath, S. Schreiber, P. Scholl, C. Pamulapati, B. Lalovic, S. Visvanathan, S. J. Padula, I. Herichova, A. Soaita, D. B. Hall, and W. O. Böcher, *Induction therapy with the selective interleukin-23 inhibitor risankizumab in patients with moderate-to-severe Crohn's disease: a randomised, double-blind, placebo-controlled phase 2 study*, The Lancet, 389 (2017), pp. 1699–1709.

[101] S. L. Field, T. Dasgupta, M. Cummings, R. S. Savage, J. Adebayo, H. McSara, J. Gunawardena, and N. M. Orsi, *Bayesian modeling suggests that IL-12 (p40), IL-13 and MCP-1 drive murine cytokine networks in vivo*, BMC Systems Biology, 9 (2015), p. 76.

[102] A. S. A. S. Figueiredo, T. Höfer, C. Klotz, C. Sers, S. Hartmann, R. Lucius, and P. Hammerstein, *Modelling and simulating interleukin-10 production and regulation by macrophages after stimulation with an immunomodulator of parasitic nematodes*, The FEBS Journal, 276 (2009), pp. 3454–3469.

[103] S. L. Fink and B. T. Cookson, *Pyroptosis and host cell death responses during Salmonella infection*, Cellular Microbiology, 9 (2007), pp. 2562–2570.

[104] H. Z. Ford, H. M. Byrne, and M. R. Myerscough, *A lipid-structured model for macrophage populations in atherosclerotic plaques*, Journal of Theoretical Biology, 479 (2019), pp. 48–63.

[105] A. Franke, T. Balschun, T. H. Karlsen, J. Sventoraityte, S. Nikolaus, G. Mayr, F. S. Domingues, M. Albrecht, M. Nothnagel, D. Ellinghaus, C. Sina, C. M. Onnie, R. K. Weersma, P. C. Stokkers, C. Wijmenga, M. Gazouli, D. Strachan, W. L. McArdle, S. Vermeire, P. Rutgeerts, P. Rosenstiel, M. Krawczak, M. H. Vatn, C. G. Mathew, and S. Schreiber, *Sequence variants in IL10, ARPC2 and multiple other loci contribute to ulcerative colitis susceptibility*, Nature Genetics, 40 (2008), pp. 1319–1323.

[106] A. Franke, D. P. McGovern, J. C. Barrett, K. Wang, G. L. Radford-Smith, T. Ahmad, C. W. Lees, T. Balschun, J. Lee, R. Roberts, C. A. Anderson, J. C. Bis, S. Bumpstead, D. Ellinghaus, E. M. Festen, M. Georges, T. Green, T. Haritunians, L. Jostins, A. Latiano, C. G. Mathew, G. W. Montgomery, N. J. Prescott, S. Raychaudhuri, J. I. Rotter, P. Schumm, Y. Sharma, L. A. Simms, K. D. Taylor, D. Whiteman, C. Wijmenga, R. N. Baldassano, M. Barclay, T. M. Bayless, S. Brand, C. Büning, A. Cohen, J. F. Colombel, M. Cottone, L. Stronati, T. Denson, M. De

Vos, R. D'Inca, M. Dubinsky, C. Edwards, T. Florin, D. Franchimont, R. Gearry, J. Glas, A. Van Gossum, S. L. Guthery, J. Halfvarson, H. W. Verspaget, J. P. Hugot, A. Karban, D. Laukens, I. Lawrance, M. Lemann, A. Levine, C. Libioulle, E. Louis, C. Mowat, W. Newman, J. Panés, A. Phillips, D. D. Proctor, M. Regueiro, R. Russell, P. Rutgeerts, J. Sanderson, M. Sans, F. Seibold, A. H. Steinhart, P. C. Stokkers, L. Torkvist, G. Kullak-Ublick, D. Wilson, T. Walters, S. R. Targan, S. R. Brant, J. D. Rioux, M. D'Amato, R. K. Weersma, S. Kugathasan, A. M. Griffiths, J. C. Mansfield, S. Vermeire, R. H. Duerr, M. S. Silverberg, J. Satsangi, S. Schreiber, J. H. Cho, V. Annese, H. Hakonarson, M. J. Daly, and M. Parkes, *Genome-wide meta-analysis increases to 71 the number of confirmed Crohn's disease susceptibility loci*, Nature Genetics, 42 (2010), pp. 1118–1125.

[107] G. Freer and L. Rindi, *Intracellular cytokine detection by fluorescence-activated flow cytometry: Basic principles and recent advances*, Methods, 61 (2013), pp. 30–38.

[108] F. Freudenberg, U. Wintergerst, A. Roesen-Wolff, M. H. Albert, C. Prell, B. Strahm, S. Koletzko, S. Ehl, D. Roos, A. Tommasini, A. Ventura, B. H. Belohradsky, R. Seger, J. Roesler, and T. Güngör, *Therapeutic strategy in p47-phox deficient chronic granulomatous disease presenting as inflammatory bowel disease*, Journal of Allergy and Clinical Immunology, 125 (2010), pp. 943–946.

[109] J. Friedman, T. Hastie, and R. Tibshirani, *Sparse inverse covariance estimation with the graphical lasso*, Biostatistics, 9 (2008), pp. 432–441.

[110] M. Friedrich, M. Pohin, and F. Powrie, *Cytokine networks in the pathophysiology of inflammatory bowel disease*, Immunity, 50 (2019), pp. 992–1006.

[111] D. M. Frucht, T. Fukao, C. Bogdan, H. Schindler, J. J. O'Shea, and S. Koyasu, *IFN-γ production by antigen-presenting cells: Mechanisms emerge*, Trends in Immunology, 22 (2001), pp. 556–560.

[112] M. Fukata, A. S. Vamadevan, and M. T. Abreu, *Toll-like receptors (TLRs) and Nod-like receptors (NLRs) in inflammatory disorders*, Seminars in Immunology, 21 (2009), pp. 242–253.

[113] S. A. Fulton, J. V. Cross, Z. T. Toossi, and W. H. Boom, *Regulation of interleukin-12 by interleukin-10, transforming growth factor-β, tumor necrosis factor-α, and interferon-γ in human monocytes infected with Mycobacterium tuberculosis H37Ra*, Journal of Infectious Diseases, 178 (1998), pp. 1105–1114.

[114] L. U. Gardner, *The similarity of the lesions produced by silica and by the tubercle bacillus*, The American Journal of Pathology, 13 (1937), pp. 13–23.

[115] J. M. Garland, A. Aldridge, J. Wagstaffe, and T. M. Dexter, *Studies on the in vivo production of a lymphokine activity, interleukin 3 (IL-3) elaborated by lymphocytes and a myeloid leukaemic line in vitro and the fate of IL-3 dependent cell lines.*, British Journal of Cancer, 48 (1983), p. 247.

[116] A. Geremia, P. Biancheri, P. Allan, G. R. Corazza, and A. Di Sabatino, *Innate and adaptive immunity in inflammatory bowel disease*, Autoimmunity Reviews, 13 (2014), pp. 3–10.

[117] R. N. Germain, M. Meier-Schellersheim, A. Nita-Lazar, and I. D. Fraser, *Systems biology in immunology: a computational modeling perspective*, Annual Review of Immunology, 29 (2011), pp. 527–585.

[118] W. Gerstner, H. Sprekeler, and G. Deco, *Theory and simulation in neuroscience*, Science, 338 (2012), pp. 60–65.

[119] E. Giacomini, E. Iona, L. Ferroni, M. Miettinen, L. Fattorini, G. Orefici, I. Julkunen, and E. M. Coccia, *Infection of human macrophages and dendritic cells with Mycobacterium tuberculosis induces a differential cytokine gene expression that modulates T cell response*, The Journal of Immunology, 166 (2001), pp. 7033–7041.

[120] J. Gillard, T. R. Laws, G. Lythe, and C. Molina-París, *Modelling early events in Francisella tularensis pathogenesis*, Frontiers in Cellular and Infection Microbiology, 4 (2014), p. 169.

[121] D. T. Gillespie, *A rigorous derivation of the chemical master equation*, Physica A: Statistical Mechanics and its Applications, 188 (1992), pp. 404–425.

[122] F. Ginhoux, M. Greter, M. Leboeuf, S. Nandi, P. See, S. Gokhan, M. F. Mehler, S. J. Conway, L. G. Ng, E. R. Stanley, I. M. Samokhvalov, and M. Merad, *Fate mapping analysis reveals that adult microglia derive from primitive macrophages*, Science, 330 (2010), pp. 841–845.

[123] F. Ginhoux and S. Jung, *Monocytes and macrophages: developmental pathways and tissue homeostasis*, Nature Reviews Immunology, 14 (2014), pp. 392–404.

[124] A. L. Glasser, J. Boudeau, N. Barnich, M. H. Perruchot, J. F. Colombel, and A. Darfeuille-Michaud, *Adherent invasive Escherichia coli strains from patients with Crohn's disease survive and replicate within macrophages without inducing host cell death*, Infection and Immunity, 69 (2001), pp. 5529–5537.

[125] P. Glendinning, *Stability, instability, and chaos : an introduction to the theory of nonlinear differential equations*, Cambridge texts in applied mathematics, Cambridge University Press, Cambridge [England] ; New York, 1994.

[126] E.-o. Glocker, D. Kotlarz, K. Boztug, E. M. Gertz, F. Noyan, M. Perro, J. Diestelhorst, A. Allroth, D. Murugan, D. Pfeifer, K.-w. Sykora, M. Sauer, H. Kreipe, M. Lacher, R. Nustede, C. Woellner, U. Baumann, U. Salzer, S. Koletzko, N. Shah, A. W. Segal, A. Sauerbrey, S. Buderus, S. B. Snapper, B. Grimbacher, and C. Klein, *Inflammatory bowel disease and mutations affecting the interleukin-10 receptor*, Receptor, 361 (2009), pp. 2033–2045.

[127] J. R. Gog, A. Murcia, N. Osterman, O. Restif, T. J. McKinley, M. Sheppard, S. Achouri, B. Wei, P. Mastroeni, J. Wood, D. Maskell, P. Cicuta,

and C. Bryant, *Dynamics of Salmonella infection of macrophages at the single cell level*, Journal of the Royal Society Interface, 9 (2012), pp. 2696–2707.

[128] M. Gogoi, M. M. Shreenivas, and D. Chakravortty, *Hoodwinking the big-eater to prosper: the Salmonella-macrophage paradigm*, Journal of Innate Immunity, 11 (2019), pp. 289–299.

[129] M. Gonzalez-Juarrero, T. S. Shim, A. Kipnis, A. P. Junqueira-Kipnis, and I. M. Orme, *Dynamics of macrophage cell populations during murine pulmonary tuberculosis*, The Journal of Immunology, 171 (2003), pp. 3128–3135.

[130] M. A. Gordon, D. L. Jack, D. H. Dockrell, M. E. Lee, and R. C. Read, *Gamma interferon enhances internalization and early nonoxidative killing of Salmonella enterica serovar typhimurium by human macrophages and modifies cytokine responses*, Infection and Immunity, 73 (2005), pp. 3445–3452.

[131] M. Guha and N. Mackman, *LPS induction of gene expression in human monocytes*, Cellular Signalling, 13 (2001), pp. 85–94.

[132] M. Guilliams, I. De Kleer, S. Henri, S. Post, L. Vanhoutte, S. De Prijck, K. Deswarte, B. Malissen, H. Hammad, and B. N. Lambrecht, *Alveolar macrophages develop from fetal monocytes that differentiate into long-lived cells in the first week of life via GM-CSF*, Journal of Experimental Medicine, 210 (2013), pp. 1977–1992.

[133] M. Guilliams and C. L. Scott, *Does niche competition determine the origin of tissue-resident macrophages?*, Nature Reviews Immunology, 17 (2017), pp. 451–460.

[134] J. Gurland, *Some applications of the negative binomial and other contagious distributions.*, American Journal of Public Health, 49 (1959), pp. 1388–1399.

[135] D. A. Hagge, N. A. Ray, J. L. Krahenbuhl, and L. B. Adams, *An in vitro model for the lepromatous leprosy granuloma: fate of Mycobacterium leprae from target macrophages after interaction with normal and activated effector macrophages*, The Journal of Immunology, 172 (2004), pp. 7771–7779.

[136] E. Hamza, S. Kittl, and P. Kuhnert, *Temporal induction of pro-inflammatory and regulatory cytokines in human peripheral blood mononuclear cells by Campylobacter jejuni and Campylobacter coli*, PLoS ONE, 12 (2017), p. e0171350.

[137] W. Hao, L. S. Schlesinger, and A. Friedman, *Modeling granulomas in response to infection in the lung*, PLoS ONE, 11 (2016), p. e0148738.

[138] D. Hashimoto, A. Chow, C. Noizat, P. Teo, M. B. Beasley, M. Leboeuf, C. D. Becker, P. See, J. Price, D. Lucas, M. Greter, A. Mortha, S. W. Boyer, E. C. Forsberg, M. Tanaka, N. van Rooijen, A. García-Sastre, E. R. Stanley, F. Ginhoux, P. S. Frenette, and M. Merad, *Tissue-resident macrophages self-maintain locally throughout adult life with minimal contribution from circulating monocytes*, Immunity, 38 (2013), pp. 792–804.

[139] J. B. Hayes, L. M. Sircy, L. E. Heusinkveld, W. Ding, R. N. Leander, E. E. McClelland, and D. E. Nelson, *Modulation of macrophage inflammatory nuclear factor κB (NF-κB) signaling by intracellular Cryptococcus neoformans*, Journal of Biological Chemistry, 291 (2016), pp. 15614–15627.

[140] B. L. Heckmann and D. R. Green, *LC3-associated phagocytosis at a glance*, Journal of Cell Science, 132 (2019), p. 222984.

[141] M. Hedl and C. Abraham, *Nod2-induced autocrine interleukin-1 alters signaling by ERK and p38 to differentially regulate secretion of inflammatory cytokines*, Gastroenterology, 143 (2012), pp. 1530–1543.

[142] M. Hedl, J. Li, J. H. Cho, and C. Abraham, *Chronic stimulation of Nod2 mediates tolerance to bacterial products*, Proceedings of the National Academy of Sciences of the United States of America, 104 (2007), pp. 19440–19445.

[143] S. Helaine, A. M. Cheverton, K. G. Watson, L. M. Faure, S. A. Matthews, and D. W. Holden, *Internalization of salmonella by macrophages induces formation of nonreplicating persisters*, Science, 343 (2014), pp. 204–208.

[144] J. Helft, F. Anjos-Afonso, A. G. van der Veen, P. Chakravarty, D. Bonnet, and C. Reis e Sousa, *Dendritic cell lineage potential in human early hematopoietic progenitors*, Cell Reports, 20 (2017), pp. 529–537.

[145] L. Helming and S. Gordon, *The molecular basis of macrophage fusion*, Immunobiology, 212 (2008), pp. 785–793.

[146] D. Heresbach, J. L. Alexandre, B. Branger, J. F. Bretagne, E. Cruchant, A. Dabadie, M. Dartois-Hoguin, P. M. Girardot, H. Jouanolle, J. Kerneis, J. C. Le Verger, V. Louvain, J. Politis, M. Richecoeur, M. Robaszkiewiczs, and J. A. Seyrig, *Frequency and significance of granulomas in a cohort of incident cases of Crohn's disease*, Gut, 54 (2005), pp. 215–222.

[147] L. Herrtwich, I. Nanda, K. Evangelou, T. Nikolova, V. Horn, Sagar, D. Erny, J. Stefanowski, L. Rogell, C. Klein, K. Gharun, M. Follo, M. Seidl, B. Kremer, N. Münke, J. Senges, M. Fliegauf, T. Aschman, D. Pfeifer, S. Sarrazin, M. H. Sieweke, D. Wagner, C. Dierks, T. Haaf, T. Ness, M. M. Zaiss, R. E. Voll, S. D. Deshmukh, M. Prinz, T. Goldmann, C. Hölscher, A. E. Hauser, A. J. Lopez-Contreras, D. Grün, V. Gorgoulis, A. Diefenbach, P. Henneke, and A. Triantafyllopoulou, *DNA Damage Signaling Instructs Polyploid Macrophage Fate in Granulomas*, Cell, 167 (2016), pp. 1264–1280.e18.

[148] L. A. Herzenberg, J. Tung, W. A. Moore, L. A. Herzenberg, and D. R. Parks, *Interpreting flow cytometry data: A guide for the perplexed*, Nature Immunology, 7 (2006), pp. 681–685.

[149] M. Hesse, M. Modolell, A. C. La Flamme, M. Schito, J. M. Fuentes, A. W. Cheever, E. J. Pearce, and T. A. Wynn, *Differential Regulation of Nitric Oxide Synthase-2 and Arginase-1 by Type 1/Type 2 Cytokines In Vivo: Granulomatous Pathology Is Shaped by the Pattern of l-Arginine Metabolism*, The Journal of Immunology, 167 (2001), pp. 6533–6544.

[150] A. M. Hine and P. Loke, *Intestinal Macrophages in Resolving Inflammation*, The Journal of Immunology, 203 (2019), pp. 593–599.

[151] G. Hoeffel, Y. Wang, M. Greter, P. See, P. Teo, B. Malleret, M. Leboeuf, D. Low, G. Oller, F. Almeida, S. H. Choy, M. Grisotto, L. Renia, S. J. Conway, E. R. Stanley, J. K. Chan, L. G. Ng, I. M. Samokhvalov, M. Merad, and F. Ginhoux, *Adult Langerhans cells derive predominantly from embryonic fetal liver monocytes with a minor contribution of yolk sac-derived macrophages*, Journal of Experimental Medicine, 209 (2012), pp. 1167–1181.

[152] A. Hoffmann, A. Levchenko, and M. L. Scott, *The IκB-NF-κB signaling module: temporal control and selective gene activation*, Science, 298 (2002), pp. 1241–1245.

[153] D. W. Hommes, T. L. Mikhajlova, S. Stoinov, D. Štimac, B. Vucelic, J. Lonovics, M. Zákuciová, G. D'Haens, G. Van Assche, S. Ba, S. Lee, and T. Pearce, *Fontolizumab, a humanised anti-interferon γ antibody, demonstrates safety and clinical activity in patients with moderate to severe Crohn's disease*, Gut, 55 (2006), pp. 1131–1137.

[154] L. Hu, M. D. Bray, M. Osorio, and D. J. Kopecko, *Campylobacter jejuni induces maturation and cytokine production in human dendritic cells*, Infection and Immunity, 74 (2006), pp. 2697–2705.

[155] H. Huang, M. Fang, L. Jostins, M. Umićević Mirkov, G. Boucher, C. A. Anderson, V. Andersen, I. Cleynen, A. Cortes, F. Crins, M. D'Amato, V. Deffontaine, J. Dmitrieva, E. Docampo, M. Elansary, K. K. H. Farh, A. Franke, A. S. Gori, P. Goyette, J. Halfvarson, T. Haritunians, J. Knight, I. C. Lawrance, C. W. Lees, E. Louis, R. Mariman, T. Meuwissen, M. Mni, Y. Momozawa, M. Parkes, S. L. Spain, E. Théâtre, G. Trynka, J. Satsangi, S. Van Sommeren, S. Vermeire, R. J. Xavier, R. K. Weersma, R. H. Duerr, C. G. Mathew, J. D. Rioux, D. P. McGovern, J. H. Cho,

M. Georges, M. J. Daly, and J. C. Barrett, *Fine-mapping inflammatory bowel disease loci to single-variant resolution*, Nature, 547 (2017), pp. 173–178.

[156] W. Hueber, B. E. Sands, S. Lewitzky, M. Vandemeulebroecke, W. Reinisch, P. D. Higgins, J. Wehkamp, B. G. Feagan, M. D. Yao, M. Karczewski, J. Karczewski, N. Pezous, S. Bek, G. Bruin, B. Mellgard, C. Berger, M. Londei, A. P. Bertolino, G. Tougas, and S. P. Travis, *Secukinumab, a human anti-IL-17A monoclonal antibody, for moderate to severe Crohn's disease: Unexpected results of a randomised, double-blindplacebo- controlled trial*, Gut, 61 (2012), pp. 1693–1700.

[157] J. P. Hugot, M. Chamaillard, H. Zouali, S. Lesage, J. P. Cézard, J. Belaiche, S. Almer, C. Tysk, C. A. O'morain, M. Gassull, V. Binder, Y. Finkel, A. Cortot, R. Modigliani, P. Laurent-Puig, C. Gower-Rousseau, J. Macry, J. F. Colombel, M. Sahbatou, and G. Thomas, *Association of NOD2 leucine-rich repeat variants with susceptibility to Crohn's disease*, Nature, 411 (2001), pp. 599–603.

[158] R. D. Huhn, E. Radwanski, J. Gallo, M. B. Affrime, R. Sabo, G. Gonyo, A. Monge, and D. L. Cutler, *Pharmacodynamics of subcutaneous recombinant human interleukin-10 in healthy volunteers*, Clinical Pharmacology and Therapeutics, 62 (1997), pp. 171–180.

[159] R. D. Huhn, E. J. Yurkow, J. G. Kuhn, L. Clarke, H. Gunn, D. Resta, R. Shah, L. A. Myers, and J. R. Seibold, *Pharmacodynamics of daily subcutaneous recombinant human interleukin-3 in normal volunteers*, Clinical Pharmacology & Therapeutics, 57 (1995), pp. 32–41.

[160] C. A. Hunter and S. A. Jones, *IL-6 as a keystone cytokine in health and disease*, Nature Immunology, 16 (2015), pp. 448–457.

[161] T. Imam, S. Park, M. H. Kaplan, and M. R. Olson, *Effector T helper cell subsets in inflammatory bowel diseases*, Frontiers in Immunology, 9 (2018), p. 1212.

[162] Y. Ishibashi and T. Arai, *Salmonella typhi does not inhibit phagosome-lysosome fusion in human monocyte-derived macrophages*, FEMS Immunology and Medical Microbiology, 12 (1995), pp. 55–61.

[163] C. Jakubzick, E. L. Gautier, S. L. Gibbings, D. K. Sojka, A. Schlitzer, T. E. Johnson, S. Ivanov, Q. Duan, S. Bala, T. Condon, N. VanRooijen, J. R. Grainger, Y. Belkaid, A. Ma'ayan, D. W. Riches, W. M. Yokoyama, F. Ginhoux, P. M. Henson, and G. J. Randolph, *Minimal differentiation of classical monocytes as they survey steady-state tissues and transport antigen to lymph nodes*, Immunity, 39 (2013), pp. 599–610.

[164] J. E. Jansen, D. Aschenbrenner, H. H. Uhlig, M. C. Coles, and E. A. Gaffney, *A method for the inference of cytokine interaction networks*, (in review).

[165] J. E. Jansen, E. A. Gaffney, J. Wagg, and M. C. Coles, *Combining mathematical models with experimentation to drive novel mechanistic insights into macrophage function*, Frontiers in Immunology, 10 (2019), p. 1283.

[166] S. J. Jenkins and J. E. Allen, *Similarity and diversity in macrophage activation by nematodes, trematodes, and cestodes*, Journal of Biomedicine and Biotechnology, 2010 (2010), p. 262609.

[167] M. A. Jones, S. Tötemeyer, D. J. Maskell, C. E. Bryant, and P. A. Barrow, *Induction of proinflammatory responses in the human monocytic cell line THP-1 by Campylobacter jejuni*, Infection and Immunity, 71 (2003), pp. 2626–2633.

[168] L. Jostins, S. Ripke, R. K. Weersma, and R. H. Duerr, *Host-microbe interactions have shaped the genetic architecture of inflammatory bowel disease*, Nature, 491 (2012), pp. 119–124.

[169] H. Jyonouchi, S. Sun, H. Le, and F. L. Rimell, *Evidence of dysregulated cytokine production by sinus lavage and peripheral blood mononuclear cells in patients with treatment-resistant chronic rhinosinusitis*, Archives of Otolaryngology - Head and Neck Surgery, 127 (2001), pp. 1488–1494.

[170] N. Kamada, T. Hisamatsu, S. Okamoto, H. Chinen, T. Kobayashi, T. Sato, A. Sakuraba, M. T. Kitazume, A. Sugita, K. Koganei, K. S. Akagawa, and T. Hibi, *Unique CD14+ intestinal macrophages contribute to the pathogenesis of Crohn disease via IL-23/IFN-γ axis*, Journal of Clinical Investigation, 118 (2008), pp. 2269–2280.

[171] V. N. Kampen, *Stochastic Processes in Physics and Chemistry*, Amsterdam; Boston; London: Elsevier, third ed., 2007.

[172] N. Kapoor, S. Pawar, T. D. Sirakova, C. Deb, W. L. Warren, and P. E. Kolattukudy, *Human granuloma in vitro model, for TB dormancy and resuscitation*, PLoS ONE, 8 (2013), p. e53657.

[173] T. Kawai and S. Akira, *Toll-like receptors and their crosstalk with other innate receptors in infection and immunity*, Immunity, 34 (2011), pp. 637–650.

[174] S. Kedia, P. Das, K. S. Madhusudhan, S. Dattagupta, R. Sharma, P. Sahni, G. Makharia, and V. Ahuja, *Differentiating Crohn's disease from intestinal tuberculosis*, World Journal of Gastroenterology, 25 (2019), pp. 418–432.

[175] B. Kessler, D. Rinchai, C. Kewcharoenwong, A. Nithichanon, R. Biggart, C. M. Hawrylowicz, G. J. Bancroft, and G. Lertmemongkolchai, *Interleukin 10 inhibits pro-inflammatory cytokine responses and killing of Burkholderia pseudomallei*, Scientific Reports, 7 (2017), pp. 1–11.

[176] Y. G. Kim, N. Kamada, M. H. Shaw, N. Warner, G. Y. Chen, L. Franchi, and G. Núñez, *The Nod2 sensor promotes intestinal pathogen eradication via the chemokine CCL2-dependent recruitment of inflammatory monocytes*, Immunity, 34 (2011), pp. 769–780.

[177] D. Kirschner, E. Pienaar, S. Marino, and J. J. Linderman, *A review of computational and mathematical modeling contributions to our understanding of Mycobacterium tuberculosis within-host infection and treatment*, Current Opinion in Systems Biology, 3 (2017), pp. 170–185.

[178] C. Klotz, T. Ziegler, A. S. Figueiredo, S. Rausch, M. R. Hepworth, N. Obsivac, C. Sers, R. Lang, P. Hammerstein, R. Lucius, and S. Hartmann, *A helminth immunomodulator exploits host signaling events to regulate cytokine production in macrophages*, PLoS Pathogens, 7 (2011), p. e1001248.

[179] A. Kole, J. He, A. Rivollier, D. D. Silveira, K. Kitamura, K. J. Maloy, and B. L. Kelsall, *Type I IFNs regulate effector and regulatory T cell accumulation and anti-inflammatory cytokine production during T cell–mediated colitis*, The Journal of Immunology, 191 (2013), pp. 2771–2779.

[180] J. K. Kolls and A. Lindén, *Interleukin-17 family members and inflammation*, Immunity, 21 (2004), pp. 467–476.

[181] K. Korla and N. Chandra, *A systems perspective of signalling networks in host-pathogen interactions*, Journal of the Indian Institute of Science, 97 (2017), pp. 41–57.

[182] S. Köster, S. Upadhyay, P. Chandra, K. Papavinasasundaram, G. Yang, A. Hassan, S. J. Grigsby, E. Mittal, H. S. Park, V. Jones, F. F. Hsu, M. Jackson, C. M. Sassetti, and J. A. Philips, *Mycobacterium tuberculosis is protected from NADPH oxidase and LC3-associated phagocytosis by the LCP protein CpsA*, Proceedings of the National Academy of Sciences of the United States of America, 114 (2017), pp. e8711–e8720.

[183] K. P. Kotredes, B. Thomas, and A. M. Gamero, *The protective role of Type I interferons in the gastrointestinal tract*, Frontiers in Immunology, 8 (2017), p. 410.

[184] T. Kucharzik, R. Stoll, N. Lugering, and W. Domschke, *Circulating antiinflammatory cytokine IL-10 in patients with inflammatory bowel disease (IBD)*, Clinical and Experimental Immunology, 100 (1995), pp. 452–456.

[185] T. Kuijpers and R. Lutter, *Inflammation and repeated infections in CGD: Two sides of a coin*, Cellular and Molecular Life Sciences, 69 (2012), pp. 7–15.

[186] R. Lahiri, B. Randhawa, and J. L. Krahenbuhl, *Infection of mouse macrophages with viable mycobacterium leprae does not induce apoptosis*, Journal of Infectious Diseases, 201 (2010), pp. 1736–1742.

[187] P. Lapaquette, M. A. Bringer, and A. Darfeuille-Michaud, *Defects in autophagy favour adherent-invasive Escherichia coli persistence within macrophages leading to increased pro-inflammatory response*, Cellular Microbiology, 14 (2012), pp. 791–807.

[188] S. K. Lathrop, K. A. Binder, T. Starr, K. G. Cooper, A. Chong, A. B. Carmody, and O. Steele-Mortimer, *Replication of Salmonella enterica serovar Typhimurium in human monocyte-derived macrophages*, Infection and Immunity, 83 (2015), pp. 2661–2671.

[189] M. Lavielle, *Mixed effects models for the population approach: Models, tasks, methods and tools*, CRC Press, 2014.

[190] G. Lay, Y. Poquet, P. Salek-Peyron, M. P. Puissegur, C. Botanch, H. Bon, F. Levillain, J. L. Duteyrat, J. F. Emile, and F. Altare, *Langhans giant cells from M. Tuberculosis-induced human granulomas cannot mediate mycobacterial uptake*, Journal of Pathology, 211 (2007), pp. 76–85.

[191] R. Leander, S. Dai, L. L. S. Schlesinger, and A. Friedman, *A mathematical model of CR3/TLR2 crosstalk in the context of Francisella tularensis infection*, PLoS Computational Biology, 8 (2012), p. e1002757.

[192] A. Leber, J. Bassaganya-Riera, N. Tubau-Juni, V. Zoccoli-Rodriguez, M. Viladomiu, V. Abedi, P. Lu, and R. Hontecillas, *Modeling the role of lanthionine synthetase C-Like 2 (LANCL2) in the modulation of immune responses to Helicobacter pylori infection*, PLoS ONE, 11 (2016), p. e0167440.

[193] J. Lee, T. Repasy, K. Papavinasasundaram, C. Sassetti, and H. Kornfeld, *Mycobacterium tuberculosis induces an atypical cell death mode to escape from infected macrophages*, PLoS ONE, 6 (2011), p. e18367.

[194] J. S. Lee, C. M. Tato, B. Joyce-Shaikh, F. Gulan, C. Cayatte, Y. Chen, W. M. Blumenschein, M. Judo, G. Ayanoglu, T. K. McClanahan, X. Li, and D. J. Cua, *Interleukin-23-independent IL-17 production regulates intestinal epithelial permeability*, Immunity, 43 (2015), pp. 727–738.

[195] B. Levine and V. Deretic, *Unveiling the roles of autophagy in innate and adaptive immunity*, Nature Reviews Immunology, 7 (2007), pp. 767–777.

[196] B. Levine, N. Mizushima, and H. W. Virgin, *Autophagy in immunity and inflammation*, Nature, 469 (2011), pp. 323–335.

[197] M. Levy, A. Arion, D. Berrebi, L. Cuisset, C. Jeanne-Pasquier, B. Bader-Meunier, and C. Jung, *Severe early-onset colitis revealing mevalonate kinase deficiency*, Pediatrics, 132 (2013), pp. e779–e783.

[198] J. Limsrivilai, A. B. Shreiner, A. Pongpaibul, C. Laohapand, R. Boonanuwat, N. Pausawasdi, S. Pongprasobchai, S. Manatsathit, and P. D. Higgins, *Meta-analytic bayesian model for differentiating intestinal tuberculosis from Crohn's disease*, American Journal of Gastroenterology, 112 (2017), pp. 415–427.

[199] P. L. Lin, C. B. Ford, M. T. Coleman, A. J. Myers, R. Gawande, T. Ioerger, J. Sacchettini, S. M. Fortune, and J. L. Flynn, *Sterilization of granulomas is common in active and latent tuberculosis despite within-host variability in bacterial killing*, Nature Medicine, 20 (2014), pp. 75–79.

[200] M. Linke, H. T. T. Pham, K. Katholnig, T. Schnöller, A. Miller, F. Demel, B. Schütz, M. Rosner, B. Kovacic, N. Sukhbaatar, B. Niederreiter, S. Blüml, P. Kuess, V. Sexl, M. Müller, M. Mikula, W. Weckwerth, A. Haschemi, M. Susani, M. Hengstschläger, M. J. Gambello, and T. Weichhart, *Chronic signaling via the metabolic checkpoint kinase mTORC1 induces macrophage granuloma formation and marks sarcoidosis progression*, Nature Immunology 2017 18:3, 18 (2017), pp. 293–302.

[201] B. S. Liu, H. L. Janssen, and A. Boonstra, *Type I and III interferons enhance IL-10R expression on human monocytes and macrophages, resulting in IL-10-mediated suppression of TLR-induced IL-12*, European Journal of Immunology, 42 (2012), pp. 2431–2440.

[202] J. Z. Liu, S. Van Sommeren, H. Huang, S. C. Ng, R. Alberts, A. Takahashi, S. Ripke, J. C. Lee, L. Jostins, T. Shah, S. Abedian, J. H. Cheon, J. Cho, N. E. Daryani, L. Franke, Y. Fuyuno, A. Hart, R. C. Juyal, G. Juyal, W. H. Kim, A. P. Morris, H. Poustchi, W. G. Newman, V. Midha, T. R. Orchard, H. Vahedi, A. Sood, J. J. Sung, R. Malekzadeh, H. J. Westra, K. Yamazaki, S. K. Yang, J. C. Barrett, A. Franke, B. Z. Alizadeh, M. Parkes, B. K. Thelma, M. J. Daly, M. Kubo, C. A. Anderson, and R. K. Weersma, *Association analyses identify 38 susceptibility loci for inflammatory bowel disease and highlight shared genetic risk across populations*, Nature Genetics, 47 (2015), pp. 979–986.

[203] Y. Liu, H. J. Van Kruiningen, A. B. West, R. W. Cartun, A. Cortot, and J. F. Colombel, *Immunocytochemical evidence of Listeria, Escherichia coil, and Streptococcus antigens in Crohn's disease*, Gastroenterology, 108 (1995), pp. 1396–1404.

[204] P. Loke, M. G. Nair, J. Parkinson, D. Guiliano, M. Blaxter, and J. E. Allen, *IL-4 dependent alternatively-activated macrophages have a distinctive in vivo gene expression phenotype*, BMC Immunology, 3 (2002), p. 7.

[205] U. Lundberg, U. Vinatzer, D. Berdnik, A. Von Gabain, and M. Baccarini, *Growth phase-regulated induction of Salmonella-induced macrophage apoptosis correlates with transient expression of SPI-1 genes*, Journal of Bacteriology, 181 (1999), pp. 3433–3437.

[206] G. B. Mackaness, *Cellular resistance to infection*, The Journal of experimental medicine, 116 (1962), pp. 381–406.

[207] S. Maeda, L. C. Hsu, H. Liu, L. A. Bankston, M. Iimura, M. F. Kagnoff, L. Eckmann, and M. Karin, *Nod2 mutation in Crohn's disease potentiates NF-κB activity and IL-1β processing*, Science, 307 (2005), pp. 734–738.

[208] T. Maier, M. Güell, and L. Serrano, *Correlation of mRNA and protein in complex biological samples*, FEBS Letters, 583 (2009), pp. 3966–3973.

[209] I. Májer, A. Hajihosseini, and A. Becskei, *Identification of optimal parameter combinations for the emergence of bistability*, Physical Biology, 12 (2015), p. 066011.

[210] G. L. Mandell and E. W. Hook, *Leukocyte bactericidal activity in chronic granulomatous disease: correlation of bacterial hydrogen peroxide production and susceptibility to intracellular killing.*, Journal of Bacteriology, 100 (1969), pp. 531–532.

[211] S. K. Manna and B. B. Aggarwal, *Interleukin-4 Down-regulates Both Forms of Tumor Necrosis Factor Receptor and Receptor-mediated Apoptosis, NF-κB, AP-1, and c-Jun N-Terminal Kinase: comparison with interleukin-13*, Journal of Biological Chemistry, 273 (1998), pp. 33333–33341.

[212] A. A. Margolin, I. Nemenman, K. Basso, C. Wiggins, G. Stolovitzky, R. D. Favera, and A. Califano, *ARACNE: An algorithm for the reconstruction of gene regulatory networks in a mammalian cellular context*, BMC Bioinformatics, 7 (2006), p. S7.

[213] S. Marino, I. B. Hogue, C. J. Ray, and D. E. Kirschner, *A methodology for performing global uncertainty and sensitivity analysis in systems biology*, Journal of Theoretical Biology, 254 (2008), pp. 178–196.

[214] S. Marino, A. Myers, J. L. Flynn, and D. E. Kirschner, *TNF and IL-10 are major factors in modulation of the phagocytic cell environment in lung and lymph node in tuberculosis: A next-generation two-compartmental model*, Journal of Theoretical Biology, 265 (2010), pp. 586–598.

[215] T. T. Marinov and K. Deng, *Characteristic line scheme for hierarchical size-structured model with nonlinear growth, mortality and reproduction rates*, in AIP Conference Proceedings, vol. 1186, 2009, pp. 123–132.

[216] ——, *Characteristic line based schemes for solving a quasilinear hierarchical size-structured model*, Journal of Scientific Computing, 46 (2011), pp. 452–469.

[217] F. Markowetz and R. Spang, *Inferring cellular networks - A review*, BMC Bioinformatics, 8 (2007), p. S5.

[218] I. Marriott, T. G. Hammond, E. K. Thomas, and K. L. Bost, *Salmonella efficiently enter and survive within cultured CD11c+ dendritic cells initiating cytokine expression*, European Journal of Immunology, 29 (1999), pp. 1107–1115.

[219] F. O. Martinez and S. Gordon, *The M1 and M2 paradigm of macrophage activation: time for reassessment*, F1000Prime Reports, 6 (2014).

[220] M. E. Martinez-Sanchez, L. Huerta, E. R. Alvarez-Buylla, and C. V. Luján, *Role of cytokine combinations on CD4+ T cell differentiation, partial polarization, and plasticity: Continuous network modeling approach*, Frontiers in Physiology, 9 (2018), p. 877.

[221] M. E. Martinez-Sanchez, L. Mendoza, C. Villarreal, and E. R. Alvarez-Buylla, *A minimal regulatory network of extrinsic and intrinsic factors recovers observed patterns of CD4+ T cell differentiation and plasticity*, PLoS Computational Biology, 11 (2015), p. e1004324.

[222] F. J. Massey, *The Kolmogorov-Smirnov Test for Goodness of Fit*, Source: Journal of the American Statistical Association, 46 (1951), pp. 68–78.

[223] A. McInnes and D. M. Rennick, *Interleukin 4 induces cultured monocytes/macrophages to form giant multinucleated cells*, Journal of Experimental Medicine, 167 (1988), pp. 598–611.

[224] I. B. McInnes, J. Sieper, J. Braun, P. Emery, D. Van Der Heijde, J. D. Isaacs, G. Dahmen, J. Wollenhaupt, H. Schulze-Koops, J. Kogan, S. Ma, M. M. Schumacher, A. P. Bertolino, W. Hueber, and P. P. Tak, *Efficacy and safety of secukinumab, a fully human anti-interleukin-17A monoclonal antibody, in patients with moderate-to-severe psoriatic arthritis: A 24-week, randomised, double-blind, placebo-controlled, phase II proof-of-concept trial*, Annals of the Rheumatic Diseases, 73 (2014), pp. 349–356.

[225] S. Meconi, A. Vercellone, F. Levillain, B. Payré, T. Al Saati, F. Capilla, P. Desreumaux, A. Darfeuille-michaud, and F. Altare, *Adherent-invasive Escherichia coli isolated from Crohn's disease patients induce granulomas in vitro*, Cellular Microbiology, 9 (2007), pp. 1252–1261.

[226] F. Mehta, *Report: economic implications of inflammatory bowel disease and its management.*, The American Journal of Managed Care, 22 (2016), pp. s51–60.

[227] M. Meier-Schellersheim, R. Varma, and B. R. Angermann, *Mechanistic models of cellular signaling, cytokine crosstalk, and cell-cell communication in immunology*, Frontiers in Immunology, 10 (2019), p. 2268.

[228] C. Meischl and D. Roos, *The molecular basis of chronic granulomatous disease*, Springer Seminars in Immunopathology, 19 (1998), pp. 417–434.

[229] J. A. J. Metz and O. Diekmann, *The dynamics of physiologically structured populations*, Springer, 1986.

[230] L. H. Miller, *Table of Percentage Points of Kolmogorov Statistics*, Journal of the American Statistical Association, 51 (1956), p. 111.

[231] M. U. Mirkov, B. Verstockt, and I. Cleynen, *Genetics of inflammatory bowel disease: beyond NOD2*, The Lancet Gastroenterology and Hepatology, 2 (2017), pp. 224–234.

[232] T. Miyamoto, *STATs and macrophage fusion*, Jak-Stat, 2 (2013), p. e24777.

[233] T. Mogues, M. E. Goodrich, L. Ryan, R. LaCourse, and R. J. North, *The relative importance of T cell subsets in immunity and immunopathology of airborne Mycobacterium tuberculosis infection in mice*, Journal of Experimental Medicine, 193 (2001), pp. 271–280.

[234] N. A. Molodecky, I. S. Soon, D. M. Rabi, W. A. Ghali, M. Ferris, G. Chernoff, E. I. Benchimol, R. Panaccione, S. Ghosh, H. W. Barkema, and G. G. Kaplan, *Increasing incidence and prevalence of the inflammatory bowel diseases with time, based on systematic review*, Gastroenterology, 142 (2012), pp. 46–54.

[235] D. C. Montgomery and G. C. Runger, *Applied statistics and probability for engineers*, vol. 19, John Wiley & Sons, 5th ed., 1994.

[236] K. W. Moore, R. D. W. Malefyt, L. Robert, and A. O. Garra, *Interleukin-10 and the interleukin-10 receptor*, Molecular and Cellular Biology, 1 (2001), pp. 683–765.

[237] J. J. Moré and D. C. Sorensen, *Computing a Trust Region Step*, SIAM Journal on Scientific and Statistical Computing, 4 (1983), pp. 553–572.

[238] P. A. Morel, R. E. Lee, and J. R. Faeder, *Demystifying the cytokine network: Mathematical models point the way*, Cytokine, 98 (2017), pp. 115–123.

[239] J. L. Moreno, I. Mikhailenko, M. M. Tondravi, and A. D. Keegan, *IL-4 promotes the formation of multinucleated giant cells from macrophage precursors by a STAT6-dependent, homotypic mechanism: contribution of E-cadherin*, Journal of Leukocyte Biology, 82 (2007), pp. 1542–1553.

[240] D. M. Mosser and J. P. Edwards, *Exploring the full spectrum of macrophage activation*, Nature Reviews Immunology, 8 (2008), pp. 958–969.

[241] J. D. Murray, *Why are there no 3-headed monsters? mathematical modeling in biology*, Notices of the American Mathematical Society, 59 (2012), pp. 785–795.

[242] R. Z. Murray and J. L. Stow, *Cytokine secretion in macrophages: SNAREs, Rabs, and membrane trafficking*, Frontiers in Immunology, 5 (2014), p. 538.

[243] Y. R. Na, M. Stakenborg, S. H. Seok, and G. Matteoli, *Macrophages in intestinal inflammation and resolution: a potential therapeutic target in IBD*, Nature Reviews Gastroenterology and Hepatology, 16 (2019), pp. 531–543.

[244] S. Nagaraja, A. Wallqvist, J. Reifman, and A. Y. Mitrophanov, *Computational approach to characterize causative factors and molecular indicators of chronic wound inflammation*, The Journal of Immunology, 192 (2014), pp. 1824–1834.

[245] M. Nakanishi-Matsui, S. Yano, N. Matsumoto, and M. Futai, *Lipopolysaccharide induces multinuclear cell from RAW264.7 line with increased phagocytosis activity*, Biochemical and Biophysical Research Communications, 425 (2012), pp. 144–149.

[246] R. J. Napier, E. J. Lee, M. P. Davey, E. E. Vance, J. M. Furtado, P. E. Snow, K. A. Samson, S. J. Lashley, B. R. Brown, R. Horai, M. J. Mattapallil, B. Xu, M. C. Callegan, L. S. Uebelhoer, C. L. Lancioni, R. K. Vehe, B. A. Binstadt, J. R. Smith, R. R. Caspi, and H. L. Rosenzweig, *T cell-intrinsic role for Nod2 in protection against Th17-mediated uveitis*, Nature Communications, 11 (2020).

[247] W. W. Navarre and A. Zychlinsky, *Pathogen-induced apoptosis of macrophages: A common end for different pathogenic strategies*, Cellular Microbiology, 2 (2000), pp. 265–273.

[248] M. F. Neurath, *Cytokines in inflammatory bowel disease*, Nature Reviews Immunology, 14 (2014), pp. 329–342.

[249] ——, *Current and emerging therapeutic targets for IBD*, Nature Reviews Gastroenterology & Hepatology, 14 (2017), pp. 269–278.

[250] J. Nocedal and S. J. Wright, *Numerical optimization*, Springer series in operations research, Springer, New York ; London, 2nd ed. ed., 2006.

[251] E. Noguchi, Y. Homma, X. Kang, M. G. Netea, and X. Ma, *A Crohn's disease-associated NOD2 mutation suppresses transcription of human IL10 by inhibiting ac-*

tivity of the nuclear ribonucleoprotein hnRNP-A1, Nature Immunology, 10 (2009), pp. 471–479.

[252] R. Nowarski, R. Jackson, N. Gagliani, M. R. De Zoete, N. W. Palm, W. Bailis, J. S. Low, C. C. Harman, M. Graham, E. Elinav, and R. A. Flavell, *Epithelial IL-18 equilibrium controls barrier function in colitis*, Cell, 163 (2015), pp. 1444–1456.

[253] J. R. Ockendon, *Applied partial differential equations*, Oxford University Press, Oxford, rev. ed. ed., 2003.

[254] E. A. Oczypok, T. D. Oury, and C. T. Chu, *It's a Cell-Eat-Cell World: Autophagy and Phagocytosis*, The American Journal of Pathology, 182 (2013), pp. 612–622.

[255] T. Ogino, J. Nishimura, S. Barman, H. Kayama, S. Uematsu, D. Okuzaki, H. Osawa, N. Haraguchi, M. Uemura, T. Hata, I. Takemasa, T. Mizushima, H. Yamamoto, K. Takeda, Y. Doki, and M. Mori, *Increased Th17-inducing activity of CD14+ CD163low myeloid cells in intestinal lamina propria of patients with Crohn's disease*, Gastroenterology, 145 (2013), pp. 1380–391.e1. Web.

[256] F. Ordikhani, V. Pothula, R. Sanchez-Tarjuelo, S. Jordan, and J. Ochando, *Macrophages in Organ Transplantation*, Frontiers in Immunology, 11 (2020), p. 2987.

[257] A. J. Pagán and L. Ramakrishnan, *The formation and function of granulomas*, Annual Review of Immunology, 36 (2018), pp. 639–665.

[258] L. J. Pallett, A. R. Burton, O. E. Amin, S. Rodriguez-Tajes, A. A. Patel, N. Zakeri, A. Jeffery-Smith, L. Swadling, N. M. Schmidt, A. Baiges, A. Gander, D. Yu, D. Nasralla, F. Froghi, S. Iype, B. R. Davidson, D. Thorburn, S. Yona, X. Forns, and M. K. Maini, *Longevity and replenishment of human liver-resident memory T cells and mononuclear phagocytes*, Journal of Experimental Medicine, 217 (2020).

[259] D. R. Park and S. J. Skerrett, *IL-10 enhances the growth of Legionella pneumophila in human mononuclear phagocytes and reverses the protective effect of IFN-gamma: differential responses of blood monocytes and alveolar macrophages.*, Journal of Immunology, 157 (1996), pp. 2528–2538.

[260] E. J. Parkinson-Lawrence, T. Shandala, M. Prodoehl, R. Plew, G. N. Borlace, and D. A. Brooks, *Lysosomal storage disease: revealing lysosomal function and physiology*, Physiology, 25 (2010), pp. 102–115.

[261] D. R. Parks, M. Roederer, and W. A. Moore, *A new "logicle" display method avoids deceptive effects of logarithmic scaling for low signals and compensated data*, Cytometry Part A, 69 (2006), pp. 541–551.

[262] S. Paul, P. Laochumroonvorapong, and G. Kaplan, *Comparable growth of virulent and avirulent Mycobacterium tuberculosis in human macrophages in vitro*, Journal of Infectious Diseases, 174 (1996), pp. 105–112.

[263] V. A. Pavlov, S. S. Chavan, and K. J. Tracey, *Molecular and Functional Neuroscience in Immunity*, Annual Review of Immunology, 36 (2018), pp. 783–812.

[264] K. A. Pawelek, D. Dor, C. Salmeron, and A. Handel, *Within-host models of high and low pathogenic influenza virus infections: the role of macrophages*, PLoS ONE, 11 (2016), p. e0150568.

[265] E. J. Pearce and A. S. MacDonald, *The immunobiology of schistosomiasis*, Nature Reviews Immunology, 2 (2002), pp. 499–511.

[266] H. Peeters, S. Bogaert, D. Laukens, P. Rottiers, F. De Keyser, A. Darfeuille-Michaud, A. L. Glasser, D. Elewaut, and M. De Vos, *CARD15 variants determine a disturbed early response of monocytes to adherent-invasive Escherichia coli strain LF82 in Crohn's disease*, International Journal of Immunogenetics, 34 (2007), pp. 181–191.

[267] O. Penack, O. M. Smith, A. Cunningham-Bussel, X. Liu, U. Rao, N. Yim, I. K. Na, A. M. Holland, A. Ghosh, S. X. Lu, R. R. Jenq, C. Liu, G. F.

Murphy, K. Brandl, and M. R. Van Den Brink, *NOD2 regulates hematopoietic cell function during graft-versus-host disease*, Journal of Experimental Medicine, 206 (2009), pp. 2101–2110.

[268] C. Petes, N. Odoardi, S. M. Plater, N. L. Martin, and K. Gee, *IL-27 amplifies cytokine responses to Gram-negative bacterial products and Salmonella typhimurium infection*, Scientific Reports, 8 (2018), pp. 1–13.

[269] P. Peyron, J. Vaubourgeix, Y. Poquet, F. Levillain, C. Botanch, F. Bardou, M. Daffé, J. F. Emile, B. Marchou, P. J. Cardona, C. De Chastellier, and F. Altare, *Foamy macrophages from tuberculous patients' granulomas constitute a nutrient-rich reservoir for M. tuberculosis persistence*, PLoS Pathogens, 4 (2008), p. e1000204.

[270] T. H. Pham, S. M. Brewer, T. Thurston, L. M. Massis, J. Honeycutt, K. Lugo, A. R. Jacobson, J. G. Vilches-Moure, M. Hamblin, S. Helaine, and D. M. Monack, *Salmonella-driven polarization of granuloma macrophages antagonizes TNF-mediated pathogen restriction during persistent infection*, Cell Host and Microbe, 27 (2020), pp. 54–67.

[271] C. W. Philipson, J. Bassaganya-Riera, M. Viladomiu, B. Kronsteiner, V. Abedi, S. Hoops, P. Michalak, L. Kang, S. E. Girardin, and R. Hontecillas, *Modeling the regulatory mechanisms by which NLRX1 modulates innate immune responses to Helicobacter pylori infection*, PLoS ONE, 10 (2015), p. e0137839.

[272] T. E. Pietilä, V. Veckman, P. Kyllönen, K. Lähteenmäki, T. K. Korhonen, and I. Julkunen, *Activation, cytokine production, and intracellular survival of bacteria in Salmonella -infected human monocyte-derived macrophages and dendritic cells* , Journal of Leukocyte Biology, 78 (2005), pp. 909–920.

[273] F. A. Post, C. Manca, O. Neyrolles, B. Ryffel, D. B. Young, and G. Kaplan, *Mycobacterium tuberculosis 19-kilodalton lipoprotein inhibits Mycobacterium smegmatis-induced cytokine production by human macrophages in vitro*, Infection and Immunity, 69 (2001), pp. 1433–1439.

[274] J. Pott, A. M. Kabat, and K. J. Maloy, *Intestinal Epithelial Cell Autophagy Is Required to Protect against TNF-Induced Apoptosis during Chronic Colitis in Mice*, Cell Host and Microbe, 23 (2018), pp. 191–202.e4.

[275] M. P. Puissegur, C. Botanch, J. L. Duteyrat, G. Delsol, C. Caratero, and F. Altare, *An in vitro dual model of mycobacterial granulomas to investigate the molecular interactions between mycobacteria and human host cells*, Cellular Microbiology, 6 (2004), pp. 423–433.

[276] M.-P. Puissegur, G. Lay, M. Gilleron, L. Botella, J. Nigou, H. Marrakchi, B. Mari, J.-L. Duteyrat, Y. Guerardel, L. Kremer, P. Barbry, G. Puzo, and F. Altare, *Mycobacterial lipomannan induces granuloma macrophage fusion via a TLR2-dependent, ADAM9-and β1 integrin-mediated pathway*, The Journal of Immunology, 178 (2007), pp. 3161–3169.

[277] J. M. Pujol, J. E. Eisenberg, C. N. Haas, and J. S. Koopman, *The effect of ongoing exposure dynamics in dose response relationships*, PLoS Computational Biology, 5 (2009), p. e1000399.

[278] A. B. Pulimood, B. S. Ramakrishna, G. Kurian, S. Peter, S. Patra, V. I. Mathan, and M. M. Mathan, *Endoscopic mucosal biopsies are useful in distinguishing granulomatous colitis due to Crohn's disease from tuberculosis*, Gut, 45 (1999), pp. 537–541.

[279] H. Rachmawati, L. Beljaars, C. Reker-Smit, H. I. Bakker, A. M. Van Loenen-Weemaes, M. N. Lub-De Hooge, and K. Poelstra, *Intravenous Administration of Recombinant Human IL-10 Suppresses the Development of Anti–Thy 1–Induced Glomerulosclerosis in Rats*, PDA Journal of Pharmaceutical Science and Technology, 65 (2011), pp. 116–130.

[280] H. Rachmawati, L. Beljaars, C. Reker-Smit, A.-m. M. Van Loenen-Weemaes, W. I. Hagens, D. K. F. Meijer, and K. Poelstra, *Pharmacokinetic and Biodistribution Profile of Recombinant Human Interleukin-10 Following*

Intravenous Administration in Rats with Extensive Liver Fibrosis, Pharmaceutical Research 2004 21:11, 21 (2004), pp. 2072–2078.

[281] A. Raue, C. Kreutz, T. Maiwald, J. Bachmann, M. Schilling, U. Klingmüller, and J. Timmer, *Structural and practical identifiability analysis of partially observed dynamical models by exploiting the profile likelihood*, Bioinformatics, 25 (2009), pp. 1923–1929.

[282] A. Raue, C. Kreutz, F. J. Theis, and J. Timmer, *Joining forces of Bayesian and frequentist methodology: a study for inference in the presence of non-identifiability*, Philosophical Transactions of the Royal Society A: Mathematical, Physical and Engineering Sciences, 371 (2013), p. 20110544.

[283] A. Raue, M. Schilling, J. Bachmann, A. Matteson, M. Schelke, D. Kaschek, S. Hug, C. Kreutz, B. D. Harms, F. J. Theis, U. Klingmüller, and J. Timmer, *Lessons learned from quantitative dynamical modeling in systems biology*, PLoS ONE, 8 (2013), p. e74335.

[284] A. Raue, B. Steiert, M. Schelker, C. Kreutz, T. Maiwald, H. Hass, and J. Vanlier, *Data2Dynamics: a modeling environment tailored to parameter estimation in dynamical systems*, Bioinformatics, 31 (2015), pp. 3558–3560.

[285] J. C. J. Ray, J. Wang, J. Chan, and D. E. Kirschner, *The timing of TNF and IFN-γ signaling affects macrophage activation strategies during Mycobacterium tuberculosis infection*, Journal of Theoretical Biology, 252 (2008), pp. 24–38.

[286] W. Reinisch, W. De Villiers, L. Bene, L. Simon, I. Rácz, S. Katz, I. Altorjay, B. Feagan, D. Riff, C. N. Bernstein, D. Hommes, P. Rutgeerts, A. Cortot, M. Gaspari, M. Cheng, T. Pearce, and B. E. Sands, *Fontolizumab in moderate to severe Crohn's disease: A phase 2, randomized, double-blind, placebo-controlled, multiple-dose study*, Inflammatory Bowel Diseases, 16 (2010), pp. 233–242.

[287] W. Reinisch, J. Panés, S. Khurana, G. Toth, F. Hua, G. M. Comer, M. Hinz, K. Page, M. O'Toole, T. M. D. Moorehead, H. Zhu, Y. H. Sun,

and F. Cataldi, *Anrukinzumab, an anti-interleukin 13 monoclonal antibody, in active UC: Efficacy and safety from a phase IIa randomised multicentre study*, Gut, 64 (2015), pp. 894–900.

[288] T. Repasy, J. Lee, S. Marino, N. Martinez, D. E. Kirschner, G. Hendricks, S. Baker, A. A. Wilson, D. N. Kotton, and H. Kornfeld, *Intracellular bacillary burden reflects a burst size for Mycobacterium tuberculosis in vivo*, PLoS Pathogens, 9 (2013), p. e1003190.

[289] O. Restif, Y. S. Goh, M. Palayret, A. J. Grant, T. J. McKinley, M. R. Clark, and P. Mastroeni, *Quantification of the effects of antibodies on the extra- and intracellular dynamics of Salmonella enterica*, Journal of the Royal Society Interface, 10 (2013), p. 20120866.

[290] B. K. Reuter and T. T. Pizarro, *Commentary: The role of the IL-18 system and other members of the IL-1R/TLR superfamily in innate mucosal immunity and the pathogenesis of inflammatory bowel disease: Friend or foe?*, European Journal of Immunology, 34 (2004), pp. 2347–2355.

[291] J. J. Rice, Y. Tu, and G. Stolovitzky, *Reconstructing biological networks using conditional correlation analysis*, Bioinformatics, 21 (2005), pp. 765–773.

[292] P. Royston, *A Toolkit for Testing for Non-Normality in Complete and Censored Samples*, The Statistician, 42 (1993), p. 37.

[293] R. C. Russo, C. C. Garcia, M. M. Teixeira, and F. A. Amaral, *The CXCL8/IL-8 chemokine family and its receptors in inflammatory diseases*, Expert Review of Clinical Immunology, 10 (2014), pp. 593–619.

[294] A. E. Saliba, L. Li, A. J. Westermann, S. Appenzeller, D. A. Stapels, L. N. Schulte, S. Helaine, and J. Vogel, *Single-cell RNA-seq ties macrophage polarization to growth rate of intracellular Salmonella*, Nature Microbiology, 2 (2016), pp. 1–8.

[295] A. Saltelli, S. Tarantola, and K. P. Chan, *A quantitative model-independent method for global sensitivity analysis of model output*, Technometrics, 41 (1999), pp. 39–56.

[296] V. C. Sanchez, P. Weston, A. Yan, R. H. Hurt, and A. B. Kane, *A 3-dimensional in vitro model of epithelioid granulomas induced by high aspect ratio nanomaterials*, Particle and Fibre Toxicology, 8 (2011), p. 17.

[297] B. E. Sands, J. Chen, B. G. Feagan, M. Penney, W. A. Rees, S. Danese, P. D. Higgins, P. Newbold, R. Faggioni, K. Patra, J. Li, P. Klekotka, C. Morehouse, E. Pulkstenis, J. Drappa, R. van der Merwe, and R. A. Gasser, *Efficacy and safety of MEDI2070, an antibody against interleukin 23, in patients with moderate to severe Crohn's disease: a phase 2a study*, Gastroenterology, 153 (2017), pp. 77–86.e6.

[298] M. G. Schäppi, N. J. Klein, K. J. Lindley, D. Rampling, V. V. Smith, D. Goldblatt, and P. J. Milla, *The nature of colitis in chronic granulomatous disease*, Journal of Pediatric Gastroenterology and Nutrition, 36 (2003), pp. 623–631.

[299] M. G. Schäppi, V. V. Smith, D. Goldblatt, K. J. Lindley, and P. J. Milla, *Colitis in chronic granulomatous disease*, Archives of Disease in Childhood, 84 (2001), pp. 147–151.

[300] L. Schlesinger, R. A. Musson, and R. B. Johnston, *Functional and biochemical studies of multinucleated giant cells derived from the culture of human monocytes*, Journal of Experimental Medicine, 159 (1984), pp. 1289–1294.

[301] J. Schott, S. Reitter, J. Philipp, K. Haneke, H. Schäfer, and G. Stoecklin, *Translational Regulation of Specific mRNAs Controls Feedback Inhibition and Survival during Macrophage Activation*, PLOS Genetics, 10 (2014), p. e1004368.

[302] A. J. Schuerwegh, L. S. De Clerck, C. H. Bridts, and W. J. Stevens, *Comparison of intracellular cytokine production with extracellular cytokine levels using*

two flow cytometric techniques, Cytometry Part B - Clinical Cytometry, 55 (2003), pp. 52–58.

[303] C. Schulz, E. G. Perdiguero, L. Chorro, H. Szabo-Rogers, N. Cagnard, K. Kierdorf, M. Prinz, B. Wu, S. E. W. Jacobsen, J. W. Pollard, J. Frampton, K. J. Liu, and F. Geissmann, *A lineage of myeloid cells independent of myb and hematopoietic stem cells*, Science, 335 (2012), pp. 86–90.

[304] R. F. Schwabe, J. W. Wiley, H. H. Uhlig, T. Schwerd, S. Koletzko, N. Shah, J. Kammermeier, A. Elkadri, J. Ouahed, D. C. Wilson, S. P. Travis, D. Turner, C. Klein, S. B. Snapper, and A. M. Muise, *The diagnostic approach to monogenic very early onset inflammatory bowel disease*, Gastroenterology, 147 (2014), pp. 990–1007.e3.

[305] W. R. Schwan, X. Z. Huang, L. Hu, and D. J. Kopecko, *Differential bacterial survival, replication, and apoptosis-inducing ability of Salmonella serovars within human and murine macrophages*, Infection and Immunity, 68 (2000), pp. 1005–1013.

[306] T. Schwerd, S. Pandey, H. T. Yang, K. Bagola, E. Jameson, J. Jung, R. H. Lachmann, N. Shah, S. Y. Patel, C. Booth, H. Runz, G. Düker, R. Bettels, M. Rohrbach, S. Kugathasan, H. Chapel, S. Keshav, A. Elkadri, N. Platt, A. M. Muise, S. Koletzko, R. J. Xavier, T. Marquardt, F. Powrie, J. E. Wraith, M. Gyrd-Hansen, F. M. Platt, and H. H. Uhlig, *Impaired antibacterial autophagy links granulomatous intestinal inflammation in Niemann-Pick disease type C1 and XIAP deficiency with NOD2 variants in Crohn's disease*, Gut, 66 (2017), pp. 1060–1073.

[307] J. L. Segovia-Juarez, S. Ganguli, and D. Kirschner, *Identifying control mechanisms of granuloma formation during M. tuberculosis infection using an agent-based model*, Journal of Theoretical Biology, 231 (2004), pp. 357–376.

[308] U. Seitzer, H. Haas, and J. Gerdes, *A human in vitro granuloma model for the investigation of multinucleated giant cell and granuloma formation*, Histology and Histopathology, 16 (2001), pp. 645–653.

[309] A. K. Shalek, R. Satija, X. Adiconis, R. S. Gertner, J. T. Gaublomme, R. Raychowdhury, S. Schwartz, N. Yosef, C. Malboeuf, D. Lu, J. J. Trombetta, D. Gennert, A. Gnirke, A. Goren, N. Hacohen, J. Z. Levin, H. Park, and A. Regev, *Single-cell transcriptomics reveals bimodality in expression and splicing in immune cells*, Nature, 498 (2013), pp. 236–240.

[310] S. S. Shapiro and M. B. Wilk, *An Analysis of Variance Test for Normality (Complete Samples)*, Biometrika, 52 (1965), p. 591.

[311] T. C. Shaw, L. H. Thomas, and J. S. Friedland, *Regulation of IL-10 secretion after phagocytosis of Mycobacterium tuberculosis by human monocytic cells*, Cytokine, 12 (2000), pp. 483–486.

[312] W. B. Shelley and H. J. Hurley, *The pathogenesis of silica granulomas in man: a non-allergic collidial phenomenon.*, The Journal of Investigative Dermatology, 34 (1960), pp. 107–123.

[313] P. Shooshtari, E. S. Fortuno, D. Blimkie, M. Yu, A. Gupta, T. R. Kollmann, and R. R. Brinkman, *Correlation analysis of intracellular and secreted cytokines via the generalized integrated mean fluorescence intensity*, Cytometry Part A, 77 (2010), pp. 873–880.

[314] W. Shurety, A. Merino-Trigo, D. Brown, D. A. Hume, and J. L. Stow, *Localization and post-Golgi trafficking of tumor necrosis factor-α in macrophages*, Journal of Interferon and Cytokine Research, 20 (2000), pp. 427–438.

[315] C. Siettos and J. Starke, *Multiscale modeling of brain dynamics: from single neurons and networks to mathematical tools*, Wiley Interdisciplinary Reviews: Systems Biology and Medicine, 8 (2016), pp. 438–458.

[316] N. Siewe, A. A. Yakubu, A. R. Satoskar, and A. Friedman, *Immune response to infection by Leishmania: a mathematical model*, Mathematical Biosciences, 276 (2016), pp. 28–43.

[317] R. F. Silver, Q. Li, and J. J. Ellner, *Expression of virulence of Mycobacterium tuberculosis within human monocytes: virulence correlates with intracellular growth and induction of tumor necrosis factor alpha but not with evasion of lymphocyte-dependent monocyte effector functions*, Infection and Immunity, 66 (1998), pp. 1190–1199.

[318] S. Skovbjerg, A. Martner, L. Hynsjö, C. Hessle, I. Olsen, F. E. Dewhirst, W. Tham, and A. E. Wold, *Gram-positive and gram-negative bacteria induce different patterns of cytokine production in human mononuclear cells irrespective of taxonomic relatedness*, Journal of Interferon and Cytokine Research, 30 (2010), pp. 23–32.

[319] C. S. Smillie, M. Biton, J. Ordovas-Montanes, K. M. Sullivan, G. Burgin, D. B. Graham, R. H. Herbst, N. Rogel, M. Slyper, J. Waldman, M. Sud, E. Andrews, G. Velonias, A. L. Haber, K. Jagadeesh, S. Vickovic, J. Yao, C. Stevens, D. Dionne, L. T. Nguyen, A. C. Villani, M. Hofree, E. A. Creasey, H. Huang, O. Rozenblatt-Rosen, J. J. Garber, H. Khalili, A. N. Desch, M. J. Daly, A. N. Ananthakrishnan, A. K. Shalek, R. J. Xavier, and A. Regev, *Intra- and Inter-cellular Rewiring of the Human Colon during Ulcerative Colitis*, Cell, 178 (2019), pp. 714–730.

[320] A. M. Smith, F. R. Adler, R. M. Ribeiro, R. N. Gutenkunst, J. L. McAuley, J. A. McCullers, and A. S. Perelson, *Kinetics of coinfection with influenza A virus and Streptococcus pneumoniae*, PLoS Pathogens, 9 (2013), p. e1003238.

[321] A. M. Smith, J. A. McCullers, and F. R. Adler, *Mathematical model of a three-stage innate immune response to a pneumococcal lung infection*, Journal of Theoretical Biology, 276 (2011), pp. 106–116.

[322] L. E. Smythies, M. Sellers, R. H. Clements, M. Mosteller-Barnum, G. Meng, W. H. Benjamin, J. M. Orenstein, and P. D. Smith, *Human intestinal macrophages display profound inflammatory anergy despite avid phagocytic and bacteriocidal activity*, Journal of Clinical Investigation, 115 (2005), pp. 66–75.

[323] A. Sokolovska, C. E. Becker, and L. M. Stuart, *Measurement of phagocytosis, phagosome acidification, and intracellular killing of Staphylococcus aureus*, Current Protocols in Immunology, (2012), pp. 14–30.

[324] C. Speckmann and S. Ehl, *XIAP deficiency is a mendelian cause of late-onset IBD*, Gut, 63 (2014), pp. 1031–1032.

[325] T. M. Stevanin, R. K. Poole, E. A. Demoncheaux, and R. C. Read, *Flavohemoglobin Hmp protects Salmonella enterica serovar typhimurium from nitric oxide-related killing by human macrophages*, Infection and Immunity, 70 (2002), pp. 4399–4405.

[326] J. L. Stow, P. Ching Low, C. Offenhäuser, and D. Sangermani, *Cytokine secretion in macrophages and other cells: Pathways and mediators*, Immunobiology, 214 (2009), pp. 601–612.

[327] K. L. Strandberg, S. M. Richards, and J. S. Gunn, *Cathelicidin antimicrobial peptide expression is not induced or required for bacterial clearance during Salmonella enterica infection of human monocyte-derived macrophages*, Infection and Immunity, 80 (2012), pp. 3930–3938.

[328] W. Strober, N. Asano, I. Fuss, A. Kitani, and T. Watanabe, *Cellular and molecular mechanisms underlying NOD2 risk-associated polymorphisms in Crohn's disease*, Immunological Reviews, 260 (2014), pp. 249–260.

[329] E. Süli and D. F. Mayers, *An Introduction to Numerical Analysis*, Cambridge University Press, aug 2003.

[330] M. H. Sung, N. Li, Q. Lao, R. A. Gottschalk, G. L. Hager, and I. D. Fraser, *Switching of the relative dominance between feedback mechanisms in lipopolysaccharide-induced NF-κB signaling*, Science Signaling, 7 (2014), p. ra6.

[331] R. J. Tanaka, N. J. Boon, K. Vrcelj, A. Nguyen, C. Vinci, D. Armstrong-James, and E. Bignell, *In silico modeling of spore inhalation reveals fungal persistence following low dose exposure*, Scientific Reports, 5 (2015), p. 13958.

[332] H. D. Tandon and A. Prakash, *Pathology of intestinal tuberculosis and its distinction from Crohn's disease.*, Gut, 13 (1972), pp. 260–269.

[333] S. R. Targan, B. Feagan, S. Vermeire, R. Panaccione, G. Y. Melmed, C. Landers, D. Li, C. Russell, R. Newmark, N. Zhang, Y. Chon, Y. H. Hsu, S. L. Lin, and P. Klekotka, *A randomized, double-blind, placebo-controlled phase 2 study of brodalumab in patients with moderate-to-severe Crohn's disease*, American Journal of Gastroenterology, 111 (2016), pp. 1599–1607.

[334] C. P. Timmerman, E. Mattsson, L. Martinez-Martinez, L. De Graaf, J. A. Van Strijp, H. A. Verbrugh, J. Verhoef, and A. Fleer, *Induction of release of tumor necrosis factor from human monocytes by staphylococci and staphylococcal peptidoglycans*, Infection and Immunity, 61 (1993), pp. 4167–4172.

[335] T. Toni, D. Welch, N. Strelkowa, A. Ipsen, and M. P. Stumpf, *Approximate Bayesian computation scheme for parameter inference and model selection in dynamical systems*, Journal of the Royal Society Interface, 6 (2009), pp. 187–202.

[336] L. H. Travassos, L. A. Carneiro, M. Ramjeet, S. Hussey, Y. G. Kim, J. G. Magalhes, L. Yuan, F. Soares, E. Chea, L. Le Bourhis, I. G. Boneca, A. Allaoui, N. L. Jones, G. Nũez, S. E. Girardin, and D. J. Philpott, *Nod1 and Nod2 direct autophagy by recruiting ATG16L1 to the plasma membrane at the site of bacterial entry*, Nature Immunology, 11 (2010), pp. 55–62.

[337] N. A. Trayanova, *Whole-heart modeling : applications to cardiac electrophysiology and electromechanics*, Circulation Research, 108 (2011), pp. 113–128.

[338] M. D. Turner, B. Nedjai, T. Hurst, and D. J. Pennington, *Cytokines and chemokines: At the crossroads of cell signalling and inflammatory disease*, Biochimica et Biophysica Acta - Molecular Cell Research, 1843 (2014), pp. 2563–2582.

[339] H. H. Uhlig and C. Booth, *A spectrum of genetic variants contributes to immune defects and pathogenesis of inflammatory bowel diseases*, Gastroenterology, 154 (2018), pp. 2022–2024.

[340] H. H. Uhlig, B. S. McKenzie, S. Hue, C. Thompson, B. Joyce-Shaikh, R. Stepankova, N. Robinson, S. Buonocore, H. Tlaskalova-Hogenova, D. J. Cua, and F. Powrie, *Differential activity of IL-12 and IL-23 in mucosal and systemic innate immune pathology*, Immunity, 25 (2006), pp. 309–318.

[341] H. H. Uhlig and F. Powrie, *Translating immunology into therapeutic concepts for inflammatory bowel disease*, Annual Review of Immunology, 36 (2018), pp. 755–781.

[342] S. Upadhyay and J. A. Philips, *LC3-associated phagocytosis: host defense and microbial response*, Current Opinion in Immunology, 60 (2019), pp. 81–90.

[343] J. M. Van den Brande, H. Braat, G. R. Van den Brink, H. H. Versteeg, C. A. Bauer, I. Hoedemaeker, C. Van Montfrans, D. W. Hommes, M. P. Peppelenbosch, and S. J. Van Deventer, *Infliximab but not etanercept induces apoptosis in lamina propria T-lymphocytes from patients with Crohn's disease*, Gastroenterology, 124 (2003), pp. 1774–1785.

[344] J. W. M. Van Der Meer, S. Endres, G. Lonnemann, J. G. Cannon, T. Ikejima, S. Okusawa, J. A. Gelfand, and C. A. Dinarello, *Concentrations of immunoreactive human tumor necrosis factor alpha produced by human mononuclear cells in vitro*, Journal of Leukocyte Biology, 43 (1988), pp. 216–223.

[345] R. D. Vigil and R. M. Ziff, *On the stability of coagulation-fragmentation population balances*, Journal of Colloid and Interface Science, 133 (1989), pp. 257–264.

[346] A. F. Villaverde and G. M. Feixas, *On testing structural identifiability by a simple scaling method: Relying on scaling symmetries can be misleading*, bioRxiv, (2020).

[347] Y. Vodovotz, A. Xia, E. L. Read, J. Bassaganya-Riera, D. A. Hafler, E. Sontag, J. Wang, J. S. Tsang, J. D. Day, S. H. Kleinstein, A. J. Butte, M. C. Altman, R. Hammond, and S. C. Sealfon, *Solving Immunology?*, Trends in Immunology, 38 (2017), pp. 116–127.

[348] D. Y. Vogel, E. J. Vereyken, J. E. Glim, P. D. Heijnen, M. Moeton, P. van der Valk, S. Amor, C. E. Teunissen, J. van Horssen, and C. D. Dijkstra, *Macrophages in inflammatory multiple sclerosis lesions have an intermediate activation status*, Journal of Neuroinflammation, 10 (2013), pp. 1742–2094.

[349] Y. Wang, T. Yang, Y. Ma, G. V. Halade, J. Zhang, M. L. Lindsey, and Y.-F. F. Jin, *Mathematical modeling and stability analysis of macrophage activation in left ventricular remodeling post-myocardial infarction.*, BMC Genomics, 13 (2012), p. S21.

[350] T. Watanabe, N. Asano, P. J. Murray, K. Ozato, P. Tailor, I. J. Fuss, A. Kitani, and W. Strober, *Muramyl dipeptide activation of nucleotide-binding oligomerization domain 2 protects mice from experimental colitis*, Journal of Clinical Investigation, 118 (2008), pp. 545–559.

[351] T. Watanabe, A. Kitani, P. J. Murray, and W. Strober, *NOD2 is a negative regulator of Toll-like receptor 2-mediated T helper type 1 responses*, Nature Immunology, 5 (2004), pp. 800–808.

[352] J. Wehkamp, J. Harder, M. Weichenthal, M. Schwab, E. Schäffeler, M. Schlee, K. R. Herrlinger, A. Stallmach, F. Noack, P. Fritz, J. M. Schröder, C. L. Bevins, K. Fellermann, and E. F. Stange, *NOD2 (CARD15) mutations in Crohn's disease are associated with diminished mucosal α-defensin expression*, Gut, 53 (2004), pp. 1658–1664.

[353] S. L. Werner, J. D. Kearns, V. Zadorozhnaya, C. Lynch, E. O'Dea, M. P. Boldin, A. Ma, D. Baltimore, and A. Hoffmann, *Encoding NF-KB temporal control in response to TNF: distinct roles for the negative regulators IKB-alpha and A20.*, Genes & Development, 22 (2008), pp. 2093–2101.

[354] J. Whittaker, *Graphical models in applied multivariate statistics*, Wiley series in probability and mathematical statistics. Probability and mathematical statistics, Wiley, Chichester [England] ; New York, 1990.

[355] R. M. Wood, J. R. Egan, and I. M. Hall, *A dose and time response Markov model for the in-host dynamics of infection with intracellular bacteria following inhalation: With application to Francisella tularensis*, Journal of the Royal Society Interface, 11 (2014), p. 20140119.

[356] T. E. Woolley, *Spatiotemporal behaviour of stochastic and continuum models for biological signalling on stationary and growing domains*, phd thesis, Oxford University, 2011.

[357] J. Xue, S. V. V. Schmidt, J. Sander, A. Draffehn, W. Krebs, I. Quester, D. De Nardo, T. D. D. Gohel, M. Emde, L. Schmidleithner, H. Ganesan, A. Nino-Castro, M. R. R. Mallmann, L. Labzin, H. Theis, M. Kraut, M. Beyer, E. Latz, T. C. C. Freeman, T. Ulas, J. L. L. Schultze, N. D. De, T. D. D. Gohel, M. Emde, L. Schmidleithner, H. Ganesan, A. Nino-Castro, M. R. R. Mallmann, L. Labzin, H. Theis, M. Kraut, M. Beyer, E. Latz, T. C. C. Freeman, T. Ulas, and J. L. L. Schultze, *Transcriptome-based network analysis reveals a spectrum model of human macrophage activation*, Immunity, 40 (2014), pp. 274–288.

[358] Q. Xue, Y. Lu, M. R. Eisele, E. S. Sulistijo, N. Khan, R. Fan, and K. Miller-Jensen, *Analysis of single-cell cytokine secretion reveals a role for paracrine signaling in coordinating macrophage responses to TLR4 stimulation*, Science Signaling, 8 (2015), p. ra59.

[359] Z. Ye, Y. Lin, Q. Cao, Y. He, and L. Xue, *Granulomas as the most useful histopathological feature in distinguishing between Crohn's disease and intestinal tuberculosis in endoscopic biopsy specimens*, Medicine (United States), 94 (2015), p. e2157.

[360] D. Yen, J. Cheung, H. Scheerens, F. Poulet, T. McClanahan, B. Mckenzie, M. A. Kleinschek, A. Owyang, J. Mattson, W. Blumenschein, E. Murphy, M. Sathe, D. J. Cua, R. A. Kastelein, and D. Rennick, *IL-23 is essential for T cell-mediated colitis and promotes inflammation via IL-17 and IL-6*, Journal of Clinical Investigation, 116 (2006), pp. 1310–1316.

[361] S. Yona, K. W. Kim, Y. Wolf, A. Mildner, D. Varol, M. Breker, D. Strauss-Ayali, S. Viukov, M. Guilliams, A. Misharin, D. A. Hume, H. Perlman, B. Malissen, E. Zelzer, and S. Jung, *Fate Mapping Reveals Origins and Dynamics of Monocytes and Tissue Macrophages under Homeostasis*, Immunity, 38 (2013), pp. 79–91.

[362] T. Yoshimura, K. Matsushima, S. Tanaka, E. A. Robinson, E. Appella, J. J. Oppenheim, and E. J. Leonard, *Purification of a human monocyte-derived neutrophil chemotactic factor that has peptide sequence similarity to other host defense cytokines.*, Proceedings of the National Academy of Sciences of the United States of America, 84 (1987), pp. 9233–9237.

[363] B. Zhang, A. Korolj, B. F. L. Lai, and M. Radisic, *Advances in organ-on-a-chip engineering*, Nature Reviews Materials, 3 (2018), pp. 257–278.

[364] L. Zhang, U. Dieckmann, and Å. Brännström, *On the performance of four methods for the numerical solution of ecologically realistic size-structured population models*, Methods in Ecology and Evolution, 8 (2017), pp. 948–956.

[365] Q. Zhang, M. J. Lenardo, and D. Baltimore, *30 years of NF-kB: a blossoming of relevance to human pathobiology*, Cell, 168 (2017), pp. 37–57.

[366] X. Zhou, R. A. Franklin, M. Adler, J. B. Jacox, W. Bailis, J. A. Shyer, R. A. Flavell, A. Mayo, U. Alon, and R. Medzhitov, *Circuit design features of a stable two-cell system*, Cell, 172 (2018), pp. 744–757.e17.

Figure acknowledgements

Figure components taken from the 'Library of Science & Medical Illustrations' by Somer-Sault1824 were used in Figures 1.1, 1.2, 1.3, 1.4, 1.5, 2.1, 1, 2, and 3.